AD-A282 729

‖‖‖‖‖‖‖‖‖‖‖‖‖

AFOSR CONTRACTORS

MEETING

IN PROPULSION

June 8 - 10, 1994

DTIC
ELECTE
JUL 28 1994
S B D

LAKE TAHOE CA / NV

AFOSR

**UNIVERSITY OF
CALIFORNIA
DAVIS**

94-23417

‖‖‖‖‖‖‖‖‖‖‖‖‖

94 7 25 059

REPORT DOCUMENTATION PAGE

Public reporting burden for this collection of information is estimated to average 1 hour per response, including the time for reviewing instructions, searching existing data sources, gathering and maintaining the data needed, and completing and reviewing the collection of information. Send comments regarding this burden estimate or any other aspect of this collection of information, including suggestions for reducing this burden, to Washington Headquarters Services, Directorate for Information Operations and Reports, 1215 Jefferson Davis Highway, Suite 1204, Arlington, VA 22202-4302, and to the Office of Management and Budget, Paperwork Reduction Project (0704-0188), Washington, DC 20503.

1. AGENCY USE ONLY (Leave blank)	2. REPORT DATE	3. REPORT TYPE AND DATES COVERED
	13 July 1994	Technical

4. TITLE AND SUBTITLE

(U) AFOSR Contractors Meeting in Propulsion

5. FUNDING NUMBERS

PE - 61102F
PR - 2308

6. AUTHOR(S)

M A Birkan and J M Tishkoff

7. PERFORMING ORGANIZATION NAME(S) AND ADDRESS(ES)

AFOSR/NA
110 Duncan Avenue, Suite B115
Bolling AFB DC 20332-0001

8. PERFORMING ORGANIZATION REPORT NUMBER

AFOSR-TR- 94 0463

9. SPONSORING/MONITORING AGENCY NAME(S) AND ADDRESS(ES)

AFOSR/NA
110 Duncan Avenue, Suite B115
Bolling AFB DC 20332-0001

10. SPONSORING/MONITORING AGENCY REPORT NUMBER

11. SUPPLEMENTARY NOTES

12a. DISTRIBUTION/AVAILABILITY STATEMENT

Approved for public release; distribution is unlimited

12b. DISTRIBUTION CODE

13. ABSTRACT (Maximum 200 words)

Abstracts are given for research in airbreathing combustion, rocket propulsion, and diagnostics in reacting media supported by the Air Force Office of Scientific Research.

14. SUBJECT TERMS

Instability, Flames, Propulsion, Gas Turbines, Combustion, Shear Layer, Supersonic, Soot, Sprays, Lasers, Fluorescence, Spectroscopy, Rocket, Plasma, Scramjets

15. NUMBER OF PAGES
210

16. PRICE CODE

17. SECURITY CLASSIFICATION OF REPORT	18. SECURITY CLASSIFICATION OF THIS PAGE	19. SECURITY CLASSIFICATION OF ABSTRACT	20. LIMITATION OF ABSTRACT
Unclassified	Unclassified	Unclassified	UL

NSN 7540-01-280-5500

TABLE OF CONTENTS

MONDAY, 6 JUN 1994

CRYO-SOLIDS I

8:30 - 12:00 Possible speakers:

> Mario Fajardo, Phillips Laboratory
> Michael Klein, U. Pennsylvania
> Greg Voth, U. Pennsylvania
> Jim Gaines, U. Hawaii
> Benny Gerber, UC Irvine
> Takeshi Oka, U Chicago
> Isaac Silvera, Harvard U.

METAL ATOMS AND CLUSTERS

1:30 - 5:00 Possible speakers:

> Pat Carrick, Phillips Laboratory
> Paul Dagdigian, Johns Hopkins U.
> Millard Alexander, U. Maryland
> Lester Andrews, U. Virginia
> Michael Duncan, U. Georgia
> Mitchio Okumura, Cal Tech
> Carl Lineberger, U. Colorado
> Dave Benard, Rockwell Science Ctr.

7:30 - 10:00 PM   **POSTER SESSION**

TUESDAY, 7 JUNE 1994

CRYO-SOLIDS II

8:30 - 10:00 Possible speakers:

> Capt. Tim Thompson, Phillips Laboratory
> David Yarkony, Johns Hopkins U.
> Ara Apkarian, UC Irvine (URI)

SOLID-PROPELLANT DYNAMICS
Chair: J Levine, Phillips Laboratory

10:30-11:30   Nonsteady Combustion Mechanisms of Advanced
Solid Propellants (URI)
M Branch, University of Colorado; M Beckstead,
Brigham Young University; M Smooke, Yale University;
V Yang, Penn State University

11:30-12:00   *Chemical Mechanisms at the Burning
Surface*
T B Brill, University of Delaware

12:00-12:30   Combustion Kinetics of HEDMs and Metallic Fuels
A Fontijn, RPI

2:00 - 3:30   **SOLID PROPELLANT DISCUSSION**

3:30 - 5:00   **HEDM PROGRAM DIRECTIONS**

        Possible speakers:

Bob Corley, Phillips Laboratory
Maj. David Lewis, Phillips Laboratory
Lt. Col. Larry Davis, AFOSR

7:30 - 9:30   **SPACE POWER AND PROPULSION
TECHNOLOGY TRANSFER AND TRANSITION
Moderator: J Levine, Phillips Laboratory
OPEN FORUM**

WEDNESDAY, 8 JUNE 1994

SOLID-PROPELLANT ROCKET CHAMBER DYNAMICS
Chair: D Weaver, Phillips Laboratory

8:30-9:00   Nonlinear Acoustic Processes in Solid Rocket Engines
D R Kassoy, University of Colorado

9:00-9:30   DNS of Acoustic-Mean Flow Interactions in Solid Rocket Motors
S Mahalingam, University of Colorado

9:30-10:00   Investigation of Active Control of Combustion Instabilities in Chemical Rockets
B T Zinn, Georgia Tech

10:00-10:30   BREAK

LIQUID-PROPELLANT ROCKETS-I
Chair: D Talley, Phillips Laboratory

10:30 - 11:00   Fundamentals of Acoustic Instabilities in Liquid-Propellant Rockets
F A Williams, University of California

11:00-11:30   Modeling Liquid Jet Atomization Processes
S D Heister, Purdue University

11:30-12:00   Theoretical Investigation of Liquid-Propellant Droplet Combustion and Dynamics at Supercritical Conditions
V Yang, Penn State

SOOT
Chair: B Ganguly, Wright Laboratory

8:45 - 9:00   Opening remarks

9:00 - 9:30   Detailed Studies of Soot Formation in Laminar Diffusion Flames for Application to Modeling Studies
R J Santoro, Pennsylvania State University

9:30 - 10:00   Evaluation of the Ionic Mechanism of Soot Formation
H F Calcote, AeroChem Research Laboratories, Inc.

10:00 - 10:30   BREAK

10:30 - 11:00	Development of Predictive Reaction Models of Soot Formation M Frenklach, Pennsylvania State University
11:00 - 11:30	Development of a Technique to Determine the Morphology and Dynamics of Agglomerates in Chemically Reacting Flows T Charalampopoulos, Louisiana State University
11:30 - 12:00	Transport Phenomena and Interfacial Kinetics in Multiphase Combustion Systems D E Rosner, Yale University
12:00 - 1:30	**LUNCH**

LIQUID-PROPELLANT ROCKETS II
Chair: A Nejad, Wright Laboratory

1:30 - 2:00	Supercritical Droplet Behavior D G Talley, Phillips Laboratory
2:00 - 2:30	Combustion Instability Phenomenon of Importance to Liquid Propellant Rocket Engines R J Santoro, Penn State
2:30 - 3:00	Liquid Rocket Motor Combustion Stability Using Coaxial Injectors M M Micci, Penn State
3:00 - 3:30	BREAK
3:30 - 4:00	Droplet Collision in Liquid Propellant Combustion C K Law, Princeton University
4:00 - 4:30	Determination of Structure, Temperature and Concentration in the Near Injection Region of Impinging Jets using Holographic Techniques D Poulikakos, University of Illinois at Chicago
4:30 - 5:00	Combustion and Plumes D Weaver, Phillips Laboratory

DIAGNOSTICS
Chair: G Roy, Office of Naval Research

1:30 - 2:15   Advanced Diagnostics for Reacting Flows
R K Hanson, Stanford University

2:15 - 2:45   Nonlinear Laser Diagnostics for Combustion and Plasma Phenomena
D Huestis, G Faris, and J Jeffries, SRI International

2:45 - 3:15   BREAK

3:15 - 3:45   Rapid Concentration Measurements by Picosecond Time-Resolved Laser-Induced Fluorescence
G B King and N M Laurendeau, Purdue University

3:45 - 4:15   Energy Conversion Device Diagnostics
B N Ganguly, WL/POOC-3

4:15 - 4:45   Nonlinear Optical Spectroscopy of Multicomponent Droplets
R K Chang, Yale University

4:45 - 7:30   **DINNER**

7:30 - 9:00   **BUSINESS SESSION** - Contractors, Grantees, and Government Laboratory Personnel Funded in Dr. Birkan's AFOSR Programs in Chemical Propulsion

7:30 - 9:30   **WORKSHOPS**

                      Soot
M Frenklach, Pennsylvania State University

                      Supersonic Combustion
M G Mungal, Stanford University

THURSDAY, 9 JUNE 1994

SPRAYS
Chair: D Littrell, Wright Laboratory

8:30 - 9:00	Droplet-Turbulence Interactions Over a Wide Spectral Range W A Sirignano and S E Elghobashi, University of California, Irvine
9:00 - 9:30	Particle Dispersion in Turbulent Sprays I M Kennedy and W Kollmann, University of California, Davis
9:30 - 10:00	Atomization of Viscous Liquid Sheets E A Ibrahim, Tuskegee University
10:00 - 10:30	BREAK
10:30 - 11:00	Use of the Maximum Entropy Principle as a Guide in Design of Spray Atomizers R S Tankin, Northwestern University
11:00 - 11:30	Fuels Combustion Research T A Jackson, WL/POSF
11:30 - 12:00	Fluorescent Diagnostics and Fundamental Droplet Processes L A Melton, University of Texas at Dallas and M Winter, United Technologies Research Center
12:00 - 1:30	**LUNCH**

SPRAYS AND SUPERCRITICAL BEHAVIOR
Chair: D Mann, Army Research Office

1:30 - 2:00	Breakup and Turbulence Generation in Dense Sprays G M Faeth, University of Michigan
2:00 - 2:30	Application of Parallel Processing to the Investigation of Supercritical Droplet Evaporation and Combustion Using Molecular Dynamics M M Micci and L N Long, Pennsylvania State University

2:30 - 3:00	Ramjet Research A S Nejad, WL/POPT
3:00 - 3:30	BREAK
3:30 - 4:00	Advanced Fuel Utilization J T Edwards, WL/POSF
4:00 - 4:30	Fuels Combustion Research I Glassman, Princeton University
4:30 - 5:00	Computer Simulation of Molecular Interactions and Dynamic Processes in Supercritical Solvents and Modeling of Particle Formation During Expansion of Supercritical Solvents P G Debenedetti, Princeton University
5:00 - 7:30	DINNER
7:30 - 9:30	**WORKSHOPS** **Supercritical Fuel Behavior** J T Edwards, WL/POSF **Turbulent Combustion** S B Pope, Cornell University

FRIDAY, 10 JUNE 1994

8:30 - 10:00	**BUSINESS SESSION** - Contractors, Grantees, and Government Laboratory Personnel Funded in Dr. Tishkoff's AFOSR Programs
10:00 - 10:30	BREAK
10:30 - 12:00	**GAS TURBINE TECHNOLOGY TRANSITIONING** - Open Forum
12:00	ADJOURN

NONSTEADY COMBUSTION MECHANISMS OF ADVANCED SOLID PROPELLANTS

M.C. Branch, University of Colorado
M.W. Beckstead, Brigham Young University
T.A. Litzinger, Pennsylvania State University
M.D. Smooke, Yale University
V.H. Yang, Pennsylvania State University

SUMMARY/OVERVIEW:

The development of advanced propellants employing new oxidizers and energetic binders such as GAP and PGN requires a more sophisticated approach than the conventional methods of testing a matrix of ingredients to arrive at a formulation empirically. Such an approach is too costly and time consuming for the large matrix of oxidizer/binder combinations. The development of a computational model to predict the sources of instability, the regression rate, as well as the temperature sensitivity and pressure and dependence of new formulations would be of tremendous value to the propellant designer in the fabrication of more energetic and stable systems.

We have initiated an exciting new collaborative research program combining the expertise of individuals from several universities to develop a new ability to predict the propulsion performance of minimum smoke, precision strike rockets. The focus of the research of nonsteady behavior is unique and the overall project is not possible at any one of the institutions participating in this coordinated research. The project will be managed so as to insure significant cooperation and coordination between the different universities in conducting the carefully selected tasks which contribute to the overall research goal. The individual tasks which we will pursue will consider solid propellant decomposition under unsteady conditions, nonsteady aspects of gas phase flame structure measurements, numerical modeling of multidimensional flame structure, propellant/flame interactions, and overall nonsteady propellant combustion characteristics in realistic rocket motor environments. Our goal is to develop general models of fundamental mechanisms of combustion instability that can be applied to a variety of new energetic materials. Progress in these tasks over the past year is outlined below.

TECHNICAL DISCUSSION:

Task 1. Condensed Phase Processes (Litzinger)

Condensed phase processes during combustion of the solid propellant are being studied using a unique Microprobe Mass Spectrometer (MPMS) system. The objective of MPMS studies is to determine the chemical mechanisms for solid propellant combustion with an initial emphasis on the decomposition of HMX and on the gas phase reactions of the products of its decomposition. A quadrupole mass spectrometer system using quartz microprobes is used to measure species profiles above the surface of the sample during CO_2 laser induced decomposition or during laser assisted deflagration of the sample. Gas Phase temperature profiles are measured with micro-thermocouples no larger than 50 micron.

The results of the studies will provide key information for the modeling of propellant combustion. It will provide the boundary conditions at the interface between the condensed and gas phases which is critical for modeling. In addition, it will provide gas phase species and temperature profiles over a range of

experimental conditions that will be used to test the models. Finally, the results will give insight into the key chemical reactions to be studied in the flame experiments.

Much of the work over the last year has focused on upgrading the mass spectrometer system to a triple quadrupole (TQMS). The TQMS is critical for detection and quantification of species with the same molecular weight such as CO, N_2, and C_2H_4. This hardware upgrade of the single quadrupole MS required substantial revision of the existing system. The control electronics, the vacuum chamber, the pumping system and the test chamber itself were redesigned. In addition, the required characteristics of the TQMS had to be specified to Extrel corporation so that they could construct the instrument.

All components for the system were received in August 1993 when the TQMS was installed by Extrel. After installation, substantial effort was expended to optimize the instrument settings for detection and separation of the species with similar molecular weights and to calibrate the instrument. Experiments with RDX and RDX composite propellants had been successfully performed including separation of $CO/N_2/C_2H_4$ and CO_2/N_2O. Work with HMX will begin as soon as HMX is available, which should be within the next several months.

Tasks 2 and 3. Gas Phase Kinetics and Chemistry (Branch, Smooke)

As described in Task 1, Condensed Phase Processes, the decomposition of solid rocket propellants and other energetic materials leads to the formation of gaseous hydrocarbons and oxides of nitrogen which react to form a flame above the surface of the solid. These flames can provide heat which is fed back to the surface and thereby influences the burning rate of the solid. In previous studies of a number of fuel/NO_x laminar premixed flames, we have developed chemical kinetic reaction mechanisms which model the essential features of the measured flame structure. The objective of the research proposed for Task 2 is to investigate the nonsteady two-dimensional effects associated with the heterogeneous nature of combustion of the solid fuel. Co-flowing laminar jet diffusion flames and counterflow premixed and diffusion flames of fuel/NO_x mixture will be established, the flame structure will be measured and the measurements will be compared to two-dimensional diffusion flame modeling. The research will therefore focus on the simultaneous effects of mixing and reaction in order to determine flame stabilization mechanisms and stability limits, and flame stretch effects important in nonsteady combustion processes.

The focus of research in Task 3 is detailed flame modeling of fuel/NO_x diffusion flames and eventual reduction of reaction mechanisms. During the past eight months our research has focused on the development of a two-dimensional computational model of fuel/N_2O flames in a Wolfhard-Parker configuration. Specifically, we have developed a model that applies detailed chemistry and complex transport to the two-dimensional flame in which a fuel stream is sandwiched between two oxidizer streams. Unlike some models in which diffusion in the downstream direction is neglected, we have treated the fully elliptic problem. A discrete solution has been obtained by combining a steady-state and a time-dependent solution method. A time-dependent approach is used to help obtain a converged numerical solution on an initial coarse grid using a flame sheet starting estimate. Grid points are inserted adaptively and Newton's method is used to complete the problem. The model developed at Yale University is currently being used to compare temperature and species profiles with experimental measurements made at the University of Colorado. Both CH_4/N_2O and CO/N_2O flames are being considered. The results of this investigation will enable us to probe the fluid dynamic and thermochemistry interaction and its effect on the structure of fuel/N_2O flames. A by-product of the study will be an assessment of various chemistry approximations that could be used in the development of propellant models. In particular, we will be able to investigate both partial equilibrium and reduced chemistry models.

Task 4. Propellant Combustion Characteristics in Isolated Environments (Beckstead)

This particular phase of the program will concentrate on developing a monopropellant model which can

be coupled with a diffusion flame model to stimulate a solid propellant. A model of the condensed phase is being developed based on previous work such as the Price-Boggs DDT model or the Bizot-Beckstead model. The model will solve the transient heat conduction equation, allowing for energy release through the solid. The model will allow for up to three decomposition reactions describing the initial bond breaking process, followed by several heterogeneous reactions describing the reactions that occur in the liquid layer on the burning surface. Calculations will eventually be performed with the model for double base binder, HMX, AP, AN, and GAP. The required kinetic input for the model will be obtained from the experiments of Brill and others. Reduced reaction mechanisms will be recommended for each of the specific ingredients to be used in conjunction with the calculations made in the combined models discussed in the following paragraphs.

Preliminary calculations have been made for the ignition of HMX using Price's model which is based on two parallel condensed phase reactions (one following the CH_2O path and one following the HCN path). A summary of those results is contained in the attached figure and table. The condensed phase values for HMX were taken from a compilation of works be a number of researchers as reported by both Boggs and Schroeder. They report decomposition activation energies of ~45-50 Kcal/mole based on a variety of methods, most at relatively low temperatures. The corresponding prefactors reported were ~10^{15} to 10^{18}. Unfortunately, these investigators only report on a single decomposition reaction. Thus, data for the two reactions modeled were not found in the literature. However, Schroeder recommends activation energies of ~49 and 53 as representative of the two reactions based on his assessment of the literature, which were therefore used in the code. Corresponding prefactor values of ~10^{18} and 10^{20} were needed to give reasonable ignition times. The ignition process was chosen as a basis of comparison because it is very dependent on the condenses phase reactions. The prefactors were slightly higher than reported data, but well within reason.

These results are both encouraging and discouraging. Using two condensed phase reactions we can model the ignition event reasonably well using essentially literature values. However, identifying the appropriate experimental test with a given reaction is difficult. It is almost impossible to separate different reaction steps from available date. Most experiments give a global result.

Another significant problem is that of determining the appropriate surface temperature as the boundary condition between the gas and condenses phases. A search of the literature has turned up essentially four studies where the surface temperature of HMX has been measured. The four studies are by Parr and Parr at NWC, Lengelle and Duterque at ONERA, Kubota and Sakamoto, and Mitani and Takahashi. None of the authors reference any of the others and each present their data as a unique set of data. Parr, Lengelle and Kubota apparently all used pressed pellets as a unique set of data. Parr, Lengelle, and Kubota apparently all used pressed pellets of pure HMX, while Mitani used pellets of 97% HMX and 3% wax. Mitani also used a counter flow burner to burn the pellets and obtain the data. Parr, Lengelle and Kutoba all report using thermocouples on the order of 5 to 15μm, which would appear to be sufficiently small to resolve the surface temperatures at the conditions cited. Kubota made his measurements up to pressures of ~90 psi while Parr's measurements were up to ~240 psi. Neither Lengelle nor Mitani report their test conditions that resulted in varying burning rates.

The agreement between investigators is not good. Parr and Lengelle both report an uncertainty of ~50K, but the general disagreement is greater than 50K. Kubota does not actually report surface temperatures. He interprets his results as a 'decomposition temperature' where reactions begin, but which is lower than what a surface temperature would be. Thus, his 'surface temperatures' would be somewhat higher than the data reported, which would be more in line with the data of either Lengelle or Mitani. Although the NWC data were obtained in what appears to be a very careful and meticulous manner, the numbers are 100 to 150K below the other measurements made at the corresponding rates. If one attempts to extrapolate the data to pressures and rates typical of rocket motors, the uncertainty becomes extreme due to the large data scatter. Additional quantitative experimental data are needed from Task 1 outlined above

3

and reduced flame mechanisms are needed from Tasks 2 and 3.

Task 5. Propellant Combustion in Rocket Motor Environments (Yang)

Results obtained from Tasks 1 through 4 provide a concrete basis for understanding the detailed combustion mechanisms of solid propellants in an isolated quiescent environment. To extend these fundamental investigations to practical motor design issues, it is important to study the propellant burning behavior at realistic rocket motor conditions. Most previous research on motor interior ballistics was either focused on cold-flow simulation or based on simplified approaches with propellant burning rates modeled by empirical formulas. Very little is known about detailed combustion mechanisms under chamber cross flows. The purpose of this task is to remedy these technical and scientific deficiencies by treating detailed flowfields and chemical reactions. Both steady and oscillatory flow conditions are considered, with emphasis placed on the interactions between propellant combustion and motor internal flows. The work mainly addresses two issues: how the local flow conditions of velocity, pressure, temperature, and turbulence intensity affect propellant burning, and how the motor internal flow is established by propellant burning.

Figure 4 shows the baseline configuration examined here, a two-dimensional (either planar or axisymmetric) rocket motor with burning solid-propellant grains. The formulation is based on the complete conservation equations of mass, momentum, energy, and species concentration for both gas and condensed phases, with full account taken of variable transport and thermodynamic properties. Only reduced chemical kinetics schemes acquired from Tasks 1 through 4 are incorporated into the flow solver to render numerical calculations manageable. Turbulence closure is achieved using a modified turbulent transport model which takes into account the wall-blowing effect arising from propellant burning.
A series of analyses have been carried out to study the combustion characteristics of double-base and nitramine homogeneous propellants in two-dimensional chambers. Emphasis is placed on the propellant burning behavior in various flow regimes in a rocket motor, including laminar, transitional, and fully turbulent regions. Specific processes investigated include:

*   motor internal flow development, including onset of turbulence and its ensuring growth;
*   detailed flame structure near the propellant surface, including effects of laminar and turbulent cross flows on propellant combustion mechanisms; and
*   coupling between gas and condenses phases, including subsurface degradation and surface regressions processes.

A parametric study is also conducted to investigate the temperature sensitivity, pressure dependence, and erosivity of propellant combustion. Furthermore, correlations for propellant burning rate are established in terms of local Reynolds number, momentum flux coefficient, turbulent kinetic energy, and strand burning rate. This information can be effectively used in predicting the performance of a rocket motor with complicated grain configuration.
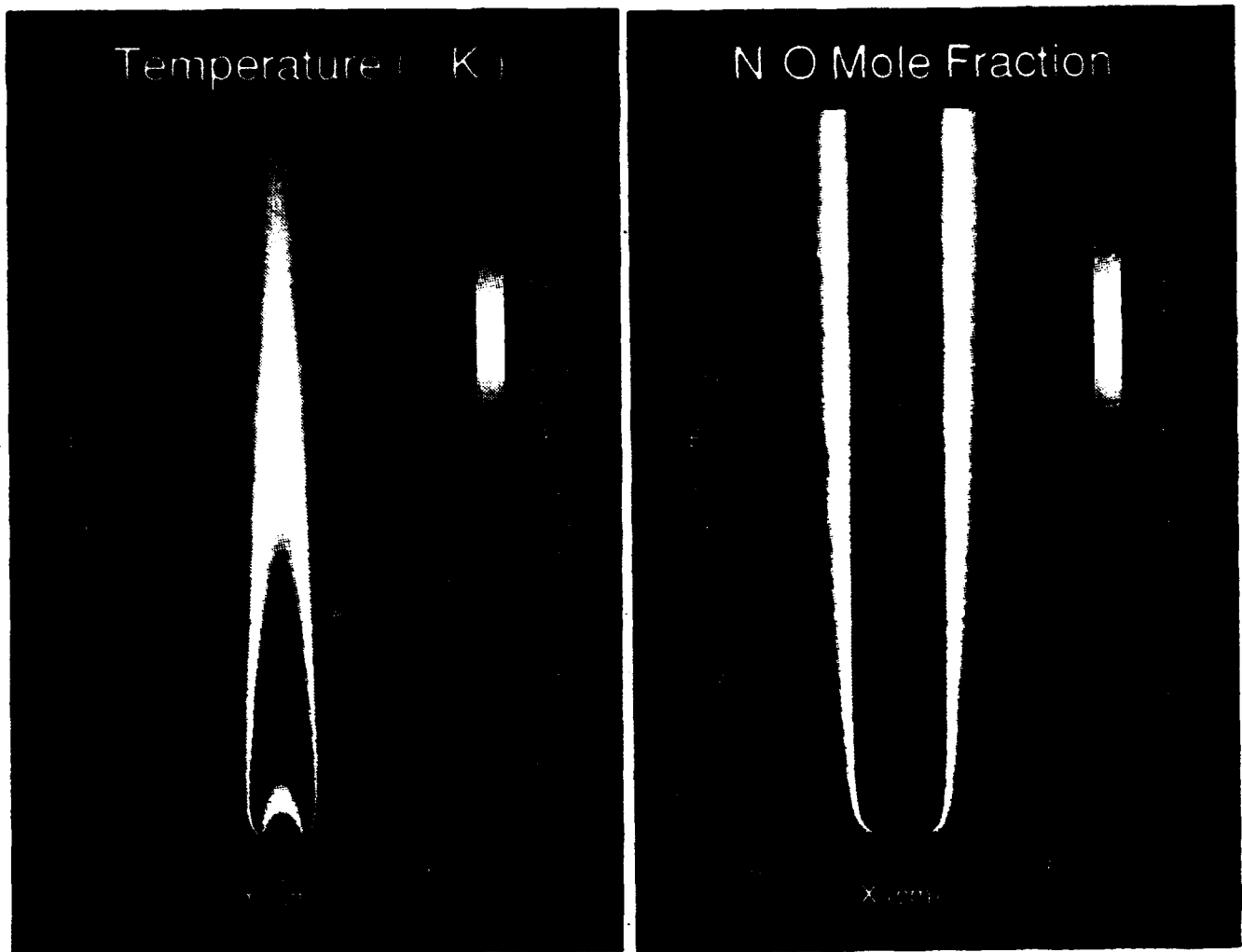
Figure 1. Flame sheet model calculation of the temperature (left) and N_2O concentration (right) in a CH_4/N_2O jet diffusion flame. Fuel (CH_4) is fed into the center, and oxidizer (N_2O) surrounds the fuel (Tasks 2 and 3)
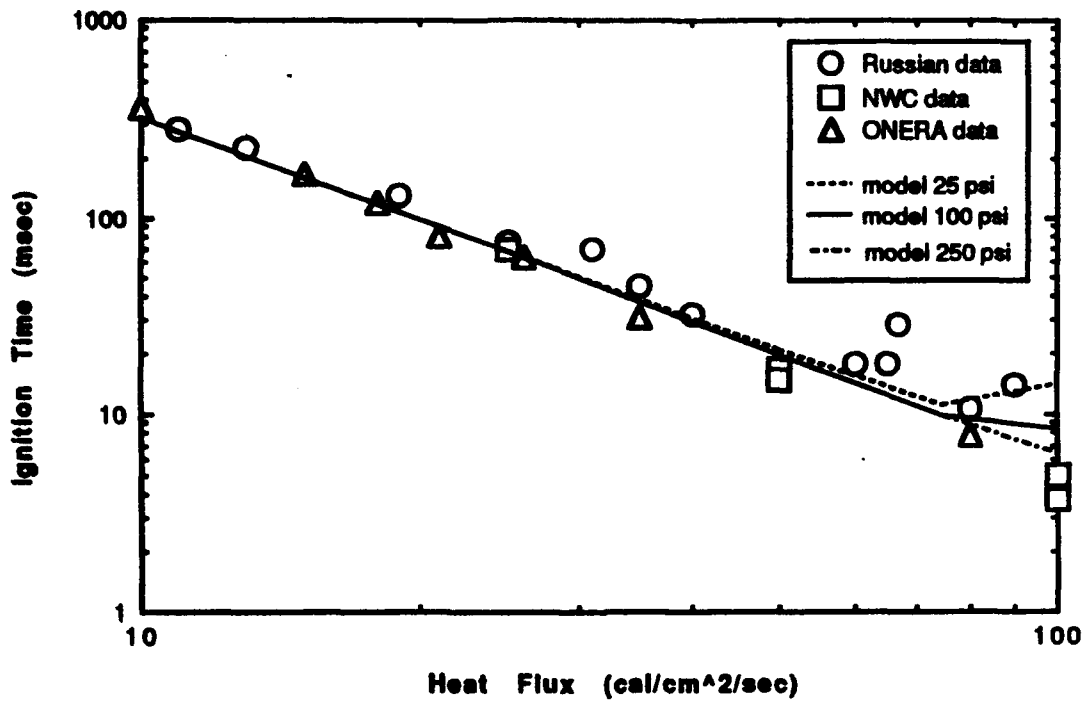
Figure 2. Comparison of calculated and measured ignition times of HMX using two parallel condensed phase reactions (Task 4)
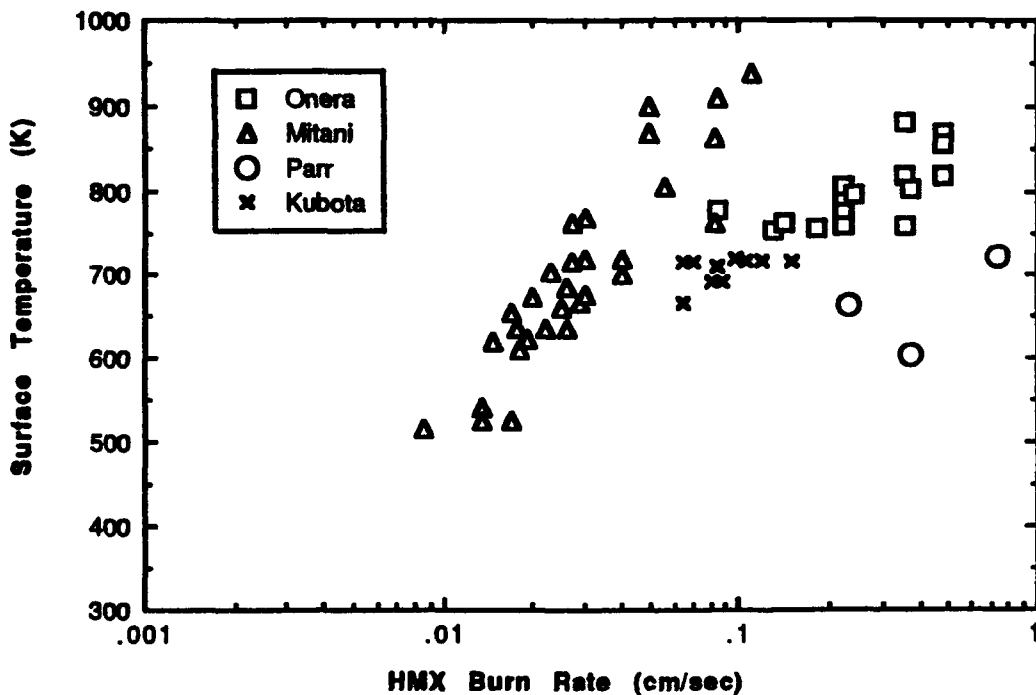
Figure 3. Comparison of measured surface temperature data (Task 4)

6

Combustion of Homogeneous Propellant in a Rocket Motor
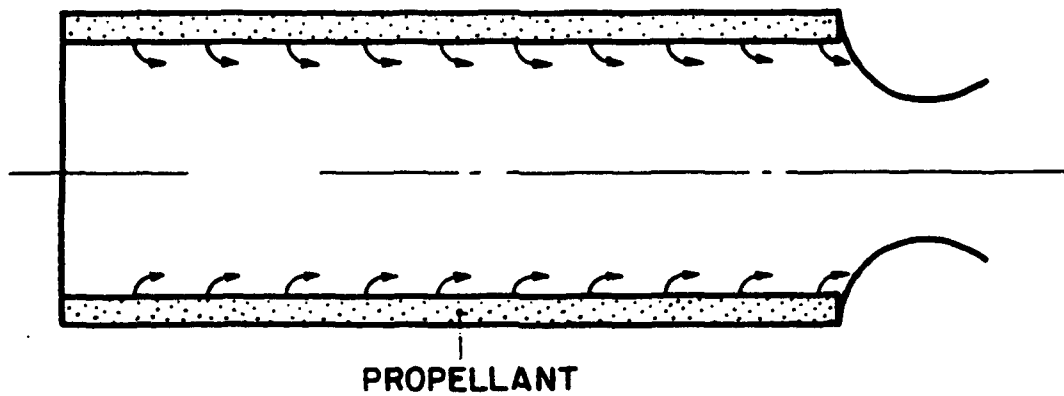
PROPELLANT

Combustion of Composite Propellant in a Rocket Motor
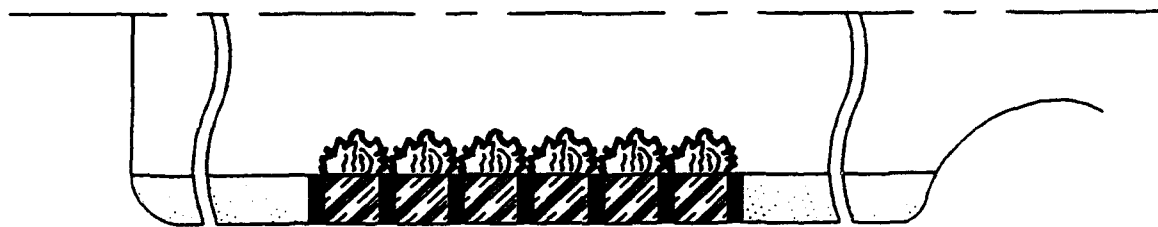
▮ Fuel binder

▨ Oxidizer

▯ Treated as homogeneous propellant

Figure 4. Two-dimensional model of rocket motor used to study propellant combustion chamber dynamics (Task 5)

CHEMICAL MECHANISMS AT THE BURNING SURFACE

AFOSR Grant Contract No. F49620-94-1-0053

Principal Investigator: Thomas B. Brill

Department of Chemistry
University of Delaware
Newark, DE 19716

SUMMARY/OVERVIEW

Determination of the rates and pathways of the decomposition and earliest exothermic reactions of solid propellant components is needed to define the chemistry of the surface during steady and non-steady combustion. Because this information has not been forthcoming from studies when the flame is present, we have developed spectroscopically-instrumented, high-rate thermolysis techniques to simulate the heating and temperature conditions at the surface during combustion. Efforts are being focused on 1) nitramine (HMX, RDX) combustion, 2) pyrolysis chemistry of non-energetic binders, and 3) pyrolysis processes of high-energy, clean-burning oxidizers, such as HNF.

TECHNICAL DISCUSSION

The surface reaction layer, which includes the reacting condensed phase and a small portion of the near field gaseous phase, plays a major, if not the dominant, role in controlling combustion of solid rocket propellants. The pressure and formulated composition influence the effective thickness of this layer, but 5-50 μm is an operable working range. Pyrolysis and exothermic reactions in this region can be outlined by the use of rapid pyrolysis techniques, such as T-jump/FTIR spectroscopy[1]. A thinly spread, small mass of sample simulates a "snapshot" view of the surface layer. By controlled heating at about 2000°C/sec to a temperature representative of combustion, the gaseous products formed and the simultaneously measured heat flow outline the chemistry.

Three issues are targets of this research program. First, the AFOSR-URI on Nonsteady Combustion has decided to model HMX combustion. In support of this effort, the relevant surface reaction zone processes must be refined as tightly as possible. Second, most oxidizer and monopropellant ingredients are formulated with a binder which pyrolyses and plays an important role in combustion. Comparatively little is known about the rates and products at high temperature and heating rate. This problem is being tackled in this program. Third, the long-term future includes the use of clean-burning, high energy solid rocket propellants. One such material is hydrazinium nitroformate (HNF). The chemistry of rapid thermolysis of HNF is being determined in our laboratory at this time. More detailed discussion of these three projects follows.

The Surface Reaction Zone of HMX

A major effort has been devoted to evaluating the merits of the published global Arrhenius kinetics for thermal decomposition of HMX in the

gaseous, liquid, and solid phases[2]. Poor agreement is found irrespective of the phase. However, the existence of a kinetic compensation effect was uncovered (Figure 1) and enables virtually all of these divergent results to be understood under a single, general, chemical phenomenon. All of these data represent valid rate measurements, but each is affected by different sample characteristics and working conditions. Consequently, there is no intrinsically "correct" rate of decomposition in the solid or liquid phase. Any E_a-lnA combination lying on the compensation line is representative of the rate under some set of conditions, but, of course, will yield a widely different rate prediction for other conditions.

Rather than employing these global rates, we are focusing on defining rates of specific decomposition and exothermic reactions that are experimentally validatable by T-jump/FTIR spectroscopy[3]. These are decomposition of HMX by two branches--one to form CH_2O + N_2O, and the other to form NO_2 + HCN. The exothermic reaction being used involves CH_2O + NO_2. Attempts are being made to refine the rates of these reactions and to scale them sensibly according to the phase[3].

Fast Decomposition of Non-Energetic Binders

The chemistry of rapid pyrolysis of polymeric, non-energetic binders is widely acknowledged to be poorly known and has a major influence on the combustion characteristics of solid propellants. We have undertaken a program to define this chemistry in much greater detail. Initial studies have begun by using T-jump/FTIR spectroscopy on polybutadiene acrylic acid acrylonitrile (PBAN), carboxyl-terminated polybutadiene (CTPB), and hydroxyl-terminated polybutadiene (HTPB). All of these polymers have the butadiene rubber backbone in common. The gaseous fragments from rapid pyrolysis are being identified and quantified by FTIR spectroscopy. These fragments are reactants for the leading edge of the diffusion flame. Figure 2 illustrates preliminary results for uncured PBAN heated to 500°C under 1 atm Ar. Two products (4-vinyl cyclohexene and butadiene monomer) are shown, but others are being identified at this time. The rate of growth of these products as a function of the pyrolysis temperature will enable the Arrhenius kinetics for decomposition at high temperature to be determined for input into models of combustion of composite propellants.

New, High-Energy, Clean-Burning Oxidizers

Rapid pyrolysis chemistry of non-standard materials is being undertaken to characterize promising energetic materials for the future. Interest in hydrazinium nitroformate (HNF), $[N_2H_5][C(NO_2)_3]$, exists at the Phillips Laboratory and at the European Space Agency (ESA). We are making progress on understanding how HNF decomposes under fast heating conditions. Figure 3 shows that proton transfer to form nitroform $[HC(NO_2)_3]$ occurs and that HNF volatilizes to some extent. A sharp transition occurs from competing endothermic sublimation and exothermic decomposition below 350°C to strongly exothermic decomposition above 400°C. These results seem to be of value to ESA in deciding the ingredients that are safe to formulate with HNF in test propellants.

Another compound of Air Force interest that we have investigated is 3-nitro-1,2,4-triazol-5-one (NTO) which is an insensitive explosive. NTO and eleven other compounds have been found to decompose upon fast thermolysis to cyclic azine polymers that are thermally stable to at least 600-700°C[4]. Each of these compounds is therefore potentially useful for burn-rate suppression

in rocket propellants. A rapid screening method to distinguish promising compounds from the test set has been devised.

1. T. B. Brill, P. J. Brush, K. J. James, J. E. Shepherd, and K. J. Pfeiffer, Appl. Spectroscopy, 46, 900 (1992).
2. T. B. Brill, P. E. Gongwer and G. K. Williams, J. Phys. Chem., submitted.
3. T. B. Brill, J. Propuls. Power, to be published.
4. G. K. Williams, S. F. Palopoli and T. B. Brill, Combust. Flame, in press.
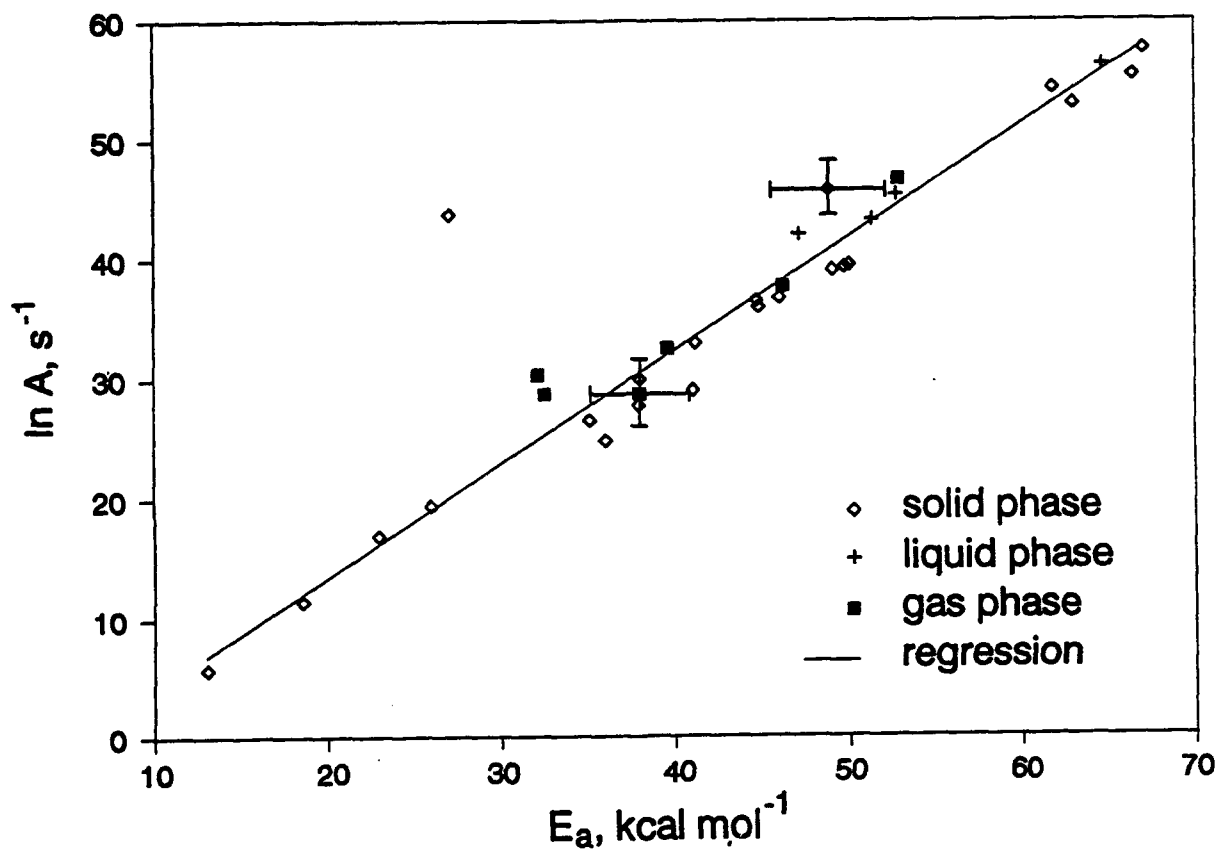
Fig. 1.   The kinetic compensation plot for thermal decompositon of HMX
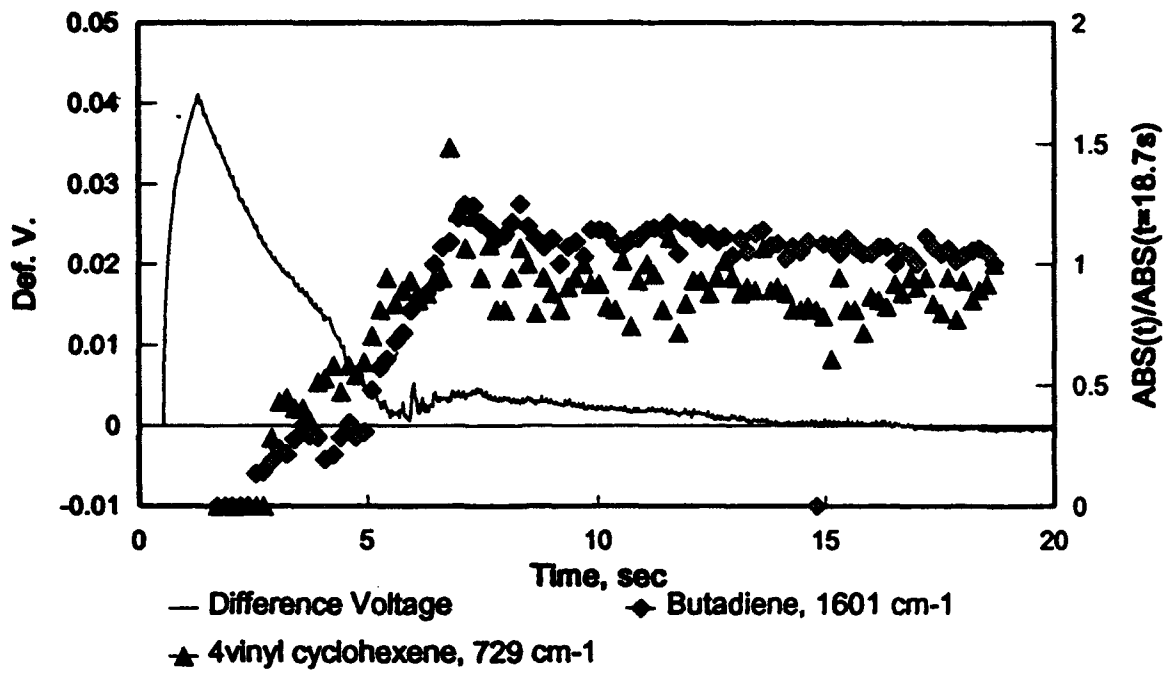
Figure 2. The rate of formation of two products of PBAN heated at 2000°C/s to 500°C under 1 atm Ar. The voltage trace shows slight exothermicity at 4-5s.
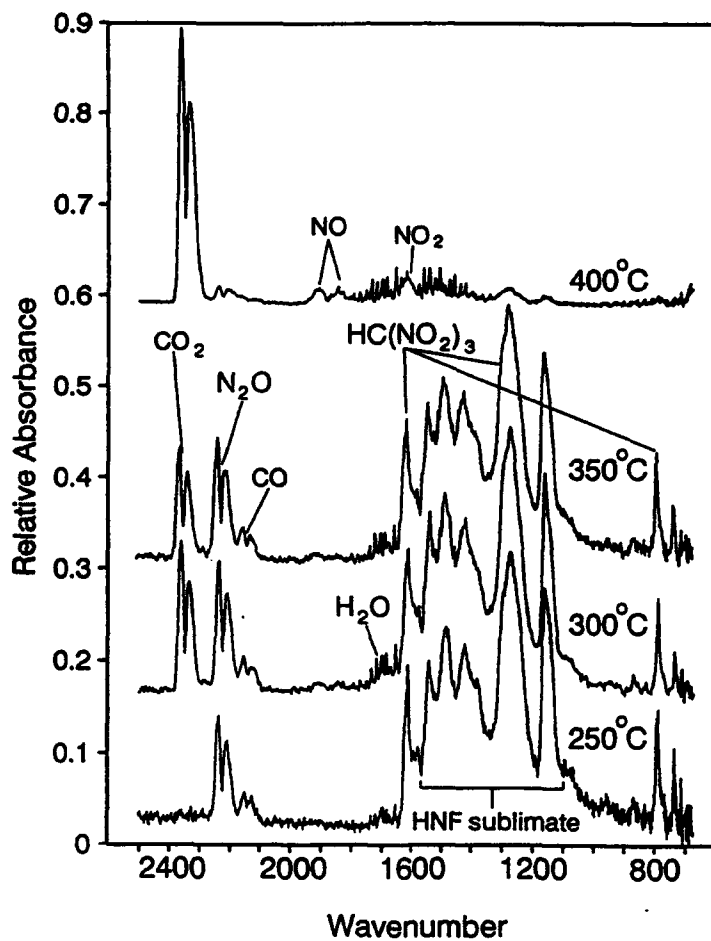
11

COMBUSTION KINETICS OF HEDMs AND METALLIC FUELS
AFOSR Grants No. F49620-92-J-0172 and -0346

Principal Investigator: Arthur Fontijn

High-Temperature Reaction Kinetics Laboratory
The Isermann Department of Chemical Engineering
Rensselaer Polytechnic Institute
Troy, NY 12180-3590

SUMMARY

The use of new advanced solid rocket propellant constituents, such as, e.g., boron as a HEDM and ammonium nitrate as replacement for halogen-containing oxidants, requires knowledge of their combustion kinetics, which needs establishing. To this end experimental rate coefficient measurements on individual important B and Al species reactions are made in the 300-1900 K temperature range in unique high-temperature reactors. Also, semi-empirical theory is being developed for predictions on further reactions. Such predictive theory existed for reactions in non-metallized propellants, but now for the first time is being developed for interactions involving metallic species.

TECHNICAL DISCUSSION

Aluminum Oxidation

Last year we discussed that the $AlO + O_2$ reaction system was not a simple one, but consists of an addition reaction with a negative temperature dependence and an abstraction reaction with a positive one. Preliminary rate data were presented. During the past year this work was completed by taking additional measurement at "low" ($T \leq 1010$ K) and "high ($T \geq 1200$ K) temperatures. The low temperature, pressure-dependent, measurements yielded an accurate rate coefficient expression for the addition reaction:

$$AlO + O_2 + Ar \rightarrow AlO_3 + Ar \qquad (1)$$

$$\log[k_1(300\text{-}1010 \text{ K})/(cm^6molecule^{-2}s^{-1})] = -24.7-1.94\log(T/K)$$

This rate coefficient expression was in turn used to ascertain that this reaction has a negligible influence under the conditions where the abstraction reaction, of greater rocket combustion importance, was to be measured. The high-temperature measurements yielded for that reaction:

$$AlO + O_2 \rightarrow AlO_2 + O \qquad (2)$$

$$k_2(1200\text{-}1700 \text{ K}) = 8.1\text{x}10^{-10}exp(-10065 \text{ K/T}) \text{ } cm^3molecule^{-1}s^{-1}$$

No measurements between 1010 and 1200 K were used, because the competition between the two processes yields less accurate results for either.

A publication on this work is being prepared. The net effect of the competition in terms of rocket combustion is that the total AlO consumption rate coefficients, i.e. the sums of $k_1(T)$ and $k_2(T)$, pass through a minimum at about 1000 K at pressures below about an atmosphere, as illustrated in Fig. 1.

Boron Oxidation

For the above measurements at 300 K a new technique for AlO production was developed. At higher temperatures it yielded results indistinguishable from those obtained by our standard evaporative technique,[1] which can not be used for reaction temperatures below about 500 K. This new technique, passing trimethyl-aluminum in argon containing 1-10 ppm O_2 through a microwave discharge, also suggested similar approaches for the production of BO and BO_2. For example, we have found that passing mixtures of B_2H_6, NO, and N_2 in Ar through such a discharge results in readily measurable constant BO signals. We are further exploring various combinations of reactants prior to studying BO and BO_2 reactions.

Predicting Temperature-Dependent Rate Coefficients

Our semi-empirical theoretical efforts at predicting rate coefficients have followed two complementary paths. In one, the pre-exponential part of temperature dependent rate coefficients $k(T)$ is predicted.[2,3] Experiments will, in general, lead to expressions of the form

$$k(T) = AT^n exp(-E/RT) \tag{3},$$

where A and n are constants, E is the reaction energy barrier and R is the gas constant. Transition-state theory allows $k(T)$ to be expressed in the form

$$k(T) = \frac{k_B T}{h} \frac{q^{\neq}}{q_{AB} q_{CD}} exp(-\Delta E^{\neq}/RT) \tag{4},$$

where k_B and h are, respectively, the Boltzmann and Planck constants, and q_{AB} and q_{CD} are the partition functions of the reactants. $q^{\neq}$ and $\Delta E^{\neq}$ are, respectively, the partition function of the transition state and its energy above the reactant ground states, both of which are unknown. By using simple ab initio methods for estimating $q^{\neq}$, and equating eqs. (3) and (4) at one temperature, $\Delta E^{\neq}$ can be found. Hence, eq. (4) can, in principle, be used to predict $k(T)$ expressions from one measurement at one temperature. To test this prediction, we chose a mid-temperature value of the experimental range and found that for reactions of the nature

$$AB + CD \rightarrow ABC + D \tag{5}$$

the predicted ln $k(T)$ versus T^{-1} plots well reproduced the experimental results, cf. Fig. 2. This effort will now be expanded to other reactants, particularly reactions of Al and B oxides.

The other effort is aimed at predicting E of eq. (3) for individual reactions. We previously observed[4-6] that for reactions of similar metal atoms with N_2O or O_2, E

13

correlates with the sum of the ionization potentials IP and s-p promotion (excitation) energies PE. The basis for this observation is that, for such "homologous reactions", E can be calculated directly by simple resonance theory once a value for a single member of a series has been determined. The metal atoms we showed this for were those with one and two valence s electrons, respectively. Using HTFFR measurements on the Al + N_2O reactions as input, we have now extended this treatment to atoms with the s^2p structure, i.e. Al, B, and further group 13 metal atoms, Fig. 3. A paper describing the measurements and the further theoretical development is in an advanced stage of preparation.

Together these semi-empirical procedures make it possible to provide reliable estimates of the temperature dependence of rate coefficients of more reactions than can be measured experimentally within reasonable periods of time.

References

1. A.G. Slavejkov, C.T. Stanton, and A. Fontijn, "High-Temperature Fast-Flow Reactor Kinetics Studies of the Reactions of AlO with Cl_2 and HCl over Wide Temperature Ranges," J. Phys. Chem. 94, 3347 (1990).

2. P.M. Futerko and A. Fontijn, "Experimental and Transition-State Theory Studies of the Gas-Phase Reactions of AlCl with N_2O, CO_2, and SO_2," J. Phys. Chem. 97, 7222 (1993).

3. P.M. Futerko, A.G. Slavejkov, and A. Fontijn, "Wide Temperature Range Kinetics of the Gas-Phase Reactions of BCl with SO_2, N_2O, O_2, and CO_2," J. Phys. Chem. 97, 11950 (1993).

4. P.M. Futerko and A. Fontijn, "Activation Barriers for Series of Homologous Reactions," I. Metal Atom Reactions with N_2O," J. Chem. Phys. 95, 8065 (1991).

5. P.M. Futerko and A. Fontijn, "Activation Barriers for Series of Homologous Reactions," II. Reactions of s^2 Metal Atoms with N_2O," J. Chem. Phys. 97, 3861 (1992).

6. P.M. Futerko and A. Fontijn, "Activation Barriers for Series of Homologous Reactions," III. Reactions of s^2 Metal Atoms with N_2O, and O_2" J. Chem. Phys. 98, 7004 (1993).
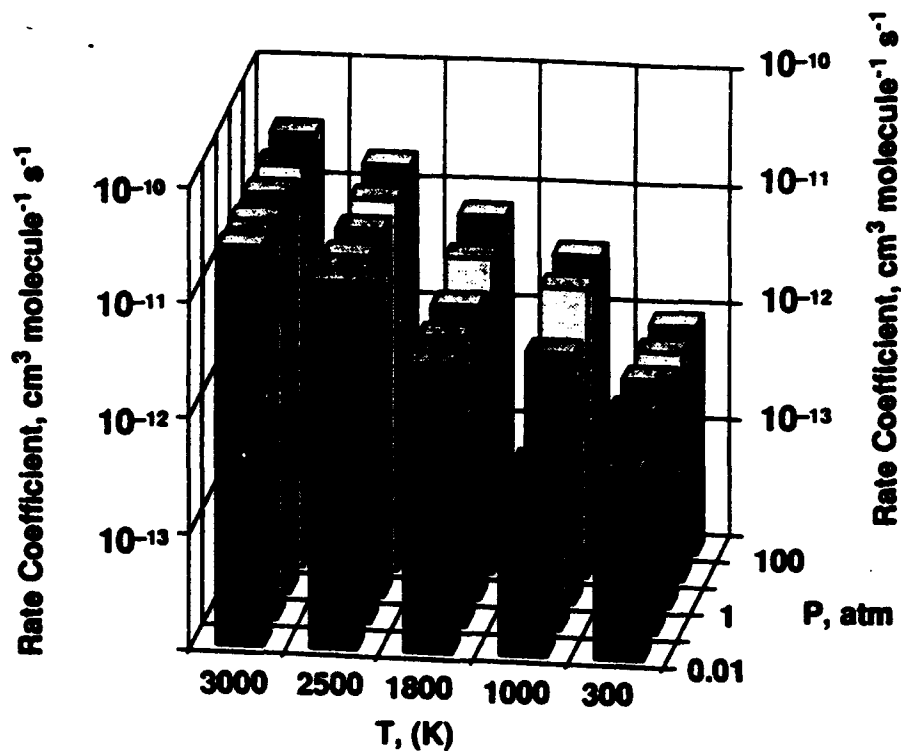
Fig. 1. Combined AlO consumption rate coefficients as functions of temperature and pressure.
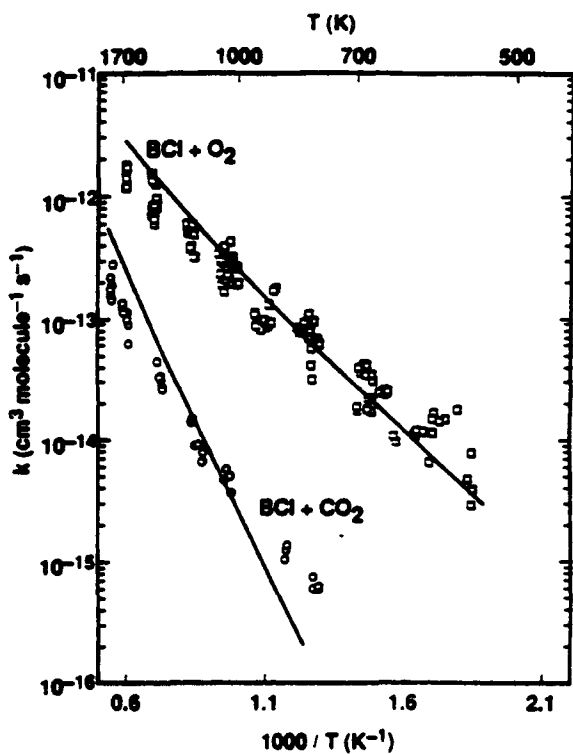
Fig. 2. Comparison of theory (lines) to experiments (points) for BCl reactions.
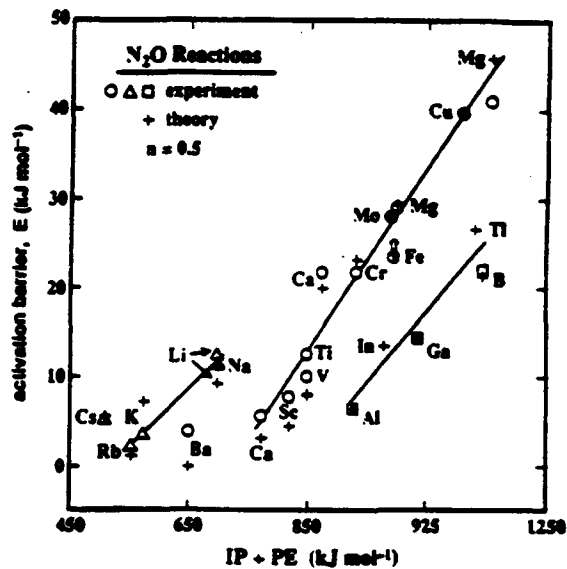
Fig. 3. Comparison of calculated and experimental E-factors for s^1 (left line), s^2 (middle line), and s^2p (right line) metal atoms.

15

NONLINEAR ACOUSTIC PROCESSES IN SOLID ROCKET ENGINES

Principal Investigator: David R. Kassoy

Mechanical Engineering Department/Center for Combustion Research
Mailing Address: Graduate School, B-26
University of Colorado, Boulder, CO 80309-0026

SUMMARY:

Fully computational methods are employed to study unsteady, nonlinear vorticity generation and evolution by an acoustic wave interaction with a sidewall injected flow in a cylindrical tube, that mimics the solid propellant surface burning in a rocket engine. The steady flow field, sustained by sidewall injection, is disturbed at the exit plane by a sinusoidally fluctuating planar pressure variation. The unsteady rotational component of the velocity field is extracted from the numerical solutions. It is shown explicitly that unsteady vorticity generated at the injecting wall is convected away from the wall towards the mainly inviscid core flow by the mean radial velocity field. Eventually, unsteady vorticity fills the entire chamber unlike that confined into traditional acoustic thin viscous layers adjacent to the sidewall. The presence of rotational flow features imply that traditional acoustic balance theories, used widely to predict solid rocket engine chamber stability, must be reevaluated.

AUTHORS: David R. Kassoy, Kadir Kirkkopru, and Qing Zhao

TECHNICAL DISCUSSION

Transient flow dynamics in a solid rocket engine chamber are strongly coupled to propellant combustion processes and related directly to overall rocket motor stability. The combustion of solid propellant generates gaseous products that induce a low Mach number ($M_{axial} = O(10^{-2} - 10^{-1})$), large Re number ($Re = O(10^4 - 10^5)$) internal shear flow in a long, narrow rocket engine chamber.

In this study, two dimensional, axisymmetric Navier-Stokes equations are solved numerically by utilizing the MacCormack explicit, predictor-corrector scheme. Sidewall mass addition is used to simulate the gasification of the burning solid propellant surface. Initially, a steady, low Mach number, large Re number, rotational flow exists in a long, narrow cylinder of an aspect ratio (length to radius) $\delta = 20$. The steady flow is disturbed at the exit plane by imposing a sinusoidally fluctuating component with frequency ω on the static pressure. Amplitudes of the oscillatory pressure disturbances (A) are chosen accordingly for different axial flow Mach numbers so that nonlinear processes affect the evolution of the unsteady flow field, an explicit result extracted from analytical studies by Zhao and Kassoy (1994) and Zhao et al. (1994). In this work rational perturbation methods are used to show that there are two disparate length scales for rotational effects; the tube radius and an $O(M)$ smaller length where significant local velocity variations are present. Information about the existence of two disparate length scales and their relationship to Mach number enables us to choose grid size and spatial distribution in

order to describe flow dynamics accurately.

The primary objective of the present study is to compute unsteady vorticity production and evolution in a cylindrical model of a rocket engine chamber. Unsteady flows arising from the exit plane planar pressure disturbances are computed for different axial flow Mach numbers ($M = 0.1, 0.05 \& 0.02$) and for different angular frequencies ($\omega = 1, 1.5 \& 2.5$).

Following a procedure used in Zhao et al. (1994), the total unsteady axial flow speed is divided into three parts

$$u(x, r, t) = u_S(x, r) + u_P(x, t) + u_V(x, r, t)$$

where u_S denotes the steady flow field which is known as an initial condition for the unsteady computations and u_P represents the irrotational, planar flow which can be computed as the difference between the unsteady axial speed and the steady axial speed on the centerline of the tube. The remaining part u_V is defined as the vortical (rotational, nonplanar) component which vanishes at the centerline at all times. It is used to describe the generation and evolution of the nonlinear unsteady vorticity field in the cylinder.

Figure 1 shows the radial variation of the unsteady axial vortical speed at midchamber($x = 0.5$) at three time values after the planar pressure disturbance is initiated at the exit plane. The flow parameters are $M = 0.1$ and $Re = 3.10^4$. The wall is located at $r = 1$ and the centerline at $r = 0$. The corresponding injection Mach number $M_i = M/\delta = 0.005$.The disturbance frequency is $\omega = 1.0$, a non-resonant frequency smaller than the first natural frequency of the tube, $\omega_1 = \pi/2$. One observes a strong velocity gradient extending out about 0.15 units from the wall at $t = 1.48$ (solid line). This is the exact radial distance travelled by the injected fluid during the time interval $t = 1.48$. The unsteady vortical axial velocity field extends out to 0.85 units from the injecting wall when $t = 11.81$. At time $t = 29.37$ unsteady rotational flow fills the entire chamber.

The spatial distribution of u_V at each time may be explained in physical terms by considering an interaction between the steady injected flow field and the propagating planar acoustic disturbances. The motion of a fluid particle injected radially into the tube from the upper sidewall at a specified location is affected by the harmonic variation of the axial pressure gradient. As a result, a given fluid particle emanating from the wall will be accelerated alternately in the positive and negative axial directions as it is convected toward the axis of the cylinder by the steady radial flow field. Part of the fluid particle response is associated with irrotational acoustic effects. The rest is rotational, resulting from vorticity generation at the wall.

Figure 2 shows the spatial oscillation of the vortical axial velocity at midchamber with respect to the radius when $t = 1.488, 11.834$ and 29.54 for a smaller $M = 0.05$ and for a larger $Re = 3.10^5$. The forcing frequency $\omega = 1.0$ is the same as for the previous case. The sharply defined region of large velocity gradient is seen in Fig. 2 at 0.07 units from the wall at $t = 1.488$. One notes that at $t = 11.834$ the wavelength of the spatial oscillation of u_V is smaller thatn that for the case $M = 0.1$. This is an expected result because the mean radial velocity field for $M = 0.05$, which transports the fluid particles into the cylinder, is characterized by a relatively lower speed than that for the $M = 0.1$ case. At $t = 29.54$ one notes spatial oscillations throughout the cylinder. It is also observed that the wavelength of the oscillatory structure decreases as the centerline is approached. This occurs basically because the mean radial flow speed vanishes as the centerline is approached.

The third case studied is for a smaller mean axial flow Mach number $M = 0.02$, Reynolds number $Re = 3.10^5$ and the forcing frequency $\omega = 1.0$. Figure 3 shows the u_V variation with respect to radius at $x = 0.5$ when $t = 3.00, 15.00$ and 30.00. It can be seen from this figure that axial velocity gradients are larger than those for larger Mach number cases presented previously. This implies that the absolute magnitude of the unsteady vorticity generated at the wall is much

larger than that of the higher Mach number flows. This unsteady vorticity field is convected away from the wall towards the center of the chamber by a relatively slower steady radial flow component.

The radial variation of unsteady vorticity at $z = 0.5$ for three cases, $M = 0.1, 0.05$ and 0.02 is shown in Figs.4a-c. Corresponding times are $t = 29.37, 29.54$ and 30.00, respectively. It is seen from these figures that the magnitude of the unsteady vorticity increases with mean flow Mach number, implying the lower the M the larger the transient shear stress on the cylinder surface. One can speculate that these transient shear stresses will impact the burning rate of an actual propellant which is the source of the "injected" fluid used in the present model. An accompanying plot, Fig. 4-d, shows the variation of the unsteady vorticity throughout the cylindrical chamber for the $M = 0.02$ case at $t = 30.00$.

Figure 5 describes the effects of forcing frequency on the oscillatory spatial structure of the vortical axial speed at times closer to $t = 17.5$ for the $M = 0.1$ case. The chosen frequencies are $\omega = 1.0$, $\omega = 1.5$(a near-resonant case) and $\omega = 2.5$. It can be seen from this plot that the wavelength of the oscillatory spatial structure decreases when ω increases. It is also noted that the local spatial gradients of vortical velocity increase for larger ω 's.

There is now a considerable body of evidence supporting the existence of an unsteady vorticity distribution in a solid rocket engine chamber. Therefore, the presence of vorticity in the chamber must be accounted for in an accurate and reliable theory of engine stability.

REFERENCES

Zhao, Q. & Kassoy, D.R. (1994), AIAA 94-0779, 32nd Aerospace Sciences meeting, Reno, NV.

Zhao, Q., Kassoy, D.R. & Kirkkopru, K. (1994), " Nonlinear Vorticity Generation by Acoustic Wave Interaction with an Injected Gas Velocity Field in a Cylinder", submitted to the J. Fluid Mech.

Kirkkopru, K., Kassoy, D.R. & Zhao, Q. (1994), " Unsteady Vorticity Generation and Evolution in a Model of a Solid Rocket Engine Chamber", submitted to the AIAA J.
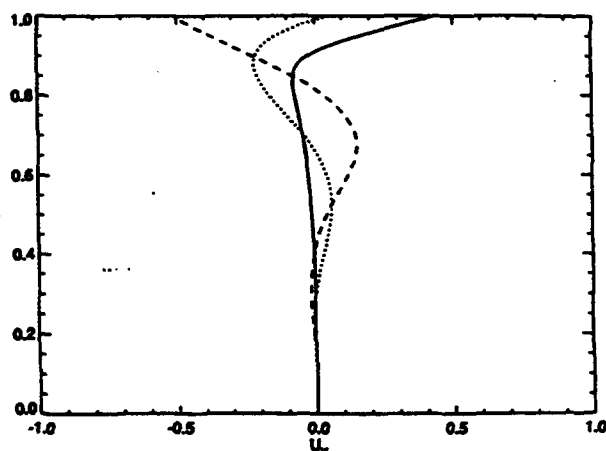
Fig. 1: The radial variation of the unsteady axial flow speed, u_V, at $z = 0.5$ when $t = 1.46$ (solid line), $t = 11.81$ (dotted line) and $t = 29.37$ (dashed line) for $M = 0.1$, $Re = 3.10^5$, $\omega = 1$ and $A = M$.
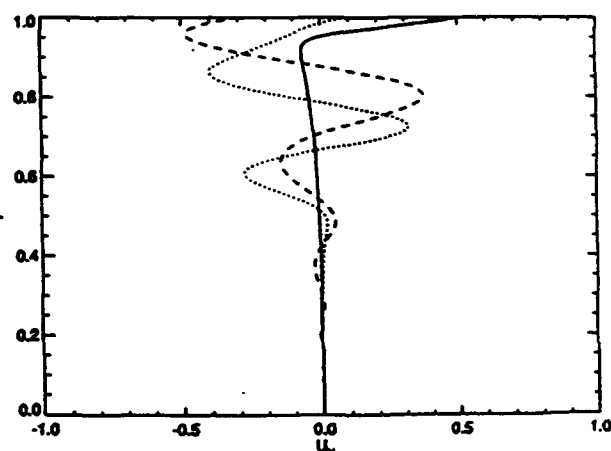
Fig. 2: The radial variation of u_V at $z = 0.5$ when $t = 1.468$ (solid line), $t = 11.834$ (dotted line) and $t = 29.54$ (dashed line) for $M = 0.05$, $Re = 3.10^5$, $\omega = 1$ and $A = M$.
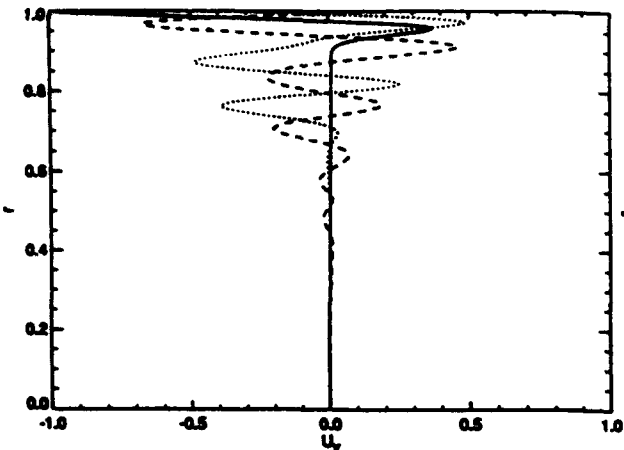
Fig. 3: The radial variation of u_φ at $z = 0.5$ when $t = 3$ (solid line), $t = 15$ (dotted line) and $t = 30$ (dashed line) for $M = 0.02$, $Re = 3.10^4$, $\omega = 1$ and $A = M$.
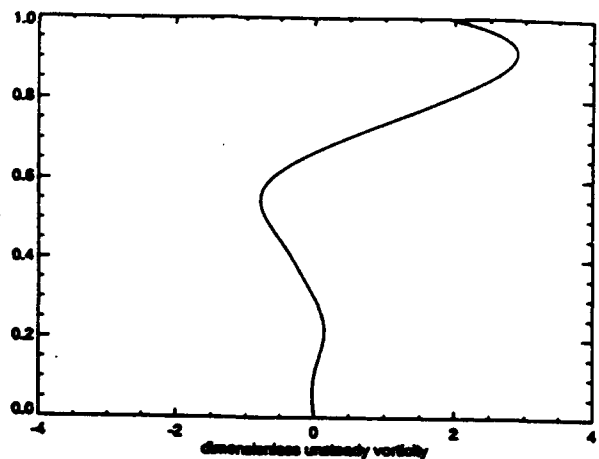
Fig. 4a: The radial variation of unsteady vorticity, Ω, at $z = 0.5$ when $t = 29.37$ for $M = 0.1$.
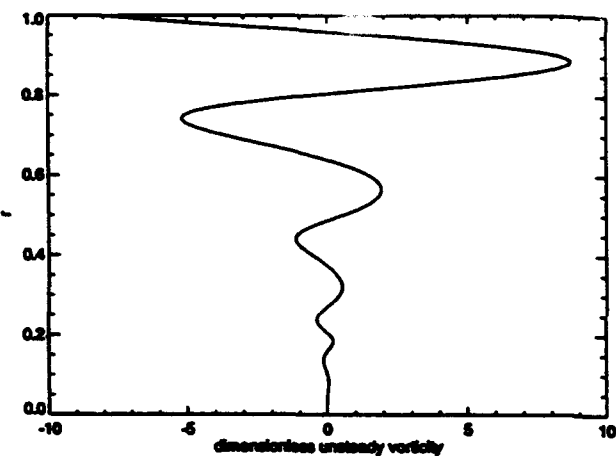
Fig. 4b: As Fig. 4a but for $M = 0.05$, when $t = 29.54$.
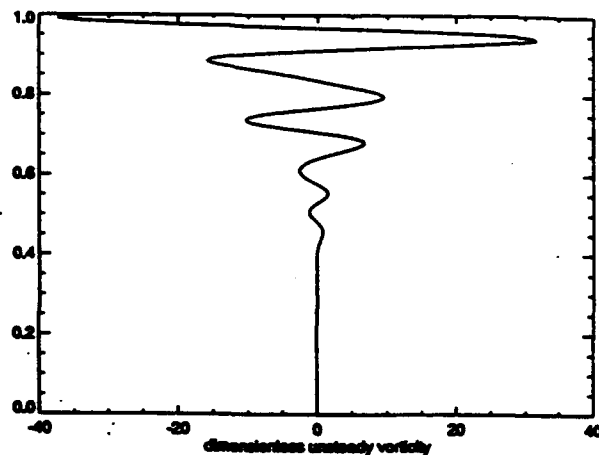
Fig. 4c: As Fig. 4a but for $M = 0.02$, when $t = 30$.
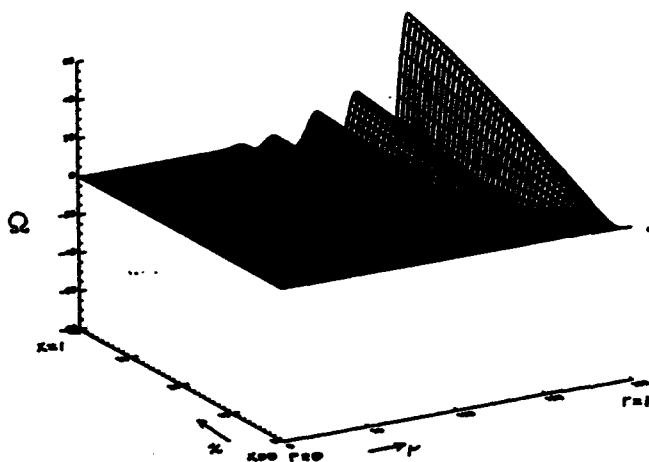
Fig. 4d: Spatial unsteady vorticity variation, Ω, throughout the cylinder at $t = 30$ for $M = 0.02$.
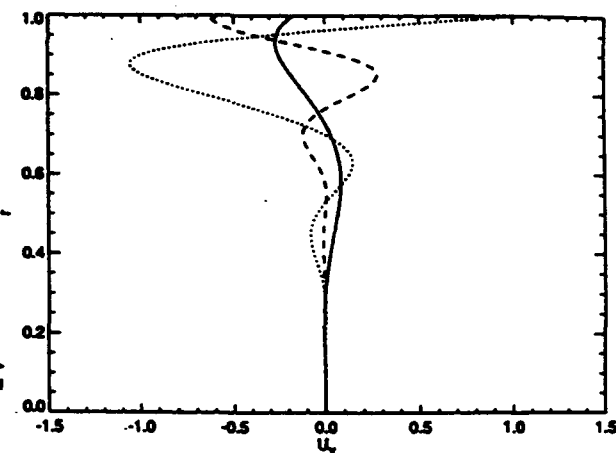
Fig. 5: The radial variation of u_φ at $z = 0.5$ when $\omega = 1$, $t = 17.72$ (solid line), $\omega = 1.5$, $t = 17.38$ (dotted line) and $\omega = 2.5$, $t = 17.77$ (dashed line) for $M = 0.1$, $Re = 3.10^4$, and $A = M$.

19

DIRECT NUMERICAL SIMULATION OF ACOUSTIC-MEAN FLOW INTERACTIONS IN SOLID ROCKET MOTORS

Principal Investigator: SHANKAR MAHALINGAM

Center for Combustion Research, Department of Mechanical Engineering
University of Colorado, Boulder, CO 80309-0427

SUMMARY/OVERVIEW:

The present research is directed towards obtaining a fundamental physical understanding of the interaction between the mean flow and acoustic disturbances in solid propellant rocket motors. An important objective of this research is the identification of acoustic mode forms from the results of direct numerical simulation. To date, acoustic traveling wave-shear flow interaction in a 2-D channel has been simulated. Phenomena that have been studied include acoustic refraction, disturbance amplification and attenuation, and the phase relationships that exist between lower and higher order acoustic modes. Current effort is being directed toward simulating the combustion response of a nonpremixed flame to acoustic excitation.

AUTHORS: Siming Mu, Stephen Hevert and Shankar Mahalingam

TECHNICAL DISCUSSION

An imbalance between energy amplification and damping mechanisms dictates whether a combustion-driven acoustic instability is sustained or weakened in a solid propellant rocket motor. The relative importance of these mechanisms is strongly dependent on the oscillation mode and type of propellant. Furthermore, due to the wave-structure of the acoustic field, its phase relative to processes contributing to amplification/damping is extremely critical to the outcome of the interaction. The focus of this research is on the mechanisms of energy exchange between the mean and acoustic flow and amongst various modes of the acoustic flow. A fundamental understanding of these processes is essential in ultimately obtaining a global understanding of the overall problem of acoustically-driven combustion instability.

Our approach is to perform direct numerical simulations of several model configurations, using higher-order accurate finite differencing schemes. Boundary conditions are treated using characteristic-based conditions developed for the Navier-Stokes equations by Poinsot and Lele (1992). The models have been carefully chosen to complement Wang and Kassoy's (1992) analytical results, and Baum and Levine's (1987) and Vuillot and Avalon's (1991) numerical simulations. Our results have enabled us to isolate different physical phenomena and thus evaluate cause and effect relationships between the mean flow and the acoustics.

To date, acoustic traveling wave-shear flow interaction in a 2-D channel has been simulated on a Cray-c90 supercomputer. The results have been compared with the analytical solution by Wang

and Kassoy (1992), and with numerical results by Baum and Levine (1987). Our analysis differs from previously published numerical work in that the current computation is able to capture the long time acoustic response. Parameters include a duct aspect ratio of 5, a centerline Mach number of 0.08, and an acoustic Reynolds number of 4000 based on the duct height. The simulation uses an 81×81 computational grid. Resolution in the transverse direction was doubled to verify that the solution is grid independent.

Our results have shown good qualitative and quantitive agreement with those by Wang and Kassoy (1992). Several interesting features associated with this problem have been observed. First, axially travelling plane waves can generate transverse waves trapped in between the upper and lower boundaries of the domain. Second, above a certain disturbance frequency, oblique waves can be generated. The interaction between oblique waves and axially traveling waves results in variation of amplitudes of acoustic pressure and velocity. Hence, our numerical simulation validates the linear perturbation analysis of the flow field in a solid rocket motor.

Other interesting features have also been noted. Amplified oblique waves due to resonant disturbances are observed for the first time. The rate of amplification of these oblique waves is much higher than that of the axially traveling waves. Also, the oblique and axial waves are 180 deg out of phase. At certain locations of the domain, this strong oblique wave interacts with the axial waves, causing a dramatic change in both wave amplitude and phase (Figure 1a). The initial increase in amplitude is due to the resonant amplification of the axial wave. Then the amplitude starts to decrease to zero due to the arrival of oblique waves, which have an opposing phase. Finally, the amplitude increases again as the oblique waves dominate over the axial waves. The wave phase at this location is changed by 180 deg. Since the oblique waves can propagate only along a fixed path, at those locations where oblique waves do not pass through, the axial wave structure remains unaffected (Figure 1b). The traveling path of the oblique wave can be best identified by examing the pressure contour (Figure 2). The arrows indicate the direction and location where the locally largest pressure gradient occurs. Thus they are also the path along which oblique waves travel.

For resonant disturbances with several transverse spatial modes, the growth rate varies significantly for different modes. It has been observed that the amplitude growth of the first mode exceeds that of all other modes, while amplitudes of all modes are observed to grow (Figure 3). This feature suggests that acoustic energy is redistributed among all spatial modes, with the most significant transfer between the zeroth mode and the first mode.

Acoustic boundary layer is another important feature of this problem. It is a very thin area along the duct wall where an overshoot of acoustic velocity occur whenever the acoustic velocity in the core changes sign, this feature is also known as Richarson's annular effect. Our numerical simulation resolved the acoustic boundary layer very well (Figure 4). The thickness estimated through our simulation is between 5 to 5.5 percent of the duct width, compared to theorectical prediction of 5.9 percent.

We are currently simulating a 2-D nonpremixed flame centered between the walls of a narrow horizontal duct with open ends. Single-step, finite rate chemistry is assumed, with the unmixed reactants diffusing into the flame zone from opposite walls of the channel. Eventually one end of the channel will be closed, and acoustic perturbations imposed on the flow field. This is the first step toward modelling the effects of acoustics on the combustion response of a nonpremixed flame confined near the surface of a burning solid propellant. In the future, this analysis will be extended to simulate the response of a premixed flame adjacent to the burning propellant.

REFERENCES

21

1. BAUM, J. D., AND J. N. LEVINE, *AIAA Journal*, **25**(12), 1577-1586, (1987).

2. LELE, S. K., AIAA Paper AIAA-89-0374, (1989).

3. POINSOT, T., AND S. K. LELE, *Journal of Computational Physics*, **101**, 104-129, (1992).

4. VUILLOT, F., AND G. AVALON, *Journal of Propulsion*, **7**(2), 231-239, (1991).

5. WANG, M, AND D. R. KASSOY, *Journal of Fluid Mechanics*. **238**, 509-536, (1992).
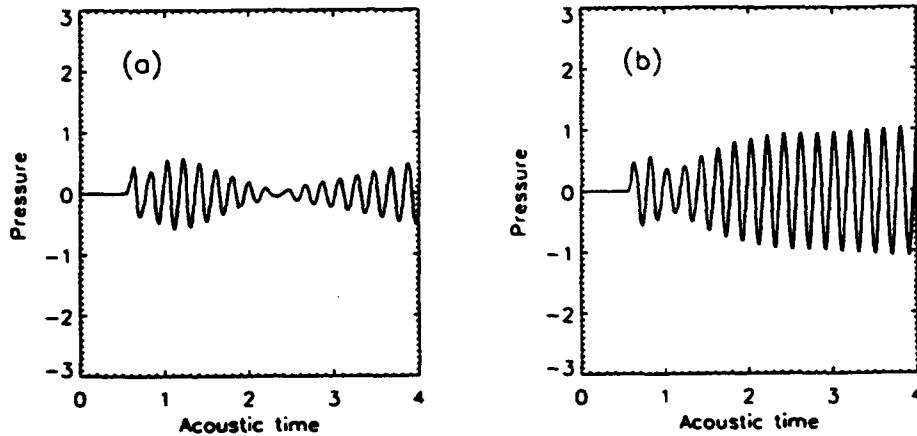
Figure 1. Acoustic pressure time history at $x = 0.6$ and (a) centerline (b) wall, under resonant condition. Note x is scaled by the duct length, and time by the duct length and reference speed of sound.
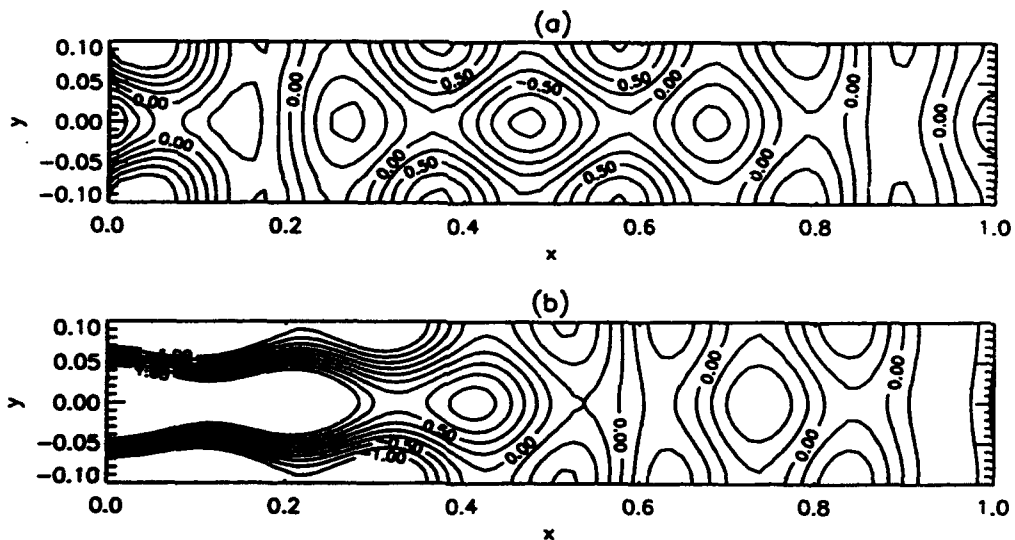
Figure 2. Acoustic pressure contours at acoustic time (a) 3.00 and (b) 3.05 under resonant condition
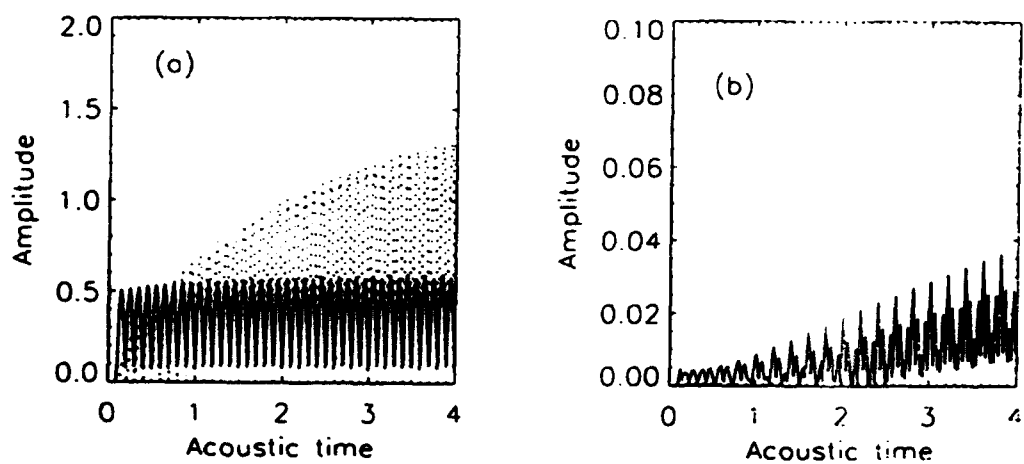
Figure 3. Time history of spatial (lateral) modes of acoustic pressure at $x = 0.5$. (a) ——— : zeroth mode; – – – – – : first mode; (b) second mode.
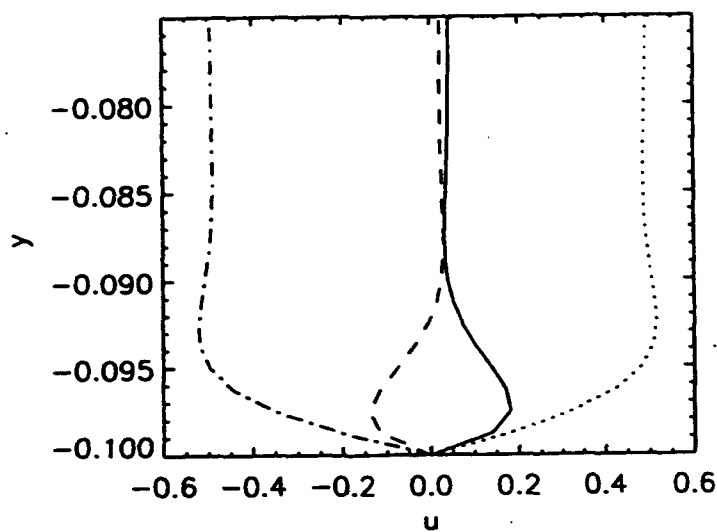
Figure 4. Axial acoustic velocity profiles at $x = 0.5$. ——— : $t=3.00$; – – – – – : $t=3.14$; – – – – : $t=3.30$; – – – – : $t=3.62$.

INVESTIGATION OF ACTIVE CONTROL OF COMBUSTION INSTABILITIES IN CHEMICAL ROCKETS

Principal Investigators: Dr. Ben T. Zinn Regent's Professor
Mr. Brady R. Daniel, Senior Research Engineer
Dr. Yedidia Neumeier, Post Doctoral Fellow

School of Aerospace Engineering
Georgia Institute of Technology
Atlanta, GA 30332

Summary/Overview

The objective of this research is to investigate active control of detrimental combustion instabilities in chemical rockets by a periodic combustion process. These efforts resulted in the development of an active control approach consisting of a sensor (i.e., a pressure transducer), an observer that determines the characteristics of the instability in real time, a controller that incorporates appropriate phase shifts and amplitude gains into each of the identified (by the observer) combustor modes and sends the resulting signal to an actuator consisting of a fuel injector with capabilities for modulating the injection rate of a secondary fuel stream into the combustor. This control system is designed to produce an oscillatory combustion process within the combustor that is out of phase with the combustor pressure oscillations, resulting in their attenuation. In a parallel effort, the development of an experimental gas rocket setup that will be used to investigate the effectiveness of the developed active control system is nearing completion. The results of this program will lead to the development of a robust active controller suitable for stabilizing a variety of unstable rocket motors and propulsion systems.

Technical Discussion

Combustion instabilities are generally driven by a periodic combustion process whose oscillations are in phase with the combustor pressure oscillations, in accordance with Rayleigh's criterion. The operation of a rocket motor becomes unstable if the driving provided by the combustion process is larger than the damping inherently present within the system due to, for example, viscous dissipation and nozzle damping. The processes responsible for the establishment of a periodic combustion process generally involve complex interactions between the combustion process and acoustic oscillations in the combustor that depend upon the rocket motor design and operating conditions. Due to their detrimental effects, there is a need for dependable engineering solutions that could be employed to stabilize rocket motors and propulsion system.

Recent progress in electronics, computers, sensors and actuators has suggested that practical active control systems capable of damping detrimental combustion instabilities in rocket motors could be developed. Such a control system generally consists of a sensor that monitors the rocket motor performance, a controller that analyzes the sensor's output and uses it to generate a signal that drives an actuator that modifies the system's performance. The development of such an active control system and an understanding of the fundamental processes that govern its operation are the objectives of this investigation.

Rayleigh's criterion indicates that acoustic oscillations are driven or suppressed when heat is added in phase or out of phase with the pressure oscillations, respectively. This suggests that combustion instability oscillations could be suppressed if effective means for generating heat addition oscillations that are out of phase with the combustor pressure oscillations could be developed. Active control of combustion instabilities investigated to date[1] utilized a time domain control approach and focused on the damping of combustion instabilities consisting of the fundamental longitudinal mode or, at most, a combination of low frequency longitudinal modes. Moreover, the application of these methods required apriori knowledge of the characteristics of the unstable modes. In reality, the characteristics of the excited instability are not known, however, in advance. Furthermore, the characteristics of the instability (e.g., its modal content) often change with time in response to changes in, for example, propellant surface diameter in a solid rocket or motor operating conditions.

A new approach for active control of rocket motor combustion instabilities that overcomes the limitations of previous active control systems has been developed under this program. The developed system consists of a sensor (a pressure transducer) that monitors the performance of the combustor, an observer that analyzes the sensor's output and determines the frequencies and amplitudes of the excited combustor oscillations in real time and a "controller" that introduces appropriate phase shifts and amplitude gains into the data provided by the observer prior to sending it to an actuator that controls the operation of a periodic fuel injection system. The novel components of this systems are its observer and "controller" whose tasks are to identify the characteristics of the instability in real time and provide the necessary phase shifts and gains to the oscillating combustor modes, respectively. The "controller's" output is then used to drive a novel actuator whose task is to produce an oscillatory fuel injection rate into the combustor that will produce combustion process heat release oscillations that are out of phase with the excited combustor oscillations.

The performance of the developed active control method were initially, investigated theoretically assuming that the flow in the combustor is described by the one dimensional, nonlinear, Euler equations. The driving of the instability by the combustion process was modeled by means of a simple linear feedback between the pressure and combustion heat addition oscillations. The combustor model was "equipped" with the developed active control system and used to investigate the its effectiveness. Numerical simulations showed that the developed active control system can damp a variety of instabilities including, for example, oscillations with amplitude as large as 25% of the mean pressure in the combustor, which were damped out within a few milliseconds of "engaging" the controller[2]

Continued theoretical studies led to the development of a more advanced numerical scheme for the unsteady reacting flow equations in unstable rocket motors. It contains a new approach for proper numerical representation of the boundary conditions at the injector face and nozzle entrance. Since the flow in the investigated combustor is one dimensional, a mixing model that can be incorporated into a one dimensional combustion model was developed. It accounts for the mixing of the fuel and air as well as the mixing of hot combustion products with the reactants. Finally, a combustion heat release model that is based upon the Arrhenius law is used to determine the reaction rate of the mixed reactants.

An important part of this research program is the development of an experimental setup that will be used to investigate the developed active control system. A block diagram of the laboratory setup is shown in Fig. 1. The active control system uses a piezoelectric pressure transducer to "sense" the combustor pressure oscillations. The measured pressure signal is fed to a Digital Signal Processor (DSP) TX320C40 DSP via an analog input board. The digital control signal that

[1] Gutmark, E., Wilson, K. J., Parr, T. P. and Schadow, K. C., Feedback Control of Multi-Mode Combustion Instability, AIAA Paper 92-0778, 30th Aerospace Sciences Jan. 1992, Reno, Nevada.

[2] Neumeier Y. and Zinn B. T., "Active Control of Combustion Instabilities Using Real Time Identification of Unstable Combustor Modes. Paper in preparation.

is generated by the DSP is converted into an analog signal and fed to the actuator. The host computer will accommodate an as yet to be developed algorithm that will determine the optimal gain and phase shift for the controller on the DSP. The DSP and the I/O interface are integrated on a single DATA TRANSLATION 3801-G board that is installed in a host IBM PC personal computer.
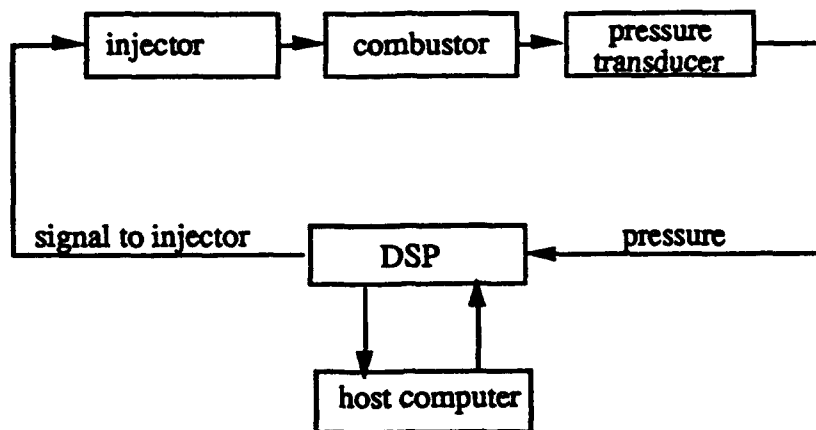
Figure 1: A Schematic of the active control system

The experimental gas rocket developed under this program is shown in Fig. 2. It consists of a reactants feed system, a combustor section with windows for observations and optical diagnostics, a nozzle and an exhaust system. To provide needed cooling, the combustor is submersed in a tank with running water. Also, the combustor length can be changed by adding or subtracting sections having the same diameter, which will provide capabilities for exciting instabilities with different frequencies. Since this combustor has a large length to diameter ratio, it is expected that axial mode instabilities with high and low frequencies will be excited in the system when short and long combustor lengths will be tested, respectively. This will provide an opportunity to investigate the effectiveness of the developed active control system in the damping of low and high frequency instabilities. The active control of high frequency instabilities will determine the frequency limit of the developed control system.
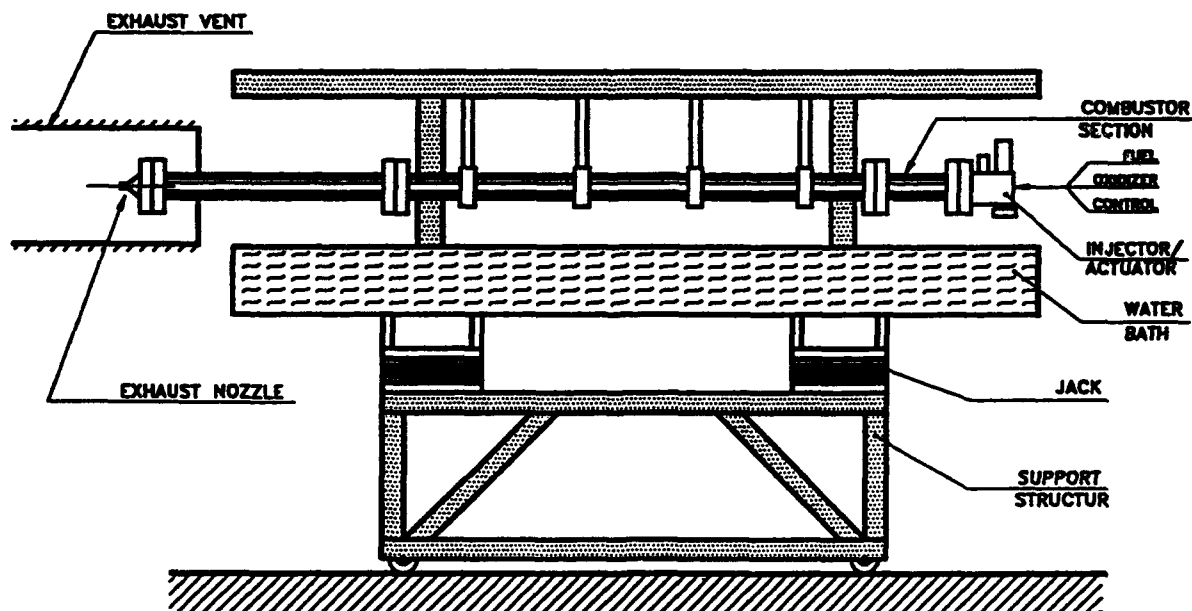
Figure 2: A schematic of the developed gas rocket setup

The developed gas rocket propellants feed system is shown in Fig. 3. It consists of one oxidizer (i.e., air) injector and two fuel injectors. The primary and secondary fuel injectors supply the combustor with specified steady and oscillatory fuel flow rates, respectively. The secondary fuel flow rate is modulated by use of a recently developed "magnetostrictive" actuator[3]. It oscillates a tapered needle up and down, producing a periodic blockage of a cross sectional area of a secondary fuel orifice. The oxidizer and fuel streams are injected at approximately 45 degrees angle and axially, respectively, into a small volume upstream of the injector plate where they mix prior to entering the combustor through the injector plate orifices. The angles and dimensions of the orifices in the injector plate have been chosen to generate recirculation zones downstream of the injector plate where the combustion process will be stabilized. In this feed system design, the main fuel flow rate is controlled by the size of the upstream orifice while the secondary fuel flow rate is regulated by the "mean" position of the oscillating actuator needle. The oscillatory needle motion is controlled by an "Etrema" actuator consisting of a Terfenol-D rod that changes its length in response to changes in magnetic field intensity[4]. This recently developed actuator is capable of providing relatively large displacement (e.g., 100 μm) in a very short response time (e.g., .2 msec.)
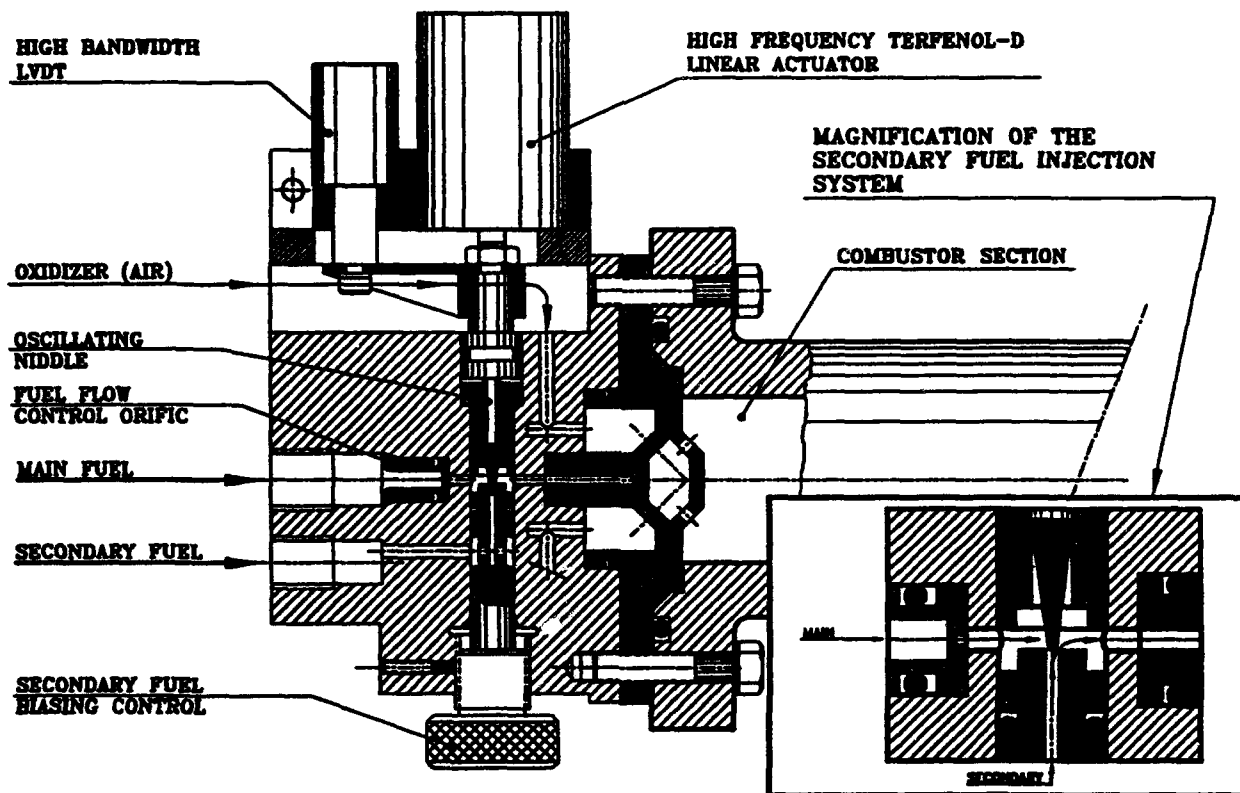
Figure 3: A schematic of the developed air and fuel feed system

[3] Savage, H. T., Clark, A. E. and Powers, J. M., Magnetomechanical Coupling and ΔE Effect in Highly Magnetostrictive Rare Earth-Fe$_2$ Compounds, IEEE Transactions on Magnetics, Vol. Mag-11, No. 5, Sep. 1975.

[4] Savage, H. T., Abbundi, R. and Clark, A. E., Permeability, Magnetomechanical Coupling and Magnetostriction in Grain-oriented Rare earth-iron Alloys.

FUNDAMENTALS OF ACOUSTIC INSTABILITIES IN LIQUID-PROPELLANT ROCKETS

Principal Investigator : F. A. Williams

Department of Applied Mechanics and Engineering Sciences
University of California at San Diego
La Jolla, CA 92093-0310

Summary/Overview

The objective of this research is to improve understanding of the mechanisms by which flow, mixing and combustion process are coupled to acoustic fields in liquid-propellant rocket motors. Particular attention has been focused on analyses of amplification mechanisms coupled with finite-rate chemical reactions by use of activation-energy asymptotics and other asymptotic methods. In addition, a simplified calculation method of the acoustic eigenmodes with spatial variations of the density and sound speed was developed.

Technical Discussion

The following discussion concerns the two advances indicated above. Future works will apply similar methods to different types of flamelets and to different types of motor-geometry nonhomogeneities. In particular, droplet combustion, with or without forced convection and supercriticality, will be considered.

Amplification Mechanisms Coupled with Finite-Rate Chemistry

Many different processes are responsible for amplification of acoustic oscillations in liquid-propellant rockets, and asymptotic analyses of these processes can help in assessing combustion instabilities. It is the intent of the present investigation to analyze a number of these processes. One such process is the strained planar diffusion flame considered here [1, 2]. Some of the results on acoustic pressure response of this type of flame were reported last year, and more detailed and extended results will be available as a publication. The analysis is extended to acoustic velocity response in order to complement the analysis of the acoustic pressure response.

Previous studies of diffusion-flame response postulated infinite chemical reaction rates (the Burke-Schumann approximation), while the present works take into account the influences of finite-rate chemistry which is the dominant nonlinear process in flows in liquid-propellant rocket engines. The results demonstrate that the high sensitivity of the chemical reaction rates to temperature fluctuations can underlie important amplification mechanisms. As an initial simplification, a one-step, irreversible Arrhenius-type chemical reaction rate is employed, and a gaseous counterflow diffusion flame is adopted to represent flamelets subjected to nonuniform flow fields caused by turbulent fluctuations. The analyses were performed by activation-energy asymptotics. The acoustic response of the flame, obtained from the linear analysis, is found to be determined by two mechanisms, namely, oscillations of the reaction sheet induced by acoustic-produced fluctuations of the reaction rate, and oscillations of the field variables produced by the transport-zone response.

The results of analyses on acoustic pressure response can be summarized in Fig. 1 showing the boundaries of neutral amplification in $Da - \omega$ plane where the Damköhler number Da and the acoustic frequency ω are normalized by the extinction Damköhler number and the strain rate exerted on the flame. The corner of large Da (near-equilibrium limit) and small ω corresponds to attenuation, while all the rest of the $Da - \omega$ plane corresponds to much stronger amplification, especially near extinction. The attenuation found in the region of large Da and small ω arises from the reduction in the rate of mass transfer associated with compression of the flow field by the acoustic pressure. As the acoustic pressure increases, the density increases in phase, and the resulting diminished axial velocity reduces the mass flux into the reaction sheet, thereby producing an attenuation effect. As ω increases the attenuation effect associated with compression of the flow field diminishes because the compression effect is lessened by unsteady accumulation. Especially in the limit of $\omega \to \infty$, the convective and diffusive transport effects fail to respond to pressure fluctuations, and the flame response can be solely determined by isentropic thermodynamic relations since they are the only processes whose relaxation times are still shorter than the acoustic time scale. Therefore, the region of large Da and ω corresponds to small amplification which arise mainly from in-phase oscillations of the mass diffusivities with acoustic pressure. As the flame approaches extinction, the flame response is dominated by acoustic-produced oscillation of the reaction rate. Since the reaction rate tends to be in phase with temperature oscillations that is, in turn, in phase with acoustic pressure oscillations, the overall response always corresponds to amplification independent of the acoustic oscillation frequency. Moreover, an extremely large sensitivity of the reaction rate to temperature perturbations yields an order-of-magnitude increase in the rate of amplification.

Extension of analysis to acoustic velocity response assumes that effects of acoustic velocity oscillation occurs through oscillation of the strain rate applied to the flame. The results show that the flame response is controlled mainly by two effects: (a) the response of the convective mass flux into the reaction sheet, which is directly related to the flow-field variation applied at the boundary, and (b) the response of the reaction sheet to adjust the residence time to that of the finite-rate chemistry. For flames near equilibrium, the former effect tends to be dominant, so that the response of the net heat release is in phase with the strain-rate oscillation. However, the finite-rate chemistry effect overtakes the fluid-dynamic effect near extinction. A typical response behavior in this limit is shown in Fig. 2 in terms of the real part of the nondimensional reaction-sheet oscillation $Re(\bar{\eta}_f)$. During a period of strain-rate oscillation, an increase in strain rate results in reduced residence time in the reaction zone, thereby reducing the reaction rate. In order to compensate for the reduced reactivity, the reaction sheet migrates toward the stagnation plane at which the local convective flux normal to the reaction sheet is much smaller, thereby resulting in negative values of $Re(\bar{\eta}_f)$. The net heat-release response of the near-extinction flame becomes out of phase with the strain-rate oscillation. Although many flame response behaviors to acoustic velocity oscillations can be explained by these two basic response mechanisms, boundaries of neutral amplification cannot be obtained from this analysis only. Since an acoustic velocity is $\pi/2$ ahead of or behind the acoustic pressure oscillation and cannot be uniquely determined unless the whole acoustic pressure field is known, a detailed inviscid calculation which relates the acoustic pressure with the unsteady strain rate must be performed in each case in order to calculate the contribution of the velocity effect to the acoustic amplification.

Acoustic Eigenmodes in Nonuniform Acoustic Media

A recent paper by Clavin et al. [3] demonstrated that nonlinear acoustic instability coupled with stochastic linear growth could lead to complicated evolution patterns of the acoustic pressure amplitude. To continue further theoretical investigation of the stochastic effects on nonlinear instability,

it is desirable to formulate nonlinear acoustic instability based on a formal singular perturbation method, since currently available nonlinear formulations are intended to be integrated numerically. In order to construct a systematic nonlinear formulation, we focus our attention to the acoustic eigenmodes in liquid-propellant rockets, previously given by a Helmholtz equation arising in a uniform acoustic medium. Because of the presence of combustion by which an order-of magnitude increase in temperature can occur, effects of spatial variations of molecular properties, such as density and sound speed, on the eigenmodes needs to be considered [4]. The wave equation with variable molecular properties is treated by a variational method which yields the acoustic oscillation frequencies and the corresponding acoustic mode shapes. For a given eigenmode, the variational principle states that the eigenvalue, that is the square of the nondimensional acoustic frequency, is the ratio of the kinetic acoustic energy to the static acoustic energy, and the eigenfunction is the minimizing function of the ratio. As a simplified model for liquid-propellant rocket engines, it is assumed that variation of the acoustic medium occurs dominantly in the longitudinal direction. In this case, the functional shapes of the transverse modes are found to be independent of the longitudinal variation, so that only the variations in the longitudinal direction need to be considered.

A sample calculation is made with the assumptions that the acoustic medium is an ideal-gas mixture and that a monotonic increase of the gas temperature is represented by the first longitudinal harmonic function $\cos(\pi z/L)$. The results exhibit two important characteristic changes of the acoustic modes. In order to minimize the kinetic acoustic energy with respect to the static acoustic energy, variations of the acoustic pressure gradients are found to be larger in the higher density region. As a consequence, Fig. 3 shows that the nodal points of the longitudinal profiles are significantly shifted toward the injector, which can provide useful information to help in determining the lengths of baffles or of acoustic liners. For the case considered in here, the length of the baffle or acoustic liner could be recommended to be about 25 % of the chamber length. The longitudinal density variation is also found to play a role in the acoustic energy transfer mechanism by which the kinetic acoustic energy of the lower mode is transfered to the adjacent higher mode. It is seen from Table 1 that the eigenvalues of the pure transverse modes have substantially larger reductions than those of the combined modes since the pure tanserve modes only lose their kinetic acoustic energy to the adjacent combined modes. The decreases of the eigenvalues in the pure transverse modes sometimes exceed more than one half of the corresponding Helmholtz eigenvalues, while the decreases in the combined modes ranges only to about 20 %. It is therefore suggested that the linear or nonlinear analyses in which the Helmholtz eigenfunctions are used as the basis functions may have significant errors for the pure transverse modes that are more frequently observed in engine tests than the combined modes.

References

[1] J. S. Kim and F. A. Williams, Contribution of Strained Diffusion Flames to Acoustic Pressure Response, to appear in *Combustion and Flame* (1994).

[2] H. G. Im, C. K. Law, J. S. Kim, and F. A. Williams, Response of Counterflow Diffusion Flames to Oscillating Strain Rates, to appear in *Combustion and Flame* (1994).

[3] P. Clavin, J. S. Kim and F. A. Williams, Turbulence-Induced Noise Effects on High-Frequency Combustion Instabilities, *Combustion Science and Technology*, **96**, 61-84 (1994).

[4] J. S. Kim and F. A. Williams, On the Eigenmodes of Acoustic Pressure in Liquid-Propellant Rocket Engines, CECR Report No. 94-02, University of California at San Diego, La Jolla, CA, 1994, also to be submitted to *Combustion and Flame*.
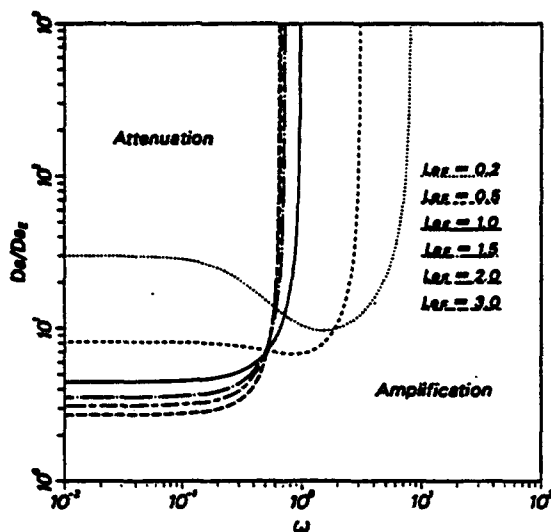
Figure 1. Response of amplification and attenuation in the $Da-\omega$ plane for various Lewis number.
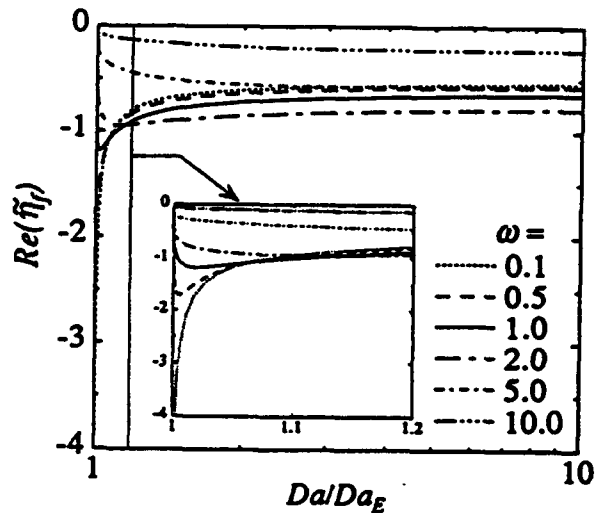
Figure 2. Real parts of the magnitude of nondimensional reaction-sheet oscillations as functions of Damköhler number for various frequencies.
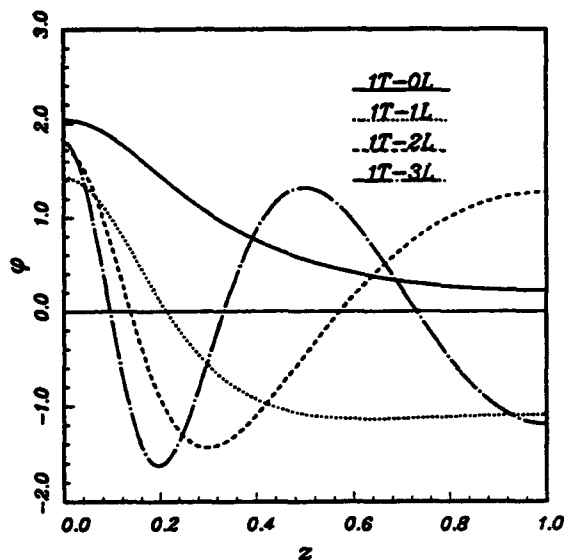
Figure 3. Longitudinal profiles of the pure and combined modes of the first tangential acoustics, 1T-0L, 1T-1L, 1T-2L, and 1T-3L.

	1T	2T	1R	3T
	8.566	17.267	24.219	27.933
0L	13.562	37.315	58.728	70.600
	21.624	43.856	58.228	65.187
1L	23.431	47.185	68.597	80.470
	41.288	66.723	90.948	102.99
2L	53.040	76.793	98.206	110.08
	77.511	98.692	120.23	133.46
3L	102.39	126.14	147.55	159.43

Table 1. Comparison of the eigenvalues with and without a variable density profile. In each mode, the large number corresponds to the eigenvalue given by the Helmholtz equation, whereas the smaller number corresponds to the eigenvalue obtained by the variational method with the variable density profile.

31

MODELING LIQUID JET ATOMIZATION PROCESSES

Stephen D. Heister

School of Aeronautics and Astronautics
Purdue University
W. Lafayette, IN 47907

Summary/Overview

The atomization of liquid jets is a fundamental problem of particular interest in determining the performance and combustion stability of liquid rocket engines. This research effort is focused on a new analytic treatment of this free surface flow utilizing Boundary Element Methods (BEMs). During the past year, this research has made two important advances. A model capable of performing nonlinear jet distortions in the presence of the orifice has been developed and verified. This model is capable of calculating jet behavior *beyond* the droplet pinchoff event. The model has been applied to a dripping flow. Results indicate that both chaotic and bifurcated behavior of droplet shedding can be predicted using this tool.

The second advancement involves a coupled nonlinear calculation of an infinite jet breaking up under the influence of both surface tension and gas-phase pressure forces in the wind-induced regime. The model predicts substantial deviations from linear predictions due to nonlinear effects. Droplet size predictions agree with the limited measurements which indicate the presence of a "main" and "satellite" droplet formed under most conditions. In addition, the model provides significant improvements to the linear theories associated with the breakup length of the jet.

Technical Discussion

Boundary Element Model for the Finite Liquid Jet

Figure 1 highlights the axisymmetric computational domain and boundary conditions employed for this problem. Potential flow is presumed in the liquid domain, so the flow within the jet can be described with a velocity potential satisfying Laplace's equation ($\nabla^2\phi = 0$). A hybrid scheme[1] has been developed whereby nodes on the free surface are "tracked" at the local surface velocity, while nodes at the inflow remain fixed for all times. On the free surface, flow kinematics require:

$$\frac{\partial\phi}{\partial r} = \frac{\partial\phi}{\partial s}sin(\beta) + qcos(\beta) = \frac{Dr}{dt} \qquad \frac{\partial\phi}{\partial z} = \frac{\partial\phi}{\partial s}cos(\beta) - qsin(\beta) = \frac{Dz}{dt} \qquad (1)$$

where β is the local wave slope and $\partial\phi/\partial s$ and q are velocities tangential and normal to the local surface, respectively. The tangential velocity is calculated using 5-point centered differences on ϕ, except near the orifice, where 3-point formulas are employed, while the normal velocity component is determined from the solution of Laplace's equation. The local wave slope, β, is calculated following the formulation of Medina[2].

We obtain a means of updating ϕ on the surface boundary by considering the unsteady Bernoulli relation. For our problem, after transforming the time derivative of ϕ from Eulerian to Lagrangian representation, the dimensionless representation of this equation is:

$$\frac{D\phi}{dt} = \frac{1}{2}(\nabla\phi)^2 - \frac{\kappa}{We} + \frac{Bo}{We}z \qquad (2)$$

where $We = (\rho v^2 a)/\sigma$ is the Weber number, $Bo = (\rho g a^2)/\sigma$ is the Bond number, and κ represents the local surface curvature. Here ρ is fluid density, a is the radius of the orifice, σ is the fluid surface tension, and g is the acceleration due to gravity. The local curvature can be expressed in terms of first and second derivatives of r and z with respect to the distance along the boundary (s). These derivatives are calculated using centered difference formulas.

Equations 1 and 2 are integrated using a fourth-order Runge-Kutta method. We employ a method to dynamically modify the time step based on the surface velocities so that the time step is decreased if the velocities become too large. In our method, no node is allowed to move more than a specified fraction of the grid spacing every time step. The model includes a smoothing routine to eliminate "zig-zag" instabilities which can appear during long time integrations[3]. In addition, surface remeshing is employed at each time step to insure roughly equal node spacing along the free surface. Cubic splines are used to describe surface geometry between nodes for the purpose of remeshing. Note that the number of nodes changes dynamically due to the alternating growth and "pinch-off" processes occurring during the unsteady simulation.

Results - Finite Length Liquid Jet

At low velocities, the breakup of a liquid jet occurs in the "dripping flow" regime. In this regime, the gas around the jet can be neglected, surface tension and gravity are the important parameters, and the droplet diameters are larger than the orifice diameter. Since the jet breakup occurs near the orifice, we can use this flow to validate the orifice treatment in the present model. Wu and Schelly present experimental results on the effects of surface tension and temperature on the dynamics of a dripping faucet[4]. Results indicate chaotic and bifurcated (bimodal) shedding frequencies over the range $0.625 < We < 1.05$ for the case where $Bo = 0.204$.

Figure 2 presents our calculation of a typical time history for the droplet shedding process. As a droplet is shed, a disturbance is sent upstream. The interaction of this disturbance with the orifice has been found to be responsible for the chaotic/bifurcated behavior observed at low We values. Results indicate that the finite-length treatment will be fruitful as we extend the model to the atomization regime in the coming year.

Figure 3 shows the droplet size spectrum as a function of the Weber number for conditions consistent with Wu and Schelly's experiment. We note the chaotic/bifurcation behavior over a range $0.4 < We < 0.9$ which is slightly lower than Wu and Schelly's result due to the stabilizing influence of viscosity in the actual measurements. However, the general character of the map is reproduced using the BEM calculation. As We (jet velocity) is increased, the jet breakup point reaches a location such that this disturbance has negligible influence on the orifice and the chaotic/bifurcated behavior vanishes. Above Weber numbers of 1.4, the model predicts a dramatic increase in jet breakup length, signaling the start of the Rayleigh breakup regime.

Nonlinear Model of Jet Atomization in Wind-Induced Regime

The "wind-induced" regime is characterized as a range of jet velocities (or Weber numbers) in which the breakup of the liquid jet is controlled primarily by surface tension and aerodynamic interactions with the surrounding gas. For relatively low speed jets, the most unstable wavelengths are longer than the jet radius and surface tension acts as a destabilizing factor. This region is typically referred to as the "first wind-induced" regime. As jet velocity (or Weber number) is increased, the most unstable wavelength decreases to a value less than the jet radius, at which point, surface tension becomes a stabilizing influence and aerodynamic interactions provide the sole destabilizing effect (second wind-induced regime).

For this calculation[5], we presume that finite disturbances, which are periodic in nature, are developed well downstream of the orifice so that an infinite wavetrain accurately represents the evolution of the jet. Under these assumptions, the domain for the calculation (and associated boundary conditions) are summarized in Fig. 4. Here, ϕ_g represents the velocity potential in the gas phase. The coordinate system is assumed to move with the liquid, and nodes are placed along the surface, along vertical planes at both ends of the wave, and along a horizontal surface (in the gas) far from the gas/liquid interface. Liquid nodes are denoted "O", while gas nodes are denoted "X" in Fig. 4.

At the interface, the Bernoulli conditions may be written:

$$\frac{D\phi}{dt} = \frac{1}{2}(\nabla\phi)^2 - \frac{\kappa}{We} - p_g \qquad\qquad \epsilon\frac{\partial\phi_g}{\partial t} = -\frac{\epsilon}{2}(\nabla\phi_g)^2 - p_g \qquad (3)$$

where p_g is the gas pressure and ϵ is the ratio of gas-to-liquid densities. We have validated a stable, accurate procedure capable of treating the coupled set of nonlinear conditions (Eqs. 1 and 3) which hold at the interface. We begin by integrating the first half of Eq. 3 to obtain new values of ϕ on the free surface. Solving Laplace's equation with this boundary condition gives the nodal velocities which in turn serve as

boundary conditions for the solution of $\nabla^2 \phi_s = 0$ for values of ϕ_s on the surface. The gas pressure is then obtained from the second half of Eq. 3 by using the current ϕ_s values to evaluate the time derivative. Nodes are moved to new locations via integration of Eq. 1.

Results - Wind-Induced Regime

Figures 5-6 summarize typical results generated using the model. In Fig. 5, the nonlinear distortion of the jet surface under conditions consistent with the first wind-induced regime is illustrated at various times in the breakup process. This illustration depicts both main and satellite droplets (as noted by other researchers[6-7] in the Rayleigh regime) forming under the selected wave number of 0.84. We calculate an overall breakup time of 267.1 as compared to a value of 238.5 as predicted by Weber[8] which indicates that the BEM calculation predicts a greater breakup length than that of Weber. Since it is well known[9] that Weber's analysis tends to overpredict the aerodynamic effect on instability, we see that the nonlinear BEM analysis provides a correction (in the proper direction) to this linear result.

In addition, we have found that predictions of droplet sizes (not shown) are in good agreement with the limited experimental data[6] in this regime. Finally, the model is currently being compared to experimental measurements of jet breakup length[9]. Preliminary results (not shown) indicate a substantial improvement over the linear theory which tends to underpredict this parameter.

Figure 6 presents the nonlinear evolution of the jet surface for conditions consistent with the second wind-induced regime. In this case, the jet surface begins to take on a "spike-shaped" appearance with a small fluid torus at the tip of the spike. As the spike becomes more pronounced, we expect flow separation on the aft portion leading to a net pressure force (exerted by the gas) in the direction of the gas flow. This force will aid in shearing the torus (and a portion of the spike) off from the main body of the jet. Droplet sizes consistent with this process will depend on the stability of the fluid sheared from the top of the spike. It is likely that secondary collisions and coalescence are important in this regime due to the close proximity of the satellite fluid to the main body of the jet.

References

1. Hilbing, J.H., and Heister, S.D., "A Boundary Element Method for Liquid Jet Atomization Processes", ILASS-94 Proceedings, 1994.

2. Medina, D. E., "On Droplets and Boundary Elements", Cornell University, FDA-89-12, 1989.

3. Longuet-Higgins, M. S., and Cokelet, E. D., "The deformation of steep surface waves on water. I. A numerical method of computation," *Proc. R. Soc. Lond. A*, 350, pp. 1-26, 1976.

4. Wu, X., and Schelly, Z. A., "The Effects of Surface Tension and Temperature on the Nonlinear Dynamics of the Dripping Faucet", *Physics D*, V40, pp 433-443, 1989.

5. Spangler, C.A.,and Heister, S.D., "Nonlinear Modeling of Jet Atomization Processes in the Wind-Induced Regime", ILASS-94 Proceedings, 1994.

6. Rutland, D.F., and Jameson, G.J., "Theoretical Prediction of the Size of Drops Formed in the Breakup of Capillary Jets", *Chem. Eng. Science*, V 25 p. 1689, 1970.

7. Mansour, N.N., and Lundgren, T.S., "Satellite Formation in Capillary Jet Breakup", *Phys. Fluids A*, V 2, No. 7, pg. 1141, 1990.

8. Weber, C., "On the Breakdown of a Fluid Jet", *Z.A.M.P.*, V 11, 1931.

9. Sterling, A.M., and Sleicher, C.A., "The Instability of Capillary Jets", *J. Fluid Mech.*, V 68, p. 477, 1975.
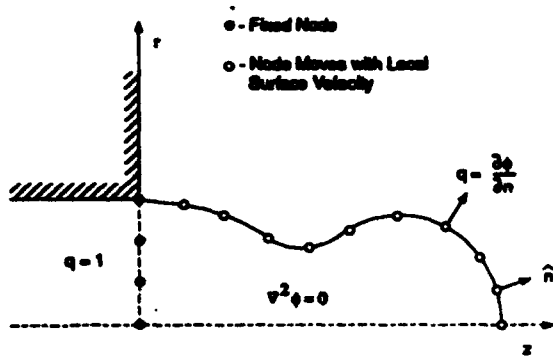
Figure 1: Schematic of Computational Domain Finite-Length Jet Model

Figure 4: Computational Domain for Wind-Induced Regime Model

Figure 2: Typical Droplet Shedding History (at equal time intervals) Indicating Interactions with Orifice, $We = 1.45$, Bo=0.204
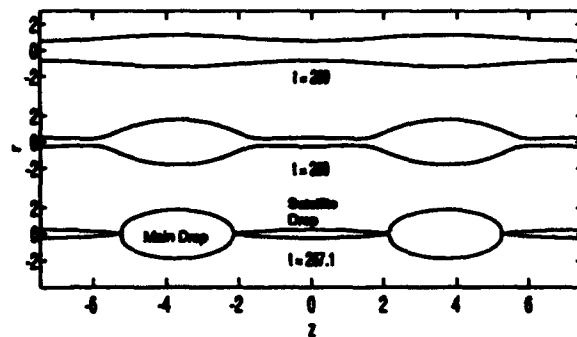
Figure 5: Evolution of Jet Surface in 1st Wind-Induced Regime: $We = 500$, k=0.84, and $\epsilon = 0.001$

Figure 3: Droplet Size Spectrum Depicting Chaotic and Bimodal Behavior at Selected We Values (Bo=0.204)
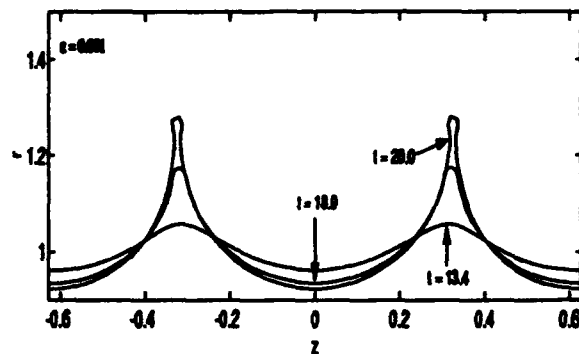
Figure 6: Evolution of Jet Surface in 2nd Wind-Induced Regime: $We = 15,000$, and k=10.0

35

THEORETICAL INVESTIGATION OF LIQUID-PROPELLANT DROPLET COMBUSTION AND DYNAMICS AT SUPERCRITICAL CONDITIONS

Vigor Yang
Department of Mechanical Engineering
The Pennsylvania State University
University Park, PA 16802

SUMMARY/OVERVIEW

A focused research program is conducted to investigate liquid-propellant droplet combustion in supercritical forced-convective environments. The purpose is to establish a solid theoretical basis for enhancing the understanding of liquid-propellant droplet vaporization, combustion, and dynamics at supercritical conditions, with emphasis placed on the effect of forced convection. A variety of liquid propellants and propellant simulants, including hydrocarbons and cryogenics, at both steady and oscillatory conditions are treated systematically. The formulation is based on the full conservation equations for both gas and liquid phases, and accommodates variable properties and finite-rate chemical kinetics. Full account is taken of thermodynamic non-idealities and transport anomalies at high pressures, as well as liquid-vapor phase equilibria for multi-component mixtures. Because the model allows solutions from first principles, a systematic examination of droplet behavior over wide ranges of temperature and pressure is made possible. Results not only enhance the basic understanding of the problem, but also serve as a basis for establishing droplet vaporization and combustion correlations for the study of liquid rocket engine combustion, performance, and stability.

TECHNICAL DISCUSSION

Liquid-droplet vaporization and combustion in supercritical environments have long been matters of serious practical concern in combustion technology, mainly due to the necessity of developing high-pressure combustion devices such as liquid-propellant rocket motors and diesel engines. Although several studies have been devoted to this problem, a number of fundamental issues regarding the attainability of critical conditions and droplet gasification and burning mechanisms at high pressures remain unresolved. Most of the existing theories are based on certain assumptions and empirical correlations that are extrapolated from atmospherical conditions, with their validity for high-pressure applications subject to clarification. Furthermore, no unified analysis of the entire droplet history, in particular the transition from the subcritical to supercritical state, was made. Almost all of the models for supercritical combustion have assumed *a priori* that the droplet reaches its critical state instantaneously upon introduction into a supercritical environment. Neither initial heatup transients nor nonuniformities of liquid-phase properties are considered. In addition, the treatment of transport properties and thermodynamic nonidealities is overly simplified to yield complete information. A recent review of this subject is given by Hsieh et al.[1].

The physical model treated here is an isolated liquid-propellant droplet (or an array of droplets) when suddenly confronted with a supercritical fluid flow. The initial temperature of

the droplet is subcritical. As the droplet is heated by the ambient gas, its temperature increases and finally exceeds the critical point. Several important aspects must be noted during this process. First, when the droplet surface approaches its thermodynamic critical state, the difference in densities of gas and liquid phases becomes smaller. The characteristic times of the transport processes near the droplet surface in both phases have the same order of magnitude. Therefore, the transient effects in the gas phase are as important as those in the liquid phase, and the quasi-steady condition may never be reached during the lifetime of the droplet. Second, the latent heat of vaporization decreases to zero at the critical point. Conventional low-pressure models may erroneously predict the vaporization rate if the variation of latent heat with pressure is not properly taken into account. In addition, if the droplet is moving, the behavior of liquid deformation and breakup may be altered considerably due to the diminished value of surface tension. Third, at high pressures, effects of thermodynamic non-idealities and property variations play decisive roles in determining transport properties and interfacial thermodynamic relationships. The solubility of the ambient gas in the liquid phase increases with pressure, and the classical Raoult's law for ideal mixtures is not applicable for phase-equilibrium analysis. One must develop a more comprehensive model for vapor-liquid interface conditions in terms of fugacity. Finally, when the droplet exceeds its critical state, it essentially becomes a "puff" of dense fluid. The entire field becomes a continuous medium, and no distinct interfacial boundary can be identified.

The primary purpose of this research project is to establish a theoretical framework within which various issues of supercritical droplet vaporization and combustion can be addressed systematically. Specific program objects are

1. to establish a complete thermodynamic and transport analysis for evaluating propellant thermophysical properties over wide ranges of temperature and pressure,
2. to study liquid-propellant droplet vaporization, combustion, and dynamics in a steady convective environment at supercritical conditions, and
3. to investigate dynamic responses of droplet vaporization and combustion to ambient flow oscillations.

A brief summary of the work scope and progress made to date for these tasks is given below.

1. Evaluation of Fluid Thermophysical Properties

Thermophysical properties, including thermodynamic and transport properties, play decisive roles in determining the droplet behavior [2,3]. Unfortunately, no complete molecular theories and evaluation techniques are currently available for thermophysical properties of constituent species as well as mixtures at high pressures, especially in the near-critical regime in which thermodynamic anomalies occur (a phenomenon referred to as critical enhancement). During this report period, efforts have been continuously made to assess a variety of property evaluation schemes and constitutive relations for both hydrocarbon and cryogenic propellants at high pressures. Generalized correlations have been established and applied to the pressure and temperature ranges of practical engine operations. In particular, asymptotic theories based on scaled equations of state and universal power laws have been incorporated in the treatment of critical phenomenon by considering the long-wavelength fluctuations of the order parameter and of other relevant hydrodynamic modes of the fluid. This technique results in the establishment of a unified scheme for evaluating fluid thermophysical properties over the entire thermodynamic state, from compressed-liquid to dilute-gas state.

37

2. Supercritical Droplet Vaporization and Combustion in Steady Convective Environments

A comprehensive theoretical analysis has been established to investigate droplet vaporization and combustion at supercritical conditions. Calculations have been carried out for hydrocarbon and liquid-oxygen (LOX) droplet vaporization and combustion under various ambient conditions. The pressure varied from one to 250 atm, and the temperature from 500 to 2000 K. The initial droplet diameter ranged from 50 to 300 μm. The effect of pressure on droplet behavior was investigated in detail. Results from the parametric study are used to develop correlations for droplet vaporization rates in terms of initial droplet diameter and ambient flow conditions. This information can be easily incorporated into existing spray codes for predicting liquid-propellant rocket engine performance and stability. Specific processes treated in this task are

1. Complete time history of droplet gasification, including the transition from the subcritical to supercritical state,
2. ignition and flame development,
3. droplet deformation, stripping, and shattering, and
4. dynamic loading (i.e., drag and lift forces) on droplets.

Figure 1. shows a typical set of results for the combustion of LOX droplet in a supercritical hydrogen flow, in which the instantaneous temperature contours in the field are presented at six different times. The droplet Reynolds number and ambient pressure are 80 and 80 atm, respectively. Ignition always occurs near the downstream edge of the droplet. The flame then propagates toward the centerline, and simultaneously tears the gasified oxygen into two fragments, with the downstream piece blown farther away from the flame zone.

3. Dynamic Responses of Droplet Vaporization and Combustion to Ambient Flow Oscillations

The dynamic responses of supercritical droplet vaporization and combustion to ambient flow oscillations are examined. The analysis extends the droplet combustion model established for steady environments, and accommodates periodic pressure and velocity fluctuations in the ambience. The oscillatory characteristics of droplet gasification and burning mechanisms are studied in detail over a broad range of pressure. Results indicate that the droplet response functions (both pressure- and velocity-coupled responses) increase progressively with pressure due to reduced thermal inertia at high pressures, as shown in Fig. 2. Furthermore, a rapid amplification of droplet vaporization/combustion response occurs when the droplet surface reaches its critical mixing point. This phenomenon may be attributed to the strong sensitivities of latent heat of vaporization and fluid transport properties to small perturbations near the critical point. Correlations of droplet response functions are also established in terms of droplet and oscillatory flow properties, and can be used effectively in liquid rocket engine combustion instability analysis.

REFERENCES

[1] Hsieh, K. C., Shuen, J. S., and Yang, V. (1991). Droplet Vaporization in High-Pressure Environment. I: Near Critical Conditions. *Combustion Science and Technology*, 76, 111.

[2] Shuen, J. S., Yang, V., and Hsiao, G. C. (1992). Combustion of Liquid-Fuel Droplets at Supercritical Conditions. *Combustion and Flame*, 89, 299.

[3]   Yang, V., Lin, N. N., and Shuen, J. S. (1994). Vaporization of Liquid Oxygen (LOX) Droplets in Supercritical Hydrogen Environments. To appear in *Combustion Science and Technology*.

[4]   Hsiao, G. C., Yang, V., and Shuen, J. S. (1994). Pressure-Coupled Vaporization Response of Liquid Fuel Droplets at High Pressures.   Submitted to *Journal of Propulsion and Power*.
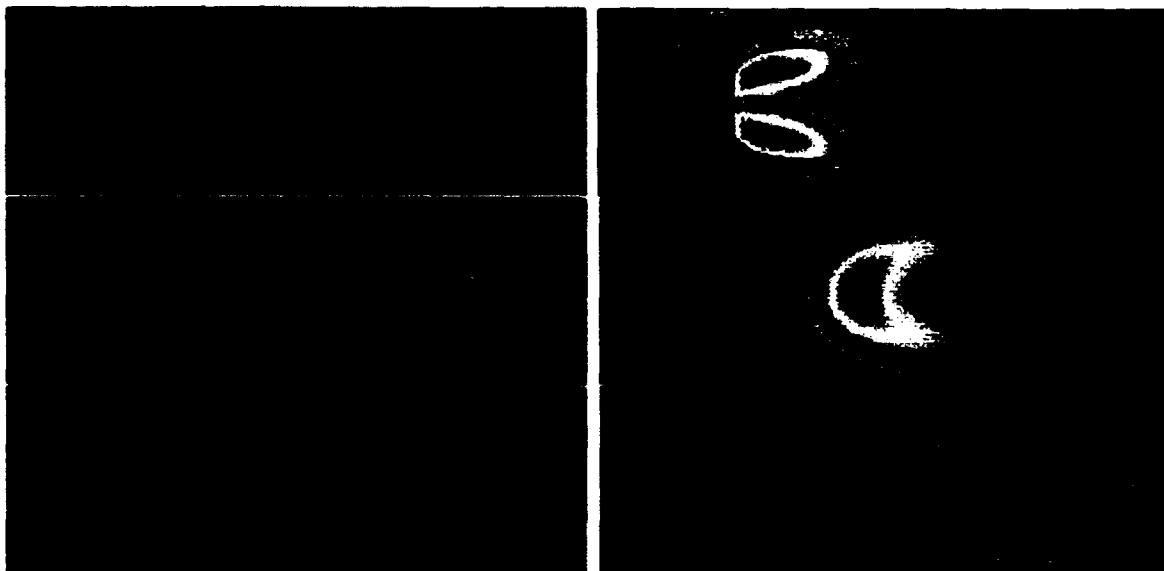
Figure 1. Time History of Temperature Contours for LOX Droplet Combustion in a Supercritical Hydrogen Flow.
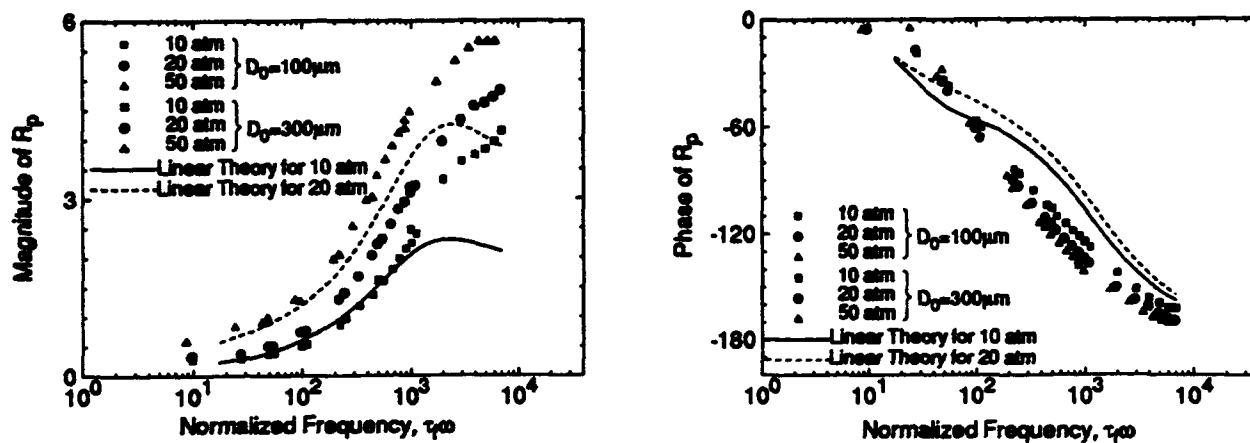
Figure 2. Effect of Pressure on Droplet Vaporization Response

DETAILED STUDIES OF SOOT FORMATION IN LAMINAR DIFFUSION FLAMES FOR APPLICATION TO MODELING STUDIES

Principal Investigator: Robert J. Santoro

Department of Mechanical Engineering
Propulsion Engineering Research Center
The Pennsylvania State University
University Park, PA 16802-2320

SUMMARY/OVERVIEW:

The primary objective of the present research program is to provide a fundamental understanding of the processes which control soot particle formation under conditions applicable to gas turbine engine operation. Current efforts emphasize laminar diffusion flames studies to elucidate the particle precursor, inception and surface growth processes important in soot formation. During the past year, using the extensive set of measurements of the gas and particle fields which has resulted from this research, a direct comparison with a detailed soot formation model has been undertaken. Additionally, species concentration results obtained as part of the present research effort have been used to established that soot surface growth in laminar diffusion flames ceases due the depletion of the gas phase hydrocarbon species involved in the surface growth process and not due to the loss of soot particle reactivity. By combining the measured temperature, velocity, soot particle and species concentration fields, it has been possible to resolve the soot formation process along individual particle paths. Using this approach, comparisons with results obtained from premixed flames show, for the conditions observed in the present diffusion flame studies, that only a small reduction in surface reactivity would be expected. Finally, a novel diagnostic technique, laser-induced incandescence, has been developed for soot volume fraction measurements and applied to laminar and turbulent diffusion flames as well as to hydrocarbon droplet studies.

TECHNICAL DISCUSSION

The objective of the present research effort is to investigate the fundamental phenomena controlling soot particle formation and destruction in combustion systems. The emphasis and approach chosen for the present studies are based on previous results which have proven the soundness of the methodology being utilized [1-5]. The present studies are conducted in well-characterized laminar diffusion flames in which fuel constituents, temperature, concentration and transport processes are systematically varied and/or measured.

Species Concentration and Soot Growth Measurements

Species concentration measurements were obtained in an ethene/air laminar diffusion flame having a fuel flow rate of 3.85 cm^3/s. Although this flame does not emit soot particles from its tip, the peak soot volume fraction observed in the flame exceeds 10^{-5}. Consequently, use of a novel electromechanical sonic microprobe, previously developed at Penn State [6], is essential to achieving measurements in this flame. The major species considered in the flame were N_2, O_2, C_2H_4, CH_4, H_2O, CO_2, H_2, C_2H_2 and Ar. Preliminary measurements were also obtained for diacetylene (C_4H_2) and benzene (C_6H_6).

By combining the species concentration measurements with previously obtained measurements of the soot particle, velocity and temperature fields, the soot formation and growth process can be followed along individual particle paths. Figure 1 shows the evolution of the soot volume fraction and acetylene (C_2H_2) concentration as a function of time along the particle path containing the maximum soot volume fraction in the flame [7]. An important point regarding this result is that the cessation of soot particle growth occurs at the location where the

C_2H_2 concentration reaches zero. Thus, it can be argued that the soot growth process ceases due to the depletion of the surface growth species, not because of the loss of surface reactivity which has sometimes been argued for premixed flames [8,9]. Similar results have been observed for other hydrocarbon species which could be important surface growth reactants such as benzene and diacetylene. Examination of other particle paths has also shown similar results to those illustrated in Figure 1 [7].

Further evidence that supports a mechanism in laminar diffusion flames which differs from that dominant in premixed flames can be gleaned by examining the temperatures along these streamlines and using the results of Dasch [8] and Woods and Haynes [9] to examine the decrease in soot particle reactivity. Equation (1) expresses the decay in the reactivity of the soot surface as taken from Dasch [8]. The term k_{SG}, which was determined from Woods and Haynes [9], is the same term as α used by Dasch.

$$\frac{k_{C_2H_2}}{k^o_{C_2H_2}} = \frac{N_s}{N_s^o} = \exp(-\alpha t) \qquad (1a)$$

$$\alpha = 3.5 \times 10^7 \exp(-T_a/T) \qquad (1b)$$

While it may not be good practice to apply the above formula for reactivity decay to non-isothermal flames, there is insight to be gained by proceeding along this line of analysis. If the maximum temperature along the streamline for the soot growth region (i.e., from initial detection of soot to the maximum soot volume fraction) is chosen, one can calculate a conservative estimate of the decrease in the soot particle reactivity along that particle path. Table 1 shows the maximum temperatures and soot residence times along three particle paths in the flame [7]. These paths correspond to the centerline of the flame, a path intermediate to the centerline and the path of maximum soot volume fraction, and the path containing the maximum soot volume fraction. In addition, the residence time for the centerline of a C_2H_4 flame discussed by Honnery and Kent [10] is also tabulated and is about five times longer than any of the residence times observed for the present study. The characteristic time, $1/\alpha$, for soot particle reactivity decrease is calculated using the activation temperature and expression of Dasch [8] (see equation (1)), since the result is more conservative than that of Woods and Haynes [9]. The results will not differ appreciably since the activation temperatures differ by approximately 1%. The fraction of initial reactivity that would remain when growth ceases is also shown in Table 1. The Arrhenius nature of the expression for the reactivity decrease can be expected to differ somewhat in the temperature range observed in the present diffusion flame. However, Woods and Haynes [9] did not expect this effect to be significant.

Using the temperatures and residence times from Table 1, the fraction of the initial reactivity available is lowest, 0.61, for the particle path designated as the maximum soot volume fraction due to the higher temperature on this particle path. Furthermore, when the data from Honnery and Kent [10] is used along the centerline of their flame, this analysis yields a fraction of initial reactivity available at the end of growth of 0.91. These values for the surface reactivity indicate that the continued growth of soot in diffusion flames to very long residence times is not in conflict with the results obtained by others in premixed flames. Furthermore, these calculations provide additional support to the interpretation that soot surface growth in laminar diffusion flames ceases due to the depletion of gas phase reactants.

Modeling of Soot and Species in a Laminar Diffusion Flame

A model of a laminar, ethene diffusion flame has been developed and compared with measurements as part of a collaborative effort with Prof. I. M. Kennedy of the University of California/Davis [11]. A system of elementary reactions is used to describe the gas phase C_1 and C_2 chemistry. The model incorporates a simple description of the growth of soot which performs a good job of reproducing the amount of soot in the flame and the transition from non-sooting to sooting conditions.

Figure 2 shows a comparison between measurements of the integrated soot volume fraction and acetylene concentration and the model predictions [11]. These results indicate that the model does quite well in terms of predicting the general profiles associated with both the soot particle and species concentration fields. Similar agreement is observed for other species in the flame.

41

Laser-induced incandescence (LII) involves the heating of soot particles to temperatures above the surrounding gas temperature due to the absorption of laser energy, and the subsequent detection of the blackbody radiation corresponding to the elevated soot particle temperatures. This technique has recently been used to obtain spatially-resolved measurements of soot volume fraction in a laminar diffusion flame, in which comparisons with laser scattering/extinction data yield excellent agreement [12]. In addition, the LII signal is observed to involve a rapid rise in intensity followed by a relatively long (ca. 600 ns) decay period subsequent to the laser pulse, while the effect of laser fluence is manifest in non-linear and near-saturated response of the LII signal with the transition occurring at a laser fluence of approximately 1.2×10^8 W/cm^2. Spectral response of the LII involves a continuous spectrum in the visible wavelength range due to the blackbody nature of the emission. Simultaneous measurements of laser-induced incandescence and light-scattering yield encouraging results concerning the mean soot particle diameter and number concentration. Thus, LII can be used as an instantaneous, spatially-resolved diagnostic of soot volume fraction without the need for the conventional line-of-sight laser extinction method. The LII technique has recently been applied to turbulent ethene/air flames as well as benzene and benzene/methanol droplet studies. The results of these studies have been encouraging regarding the use of LII in unsteady combustion environments.

REFERENCES

1. Santoro, R. J., Semerjian, H. G. and Dobbins, R. A., "Soot Particle Measurements in Diffusion Flames," *Combustion and Flame*, 52:204-218 (1983).
2. Santoro, R. J., Yeh, T. T., Horvath, J. J. and Semerjian, H. G., "The Transport and Growth of Soot Particles in Laminar Diffusion Flames," *Combustion Science and Technology*, 53:89 (1987).
3. Puri, R., Richardson, T. F., Santoro, R. J. and Dobbins, R. A., "Aerosol Dynamic Processes of Soot Aggregates in a Laminar Ethene Diffusion Flame," *Combustion and Flame*, 92:320-333 (1993).
4. Puri, R., Moser, M., Santoro, R. J. and Smyth, K. C., "Laser-Induced Fluorescence Measurements of OH Concentration in the Oxidation Region of Laminar, Hydrocarbon Diffusion Flames," *Twenty-Fourth Symposium (International) on Combustion*, The Combustion Institute, Pittsburgh, PA, pp. 1015-1022 (1992).
5. Puri, R., Santoro, R. J. and Smyth, K. C., "The Oxidation of Soot and Carbon Monoxide in Hydrocarbon Diffusion Flames," *Combustion and Flame*, 97:125-144 (1994).
6. Puri, R., "The Interaction of Soot Particles and Carbon Monoxide in Laminar Diffusion Flames," Ph.D. Thesis, The Pennsylvania State University (1992).
7. Rapp, D. C. and Santoro, R. J., "Growth Species and Soot Surface Growth in a Laminar Diffusion Flame," Paper #WSS/CI 94-052, 1994 Spring Meeting, Western States Section of The Combustion Institute, University of California at Davis, Davis, CA, March 21-22, 1994.
8. Dasch, C. J., "The Decay of Soot Surface Growth Reactivity and Its Importance in Total Soot Formation," *Combustion and Flame*, 61:219-225 (1985).
9. Woods, I. T. and Haynes, B. S., "Soot Surface Growth at Active Sites," *Combustion and Flame*, 85:523-525 (1991).
10. Honnery, D. R. and Kent, J. H., "Soot Formation in Long Ethylene Diffusion Flames," *Combustion and Flame*, 82:426 (1990).
11. Kennedy, I. M., Rapp, D. C., Santoro, R. J. and Yam, C., "Modeling and Measurements of Soot and Species in a Laminar Diffusion Flame," Paper #WSS/CI 94-053, 1994 Spring Meeting, Western States Section of The Combustion Institute, University of California at Davis, Davis, CA, March 21-22, 1994.
12. Quay, B., Lee, T.-W., Ni, T. and Santoro, R. J., "Spatially-Resolved Measurements of Soot Volume Fraction Using Laser-Induced Incandescence," *Combustion and Flame* (in press).
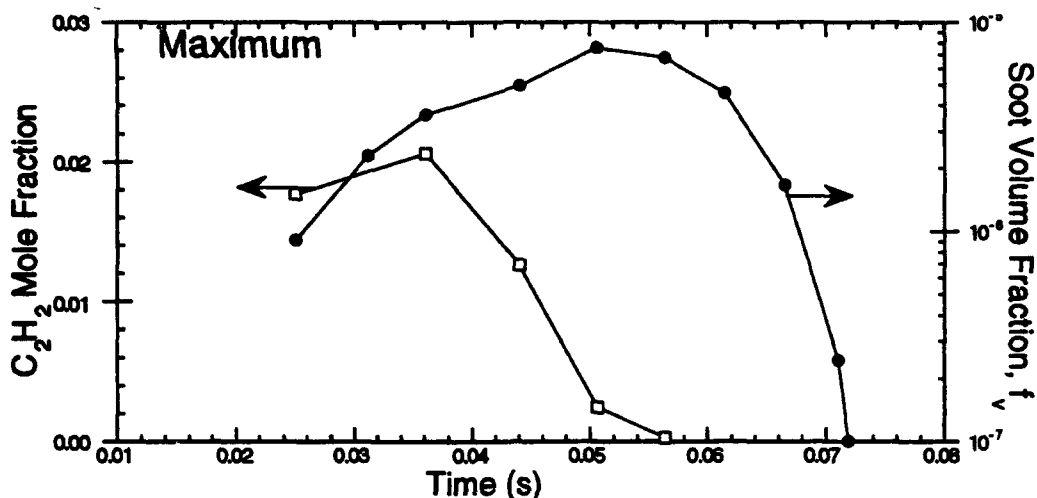
FIGURE 1 Plots of soot volume fraction, f_V, and the mole fraction of C_2H_2 as a function of time for the particle path containing the maximum f_V.

(a)

(b)
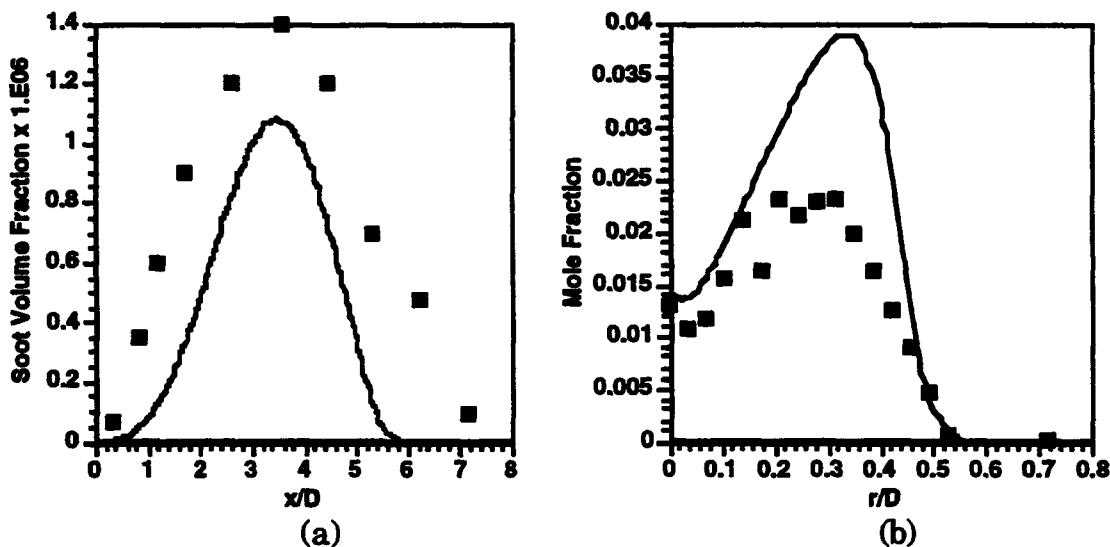
FIGURE 2 Measured and predicted values for (a) soot volume fractions integrated across the ethene/air flame as a function of nondimensional axial position and (b) radial profiles of the C_2H_2 mole fractions at 7 mm from the fuel tube exit. In these plots, D is the diameter of the fuel jet (1.11 cm).

TABLE 1 Data for calculation of particle reactivity decrease along several particle paths

Particle Path	Maximum Temperature (K)	Soot Residence Time (sec)	Characteristic Time (sec)	Fraction of Initial Reactivity
Centerline	1439	0.017	0.196	0.92
Middle	1449	0.035	0.175	0.82
Maximum	1572	0.026	0.0518	0.61
Honnery and Kent (1990)	≈1250	>0.2	2.11	0.91

43

MODELING STUDY TO EVALUATE THE IONIC MECHANISM OF SOOT FORMATION

(AFOSR Contract No. F49620-94-C-0014)

Principal Investigator: H.F. Calcote

AeroChem Research Laboratories, Inc.
P.O. Box 12, Princeton, NJ 08542

SUMMARY/OVERVIEW

This research program addresses: (1) the nucleation step in the mechanism of soot formation in flames, and (2) the mechanism of formation of the large cations observed in flames. The ionic mechanism of soot nucleation is studied by computer modeling to evaluate its potential for accounting for the experimental results. This involves the immediate task of developing a mechanism for production of the large ions observed in flames. This requires development of thermochemistry of large ions, development of a detailed mechanism with appropriate rate coefficients, and examination of the theoretical basis of the Langevin theory of ion-molecule reactions when large ions at flame temperatures are involved. During the last year, we improved the thermochemical and kinetics data bases, improved and extended the correlation between model and experiment to ion mass 301, $C_{24}H_{13}^+$. We also further explored the non-equilibrium nature of soot and acetylene formation in flames.

TECHNICAL DISCUSSION

In extending the model to larger ions, the dominant role of temperature became increasingly apparent. The maximum measured flame temperature in the C_2H_2/O_2, 2.67 kPa, 50 cm/s unburned gas velocity that we are modeling, the standard flame, is 2,200 K. It was of concern that to obtain agreement between model and experiment we had to reduce the temperature profile from 0% at the burner to 10% at the temperature maximum. At greater cation masses it became evident that even a lower maximum temperature, 1700 K, was required to obtain agreement. Reaction rates also seemed to be too fast: large ions were produced very early in the flame front. Reducing all reaction rate coefficients by a factor of 100 gave some improvement, but confirmed the previous observations that thermochemistry plays the dominant role in the mechanism. The premise of the model for ion growth is that the chemiion, HCO^+, which is in great excess of equilibrium, continues to grow to larger and larger ions by the addition of acetylene, diacetylene and other small neutrals. Thus large ions cannot exceed the equilibrium concentration calculated from the experimental HCO^+ concentration .

HCO^+ is not observed in these very rich flames because it reacts extremely rapidly to produce H_3O^+, $C_3H_3^+$ and $H_5C_6^+$ [the order of C and H distinguish isomers] which are observed experimentally. Thus to determine the extent to which equilibrium was attained in the model, recognizing that odd carbon number ions and even carbon number ions are produced in parallel paths, initiated by $C_3H_3^+$ and $H_5C_6^+$ respectively, we calculated the pseudo-equilibrium concentration of the large ions from the equilibrium constant with respect to $C_3H_3^+$ and $H_5C_6^+$, using experimental concentrations of $C_3H_3^+$, $H_5C_6^+$, C_2H_2 and H_2. Because the free energy of formation increases rapidly with increasing temperature, e.g., perinaphthenyl cation, $\Delta_f G = 1059$ and 1502 kJ/mol at 500 and 2000 K respectively, the equilibrium concentration decreases with increasing temperature. At the experimental maximum flame temperature, 2020 K, the experimental concentrations of many of the ions exceed the calculated pseudo equilibrium concentrations. This

cannot be true if our premise is correct, unless there is a mechanism for directly producing large ions, e.g., thermal ionization. However this raises the more difficult inverse question: how are small ions produced from large ions?

Thus, for each observed ion, a flame temperature was calculated below which the experimental ion concentration would be less than the pseudo-equilibrium concentration with $C_3H_3^+$ or $H_5C_6^+$. Some of the temperatures are very low, e.g., about 1750 K for $C_{11}H_8H^+$, $C_{13}H_6H_3^+$, and $C_{15}H_{10}H^+$. The flame code was run by fixing the maximum flame temperature at 1700 K. The results are presented in Fig. 1 in which the ratio of the maximum experimental concentrations to the calculated concentrations are presented. Maximum concentrations are a good means of comparison because the calculated cation profiles parallel the experimental profiles and are simply displaced in concentration. The agreement between model and experiment is generally excellent, except for $C_{14}H_7H^+$. Any ratio less than zero, i.e., the bar to the left of zero, could be adjusted by reducing the reaction rate coefficient, always an easy thing to do. In the current model, using 1700 K maximum flame temperature, the experimental concentrations are less than the pseudo-equilibrium calculations. Furthermore, the mole fractions calculated with the model are also less than given by the pseudo-equilibrium calculations, indicating that equilibrium has not been attained. These differences become very large, ratios of model to pseudo-equilibrium concentrations are 10^{-5} to 10^{-10} for large ions.

Why $C_{14}H_7H_4^+$, protonated anthracene, is uniquely underestimated is not presently understood. As suggested below, proton, hydride ion or hydrogen atom transfer between species may be involved, but has not yet been incorporated into the mechanism. We have restricted the reactant and product species considered to those which have been observed. Potential species resulting from proton or hydrogen atom transfer have never been observed in flames. The present mechanism includes 35 ions and has been reduced to 103 reactions by including only those reactions which contribute greater than one percent to the ion flux. These reactions were chosen from a data base of 360 ion-molecule reactions and 30 ion-electron recombination reactions.

The major concern is the need to reduce the flame temperature to obtain agreement. The following lines of reasoning are being considered: (1) The original premise is incorrect. It is too soon to reject a concept that seems to be consistent with a large number of facts, and were the premise wrong, why can such good agreement be obtained by just altering the temperature; (2) The experimental temperature is incorrect. This is reject because it cannot be incorrect by this large an amount; (3) The thermochemistry may not be sufficiently accurate. The calculations are very sensitive to thermochemistry and with a "maximum uncertainty of $\pm$ 25 kJ/mol in the enthalpy of reaction" [Stein, 1983] and an estimated accuracy for entropies of reaction of $\pm$ 5 J/mol K [Stein, 1983] it offers an opportunity to improve the agreement. This has only been employed in one case where there was a question of the degree of aromaticity; (4) The ion concentrations may be off, as they were very difficult to measure. We are examining this possibility. Our total ion concentrations obtained by Langmuir probe were in agreement with total ion profiles in similar flames subsequently measured by Delfau, Michaud and Barrassin (1979), and Homann and Stroefer (1983). Gerhardt and Homann (1990) reported ion profiles in similar flames in which the total is about an order of magnitude smaller than the totals referenced above. We are combining the two sets of data which will lower our concentrations in the region of 200 u and increase them above about 400 u; (5) As proposed by Stein [Stein, 1983] the observed ions are not the ions in the flame but ions which have been formed in the sampling cone by addition of a hydrogen atom, where the gases are cooled by expansion. This would not alter the original premise, but would complicate its interpretation by adding a whole new set of reactions to the mechanism. The proposed new ions are more stable at high temperatures. Thus, e.g., the $C_{14}H_{11}^+$ ion might be in equilibrium:
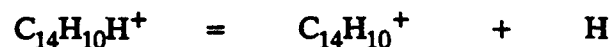
$$C_{14}H_{10}H^+ \quad = \quad C_{14}H_{10}^+ \quad + \quad H$$

for which Stein calculates an equilibrium ion ratio, $C_{14}H_{10}{}^+/C_{14}H_{10}H^+$ of 1.8 and 550 at 1600 and 2200 K respectively.

Equilibrium calculations of soot, acetylene and other neutral and ion species are being compared with available measurements of such quantities, Fig.2. One of the surprising discoveries is that, with one exception, for all flames compared thus far, soot and acetylene concentrations are in great excess of equilibrium and occur at C/O ratios below where soot is expected to form. But, for the widely studied standard acetylene flame, soot only appears where predicted by thermodynamics, and is less than predicted by equilibrium. Acetylene concentrations exceed equilibrium. Thus in most flames, soot exceeds equilibrium, in the acetylene flame it is less than equilibrium.

Immediate future plans are to extend the model to $C_{45}H_{17}{}^+$, mass 557. To do this we will extrapolate the available thermodynamic data on large cations to $C_{45}H_{17}{}^+$. The thermodynamic and kinetic data necessary to incorporate hydrogen atom reactions, proton transfer and hydride transfer reactions in the mechanism will also be developed and incorporated in the data base. We will also search for a more typical sooting flame to study on which there is sufficient data, this will probably be the benzene flame.

The following people have participated in this program: Drs. R.J. Gill, D.G. Keil, C.H. Berman, AeroChem, and Prof. F. Egolfopoulos, University of Southern California.
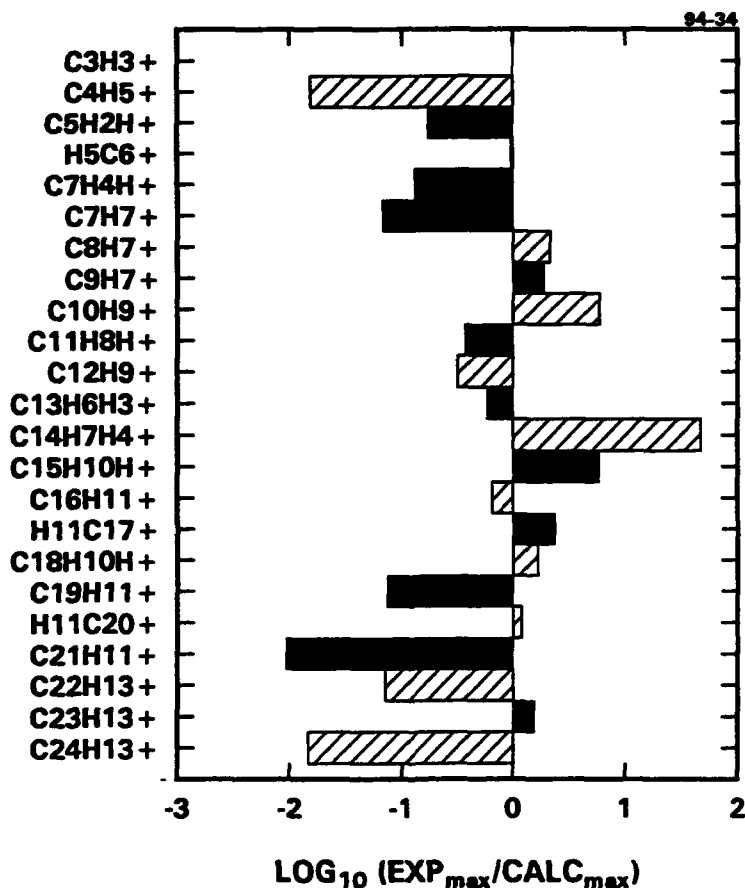
FIGURE 1   COMPARISON OF EXPERIMENTAL (EXP)$_{maximum}$ AND CALCULATED (CALC)$_{maximum}$ CATION CONCENTRATIONS.
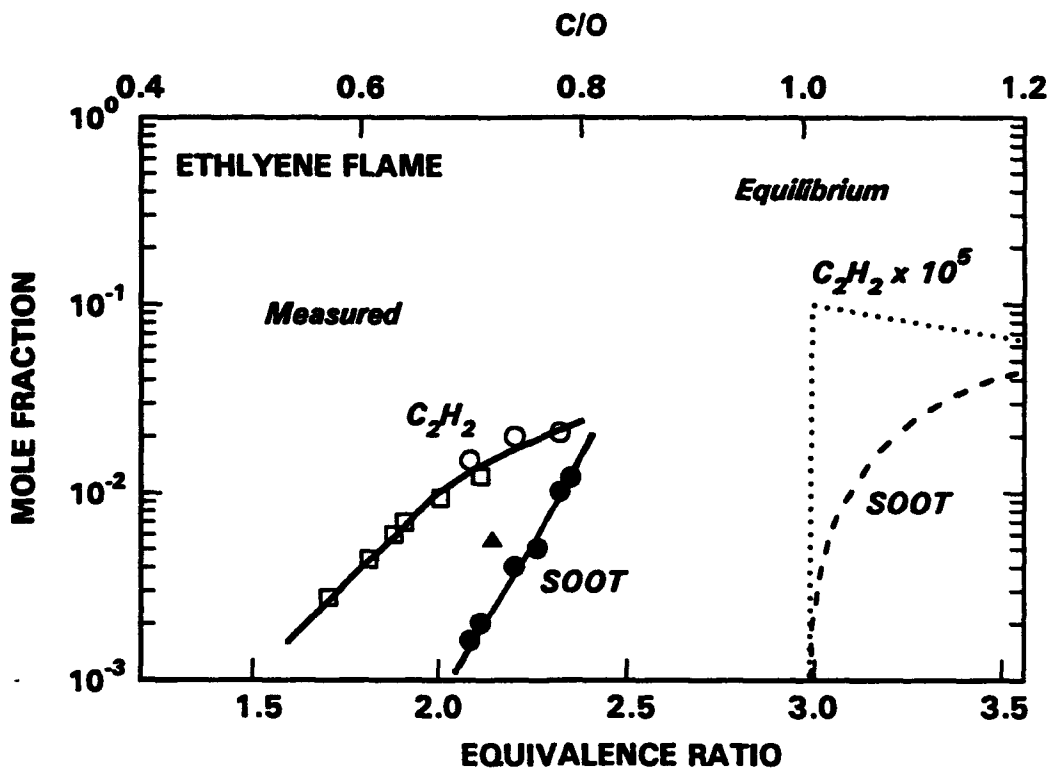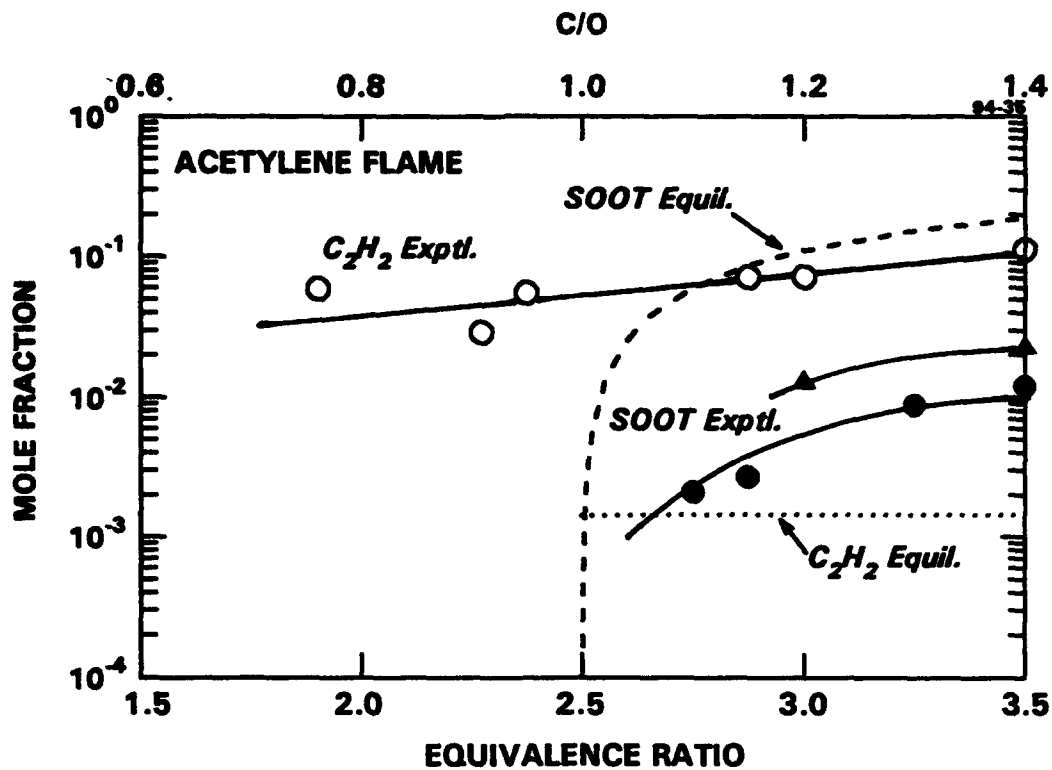
FIGURE 2 COMPARISON OF EXPERIMENT AND EQUILIBRIUM ACETYLENE AND
SOOT CONCENTRATIONS FOR ACETYLENE/OXYGEN FLAME AT 2.7 kPa AND
ETHYLENE/AIR FLAME AT 100 kPa.

Acetylene flame data from Homann, et.al. (1965), Bonne, et.al. (1965), and Wersborg, et.al. (1975); measured flame temperature from lean to rich 2000 to 1900 K. Ethylene flame data from Millikan (1962), Harris and Weiner (1983), and Bonig, et.al. (1990); measured flame temperature scattered 1650 to 1820 K.

47

DEVELOPMENT OF PREDICTIVE REACTION MODELS OF SOOT FORMATION

(AFOSR Grant No. F4620-94-1-0226)

Principal Investigator: M. Frenklach

Fuel Science Program
Department of Materials Science and Engineering
The Pennsylvania State University
University Park, PA 16802

SUMMARY/OVERVIEW:

The ultimate goal of this program is to develop a predictive reaction model for soot formation in hydrocarbon flames. The specific objectives of the current 3-year period are to attempt modeling of soot formation in environments closer related to practical combustors, like diffusion and turbulent flames, and to undertake a theoretical investigation into the chemistry and physics of soot-particle surface processes and their relationship to particle dynamics. During the past year, progress has been made in the following areas: (1) Computer simulations of the effect of pressure on soot formation in laminar premixed flames were completed; (2) A reduced model of PAH and soot formation in turbulent reactive flows was developed and applied to simulation of soot formation in natural-gas fueled diesel combustion.

TECHNICAL DISCUSSION

Pressure Effect on Soot Formation

The ability to predict soot formation at high pressures is of considerable interest because most practical combustion devices operate at elevated pressures. The objective was to test whether our recently developed soot formation model[1] is able to account for the formation of soot in experimental 10 bar flames of Jander, Wagner and co-workers.[2] The computational model consisted of the following principal processes: initial aromatic ring formation during small hydrocarbon pyrolysis and oxidation, growth of planar polycyclic aromatic hydrocarbons (PAH) through the hydrogen-abstraction–acetylene-addition (HACA) reaction mechanism, particle nucleation through coalescence of PAHs into three-dimensional clusters, particle growth by coagulation and surface reactions of the forming clusters and particles.

A recently updated 500-reaction and 100-species mechanism was used to describe the initial hydrocarbon pyrolysis and oxidation, and PAH formation and growth up to coronene. The PAH growth beyond pyrene was described by a replicating HACA reaction sequence. The formation of soot particles was assumed to be initiated by the coalescence of two PAH molecules. The subsequent growth of soot particles proceeds through particle-particle and particle-PAH coagulation and through surface reactions. Modeling of PAH growth beyond pyrene and of soot particle dynamics was accomplished using the method of moments.[1] Particle coagulation was

assumed to be in the free-molecular regime and surface growth was described in terms of elementary chemical reactions.

Three 10 bar, burner-stabilized, ethylene-air flames were selected for the simulation. To examine the influence of pressure on soot production, an 1 bar, burner-stabilized flame was also considered. The kinetic model predicted reasonably well measured species concentrations. The comparison of the computed and experimental profiles of soot volume fractions are presented in Fig. 1. Inspection of this figure indicates that the shape of the experimental soot profiles for all of the flames is well predicted by the model. The quantitative agreement was obtained by adjusting a single parameter—the fraction of soot surface sites available for reaction.

An important feature of the present study is that the experimentally observed effect of pressure on soot volume fraction is well accounted for by the model. Experimentally, Bönig et al.[2] determined in ethylene-air flames that the final soot volume fraction, $f_{v\infty}$, is proportional to P^2 for $P \leq 10$ bar. Above 10 bar, the dependence of soot production on pressure weakens and $f_{v\infty}$ is proportional[3] to P. It was suggested[3] that the weakening pressure dependence is due to the increasing acetylene consumption by soot surface reactions, thus depleting the principal surface growth species. Analysis of the computational results of the present study indicated that the consumption of acetylene by soot particle surface growth is insignificant up to 10 bar. The influence of pressure on soot production arises mainly from a larger concentration of acetylene at high pressure, which affects both the soot surface growth and the nucleation of soot particles.

To understand the factors governing the observed pressure dependence of soot production, the rates of nucleation, coagulation and surface growth of the soot particles were examined. As described earlier, the present model assumes that the nucleation of soot particles is initiated by PAH coalescence. Consequently, the nucleation rate depends strongly on PAH concentrations. Inspection of the computed results indicated that the influence of pressure on the total concentration, particularly on the concentration of acetylene, has the strongest effect on the production of PAHs and hence on the nucleation of soot particles.

A secondary effect of pressure on the production of PAHs arises from the pressure dependence of reaction rate coefficients. This pressure effect arises from the reactions whose energized adducts undergo collisional stabilization. A test run under the conditions of a 10 bar flame, but with the pressure-dependent rate coefficients set equal to those at 1 bar, resulted in the peak concentration of naphthalene that is a factor of 4 lower than that computed with the rate coefficients at 10 bar.

Reduced Model for PAH and Soot Formation

The entire reaction mechanism—from the initial hydrocarbon to soot particles—can be divided into three parts, each reduced with a different method: small-molecule reactions describing the main combustion environment and the formation of the first aromatic ring; its growth to pyrene; and nucleation, growth and oxidation of soot particles. The former part, small-molecule chemistry, is a subject of continuous efforts of the research community; and the latter, particle dynamics, has been addressed by us previously using the method of moments. Here, a reduced model for PAH formation and growth, the central part of the soot-precursor chemistry, is addressed.
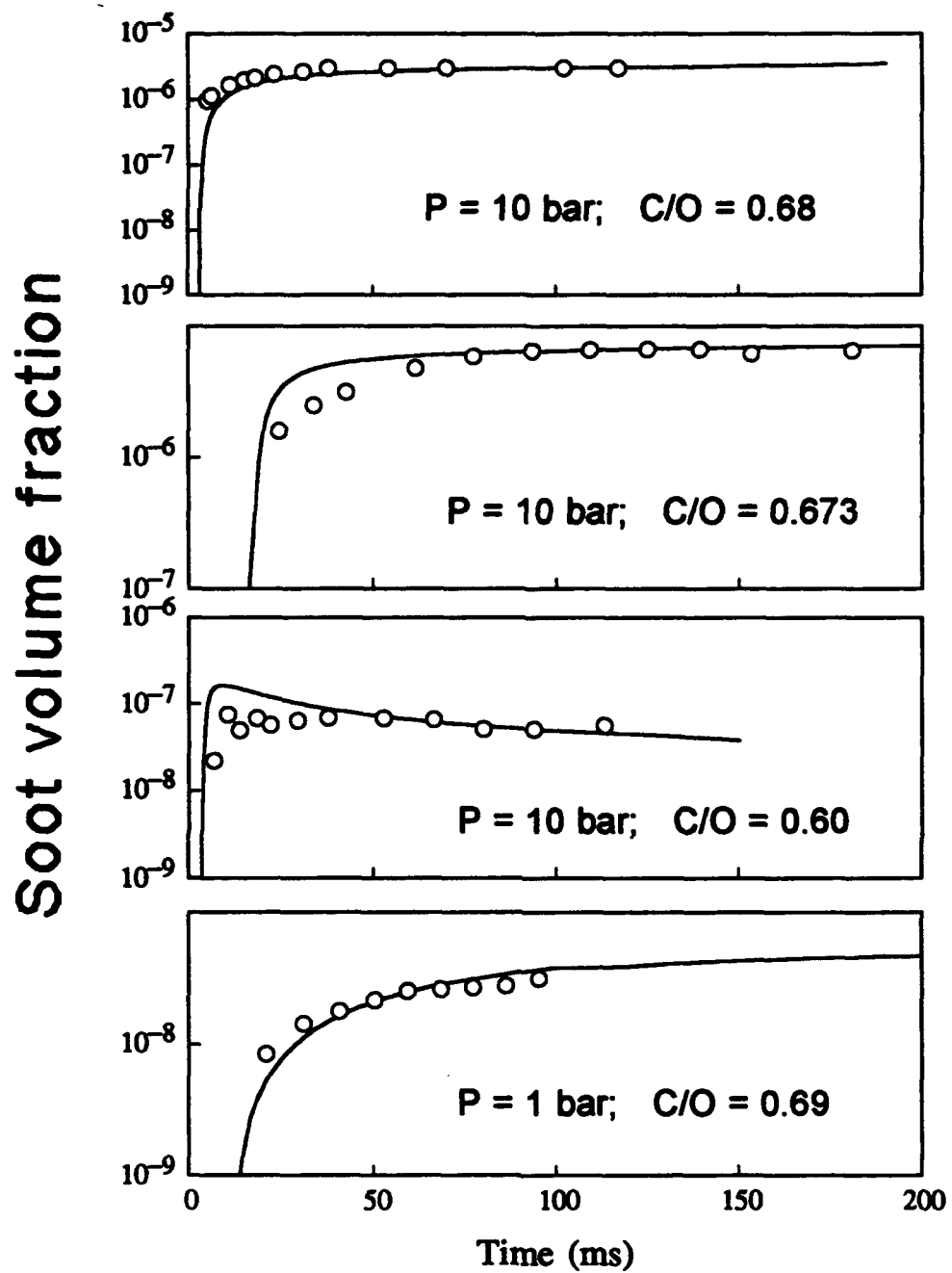
Figure 1. Comparison of model predictions and experimental data[3] for soot volume fraction in laminar premixed flames of ethylene.

50

An analytical expression relating the concentrations of pyrene and benzene was developed assuming a combination of steady states applied for the radicals and partial equilibrium assumed for selected reaction steps in the reaction sequence of PAH growth. The accuracy of this reduced model was tested by performing kinetic calculations on an individual fluid cell whose initial conditions were typical of those producing soot in high-pressure turbulent combustion. The results, shown in Fig. 2, indicate that the reduced model overpredicts the pyrene concentration in the beginning, but gets closer to it at times around 1 ms, the average cell reaction time. The difficulty of obtaining a more accurate reduced model for the PAH reaction scheme resides in the complex kinetic behavior of two- and three-ring aromatic molecules: they accumulate at first and then react at the later stages of reaction. A compromise solution was developed, which included the biphenyl channel, whose importance is demonstrated in Fig. 2.
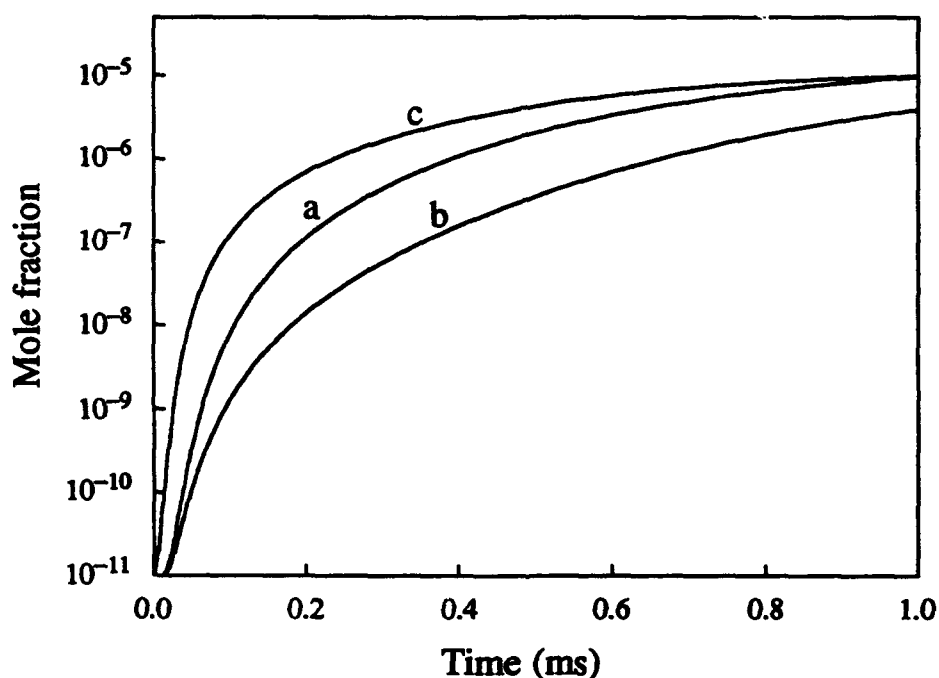
Figure 8. Calculated mole fraction of pyrene for the following initial conditions of a single fluid cell: $P_0 = 39$ atm, $T_0 = 1954$ K, $\phi = 3.68$, pyrene mole fraction 9.3×10^{-12}. a) Computed with the full reaction scheme for PAH growth. b) The same as (a) but without the biphenyl reaction channel. c) Computed with the reduced model of PAH growth.

REFERENCES

1. Frenklach, M. and Wang. H., *Twenty-Third Symposium (International) on Combustion*, The Combustion Institute, Pittsburgh, 1991, p. 1559; in *Proceedings of the International Workshop on Mechanisms and Models of Soot Formation* (H. Bockhorn, Ed.), Springer-Verlag, Heidelberg, in press.
2. Bönig, M., Feldermann, Chr., Jander, H., Lüers, B., Rudolph, G., and Wagner, H. Gg., *Twenty-Third Symposium (International) on Combustion*, The Combustion Institute, Pittsburgh, 1991, p. 1581.
3. Böhm, H., Feldermann, Chr., Heidermann, Th., Jander, H., Lüers, B., and Wagner, H. Gg., *Twenty-Fourth Symposium (International) on Combustion*, The Combustion Institute, Pittsburgh, 1993, p. 991.

DEVELOPMENT OF A TECHNIQUE TO DETERMINE THE MORPHOLOGY AND DYNAMICS OF AGGLOMERATES IN CHEMICALLY REACTING FLOWS

Principal Investigator: Tryfon Charalampopoulos

Mechanical Engineering Department
Louisiana State University
Baton Rouge, LA 70803

SUMMARY/OVERVIEW

Agglomerated particulate structures of variable degree of complexity occur in environments such as combustion systems, and atmospheric and colloidal dispersions. In particular, combustion generated soot particulates have wide ramifications in radiative transfer from luminous and pollution control. Yet there are difficulties for a complete in-situ characterization of the agglomerate morphology due to: a) lack of knowledge of the physiochemical properties of the primary particles and b) suitable theoretical models for the data inversion. The objective of this study is to remove these difficulties by developing both the experimental and theoretical framework for determining the agglomerate morphology and dynamics under in-situ conditions. Towards this end it has been shown that the agglomerated soot structures do not satisfy the reciprocity relations and an exact formulation has been developed for the internal field of an assembly of particles which: (a) satisfies the energy conservation requirement (b) accounts for self-contribution and multiple scattering field effects (c) is invariant to coordinate transformation and is particularly useful for soot and/or other particulate diagnostics at wavelengths UV. The new formulation results in 99% reduction in computational demand. In addition experiments are being developed that allow in-situ measurements of the anisotropic properties of the agglomerates along with the generation of specific particles shapes such as straight chains.

TECHNICAL DISCUSSION

a. Analysis
There are two methods for the study of the characteristics of flame particulates: ex-situ and in-situ. The ex-situ method, although simple to use, possesses disadvantages because the sampling process perturbs the flow field, and the sampling probes may not sustain adverse temperatures and/or reactive conditions. The in-situ technique though more complex, can yield valuable information about the size and shape of the particles. In this respect it should be noted that Jones formulation [1,2] for the predictions of light scattering properties from assemblies of Rayleigh size particles has been used by several investigators in recent years especially in the context of analysis of scattering/absorption measurements from sooting flames. Because for most sooting flames the primary particles are sphere-like and conducting, Jones formulation was very well suited for data inversion [3-5]. Jones solution [1] has been corrected for the appropriate representation of the complex refractive index of the particles [6] as well as for the extinction efficiency factors [7]. In addition in the course of this study it was demonstrated [8] that the agglomerated structures do not satisfy the reciprocity relations and this provides an additional diagnostic tool both for sooting flames and colloidal dispersions. In this study a detailed approach is undertaken that utilizes Saxon's integral equation [9] to arrive at a general form for

the governing equation of the internal field of an assembly of particles which satisfy the Rayleigh approximation and the energy conservation requirement.

For an assembly of N small spheres in the Rayleigh approximation, Jones [1] obtained a set of linear simultaneous equations in the form

$$E(r_l) = \frac{3}{\varepsilon+2} E_{inc}(r_l) + \frac{\varepsilon-1}{\varepsilon+2} \sum_{j=1,\neq l}^{N} (kR_j)^3 T_{lj} E(r_j) \qquad (1)$$

$$l = 1,2,...,N$$

These equations can be solved for the three rectangular field components (Ex, Ey, Ez) of any particle in the agglomerate. This formulation has been utilized for data inversion [3-5] and it has been generally assumed that the agglomerated structure is randomly oriented with respect to the incident wave. This assumption makes it necessary to perform computations of the respective scattering quantities over a large number of orientations, typically 600 or more for a flame soot agglomerate [4], and average the results. As the number of primary particles in the agglomerate increases, this process becomes computationally cumbersome. To circumvent this difficulty, let us rewrite equation (1) in matrix form, namely

$$ME = B, \qquad (2)$$

where M is a 3N*3N matrix, E and B 3N*1 matrices representing the unknown internal field and the incoming wave, and N is the number of particles in the agglomerate. Conventionally, this linear system of equations is solved in an incident-measuring coordinate system, see Fig. 1. Instead let us fix the agglomerate in the coordinate system (x',y',z'), which will refer to as: the structural coordinate system. Then matrix M is invariant while B varies as the structural system (x',y',z') rotates. By rotating the incoming wave instead of the agglomerate, we need to establish M and solve its inverse matrix only once for a solution for the scattering field matrix M needs to be set up and inverted only once instead of 100 times. This reduces the computational demand by approximately 99 percent when solving for the internal field. It should be noted that the selection of the structural coordinate system is based on the invariance of the governing equation (1). Noting that T in vector equation (1) must be a tensor let us consider the cartesian coordinate system in Figure 1. A second order tensor satisfies the relation [10]

$$T_{ij} = \sum_{m=1}^{3} \sum_{n=1}^{3} a_{im} T'_{mn} a_{jn} \text{ or } T = AT'A^t \qquad (3)$$

where T_{ij}, T'_{mn} are elements of tensor T under xyz coordinate system and the primed system respectively, and a_{im}, a_{jn} are elements of matrix A. With this definition of T' matrix a general form of the internal field equation is obtained [10]:

$$E(A) = E_{inc}(A) + \frac{\varepsilon-1}{3}\left[-3+2i(kR_A)^2 h_1(kR_A)\right]E(A)$$
$$+ \frac{\varepsilon-1}{3} i(kR_B)^2 j_1(kR_B)TE(B), \qquad (4)$$

The coefficients preceding E(A) on the right of equation (4) is the complete form of self-contribution field term whereas the coefficients of TE(B) account for multiple scattering effects. The scattered field from an adjacent sphere B may be shown to be

$$E_{scat} = (\varepsilon-1)(kR_B)^2 j_1(kR_B)\frac{e^{ikr}}{kr} e^{-ikr_B \cos\beta} (\Theta e_\theta - \Phi e_\phi), \qquad (5)$$

Using this form of the scattered field along with the definition of the scattering cross-section it can be shown [10] that

$$C_{sca} = C_e - C_a + \frac{4\pi R^2}{3} j_1(x)|\varepsilon - 1|^2 \sum |E_j|^2 \left[\mathrm{Im}(F_0) + 2x^2 j_1(x) \right], \qquad (6)$$

where $\left[F_o = (3 - 2ix^2 h_1(x)) \right]$ the extinction cross section C_e is given in accordance with the optical theorem as

$$C_e = 4\pi R^2 j_1(x) \mathrm{Im}\left[(\varepsilon - 1) \sum_{j=1}^{N} \mathbf{E}_j \cdot \mathbf{E}_{inc}^* \right] \qquad (7)$$

and the absorption cross section C_a is

$$C_a = 4\pi R^2 j_1(x) \mathrm{Im}(\varepsilon - 1) \sum_{j=1}^{N} |E_j|^2 . \qquad (8)$$

When j_1 is approximated by $kR/3$ or $x/3$, equations (7) and (8) reduce to the more familiar form of C_a and C_e.

A detailed comparison of the present solution with the original Jones solution [1], the Purcell & Pennypacker (P-P) solution [11], its later development by Goedecke & O'Brien (G-O) [12], and the Iksander, Chen & Penner (I-C-P) [13] solution in terms of: (i) energy conservation requirement, (ii) self-contribution term, (iii) multiple scattering factor, (iv) conformity to coordinate rotations, and (v) the volume element is presented in Ref [10]. The present solution degenerates into the I-C-P formulation when $j_1(x)$ is approximated with $x/3$; it further reduces to the G-O formulation after the self-contribution term is approximated to its third order and the P-P or the original Jones solution if the self-contribution term is approximated to its first order. In addition it was found that only the present solution and the G-O solution satisfy the energy conservation requirement. Specifically equation (6) reveals that the energy balance will be violated if approximations of F_0 (self contribution term) and j_1 (field interaction term) are incompatible. Since a compatible approximation requires that F_0 is two orders higher than j_1, the lowest order compatible approximation of j_1 should be $x/3$ and F_0 should be $\left(1 - x^2 - \frac{2}{3} x^3 i\right)$. The (I-C-P) and the (G-O) results were found to be within 1 percent of the exact result for x_p parameters up to 0.2 (Fig. 2). For larger size parameters the differences become more pronounced. Considering also that the I-C-P solution does not obey the energy conservation law, the third order approximation of the general form should be used for primary particle size parameters less than 0.15. For larger size parameters, higher order compatible approximations of the exact solution or the exact solution itself can be utilized. Such will be the case, for example, when the interaction of laser light in the deep uv part of the spectrum ($\approx$ .275 μm) is to be used for flame soot studies or similar applications where the size parameters will be of the order of 0.3 or higher.

b. Experimental

Experiments are being developed to allow the in-situ determination of the rotational diffusion coefficient and aspect ratio of agglomerated structures. The experimental set-up (Fig. 3) includes a CO-AIR flame doped with iron-pentacarbonyl $Fe(CO)_5$ vapor. As may be seen from the attached electromicrographs the system produces chain-like aggregates. Evident is the variability of primary particle size within a chain as well as the distribution of the aspect ratio. Work is under way to determine the aspect

54

ratio of the chain-like aggregates from the rotational depolarized optical spectrum at 0.488 μm.

References

1. Jones, A.R. (1979) Proc. R. Soc. A 336 111-27.
2. Jones, A.R. (1979) J. Phys. D: Appl. Phys. 12:1661-72.
3. Chang, H. and Charalampopoulos, T.T. (1990). Proc. R. Soc. 430A 577-591.
4. Charalampopoulos, T.T. and Chang, H. (1991). Combust. Flame 87:89-99.
5. Charalampopoulos, T.T. (1992). Prog. Energy Combust. Sci. 18:13-45.
6. Kumar, S. and Tien, C.L. (1989). Combust. Sci. Tech. 66:199-216.
7. Ku, J.C. and Shim, K.H. (1992). JQSRT 47(3):201-20.
8. Charalampopoulos, T.T. and Panigrahi, P.K. (1993) J. Phys. D: Appl. Phys. 26 2075-2081.
9. Saxon, D.S. (1974). NASA Report CR140816 pp 111-27.
10. Lou, W. and Charalampopoulos, T.T. Submitted to the Journal of Physics D: Appl. Phys. (Paper No. D/54634/PAP)
11. Purcell, E.M. and Pennypacker, C.R. (1973). Astrophys. J. 186:705-14.
12. Goedecke, G.H. and O'Brien, S.G. (1988). Appl. Opt. 27:2431-38.
13. Iksander, M.F., Chen, H.Y. and Penner, J.E. (1989). Appl. Opt. 28:3083-91.

Measuring coordinate: (x,y,z)

Structural coordinate: (x',y',z')
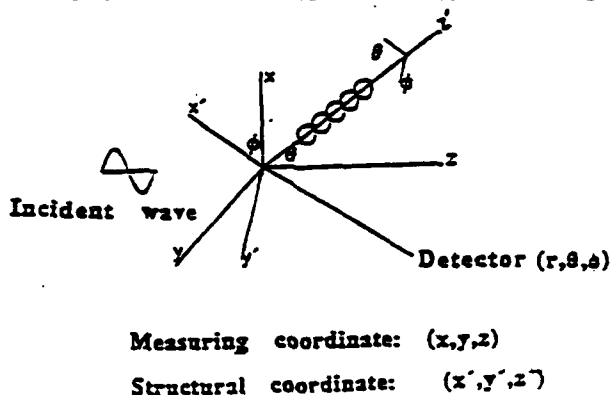
Figure 1

TOTAL FUEL FLOWRATE: CO = 450 cc/min

CARRIAGE GAS FLOW RATE: CO = 20 cc/min

H.A.B = 35 mm

THERMOPHORETIC PROBE

Primary particle size parameter, x_p

Figure 2

0.5 micron
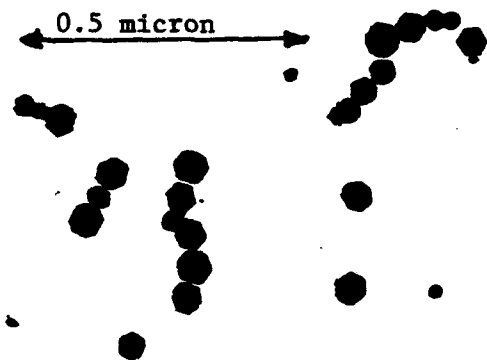
Chain-like Aggregates

Magnification 120 k
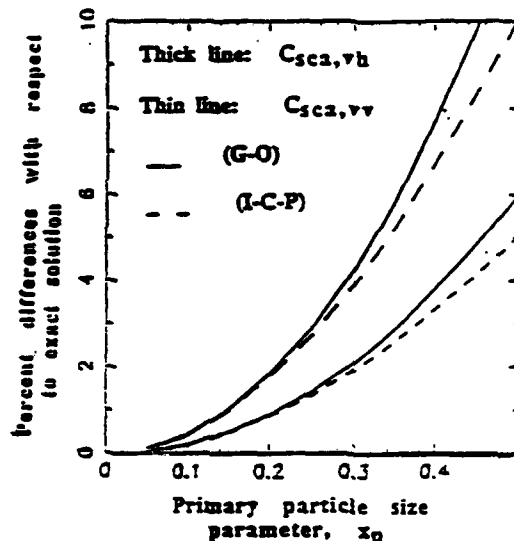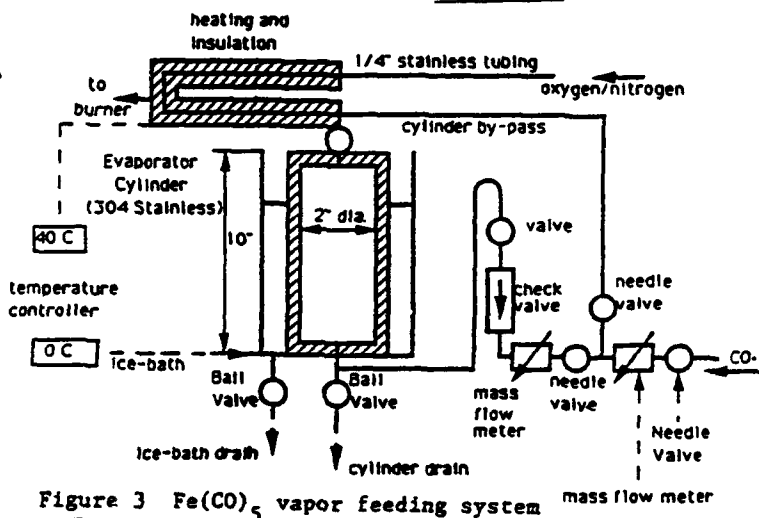

Figure 3 Fe(CO)$_5$ vapor feeding system

TRANSPORT PHENOMENA AND INTERFACIAL KINETICS IN MULTIPHASE COMBUSTION SYSTEMS

AFOSR Grant No. 94-1-0143

Principal Investigator: Daniel E. Rosner
High Temperature Chemical Reaction Engineering Laboratory
Department of Chemical Engineering, Yale University
New Haven, CT 06520-8286,USA

SUMMARY / OVERVIEW

The performance of ramjets burning slurry fuels (leading to oxide aerosols and deposits), and gas turbine engines in dusty atmospheres depends upon the formation and transport of small particles, often in non-isothermal combustion gas boundary layers (BLs). Even airbreathing engines burning "clean" hydrocarbon fuels can experience *soot* formation/deposition problems (*e.g.*, combustor liner burnout, turbine blade erosion,...). Moreover, particle formation and transport are important in chemical reactors used to synthesize or process aerospace materials (turbine coatings, optical waveguides, ceramic precursor powders,...). Accordingly, our research is directed toward providing chemical propulsion system and aerospace materials engineers with new techniques and quantitative information on important particle- and vapor-mass transport mechanisms and rates. An interactive experimental/theoretical approach is being used to gain an understanding of performance-limiting chemical-, and mass/energy transfer-phenomena at or near interfaces. This includes the development and exploitation of seeded laboratory burners (Fig. 1), flow-reactors (Fig. 5), and new diagnostic/characterization techniques (Fig. 3). Resulting experimental data, together with the predictions of asymptotic theories, are then used to propose and verify simple viewpoints and rational engineering correlations (Figs. 4,5,8) for future design/optimization.

TECHNICAL DISCUSSION / RECENT RESEARCH PROGRESS

1. FORMATION, TRANSPORT AND STABILITY OF COMBUSTION-GENERATED PARTICLES:
   SEEDED LAMINAR COUNTERFLOW DIFFUSION FLAME EXPERIMENTS

Based on our recent measurements of the *thermophoretic diffusivity* of flame-generated submicron "soot" particles using a $TiCl_4(g)$-seeded low strain-rate counterflow laminar diffusion flame (CDF-) technique (Gomez and Rosner, 1993) we showed that a knowledge of the relative positions of the gas and particle phase stagnation planes and the associated local chemical environments, can be used to control the composition and morphology of flame-synthesized particles. These factors will also influence particle production and *radiation* from *turbulent* non-premixed "sooting" flames.

To obtain fundamental information on the nucleation, growth and restructuring kinetics of flame-generated aggregates, during this past year we have exploited an improved "slot-type" burner seeded with the $TiO_2(s)$ vapor precursor: titanium tetra-iso-propoxide (TTIP) (Fig. 1) to carry out *in situ* measurements of aggregate dynamics and morphology evolution. For the latter we use the morphology-insensitive *thermophoretic sampling* technique (Rosner, Mackowski and Garcia-Ybarra, 1991) with carbon film-coated copper gridsto extract aggregates from various positions in the seeded-CDF for morphological analysis using transmission electron microscope (TEM-)images (Fig. 2a). Aggregate data obtained from CH_4 flames seeded with TTIP- vapor are now being obtained and analyzed using the theoretical methods briefly outlined in Section 2. Apart from characterizing the *fractal dimension*, D_f, of aggregates sampled from various points within the CDF, we are currently examining the distribution of the angles between triplets of primary particles, based on their projected TEM images. When corrected for the fact that the centroids of the particles comprising the aggregate are not all in one plane, we believe these histograms will be useful to characterize the degree of aggregate restructuring of moderate size aggregates in high temperature flames (see Section 2 and Cohen and Rosner,1993,1994).

---

2. TRANSPORT AND RESTRUCTURING PROPERTIES OF FLAME-GENERATED AGGREGATES: THEORY

The ability to reliably predict the transport properties and morphological stability of *aggregated* flame-generated *particles* (carbonaceous soot, Al_2O_3, SiO_2,...) is important to many technologies, including chemical propulsion and refractory materials fabrication. Needed are methods to anticipate coagulation and ultimate deposition rates of suspended populations of such particles in combustion systems. Toward this end we are developing efficient methods for predicting the transport properties of large 'fractal' aggregates *via* a spatially variable effective porosity pseudo-continuum model . Since "young" small aggregates are frequently "stringy" (fractal dimensions much less than 2) we are also introducing an aggregate statistical characterization based on the *pdf* of angles between triplets of primary particles (Fig. 3 a,b), and developing methods to predict the evolution of such *pdf*s due to the *restructuring* mechanisms of Brownian motion, surface energy driven viscous flow, and/or capillary-condensation (Cohen and Rosner, 1993,1994). Indeed, these factors determine the observed size of the apparent "primary" particles comprising soot particles, and the "collapse" of surface area observed in some high temperature systems.

These new methods/results, together with our recent estimates of the *spread* of aggregate sizes in coagulating populations, are now being used to predict particle *capture rates* on solid surfaces by the mechanisms of convective-diffusion, turbulent eddy-impaction, and thermophoresis (Rosner, Tassopoulos and Tandon, 1993,1994). Also under development are methods to predict interactions between aggregates and their surrounding *vapor* environment---interactions which can lead to primary particle growth, or burn-out. Toward this end, we have also developed new and efficient methods to predict the "accessible surface area" of populations of aggregates (expressed as a fraction , η_{pop}, of the true total surface area in Fig. 4), including its dependence on mean aggregate size $(\bar{N})$, probing molecule reaction probability α, and pressure level (*via* Knudsen number based on primary particle diameter) for aggregates of a prescribed structure (fractal dimension, D_f). Figure 4 shows the results of applying to a log-normal *population* of aggregates our "effective Damkohler number" correlation approach to calculate η for each individual aggregate (Rosner and Tandon,1994) in the population.

We are now carrying out theoretical studies on the structure of thin reaction-nucleation-coagulation 'sublayers' within laminar mixing- and boundary- layers (Fig.7 below), including stagnation flows similar to those achieved in our counterflow burner (Fig. 1) and CVD-impingement flow reactor (Fig. 5).An account of our recent studies of the *unusual population dynamics* of coagulating absorbing-emitting particles in strong *radiation fields* will be found in *Aerosol Sci. Tech.* (Mackowski *et.al.*, 1993). For a useful overview of our work on these and other effects of energy transfer on suspended particle dynamics, see our *IEC-Research* paper: Rosner, *et. al.*, 1992.

3 FORMATION KINETICS AND MORPHOLOGY OF CVD-MATERIALS: THEORY OF MULTI-PHASE WITH NUCLEATION, GROWTH AND THERMOPHORESIS

A small impinging jet (stagnation flow) reactor (Fig. 5) has been used to study the chemical vapor deposition (CVD-) rates of refractory layers on inductively (over-)heated substrates in the presence of complicating homogeneous reactions of the vapor precursor. These measurements are being used to understand deposition rates and associated deposit microstructures observed in highly non-isothermal, often particle-containing local CVD environments. Figure 6 shows (logarithmic ordinate) our apparent deposition probability *vs.* reciprocal surface temperature for $TiO_2(s)$ films obtained from TTIP(g) over the broad surface temperature range: 600-1600K. A mathematical model incorporating finite-rate reagent depletion near the hot surface captures the experimentally observed deposition rate trends (Fig. 6; curve marked $Dam_{hom} = A_{hom}\delta^2/D = 8.7x10^4$). A more detailed mathematical model (Tandon and Rosner, 1994) tracks the size distributions of nucleated particles within such BLs (Fig. 7), including the particle+vapor "co-deposition" rate at the surface y=0.

Missing from previous predictions of film deposition rates has been essential information about deposit microstructure and ancillary thermophysical properties. Toward this end we have investigated the possibility of a rational correlation of vapor *deposit* grain *densities* based on the

notion that close-packed dense deposits should be possible only when the characteristic time for adatom(molecule) *surface diffusion* is short compared to the time for *surface reaction* and "burial". Our preliminary results (Fig. 8; after Kho, Collins and Rosner,1994) are encouraging and the addition of further relevant characteristic times to our scheme may open the door to the corelation/'anticipation' of other important deposit characteristics.

CONCLUSIONS, FUTURE RESEARCH

In our 1993-1994 OSR-sponsored Yale HTCRE Lab research (briefly described above, and in greater detail in the archival references cited and updated below) we have shown that new methods for rapidly measuring vapor- and particle-mass transfer rates , combined with advances in multiphase transport theory, provide useful means to identify and incorporate important, often previously neglected, transport phenomena in propulsion/materials engineering design/ optimization calculations. As indicated in Section 2, we are now extending our work on transport effects involving *aggregated particles* to include their stability (with respect to high temperature *restructuring*, leading to a loss of surface area). For this purpose an improved CDF burner has been employed (Fig. 1), along with supplementary optical and thermophoretic sampling/TEM diagnostics (Figs. 2,3) . These techniques, together with closely coupled theoretical calculations of particle birth/dynamics in mixing/boundary layers (Fig. 7) , promise to lead to a valuable understanding of combustion-generated ultra-fine particles and films (including their deposition or erosion (Rosner and Tandon, 1994, Kho, Rosner and Tandon,1994)).

REFERENCES

Albagli, D. , Xing, Y. and Rosner, D.E., "Experimental Studies of the Morphology of Combustion-Generated Ultrafine Particles", (in preparation, 1994).

Cohen, R.D., and Rosner, D.E., "Kinetics of Restructuring of Large Multi-Particle Aggregates ", in prep., 1994.

Collins, J. , **Effects of Homogeneous Reaction on the Chemical Vapor Deposition of Titanium Dioxide**, Yale University Graduate School, PhD Dissertation, May, 1994

Collins, J. and Rosner, D.E., "Deposition Rates and Deposit Quality for Heated Surface CVD in the Presence of Simultaneous Homogeneous Reaction: Deposition of TiO_2 Films from TTIP", for *J. Electrochem. Soc.* (1994)

Gomez, A., and Rosner, D.E., "Thermophoretic Effects on Particles in Counterflow Laminar Diffusion Flames", *Combust. Sci. and Tech.* **89**, 335-362 (1993).

Kho, T. , Collins, J. and Rosner, D.E.,"Development, Preliminary Testing and Future Applications of a Rational Correlation for the Grain Densities of Vapor-Deposited Materials", *J. Materials Science*, submitted, 1994

Kho, T. , Rosner, D.E. and Tandon, P., " Simplified Erosion Rate Prediction Technique for Cylindrical Targets in the Crossflow of Abrasive 'Polydispersed' Suspensions", (in preparation, 1994)

Konstandopoulos, A.G. and Rosner, D.E.,"Inertial Effects on Thermophoretic Transport of Small Particles to Walls With Streamwise Curvature—I. Experiment, II. Theory", *Int. J. Heat Mass Transfer* (in press 1994).

Mackowski, D.W., Tassopoulos, M. and Rosner, D.E.,"Effect of Radiative Heat Transfer on the Coagulation Dynamics of Combustion-Generated Particles", *Aerosol Sci. Technol (AAAR)* (in press 1994).

Rosner, D.E., **Transport Processes in Chemically Reacting Flow Systems**, Butterworth-Heinemann (Stoneham MA), 3d Printing (1990) sold out; for 4th printing contact author directly..

Rosner, D.E., Cohen, R.D. and Tandon, P., "Development of Pseudo-Continuum Theories of the Restructuring Kinetics of Large (Multi-Particle) Aggregates in Combustion Systems", presented at **AAAR 1993 Annual Mtg.**, Oak Brook, IL (Oct. 11-15, 1993).

Rosner, D.E., Collins, J. and Castillo, J.L., "Onset Conditions for Gas Phase Reactions and Particle Nucleation/Growth in CVD Boundary Layers", Proc. 12th **International Conference on CVD**, Electrochem. Soc., Proc. Vol. 93-2, 1993, pp. 41-47

Rosner, D.E., Konstandopoulos, A.G., Tassopoulos, M., and Mackowski, D.W, "Deposition Dynamics of Combustion-Generated Particles: Summary of Recent Studies of Particle Transport Mechanisms, Capture Rates, and Resulting Deposit Microstructure/Properties", *Proc. Engineering Foundation/ASME Conference*: **Inorganic Transformations and Ash Deposition During Combustion**, 585-606 (1992).

Rosner, D.E., Mackowski, D.W and Garcia-Ybarra, P., "Size and Structure-Insensitivity of the Thermophoretic Transport of Aggregated 'Soot' Particles in Gases", *Comb. Sci & Technology* **80** (1-3), 87-101 (1991).

Rosner, D.E., Mackowski, D.W, Tassopoulos,M., Castillo, J.L., and Garcia-Ybarra, P., "Effects of Heat Transfer on the Dynamics and Transport of Small Particles in Gases", *I&EC-Research (ACS)* **31** (3), 760-769 (1992).

Rosner, D.E. and Tandon, P., "Pseudo-Continuum Theories of the Transport Properties of Large (Multi-Particle) Suspended Aggregates", prepared for presentation at the AIChE **1993 Annual Mtg.**, St. Louis, MO (Nov. 8-12, 1993).

Rosner, D.E.and Tassopoulos, M.,"Deposition Rates from 'Polydispersed' Particle Populations of Arbitrary Spread", *AIChE J.* **35** (9) 1497-1508 (1989)
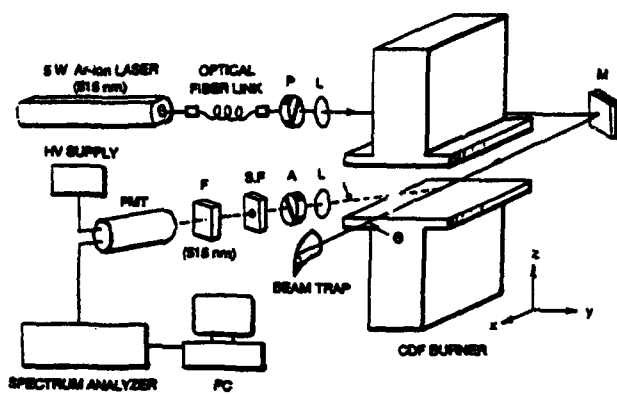
Fig.1 "Slot"-type counterflow diffusion flame (CDF-) burner set-up for *in situ* and extractive experimental studies of the nucleation, growth, transport and restructuring of aggregates in flames (after Albagli and Rosner, 1994; see, also Gomez and Rosner, 1993)
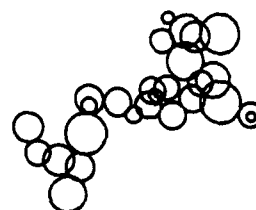
Fig. 2 Typical multi-particle aggregate thermophoretically extracted from laminar CDF ($CH_4/O_2/N_2$, equiv. ratio: 0.833, nom. strain rate 4 s^{-1}) seeded with TiO_2 precursor TTIP vapor. TEM image (a) compared with 'touching sphere' idealization (b) (after Albagli, Xing and Rosner, 1994)
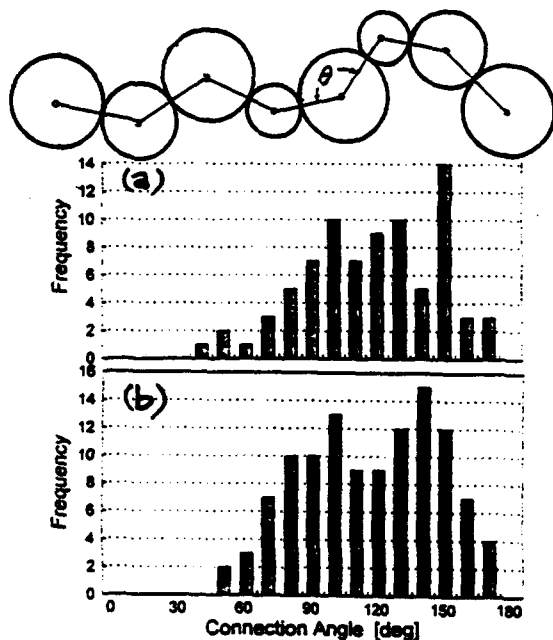
Fig. 3 Distribution of angles (projected) between touching 'primary' particles in sample of 7 multiparticle aggregates thermophoretically extracted from two locations on oxidizer side of laminar CDF seeded with TTIP: a) 5 mm from flame, b) 2 mm from flame (after Albagli, Xing and Rosner, 1994; see, also, Cohen and Rosner, 1993,1994))
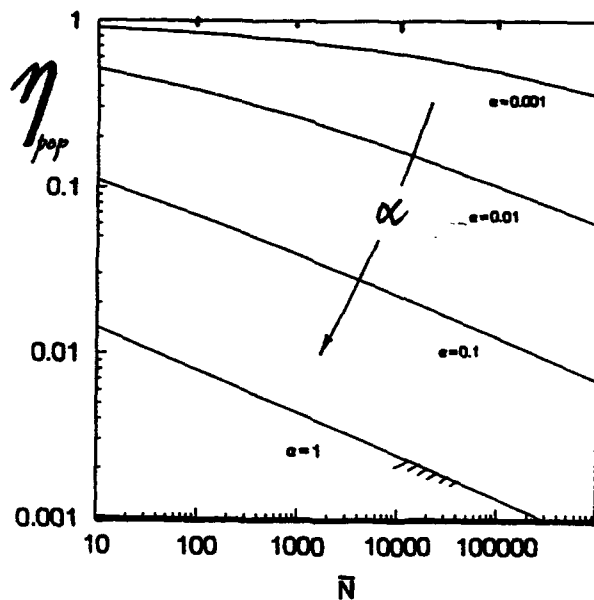
Fig.4 Predicted accessible area fraction for a population of aggregates *via* "porous sphere" model of each large fractal aggregate (D_f=2.5) in the high pressure limit ; $\bar{N}$ is mean number of primary particles per aggregate and α = probability for gas/surface reaction (after Rosner and Tandon, 1993)

59
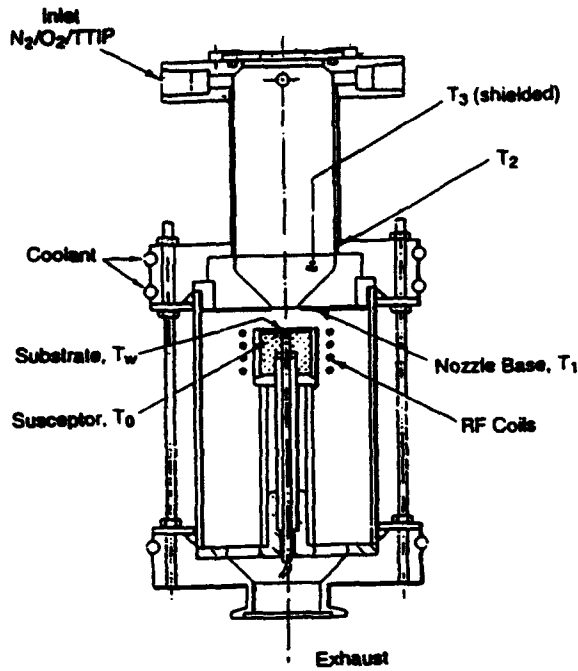
Fig. 5 Axisymmetric impinging jet CVD-flow reactor with inductively heated "pedestal" for studies of vapor + particle co-deposition across laminar BLs (after Rosner, Collins and Castillo, 1993, Collins, 1994)
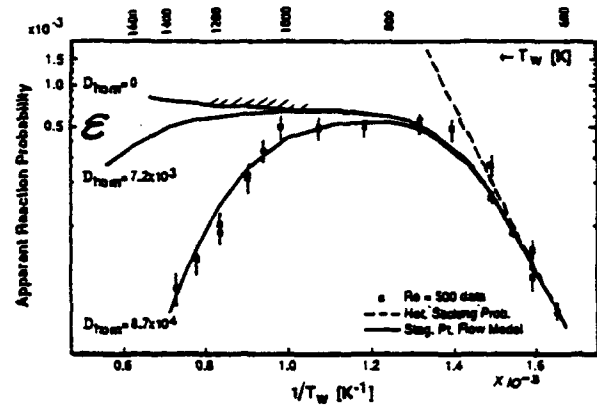
Fig.6 TiO$_2$(s) deposition rate data (reported as apparent heterogeneous reaction probability ε) from TTIP/O$_2$/N$_2$ mainstream showing calculated deposition rate behavior in presence of *homogeneous* reactions to form non-depositing species (after Rosner, Collins and Castillo, 1993, Collins, 1994, Collins and Rosner, 1994)
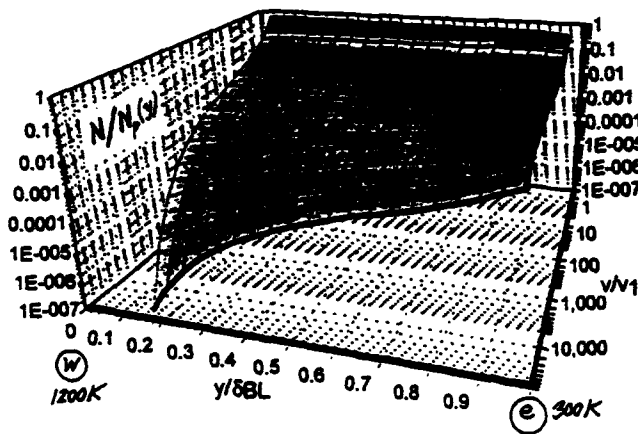
Fig. 7 Predicted local size distributions of particles nucleated within thermal boundary layer near hot deposition surface. y/δ_{BL} = relative position in LBL; v/v_1 = particle volume in monomer volume units (after Tandon and Rosner, 1994)
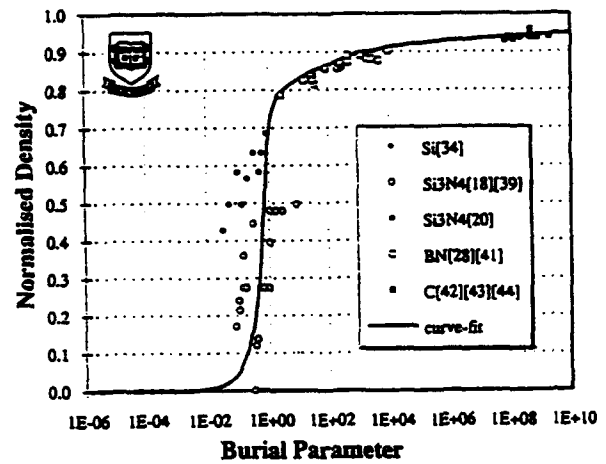
Fig. 8 "Universal" correlation of experimentally reported solid deposit densities based on a Damköhler number ("burial" parameter) comparing the characteristic times for surface reaction and surface diffusion (after Kho, Collins and Rosner,1994)

60

SUPERCRITICAL DROPLET BEHAVIOR

AFOSR Task 2308AP

Principle Investigator: D.G. Talley

Combustion Branch, Fundamental Technologies Division
Propulsion Directorate
OLAC Phillips Laboratory
Edwards AFB, CA 93524-7660

Summary/Overview:

The objective of this research is to explore the transcritical behavior of vaporizing and burning droplets. By this is meant the behavior of droplets injected at supercritical pressures but initially at a subcritical temperature, which then undergo a transition to a supercritical state as they are heated in a hot environment. An experimental approach is taken using a free droplet technique, whereby monodisperse droplets are studied as they fall freely in a pressure chamber. At present, Raman visualizations of LOX droplets falling in a high pressure shock tube are being performed. The goal is to measure velocity fields and temperature and species concentration profiles, measurements that have not previously been available. In addition, a simple way to simulate the deformation and breakup behavior of zero surface tension droplets has also been explored, in which one liquid is injected into another miscible liquid. The results confirm that breakup regimes of zero surface tension droplets depend on the Reynolds number.

Authors: D.G. Talley, R.D. Woodward, and J.C. Pan

Technical Discussion:

Background and Objectives

Reducing the cost of future Air Force rocket and airbreathing propulsion systems requires an improved understanding of combustion fundamentals. In large rocket engines, for example, an error of even a fraction of a percent in predicted combustion efficiency can magnify into a change in payload capability worth millions of dollars per launch. Saving the necessity for even one engine test during engine development can be worth many hundreds of thousands of dollars. Needs exist to better understand and predict mechanisms leading to combustion performance, chamber wall and injector faceplate heat transfer, and combustion instabilities. This is particularly true in high pressure systems which exceed the critical pressure of the propellants. In many cases the fuel or oxidant (liquid oxygen in rocket propulsion systems) is injected at supercritical pressures but initially at a subcritical temperature. The propellant then undergoes a transition to a supercritical state as it is heated and burned in the combustion chamber—the so-called transcritical process. Compared with the analogous subcritical case, transcritical and supercritical injection and combustion remains relatively poorly understood.

Droplets remain the simplest and most easily studied of spray systems, and despite the added complexities of full fledged sprays many of the interfacial transport and breakup mechanisms applicable to them can be understood from single droplets. The goal of this work is to better understand these applicable mechanisms for transcritical spray injection, through a better understanding of droplet processes. There are a number of differences from the subcritical case that need to be addressed. Gas/liquid density ratios are near unity, so the quasi steady gas phase assumption commonly employed in subcritical studies is no longer valid. The equilibrium "wet bulb" condition may also not exist. Thus transcritical droplet vaporization/combustion is a fully unsteady phenomenon. The computation of properties becomes significantly more complicated in that properties such as diffusion coefficients become functions of pressure as well as temperature, and the solubility of the gas phase in the liquid phase increases significantly. The latter effect can mean that the effective critical pressure of the mixture can be several times the critical pressure of the pure phase. Other property anomalies can to singular

61

behavior near the critical condition. For instance, the burning rate has been observed to reach a maximum near the critical pressure, and the potential to couple with combustion instabilities may be increased. The surface tension also vanishes, potentially leading to significantly different droplet deformation and breakup mechanisms. These latter mechanisms can be particularly important because they have a direct effect on mixing.

Past experimental studies of transcritical droplet processes have been mostly limited to global measurements such as the variation of droplet lifetimes and burning times as a function of pressure [1-4]. While useful, these provide an incomplete picture of the transport and breakup mechanisms that can contribute to mixing and the potential to couple with combustion instabilities. On the other hand, the theoretical understanding of transcritical droplet vaporization, combustion, and breakup has advanced significantly in recent years due to the introduction of new models [5,6]. However, these remain unverified experimentally. The objective of this work is to provide detailed measurements of transcritical droplet flow fields and temperature and composition profiles that can be used to validate these models, as well as to develop semi-empirical correlations for direct use in comprehensive engine design codes. These measurements will be performed both in quiescent environments and in the presence of acoustic disturbances representative of combustion instabilities.

Drop Generation and Diagnostics

Detailed measurements of droplet flow fields and temperature and composition profiles are believed to be feasible through a combination of 1) precise control of the droplet generation process to achieve repeatable, monosized droplets, and 2) incorporation of "drop slicing" [7] and other innovative droplet diagnostic techniques that have recently been developed. Progress in these two areas is summarized below.

Since the primary application at the Phillips Laboratory is rocket propulsion where the transcritical fluid is liquid oxygen, a piezoelectric droplet generator has been developed which is capable of producing a monodisperse stream of cryogenic droplets at high pressures. As of the date of this writing, the generator has successfully produced monodisperse streams of liquid nitrogen and liquid oxygen droplets in an acoustically excited Rayleigh breakup mode at pressures to 700 psi. Extension to higher pressures is in progress, and will be reported at the meeting. The generator has also successfully operated in a drop-on-demand mode for hydrocarbon and water droplets at atmospheric pressure, but the severe heat transfer environment has so far precluded operating in this mode with cryogenic fluids. Drop-on-demand operation at elevated pressures has not yet been attempted for non-cryogenic fluids.

Advanced droplet diagnostics have been under development for a number of years under AFOSR and Phillips Laboratory funding by several researchers [7-9]. These have been limited almost exclusively to subcritical droplets. Application of these and other techniques is currently being evaluated in a collaborative effort with the United Technologies Research Center. Promising candidates will be further exercised at the Phillips Laboratory. At present, Raman imaging appears attractive at high pressures due to the increased signal from the high molecular number density, and can potentially provide both species and temperature measurements. Raman imaging of LOX droplets at high pressures is currently being performed in the UTRC shock tube facility by one of the authors (Woodward). Results will be reported at the meeting.

Deformation and breakup of zero surface tension fluid particles

As mentioned previously, deformation and secondary breakup of droplets contributes directly to mixing. Understanding this process for transcritical droplets as the droplet surface becomes critical and surface tension vanishes is one of the important unknowns to be addressed in this work. In parallel with the above experimental effort, an extraordinarily simple and inexpensive way to produce zero surface tension droplets in simulation of transcritical droplets has also been explored. The results are summarized below. First, however, some theoretical considerations will be presented. In view of the highly nonspherical shapes of zero surface tension "droplets," they will hereinafter be referred to as "particles," while the surroundings will be referred to as the "fluid."

Deformation and breakup of particles is largely characterized by the following primitive variables: the fluid and particle densities ρ and ρ_p (the subscript "p" refers to the particle and a lack of subscript refers to the surrounding), the fluid and particle viscosities μ and μ_p, the particle size D, the particle-fluid relative velocity V, the particle acceleration a, and the surface tension σ. These are typically grouped into the following five dimensionless variables:

Density ratio: $\quad\quad\quad Dr = \rho_p / \rho$ $\quad\quad\quad\quad\quad\quad\quad\quad\quad\quad\quad\quad$ (1)

Viscosity ratio: $\quad\quad\quad Vr = \mu_p / \mu$ $\quad\quad\quad\quad\quad\quad\quad\quad\quad\quad\quad\quad$ (2)

Weber number: $\quad\quad\quad We = \rho D V^2 / \sigma$ $\quad\quad\quad\quad\quad\quad\quad\quad\quad\quad\quad$ (3)

Eotvos number: $\quad\quad\quad Eo = a \rho_p D^2 / \sigma$ $\quad\quad\quad\quad\quad\quad\quad\quad\quad\quad$ (4)

Reynolds number: $\quad\quad\quad Re = \rho V D / \mu_p$ $\quad\quad\quad\quad\quad\quad\quad\quad\quad\quad$ (5)

Alternatively, the Ohnesorge number, $Oh = \mu_p / (\rho_p D \sigma)^{1/2}$, can be used in place of one of these numbers, but not in addition to them in view of the relationship $We = \left[Dr Re^2 \right] Oh^2$. As surface tension vanishes, both We and Eo, as well as Oh, become infinite, and these numbers no longer become useful. The effect of acceleration is then more effectively described by taking the ratio

$$Eo / We = Dr(aD / V^2)$$
$$(6)$$

where the number aD / V^2 is a ratio of hydrostatic forces in the droplet caused by acceleration to the dynamic pressure, and to our knowledge has been given no name. When particle acceleration is not important, this number becomes zero, and deformation and breakup behavior should depend only on the Reynolds number and the two property ratios. This makes sense, for as defined here the Reynolds number is the ratio of the inertial forces, which tend to cause deformation and breakup, and the particle viscous forces, which tend to resist. Some experimental evidence exists that this is true. According to the relationship preceding eq. 6, a constant Reynolds number should be represented as straight lines with slope 2 on a log plot of We vs. Oh. The high Ohnesorge number data of Hsiang and Faeth [10] approaches this slope, which could be interpreted to imply that in the limit of zero surface tension breakup regimes can be determined by the Reynolds number and density ratio alone. To our knowledge, this hypothesis has not been suggested before, but little experimental evidence besides that of Hsiang and Faeth has so far existed to validate it. In the transcritical regime where $Dr \approx 1$, deformation and breakup should in fact depend only on Re and possibly the viscosity ratio Vr.

To provide further evidence, a simple way to produce zero surface tension particles is suggested in which a fluid particle is injected into another fluid with which it is miscible. Surface tension is caused by an asymmetry of molecular forces at a surface over a distance of a few molecules [11]. As initially separate miscible fluids begin to co-dissolve into each other, the gradient between the two rapidly flattens over many thousands of molecules, and the "surface," along with the surface tension, is effectively destroyed. Fortuitously, such a system has other similarities with transcritical droplets as well. For instance, liquid densities simulate the densities of high pressure fluids, and miscible liquids can easily be found where the density ratio is near unity. Additionally, the co-dissolving effect may also simulate the high solubility of the gas phase into the liquid phase as the critical point is reached. On the other hand, transport phenomena may not be well simulated, but this should not be relevant to the purely kinematic behavior of deformation and breakup, as long as these occur faster than transport time scales.

Visualizations were performed of simple sucrose solutions in water, where the sucrose densities were slightly greater than the water so that the sucrose particles would fall. Reynolds numbers were varied by initially diluting the sucrose with small amounts of water, thus changing the viscosity. A dependence of

the breakup regimes on the Reynolds number was confirmed. Highly viscous particles were observed to initially flatten into pancake shapes as they fell. Eventually, as water became dissolved into the particles and viscosity was reduced, the particles appeared to suddenly breakup into a small number (<5) of smaller globules, as in a bifurcation ("n-furcation"). This appeared to be due to some fluid dynamic instability. Further down, the small globules would similarly break down into even smaller globules in a manner which suggests fractal behavior. Less highly viscous particles would "n-furcate" more quickly, and possibly into a larger number of globules. The net effect was that highly viscous zero surface tension particles tended to behave particle-like, maintaining their coherence with relatively higher terminal velocities. Less viscous particles dissipated rapidly, with correspondingly slower terminal velocities. In application one would expect the latter to be better mixers.

Future work

Operation of the monodisperse droplet generator to produce transcritical droplets to 2000 psi should be feasible within the next few months. The initial focus over the next year will primarily be on steady conditions. However, acoustically perturbed measurements are eventually planned using a high pressure piezoelectric acoustic driver (UTRC will separately be performing shock tube experiments). Measurements of the velocity fields and temperature and composition profiles of transcritical droplets will be made using Raman imaging. Other diagnostic methods will also be explored. Emphasis will be placed on determining how interfacial behavior affects breakup and vaporization. Finally, the analogy with miscible liquids will be further explored.

References

1. Faeth, G.M. Dominicis, D.P. Tulpinsky, J.F., and Olson, D.R., "Supercritical Bipropellant Droplet Combustion," *Twelfth Symposium (International) on Combustion*, The Combustion Institute, pp. 9–18 (1969).
2. Sato, J., Tsue, M., and Kono, M., "Effects of Natural Convection on High Pressure Droplet Combustion," *Comb. Fl.* 82: 142–150 (1990).
3. Natarajan, R., and Brzustowski, T.A., "Some New Observations on the Combustion of Hydrocarbon Droplets at Elevated Pressures," *Comb. Sci. and Tech.* 2: 259–269 (1970).
4. Sowles, R.E., "An Experimental Study of Carbon Dioxide Droplets Falling Through Inert High Pressure High Temperature Environments," Ph.D. Thesis, Dept. of Mech. Eng., University of Wisconsin (1973).
5. Shuen, J.S., Yang, V., and Hsiao, C.C., "Combustion of Liquid Fuel Droplets in Supercritical Conditions," *Comb. Fl.* 89: 299–319 (1992).
6. Delplanque, J.-P., and Sirignano, W.A., "Numerical Study of the Transient Vaporization of an Oxygen Droplet at Sub- and Supercritical Conditions," *Int. J. Heat Mass Transfer* 36: 303–314 (1993).
7. Winter, M., "Droplet Slicing Measurements of Internal Circulation," 31st AIAA Aerospace Sciences Meeting & Exhibit, Reno, NV, paper 93–0900 (1993).
8. Winter, M., and Melton, L., "Fluorescent Diagnostics and Fundamental Droplet Processes," presented at this meeting.
9. Chang, R.K., "Nonlinear Optical Spectroscopy of Multicomponent Droplets," presented at this meeting.
10. Hsiang, L.-P., and Faeth, G.M., "Secondary Drop Breakup in the Deformation Regime," 30th Aerospace Sciences Meeting & Exhibit, paper AIAA 92-0110 (1992).
11. Probstein, R.F., "Physicochemical Hydrodynamics," Butterworths, 1989.

COMBUSTION INSTABILITY PHENOMENON OF IMPORTANCE TO LIQUID PROPELLANT ROCKET ENGINES

Principal Investigators: R.J. Santoro and W.E. Anderson

Propulsion Engineering Research Center
and
Department of Mechanical Engineering
The Pennsylvania State University
University Park, PA 16802

SUMMARY/OVERVIEW:

The performance, heat transfer, and combustion stability characteristics exhibited by liquid rocket combustors are largely dictated by the injector design. Studies of impinging jet, swirl coaxial, and shear coaxial injector elements used for liquid-liquid, liquid-gas, and gas-gas propellant injection comprise a comprehensive research effort undertaken at Penn State to develop a detailed understanding of common injector element types through experimentation and analysis. The results of this research will provide a basis for the development of advanced combustor design analysis models that can accurately predict the injector's geometric and operational effects. Under the present AFOSR support, studies of swirl coaxial and impinging jet injector elements have been undertaken for liquid-gas and liquid-liquid applications, and have focused on their primary atomization and spray formation processes under both cold- and combusting-flow conditions. Progress made over the last year related to these impinging jet and swirl coaxial injector studies is described in more detail below.

TECHNICAL DISCUSSION:

Work to date on impinging jet injectors has strongly suggested that combustion stability can often be directly related to the periodicity of primary atomization. The appearance of waves near the impingement point that eventually lead to periodic breakup further suggests that interactions between jet flow instabilities in the stagnation region may be a root cause of combustion instability. Studies are underway to provide conclusive substantiation regarding this mechanism of combustion instability.

Previous work as part of this research effort on impinging liquid jets included measurements of fan breakup length, drop size, and surface wave and periodic ligament formation phenomena under cold-flow, atmospheric pressure conditions.[1] Studied parameters included orifice length-to-diameter ratio (L_o/d_o), orifice diameter, impingement angle, impingement length (L_{imp}), jet flow condition (turbulent or laminar), and jet velocity. In summary, the results indicated that primary breakup of turbulent impinging jets is closely related to wave-like disturbances formed very near the impingement point. The distance between these disturbances was linearly dependent on jet diameter and was relatively independent of jet velocity. These characteristics are consistent with a process whereby long wave helical disturbances on the jet are transmitted to the fan surface. Linear stability analysis of long wave disturbances on a jet indicate that the fastest growing helical disturbance has a wavelength of about ten times the jet diameter and is independent of jet velocity; predominant observed disturbances on the sheet formed by the impinging jets exhibited wavelengths of about two - five jet diameters.

Work over the past year has concentrated on fan breakup length and drop size measurements under high pressure and oscillatory pressure conditions and development of a primary atomization model for impinging liquid jets. The high-pressure acoustic chamber used in the cold-flow characterization tests has interior dimensions of 0.254 m in width, 0.305 m in height, and 0.102 m in depth. Plexiglas walls allow optical access into the chamber. Maximum operating pressure is 1.03 MPa (150 psia). A compression driver attached to a chamber side wall is used to drive the first (1W), second (2W), and third (3W) resonant modes in the 0.254 m width dimension. Frequencies on the order of 1000 hertz, typical of rocket combustion instabilities, are driven at amplitudes up to 4% of chamber pressure. The impinging jet injector element fits into the center of the top plate of the chamber, enabling evaluation of velocity-coupled effects for the 1W and 3W modes and evaluation of pressure-coupled effects for the 2W mode. To date, one twist-drilled injector ($L_o/d_o=10$; $L_{imp}/d_o=14$) has been used in this chamber. Jet Reynolds numbers have ranged from 3420 to 17000 ($3.4<U_j<17$ m/s), and chamber pressures have been varied from atmospheric to 915 kPa.

The nondimensional breakup length, x_b/d_o, obtained from instantaneous images of the impinging jet spray with a solid state CID camera is plotted as a function of Weber number (We = $\rho_l U_j^2 d_o/\sigma$) and chamber pressure in Figure 1. Each symbol represents an average breakup length from 17 measurements. Also shown in this figure is the breakup length data for a 1.02 mm diameter, $L_o/d_o=50$ precision-bore glass tube set of impinging jets. At atmospheric conditions, there is little apparent difference between the breakup length measured for the long orifice,

long impingement length glass tubes and the shorter orifice, shorter impingement length twist-drilled injector. Increased ambient density reduces the sheet breakup length as jet velocity increases. It was difficult to obtain measurements of breakup length at elevated chamber pressures for jet velocities greater than about 10 m/s since the turbulent nature of the impinging jet spray and window-wetting lead to low contrast images. The effect of the three chamber resonant modes on breakup length is shown in Figure 2. In all cases, the breakup length is essentially independent of Weber number. Shorter breakup lengths were observed for the sheet in the presence of the 1W and 3W modes than for either the quiescent case or the case where the 2W mode was present. These results suggest that oscillating velocity effects are greater than oscillating pressure effects on breakup length. Drop size measurements in this chamber are underway, but difficulties apparently related to recirculation zones within the chamber that tend to trap small drops resulting in erroneous measured size distributions are hindering progress.

Modeling efforts in the past year have centered on the use of a finite difference Navier-Stokes code to investigate the effects that spatial and temporal jet flow oscillations have on the primary breakup of the impinging jet fan into ligaments. Directly opposed jets are chosen for study to simplify the analysis. Representative computational results showing the free surface contour maps are illustrated in Figure 3. Spatial and temporal disturbances were imposed on the jets as boundary conditions. The cases presented include imposed sinusoidal disturbances of 500, 1000, and 2000 s^{-1} on each jet that are 180° out of phase with each other. This work is ongoing. The results of planned cold-flow experiments that focus on the impingement region will be used to help define a new analytical approach that will be undertaken in the future.

Work on swirl coaxial liquid-gas injector elements has emphasized experimental characterization of the LOX spray field produced under high-pressure and combusting-flow conditions in an optically-accessible combustor at the Combustion Cryogenic Laboratory (CCL). The location and extent of the liquid oxygen (LOX) spray cone and intact LOX sheet have been grossly determined. Because the swirl element provides superior atomization and mixing, and is less well understood than a shear coaxial element, its characteristics are being closely detailed. Figure 4 (left) shows the water spray formed by a swirl coaxial injector element with a coflowing gas. Figure 4 (right) shows an image of the combusting LOX spray using the same injector used in the cold-flow studies. Measurements of the drop size distribution and of the location of the LOX spray are also being made to provide information related to atomization and mixing.

The ability to use oxygen as a working fluid is an important feature of future SSTO rocket propulsion systems. This includes the use of oxygen-rich preburners (O/F mass ratio>100) in staged combustion propulsion systems. The enhanced spray formation and drop dispersion resulting from the swirling action of the LOX leads to improvements in ignition and flame stability, leading to the ability to operate the swirl coaxial element at very high LOX/H$_2$ mass ratios. Figure 5 is a plot of the characteristic exhaust velocity efficiency versus O/F mass ratio obtained in an optically-accessible combustor at the CCL using the swirl coaxial injector shown in Figure 4. In all tests, ignition occured readily and stable combustion was observed. These results from uni-element studies demonstrate the potential for robust injector performance at oxygen-rich conditions comparable to current technology interests for preburner designs.

Based on these results future work will emphasize high-pressure combusting-flow studies of both impinging jet and swirl coaxial injectors. Comparative work will also be intitiated on gas-gas injectors. This work will build on current experience at Penn State with shear gas-gas coaxial injectors.[2] Work on the swirl coaxial injector will also be compared to ongoing studies of shear coaxial liquid-gas injectors.[3] With these objectives in mind, certain experimental capabilities have been improved. Liquid hydrocarbon fuel test capability for impinging jet combusting-flow tests was added to the Cryogenic Combustion Laboratory (CCL). A high-pressure, optically-accessible combustor in which oscillating pressure fields can be generated has been designed to enable experimental studies under simulated combustion instability conditions at the CCL. A short orifice (L_o/d_o=5), short impingement length (L_{imp}/d_o=5) injector that matches practical injector designs has been fabricated for cold-flow characterization prior to its use in the combustion instability chamber and is presently being tested.

1. Ryan, H.M., W.E. Anderson, S. Pal and R.J. Santoro, "Atomization Characteristics of Impinging Liquid Jets," AIAA Paper 93-0230, 31st Aerospace Sciences Meeting, Reno, NV, January 11-14, 1993 (accepted for publication by Journal of Propulsion and Power, 1993).
2. Moser, M.D., J.J. Merenich, S. Pal and R.J. Santoro, "OH Radical Imaging and Velocity Field Measurements in a Gaseous Hydrogen/Oxygen Rocket," AIAA Paper 93-2036, 29th AIAA/SAE/ASME/ASEE Joint Propulsion Conference, Monterey, CA, June 28-30, 1993.
3. Pal, S., M.D. Moser, H.M. Ryan, M.J. Foust and R.J. Santoro, "Flowfield Characteristics in a Liquid Propellant Rocket," AIAA Paper 93-1882, 29th AIAA/SAE/ASME/ASEE Joint Propulsion Conference, Monterey, CA, June 28-30, 1993.
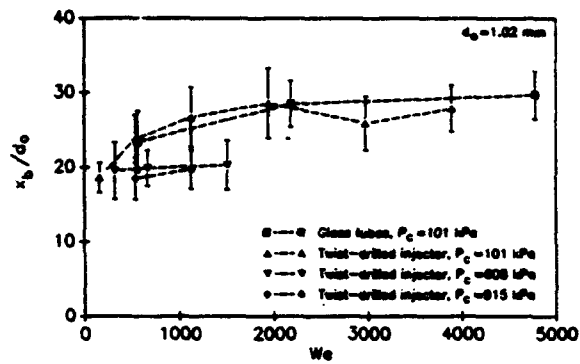
Figure 1. Nondimensional breakup length, x_b/d_o, plotted as a function of Weber number, We, and chamber pressure, P_c, for both glass tube and twist-drilled injectors. Impingement angle for both injector types is 60°.
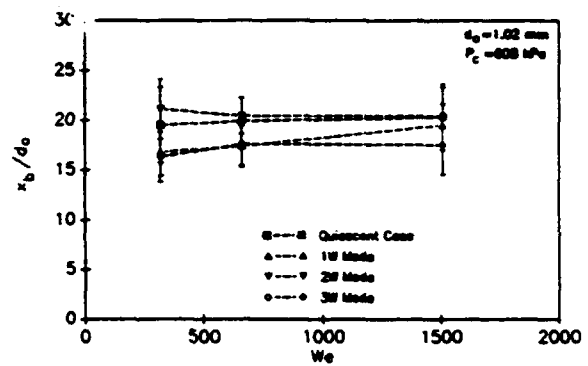
Figure 2. Nondimensional breakup length, x_b/d_o, plotted as a function of Weber number, We, and chamber resonant mode for the twist-drilled injector at a chamber pressure of 608 kPa.
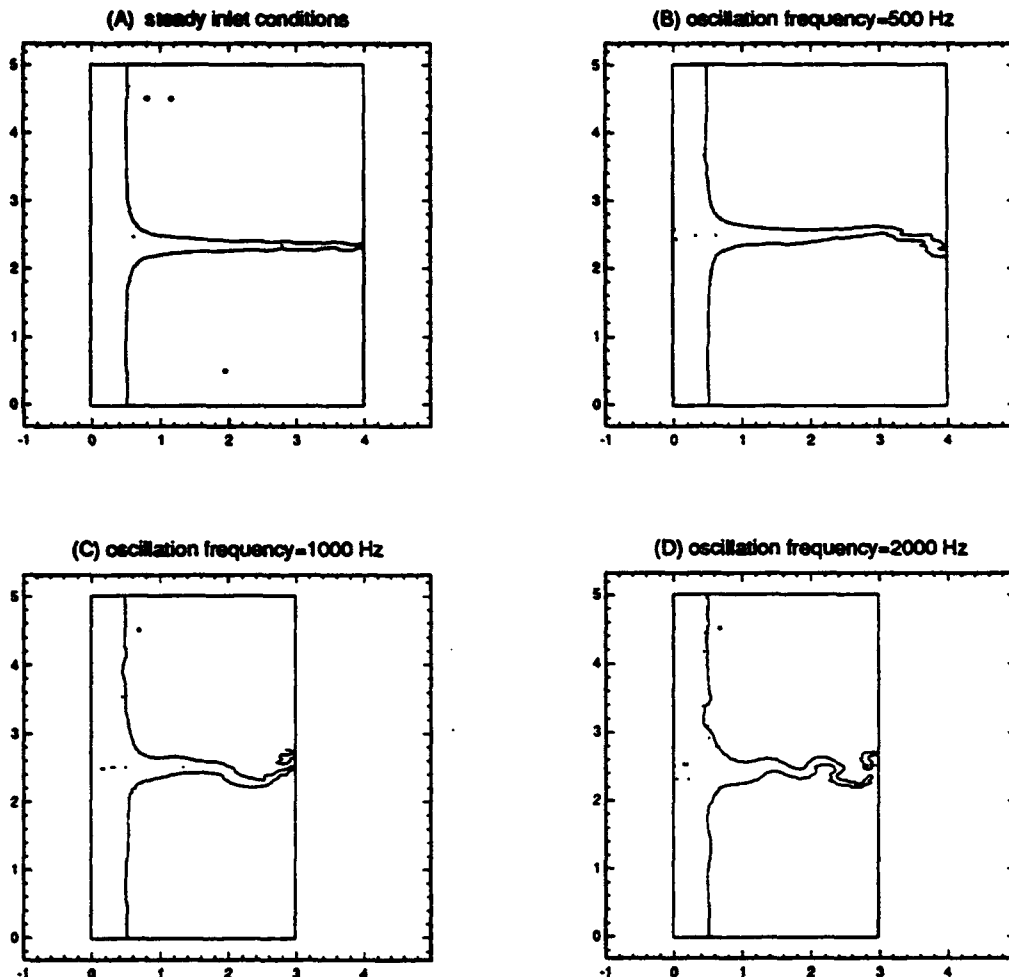
Figure 3. Contour maps of the free surface formed by two opposed liquid jets. Jets enter from the top (y=5 mm) and bottom (y=0 mm) of the computational domain and form a radial sheet that has a thinning cross section with increasing radius. Initial mean jet velocity is 10 m/s; initial jet diameter is 1 mm. Impinging jets shown in (A) have steady inlet conditions. Jets in (B), (C), and (D) show effects of spatially sinusoidal velocity fluctuations at 500, 1000, and 2000 s⁻¹, respectively, imposed at the jet inlet. The amplitudes of the velocity fluctuations are 5% of the mean velocity.

67
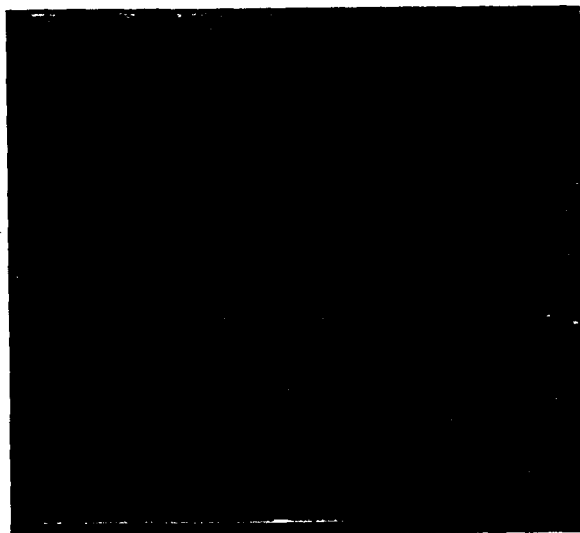
Figure 4. Images of swirl coaxial injector sprays. Instantaneous image on the left is of the near injector spray flowfield under non-combusting conditions. Water and air are used as simulants. Water flow is 0.2 lb/s issuing from the 3.3 mm diameter post, and air flows through the 1.4 mm annular gap. The image on the right is of the combusting spray formed by the same injector shown on the left. Window diameter is 50.8 mm. Propellants are LOX/GH$_2$ at an O/F ratio of 5.5. The LOX flowrate is 0.4 lb/s and the chamber pressure is 420 psia.
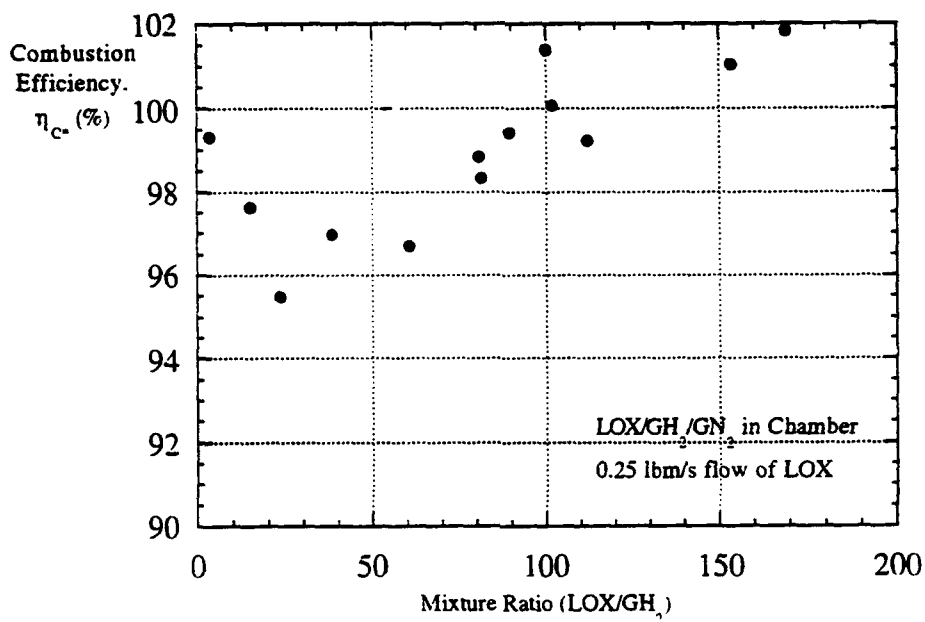
Figure 5. Measured characteristic exhaust velocity efficiency as a function of mass O/F ratio obtained in an optically-accessible rocket equipped with the swirl coaxial injector shown in Figure 4. Data is uncorrected for chamber wall heat transfer and nozzle discharge coefficient effects; corrected data will differ from raw data by less than +/-5%. Chamber pressures range from 140 to 340 psia.

68

LIQUID ROCKET MOTOR COMBUSTION STABILITY
USING COAXIAL INJECTORS

AFOSR Grant No. F49620-93-1-0126

Michael M. Micci

Aerospace Engineering Department &
Propulsion Engineering Research Center
The Pennsylvania State University
University Park, PA 16802

SUMMARY/OVERVIEW:

Although the hydrogen temperature ramping technique is used to determine the stability characteristics of hydrogen/oxygen coaxial liquid rocket motor injectors, there is no definitive knowledge of the effect of the hydrogen temperature on the stability characteristics of the injectors. Possible explanations are a detrimental change in the atomization characteristics due to a decrease in the velocity ratio, the disappearance of a stabilizing recirculation region at the base of the LOX post or a change in the gas side injector pressure drop allowing acoustic coupling to the propellant feed system. This program will provide the first quantitative measurements of droplet size and velocity distributions as a function of the injector velocity ratio and of injector pressure drop as a function of gas temperature. It will also be the first experimental examination of the recirculation region at the base of the injector LOX post. Due to the ability to use liquid oxygen at pressures occurring in actual liquid rocket motors, a high level of similitude can be achieved.

TECHNICAL DISCUSSION:

Although stable operating regimes for cryogenic coaxial injectors have been empirically determined, there is no knowledge of the spray characteristics corresponding to stable operation or the physical processes which produce the atomization patterns that result in stable or unstable operation. The current engineering method for determining the stable operating regime of a cryogenic coaxial injector is the "hydrogen temperature ramping" method, however there is still no definitive knowledge of the effect of the hydrogen temperature on the stability characteristics of coaxial injectors. The physical significance of the hydrogen temperature ramping technique may come from the atomization process occurring in coaxial injectors where the high velocity outer gaseous hydrogen flow strips droplets from the lower velocity inner liquid oxygen flow. Experiments at ONERA using water as the liquid oxygen simulant have shown that a higher relative velocity between the two flows results in smaller droplets and complete atomization closer to the injector exit[1]. Lowering the gaseous hydrogen temperature increases its density, thus lowering its injection velocity relative to the liquid in order to maintain the same mass flow.

---

[1]Vingert, L., "Coaxial Injector Spray Characterization for the Ariane 5 Vulcain Engine," 6th Annual Conference "Liquid Atomization and Spray Systems - Europe," July 4-6, 1990.

Wanhainen et al have shown that it is not the hydrogen temperature itself causing the transition to instability but the ratio of the gas to liquid injection velocities[2]. From this one might infer that the instability arises because of an increase in the liquid oxygen drop sizes along with an extension in the length of the atomization zone. A primary purpose of the experiments is to identify what effect the velocity ratio has on atomization.

Another proposed explanation for the emergence of unstable operation in the hydrogen temperature ramping test is that a recirculation region acting as a flameholder exists downstream of the LOX post tip. Below a minimum relative velocity between the liquid oxygen and gaseous hydrogen, the recirculation region becomes too weak to act as a flameholder and the combustion zone moves away from the injector face to a location where it can interact more strongly with the chamber acoustic modes. Liang and Schumann have examined this idea with an experimental and computational investigation of gaseous oxygen and hydrogen coaxial injectors[3]. They examined several injectors designed to produce recirculation regions of different sizes but found that all injectors tested showed the combustion region anchored to the base of the injector.

A liquid nitrogen cooled heat exchanger to lower the temperature of the injected gas, either hydrogen or helium, from ambient down to 80K has been designed and construction is in progress. The heat exchanger will be used for the final series of experiments to simulate the hydrogen temperature ramping test and examine the effect of temperature induced gas velocity changes on the resultant atomization and its subsequent effect on motor instability.

An injector with full-scale dimensions derived from the SSME preburner injector has been constructed. The SSME preburner injector was selected because the test facility is capable of providing the required gas and liquid mass flow rates for a full size injector and as large an injector as possible was desired to provide the possibility of optical access. A second LOX post was fabricated with a 7° taper at the tip to match the shape of the production injector element. Liquid nitrogen was used to simulate the liquid oxygen while gaseous nitrogen was used to simulate the gaseous oxygen.

To gain qualitative insight into the overall morphology of a shear coaxial injector spray, the spray was examined by imaging the scattered light from a laser sheet passing through the axis of the spray and, in a separate test series, from a stroboscope illuminating the backside of the spray. For the laser sheet imaging tests a frequency doubled Nd:YAG laser (532 nm), pulsed at 10Hz with a pulse duration of 10 ns, was used with a spherical and cylindrical lens combination to form a laser sheet with a thickness of 0.15 mm and negligible divergence at the injector centerline. In an effort to ascertain whether a more extensive droplet flow field exists beyond the observable limits of the laser sheet images, a modified approach to spray visualization was undertaken with the stroboscope. Based on previous flow visualization experience with water/air sprays at atmospheric pressure[4], the strobe light was directed toward

[2]Wanhainen, J.P., Parish, H.C. and Conrad, E.W., Effect of Propellant Injection Temperature on Screech in 20,000-Pound Hydrogen-Oxygen Rocket Engine, NASA TN D-3373, April 1966

[3]Liang, P.-Y. and Schumann, M.D., "A Numerical Investigation of the Flame-Holding Mechanism Downstream of a Coaxial Injector Element," Proceedings of the 24th JANNAF Combustion Meeting, CPIA Publication 476, Vol. 3, Oct. 5-9, 1987, pp. 599-610.

[4]Kaltz, T., Milicic, M., Glogowski, M. and Micci, M. M., "Shear Coaxial Injector Spray Characterization," AIAA Paper 93-2190, 29th Joint Propulsion Conference, Monterey, CA, June 28-30, 1993.

the backside of the spray, off center from the camera and in the direction of the injector face. With this orientation both the dispersed droplet region and the structure of the liquid core may be imaged with a 35 mm camera. The flash rate of the strobe was set at 10 Hz with a flash duration of 3 μs.

In general, the laser sheet photographs depict an overall contraction of the large scale liquid structures (liquid core and detached ligaments) and droplet flow regions with increasing ambient pressure. Regions of droplet flow are most evident downstream of the liquid structures, while very little droplet production is observed along the liquid column close to the injector exit. When the gas mass flow rate was decreased to approximately half of its original value, it resulted in a larger, more dispersed spray indicating a strong effect of mixture ratio on the atomization and vaporization of liquid nitrogen. The behavior of the spray with respect to increasing chamber pressure follows the same trend as the previous tests, in that the LN_2 spray contracts in size as the chamber pressure increases. Other tests were performed with the tapered LOX post using the stroboscope to visualize the spray. The stroboscope photographs showed the same contraction of the liquid and droplet flow regions with increasing pressure, but contradictory to the observed contraction of the spray with increasing pressure, the liquid core breakup length increased significantly for a chamber pressure greater than the critical pressure (3.4 MPa). Stroboscope tests with the nontapered LOX post under similar operating conditions revealed the same behavior for pressures above and below the critical point but indicated little differences in spray morphology between the two LOX post designs.

Quantitative information on the spray was pursued with a phase Doppler interferometric (PDI) device, developed by Aerometrics, which enabled simultaneous measurement of the temporarily averaged droplet size and velocity distribution at a point within the spray. The effect of gas mass flow rate on the droplet size distribution is seen in Fig. 1. Measurements were made along the axis 10 cm downstream from the injector for this test, which marks the approximate end of the spray according to the photographic results. The droplet size distributions have been superimposed in Fig. 1 to illustrate the general behavior of the spray with varying liquid to gas mixture ratios. At the lowest mixture ratio, which corresponds to full scale operation of the SSME preburner, the majority of droplets fall in the smallest size range of Fig. 1. As the gas mass flow rate decreases to 3/4 and 1/2, the droplet distribution shifts to larger droplet sizes. The small number of large droplets at the upper end of the size range, observed during all of the tests, may be due to remnants of the liquid core and/or coalesced small droplets.

In order to determine if a recirculation region exists at the base of the LOX post, a miniature diode laser LDV system has been assembled and is being used to probe the region at the base of the LOX post to determine under what circumstances a recirculation region exists. The LDV uses liquid droplets produced by the atomization process as the seeding particles. A pyrex tube was used for the exit region of the injector to allow LDV probing of the region immediately downstream of the LOX post in the injector recess region. Initial tests were conducted with water and air at atmospheric pressure. Downstream of the injector face the LDV measured all positive flow velocities, with the maximum occurring at positions directly downstream of the injector gas annulus. However, with the LDV probe volume moved into the recess region, positive velocities are measured in the core of the annular gas flow but decrease to zero as one moves radially inward and become negative directly downstream of the LOX post, thus indicating flow reversal. Tests are currently underway to more extensively map the flow in the recess region and to determine the effect of operating conditions and injector design on the strength of the recirculation region. Future tests are planned at elevated pressures under combusting conditions.

In the course of an extensive literature review, some previous experimental evidence was found that indicated that the spontaneous stability condition for a hydrogen/oxygen rocket was determined by the hydrogen pressure drop through the injector[5,6]. Below a critical minimum value for the pressure drop, chamber oscillations evidently can couple to the propellant feed system, causing a combustion instability in the chamber. However, the value of this critical pressure drop was a function of the injector and chamber design. A linearized, lumped-element model based on the Rayleigh criterion was generated to describe the fluid dynamics of several processes in the system and to illustrate the effect of injector geometry and fuel temperature on combustion stability. Response factors have been computed for the full scale injector operating under cold flow conditions and have confirmed a transition from stable to unstable operation as fuel temperature decreases. To verify these results, high frequency pressure transducers were mounted on the pressure chamber and injector fuel plenum and measurements were acquired under cold flow conditions using liquid and gaseous nitrogen and analyzed by fast Fourier transform. A strong correlation was found between the predicted injector response and the measured chamber pressure oscillation amplitudes relative to those measured in the injector fuel plenum.

A pressure chamber rated to 10 MPa for combusting experiments is currently being designed for use with liquid oxygen and gaseous hydrogen and will be able to operate at the full scale fuel and oxidizer flow rates. Future tests will involve PDPA measurements under combusting conditions for comparison to the cold flow results. Oscillatory pressure measurements will be made in the chamber injector and fuel plenum to verify the predicted injector responses under combusting conditions.
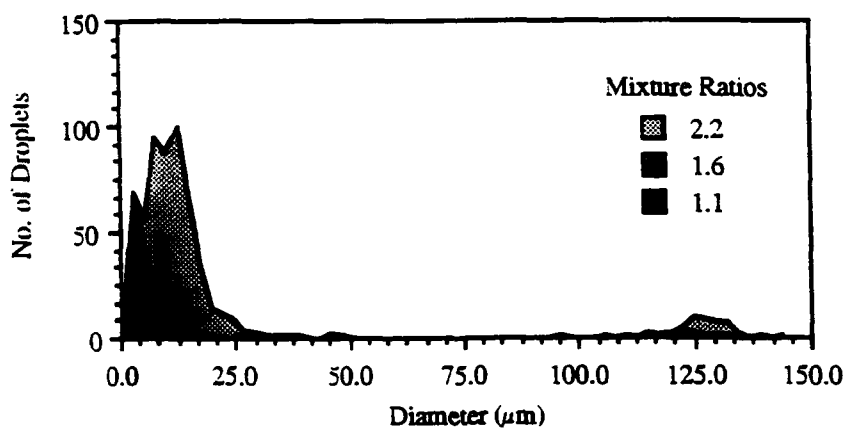
Fig. 1 Droplet size distributions for three oxidizer to fuel mixture ratios (P_c = 2.4 MPa).

[5]Conrad, E.W, Bloomer, H.E., Wanhainen, J.P. and Vincent, D.W., Interim Summary of Liquid Rocket Acoustic-Mode-Instability Studies at a Nominal Thrust of 20,000 Pounds, NASA TN D-4968, Dec. 1968.

[6]Hannum, N.P., Russell, L.M., Vincent, D.W. and Conrad, E.W., Some Injector Element Detail Effects on Screech in Hydrogen-Oxygen Rockets, NASA TM X-2982, Feb. 1974.

DROPLET COLLISION IN LIQUID PROPELLANT COMBUSTION

(AFOSR GRANT No. F49620-92-J-0355)

Principle Investigator: Chung K. Law

Princeton University
Princeton, NJ 08544

SUMMARY/OVERVIEW

Droplet collision is an essential process in spray combustion, intimately influencing the spray characteristic in the dense spray region. The present study aims to gain fundamental understanding on the mechanisms governing the observed phenomena of permanent coalescence, bouncing, and separation upon collision. Specific issues of interest include the extent of droplet deformation, the dynamic of the inter-droplet flow, the relative importance of the gas resistance force as compared to the collision inertia, and the relevant rheological properties of the gases and liquids. Extensive experiments have been performed for various liquids, environment gases, and system pressures. Valuable insight have been gained regarding the specific mechanisms and factors controlling the various droplet collision outcomes, especially on the bouncing propensity.

TECHNICAL DISCUSSIONS

Our previous experimental results indicated that the collisional dynamics of hydrocarbon droplets can be significant different from those of water droplets. Specifically, earlier results on water droplet collision at one atmosphere pressure showed that coalescence and separation are respectively favored for small and large Weber number (We), as shown in Fig. 1a, in which B is the collision impact parameter. Our experimental observation, however, showed that the transition between coalescence and separation for hydrocarbon droplets at one atmosphere is far from being monotonic. Indeed, as shown in Fig 2b, there are five collision outcome regimes, representing (I) coalescence with small droplet deformation, (II) bouncing, (III) coalescence with large droplet deformation, (IV) Separation after near head-on coalescence, and (V) separation after off-center coalescence. Regimes I to IV occur for near head-on collisions with increasing We, while Regime V is characteristic of large values of We and B. Regime II is very small for water droplet such that Regimes I and III merge.

The crucial factor responsible for the different behavior of water and hydrocarbon droplet is clearly the transition between Regimes I, II and III. Here, as the droplets collide, they become deformed due to the pressure buildup in the gas film between the droplets. This deformation absorbs the kinetic energy of collision, therefore reduces the ability for inter-droplet gas film to be squeezed out in order to effect coalescence. Since the extent of deformation depends on the surface tension of the liquid, it is reasonable to expect a difference behavior for water and hydrocarbon. Further, since displacement of the gas film depends on the density and viscosity of the gas, one may also expect the collision outcome depends on the gas properties.

In the present investigation we have manipulated the effects of the gas and liquid properties by conducting experiments with both water and hydrocarbon droplets in environment of different gases (air, nitrogen, helium, hydrogen and ethylene) and pressures (ranging from 0.6 to 12 atmospheres). The experimental results show that the collision behavior of water and hydrocarbon droplets are actually similar, when the influence of the environment gas density is taken into account.

To substantiate these observation, we note that the gas density can be manipulated in two ways, by changing either gas pressure or the gas molecular weight. Figures 1, 2, and 3 separately show that the effects caused by these two changes in terms of various and separated regimes.

We first note that in order to promote the occurrence of bouncing for water droplets, which is not previously observed for one atmosphere air, we should increase the density of the gas. In the course of the experimental exploration, we have found that water droplets actually do exhibit the bouncing phenomenon at one atmosphere air or nitrogen, albeit at high values of B, as shown in Fig. 1a. This regime apparently has been mostly overlooked. We have subsequently found that, with increasing pressure, this regime expands and moves to include small values of B. When the pressure is increased to around 2.8 atmosphere (fig 1b), a fully-developed Regime II is observed in that droplet bouncing now occurs for both off-center and head-on collisions. We have therefore demonstrated that the five collision regimes for hydrocarbons also exist for water, at elevated pressures.

Recognizing that increasing pressure promotes bouncing, it is then reasonable to expect that decreasing pressure should suppress bouncing. Figures 2a and 2b for tetradecane droplets show that this is indeed the case in that, while the five regime response is observed at one atmosphere, the head-on bouncing regime is suppressed as the pressure is reduced to 0.6 atmosphere.

We have further found that, by increasing the pressure to 8 atmospheres for water and 2.4 atmospheres for tetradecane, Regime II can be expanded to such an extent that Regime I can not be experimentally detected. Realistically, of course, two droplets will merge when slowly brought together. We have, however, not been able to simulate such a slow rate of collision in our experiments. The important point to note is that low-We head-on collision at high pressures could very likely result in bouncing. This is to be contrasted with the previous concept, based on water at one atmosphere, that low-We head-on collision always results in coalescence.

To further demonstrate the influence of the inertia of the gas film through the gas density, additional experiments have been conducted for the "lighter" helium environment. The collision response regimes for tetradecane are shown in Fig. 3. The results clearly show that, because of the reduced molecular weight and hence density of the helium atmosphere, a higher pressure is needed to induce bouncing in Regime II and suppress merging in Regime I.

Gas density, however, is not the only parameter influencing the collision outcomes. To demonstrate this point, we note that while the gas density for 0.6 atmosphere nitrogen in Fig. 2a is almost the same as that for 4.4 atmosphere helium in Fig. 3c, bouncing is clearly more prominent for the helium atmosphere. The difference is possibly caused by the higher dynamic viscosity of helium. As discussed earlier, as the gas is drained from the gap, a higher pressure differential is required to overcome the shear force for gas with higher viscosity, which in turn increases the gas resistance force acting on the droplet. This viscous effect is further shown by comparing Figs. 2a and 3a. It is seen that while the density of helium at 0.7 atmosphere is lower than that of nitrogen at 0.6 atmosphere, bouncing is still observed for the more viscous helium atmosphere.

Another important factor which influences the bouncing property is the similarity of the molecular structure of the liquid and gas. Figure 4 shows the collision outcomes for tetradecane in an environment of nitrogen and ethylene with different compositions; the transition boundaries between Regimes III and IV, and Regime III and V, are not shown. Ethylene is chosen because its molecular structure is similar to that of tetradecane, while its molecular weight is the same as that of nitrogen. It is seen that coalescence is promoted with increasing amount of ethylene. This is an important result because the spray interior invariably contains some fuel vapor produced through droplet vaporization. The presence of the fuel vapor thus promotes droplet coalescence. There are two possible causes for this result. The presence of ethylene could modify the surface tension which affects the merging tendency of the two surfaces. Second, since ethylene is readily soluble in tetradecane, its absorption during collision reduces the gas density in the inter-droplet spacing, hence promoting coalescence. More study is needed to identify the dominant cause.
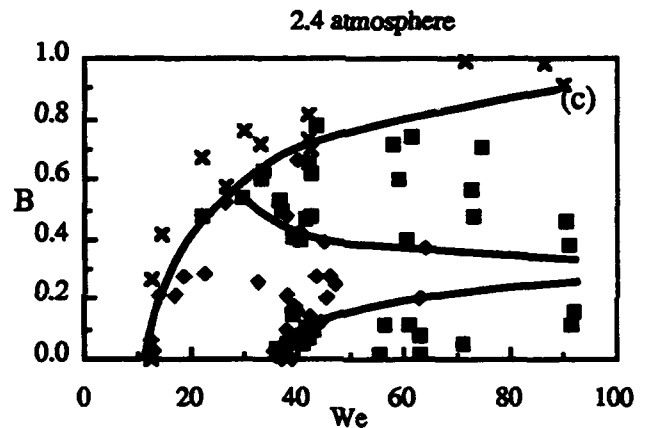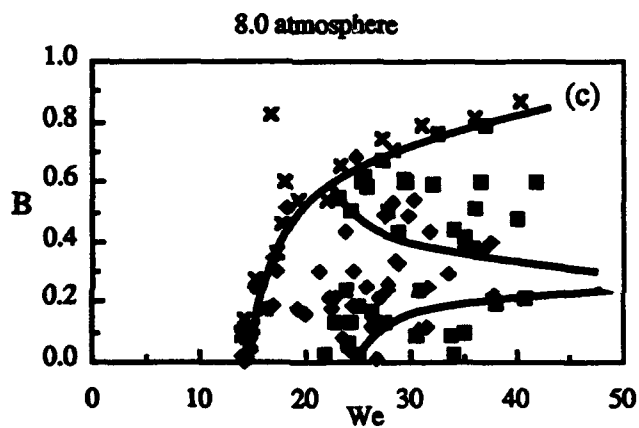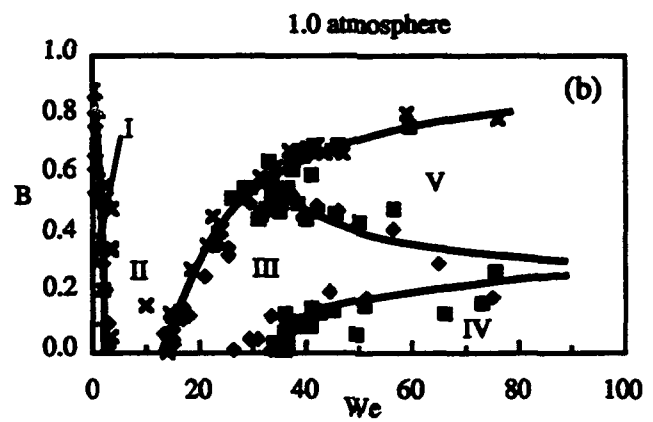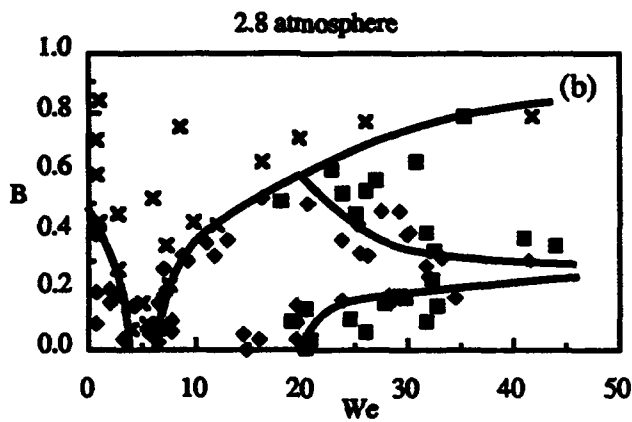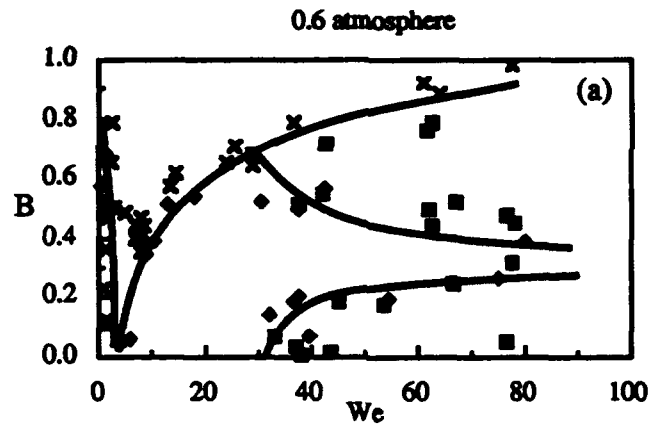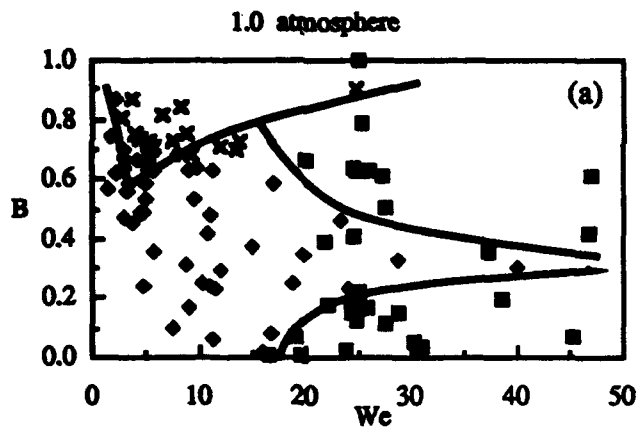
Figure 1. The transitions of water droplet collision regimes versus pressures in the nitrogen environment.

Figure 2. The transitions of tetradecane droplet collision regimes versus pressures in the nitrogen environment.
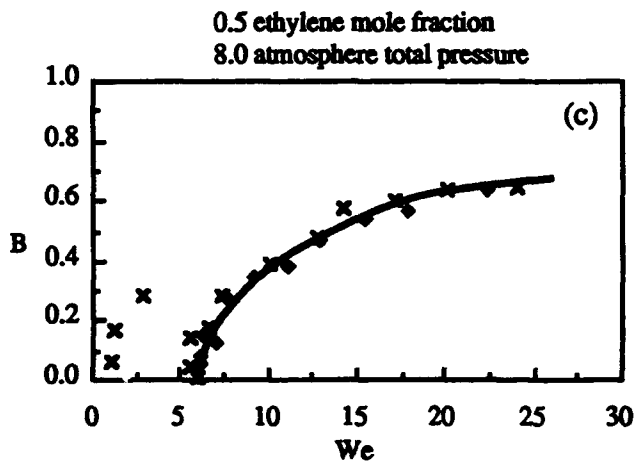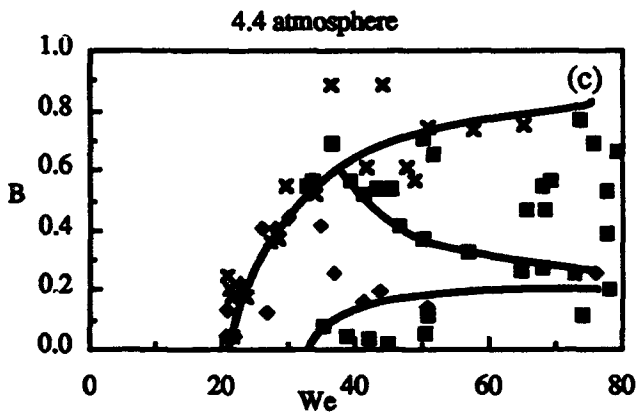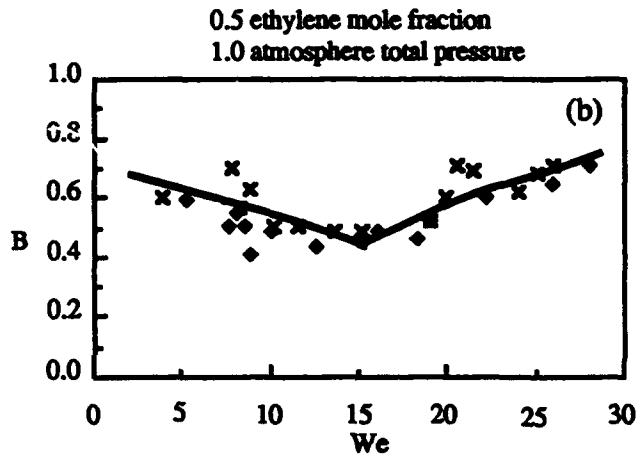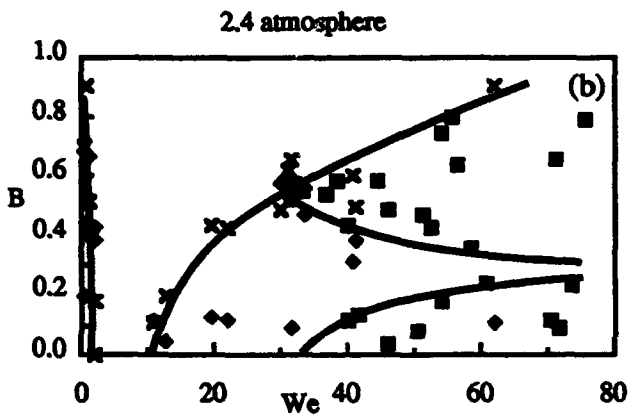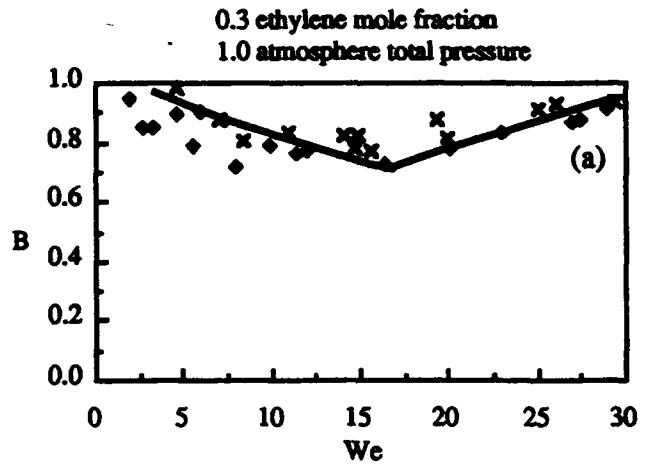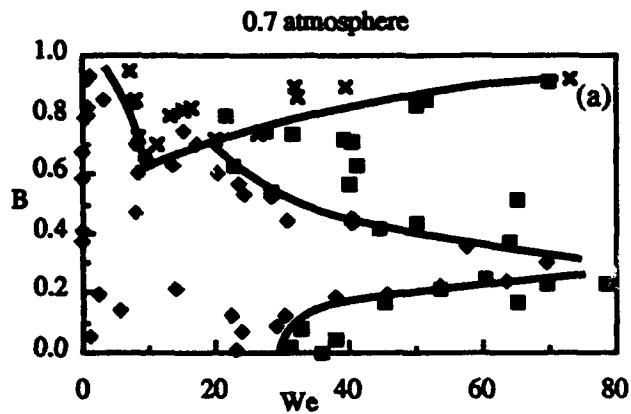
Figure 3. The transitions of tetradecane droplet collision regimes versus gas pressures in helium environment.

Figure 4. The transition of the boundaries between coalescence and bouncing versus erthylene mole fraction in the the mixture of nitrogen and ethylene environment.

DETERMINATION OF STRUCTURE, TEMPERATURE AND CONCENTRATION IN THE NEAR INJECTOR REGION OF IMPINGING JETS USING HOLOGRAPHIC TECHNIQUES

Principal Investigator : Prof. Dimos Poulikakos

Department of Mechanical Engineering
University of Illinois at Chicago
842 W. Taylor St.
Chicago, IL 60607-7022

SUMMARY/OVERVIEW

The purpose of this research is to investigate the dense region of a spray generated by two high speed impinging jets, using a novel, pulse holography technique. The effect of several parameters such as the impingement angle, the liquid jet velocity, and the orifice diameter on the atomization process was investigated in the past year. It was shown that in the dense spray region the liquid elements were not spherical. Smaller and faster droplets were generated with larger impingement angles, higher jet velocities, and smaller orifice diameters. The structure of the liquid elements near the jet impact point is indicative of the mechanisms of the disintegration process.

TECHNICAL DISCUSSION

During the second year of the research, the procedures for the reliable fabrication of double pulse holograms and the subsequent image analysis of these holograms for the measurement of size and velocity of the liquid elements in the dense spray region were perfected. The measurements focused on the determination of the effect of the impingement angle, liquid jet velocity, and orifice diameter on the near impingement region of the spray. Representative results will be discussed next.

Figure 1 demonstrates the ability of the double pulse holographic technique to record the size and position of liquid elements at two different times. The region shown is downstream along the spray axis. The droplet identified as no. 1 in Figure 1 (a) corresponding to the first pulse moved to the location identified as no. 1 in Figure 1 (b) corresponding to the second pulse. This photograph also demonstrates the size diversity of the liquid elements as well as the fact that these elements are largely non-spherical. The photographs of the holograms in Figure 2 reveal clearly the disintegration process of the liquid sheet produced by two impinging jets. The impact

wave produced at the impaction point due to the obliquely colliding high speed jets causes the detachment of arc shaped liquid ligament from the liquid sheet as shown in Figure 2 (a). These ligaments progressively disintegrate as they move downstream as shown in Figure 2 (b). Further downstream, Figure 2 (c), only small size droplets are observed. Compared to the droplets in Figure 1, droplets in Figure 2 are smaller because the impingement angle is increased from 60° in Figure 1 to 90° in Figure 2 with all the other parameters kept unchanged.

Figures 3 and 4 show the effect of the impingement angle, liquid jet velocity, and orifice diameter on the droplet diameter and velocity, respectively. These results were obtained by averaging the measurements for all droplets taken at six different locations. The sampling area in each location was 1.0 cm x 1.5 cm. Figure 3 shows that, in an average sense, smaller droplets (desirable from the combustion standpoint) were produced with larger impingement angles, higher jet velocities, and smaller orifice diameters. With reference to Figure 4, V_x, V_y, and V_m indicate the horizontal velocity, the vertical velocity, and the magnitude of the velocity vector, respectively. Increasing the impingement angle or the jet velocity increases the droplet velocity. On the other hand, increasing the jet diameter decreases the droplet velocity. The effect of the aforementioned factors, is considerably stronger on the droplet diameter than it is on the droplet velocity. To exemplify, increasing the jet impingement velocity from 12 m/s to 20 m/s decreases the Sauter Mean Diameter from about 440 μm to about 300 μm (Figure 3). An increase in the jet impingement velocity from 12 m/s to about 15.5 m/s, increased the horizontal component of the mean velocity from about 4 m/s to about 5 m/s (Figure 4).

5mm

(a)   (b)
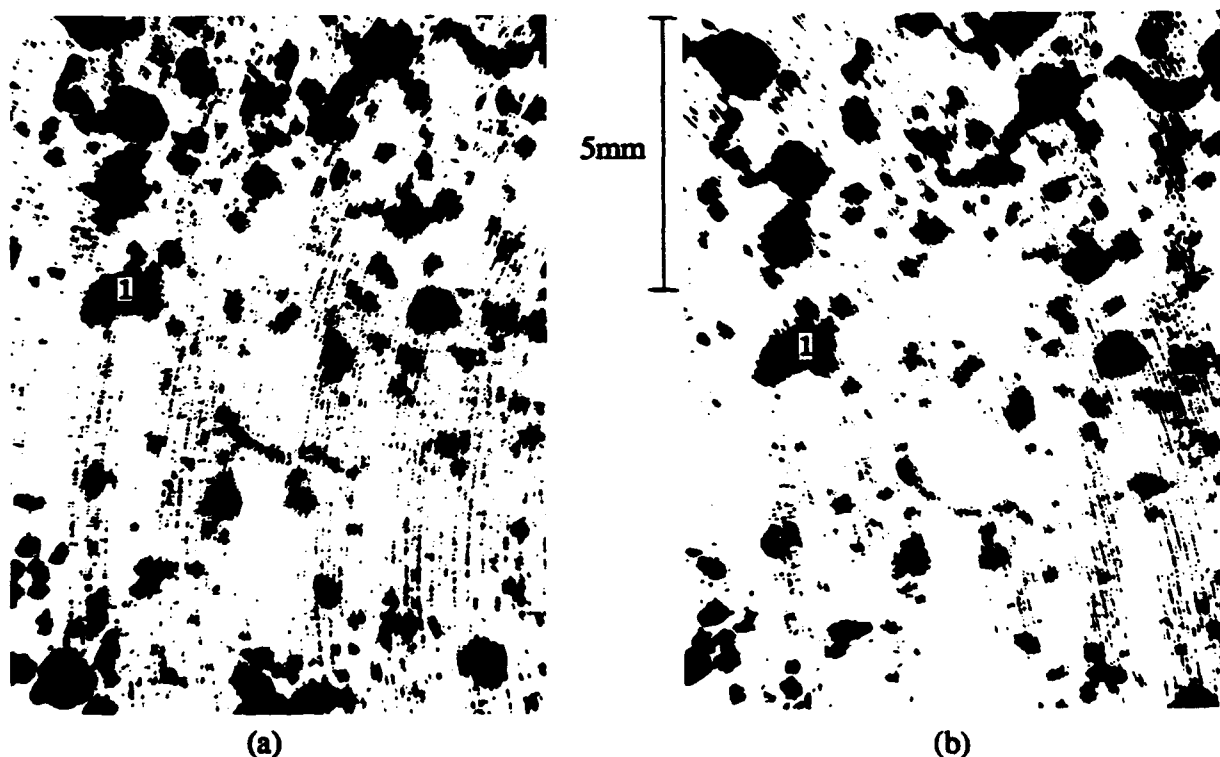
Figure 1 Photographs of hologram revealing droplet images at the first and the second pulse with impingement angle $2\theta = 120°$, $V_j = 12.0$ m/s, $D_j = 1.0$ mm, (x, y) = (0.0 cm, 4.0 cm) (a) droplet images at the first pulse, (b) droplet images at the second pulse.
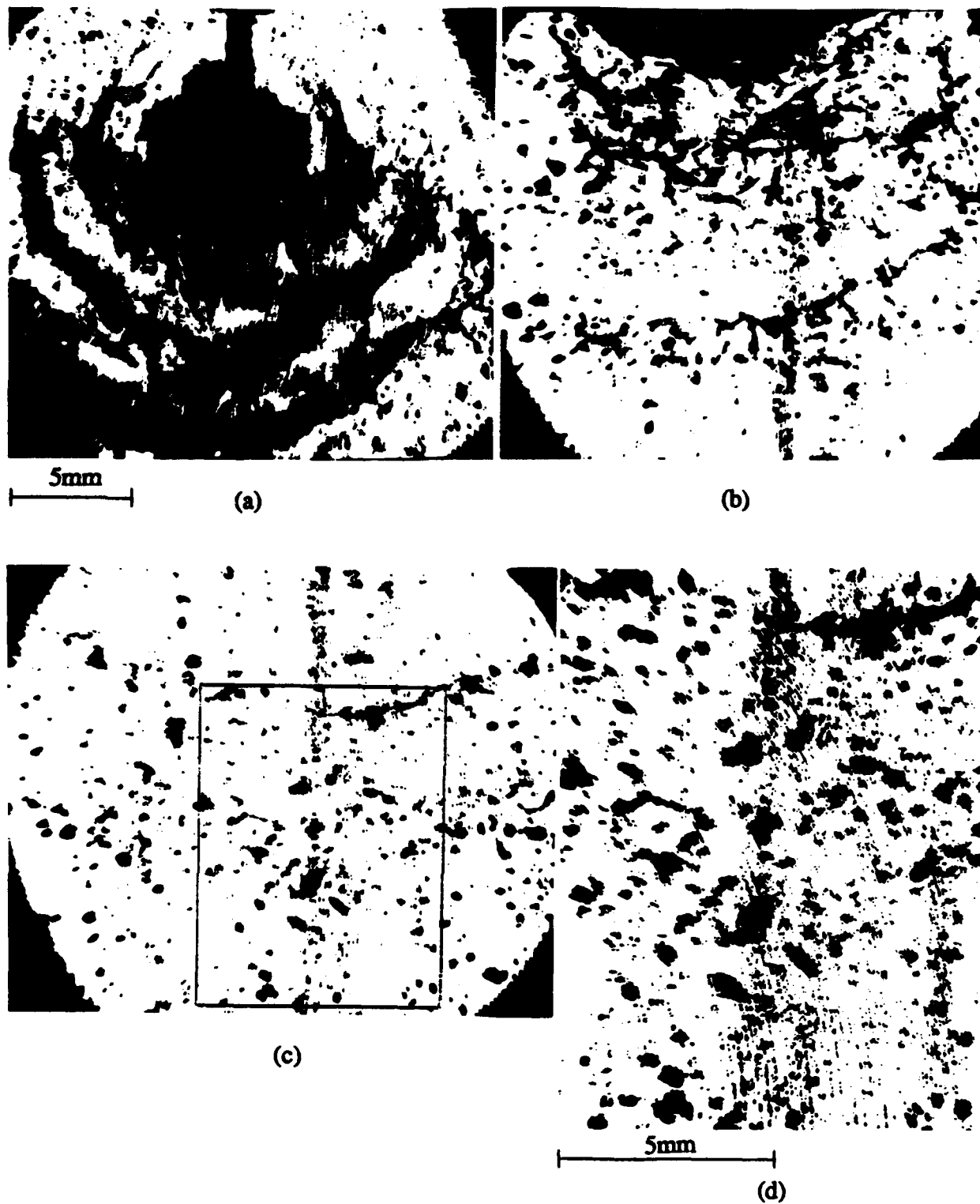
Figure 2 Photographs of hologram revealing the structure of the sheet disintegration with impingement angle $2\theta = 90°$, $V_j = 12.0$ m/s, $D_j = 1.0$ mm (a) y = 0.0 to y = 1.5 cm, (b) y = 1.5 to y = 3.0 cm, (c) y = 3.0 to y = 4.5 cm, (d) microscopic detail of the region identified by a square in Figure 2 (c).
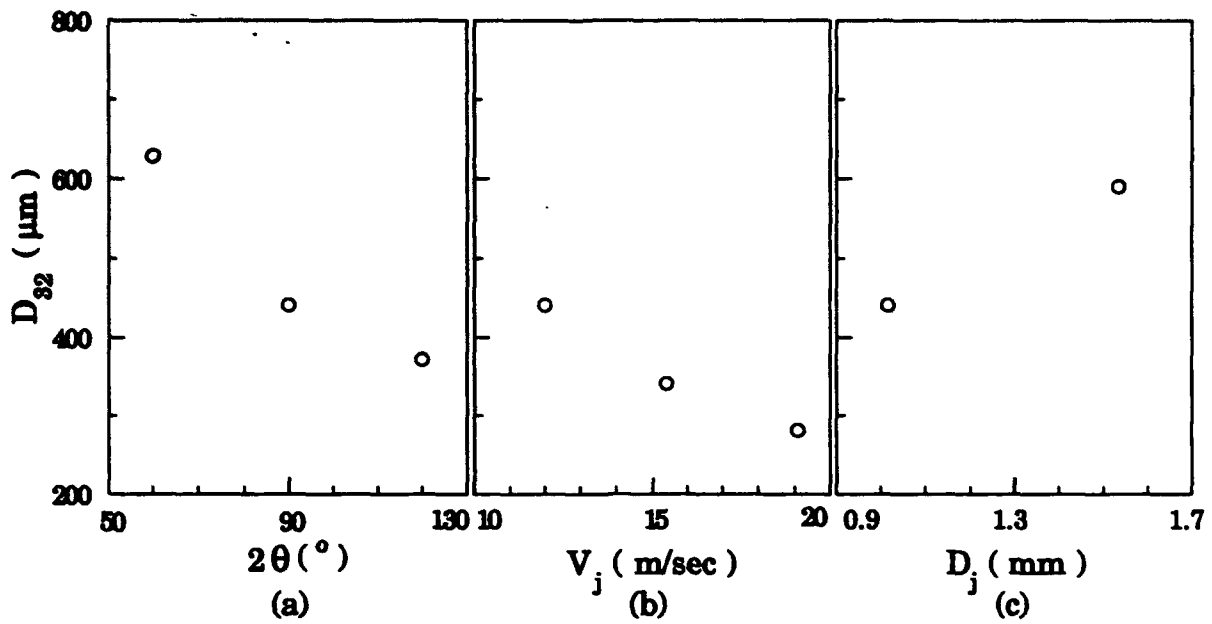
Figure 3 Effect of impingement angle, liquid jet velocity, and orifice diameter on Sauter Mean Diameter (a) Dj = 1.0 mm, Vj =12.0 m/s, (b) Dj = 1.0 mm, 2θ = 90°, (c) Vj =12.0 mm, 2θ = 90°.
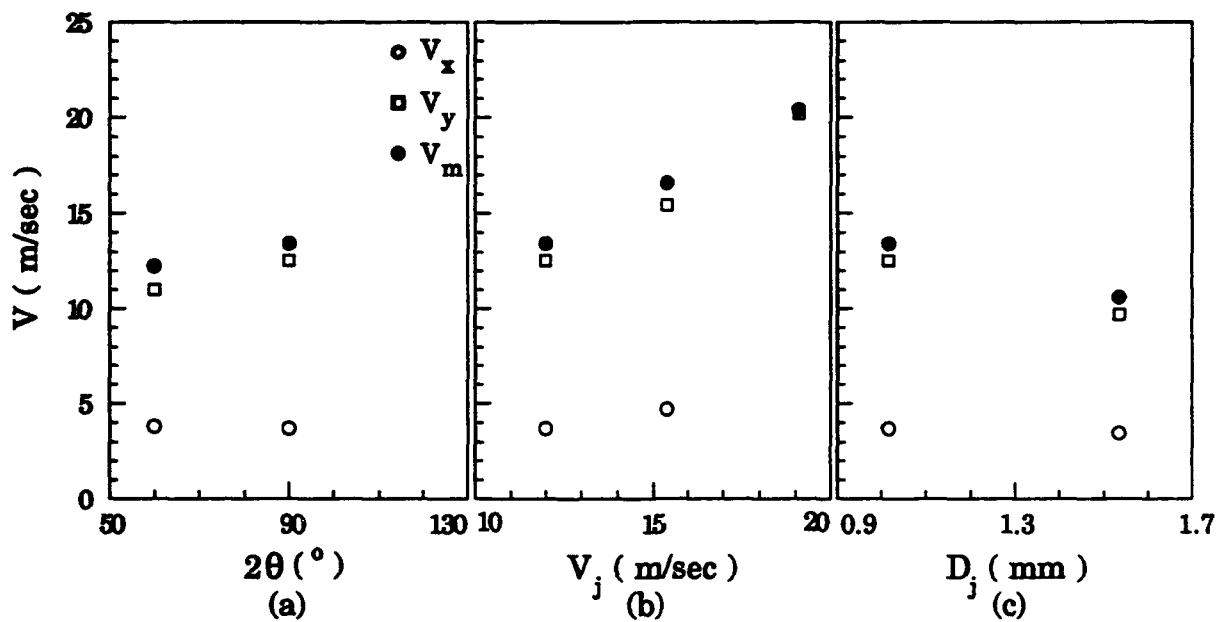
Figure 4 Effect of impingement angle, liquid jet velocity, and orifice diameter on mean droplet velocity (a) Dj = 1.0 mm, Vj =12.0 m/s, (b) Dj = 1.0 mm, 2θ = 90°, (c) Vj =12.0 mm, 2θ = 90°.

Combustion and Plumes

(AFOSR Task 2308 M1)

Principle Investigators: D. P. Weaver, D. H. Campbell, I. J. Wysong, G. L. Vaghjiani, and A. Alfano

Phillips Laboratory, OLAC PL/RKFA
Rocket Propulsion Directorate
10 Saturn Blvd.
Edwards AFB, Ca. 93524-7660

SUMMARY/OVERVIEW:

In this program, research is performed in the areas of rocket exhaust plume physics and rocket propellant combustion. Both experimental measurements and theoretical computational investigations are carried out. Laser diagnostic techniques are used in both areas to map the properties, such as temperature and density, of gases in various combusting and non-combusting environments. Chemical kinetic measurements are also carried out to determine the specific reaction pathways and kinetic rates for specific reactions of interest. Results of these investigations are used to help in the design of future rocket propellants and to further our understanding of the chemical and collisional processes in rocket exhaust plumes that give rise to emissions in the infrared, visible and ultraviolet spectral regions so that better predictions of these emissions can be used in designing ballistic missile detector systems. Typical results obtained in several of the research areas are detailed below.

TECHNICAL DISCUSSION:

Accurate prediction of plume signatures in both the high density plume core and in the plume-atmosphere interaction region at high altitudes requires specific knowledge of molecular vibrational transfer processes. Specifically, state-specific vibrational energy transfer rates are required for the important plume species. NO is one of these important species. Vibrational relaxation rates have been successfully measured for NO $v=1$, 2 and 3 with various collision partners using a laser pump/probe technique. The NO-NO V-V transfer rate has been measured for the first time below room temperature, showing that the relaxation probability increases with decreasing temperature, as does the V-T rate for $v=1$. This indicates the importance of attractive, long-range forces in the near-resonant V-V process. The V-V rates for various other collider species, the temperature dependence of the NO-NO V-T rate, and the electronic state dependence of vibrational relaxation, all demonstrate the complexity of

the physical mechanism for vibrational energy transfer, and no single theory yet proposed appears to explain all aspects of the experimental results.

The direct simulation Monte Carlo (DSMC) computational technique is the preferred method of flowfield prediction for high altitude rocket exhaust plumes. A series of computations are being conducted using the DSMC technique to evaluate this technique's ability to predict accurate flowfield parameters, internal energy state populations, and chemical species reaction processes. These include: (1) simulations to compare to nitrogen jet experimental measurements taken at UC Berkeley and USC, (2) simulations for comparison to NO vibrational population measurements and (3) simulations to compare to high altitude plume-freestream interaction number density measurements taken at AEDC. Calculations were completed for comparison to the UC Berkeley free jet rotational temperature data and the results of the DSMC simulation match well with the data. Implementation of the DSMC code on a massively parallel computer has allowed more accurate simulation of the AEDC plume-freestream experiment.

The experimental data obtained during the NO vibrational energy exchange rate measurements provide a time resolved population distribution in the lower levels of NO. This data has been used to check the ability of the DSMC computational model to predict chemical reaction processes by treating each vibrational state as a separate chemical species in the computation. A DSMC simulation for comparison to the NO vibrational population measurements has been completed using Bird's DSMC code for a set of 3 species (NO v=0, 1, and 2) using 6 reactions with one cell simulating a coincident pump and probe experimental condition. The comparisons to the measured populations in v=1 and 2 are very good. In order to obtain calculations in which the pump and probe beams are not coincident, the calculations will require use of species weighting factors. The comparisons to the experimental data will allow verification of the various weighting factor schemes now in development.

A key element in the understanding of the influence of nonequilibrium processes on flow phenomena is an experimentally verified analytical tool of sufficient capability to allow assessment of the interrelated influences of translational, rotational, vibrational, and electronic nonequilibriums as well as the influence of chemistry on the fluid flow properties of concern. Current monoprocessor code development is well below the computational capability required for such analysis, and as a result, an effort has been started to develop a multiprocessor based approach to direct simulation modeling that will significantly increase our computational power. Initial results from a parallel processing DSMC effort will be presented and implications regarding nonequilibrium flow prediction will be discussed.

Construction of a second-generation, higher flux atomic oxygen source flow was completed. This new continuous source is housed in a cryogenically-pumped cell that can provide a flow field simulation of the plume/freestream interaction. Initial work with the new source has demonstrated at least an order of magnitude increase in oxygen flux and a much reduced energy spread. A new resonance charge exchange approach

for neutralizing atomic oxygen was evaluated and much higher flux levels were obtained from the new source than originally anticipated. Several new ceramic ring jet sources were tried and the resulting best design determined. Summary results will be presented.

Work has continued on the gas phase reaction measurements of hydrazine. High temperature second-order rate coefficient measurements for H + N_2H_4 reaction has been completed. The rate coefficients for reactor temperatures of up to 893 K have been measured. However, at such high temperatures the N_2H_4 was also undergoing significant heterogeneous decomposition at the reactor walls. If this effect is not accounted for in the H + N_2H_4 gas phase work, there will be a corresponding error in the determination of the homogeneous second-order rate coefficient for this reaction. The activation energy for heterogeneous decomposition of N_2H_4 has been established to be 9.4 ± 0.3 kcal mol^{-1} in the temperature range 657-893 K. This value is typical for heterogeneous reactions for the surface-to-volume ratio of the reactor employed in this work. Below 657 K, the degree of heterogeneous decomposition of N_2H_4 is small (only a few percent). Thus, the rate coefficient measurements should be relatively free from errors due to uncertainty in the gas phase [N_2H_4] in the reaction zone at temperatures below this compared to that at higher temperatures. For temperatures below 222 K the second-order rate coefficient falls rapidly as does the saturated vapor pressure of N_2H_4. Therefore, experimentally it is difficult to accurately determined the rate coefficient beyond this low temperature limit. Thus, the most extended temperature range available for studying the gas phase reaction between H-atoms and N_2H_4 is 222-657 K. The rate coefficient for O+N_2H_4 reaction at room temperature has also been accomplished, and detection of the OH produced in this reaction has produced strong evidence against one hypothesis for production of ultraviolet signatures in hydrazine fueled rockets.

The necessity to understand the critical energy release mechanisms of high energy density propellants has created a need for an experimental capability to accomplish the simultaneous objectives: detection of molecular/ radical intermediates and stable products during combustion/pyrolysis; conservation of sample size due to limited availability of candidate propellant molecules; and inclusion of a general diagnostic to complement optical techniques. This need has resulted in the construction of a new facility to heat these reactive species to over 1000 K in a few microseconds and to determine the pyrolysis and combustion products. A CO_2 laser has been obtained along with gas chromatographic and mass spectrometric diagnostic equipment to obtain this information. A conventional flow reactor with controlled temperatures in excess of 1000 C has also been constructed. The calibration of this apparatus using the well known pyrolysis mechanism and kinetics of propane as a standard has been completed. Strained ring hydrocarbon molecules, quadricyclane and triangulanes, have been studied initially to determine their mechanisms of thermal decomposition and combustion. These molecules are currently being evaluated as performance boosting additives for RP-1 fuel. Early results of decomposition studies on quadricyclanes will be presented.
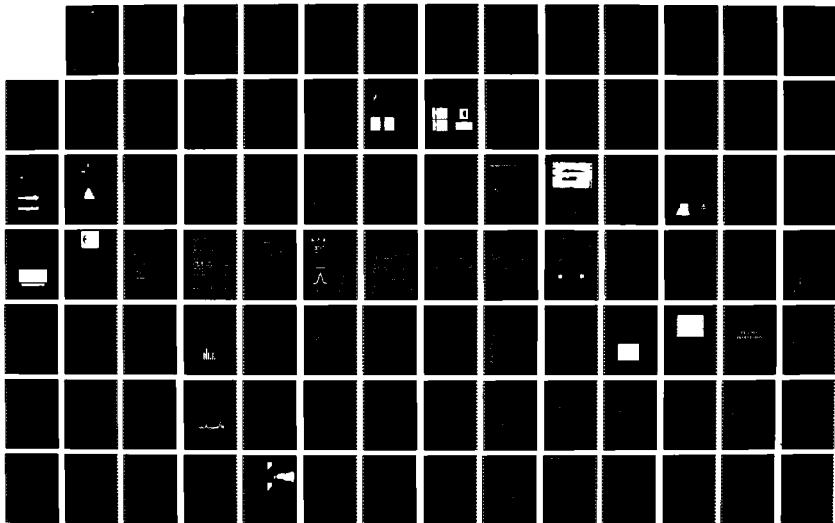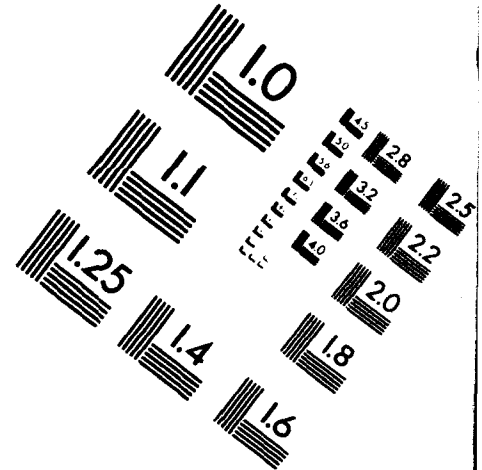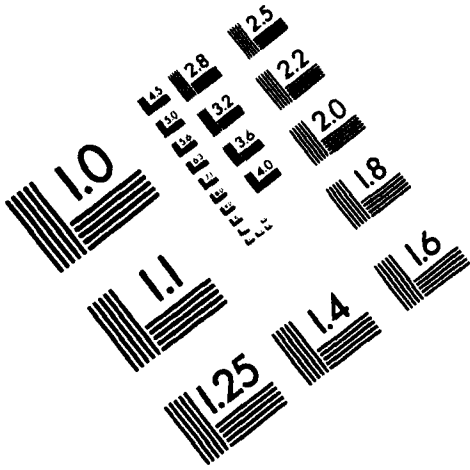
Centimeter
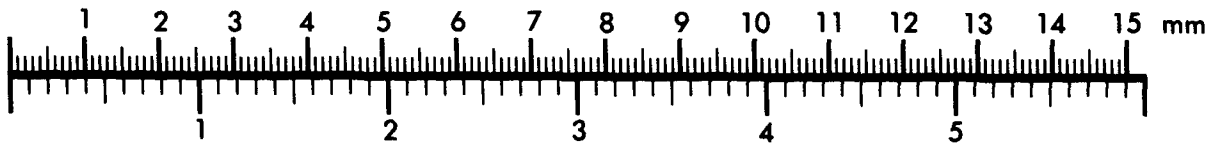
Inches
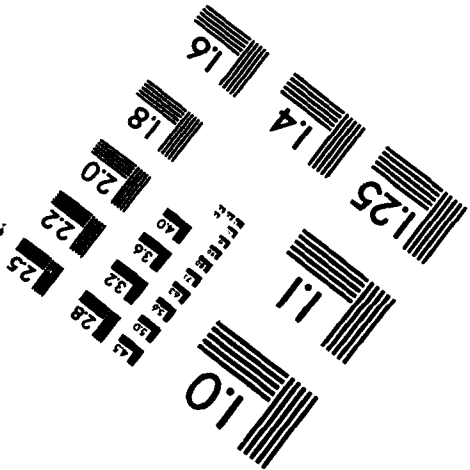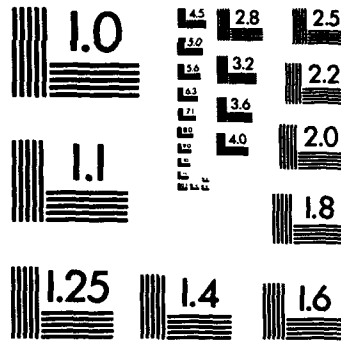
MANUFACTURED TO AIIM STANDARDS

BY APPLIED IMAGE, INC.
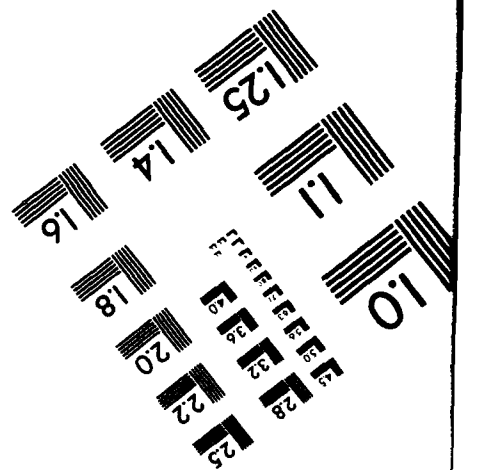
The activation energies for the following reactions were measured over the temperature range 211-472 C with a flow reactor modified to conserve sample size during kinetics studies:

(1) Quadricyclane -----> Norbornadiene
(2) Norbornadiene -----> Cyclopentadiene + Acetylene
(3) Norbornadiene -----> Cycloheptatriene
(4) Norbornadiene -----> Toluene
(5) Cycloheptariene -----> Toluene

The results agree with previously reported values and the sample size required was only ca. ten micrograms at each temperature studied. In the temperature range from 368-472 C the Arrhenius plot for the rate constant of reaction (2) exhibits the characteristic two slope behavior typical of a heterogeneous reaction. This has not been previously observed.

ADVANCED DIAGNOSTICS FOR REACTING FLOWS

AFOSR 89-0067-G

Principal Investigator: Ronald K. Hanson

High Temperature Gasdynamics Laboratory
Mechanical Engineering Department
Stanford University, Stanford, CA

SUMMARY/OVERVIEW:

This research is directed toward innovation of advanced diagnostic techniques applicable to combustion gases and plasmas, with some emphasis on high speed flows. The primary flowfield parameters of interest are species concentrations, temperature, pressure, mass density, electron density, velocity, and quantities derivable from these parameters such as mass flux and thrust (calculable from mass density and velocity). Principal techniques under study include spectrally-resolved absorption and fluorescence, using wavelength-modulated cw semi-conductor diode laser sources; planar laser-induced fluorescence (PLIF), using tunable pulsed laser sources (excimer-pumped dye and narrow-linewidth excimer); and diagnostic techniques based on degenerate four-wave mixing.

TECHNICAL DISCUSSION

In the following paragraphs we highlight primary activities of the past year.

Plasma and High-Enthalpy Air Diagnostics

Recent work has focussed on the development of a diagnostic strategy based on measurement of spectrally resolved absorption lines associated with transitions between excited electronic states of atoms. This approach is suggested by the fact that gases at very high temperatures, such as found in hypersonic flight and in various plasma-based propulsion systems, are primarily neutral or ionized atoms; the further influence of high temperatures is to produce substantial populations of these species in excited electronic quantum states. A particular advantage of the proposed measurement scheme is that it utilizes a tunable semiconductor diode laser source, which is attractive owing to its rapid tuning capabilities, low cost, and compatibility with fiberoptic transmission. In brief, the shape and amplitude of the absorption line, recorded either with fluorescence or absorption detection, contain the primary information of interest, namely the kinetic and electronic temperatures of the species.

During the past year we have investigated application of this diagnostic to three species: xenon, atomic oxygen and atomic nitrogen. The work with xenon utilized the 6s-6p transition at 823 nm (GaAlAs laser) and involves measurements in a low pressure dc discharge. Xenon is of practical interest owing to its use in ion thruster propulsion systems, and it is of fundamental interest owing to the complex nature of Xe spectra. For example, owing to the significant number of major isotopes in Xe (9 with mol fractions of about 1% or more), and its complex nuclear splitting, the spectrum of the 6s-6p transition involves a convolution of 21 individual spectral features. A recent measurement of the absorption line, and a comparison with theory, is shown in Fig. 1. Such a measurement, once fully understood, has potential for monitoring temperature, density and velocity of xenon atoms.

In related work we have applied a similar strategy to monitor excited-state transitions of O-atoms (772 nm, 3s-3p) and N-atoms (821.6 nm, 3s-3p) in gases heated (by reflected shock

waves in a shock tube) to temperatures of 6000-13,000 K. Such conditions are representative of those found behind bow shocks in hypersonic flight. An example of recent data for N-atoms is given in Fig. 2. Here a best Voigt fit of the profile allows a determination of the kinetic and electronic temperatures, both near 9000 K and in good agreement with the temperature calculated from the measured shock speed. We are unaware of any previous diagnostic methods with similar potential for probing such high temperature environments. Further information may be found in Refs. 1-3.

PLIF Imaging in Shock Tube Flows

Shock tubes and tunnels provide a convenient environment for the development of advanced diagnostic methods relevant to advanced air-breathing propulsion systems. A wide variety of high-enthalpy and high-velocity flows can be easily generated, and at modest expense relative to continuous-flow facilities. During the past year we continued to use a pressure-driven shock tube and tunnel to investigate diagnostics for scramjet and nonequilibrium hypersonic flow studies. A particular accomplishment was the completion of work which demonstrated quantitative, single-shot imaging of temperature in a model scramjet flow. Two tunable lasers and two CCD cameras were used to allow essentially instantaneous recording of two PLIF images which could be ratioed to extract temperatures. Successful temperature images, accurate to about 5-10%, were achieved with both OH and NO imaging. Dual imaging of both species was also demonstrated, with NO used as a tracer of the H_2 fuel and OH used as a marker of combustion. A schematic of the flowfield studied is given in Fig. 3; details of the work can be found in Refs. 4 and 5. (Ref. 4 was featured on the cover of Applied Optics in the December, 1993 issue.) In related work we also demonstrated approaches for single- and dual-laser PLIF imaging of nonequilibrium shock tunnel flows, including imaging of velocity (2 components) and both rotational and vibrational temperatures. Further details of this work may be found in Ref. 6.

Laser Diagnostics for Multi-Parameter Measurements

For the past few years we have worked to develop a diagnostics strategy which allows simultaneous determination of multiple gasdynamic parameters from spectrally resolved absorption spectra. For example, LIF monitoring of UV absorption line pairs of NO was used for simultaneous determination of velocity (Doppler shift), temperature, pressure and density in a supersonic jet, with submillimeter spatial resolution and at a measurement repetition rate of 4kHz. Work with line-of-sight absorption has been conducted with both O_2 (at 760 nm) and H_2O (at 1.4 microns), in both cases using a shock tube to produce controlled supersonic gas flows at known conditions. In both studies, the measurements yielded high repetition rate determinations of velocity (1 component), temperature, pressure and density, and the derived quantities of mass flux and momentum flux. These latter quantities are of particular interest to propulsion engineers wishing to monitor inlet and exhaust flows of advanced supersonic combustors. Indeed, the technology we developed is now being employed in several large-scale facilities in this country and elsewhere. An example data trace in H_2O is shown in Fig. 4; inferred and known flow properties are indicated. Further information appears in Refs. 7-10.

Other Diagnostics Efforts

During the past year we completed work on a scheme to extend PLIF to 3-D imaging. The objective has been to develop methods for probing flows which include important three dimensionality. Another project, still underway, is an investigation of fundamental issues in degenerate four-wave mixing; details of progress on that effort may be found in Ref. 11. Finally, we have initiated a new effort to investigate diagnostics strategies for high-pressure flows, for example in connection with advanced high-pressure combustors, rockets, and other propulsion systems. The conditions of interest in these devices introduce significant changes in the physical phenomena which underly both modelling of such flows and their measurement via laser diagnostic strategies. This will be a fruitful area for fundamental and applied investigation.

REFERENCES

1. R. J. Cedolin, R. K. Hanson and M. A. Cappelli, "Semiconductor Laser Diagnostics Development for Xenon Plasmas," submitted to Joint Propulsion Conference, Indianapolis, June, 1994.

2. H. A. Chang, D. S. Baer and R. K. Hanson, "Semiconductor Diode Laser Absorption Diagnostics of Atomic Nitrogen for Hypersonic Flowfield Measurements," paper AIAA-94-0385 at 32nd AIAA Aerospace Sciences Meeting, Reno, Jan. 10-13, 1994.

3. H. A. Chang, D. S. Baer and R. K. Hanson, "Semiconductor Laser Diagnostics for Simultaneous Determination of Kinetic and Population Temperatures in High-Enthalpy Flows," 19th Int. Symp. on Shock Waves (ISSW 19), Marseille, July 26-30, 1993.

4. B. K. McMillin, J. L. Palmer and R. K. Hanson, "Instantaneous Temperature Imaging of a H_2/NO Jet in Supersonic Crossflow Using Two-Line PLIF," Applied Optics 32, 7532-7545 (1993).

5. B. K. McMillin, J. M. Seitzman and R. K. Hanson, "Comparison of NO and OH PLIF Temperature Measurements in a Scramjet Model Flowfield," paper AIAA-93-2035 at 29th AIAA/SAE/ASME/ASEE Joint Propulsion Conf., Monterey, CA, June 1993; also AIAA J., submitted 8/93.

6. J. Palmer and R. K. Hanson, "PLIF Measurements of Temperature and Velocity in a Reacting Supersonic Free Jet with OH, paper AIAA-94-0168 at 32nd AIAA Aerospace Sciences Meeting, Reno, Jan. 10-13, 1994.

7. M. D. DiRosa, A. Y. Chang and R. K. Hanson, "CW Dye Laser Technique for Simultaneous, Spatially-Resolved Measurements of Temperature, Pressure and Velocity of NO in an Underexpanded Free Jet," Applied Optics 32, 4074-4087 (1993).

8. M. P. Arroyo, S. Langlois, and R. K. Hanson, "Diode Laser Absorption Technique for Simultaneous Measurements of Multiple Gasdynamic Parameters in High-Speed Flows Containing Water Vapor," Applied Optics, in press.

9. M. P. Arroyo, T. P. Birbeck, D. S. Baer and R. K. Hanson, "Dual Diode-Laser Fiberoptic Diagnostic for Water Vapor," Optics Letters, submitted 2/94.

10. L. C. Philippe and R. K. Hanson, "Laser Diode Wavelength-Modulation Spectroscopy for Simultaneous Measurement of Temperature, Pressure and Velocity in Shock-Heated Oxygen Flows," Applied Optics 32, 6090-6103 (1993).

11. P. M. Danehy, E. J. Friedman-Hill, R. P. Lucht and R. L. Farrow, "Effects of Collisional Quenching on Degenerate Four-Wave Mixing," App. Phys. 57, 243-248 (1993).
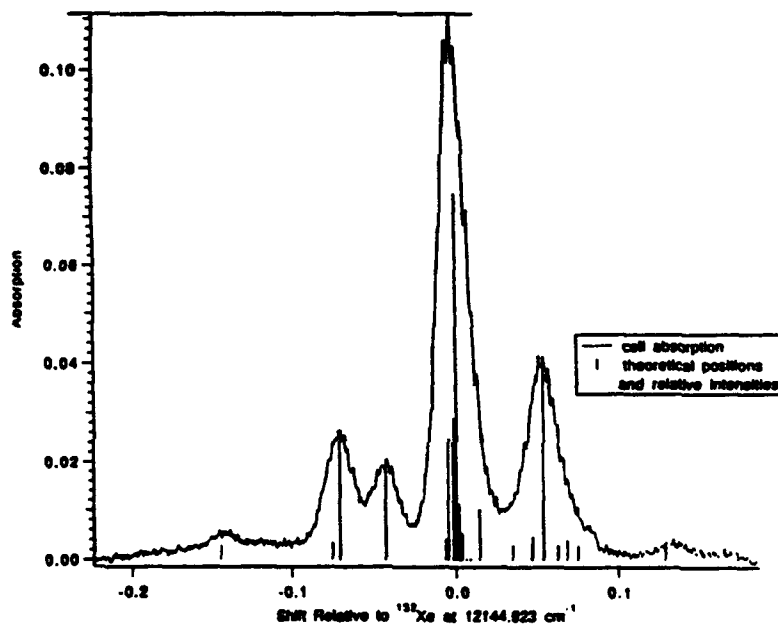
Fig. 1. Measured profile of Xe 3s-3p transition at 823 nm, and theoretical positions/intensities of component lines.

Reduced N-Atom Absorption Lineshape
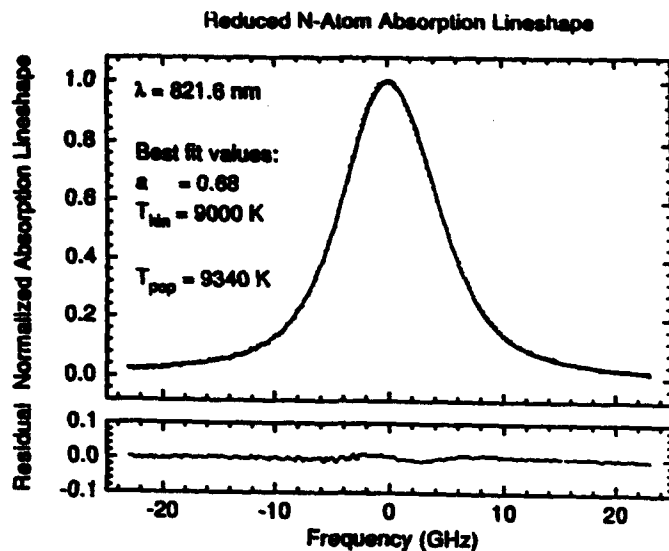
Fig. 2.   Best Voigt fit to N-atom transition at 821.6 nm (3s-3p) in shock-heated nitrogen.
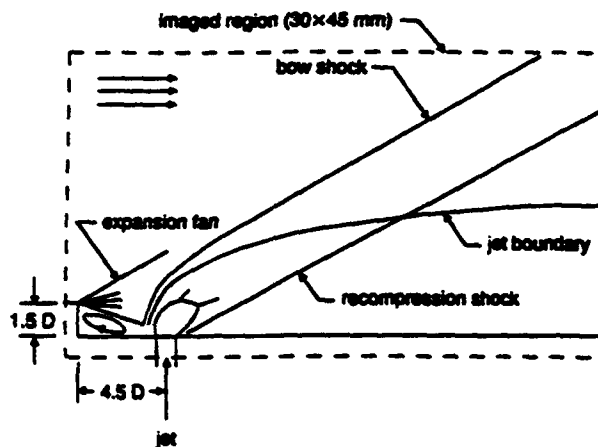
Fig. 3.   Schematic diagram of the model scramjet flowfield used to develop PLIF imaging of temperature. The fuel is H_2 and the supersonic crossflow is high temperature air or other gas mixtures. Jet diameter $D = 2$ mm.
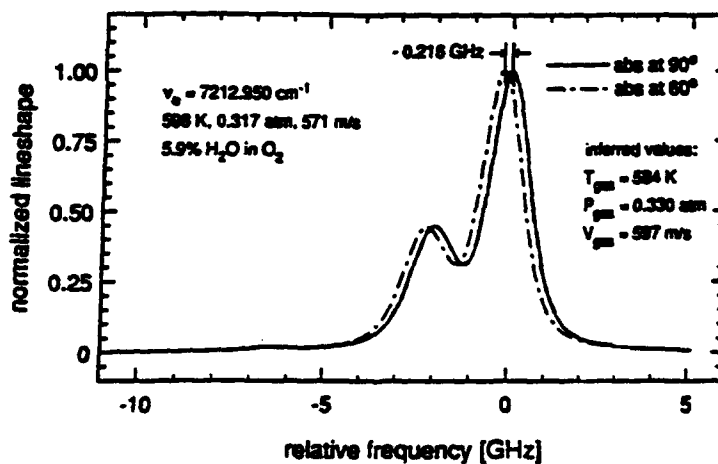
Fig. 4.   Reduced shock tube absorption data for single scan of the $6_{42} \leftarrow 6_{43}$ and $3_{13} \leftarrow 3_{12}$ lines in the $v_1 + v_3$ band of H_2O. The gasdynamic parameters inferred from a Voigt profile analysis are indicated along with the values calculated with shock wave theory. From Ref. 8.

88

NONLINEAR LASER DIAGNOSTICS FOR COMBUSTION AND PLASMA PROCESSES

(AFOSR Contract No. F49620-94-C-0027)

Principal Investigators: David L. Huestis, Gregory W. Faris, and Jay B. Jeffries

SRI International
Molecular Physics Laboratory
Menlo Park, CA 94025

SUMMARY/OVERVIEW:

Task 1: UV and VUV Generation and Detection Techniques

We are developing techniques to extend laser-based diagnostics into the vacuum ultraviolet (vuv) region for the detection of atomic ions, planar imaging of light atoms, and other applications. To date, we have developed a high-power widely-tunable vuv source producing over 65 µJ at 133 nm, demonstrated two-photon-excited fluorescence at this wavelength, and discovered some technical challenges specific to vuv-based diagnostics. Future work will be to investigate solutions to materials-related problems.

Task 2: Laser-Excited Amplified Spontaneous Emission (ASE)

Two-photon-excited ASE of atomic hydrogen and oxygen has been explored in a variety of low-pressure flames as a method to measure concentration, gas velocity, and gas temperature. We discovered that ASE intensity is more sensitive to the collisional environment than LIF, which makes the interpretation of the ASE signal quite difficult. Direct gain of a probe laser pulse tuned to the ASE transition avoids this difficulty. The probe pulse can stimulate the emission in a time short compared to the collision time and the observed gain is proportional to the population inversion created by the laser. Demonstration measurements and model calculations for atomic oxygen in a low-pressure hydrogen/oxygen flame are reported.

TECHNICAL DISCUSSION

Task 1: UV and VUV Generation and Detection Techniques (G. W. Faris)

While great progress has been made on laser-based detection techniques, some significant challenges remain. Among these are the detection of atomic ions and the single-photon detection of light atoms. These detection problems are similar in that they both require high power vacuum ultraviolet radiation.

The ability to perform quantitative detection of atomic ions is important for studying plasma propulsion, highly-ionized flows, plasma etch lithography, magnetically-confined fusion, astronomy, and astrophysics. Detection of light atomic ions is difficult because the single-photon transitions from the ground state lie in the extreme ultraviolet (xuv) and no window materials are available in this region. Our approach is to use two-photon-excited fluorescence in the vuv, allowing the use of windows such as MgF_2 and LiF.

Light atoms can be detected through two-photon techniques in the near ultraviolet region. An alternative technique to two-photon detection is single-photon detection using vuv. While more complicated than the two-photon approaches, single-photon vuv detection of light atoms allows more sensitive detection, can avoid photo-induced changes due to high optical intensities, and provides the possibility for planar imaging. Areas where single-photon detection techniques may prove useful include arc jets and hot rarified flows. Other applications of vuv diagnostics include single- or multiple-photon ionization for very high sensitivity detection techniques and single-photon calibration of multiple-photon diagnostic techniques.

To produce high-power widely-tunable, vuv radiation, we have developed a source based on two-photon-resonant difference-frequency generation.[1] In this approach the output of a tunable ArF excimer laser at frequency v_{ArF} is mixed with the fundamental or frequency-doubled output from a Nd:YAG-pumped dye laser at frequency v_{dye} to produce radiation at frequency $v_{vuv} = 2 \times v_{ArF} - v_{dye}$. Enhanced efficiency is provided by tuning the ArF laser onto resonance with two-photon transitions in the mixing gas (krypton or hydrogen). By tuning the dye laser frequency, the vuv wavelength can be varied from 110 to 180 nm. To date, we have obtained over 65 µJ at a wavelength of 133 nm using this technique. Larger powers can be obtained over a limited tuning range by directly Raman-shifting the ArF laser output.[2]

We have evaluated the performance of the vuv-based multi-photon spectroscopy through 1+1 REMPI on xenon at 147 nm and two-photon-excited fluorescence in neon using 133 nm light.[3] The latter constitutes a demonstration of the two-photon-excited fluorescence technique in an appropriate wavelength region for atomic ion detection. The neon measurements were performed at a pressure of about 1 Torr, however, which is too high for most useful applications for atomic ion detection. Further improvement in laser power is required in order to achieve useful detection of atomic ions. We have minimized the path length for the vuv through the optics by using an off-axis lens instead of a prism to separate the beams. This resulted in more than a factor of 3 improvement in vuv energy over that we had available for the neon measurements. Further improvement in energy is still required, however.

There are two avenues we can pursue to further improve our laser power. Both concern materials problems. The first involves loss mechanisms that build up due to the length of exposure to the high power vuv. The second deals with mechanisms to improve the efficiency of the mixing gas. During exposure to the vuv radiation, the transmission of our vuv optics is gradually degraded. We believe that this is due to color center formation, and are further investigating the process. Color center losses may be mitigated by reducing the vuv fluence on the optics (using larger diameter beams and optics), by heating the optics to speed recombination of the color centers, or by separating the vuv beam from the input beams using a concave grating instead of transmissive optics.

The efficiency of the vuv generation is related to the nonlinear optical polarizability, which is proportional to the square of the mixing gas density. Improvement in vuv power cannot be realized by increasing the gas density alone, because of index of refraction dispersion for the gas between the input and output beam wavelengths. By reducing the effects of the material dispersion (phasematching) we can achieve significant improvement in vuv energy. Phasematching can be achieved through using a mixture containing a gas having negative dispersion at the vuv wave-length. Other approaches include noncollinear mixing and "quasi-phasematching." It currently appears that some phasematching will be required to achieve significant powers near 120 nm.

In order to better characterize these aspects of the mixing process in the absence of time-varying, irradiation-dependent window absorptions, the apparatus has been modified to allow windowless detection of the generated VUV and XUV through the use of a differentially-pumped gas cell. The 100 cm^3 cell is filled with hydrogen at a rate of 10 Hz using a pulsed valve to attain peak pressures of several hundred Torr. The ArF and dye laser beams enter and exit through optical access holes 1 mm diameter on either side of the cell, separated by 5 cm, and are timed to

coincide with the pressure envelope maximum. The volume of the mixing cell is continually pumped by a high volume mechanical pump and the optical path outside the cell is maintained at $< 10^{-4}$ Torr using a trapped diffusion pump. The ultraviolet wavelengths generated by the mixing process pass from the cell directly into a Spex 1500SP 0.5 meter vacuum ultraviolet spectrometer, where they are dispersed and detected by either a photomultiplier or pyroelectric energy detector. The peak pressure in the mixing cell is determined through comparison of MPI signal levels of the Q(1) branch in H_2 for the pulsed, flowing condition with a static cell volume. Because the source has no windows, we can insert optics into the beam after mixing to determine the effects of exposure independently of the mixing. By flowing gas mixtures through the source, we can study phasematching without constraints due to the focusing/collection geometry for the mixing, and difficulties due to time-dependent degradation of the vuv radiation.

Task 2: Laser-Excited Amplified Spontaneous Emission (ASE) (J. Jeffries)

Laser-excited amplified spontaneous emission (ASE) is an attractive method to detect atomic species in reacting gas flows and plasmas because the signal shares the same beam path with the excitation laser light. Multiphoton laser excitation of atoms is traditionally detected by fluorescence or ionization which either requires large solid angle fluorescence collection or a probe for ion/electron collection. ASE provides an alternative detection method which requires minimal optical access and no intrusive probes; however, quantitative ASE requires understanding the non-linear optical gain in the laser excited sample. For example, two-photon selection rules produce atoms in excited states which do not have allowed one-photon transitions back to the ground state but radiate instead to an intermediate excited state. For atomic species found in propulsion like hydrogen and oxygen, these intermediate states are more than 10 eV above the ground state, and at combustion temperatures there is nearly no thermal population in states with such a large excitation energy. Thus, a population inversion can readily be produced by the laser two-photon excitation; any spontaneous emission along the excitation laser beam can experience gain. This gain produces ASE propagating forward and backward along the laser beam.

ASE has been observed in a variety of low-pressure flames with an experimental arrangement shown in Figure 1. The schematic also shows a diode laser probe beam which crosses the
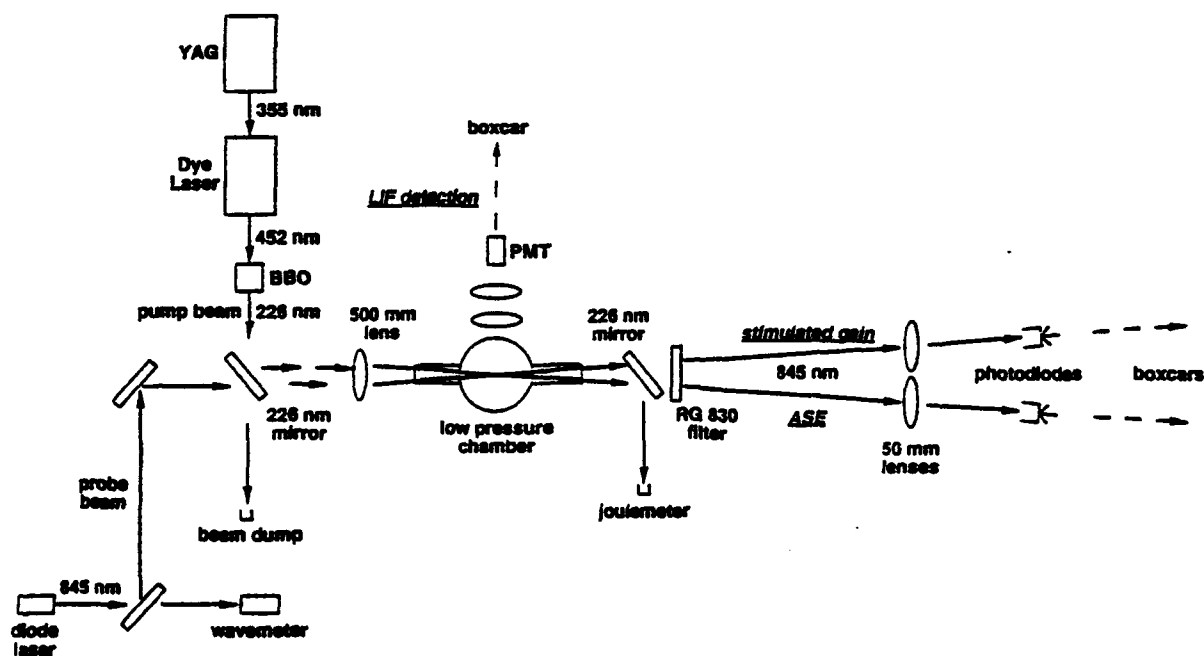
Figure 1. The experimental setup used to measure both the ASE and stimulated gain signals.

91

excitation beam at a small angle. The excitation laser was tuned to line center of the $3p^3P_2$ $\leftarrow 2p^3P_2$ transition in atomic oxygen at 225.6 nm. The forward ASE signal at 845 nm is observed from the $3p^3P_2 \rightarrow 3s^3S_1{}^o$ transition; the probe laser was tuned to line center of the ASE transition.

To demonstrate the ASE loss/probe gain technique, we first operated the diode laser at 38 mW and monitored both the probe beam as it exited the low-pressure chamber and the ASE signal while alternately blocking the pump and probe beams before they entered the chamber. The results of this test are shown in Figure 2 where the ASE signal and the ac component of the cw probe beam are plotted. In region I both the pump and probe beams are blocked establishing the background level for both types of signal. Region II shows the probe intensity with no gain as the pump beam is blocked. In region III, the probe has been blocked while the pump is unblocked resulting in a large ASE signal. With both beams unblocked (region IV) the probe beam experiences a small (20%) gain while the ASE signal experiences 100% loss.

The relative ASE signal is shown in Figure 3 as a function of the incident probe beam intensity while the pump beam intensity was held fixed. The probe intensity is normalized to the saturation intensity ($2W/cm^2$) for analysis purposes. The ASE signal falls in a smooth way as the incident probe intensity is increased. The solid line in Figure 3 is from a single pass amplifier theoretical fit with laser excited atomic oxygen the gain medium. The inversion population density given by the measured gain in Figure 2 and loss in Figure 3 agree within a factor of two with each other and within the estimated uncertainty of a model calculation of the atomic oxygen concentration.
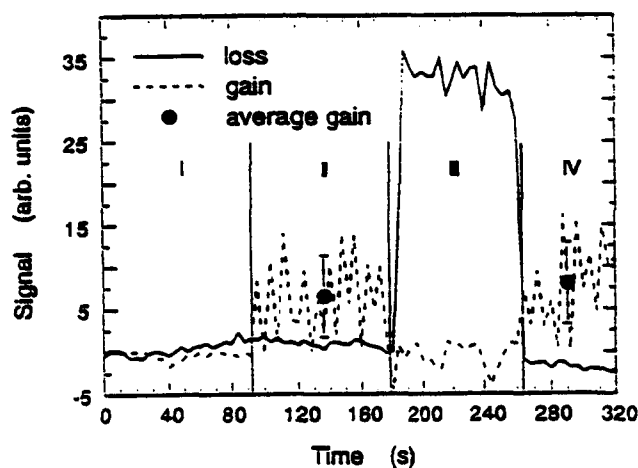
Figure 2. Simultaneous observation of the probe (gain) and ASE (loss) signals for the four input combinations of I - both pump and probe beams blocked, II - pump beam blocked, III - probe beam blocked and IV - neither beam blocked.
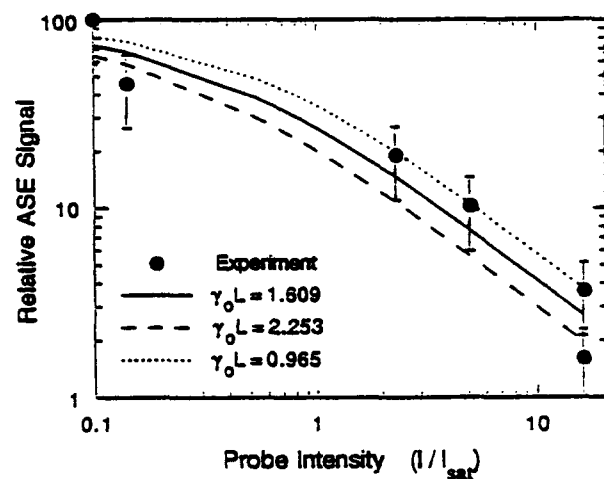
Figure 3. The relative ASE signal as a function of the probe beam intensity. The solid line indicates a best fit (γ_0 = 1.609) found using the model. Dashed lines indicate theoretical curves for $\gamma_0\ell$ = 1.609 ± 40 %.

REFERENCES

1. G. W. Faris and M. J. Dyer, in *Short Wavelength Coherent Radiation: Generation and Applications*, Philip H. Bucksbaum and Natale M. Ceglio, Eds. (Optical Society of America, Washington, DC, 1991).

2. G. W. Faris and M. J. Dyer, J. Opt. Soc. Am. B, **10**, 2273-2286 (1993).

3. G. W. Faris and M. J. Dyer, Opt. Lett. **18**, 382-384 (1993).

RAPID CONCENTRATION MEASUREMENTS BY PICOSECOND TIME-RESOLVED LASER-INDUCED FLUORESCENCE

Galen B. King
Normand M. Laurendeau

Flame Diagnostics Laboratory
School of Mechanical Engineering
Purdue University
West Lafayette, IN 47907-1288

SUMMARY/OVERVIEW:

This research is concerned with the development of a laser-based diagnostic technique for the measurement of species concentrations in turbulent flames called picosecond time-resolved laser-induced fluorescence (PITLIF). Current diagnostic techniques have the capability to measure probability distribution functions (PDFs), but in many cases they lack the temporal resolution needed to measure power spectral densities (PSDs). The PITLIF instrument employs a high repetition rate mode-locked laser which gives it the temporal resolution and power necessary to rapidly obtain PSDs in addition to PDFs. The specific objective of this project is to develop the PITLIF instrument and to demonstrate its viability for obtaining PDFs and PSDs of minor species concentrations in turbulent flames.

TECHNICAL DISCUSSION:

Turbulent flames are characterized by random fluctuations in flow variables such as velocity or concentration.[1] These fluctuations must be described statistically using PDFs and PSDs. Laser Doppler velocimetry (LDV) can be used to measure PDFs and PSDs of velocity in a turbulent flame.[2] Laser-induced fluorescence (LIF) is commonly employed for measurement of minor species concentrations.[3] Typically, CW or Q-switched laser systems are employed for LIF measurements of PDFs, but these systems lack the power and temporal resolution necessary to measure PSDs of concentration in turbulent flames. Both the PDF and the PSD must be known to completely describe the random fluctuations in concentration. We report here on current investigations with picosecond time-resolved laser-induced fluorescence (PITLIF), a new diagnostic technique which has the potential to rapidly and

Figure 1. Schematic diagram of the PITLIF instrument.

simultaneously measure both PDFs and PSDs of concentration in a turbulent flame.

A block diagram of the PITLIF instrument is shown in Fig. 1. The laser system consists of a broadband dye laser synchronously pumped by a mode-locked frequency-doubled Nd:YAG laser. The laser system delivers a series of mode-locked laser pulses 20-50 ps FWHM and a repetition rate of 82 MHz. The laser system irradiates a region of the flame, and through interaction with atoms or molecules in the flame, light is absorbed and spontaneously emitted. The detector, a photomultiplier tube, measures some of this emitted light. The output of the detector is fed into two parallel data acquisition channels. The low-bandwidth acquisition system uses a low-pass filter to filter out individual laser pulses and records the integrated fluorescence signal which provides a measure of the low frequency (<10 kHz) fluctuations in the LIF signal. The low-bandwidth system can be used alone to measure concentration fluctuations in systems where the variation in quenching is small. The high-bandwidth acquisition system (0-2 GHz real-time) has the temporal resolution necessary to resolve individual fluorescence decays, and thus can be used to measure the lifetime of the decay for the excited state. From this measurement of lifetime, we can determine the magnitude of the quenching rate coefficient. Thus, when the high-bandwidth system is used in conjunction with the low-bandwidth system, the PITLIF instrument can correct the measured concentration fluctuations for large variations in quenching.

Previous investigations with the PITLIF instrument have been concerned with the development of non-concurrent low- and high-bandwidth acquisition. We studied atomic sodium seeded into a laminar diffusion flame. The burner is a concentric tube design in which hydrogen flows through a circular tube, and an oxygen/argon mixture flows through a surrounding annulus. Sodium is seeded into the oxygen/argon mixture using an atomizer; the fluctuations in sodium are caused primarily by the atomization process. Using this simple flame, we were able to demonstrate the utility of the technique for systems in which concentration fluctuations are caused by turbulent mixing in the flame. In particular, the low-bandwidth system has been shown to be very effective in obtaining the PDFs and PSDs of the sodium concentration[4].
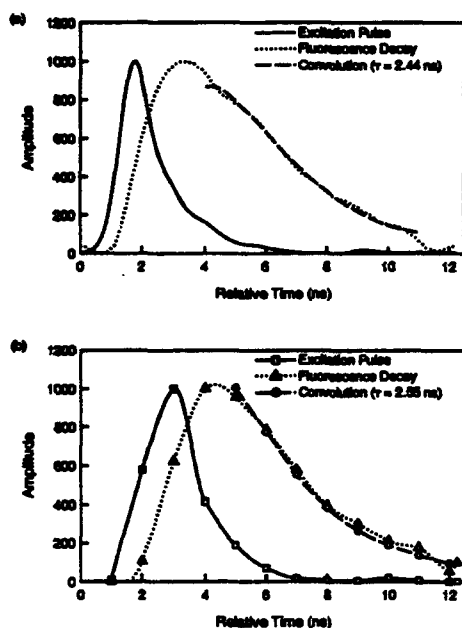
Figure 2. Normalized equivalent- and real-time instrument responses and fluorescence decays induced by the picosecond pulsed laser. Each waveform in (a) was obtained using equivalent-time sampling averaged over 500 waveforms and smoothed using a digital n-pole Bessel filter with a 700 ps risetime. Each waveform in (b) was obtained by summing 20 individual records of 20464 points acquired at 1 GHz. The symbols in (b) designate actual data points, while the lines in (a) and (b) are cubic spline fits between data points. Due to the greater point density for the equivalent-time data, individual data are not displayed in (a).

The high-bandwidth portion of the PITLIF instrument enables measurement of the local quenching environment. Each laser pulse induces a fluorescence decay which is depicted in Fig. 2(a). The instrument response to scattering from a laser pulse is also included in Fig. 2(a). Data were acquired using random equivalent time sampling at an effective rate of 20 Gsamples/s. The waveforms in Fig. 2 were smoothed using a digital n-pole filter with a time constant of 700 ps after averaging approximately 500 waveforms. The FWHM of the laser pulse is approximately 2 ns while that of the fluorescence decay is

approximately 6 ns. Since the instrument response time is on the same order of magnitude as the lifetime of the decay, a convolute-and-compare technique must be utilized to obtain the lifetime.

Because the equivalent-time mode requires an acquisition time greater than the time scale of turbulence, it is only suitable for measuring the average quenching environment at a specific location in the flame. A technique employing real-time sampling of the fluorescence decays yields similar results to the equivalent-time method while utilizing an acquisition rate on the time scale of turbulence[5]. To simulate real-time data samples without re-arming, successive real-time data samples were combined via a trigger from the laser mode-locker. A record of the fluorescence signal is analyzed by dividing it into data ranges, the temporal width of the ranges being equal to the inverse of the laser repetition rate. Each of these data ranges is divided into bins with a temporal width equal to the inverse of the acquisition rate. The data points are accumulated to generate a composite decay. Unfortunately, multiple data files are required to reconstruct a suitable decay. At the acquisition rate of 1 Gsample/s, the maximum number of points which can be acquired before the system must re-arm is 20464. The resulting 20.5 μs sampling time was not sufficient to adequately resolve the decay from the background emission. By obtaining 20 files at 1 Gsample/s (for a total sampling time of 409 μs), a meaningful fluorescence decay can be reconstructed. Figure 2(b) displays a composite fluorescence decay of sodium using the real-time technique, as well as the measured system response to scattered laser light. If not limited by the memory of the high-bandwidth channel, PITLIF could be used to correct the fluorescence signal for variations in the quenching environment on the time scale of turbulence.

A quantitative comparison of equivalent-time and real-time lifetimes was conducted by measuring the fluorescence lifetime via each method as a function of position in the flame. The results are shown in Fig. 3. The error bars (±2σ) were determined from a statistical analysis using 20 trials of each method at one location in the flame (r = 2 mm). The mean (μ) and sample standard deviation (σ) of the fluorescence lifetimes were calculated for both groups of 20 trials and fractional errors (μ/σ) were determined. The resulting fractional error was 0.100 for the equivalent-time method and 0.087 for the real-time method. These fractional errors are assumed to be independent of position in the flame.
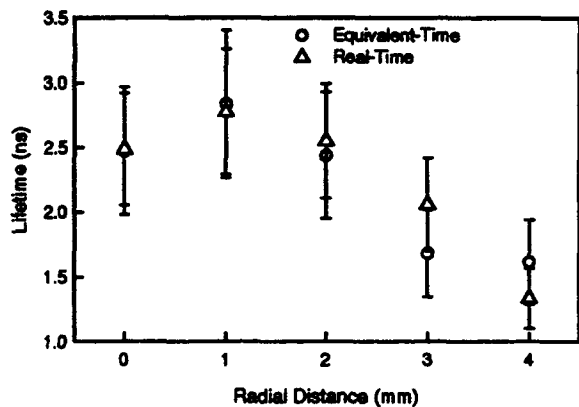
Figure 3. Equivalent-time and real-time fluorescence lifetimes at x = 10 mm for different radial positions. The uncertainty ranges for both methods (± 2σ) are calculated from a fractional error determined from the standard deviation of 20 lifetimes acquired at r = 2 mm.

We are currently applying the PITLIF technique to obtain time-resolved measurements of OH in laminar and turbulent $CH_4/O_2/N_2$ flames. Fluorescence techniques for OH require laser wavelengths in the ultraviolet (e.g., ~308 nm). This is accomplished with the use of an $LiIO_3$ crystal which frequency-doubles visible light from the dye laser to the ultraviolet. The current system also utilizes a cavity-dumper to increase peak pulse power (while lowering the pulse repetition rate); this allows for more effective frequency-doubling to the ultraviolet wavelengths. A 1/4-meter monochromator placed

95

in the detection path is used to reduce background flame emission. Figure 4 displays an OH fluorescence decay obtained 4 mm above the burner surface in a flat laminar $CH_4/O_2/N_2$ flame with unity equivalence ratio. The decay was obtained using random equivalent-time sampling at an effective rate of 10 Gsamples/s. A total of 500 waveforms were averaged and a 900 ps n-pole Bessel filter was utilized to obtain a smooth fluorescence decay. A fluorescence lifetime of 1.9 ns was measured using the convolute and compare method. Bergano et al.[4] measured the lifetime of OH to be 1.83 ns in a laminar, premixed CH_4/air flame using a streak camera and a low-repetition rate (10 Hz) laser system.
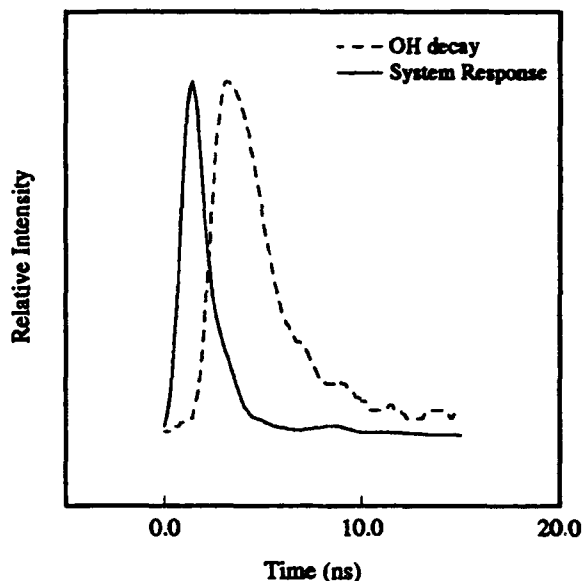
Figure 4. Normalized equivalent-time instrument responses and OH fluorescence decays induced by the picosecond laser. Each waveform was obtained using equivalent-time sampling averaged over 500 waveforms and smoothed using a digital n-pole Bessel filter with a 900 ps risetime.

We have demonstrated that variations in the quenching environment can be measured utilizing the high-bandwidth system in a random equivalent time sampling mode and also via real-time sampling. These measurements make it possible to correct the concentration measurements for collisional quenching. Future work will focus on measuring quenching rate coefficients of OH measured in near-adiabatic, laminar $CH_4/O_2/N_2$ flames and comparing these to quenching rate coefficients determined by assuming equilibrium chemistry and using known collisional cross-sections for the major quenchers in these flames. PDFs and PSDs of OH concentration obtained in turbulent flames will show the potential of the technique to make quantitative measurements of minor species concentrations in practical combustion systems.

1. J. O. Hinze, *Turbulence*, McGraw Hill, New York (1975).

2. J. O. Keller, J. L. Ellzey, R. W. Pitz, I. G. Shepherd and J. W. Daily, "The structure and dynamics of reacting plane mixing layers", *Experiments in Fluids*, 6, 33 (1988).

3. M. C. Drake and R. W. Pitz, "Comparison of turbulent diffusion flame measurements of OH by planar fluorescence and saturated fluorescence", *Experiments in Fluids*, 3, 283 (1985).

4. M. S. Klassen, B. D. Thompson, T. A. Reichardt, G. B. King and N. M. Laurendeau, "Flame concentration measurements using picosecond time-resolved laser-induced fluorescence", *Comb. Sci. Tech.*, in press (1994).

5. T. A. Reichardt, M. S. Klassen, G. B. King, and N. M Laurendeau, "Real-time acquisition of laser-induced fluorescence decays", *Optics Letters*, in review (1994).

6. N. S. Bergano, P. A. Jaanimagi, M. M. Salour and J. H. Bechtel, "Picosecond laser-spectroscopy measurement of hydroxyl fluorescence lifetime in flames", *Optics Letters*, 8, 443 (1983).

Energy Conversion Device Diagnostics
Prinicipal Investigator: B.N. Ganguly
Wright Laboratory
Wright-Patterson AFB, OH 45433-7919

SUMMARY/OVERVIEW: The effect of reacting and non-reacting gas additives on soot formation in premixed propane-oxygen flame has been investigated.   Transmission, scattering and temperature measurements were made at several downstream locations. The soot volume fraction, particle radius, and number density were derived from 488 nm laser beam transmission and Mie scattering measurements.   The temperature was measured by a two color pyrometer.   The sooting characteristics show nearly identical behavior with argon and nitrogen flame dilution.   The small quantities of SF_6 additive were found to be an effective soot suppressor for propane-oxygen flame.

TECHNICAL DISSCUSSION: The effects of additives on soot growth/suppression are being studied in a premixed propane-oxygen flame, using a flat flame burner. The soot volume fraction, soot diameter, soot density and the flame (soot) temperature have been simultaneously measured to permit correlation of soot reduction with nitrogen, argon and SF_6 gas additives.

Three non-intrusive optical techniques are used to measure the Mie scattering, the laser transmission and the flame (soot) temperature[1]. The Mie scattering is measured at a 90° scattering angle with both the incident and the scattered beam vertically polarized. The extinction measurement is performed with the laser beam split into a 50-50 ratio before entering a mechanical chopper. The reference and the probe beams are aligned to yield a 180° out of phase signal so that in absence of any attenuation of the probe beam, the signal obtained from the lock-in amplifier is zero. This detection arrangement not only removes incoherent noise, it also helps to reduce coherent laser and detector noise.   This experimental approach significantly improves the signal to noise for beam attenuation measurement under low extinction (low soot) conditions.

A line of sight integrated two color pyrometric technique is used to measure soot temperature. The radiometric measurements at 980 nm and 1600 nm are corrected for the optical signal attenuation to obtain the soot surface temperature. The gas temperature, for optically thin flames, is obtained by the same radiometric setup with a 10 micron SiC fiber acting as a grey body emitter[2].

The effect of gas dilution on soot has been measured for the equivalence ratios between 2.0 and 2.7, at several post reaction zone locations, with nitrogen, argon and SF_6.   The influence of

97

argon flow on temperature, Mie scattering and transmission are shown in figure 1 for Φ=2.06 and 8 mm above the burner head. Note that the transmission and the temperature variations both exhibit monotonic dependance on argon flow. The observed soot temperature increase is due to the flame streching and the soot volume fraction reduction (inversely proportional to the transmission) is due to both the temperature increase and the flame dilution.

The flame dilution with nitrogen exhibit soot behavior similar to the argon flame dilution. A comparison of the soot volume fraction change with temperature (flow rate) for argon and nitrogen flame dilution is shown in figure 2. This measurement was made at 19 mm from the burner head and at the same equivalence ratio as the data shown in figure 1.

The SF_6 additive has been known to reduce soot in ethylene flame[3]. The effect SF_6 additive on transmission, Mie scattering and soot temperature in a heavily sooted (ϕ=2.57) propane-oxygen flame is shown in figure 3. Note that a small amount of SF_6 additive (~ 100 ml/min) significantly increases the transmission and decreases Mie scattering intensity. Obviously SF_6 participates in the flame chemistry to modify soot formation.

The soot volume fraction change with the SF_6 flow rate is shown in figure 4. Assuming the soot particles are spherical and that no agglomeration occurs, the soot particle radius and soot number density can be estimated from the transmission and the Mie scattering measurements. The scattering intensity is normalized with respect to the N_2 Rayleigh scattering measurement. The soot particle radius and the number density variation with the SF_6 flow rate are also shown in figure 4. Note that at low SF_6 flow rate the soot particle radius does not change and the soot number density decreases. This behavior is opposite to the effects demonstrated by the metal additives.

REFERENCES
1. O. L. Gulder and D. R. Snelling, Combust. Flame 92, 115-124 (1993) and other references therein.

2. L. P. Goss, V. Vilimpoc, B. Sarka and W. F. Lynn, Jour. Engr. Gas Turb. Pwr. 111, 46-52 (1989).

3. J. B. A. Mitchell and D. J. M. Miller, Combust. Flame 75, 45-55 (1989).
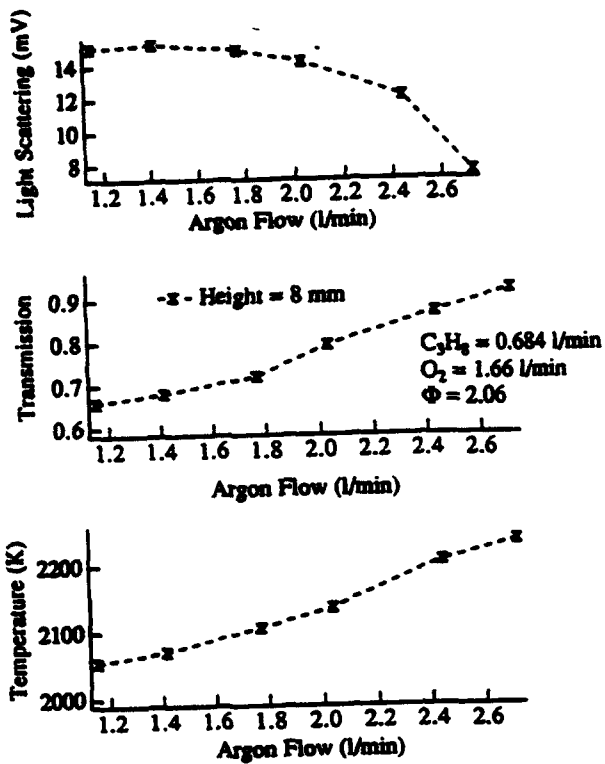
Figure 1: Effect of Argon flow on soot temperature, light scattering and extinction at a downstream location.
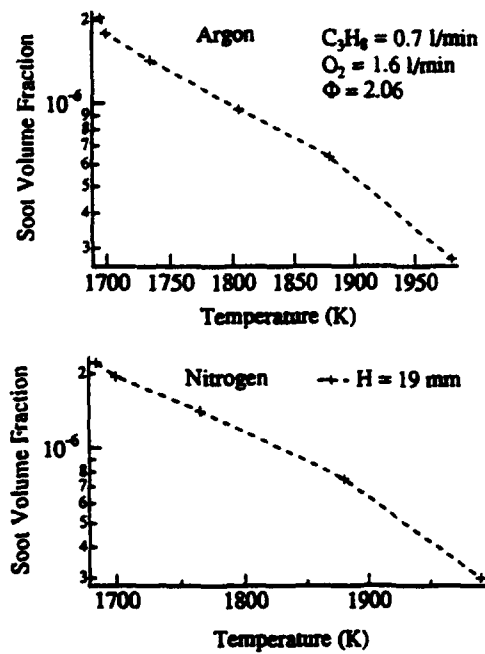
Figure 2: Comparison of soot volume fraction change with Argon and Nitrogen flame dilution at a downstream location.
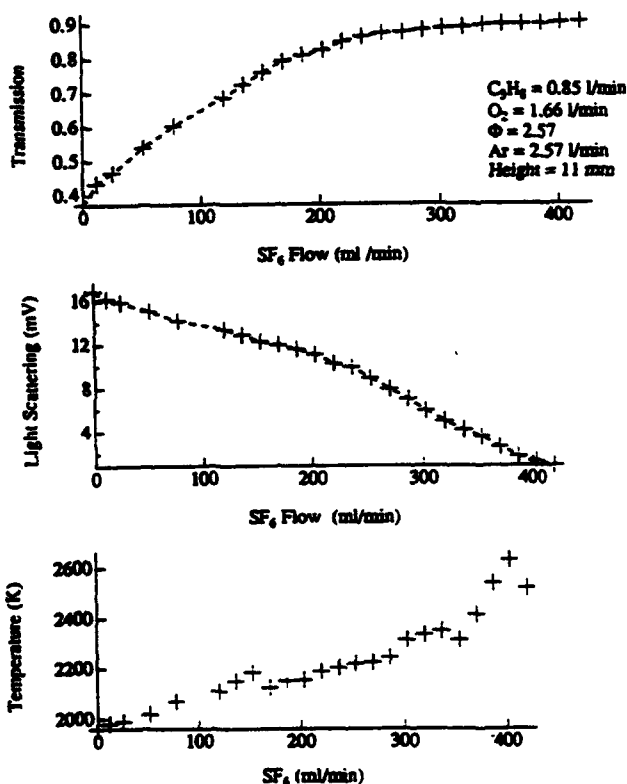
Figure 3: The effect of SF_6 additive on transmission, Mie scattering and soot temperature in a propane-oxygen flame.
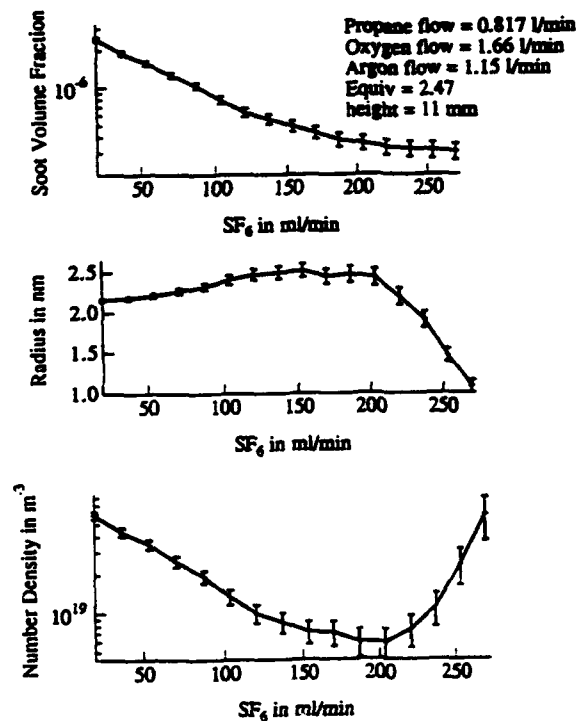
Figure 4: Soot volume fraction, soot radius and number density variations with SF_6 flow rates.

NONLINEAR SPECTROSCOPY OF MULTICOMPONENT DROPLETS

(AFOSR Grant No. 94-1-0135)

Co-Principal Investigator: Richard K. Chang

Yale University
Department of Applied Physics and Center for Laser Diagnostics
New Haven, Connecticut 06520-8284

SUMMARY/OVERVIEW

Noninstrusive in-situ optical diagnostics techniques have the potential to determine the chemical species and physical properties of multicomponent liquid droplets in a spray combustor. Our research is directed toward the understanding of nonlinear optical interactions occuring within individual droplets which decrease in size because of the evaporative process and are deformed in shape because of inertial effects. One of the key objectives of the research is to extract from the nonlinear optical spectra, information pertaining to the evaporation rate of closely spaced flowing droplets and to droplet shape deformations. The two main research results during the past year are: (1) the determination of evaporation rates of various droplets in a segmented stream flowing at a constant speed;[1] (2) the realization that the wavelength of the lasing emission emerging from different portions of the droplet rim contains information on the droplet deformation shape (i.e., whether it is an oblate or prolate spheriod), as well as on the droplet deformation amplitude.[2]

TECHNICAL DISCUSSION

The spherical liquid-air interface of a droplet, with radius a much larger than the wavelength, acts as an optical cavity. The normal modes of a dielectric sphere are referred to as morphology-dependent resonances (MDRs), which occur at discrete size parameters $x_{n,\ell} = 2\pi a/\lambda_{n,\ell}$, where $(\lambda_{n,\ell})$'s are discrete wavelengths. The index n designates the MDR mode number, angular momentum of the mode, or 1/2 of the number of intensity maxima around the equatorial plane. The index ℓ designates the mode order, radial mode number, or the number of angle-averaged intensity maxima along the radial direction. For a perfect sphere, a MDR at $x_{n,\ell}$ is $(2n + 1)$ degenerate, i.e., the frequency of this MDR is independent of the azimuthal mode number m, which can assume values $\pm n$, $\pm(n - 1)$,....,0.

For a spheroid with an axisymmetric z-axis, perturbation theory has shown that each of the $(n + 1)$ MDRs is frequency shifted from the $(2n + 1)$-degenerate MDR of a spherical droplet. When the distortion amplitude is small, the perturbtion theory[3] provides an analytical expression for the MDR frequency of a spheroid that depends on m^2,

$$\frac{\Delta\omega(m)}{\omega_0} = -\frac{e}{6}\left[1 - \frac{3m^2}{n(n+1)}\right],$$

where ω_0 is the frequency of a MDR at $x_{n,\ell}$, and the distortion amplitude is $e = (r_e - r_p)/a \ll 1$. The droplet polar and equatorial radii are r_p and r_e, respectively. The radius of the equivolume sphere is a. Note that the frequency shift to the "red" or to the "blue" (i.e., $\Delta\omega = \pm$) is dependent on the sign

of e. Thus, the shape deformation (whether it is oblate or prolate) as well as the distortion amplitude can be spectroscopically determined.

We make use of the frequency shifts of MDRs to deduce the radius decrease of droplets which are closely spaced and hence, hydrodynamically affecting the evaporation rate of various droplets in the flow field.[1] The wavelength shift of a MDR ($\Delta\lambda$) is simply related to the droplet radius change as follows: $\Delta a = (a/\lambda) \Delta\lambda$. Results from a continuous stream and a segmented stream are compared.[1] We also make use of the degeneracy-split spectra of MDRs to determine the deformation amplitude as well as the deformation shape of flowing droplets.[2]

In order to determine the evaporation rate, Fig. 1 shows the experimental setup that is able to detect simultaneously the MDR peaks in the lasing emission from numerous droplets in a continuous droplet stream or in an isolated droplet-stream segment. When the droplet a decreases to a - Δa, the wavelength location of each MDR is correspondingly "blue" shifted (- $\Delta\lambda$), because a shorter wavelength is needed to fit into the new circumference (see Fig. 2). The lasing MDR spectra from closely spaced droplets in a segmented stream is shown in Fig. 3. Note that the lasing MDR wavelengths of leading droplets occur at progressively shorter wavelength, indicating that these droplets are smaller than the trailing droplets (see Fig. 3). The lasing spectrum of the lead droplet is a continuum, because the lead droplet has three times the volume of the trailing droplets and consequently, largely distorted. The evaporation rates of different droplets in the segmented stream are summarized in Fig. 4.

In order to determine the deformation shape and amplitude, we use the same experimental setup that is shown in Fig. 1. We realized that the different azimuthal modes m have a different inclination with respect to the droplet axisymmetric axis, z. The lasing emission along the entire droplet rim would have a different frequency, because each ±m modes of a spheriod have a different frequency. The wavelength variation should from a parabola (see Fig. 5), starting from the droplet poles and ending on the droplet equatorial plane. When the individual droplets are imaged onto the entrance slit of an image-preserving spectrograph (see left side of Fig. 6), the resultant lasing spectra from five droplets are shown on the right side of Fig. 6. By observing the $\supset$- and $\subset$-shaped spectra, we can deduce that the droplet shape varies from prolate to nearly spherical to oblate, even though the actual photographs indicate that the droplets are spherical, at 15 mm down stream from the orifice. Figure 7 shows the lasing spectrum from a single droplet, which is greatly magnified onto the entrance slit. The spatially preserved lasing spectrum forms a parabolic shape. We deduce from the $\supset$- shaped spectrum that this droplet has a deformed shape of a prolate spheriod with a deformation amplitude of $e = 4 \times 10^{-3}$.

REFERENCES

1. Gang Chen, Ali Serpengüzel, Richard K. Chang, and William P. Acker, "Relative Evaporation of Droplets in a Segmented Stream Determined by Cavity Droplet Fluorescence Peak Shifts," in Proceedings of the SPIE Conference on Laser Applications in Combustion and Combustion Diagnostics, Vol. 1862 (SPIE, Bellingham, Washington, 1993) p. 200.
2. G. Chen, Md. M. Mazumder, Y. R. Chemla, A. Serpengüzel, R. K. Chang, and S. C. Hill, "Wavelength Variation of Laser Emission Along the Entire Rim of Slightly Deformed Droplets," Opt. Lett. 18, 1993 (1993).
3. H.M. Lai, P.T. Leung, K. Young, P.W. Barber, and S.C. Hill, "Time-Independent Perturbation for Leaking Electromagnetic Modes in Open Systems with Application to Resonances in Microdroplets," Phys. Rev. A41, 5187 (1990).
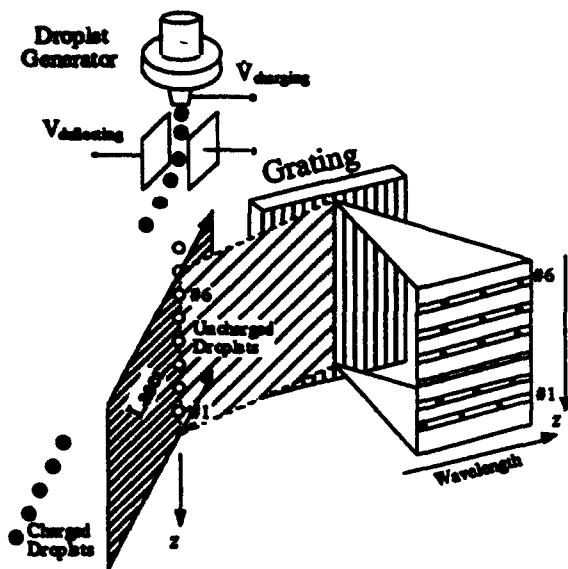
Figure. 1 The experimental arrangement. A laser beam is focused into a sheet and irradiates an isolated segmented droplet stream. The dye-lasing signals from the droplets are collected at 90° with respect to the laser sheet. A CCD camera (not shown) records simultaneously the wavelength dispersed lasing spectra (along the horizontal axis) and the spatial location of each droplet (along the vertical z-axis).

$$\Delta\lambda = (\lambda/a)\Delta a$$
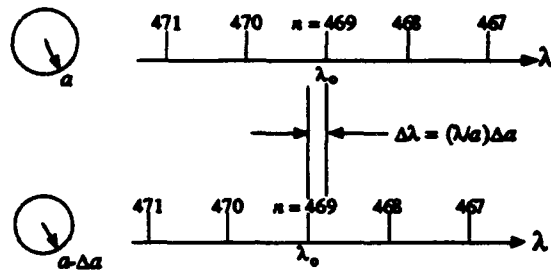
Figure 2 Two sets of MDR peaks with the same mode number n's from two droplets with different sizes. The consecutive n's imply that these MDR peaks are associated with the same order number ℓ.

(a) 20 mm below the orifice

(b) 25 mm below the orifice

Distance from orifice

wavelength (nm)

#n	○	$\frac{dA}{dt} = -7.2 \times 10^{-4}$ cm^2/sec
#7	○	$\frac{dA}{dt} = -7.3 \times 10^{-4}$ cm^2/sec
#6	○	$\frac{dA}{dt} = -7.5 \times 10^{-4}$ cm^2/sec
#5	○	$\frac{dA}{dt} = -8.1 \times 10^{-4}$ cm^2/sec
#4	○	$\frac{dA}{dt} = -8.7 \times 10^{-4}$ cm^2/sec
#3	○	$\frac{dA}{dt} = -9.2 \times 10^{-4}$ cm^2/sec
#2	○	$\frac{dA}{dt} = -11.2 \times 10^{-4}$ cm^2/sec
#1	⬭	? (continuum spectrum)

Figure 4 The tabulation of droplet evaporation rates (expressed as the decreasing rate of the droplet surface area) for the first several droplets in a segmented droplet stream. Because the lead droplet is so distorted that evaporation rate cannot be determined with the spectroscopic technique.

Figure 3 The spectrally and spatially resolved CCD recordings of an isolated segmented droplet stream at (a) 20 mm below the orifice and (b) at 25 mm below the orifice. Between (a) and (b), the time delay of the pump laser pulse is 0.5 ms. The lasing spectrum of the lead droplet is a continuum. Droplet #2, which is distinct in (a), is just about to coalesce with the lead droplet in (b).

102
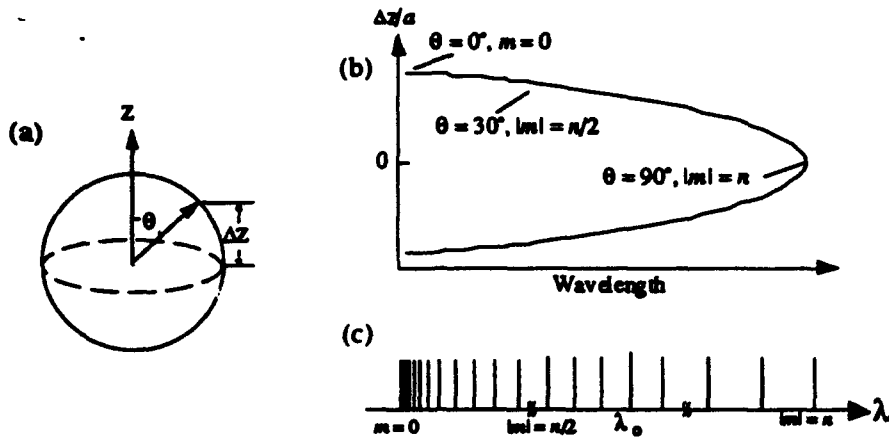
Figure 5 (a) Shows the definition of θ and Δz. (b) Illustrates the wavelength dependence of the light from different positions (with different θ and Δz) on an oblate droplet rim. Various parts of the parabolic λ(Δz) curve can be related to the different *m*-MDRs. (c) The MDRs mode splitting and frequency shifts are based on Eq. (1)
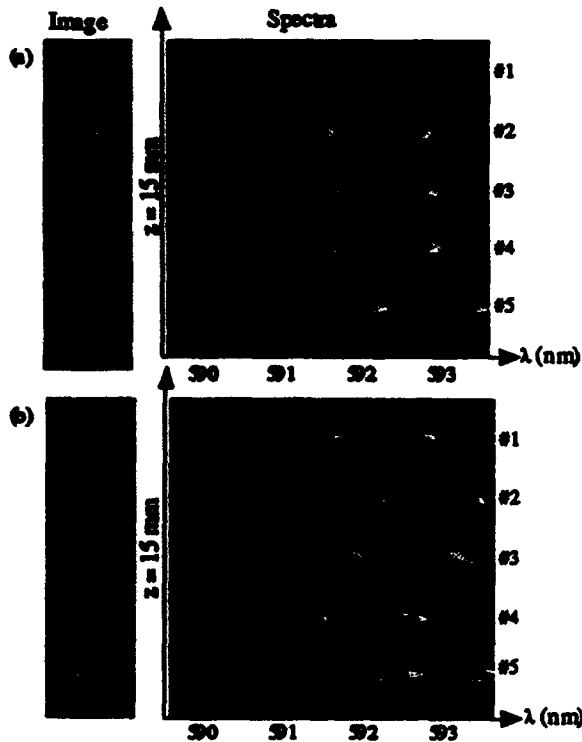
Figure 6 At medium magnification (5x), the CCD image of the lasing droplets (15 mm below the orifice) as they appear at the entrance slit (250 μm wide) of a spectrograph (left column). For (a) the right-half rim and for (b) the left-half rim is imaged onto the slit. The spatially preserved wavelength-dispersed data captured by a CCD camera are shown on the right side. Note the ⊃- and ⊂-shaped curves are better resolved spatially than in Fig. 13.
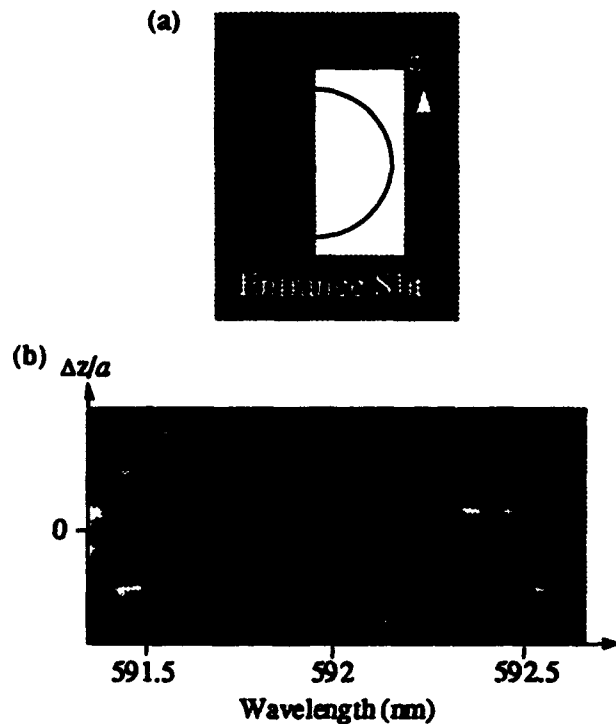
Figure 7 (a) At larger magnification (20x), the right half of circular image of a single droplet (10 mm below the orifice) fits into the entrance slit (800 μm wide) of a spectrograph. (b) The spatially preserved wavelength-dispersed data captured by a CCD camera.

DROPLET-TURBULENCE INTERACTIONS
OVER A WIDE SPECTRAL RANGE

PRINCIPAL INVESTIGATOR:

W.A. Sirignano

Department of Mechanical and Aerospace Engineering
University of California
Irvine, CA 92717

SUMMARY/OVERVIEW:

The research program concerns the detailed three-dimensional interactions of simulated turbulent flow structures with individual droplets. Initially cylindrical vortices advect past a sphere. Navier-Stokes equations describe the unsteady flow field. Finite-difference computations yield flow properties plus temporal behavior of lift, drag, and moment coefficients on the sphere. Useful correlations for these coefficients are obtained.

AUTHORS

W.A. Sirignano   S.E. Elghobashi   I. Kim

TECHNICAL DISCUSSION

Droplet – Turbulent Interaction Over a Wide Spectral Range

A theoretical/computational analysis of the interactions of droplets with a turbulent field is being conducted. We are particularly interested in the important and challenging high-frequency domain where turbulent length scales are comparable to droplet size. To simulate the three-dimensional, unsteady interactions, a Navier-Stokes solver was developed. The alternating-Direction-Predictor-Corrector scheme and a pressure correction equation are employed.

We first investigated three-dimensional flow interactions between a vortical (initially cylindrical) structure flowing with the free stream and a spherical particle fixed in space. A schematic of this problem is shown in Figure 1-a where the vortex tube, whose diameter is of the order of the sphere diameter, is initially located ten radii upstream from the center of the sphere. The vortex tube has a small core region with a radius σ normalized by the sphere radius. The velocity induced by a vortex tube approaches zero as the distance from the center of the vortex tube goes to zero, and at distances greater than σ, the induced velocity is similar to the point vortex. Initially, the lift forces are positive due to upwash on the sphere, then become negative due to downwash and higher fluid velocity near the bottom of the sphere when the vortex tube passes the sphere.

We examined the effects of the size of the vortex tube on the flow field by performing computations for Re (Reynolds number) = 100, d_{off} (offset distance) = 0, and five different sizes of the

vortex tube, $0.25 \leq \sigma \leq 4$ in addition to the base case $\sigma = 1$. Each simulation is performed with two different values of $v_{max} = 0.1$ and 0.3, where v_{max} denotes the maximum fluctuation velocity due to the vortex tube and equals to the circulation of the vortex tube divided by (2π). Table 1 shows the rms lift and moment coefficients as a function of v_{max} for six different initial radii of the vortex tube, $\sigma = 4, 3, 2, 1, 0.5$, and 0.25. The root mean square (rms) is evaluated for the dimensionless time span 23.4. All the coefficients are linearly proportional to v_{max} at each σ. When $\sigma \geq 2$, all the coefficients become *independent* of σ. When σ approaches zero, all the coefficients should be proportional to (σv_{max}) which is the *circulation* of the vortex tube divided by 2π ($\Gamma_v = 2\pi\sigma v_{max}$). For example, $C_{L,rms}$ is expressed by

$$C_{L,rms} = c_1 v_{max}, \quad 2 \leq \sigma \leq 4 \tag{1}$$
$$= c_2 v_{max} \sigma^n, \quad 0.25 \leq \sigma < 2, \quad 0.75 \geq n \geq 0.5, \tag{2}$$

where the constant $c_1 = 1$ and $c_2 = 0.65$, and n depends on σ and should approach unity as σ reaches zero. $C_{M,rms}$ are also expressed by equation (1) and (2) with $c_1 = 0.055$ and $c_2 = 0.05$. The time averaged value of the deviation of the drag coefficient from that of the axisymmetric flow past a sphere for all values of σ is nearly zero ($O(10^{-4})$).

In summary, the lift and moment coefficients depend only on circulation at small values of σ while they depend only on v_{max} (and not σ) at large values of σ. For mid-range values of σ, they depend on both σ and v_{max} (or equivalently both σ and Γ_v).

In order to examine in more detail the effects of the size of the vortex tube to the drag on the sphere, we performed the same calculation as the above but with $d_{off} = -2$. The behavior of the deviation of the drag coefficient from that of the axisymmetric flow past a sphere is similar to that of the lift and moment coefficients described above. For example, $C_{D,ave}$ averaged over time span 23.4 is expressed by

$$C_{D,ave} = C_{D,axi} + c_1 v_{max}, \quad 2 \leq \sigma \leq 4 \tag{3}$$
$$= C_{D,axi} + c_2 v_{max} \sigma^n, \quad 0.25 \leq \sigma < 2, \quad 0.75 \geq n \geq 0.5, \tag{4}$$

where the constant $c_1 = -0.45$ and $c_2 = -0.28$, and n depends on σ and should approach unity as σ reaches zero. $C_{D,axi}$ in equations (3) and (4) represents the time averaged value of the drag coefficient in the case of $v_{max} = 0$.

The effect of Reynolds number ($20 \leq Re \leq 80$) on the rms lift and moment coefficients was investigated for the vortex size $1 \leq \sigma \leq 4$. The rms lift and moment coefficients are linearly proportional only to v_{max} and independent of σ when $\sigma \geq 2$ at fixed Reynolds number as described above for $Re = 100$ and expressed by

$$C_{L,rms} = 6.3 v_{max} Re^{-0.4} \tag{5}$$
$$C_{M,rms} = 2.9 v_{max} Re^{-0.86}, \tag{6}$$

where the root mean square (rms) is evaluated for the dimensionless time span 23.4.

We summarize our findings which are directly relevant to practical applications as below.

(i) The deflection of the particle path will depend on the magnitude of the rms lift coefficient (equation (5)) and the ratio, ρ_r, of the particle density to that of the carrier fluid ($C_L = \frac{8}{3}\rho_r A$, where A is the dimensionless acceleration of the particle due to the lift force). This result provides a simple method to estimate the deflection of particle trajectory in the dilute particle-laden turbulent flow. Equation (5) and the nondimensionalized Newton's second law shows that the deflection becomes slowly higher as Reynolds number becomes smaller.

(ii) The magnitude of the rms moment coefficient of the particle is one order magnitude less than that of the rms lift coefficient when $Re \geq 20$. However, we can deduce from equation (6) that the moment will be important, and its magnitude will be comparable to that of the lift when $Re < 1$.

(iii) When a vortex tube advected by a uniform free stream approaches a sphere, the sphere experiences *lower drag* than that of a sphere subjected to an axisymmetric flow if the sphere were *free to move* rather than fixed, unless the initial offset distance of the vortex tube is large positive. The lower drag is caused by the upward motion of the sphere due to the upwash of the approaching vortex tube, and thus the center of the vortex tube would be located below the front stagnation point of the sphere. This causes lower dynamic pressure ahead of the front stagnation point.

(iv) We observe some interesting flow phenomena in the near wake as a function of time on the passage of the vortex tube as shown in Figure 2, which displays the pseudo-streamlines (left column) and y-component of the vorticity (right column) in the x-z symmetry plane at $t = 0, 1, 6, 9, 10$, and 11 for $Re = 100$, $d_{off} = 0$, $\sigma = 1$, and $v_{max} = \Gamma_v/(2\pi\sigma) = 0.4$. The contour values of the pseudo-streamlines are $0, \pm 0.02, \pm 0.1, \pm 0.3$. The contour values of the vorticity are $\pm 0.4, \pm 0.5, \pm 0.8, \pm 1.4, \pm 2$, with the highest magnitude at the sphere surface.

We now investigating three-dimensional flow interactions between a pair of vortex tubes flowing with the free stream and a spherical particle fixed in space as shown in Figure 1-b.

The lift coefficients of the sphere as a function of time were computed for $Re = 100$, $d_{off} = 1.5$, and $\sigma = 1$ with for four different maximum fluctuation velocities due to the vortex tubes rotating counter-clockwise. The rms lift coefficient is linearly proportional to v_{max} as in the case of the interaction of a single vortex tube with a sphere. More investigations, for example, on the vortex tubes rotating in different direction, are underway.
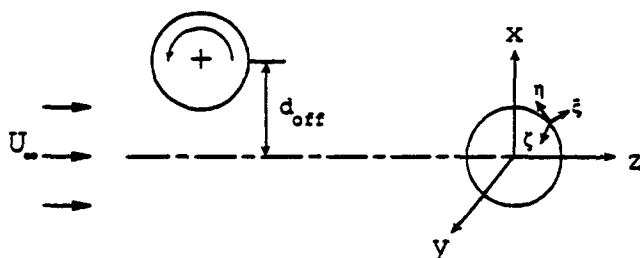
Figure 1-a Flow geometry and coordinate for one vortex tube
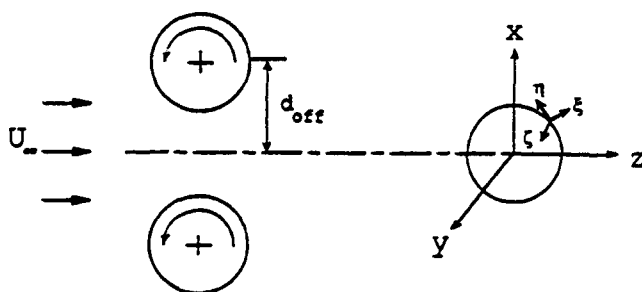
Figure 1-b Flow geometry for a pair of vortex tubes

v_{max}	$C_{L,rms}$	$C_{M,rms}$
$\sigma = 4$		
0.3	0.307	0.0161
0.1	0.102	0.00546
$\sigma = 3$		
0.3	0.299	0.0169
0.1	0.0997	0.00577
$\sigma = 2$		
0.3	0.271	0.0169
0.1	0.0907	0.00593
$\sigma = 1$		
0.3	0.195	0.0138
0.1	0.0658	0.00514
$\sigma = 0.5$		
0.3	0.119	0.00953
0.1	0.0402	0.00355
$\sigma = 0.25$		
0.3	0.0660	0.00587
0.1	0.0221	0.00210

Table 1. Rms lift and moment coefficients as a function of v_{max} for six different radii of the vortex tube.
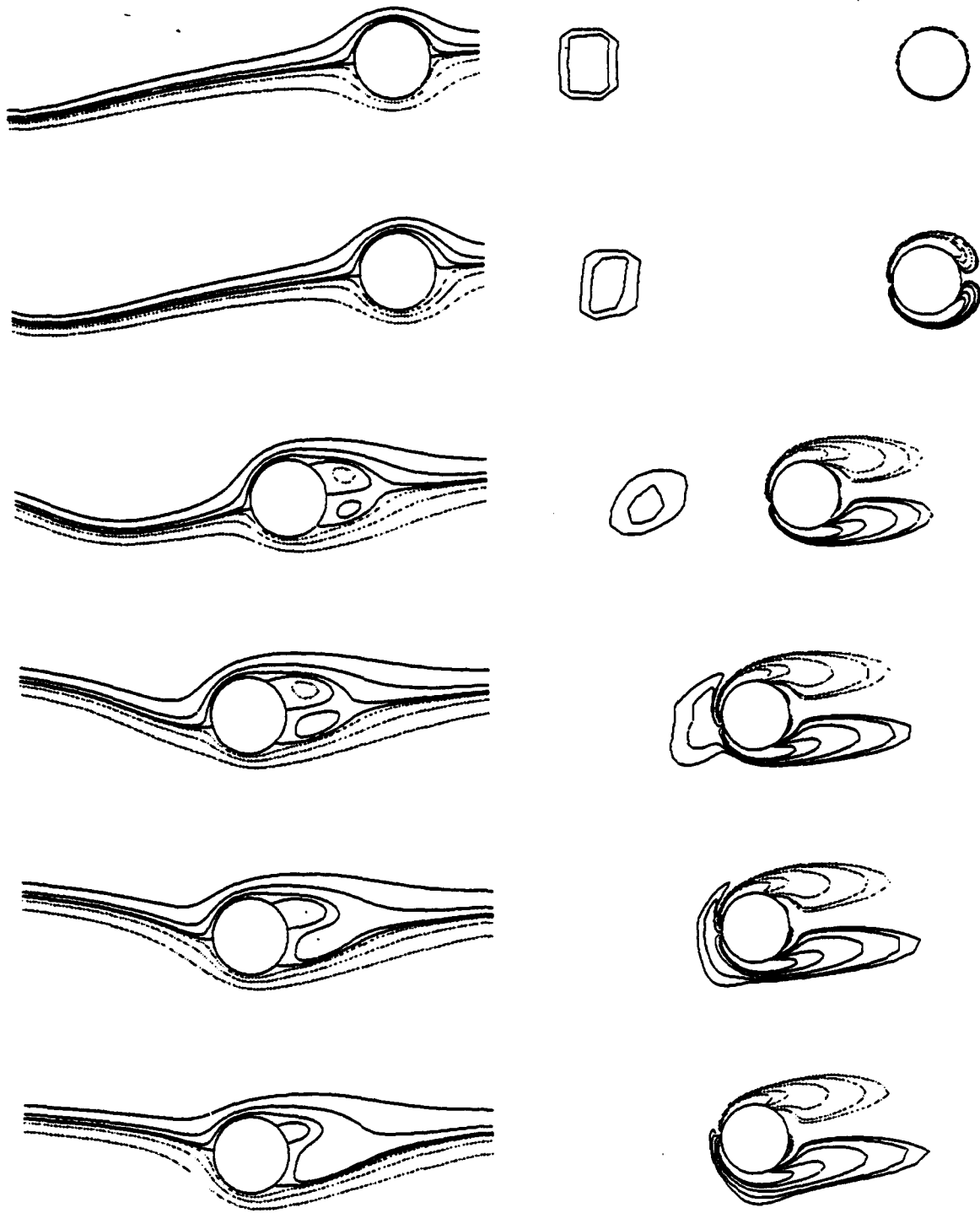
Figure 2. Pseudo-streamlines (left column) and vorticity contours (right column) in x-z plane at $t = 0, 1, 6, 9, 10$, and 11 for $Re = 100$, $d_{off} = 0$, $\sigma = 1$, and $v_{max} = 0.4$.

PARTICLE DISPERSION IN A TURBULENT SHEAR FLOW

Principal Investigators: Ian Kennedy and Wolfgang Kollmann

Department of Mechanical and Aeronautical Engineering
University of California
Davis CA 95616

SUMMARY

An experimental and computational effort has been directed towards aspects of the interaction between spray droplets and turbulence in a shear flow. Earlier phases of the project were concerned with single droplets in a round, turbulent jet. The experimental results have shown that a turbulent Stokes number near unity leads to a particle diffusivity greater than the fluid diffusivity. Large Eddy Simulations of the process were completed with a Smagorinsky model for sub-grid scale effects. Current efforts are directed towards extending the research into actual sprays. The experimental group recently demonstrated that it is possible to track the motion of an individual fluorescent particle within a turbulent spray. The numerical scheme has been extended to include many particles in the flow that modify the turbulence of the continuous phase.

TECHNICAL DISCUSSION

Theory and Computation

Direct simulation of turbulent round jets and turbulent sprays is not within the capabilities of present computers. The mass loading of realistic sprays in a turbulent environment is several orders of magnitude too high for the available computer memory and speed. Therefore, the computation of the turbulent flow field is based on the notion of simulating the large eddies and modelling the effect of the small and unresolved eddies on the large and resolved ones as described in the contract proposal. The work on the LES model for the continuous phase is concluded using the Smagorinsky model for the sub-grid-scale motion. Furthermore, a simple model for the effect of the particles on the continuous phase was developed, which is essentially a momentum balance for a fluid volume containing particles moving relative to the continuous phase. The current theoretical work is aimed at the simulation of particle subsets using stochastic differential equations that reflect not only the interaction of particles with the continuous phase, but also the change in particle numbers in a subdomain of the flow field that moves with a velocity averaged over the particles. The result should allow a Lagrangian -type treatment of higher particle loading without using two-fluid models for the particulate phase.

The present status of the prediction model for particle transport in turbulent jets is illustrated in Fig.1 and Fig.2. The turbulent flow in a round jet at the Reynolds number Re=13000 is simulated with the LES model; particles are injected uniformly at the entrance section with a velocity $v_p = 0.448$ m s^{-1} smaller than the velocity of the continuous phase, which is $v = 13$ m s^{-1} in the core region. Thirty four particles are injected every tenth time step corresponding to a mass loading of 2.3%. The first

figure shows the scatter plot of the particles at x/D=14. The model for the effect of the unresolved motion of the continuous phase is not yet included in the particle equations. Hence, particles form in some instances coherent strings which would be diffused by the random process describing the small scale effects. The particles have a distinct effect on the continous phase as Fig.2 shows. The upper graph contains the flow field without the effect of the particles on the continuous phase and the lower graph the flow field for the same conditions with the particle effect. The particles are injected at lower velocity than the continuous phase and act as an additional disturbance. The roll-up of the shear layer is accelerated and starts further upstream than in the lower graph, but the development of large structures downstream is reduced.

Experiments

Droplet dispersion has been measured in a turbulent round jet of air issuing into still air. Individual droplets were formed with a piezo-electric device; they were injected onto the centerline of the jet. Their location across the jet was measured at different axial stations with a laser sheet and position sensing photomultiplier tube.

Measurements of droplet dispersion in an isothermal, non-reacting flow have been obtained with variations in droplet response times and turbulence time scales. The Reynolds numbers of a round jet have been varied from 10,000 to 30,000. The nozzle diameter has been varied from 7 to 12 mm. Two droplet sizes have been investigated viz., 60 µm and 90 µm. Results were analyzed in terms of the turbulent Stokes numbers based on the droplet response time and the integral time scale.

Dispersion (mean square displacement of the droplets from the centerline of the jet) was measured as a function of time of flight. The curve of mean square displacement has been differentiated with respect to time to obtain droplet diffusivity. The droplet diffusivity has been compared with the eddy diffusivity in terms of an inverse particle Schmidt number as a function of the turbulence Stokes number. The results that are presented in Fig. 3 indicate that as the Stokes number tends to zero, the Schmidt number tends to unity as the droplets approach the behavior of a fluid particle. At large Stokes numbers, the inverse Schmidt number attains a maximum around a Stokes number of 1.

The latest phase of the experimental research involves the addition of a spray to the jet. an ultrasonic atomizer is use produce a fine spray with a SMD of around 50 µm. The spray is introduced tangentially to the flow of air through a chamber as shown in Fig. 4. The chamber is designed to have a small flow of air through the walls and through the central tube to prevent the spray hitting the walls and creating drips. Single droplets that are seeded with fluorescein dye are created at the top of the chamber with a piezoelectric droplet generator. The fluorescent droplet passes through the spray to leave the nozzle on the centerline. As it passes through an Argon ion laser sheet, it emits fluorescence at a longer wavelength. The fluorescence is detected by a position sensing photomultiplier tube to yield a measure of the location and velocity of the particle.

A major challenge over the past year has been to obtain good signals from the fluorescent particles in the very strong background Mie scattering from the spray. The background scattering has been blocked with a Raman filter followed by a colored glass long pass filter. The combination of filters offers up to 6 orders of magnitude rejection of the laser wavelength.

It has been demonstrated recently that it is possible to detect droplets as small as 30 μm against the scattering from a spray with a mass loading as high as 7%. The signal to noise ratio is excellent. It will be possible with this technique to determine the impact of the mass loading on the dispersion of the individual droplet a function of the time of flight and the droplet velocity.
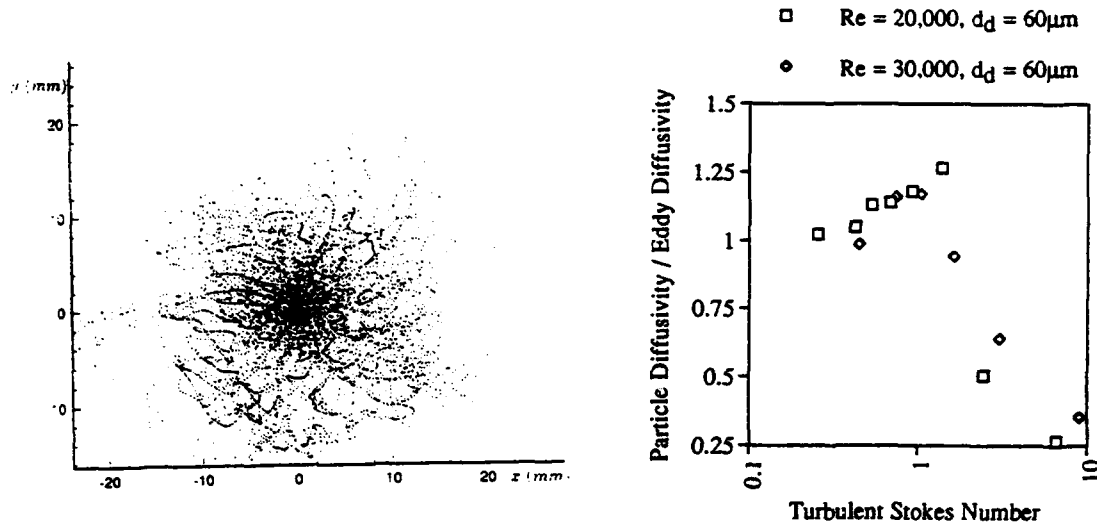
Fig.1 Scatter plot of particle location at x/D. =14 in a turbulent jet with Re = 13000

Figure 3 Inverse Particle Schmidt Number as a function of Turbulent Stokes Number for two Reynolds Numbers
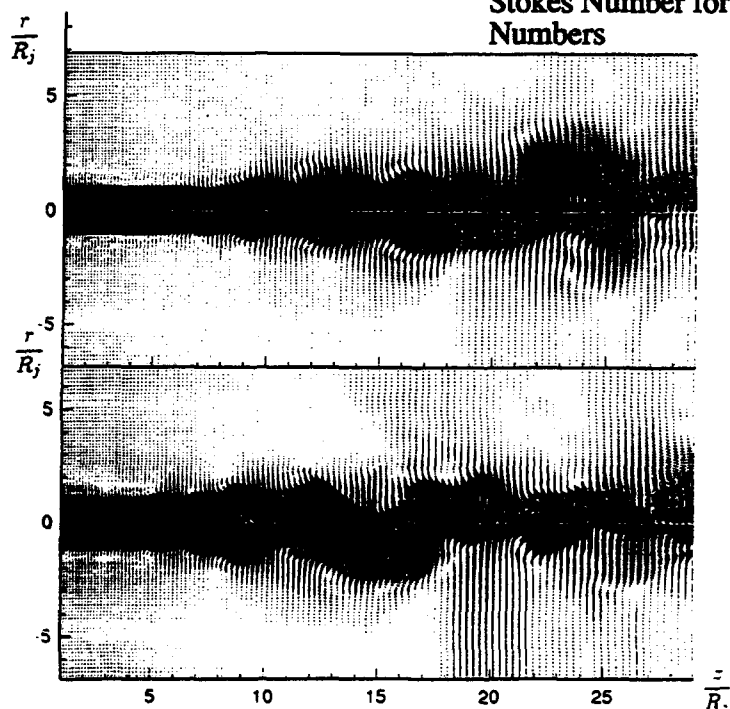
Fig.2 Velocity field without particles (upper graph) and with particles (lower graph) in a turbulent jet at Re = 13000.
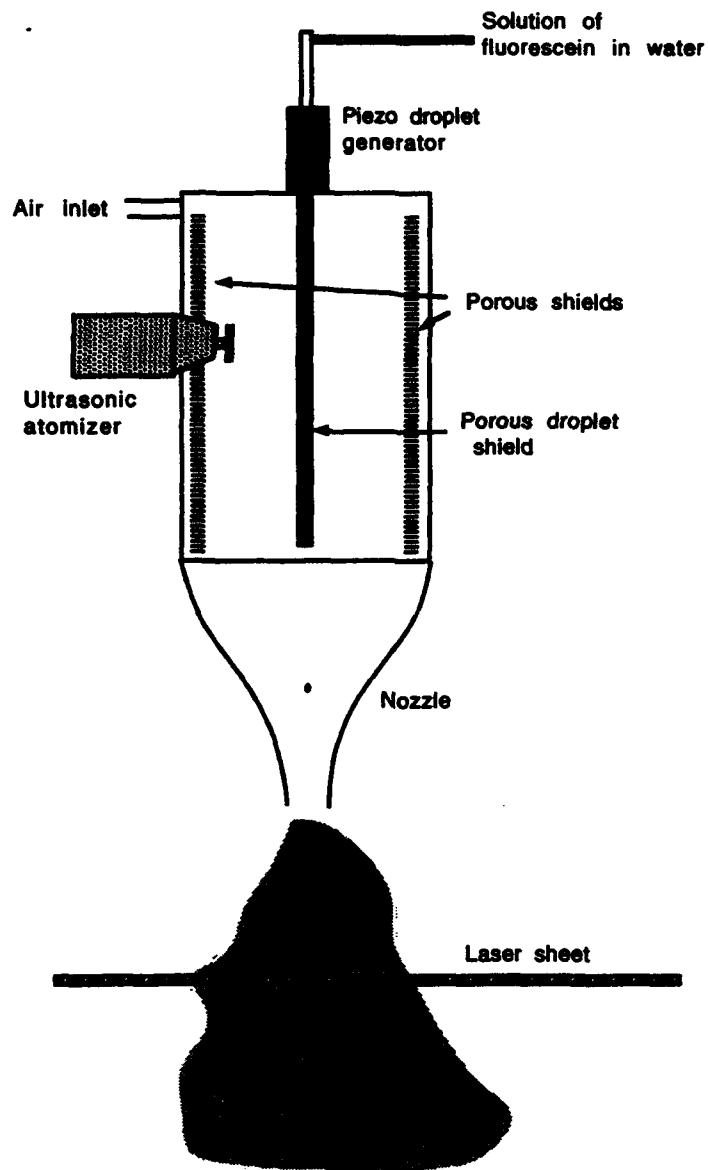
Figure 4 Apparatus for tracking Fluorescent Particles in Turbulent Spray

ATOMIZATION OF VISCOUS LIQUID SHEETS

Principal Investigator: E. A. Ibrahim

Mechanical Engineering Department
Tuskegee University
Tuskegee, Alabama 36088

SUMMARY

A numerical solution of the problem of the nonlinear instability of
a viscous liquid sheet issued in a quiescent inviscid gas has been
obtained by the Spectral method. The temporal and spatial evolution
of the liquid-gas interface undergoing symmetric or antisymmetric
disturbances is investigated. The sheet breakup-length and the size
of the drops produced by the disintegration of the sheet are
estimated. The effects of the physical properties of the sheet and
surrounding gas on instability are examined.

TECHNICAL DISCUSSION

We consider the problem of nonlinear instability of a viscous
liquid sheet of thickness 2a that is issued from a nozzle at a
velocity U into a quiescent inviscid gas medium. The velocity U is
small compared to the velocity of sound; thus the assumption of
incompressibility for both fluids is valid. The viscosity of the
gas is neglected following Taylor's[1] treatment of a related problem.
The x-axis is parallel to the direction of the velocity U, and the
y-axis is normal to the undisturbed sheet with its origin at the
midplane of the sheet. The Orr-Sommerfeld equation governing the
liquid motion is given by:

$$\nabla^2 \psi_t - \nu \nabla^2 (\nabla^2 \psi) + U \nabla^2 \psi_x + \psi_y \nabla^2 \psi_x - \psi_x \nabla^2 \psi_y = 0$$

where ψ is the stream function, t is time, ν is kinematic viscosity
of liquid and $\nabla^2 = \partial_{xx} + \partial_{yy}$. Subscripts t, x, and y denote partial
differentiation. The boundary conditions are that the y-component
velocity at the interface is equal to the total derivative of the
interface displacement. Since the surrounding gas medium is assumed
to be inviscid, the tangential stresses should vanish at the
interface. The normal stresses across the interface should be
balanced. Hence, at $y = \eta_j - (-1)^j a$, where j=1 for the upper and
j=2 for the lower interface, η is the surface disturbance, we have

$$v = \eta_{jt} + (U + u) \eta_{jx}$$

$$\mu \left(\frac{\partial u}{\partial y} + \frac{\partial v}{\partial x} \right) = 0$$

$$- p + 2 \mu \frac{\partial v}{\partial y} = - p_{gj} - (-1)^j p_{\sigma j}$$

where, u, v are the velocity components in the x, y directions, respectively, μ is the liquid dynamic viscosity, p is the liquid pressure, p_g is the gas pressure, and p_σ is the pressure due to surface tension, $p_{\sigma j} = \sigma \eta_{jxx} (1 + \eta^2_{jx})^{-3/2}$. The continuity equation for the inviscid gas medium may be expressed in terms of a velocity potential, ϕ_j, such that $\nabla^2 \phi_j = 0$. The boundary conditions for the gas require that across the liquid-gas interface the normal velocity be continuous, and far away from the liquid surface the disturbance decay to zero. Hence,

$$v_{gj} = \eta_{jt} + u_g \eta_{jx} \qquad at \qquad y = \eta_j - (-1)^j a$$

$$v_{gj} = 0 \qquad at \qquad y = \pm \infty$$

The liquid and gas pressures may be expressed in terms of ψ, ϕ_j, respectively, by using the relevant momentum equation. It is assumed that ψ, ϕ_j, and η admit expansions in the form of Fourier series in x, with the coefficients function of t only. The series expansion for ψ, ϕ_j are multiplied by a term that is a function of {"only derived from the corresponding linear instability solution given by Ibrahim[2]. The series representation of η is multiplied by η_0, the amplitude of the initial disturbance. The Spectral method is used to obtain a numerical solution of the problem. The unknowns are the coefficients in the Fourier series expansions. The initial conditions are provided by the linear instability solution of Ibrahim[2]. The resulting initial-value problem is solved by a fourth-order multistep predictor-corrector scheme similar to that described in Burden and Faires[3].

The numerical solution provides the temporal and spatial evolution of the liquid-gas interface originating from symmetric or antisymmetric disturbances. It is found that maximum thinning and subsequent rupture of the sheet into ligaments occur at positions corresponding to one or one-half of the length of the fundamental wave for symmetric and antisymmetric disturbances, respectively. This is in agreement with the results of Dombrowski and Hooper[4] and Rangel and Sirignano[5]. The breakup length of an attenuating sheet may be defined by the implicit equation, $\eta_2(x^*, t^*) - \eta_1(x^*, t^*) = 2a$, where x^* denotes the breakup length and t^* is the breakup time. Figure 1 shows representative results of the variation of dimensionless breakup length with liquid Weber number for water sheet in atmospheric air. The values of breakup length compare favorably with the experimental measurements of Dombrowski and Hooper[4]. To estimate the size of the drops produced by the

fragmentation of ligaments, we employ the secondary breakup formula of O'Rourke and Amsden[6]

$$R_{32} = R \left[\frac{7}{3} + \frac{\rho R}{2\sigma} \left(\frac{dy}{dt} \right)_b^2 \right]^{-1}$$

where R_{32} is the Sauter mean radius, R is the radius of the ligament, ρ is liquid density, σ is surface tension and $(dy/dt)_b$ is the rate of drop deformation at breakup which is provided by Ibrahim et al.[7] The radius of the ligament at breakup is calculated by a mass balance to be R = $(8a/k)^{1/2}$ where k is the wave number. Some preliminary computations of the variation of dimensionless drop Sauter mean radius with Reynolds number are shown in Figure 2. The size of the drops fall within the experimental values reported in Mansour and Chigier[8]. However, more validations and refinements of the computational technique are still needed. Figure 3 shows the effect of liquid viscosity on the instability of liquid sheets. It is seen that liquid viscosity, affected through Reynolds number, reduces both the disturbance growth rate and shifts the dominant wave the disturbances to a longer wavelength. Figure 4 illustrates the effect of gas to liquid density ratio on the growth rate of instability due to antisymmetrical disturbances. It is shown that an increase in gas to liquid density ratio increases the growth rate and dominant wavenumber of the antisymmetrical disturbances as long as the density ratio is less than the gas Weber number. Once the density ratio becomes greater than the gas Weber number the disturbance growth rate is reduced. A density ratio higher than the gas Weber number shifts the mechanism of instability from aerodynamic to the viscosity enhanced instability discovered by Li and Tankin[9]. The effect of surface tension is to oppose the development of instability.

REFERENCES

[1]Taylor, G. I., The Scientific Papers of G. I. Taylor, Cambridge University Press, Cambridge, England, Vol. 3, pp. 244-254, (1963).
[2]Ibrahim, E. A., AIAA Paper 94-0562, presented at the 32nd Aerospace Sciences Meeting, Reno, NV, Jan. 10-13, (1994). Also accepted by Journal of Propulsion and Power.
[3]Burden, R. L., and ʳaires, J. D., Numerical Analysis, 5th ed., PWS Publishing Company, ρp. 270-282, (1993).
[4]Dombrowski, N., and Hooper, P. C., Chemical Engineering Science, Vol. 17, pp. 291-305, (1962).
[5]Rangel, R. H., and Sirignano, W. A., Physics of Fluids A, Vol. 3, pp. 2392-2400, (1991).
[6]O'Rourke, P. J., and Amsden, A. A., SAE Paper 87-2089.
[7]Ibrahim, E. A., Yang, H. Q., and Przekwas, A. J., Journal of Propulsion and Power, Vol. 9, pp. 651-654, (1993).
[8]Mansour, A., and Chigier, N., Physics of Fluids A, Vol. 2, pp. 706-719, (1990).
[9]Li, X., and Tankin, R. S., Journal of Fluid Mechanics, Vol. 226, pp. 425-443, (1991).
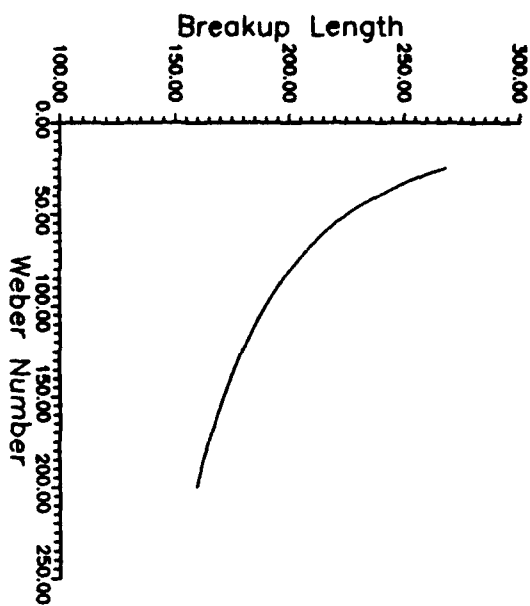
Fig. 1 Effect of Weber number on sheet breakup length.
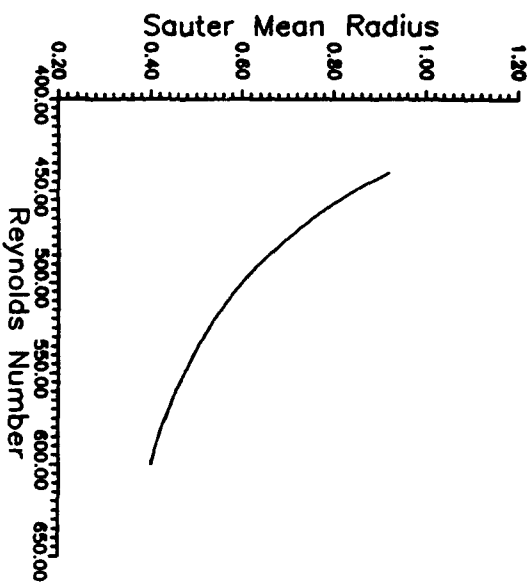
Fig. 2 Effect of Reynolds number on Sauter mean radius of drops.
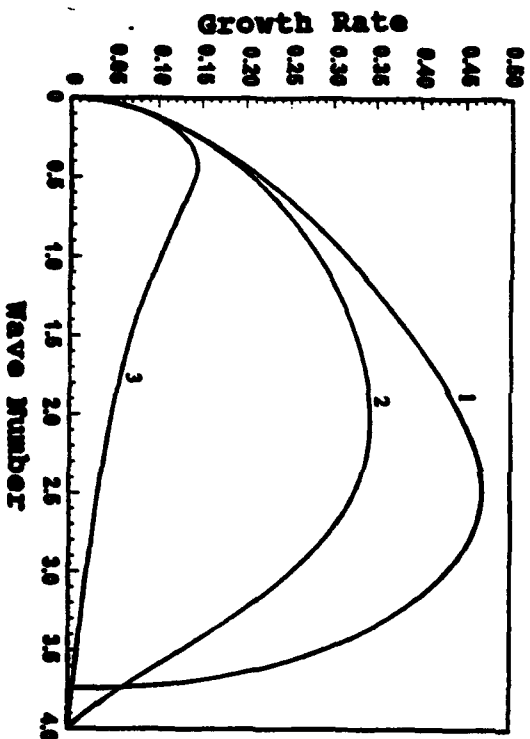
Fig. 3 Effect of liquid viscosity. ρ = 0.1 and We_g = 4.0. Curve 1, Re = ∞, curve 2, Re = 63.25, curve 3, Re = 1.25.
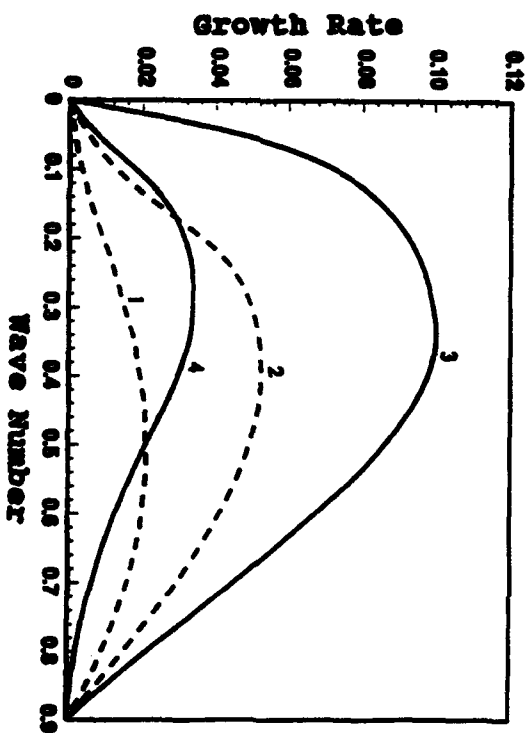
Fig. 4 Effect of density ratio. We_g = 0.9 and Re = 1.0. Curve 1, ρ = 2.0, curve 2, ρ = 1.0, curve 3, ρ = 0.1, curve 4, ρ = 0.01.

115

USE OF MAXIMUM ENTROPY PRINCIPLE AS A GUIDE
IN DESIGN OF SPRAY NOZZLES

Principal Investigator: Richard S. Tankin

Mechanical Engineering Department
McCormick School of Engineering
Northwestern University
Evanston, Illinois 60208

SUMMARY:

An Ektapro motion analyzer was used to measure the size distribution of droplets generated by the disintegration of a cylindrical liquid jet. The liquid jet breakup under consideration contains satellite droplets interspersed among the primary droplets - thus resulting in a bi-modal size distribution. The maximum entropy principle is used to model this phenomenon. Agreement between the model and the measurements is reasonably good.

AUTHORS:

Long P. Chin. Systems Research Laboratories, Inc.; Thomas Jackson, Wright-Patterson Air Force Base; P. C. Hsing and Richard S. Tankin, Northwestern University

TECHNICAL DISCUSSION:

The purpose of the present study is to show that the maximum entropy model is very robust. It has been applied successfully yielding a uniform size distribution and a skewed mono-modal size distribution. In this presentation, it will be shown that it can yield a bi-modal size distribution. The distribution depends on the initial flow conditions and the constraints imposed. A schematic diagram of the apparatus used to study the evolution of the bi-modal droplets is illustrated in Figure 1. A compressed air supply forces the water from a reservoir through a filter to a nozzle assembly. The nozzle assembly, consisting of a sapphire orifice with a 0.08 cm hole, is positioned vertical with the fluid exiting downward. An image analyzer system manufactured by Kodak was arranged to take pictures of the water droplets. The water issues from the nozzle assembly as a liquid column. This liquid column breaks up into droplets about 10cm from the orifice. In the experiment, a total of 1017 primary droplets and 877 satellite droplets were counted and analyzed.

Thus the measured ratio of the number of primary droplets to number of satellite droplets at breakup is 1.16

In Figure 2, are images of the drops - both primary and satellite.There is little problem in determining the diameter of the satellite drops - their shape is nearly spherical and for measurement their size was enlarged and enhance with appropriate software. The size of the drop was estimated by fitting (by eye) a circle to the enlarged and enhanced image. On the other hand, the primary (large) droplets are far from spherical; thus it was necessary to characterize their size with an effective diameter. It was assumed that the droplets were ellipsoidal in shape and by measuring their major and minor axes an area was computed using the software *Image Processing and Analysis, v1.43*. The diameter of a circle with an equivalent area was calculated and its diameter becomes the effective diameter for the droplet. Figure 3 contains a plot of the experimentally determined size distributionThe important point is that the size distribution has two large peaks - one due to the satellite drops and the other due to the primary drops - with essentially no droplet sizes between these peaks.

Detailed formulation and derivation of the maximum entropy principle have been published[1,2]. However, there is one significant modification in the theory. The theory, as presented previously, is based on the assumption that the droplets are spherical. In the present study, there is no major problem with the satellite drops - in most instances they are nearly spherical; however the primary (large) drops are far from spherical. To account for this non-spherical shape, two new constraints were introduced that are related to mean surface to volume ratio. One constraint is proportional to $\overline{D}$ and the other is inversely proportional $\overline{D}$.

Once the source terms are estimated, the distribution for droplet size is obtained from the following equation:

$$\frac{dN}{d\overline{D}} = \frac{3}{2}(\frac{\pi\overline{D}}{\alpha_3})^{\frac{1}{2}}[\ erf(X_{max}) - erf(X_{min})] \times exp[\ -\alpha_0 - (\alpha_1\frac{\alpha_2^2}{4\alpha_3})\overline{D}^3 - \alpha_4 B\overline{D}^2 - \alpha_5\overline{D} - \alpha_6\overline{D}^{-1}]$$

where erf(X) is the error function of X :

$$X_{max} = (\overline{U}_{max} + \alpha_2/2\alpha_3)(\alpha_3\overline{D}^3)^{\frac{1}{2}}\ ,$$

$$X_{min} = (\overline{U}_{min} + \alpha_2/2\alpha_3)(\alpha_3\overline{D}^3)^{\frac{1}{2}}\ .$$

This equation is plotted in Figure 3. One can see there is reasonably good agreement between the experimental size distribution and the computed size distribution. Also shown in Figure 3 is the size distribution (with the same source terms) but with assumption that the droplets are spherical. As one can see this plot is not bi-modal and disagrees with the experimental data.

REFERENCES

[1]X. Li, L. P. Chin, R. S. Tankin, T.Jackson, J. Stutrud, and G. Switzer, _Comparison Between Experiments and Predictions Based on Maximum Entropy for Sprays from a Pressure Atomizer_, Combustion and Flame, 86, (1990).

[2] L. P. Chin, P. G. LaRose, R. S. Tankin, T. Jackson, J. Stutrud, and G. Switzer, _Droplet Distributions from the Breakup of a Cylindrical Liquid Jet_, Phys. Fluids A 3 (8) (1991).

1. Pressure source
2. Pressurized water tank
3. Water filter
4. Pressure nozzle
5. Synchronized strobe
6. Convex lens
7. Microscope
8. High speed camera
9. Monitor
10.Kodak image processor
11.Synchronous cable
12. Micromanipulator
13.Water droplet collector
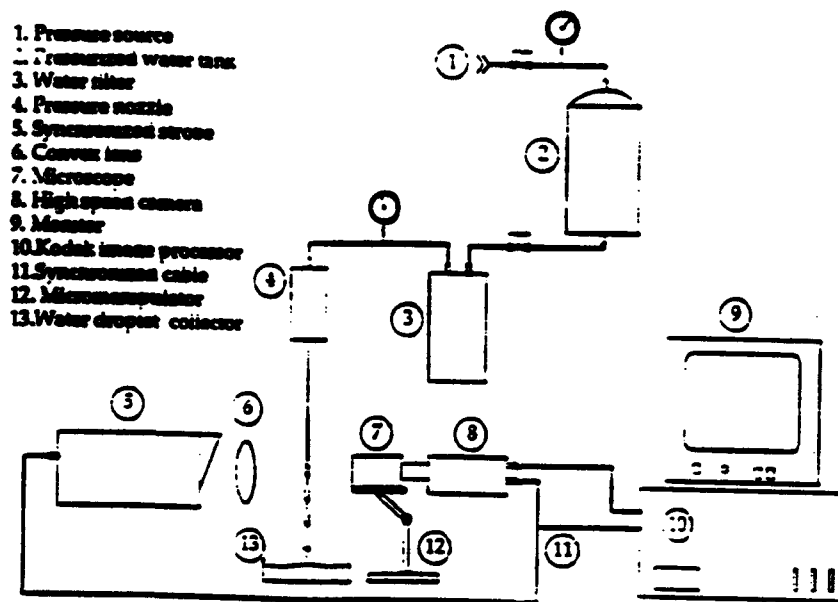
Figure 1. Schematic drawing of the droplet generator setup.
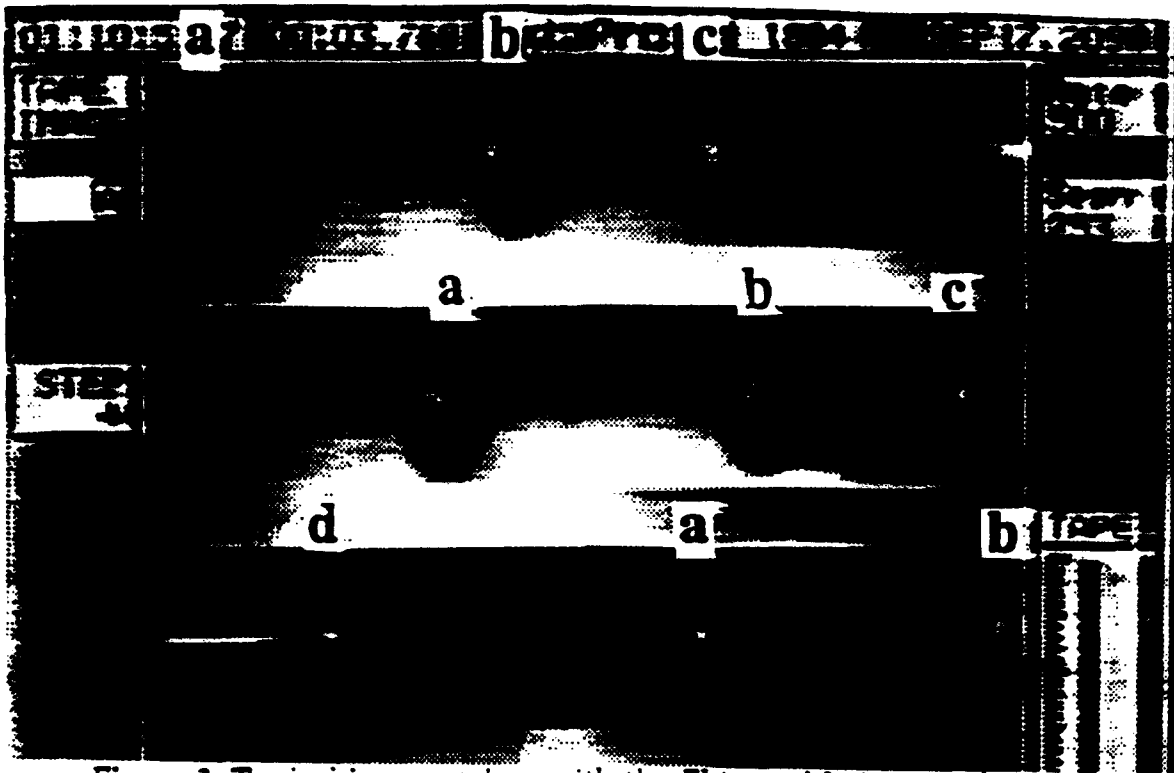
Figure 2. Typical images taken with the Ektapro Motion Analyzer.
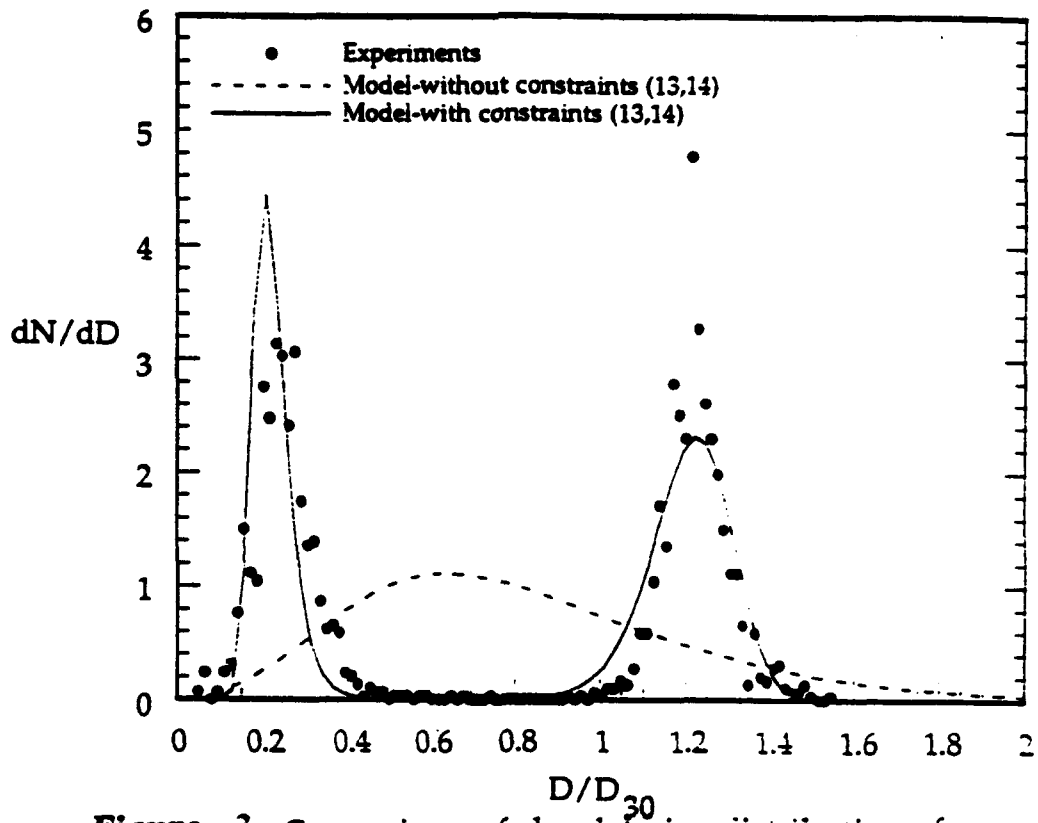
Figure 3. Comparison of droplet size distributions from a cylindrical liquid jet having satellite droplets

FUELS COMBUSTION RESEARCH

AFOSR Task 2308 S7

Principal Investigators: T. A. Jackson and W. M. Roquemore

USAF Wright Laboratory
WL/POSF Bldg 490
1790 Loop Rd N
Wright-Patterson AFB OH 45433-7103

SUMMARY/OVERVIEW:

The focus of this research task is to develop and assimilate the necessary fundamental understanding of fuel injection and fuel-air mixing processes to advance the technology of gas turbine combustion. Research on fuel injection has included studies of isolated and interacting droplets, the atomization process itself, and non-intrusive measurements of dense, reacting sprays. Research on fuel-air mixing has included buoyancy-driven, gaseous-fueled flames and swirl-driven, turbulent, liquid-fueled flames. The impact of turbulence on reaction processes is of primary consideration. The specific direction of research in both general areas is set by a continuous dialogue with the gas turbine community on pressing issues such as flame stability, emissions control, and efficient, high temperature rise combustion; these "application" problems expose the lack of fundamental understanding of key mixing and kinetic phenomena. This abstract addresses only the spray research portion of the task.

TECHNICAL DISCUSSION:

Advances have been made over the last year in three areas of spray research within this task. These have included studying the evaporation of interacting, single droplets, enhancing the energy of atomization through the use of acoustic stimulation, and completing the full formulation of an atomization modeling approach.

Experiments were conducted on an array of droplets emitted by a customized, acoustically-driven droplet generator to observe the evaporation of individual droplets as a function of their relative position in the array. Droplets were either ethanol or ethanol/acetone blends. Small changes in droplet size were identified by measuring the spherical morphology (morphology-dependent resonances) of each drop. Droplet evaporation rates varied according to the extent to which the droplet is surrounded by other droplets (Figure 1). Those at the very center of the array evaporated slower than those along an edge, which evaporated slower than those along the corners of the array.[1] This study complements previous single droplet studies under this task which looked at intradroplet heat and mass transport and droplet-vortex interaction. Collectively the work supports subgrid-scale modeling efforts such as those of Bellan et al.[2]

Research has continued into techniques to enhance the atomization of a fluid column beyond conventional fluid pressure and air acceleration approaches. Acoustic drivers have been applied to conventional atomizers[3] in an attempt to utilize technology developed by Fluid Jet Associates in the area of acoustically driven liquid breakup. Photographs of undriven and driven atomizer behavior are illustrated in Figure 2.

The full Maximum Entropy model for predicting the resultant spray from an atomization process has been formulated.[4] This formulation is three-dimensional and includes source terms for liquid-gas heat transfer as well as for mass and momentum transfer and liquid sheet-droplet surface

energy exchange. Our original expectation of this approach as a predictive/design tool for liquid fuel injection has been modified. The behavior of the model is very sensitive to source term specification. In practice this would necessitate a large amount of measurements of the gas phase surrounding the spray as it develops. Such effort could as easily be applied to the spray itself, partially negating the value of the prediction. An alternative application is the prediction of variations in an atomization process from some well established, nominal performance. The utility of such a model would be a predictive capability for assessing nozzle performance variations due to manufacturing processes or variations in wear patterns. It is the prospect of such applications that have redirected our research on the Maximum Entropy model towards modeling well documented and classic spray problems. This has recently begun.

1. "Local Environment Effects on Evaporation Rates of Flowing Droplets," by J. Christian Swindal, Final Report for Graduate Student Research Program, Air Force Wright Laboratory, Sep 1993.

2. "The Behavior of Polydisperse Dense and Dilute Collection of Droplets in Vortical Flows," by J. Bellan, Final Report for Air Force Wright Laboratory, Jan 1994.

3. "Characteristics of a Velocity-Modulated Pressure-Swirl Atomizing Spray Measured by the Phase-Doppler Method," by F. Takahashi, W.J. Schmoll, and J.L. Dressler, AIAA 94-0558, 32nd Aerospace Sciences Meeting, Jan 1994.

4. "Maximum Entropy Formulation of Joint Droplet Distributions in Sprays," by L.P. Chin, R.S. Tankin, T.A. Jackson, J.S. Stutrud, and G.L. Switzer, to be submitted for publication.
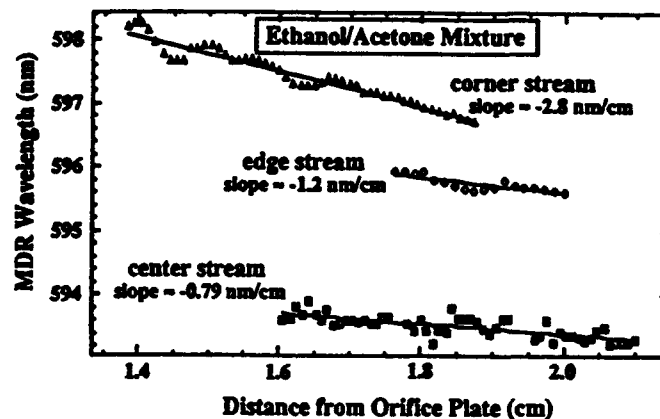
Figure 1. Droplet size as a function of distance from injector and relative position in a rectangular array of droplets (reproduced from Ref 1, Figure 9)
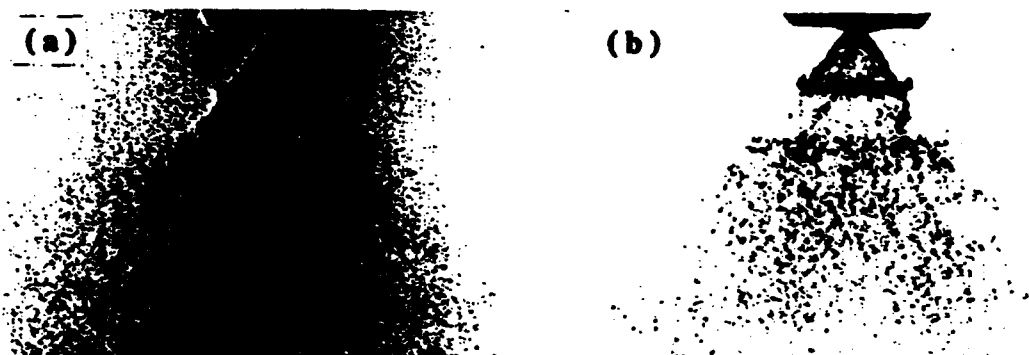
Figure 2. Delevan Pressure Atomizer, (a) undriven, and (b) driven at f=5kHz, 800V$_{p-p}$ (reproduced from Ref 3, Figure 3)

FLUORESCENT DIAGNOSTICS AND FUNDAMENTAL DROPLET PROCESSES

Principal Investigator: Lynn A. Melton
Co-Principal Investigator: Michael Winter*

Department of Chemistry
University of Texas at Dallas
Richardson, TX 75083-0688

SUMMARY/OVERVIEW:

This talk will focus on the extension of Droplet Slicing Imaging (DSI) measurements to systems in which simultaneous Planar Laser Induced Fluorescence (PLIF) measurements are carried out in a droplet and in the surrounding gas phase flow field. As a result of such experiments, a new method for imaging the flowfields within droplets, called "layered droplets" has been developed. In these experiments, acetone, which is used for PLIF imaging of the gas phase flow field, condenses on the surface of the hydrocarbon droplet and can also be used to image liquid phase streamlines originating at the surface of the droplet.

New developments in exciplex fluorescence thermometry, including methods for use of PYPYP [bis-1,3-(1-pyrenyl)-propane] which make possible its use as a thermometer in combusting systems, will also be discussed.

TECHNICAL DISCUSSION:

"Layered Droplets" (UTRC)

Acetone has proved to be a useful fluorescent dopant for combustion studies.[1] It is volatile, and its fluorescence quantum yield is independent of the oxygen concentration. At UTRC, DSI measurements on decane droplets generated with an aerodynamic droplet generator[2] have used acetone seeded into the coflow to provide visualization of the flow patterns in the gas phase surrounding a falling droplet. Figure 1 shows results obtained in such experiments.

In an aerodynamic droplet generator the droplet liquid is suspended on the end of a hypodermic needle which is located in the throat of a gas nozzle. The surrounding gas flow strips off the liquid and forms a droplet.

When the acetone partial pressure in the gas flow of the aerodynamic droplet generator is sufficiently high, a portion of the acetone seeded into the gas continuously condenses on the surface of the decane droplet and forms a "layered droplet" in which

---

*United Technologies Research Center, East Hartford, CT 06108

the liquid phase acetone also fluoresces. Controlling acetone partial pressure and the droplet fall speed (residence time in the jet) directly controls the thickness of the acetone layer deposited on the droplet.

The "layered droplets" have distinct advantages over the naphthalene seeded droplets which have been used in previous DSI experiments.[3] In both cases, surface liquid is carried in to the interior of the droplet as a result of internal circulation. The naphthalene seeded droplets rely on the quenching of fluorescence by oxygen (streamlines by oxygen quenching, SOQ) and result in a decreased fluorescence which much be measured against a light background. In the "layered droplet" experiments, the decane droplet does not fluoresce, and the condensing acetone results in a bright streamline against a dark background. The liquid phase diffusion coefficient of acetone is smaller than that of oxygen, and hence, diffusion within the liquid is lessened. As a result, in contrast with the naphthalene based SOQ experiments, the "layered droplet" technique yields stronger fluorescence signals, enhanced image contrast and dynamic range, and more sharply defined streamlines. These "layered droplets" can provide new insights into the fundamental mechanisms of droplet heating, evaporation, and combustion. Figure 2 shows a PLIF/DSI image of a "layered droplet".

In the naphthalene based DSI/SOQ experiments, the naphthalene concentration is carefully chosen so that the absorbance of a laser ray along the droplet diameter is approximately 1. This provides reasonable illumination over the entire droplet. The optimum concentration of naphthalene is, however, dependent on the droplet size. This constraint does not apply to "layered droplets", since in those droplets the streamline appears bright against a dark background.

Extensions of Exciplex Fluorescence Thermometry (UTD) PYPYP has already found use in exciplex fluorescence thermometry measurements of falling droplets.[4] However its utility in combustion applications has been limited by its sensitivity to oxygen quenching: the ratio of the exciplex intensity to the monomer intensity is affected both by temperature (good) and oxygen (bad). A modified use of PYPYP, in which the temperature-dependent shift of the exciplex band (to higher energies as the temperature increases) is used as the basis for an exciplex shift thermometer (EST), is under investigation. Preliminary studies show that, even though the total intensity in the exciplex band decreases as the oxygen concentration increases, the band shape does not change. As a result, it appears that EST systems can be developed for use with oxygen partial pressures of at least one atmosphere air and perhaps higher.

Figure 3 shows fluorescence spectra of PYPYP in decane as a function of temperature. The blue shift of the exciplex band is apparent. Figure 4 shows calibration curves obtained for three cases; (1) nitrogen purged solutions, (2) air purged solutions, and (3) oxygen purged solutions. The near linearity of these calibration curves meets the criterion described in earlier analyses of potential systematic errors in EFT measurements of transient droplet temperatures,[5] and consequently, use of EST systems instead of EFT systems should result in accurate "volume averaged" droplet temperatures. The curve for the air purged solutions is sufficiently close to that for the nitrogen purged solutions that the effect of variable oxygen concentration within the droplet may be neglected. The EST systems are not as sensitive as the previous EFT systems, and it is estimated that the EST

temperatures will be determined within +/- 10°C instead of the +/- 3°C obtained with EFT.

Further work is underway in the analysis of EST data to determine whether there are appropriate wavelength regions for which the intensity ratios will be oxygen independent.

In an example of "dual use technology", the PYPYP EST systems have already been used in a project funded by Ford Motor Company. Two dimensional temperature images of a hydrocarbon liquid which had been sprayed onto a hot steel plate were obtained as a function of time, and the evaporation of the residual liquid was followed.

REFERENCES

1. A. Lozano, B. Yip, and R. K. Hanson, "Acetone: a tracer for concentration measurements in gaseous flows by planar laser-induced fluorescence", Experiments in Fluids, 13, 369 (1992).

2. G. J. Green, F. Takahashi, D. E. Walsh, and F. L. Dryer, "Aerodynamic Device for Generating Mono-Disperse Droplets", Rev. Sci. Instrum., 60, xx (1989).

3. M. Winter and L. A. Melton, "Measurement of Internal Circulation in Droplets", Appl. Opt., 29, 4574 (1990).

4. T. R. Hanlon and L. A. Melton, "Exciplex Fluorescence Thermometry of Falling Hexadecane Droplets", Trans ASME, J. Heat Transfer, 114, 450 (1992).

5. J. Zhang and L. A. Melton, "Potential Systematic Errors in Droplet Temperatures Obtained by Fluorescence Methods", Trans ASME, J. Heat Transfer, 115, 325 (1993).
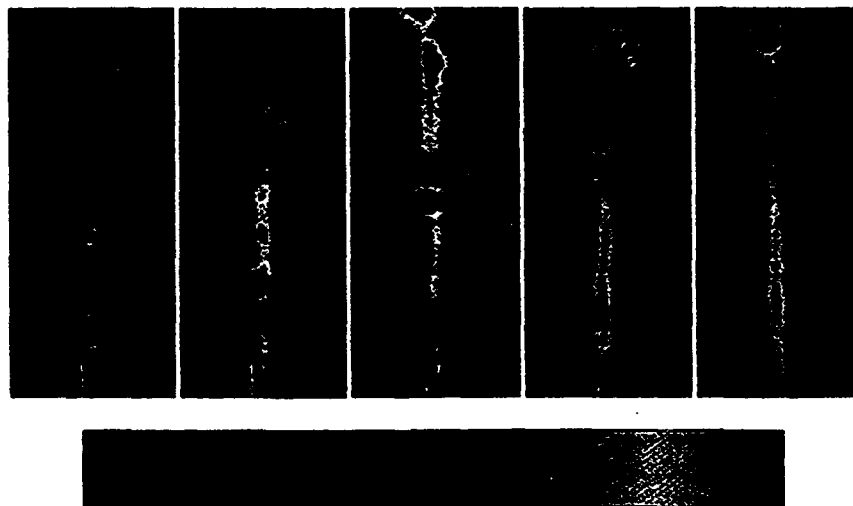
Figure 1. Laser-induced fluorescence from both the gas and liquid phases. Each image was recorded after an increasing time delay after the droplet passed a fixed point in the laboratory frame of reference.
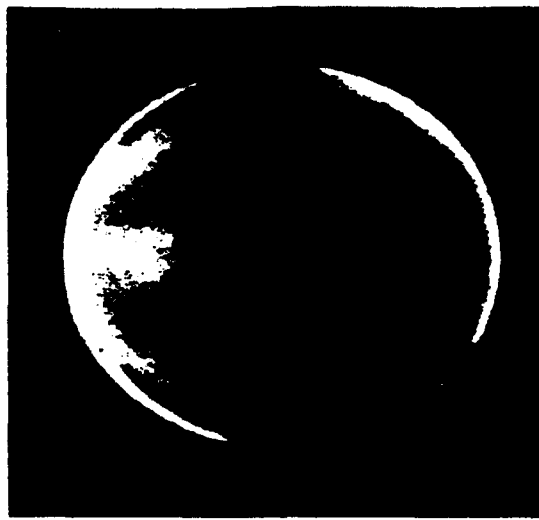
Figure 2. Internal structure of a bicomponent layered droplet using droplet slicing techniques.
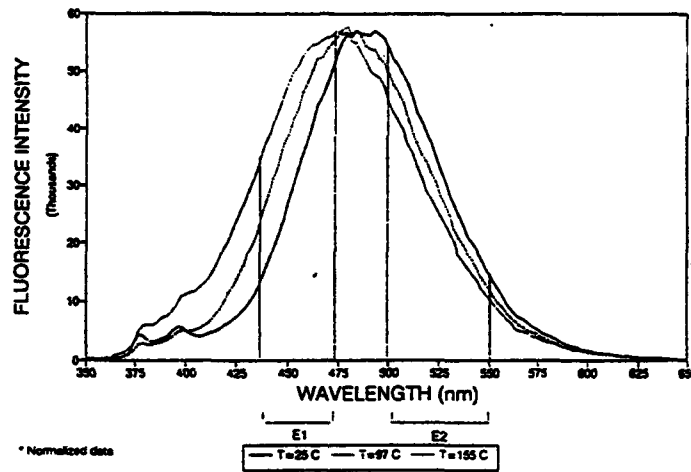
Figure 3. Fluorescence spectra at different temperatures (2E-5M PYPYP/decane).
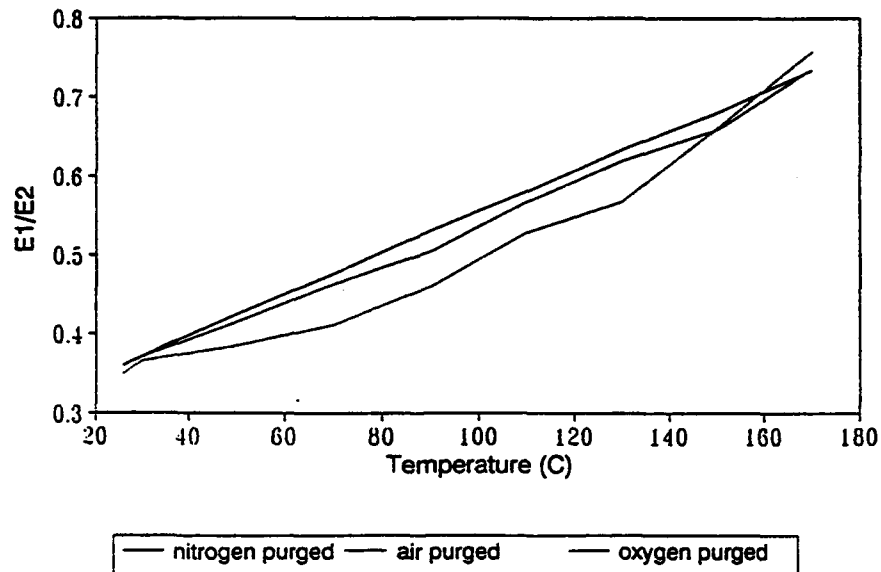
Figure 4. Fluorescent spectra at different temps. (PYPYD in Decane).

125

BREAKUP AND TURBULENCE GENERATION IN DENSE SPRAYS

Principal Investigator: G. M. Faeth
Department of Aerospace Engineering
3000 FXB Building
The University of Michigan
Ann Arbor, Michigan 48109-2118

SUMMARY/OVERVIEW:

Secondary drop breakup and turbulence generation by drops are being studied. Work on secondary drop breakup has yielded information about the regimes, the dynamics, and the outcomes, of drop deformation and breakup. Results for both shock-wave (step) and steady disturbances have been found using pulsed holography and photography for both shock tubes and drop towers. The results have yielded new understanding about drop behavior at conditions encountered during practical combustion processes at high pressures. Current work is emphasizing effects of phase density ratios that are crucial for understanding, and simulating, the properties of sprays at high pressures.

Work on turbulence generation has shown that drop-generated turbulence differs from conventional turbulence, and suggests that the properties of this flow involve a stochastic combination of randomly-arriving drop (particle) wakes. Present studies show that wake properties for these conditions exhibit a new laminar-like turbulent wake behavior, even when drop Reynolds numbers are small, as well as a new fast-decay region as wake mean velocities approach ambient velocity fluctuations. Current work involves utilizing this information to interpret the properties of drop (particle)-generated turbulence and its interactions with conventionally-generated turbulence.

TECHNICAL DISCUSSION

Introduction. Past work on the structure of dense sprays has highlighted the importance of secondary drop breakup and turbulence generation by drops (Faeth, 1990; Ruff et al., 1989, 1991, 1992, 1994; Tseng et al., 1992a, b, 1994; P-K. Wu and Faeth, 1993; Wu et al., 1991, 1992, 1994). Work under the present investigation is studying these processes as discussed in the following.

Secondary Drop Breakup. Studies of liquid atomization have shown that drops produced by primary breakup generally are unstable to secondary breakup (Ruff et al., 1989, 1991, 1992, 1994; P.-K. Wu and Faeth, 1993; Wu et al., 1991, 1992, 1994). Thus, secondary breakup is being studied during this phase of the investigation, see Hsiang and Faeth (1992, 1993, 1994) for findings thus far.

The deformation and secondary breakup of individual drops are being observed within both a shock tube and drop (liquid/gas, liquid/liquid) towers. Flash cinematography and pulsed holography are used to observe the dynamics and outcomes of breakup, while phenomenological theories are used to interpret the measurements. Various drop generating techniques are used to create drops having a wide range of properties — acoustic levitation, electrostatic selection and vibrating capillary tubes.

Reconsideration of drop deformation and breakup regimes has modified past thinking about drop breakup at high pressures near the thermodynamic critical point. The earliest hypothesis was that drops broke up near the critical point; subsequently, it was thought that high Ohnesorge (Oh) number effects, due to liquid viscosity, prevented drop deformation and breakup near the critical point entirely. Our newest results concerning breakup regimes are illustrated in Fig. 1. In this case, phenomenological theory suggests that breakup Weber numbers (We) become proportional to Oh at large Oh; thus, deformation and breakup are only inhibited at large Oh conditions, not eliminated!

A second important flow regime finding has involved the transition between dome-shaped (flat at forward stagnation point) and bowl-shaped (flat at rear stagnation point) drops. This transition is important because it fixes the transition between bag and shear breakup, which involve dome-and bowl-shaped drops, respectively. These results are illustrated in Fig. 2 where measurements for drops in both liquids and gases are summarized. In agreement with phenomenological theory, the transition We is proportional to the square root of the Reynolds number, Re. This finding is very important because it implies that the bag breakup regime becomes larger as liquid/gas density ratios approach unity, which is representative of high-pressure combustion conditions. Subsequent work will seek to confirm this behavior, as well as develop methodology needed to treat breakup as a rate process at high pressure conditions.

Hsiang and Faeth (1992, 1993, 1994) should be consulted for other findings about drop deformation and breakup during the present study. Current work is emphasizing effects of liquid/gas density ratio on these properties.

Turbulence Generation. Turbulence generation by drops controls turbulence properties within dense sprays (Faeth, 1990; Ruff et al., 1989, 1991, 1992, 1994). Drop-generated turbulence differs from conventional turbulence; however, stochastic analysis based on the random arrival of drop wakes appears to be promising for describing this flow (Parthasarathy and Faeth, 1990; Mizukami et al., 1992). This approach requires information about drop wakes at intermediate Reynolds numbers in both nonturbulent and turbulent environments, which has been the focus of current work as described by J.-S. Wu and Faeth (1993, 1994a, b).

Wakes in nonturbulent environments exhibit classical turbulent and laminar wake regions (J.-S. Wu and Faeth, 1993). In contrast, wakes in turbulent environments only exhibit a laminar-like turbulent wake region that has not been observed before (J.-S. Wu and Faeth, 1994a, b). Distributions of mean streamwise velocities, $\bar{u}$, are plotted in Fig. 3 as a function of similarity variables for laminar wakes but with an enhanced effective viscosity, v_t, due to the presence of turbulence (see J.-S. Wu and Faeth (1994a, b) for other notation). It is evident that the wakes exhibit laminar-like scaling.

The key factor for laminar-like turbulent wake behavior involves the behavior of v_t. Figure 4 is an illustration of v_t normalized by the molecular viscosity, v, plotted as a function of the sphere Reynolds number, Re, with turbulence intensity as a parameter. Values of v_t/v are independent of position in the wake but increase with increasing Re. Additionally, v_t/v exhibits low and high Re regimes at lower ambient turbulence intensities, with transition between these regimes for Re in the range 300-600. This transition is related to the onset of vortex shedding from the spheres, which begins at a Re of roughly 300, while phenmemalogical analysis appears to explain the other features of v_t, see J.-S. Wu and G. M. Faeth (1994b).

Current work is emphasizing the application of sphere wake properties to the measurements of effects of turbulence generation by Parthasarathy et al. (1990) and Mizukami et al., (1992).

REFERENCES

Faeth, G.M. (1990) Twenty-Third Symposium (International) on Combustion, The Combustion Institute, Pittsburgh, 1315-1352.

Hsiang, L.-P. and Faeth, G.M. (1992) Int. J. Multiphase Flow, 18, 635-652.

Hsiang, L.-P. and Faeth, G.M. (1993) Int. J. Multiphase Flow, 19, 721-735.

Hsiang, L.-P. and Faeth, G.M. (1994) Int. J. Multiphase Flow, submitted.

Mizukami, M., Parthasarathy, R.N. and Faeth, G.M. (1992) Int. J. Multiphase Flow, 18, 397-412.

Parthasarathy, R.N. and Faeth, G.M. (1990) J. Fluid Mech., 220, 485-537.

Ruff, G.A., Sagar, A.D. and Faeth, G.M. (1989) AIAA J., 27, 901-908.

Ruff, G.A., Bernal, L.P. and Faeth, G.M. (1991) J. Prop. Power, 7, 221-230.

Ruff, G.A., Wu, P.-K., Bernal, L.P. and Faeth, G.M. 1992) J. Prop. Power, 8, 280-289.

Ruff, G.A. and Faeth, G.M. (1994) Prog. Astro. Aero., invited.

Tseng, L.-K., Ruff, G.A. and Faeth, G.M. (1992a) AIAA J., 30, 1537-1544.

Tseng, L.-K., Wu, P.-K., and Faeth, G.M. (1992b) J. Prop. Power, 8, 1157-`66.

Tseng, L.-K., Ruff, G.A., Wu, P.-K. and Faeth, G.M. (1994) Prog. Astro Aero, invited.

Wu, J.-S. and Faeth, G.M. (1993) AIAA J., 31, 1448-1455.

Wu, J.-S. and Faeth, G.M. (1994a) AIAA J., 32, 535-541.

Wu, J.-S. and Faeth, G.M. (1994b) AIAA J., submitted.

Wu, P.-K. and Faeth, G.M. (1993) Atom. Sprays, 3, 265-289.

Wu, P.-K., Ruff, G.A. and Faeth, G.M. (1991) Atom. Sprays, 1, 421-440.

Wu, P.-K., Tseng, L.-K. and Faeth, G.M. (1992) Atom. Sprays, 2, 295-317.

Wu, P.-K., Miranda, R.F. and Faeth, G.M. (1994) Atom. Sprays, submitted.
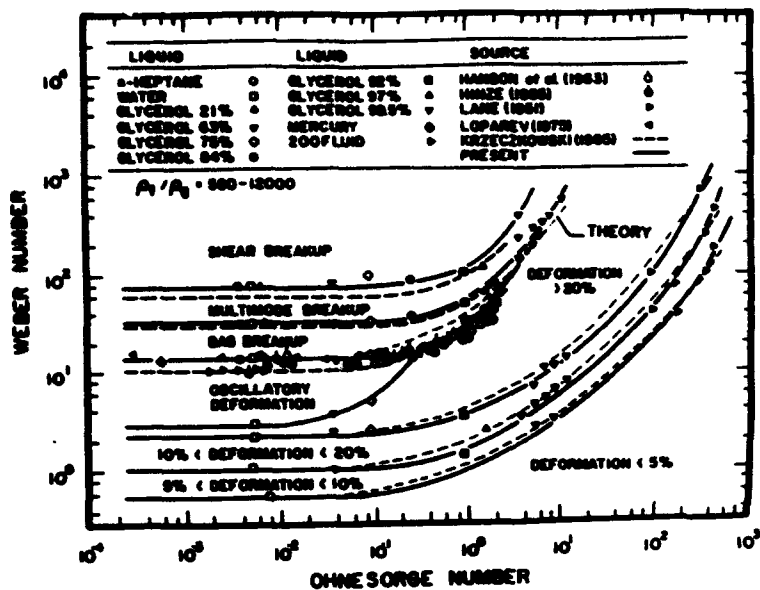
Fig. 1 Drop deformation and breakup regimes for shock-wave disturbances.
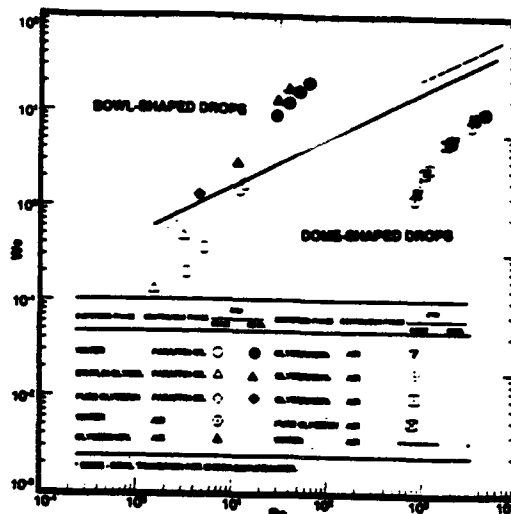
Fig. 2 Dome-and bowl-shaped drop transition.
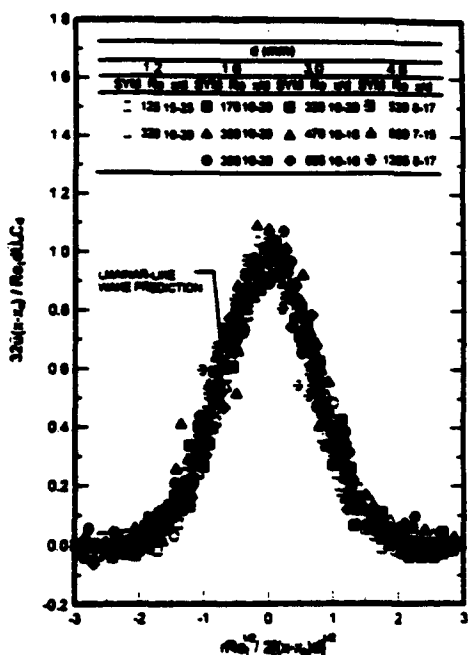
Fig. 3 Radial profiles of mean streamwise velocities in laminar-like turbulent wakes for an ambient turbulence intensity of 9.5%.
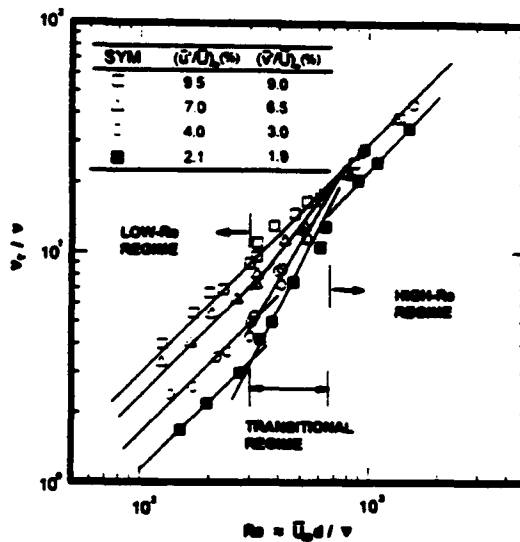
Fig. 4 Effective turbulent viscosities in laminar-like turbulent wakes at various sphere Reynolds numbers and ambient turbulence intensities.

129

Application of Parallel Processing to the Investigation of Supercritical Droplet Evaporation and Combustion Using Molecular Dynamics

M. M. Micci and L. N. Long

Dept. of Aerospace Engineering
The Pennsylvania State University
University Park, PA 16802

SUMMARY/OVERVIEW:

Supercritical droplet evaporation (and eventually combustion) is being modeled using molecular dynamics. The use of molecular dynamics reduces the required material properties to only the two Lennard-Jones interaction parameters, ϵ and σ, and reproduces both liquid and gas phases seamlessly without the need for an interface model. In order to handle the numerically intensive computations, algorithms for implementation on current and future massively parallel processors are being developed. Algorithms have been written using both a data parallel approach and a message passing approach. Results have been obtained to date for an argon droplet coexisting in equilibrium with its vapor at subcritical conditions.

TECHNICAL DISCUSSION:

Supercritical droplet evaporation and combustion is one of the least understood processes occurring in current and future aerospace propulsion systems. It occurs in current cryogenic rocket motor chambers when oxygen is injected (in the liquid state at supercritical pressure) into a combusting environment which is above its critical temperature while the injected hydrogen gas is already above its critical pressure and temperature. Supercritical droplet evaporation and combustion will also be present in future high speed airbreathing propulsion systems where the fuel, either hydrocarbon based or liquid hydrogen, will be used for cooling the engine and airframe and will thus be preheated above its critical temperature before injection into the combustion chamber.

Above the critical pressure and temperature, the distinction between liquid and gas phases breaks down as their densities become equivalent and dramatic changes in material properties occur, for example the liquid surface tension and heat of vaporization go to zero and the viscosity decreases significantly while the gas solubility into the liquid phase increases. The droplet lifetime no longer follows the d^2 law and analysis of the process by standard methods (i.e., solution of the conservation equations) is difficult due to the highly transient nature of the problem and the need for submodels to obtain the gas and liquid thermodynamic and transport properties. At the same time, knowledge of the droplet lifetimes is essential for the prediction of combustor performance and stability.

The authors have begun modelling these problems using molecular dynamics (MD), which is the field of science concerned with the motions of individual atoms or molecules. The forces between individual particles are modeled based on quantum mechanical or experimental results and used in Newton's Law ($F = ma$) to solve for a variety of thermodynamic or transport properties such as the virial coefficients in the high pressure equation of state or the

coefficients of viscosity, thermal conductivity or diffusion. Indeed, one of the more common applications of molecular dynamics is to solve for such properties near or beyond the critical point where experimental measurements are difficult if not impossible. Because such properties are not dependent on the size of the system being studied, the extremely small systems composed of the few thousand atoms or molecules which could be computationally handled were adequate and there was no motivation to go to larger systems.

Molecular dynamics (MD) analyzes the motions of atoms or molecules which are the result of forces between the same atoms or molecules. Several mathematical representations of the force have been used in the search for increasing accuracy, including the rigid impenetrable sphere, the square-well potential, and the point center of repulsion potential. The most commonly used potential is the Lennard-Jones 12-6 potential

$$\phi(r) = 4\epsilon \left[(\sigma/r)^{12} - (\sigma/r)^6\right]$$

where σ is the zero energy separation distance and ϵ is the minimum energy. The sixth-power term is attractive out to long ranges and can be derived from quantum mechanics where it is referred to as the induced-dipole-induced-dipole interaction. The twelfth-power term is repulsive and acts primarily at short ranges. There is no rigorous derivation of the value of twelve other than that it appears to accurately model the repulsive force when compared to experiments and is been accepted as a standard world wide to facilitate communication and comparison of results. Since the assumed potential seeks to represent all the forces acting on an atom or molecule, there is no need for additional models and the above potentials are valid with constant values of σ and ϵ as one moves from the solid to the liquid to the gas phase.

The intermolecular force is derived from the spatial gradient of the potential. Newton's Laws are then solved for each particle, either deterministically by finite differencing $F = ma$ or stochastically by a Monte Carlo method. Molecular dynamics refers to the deterministic approach and is the most commonly used method to date for determining fluid static and dynamic properties. The properties which can be determined from molecular dynamics include the entropy, specific heats and coefficients of viscosity and thermal and mass diffusion. Two-phase behavior such as droplet formation and evaporation has been simulated. The system of equations can be easily programmed to run on parallel machines by assigning one (virtual) processor to each particle.

The above potentials all assume a spherically symmetric molecule (nonpolar). For nonsymmetric (polar) molecules an angular dependence can be given to the potential by using multiple site Lennard-Jones potentials and Newton's Law for rotational motion is solved simultaneously with that for translational motion. Flexible molecules can also be handled by adding additional degrees of freedom.

In the past, supercomputers were able to simulate systems with tens of thousands of particles. Today, with advanced massively parallel computers, it is possible to model millions of particles[1]. The 1024-processor CM-5 at Los Alamos National Lab has a peak speed of 128 gigaflops (61 gigaflops have been sustained[2]) and has 32 gigabytes of main memory. This

[1]Lomdahl, P.S., Tamayo, P., Greebech-Jenson, N., and Beazley, D.M.; "45 Gflops Molecular Dynamics on the Connection Machine 5," IEEE Supercomp. '93 Conf., Nov. 1993.

[2]Long, L. N. and Myczkowski J., "Solving the Boltzmann Equation at 61 Gigaflops on a 1024-node CM-5," IEEE Supercomp. '93 Conf., Nov. 1993.

abstract describes our efforts to use the CM-5 for MD, but in addition we will also describe efforts to use a completely different kind of parallel computer: clustered workstations. The CM-5 is most often programmed as a data parallel computer using Fortran 90, while clustered workstations are most often programmed using Fortran 77 and Parallel Virtual Machine (PVM). These approaches both have advantages and disadvantages for MD problems.

The equations of motion for a system of argon atoms were implemented using the well-known Verlet molecular dynamics algorithm on several massively parallel and vector computers. The Verlet algorithm is simply

$$\vec{x}_{n+1} = 2\vec{x}_n - \vec{x}_{n-1} + \Delta t^2 \vec{a}_n$$

where $\vec{x}$ and $\vec{a}$ are the molecular positions and accelerations, respectively. The n denotes time level. The advantage of this algorithm is that it is second-order accurate while avoiding the need to compute any velocities.

The Lennard-Jones 12-6 potential was used with no cut-off initially, which results in an $O(N^2)$ algorithm where N is the number of particles. While the $O(N^2)$ MD algorithm may be required for some problems, it is not practical for the majority of problems since the computer time quickly becomes excessive. For this reason we have also implemented MD algorithms with a cut-off scheme on the CM-5 and clustered workstations. Since the intermolecular force decays very rapidly with distance, beyond a certain distance we can just neglect their effect. This dramatically reduces the computer time from $O(N^2)$ to $O(N)$, which means for a million particles the cut-off scheme should be roughly a million times faster than the full scheme. For Lennard-Jones interactions, one typically uses between 2.5σ and 5σ for the cut-off distance. Figures 1a and 1b show the initial and equilibrium conditions for a simulation involving 996 argon atoms. The results were obtained using the $O(N)$ scheme on a single RS/6000 workstation. In the figures, all of the particles are argon atoms, but the atoms which begin in the gas phase are lightly colored while those that begin in the liquid droplet are shaded dark. Figure 1b shows the intermixing representative of equilibrium.

On the CM-5 we have implemented a data parallel MD algorithm that relies heavily on sorting and the Fortran-90 command CSHIFT. These two functions have been highly optimized on the CM-5. All of the data associated with the particles (e.g positions, velocities, etc.) are arranged in 1-dimensional arrays, even though we are solving 3-dimensional problems. The physical domain is divided into small 3-dimensional cells, each side of which is length equal to the cut-off distance. To determine which cell a molecule is in, we simply truncate the position vectors (x,y,z) of each particle by converting them from real numbers to integers. These three integers can then be easily combined into a single integer denoting the cell location using:

ICELL = K*XCELLS*YCELLS+J*XCELLS+I.

Once we know which cell each particle is in, we can sort them according to their cell number using the CMF_ORDER routine. A general purpose Fortran-90 send command then arranges all the particles in order of their cell location. All the molecular interactions can be computed by making a duplicate of the sorted arrays and repeatedly using CSHIFT on the duplicated array. After each CSHIFT, interactions are computed. Typically, one must use M CSHIFT's, where M is the maximum number of particles in a cell. This process must be performed not only for all the particles within each cell, but for all the neighboring 26 cells as well.

The above code was run on a 128-node CM-5 using up to 1,000,000 particles. The code requires roughly 59 words of memory per particle and achieved roughly 8% of the peak speed of the CM-5. We were able to sustain 1.8 gigaflops. This program required roughly 27

μseconds per particle per time step.

In addition to implementing a data parallel approach, we have also used a completely different programming paradigm: message passing. This approach uses essentially Fortran-77 with Parallel Virtual Machine (PVM) to send data from processor to processor. This has been implemented on clusters of IBM RS/6000 workstations. Penn State also has a 32-node IBM SP-1 computer, and results from running the program on this machine will be available in the near future.

In this approach we also use the Lennard-Jones model, but physical space is divided into larger subdomains, with the number of subdomains equal to the number of processors. Within each subdomain we have implemented a linked-list MD code with a cut-off. A three-dimensional grid with cell discretization at $O(\sigma)$ is used within each subdomain to establish the linked-list connectivity of the molecules. Imposing the cell structure dramatically reduces the computation of molecular interactions from $O(N^2)$ to $O(N)$. Due to the cell structure, only interactions within a cell and the 26 neighboring cells are required. Thus the calculation of the intermolecular potential is greatly reduced. We can therefore retain the efficiency of the linked-list algorithm and yet explore the power of the domain-decomposition parallelism. In this approach we can obtain the full power of the RISC processor while keeping the network contention low. Essentially this approach can be described as a two-grid-level algorithm with parallelism implemented on the coarse grid level.

During each time step the particles move according to their velocities. These are strictly local computations and require no communication. After the move we determine which particles have left their subdomains. All the particles that leave their domain are sent to a master processor. The master processor sorts all these particles and resends them to the proper processor. The master-slave approach was used to simplify the programming, minimize network contention, and achieve better scaling as processors are added.
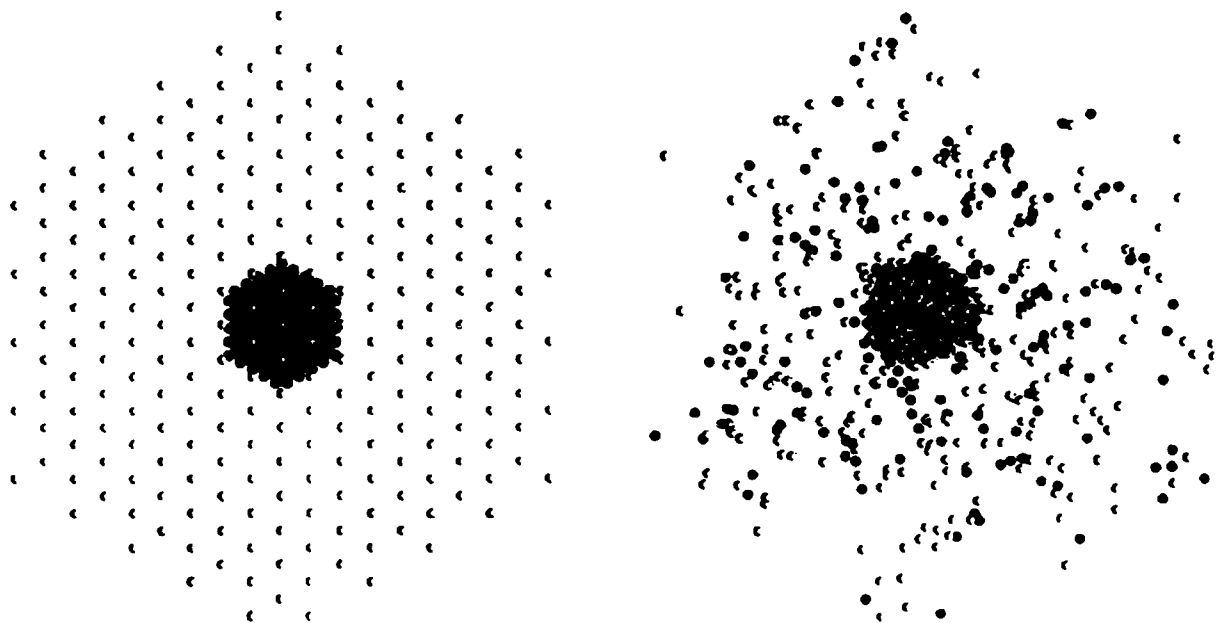
Figure 1a, 1b. Initial conditions and equilibrium (60,000 time steps) for a subcritical argon droplet ($T^* = 0.7$) using periodic boundary conditions.

133

ATOMIZATION OF SUPERCRITICAL FLUIDS IN GASES

AFOSR TASK 2308BW

Wu, P.-K., Chen, T.H. and Nejad, A.S.

Aero Propulsion and Power Directorate
Wright-Patterson AFB, Ohio 45433-7655

SUMMARY

A plan for studying the atomization processes of supercritical fuels injected into a quiescent gas is presented. The goal of this research is to study two processes: a) thermodynamic state transition of supercritical fuel within a nozzle passage; b) mixing processes of supercritical fuel with the surrounding gas. Nozzles of different L/d's will be tested to illustrate thermodynamic state transition and nozzle geometry effects on atomization and mixing. Ethylene and nitrogen are used in the present study to simulate interactions of supercritical fuel and air. Qualitative and quantitative measurements will be made to characterize the flow field. Fuel penetration lengths will be determined by studying shadowgraphs. Spontaneous planar Raman scattering method will be used to measure the ethylene concentration and temperature distributions. The results generated will aid the understand of atomization processes as well as quantify the mixing efficiency of supercritical fuels.

OVERVIEW

For hypersonic flights, e.g. flight Mach number greater than 8, cooling of the airframe becomes an engineering challenge. The use of endothermic fuels has been proposed as a means for regenerative cooling of the airframe components subjected to severe aerodynamic heating. This approach, however, increases the fuel temperature and pressure and usually the fuel is in supercritical state before injection [1]. For example, in a typical scramjet cycle, supercritical fuel is injected into a superheated combustor environment, see Figure 1. To simulate these conditions, an experiment must be devised to allow study of fuel/gas(air) mixing over a wide range of temperatures and pressures.

For supercritical fluids, thermodynamic and transport properties exhibit unusual behavior near the supercritical point, e.g. zero surface tension, liquid-like density, gas-like diffusivities, etc. [1,2,3]. A ρ-P diagram is shown in Figure 2. Near the critical point the gradient of fluid density with respect to temperature and pressure is extremely large. A 10% decrease in the fluid pressure results in a 50% reduction in fluid density, if an isothermal process at the critical temperature and pressure is assumed. These unusual properties will affect atomization and mixing processes. Chen [4] recently studied the atomization processes of supercritical SF_6 injected into quiescent gases and found that the supercritical fluid exhibited an opaque core which persisted for a long distance before disappearing as a result of mixing and/or change of its thermodynamic state. However, the core lengths observed were much smaller than those produced by subcritical liquids injected under the same test conditions. Hermanson et al. [5] studied the supercritical (cryogenic) nitrogen injected into supersonic flow streams and attributed a reduction in penetration height, when compared to subcritical ethanol injection, to a larger degree of superheat. These studies indicate that atomization and mixing processes of supercritical fluids are vastly different from those observed in subcritical conditions. Nevertheless, the results obtained from injection of liquids in a subcritical state can be used as a frame of reference when one studies supercritical fluid injection. Liquid atomization of subcritical liquids has been reviewed and summarized in many recent articles [6,7]. It is generally agreed that liquid atomization is caused by liquid turbulence, liquid

vorticity, liquid cavitation, and aerodynamic forces. Aerodynamic forces can be important at some conditions, however, the dominant factors are related to the flow conditioning at the nozzle exit. Experiments of Ruff et al. [8] and Wu et al. [9] have shown the influence of fluid flow quality and profile at the injector exit on mixing and droplet size distribution immediately downstream of the injector. The present effort will also study the effect of nozzle geometry on atomization and mixing of supercritical fluids over a wide range of operating conditions.

TECHNICAL DISCUSSION
Experimental Approaches

The proposed experimental approach is to inject supercritical fluid vertically downward into a large injection chamber filled with an inert gas. A sketch of the apparatus is shown in Figure 3. The experimental setup consists of a liquid fuel tank, a solenoid valve, a fluid temperature control unit, a nozzle section, and a test chamber. The fuel tank assembly is designed to allow preset operating conditions (mass, pressure, and temperature). A fast-acting solenoid valve with a response time of 30-45 ms will be used to control the injection time period. Injection run times will be limited to few seconds in order to minimize the consumption of supercritical fuel and maximize the number of test runs before reaching a significant fuel vapor partial pressure in the injection chamber.

The supercritical fuel temperature is monitored by using thermocouples and controlled by flowing coolant outside the fuel pipe along the fuel delivery line. The coolant temperature is accurately controlled over the range of 247 to 422 K by using a commercially available heat exchanger device. The liquid pressure and temperature are measured by a piezoelectric pressure transducer and a type K thermocouple respectively at one fuel pipe diameter upstream of the nozzle orifice. The measured pressure and temperature are then used to determine the fluid density with a 32 term modified Benedict-Webb-Rubin (MBWR) equation [3].

Nozzles are limited to 1 mm in diameter at the exit with an aspect ratio of 104:1 to reduce fluid turbulence level and to minimize upstream flow disturbances. The nozzle length to diameter ratio is an important parameter in this study and will involve L/d of 0.5, 4, 50, and 100. In order to prevent cavitation, the entry to all nozzle passages is rounded. Test fluid will be limited to ethylene for two reasons. First, in a real engineering system, thermal cracking and endothermic conversion of hydrocarbon fuels result in production and injection of ethylene. Second, the critical temperature of ethylene is close to the ambient room temperature which reduces system safety requirements. To simulate the scamjet combustor operating conditions, a large high temperature/high pressure optical injection chamber, 420 mm in diameter and 940 mm in height, has been designed. The gas pressures and temperatures can be varied over a wide range, up to 7500 kPa at 811 K.

Qualitative and quantitative optical measurements will include high-speed photography, back-lighted shadowgraphy and spontaneous planar Raman scattering method. Photography will be used for flow visualization to identify the thermodynamic phase (i.e. gas/liquid) of the supercritical fluid immediately downstream of the injector nozzle. Shadowgraphy will be used to measure the mean length of the opaque fluid core, while the spontaneous planar Raman scattering method will be used to estimate concentration and temperature distributions. The 532 nm line of a Nd:Yag laser operating at 400 mJ will be used for all these measurements. For the planar Raman scattering method, the laser beam will be expanded into a thin sheet and the 3020 cm^{-1} shift of ethylene and the 2331 cm^{-1} shift of nitrogen will be employed to provide the total number density at each location [10]. Knowing the total number density and total pressure inside the test chamber, concentration and temperature distributions can easily be obtained.

Study Plan

The present study is designed to address two critical issues involved with injection and atomization of supercritical fuels: a) the effects of thermodynamic state transition inside the injector passage and its influence on the ensuing flow field; b) the observation of the mixing and entrainment processes pertaining to injection of supercritical fluids immediately downstream of the injector.

Thermodynamic State Transition:

The understanding of the thermodynamic state variation within the nozzle passage is crucial because it determines the initial conditions for fuel/gas mixing. It is well known that different injector geometries result in different atomization phenomena for subcritical liquids since the liquid flow properties at the nozzle exit dominate the atomization processes. For atomization of supercritical fluids, the situation becomes more complicated due to the possibility of a thermodynamic state transition/change caused by the pressure drop within the injector nozzle. Nozzles of different L/d's are to be used to illustrate the geometry effects. The flow residence time in short L/d nozzles is insignificant and no thermodynamic transition will be assumed. Therefore, to identify the fluid conditions at the nozzle exit, the flow can be approximated with a frozen flow model and treated as an incompressible fluid. Nozzles with longer L/d have a longer passage and therefore a longer flow residence time for the same mass flow rate. For these studies the thermodynamic properties of the supercritical fluid can drastically change as it passes through the injector nozzle. If the fluid residence time within the nozzle passage is large, one can assume that the fluid reaches a thermodynamic equilibrium. Then the isentropic flow relations can be used to determine the fluid properties at the nozzle exit. The validity of the above two assumptions will be tested against the experimental observations. Note that the measurements and flow visualizations will allow us to determine whether the fluid is in supercritical state or in a gas phase just outside of the injector nozzle.

Mixing Processes:

For liquid atomization, the intact core length is an important parameter for both fundamental studies and practical applications. The opaque core length of the supercritical jet will be measured to provide penetration and mixing information. The results from different nozzles are also to be compared to illustrate the nozzle geometry effects.

Another objective of this study is to quantify the mixing process by measuring concentration and temperature distributions. Injection of supercritical fluids is a process that falls between injections of incompressible liquids and compressible gases. The concentration and temperature distributions within the fuel plume will be valuable for the validations of future computational simulations. It is also important to quantify and differentiate the mixing processes of subcritical and supercritical fluids to provide much needed engineering guideline for the design of advanced combustors. Test conditions of the present study are summarized in Table 1.

REFERENCES

1. Edwards, T., "USAF Supercritical Hydrocarbon Fuels Interests," AIAA 93-0807, 1993.
2. McHugh, M. and Krokonis, V., *Supercritical Fluid Extraction: Principle and Practice*, Butterworths Publ., 1-5, 1993.
3. Holland, P.M., Eaton, B.E., and Hanley, H.J.M., "A Correlation of the Viscosity and Thermal Conductivity Data of Gaseous and Liquid Ethylene," J. Phys. Chem. Ref. Data, 12, 917-932, 1983.
4. Chen, L.D., "Supercritical Atomization Studies," AFOSR Supercritical Fuels/Combustion Workshop, WPAFB, Ohio, Feb. 1994.
5. Hermanson, T.C., Papas, P., and Kay, I.W., "Structure and Penetration of a Traverse Fluid Jet Injected at Supercritical Pressure into Supersonic Flow," AIAA 92-3652, 1992.
6. Faeth, G.M., "Structure and Atomization Properties of Dense Sprays," Twenty-Second Symposium (International) on Combustion, 1334-1352, 1990.
7. Chigier, N.A., "The Physics of Atomization," Fifth International Conference on Liquid Atomization and Spray Systems, Gaithersburg, MD., 1-15, 1991.
8. Ruff, G.A., Wu, P.-K., Bernal, L.-P., and Faeth, G.M., "Continuous and Dispersed-Phase Structure of Dense Nonevaporating Pressure-Atomized Sprays," J. Prop. Power, 8, 280-289, 1992.
9. Wu, P.-K., Miranda, R.F., and Faeth, G.M., "Effects of Initial Flow Conditions on Primary Breakup of Nonturbulent and Turbulent Liquid Jets," AIAA 94-0561, 1994.

10. Eckbreth, A.C., *Laser Diagnostics for Combustion Temperature and Species*, Abacus Press, Cambridge, 162-206, 1988.

Table 1 Summary of Test Conditions (Pc=50.5 atm., Tc=283 K)

Parameters	Ranges
Pj/Pc	1.1
Tj/Tc	0.9, 1.0, 1.1
Pg/Pc	0.1, 0.5, 0.85, 1.0
Tg/Tc	1.05, 1.2, 1.5, 2.5
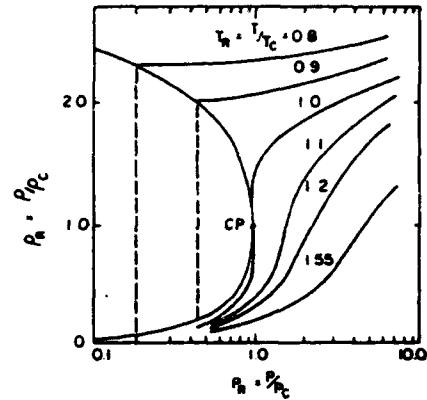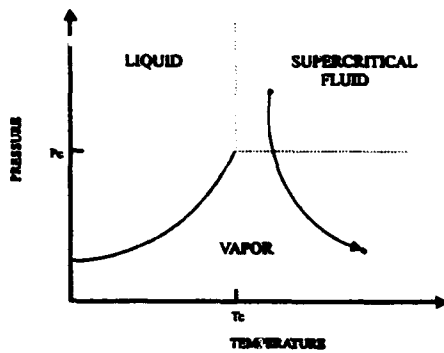
Figure 1 Operating Conditions for a Typical Scramjet Cycle.

Figure 2 Variation of the Reduced Density of a Pure Component Near Its Critical Point. [2].
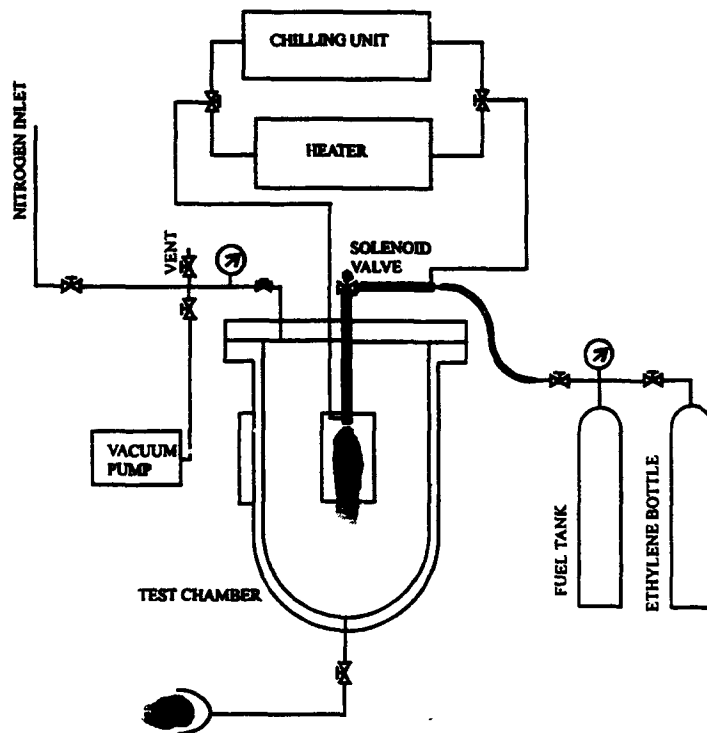
Figure 3   Sketch of Supercritical Fluid Atomization Test Apparatus

ADVANCED SUPERCRITICAL FUELS

AFOSR Task # 93WL002

Principal Investigators: Tim Edwards, Jim Gord, Mel Roquemore

USAF Wright Laboratory
WL/POSF Bldg 490
1790 Loop Rd N
Wright Patterson AFB, OH 45433-7103

SUMMARY/OVERVIEW:

Increases in aircraft and engine performance are increasing the heat load being transferred into an aircraft's primary coolant--the fuel [1]. This research is aimed at understanding the limitations of operation of fuel heated to 480 °C (900 °F). Important areas are expected to be thermal stability, heat transfer/flow instabilities, and injection properties. This discussion focuses on thermal stability.

TECHNICAL DISCUSSION

"Thermal stability" refers to the ability of a fuel to absorb heat without the formation of undesirable solid deposits or other reaction products. Current jet fuels are thermally stable up to temperatures of ~170 °C (325 °F). This research is aimed at determining the barriers to the use of a hydrocarbon fuel at 480 °C (900 °F). Two distinct types of fuel reactions are involved in thermal stability at these temperatures: thermal-oxidative and pyrolytic reactions. Thermal-oxidation stability has been studied in single-tube heat exchangers, where it has been found that naphthenic and paraffinic hydrocarbons, both pure and refined mixtures, are of about equal thermal stability at these high temperatures [2,3]. Recent work has shown that detergent/dispersant additives, found to be effective in other thermal stability tests at lower temperatures, can dramatically reduce the surface deposition from jet fuels heated to 480 °C (900 °F). This is illustrated in Figure 1. The mechanism of this reduction in deposition is under investigation. Pyrolytic stability has also been examined in flowing tests. It has been found that naphthenic and paraffinic hydrocarbons were again of comparable thermal stability [4]. This is in contrast to batch reactor work, where naphthenes were found to be more stable than paraffins. The pyrolytic deposition from jet fuels heated to ~590 °C (1100 °F) was found to be very dependent upon the presence of additives. Benzyl alcohol and tetralin were found to reduce deposition (probably by acting as high temperature hydrogen donors), as were glycol ether fuel system icing inhibitor and fuel oxidation products [4].

A unique CFD/chemical kinetic model of the fuel oxidation and deposition processes has been constructed and is under refinement [5,6,7,8]. The model has been successful in predicting deposition behavior in nozzle and heat exchanger environments. The global chemistry/deposition scheme used in the model is shown in Figure 2. The rate constants for the

reactions are determined from calibration tests in various thermal environments. Problem areas under current study include the effect of the fuel thermal history (e.g., preheating), calibration for different fuels, and low temperature initiation processes. The relationship between the oxidation reactions and the deposition can be quite complex [1,7,8].

A better understanding of the fuel deposition processes will require better diagnostic probes. The quartz crystal microbalance (QCM) is being used as a very sensitive probe of surface deposition [9,10]. This in situ probe allows deposition measurements in real time. Simultaneous application of the QCM and photon correlation spectroscopy is being explored to examine the mechanisms of surface deposition. There is still debate as to the mechanisms of thermal-oxidative surface deposition, with two possibilities being transport of insoluble macroscopic particles from the bulk fuel to the surface, or transport of smaller soluble "precursors" from the bulk to the surface. An alternative view of this second possibility is adsorption of precursor-type species by the deposit from the bulk fuel. Inverse liquid chromatography is being used to study to adsorption properties of deposits [11]. There is evidence that the deposits can preferentially absorb polar species similar to precursors from the fuel, as can metal surfaces.

Ultrafast laser diagnostics are being used to probe the chemical environment of high temperature fuels. Buildup of a system to examine the "clustering" seen in supercritical solvents is underway, with application to high temperature fuels (typical fuel T_C ~385 °C (725 °F)). Two-photon fluorescence is also being studied as a chemical probe [12]. The inherent weakness of the two -photon process is offset by the high power densities in the ultrafast pulse, and the specificity of the process allows discrimination between the desired signal and the large one-photon fluorescence seen in jet fuels. Interestingly, the two-photon signal from jet fuels correlates with their thermal stability, as shown in Figure 3. The best fuels (as shown in Figure 1) produce the lowest two-photon signal from IR excitation. The source of the two-photon emission is under investigation.

1.   Edwards, T., Roquemore, W. M., Harrison, W. E., Anderson, S. D., "Research and Development of High Thermal Stability Fuels," AGARD 81st Symposium on Fuels and Combustion Technology for Advanced Aircraft Engines, Colleferro, Italy, May 1993, AGARD-CP-536.
2.   Edwards, T., and Liberio, P., "The Thermal-Oxidative Stability of Fuels at 480 °C (900 °F)," ACS Petroleum Chemistry Division Preprints, Volume 39, No. 1, pp. 86-91, 1994.
3.   Edwards, T., Zabarnick, S., "Supercritical Fuel Deposition Mechanisms," *Industrial and Engineering Chemistry Research.*, Vol. 32, 3117-3122, 1993.
4.   Edwards, T., and Liberio, P., "The Relationship Between Oxidation and Pyrolysis in Fuels Heated to ~590 °C (1100 °F)," ACS Petroleum Chemistry Division Preprints, Volume 39, No. 1, pp. 92-96, 1994.
5.   Katta, V. R., and Roquemore, W. M., "Numerical Method for Simulating Fluid-Dynamic and Heat-Transfer Changes in Jet-Engine Injector Feed-Arm Due to Fouling," *AIAA J. Thermophys. Heat Trans.* 7(4), 651-660 (1993).
6.   Katta, V. R., Jones, E. G., and Roquemore, W. M., "Development of a Mathematical Model for Jet Fuel Thermal Stability Based on the Observations Made from Static and Flowing Experiments," AGARD 81st Symposium on Fuels and Combustion Technology for Advanced Aircraft Engines, Colleferro, Italy, May 1993.

7.   Chin, L. P., Katta, V. R., Heneghan, S. P., "Numerical Modeling of Jet Fuel Autoxidation in Flowing Systems," ACS Petroleum Chemistry Division Preprints, Volume 39, No. 1, pp. 19-25, 1994.

8.   Zabarnick, S., Industrial and Engineering Chemistry Research, Vol. 32, 1012-1017, 1993.

9.   Zabarnick, S., "Studies of Jet Fuel Thermal Stability and Oxidation Using a Quartz Crystal Microbalance and Pressure Measurements," Industrial and Engineering Chemistry Research., in press.

10.   Zabarnick, S., and Grinstead, B. R., "Studies of Jet Fuel Thermal Stability and Autoxidation Using a Quartz Crystal Microbalance," ACS Petroleum Chemistry Division Preprints, Volume 39, No. 1, pp. 51-57, 1994.

11.   Striebich, R.C., and Rubey, W. A., "Surface Adsorption Studies Using Inverse Gas Chromatography and Inverse Liquid Chromatography," ACS Petroleum Chemistry Division Preprints, Volume 39, No. 1, pp. 64-66, 1994.

12.   Gord, J. R., Weaver, W. L., Grinstead, K. D., Lytle, F. E., "Fuel Thermal Stability Studies with Two-Photon Fluorescence Spectroscopy," paper to be presented at 6/94 Central States Section/Combustion Institute Meeting.
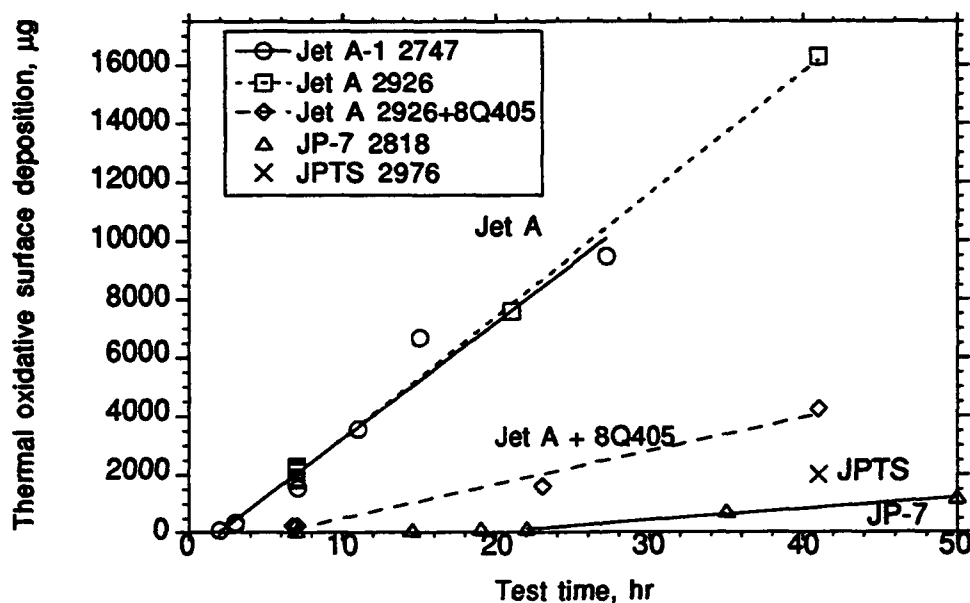
Figure 1. The effect on surface deposition of adding 100 mg/L of a dispersant ("8Q405") to air-saturated jet fuel. Test parameters: 12 mL/min flow, 69 atm, fuel heated to 480 °C (900 °F), 1.4 mm ID 316 SS tubing. JPTS and JP-7 are highly processed, higher cost, thermally stable fuels.
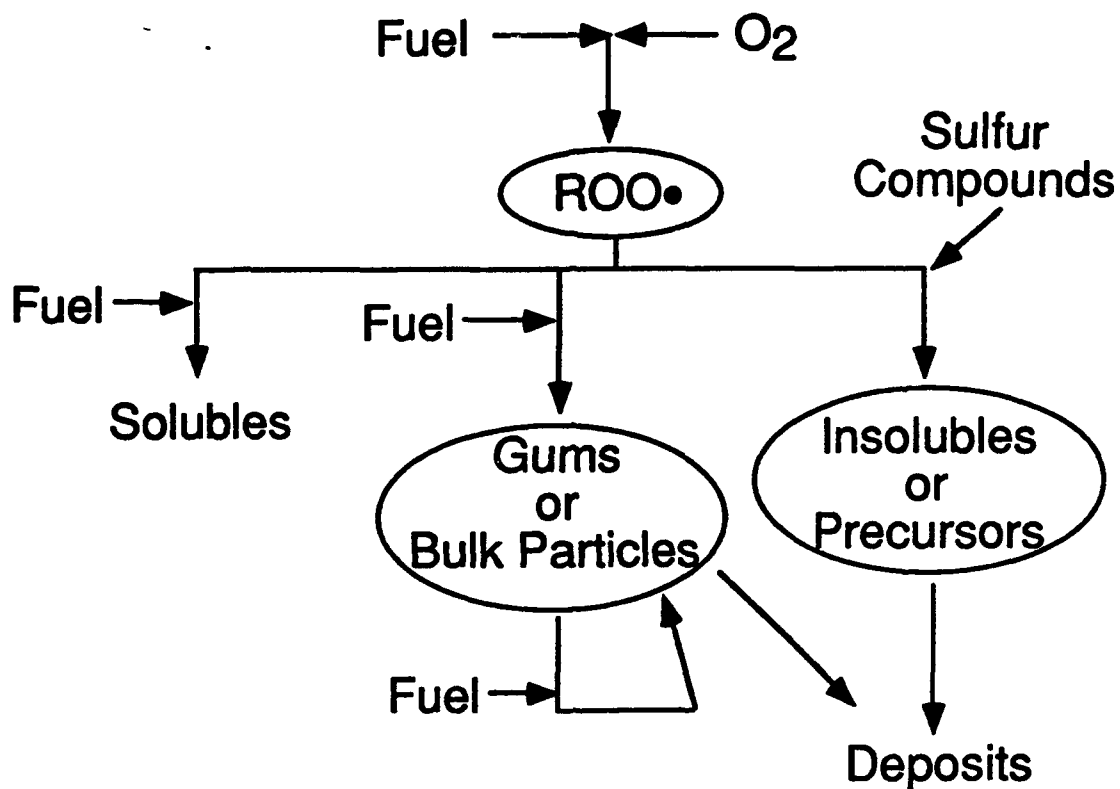
Figure 2. Global mechanism used in CFD deposition model [5,6,7].
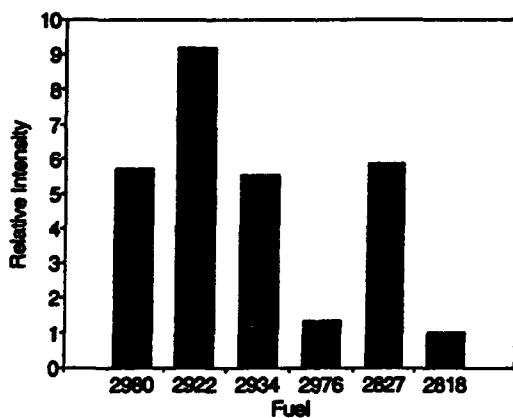
Figure 3. Relative two-photon fluorescence signals for jet fuels [12]. Note that the fuels with the small signals are the high thermal stability fuels shown in Figure 1. The other fuels are Jet A fuels of lower thermal stability than the two Jet A fuels in Figure 1.

FUELS COMBUSTION RESEARCH

(AFOSR GRANT 89-0034)

Principal Investigators: I. Glassman and K. Brezinsky

Department of Mechanical and Aerospace Engineering
Princeton University
Princeton, NJ 08544

SUMMARY

Challenging projected new fuel characteristics of concern to the Air Force, Princeton's Fuels Combustion research program has evolved into an integrated effort that now focuses, in order of priority, on: a) the thermal degradation of jet fuel components under sub- and super-critical conditions; b) the pyrolysis and oxidation of protypical endothermic fuels; c) the oxidation kinetics of aromatic fuels, including the polynuclear aromatics, and aromatic-aliphatic fuel blends and d) soot formation and destruction processes. This integrated research program is unique not only in the programs, but also in the integration of the various components by considering identical fuel compounds in each element.

TECHNICAL DISCUSSION

1) Sub- and Super-Critical Fuel Degradation Study

Degradation studies of toluene, methylcyclohexane (an endothermic fuel) and toluene/methyl cyclohexane mixtures were studied at unique combinations of temperatures and pressures in the sub/super-critical liquid flow reactor apparatus described last year as being developed. Fig. 1 graphically portrays the matrix of experimental conditions examined in the now fully developed reactor. The figure contains critical temperature and pressure information on toluene and methylcyclohexane. To date most of the experiments conducted have been at temperatures and pressures above the critical points of the pure fluids and probably above those for the toluene/methyl cyclohexane mixture. The residence times in the flow reactor have been varied from almost 20 minutes to as little as almost 1 minute.

As can be observed in Figure 1, one set of systematic experiments examining the chemical changes in pure methyl cyclohexane has been conducted as a function of temperature. This set is shown on the figure by solid black squares. As the methyl cyclohexane is heated it approaches temperatures at which solid material forms and clogs the reactor tube. Cases where this clogging has been observed are shown on the figure.

The experiments conducted at temperatures just preceding that which causes clogging have yielded fluid samples that were analyzed by gas chromatography - Fourier Transform spectroscopy. The preliminary results indicate that the methyl cyclohexane fragments on heating to produce light gases such as methane and a variety of four and five carbon species. These latter species are being examined more closely in order to determine their identities. Also benzene appears to be formed. What does not appear to be formed are large molecular species such as polynuclear aromatics or polymers that would constitute the precursor species to deposit formation. Investigation of the liquid phase chemistry is continuing.

Two of the three experiments that led to clogging have yielded solid samples suitable for analysis. The first experiment, indicated on the figure by a solid black up triangle marked clogged, was conducted with a 90% toluene, 10% methylcyclohexane mixture at 797K, 4.63MPa and a residence time of 1.05 minutes. The second, indicated on the figure by a solid black circle labeled "clogged", is the methyl cyclohexane experiment at 657K, 4.14 MPa and residence time of 4.12 min.

These two experiments exhibited the onset of particulate formation clogging by a rapid rise in the fluid pressure as the blockage developed in the nickel tubing. As this pressure rise occurred, the flow rate was drastically increased in order to drive the blocking material out of the tubing. The black powdery

material that exited the reactor in the reactant fluid was captured and subsequently analyzed using transmission electron microscopy (TEM), energy loss and electron diffraction spectroscopy.

Analysis was conducted with a CM 20 Philips TEM. The TEM and energy loss analysis indicated that the black powdery material consisted of filaments of graphitic platelets aligned parallel to the long axis of the filament. The EDAX (electron diffraction) analysis also indicated that the filaments contained, occluded within the filament, nickel particles. Copper was also shown to be present but only in the supporting grid necessary for the TEM analysis. Photographs were subsequently generated from the TEM analysis.

Three unusual characteristics exhibited by these filaments appear to be unique. First, the whole length of the filament is composed of a gently curving rod without any kinks or sharp changes in direction. Kinks generally are sites of weakness in a fiber and lead to fracture at the kink location. Secondly, the nickel particles are contained within the length of the filament not just at the ends. The literature on this subject indicates that metal particles such as nickel occur at the end of the filament and serve as the base from which the filament grows. Graphitic filaments as produced here have not been observed to contain nickel particles within, especially particles that appear to be faceted. Thirdly, although there appears to be the hint of a hollow core in these filaments, they are primarily solid rodlike structures. Graphitic filaments generally contain a substantial hollow center core. A unique characteristic of these filaments not obvious from the photos is that the conditions of production involve higher pressures and much lower temperatures i.e. nominally 800K rather than 2000K, than have been required in other processes. Consultation with Structural Materials Branch of WPAFB have revealed these filaments to be unique and perhaps of great value.

The essential discovery of importance to the Air Force is a method of fabrication of graphitic filaments in the presence of metal particles when exposed to hydrocarbon fluids either in the supercritical state, i.e. at high pressures and at temperatures above the critical point, pressures and temperatures and, possibly when exposed to fluids at high pressure, and modest temperatures so that the hydrocarbons remain in the liquid state.

2) Pyrolysis and Oxidation of Endothermic Fuels and Fuel Blends

The initial results on the study of the methylcyclohexane (MCH)/toluene blends have been most enlightening and encouraging in that blend studies may follow a pattern that precludes detailed variation of the blend components. Examination of pure MCH during pyrolysis and oxidation revealed that ethane, butadiene, methane and propene were the major stable intermediates. Since the pyrolysis and oxidation characteristics of these intermediates had already been studied in the program, the overall mechanistic character of these processes now appear to be understood.

The oxidation experiments of MCH/toluene blends have led to three significant findings relevant to component selection in multi-component JP fuels. They are:

1) Toluene, commonly thought to be a reaction inhibitor, has little effect on the rate of oxidation of MCH.
2) Early in the oxidation process MCH produces an extensive radical pool which is not only sufficient to insure MCH's rapid oxidation, but also to serve to accelerate the oxidative pyrolysis of toluene.
3) When oxidized as a blend, MCH/toluene, despite sharing a radical pool, each appear to follow their own oxidation mechanism as pure species.

3) The Oxidation and Pyrolysis of Hydrocarbons

Previous investigations of the oxidation characteristics of aromatics considered benzene, mono-alkylated benzenes particularly toluene and the di-alkylated benzenes, particularly o, m and p-xylenes. The recent focus of the research was on the oxidation of 1-methylnaphthalene and has provided the first detailed oxidation results for any polycyclic aromatic hydrocarbon (PAH), despite the presence of PAH's in many practical fuels. The results of this study can be summarized succinctly as follows.

143

Detailed intermediate species profiles for the oxidation of 1-methylnaphthalene have been obtained by gas-phase sampling from the atmospheric-pressure flow reactor operating at about 1170 K. No evidence was found to indicate that fuel consumption through ring reactions was competitive with consumption through attack of the methyl side chain. Based on the observed intermediate species profiles, a mechanism has been proposed for the oxidation of 1-methylnaphthalene which is strongly analogous to a previously developed mechanism for the oxidation of toluene under flow reactor conditions. In this mechanism, the resonantly stabilized 1-naphthylmethyl radical undergoes radical-radical reactions to form 1-naphthaldehyde, which decomposes to 1-naphthyl radical. Naphthalene and 1-naphthyl radical are oxidized to 1-naphthoxy radical, which decomposes to indenyl radical. Further reaction and decomposition results in the formation of phenylacetylene, styrene, phenyl radical, and acetylene. This mechanism is consistent with the observed sequential formation of the major aromatic intermediates 1-naphthaldehyde, naphthalene, indene, phenylacetylene, and benzene. Other pathways to the formation of minor intermediates such as 2-methylnaphthalene, acenaphthylene, 2-naphthol, and 1-methylindene are considered.

4) Soot Formation and Destruction Process

The impact of the program's effort on soot formation and destruction processes has been well established and well recognized. The general activity in this aspect of the overall program has been diminishing. A major aspect of the soot problem that was resolved during this report period was with regard to the critical temperature for soot nucleation. By measuring the temperature along the center-line of a burning fuel jet which had been diluted with an inert gas until it was no longer luminescent, it was possible to establish a critical temperature at which a given fuel would not longer soot. The range of temperatures observed for the fuels evaluated in this manner was extremely narrow. The preliminary results reported previously were indeed validated by more extensive experimentation. These results showed about 100 K variation in the critical temperature to prevent sooting and the order would indicate that the dilution technique could have affected the results to give this variation. The fuels that had the least tendency to soot demanded the least amount of dilution and gave the highest critical temperature. It would appear then that a single critical temperature for soot nucleation in diffusion flame tests exists and that the actual temperature is in the 1600-1700 K range regardless of the fuel. Since the mechanism for the formation of the initial fuel particle is the same regardless of the fuel, some high activation process in the soot formation mechanism would appear to control initial particle nucleation.

This result permitted the first complete explanation of the temperature effect in sooting diffusion flames, particularly those using circular fuel jets. Essentially the critical temperature isotherm, say 1650 K, is the point at which soot particles nucleate. The soot volume fraction grows by mass addition to the particles until the particles enter the higher temperature flame front. As the volumetric flow rate of the flow is increased, the separation distance of the flame and critical temperature isotherms remains essentially the same, but the amount of particles nucleated increase the soot volume fraction so that the particles penetrate the flame front and a smoke height is reached. Different fuels will form different number of nucleated particles at the 1650 isotherm, so different smoke heights are obtained for different fuels. When the fuel is diluted with an inert gas, the flame temperature drops and the 1650 isotherm moves closer to the flame temperature isotherm. Thus the growth period of the nucleated particles decreases and the soot volume fraction entering the flame is less. To create a smoke point for this diluted condition, the volumetric flow rate of the fuel-inert mixture must be increased so that more particles will form.

Pressure Transducer Limit

Sandbath Temperature Limit

■ MCH series 3
□ MCH series 1
● MCH series 2
○ Toluene
▲ [0.9] Toluene, [0.1] MCH mixture

Clogged

Tc Toluene

Tc MCH

Clogged

Pc Toluene

Pc MCH

Pressure [MPa]

Temperature [K]

900

800

700

600

500

3   4   5   6   7

145
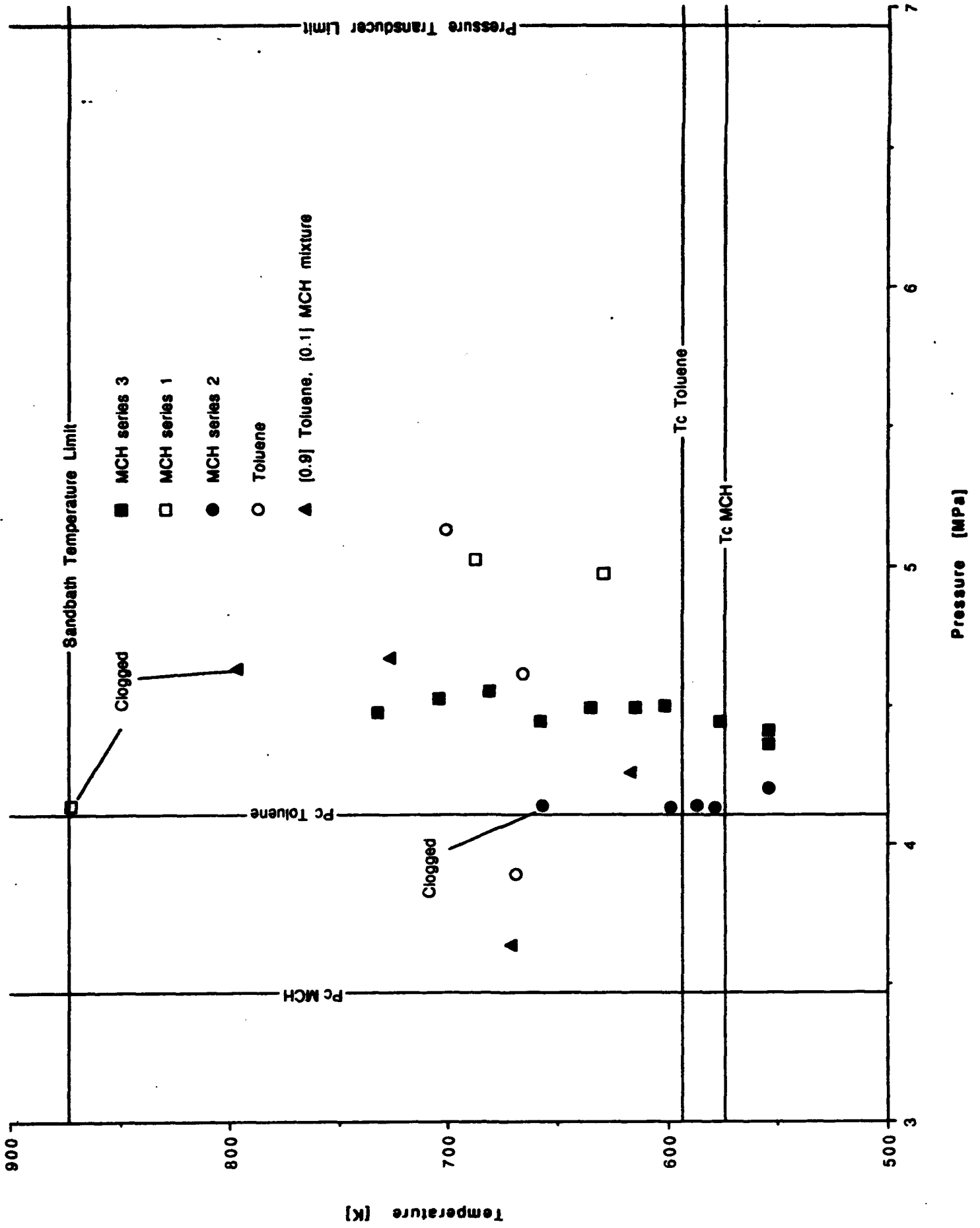
COMPUTER SIMULATION OF MOLECULAR INTERACTIONS IN SUPERCRITICAL SOLVENTS; PARTICLE FORMATION FROM SUPERCRITICAL FLUIDS

Principal Investigator: Pablo G. Debenedetti

Department of Chemical Engineering
Princeton University
Princeton, NJ 08544-5263

SUMMARY/OVERVIEW

This research program has two components. In one, we use molecular dynamics computer simulations to investigate solvation in supercritical solvents. In the other, we conduct experimental and theoretical studies of particle formation from supercritical fluids. The simulation studies seek to understand the mechanisms of solvation in supercritical solvents, and how these depend on differences in size, shape, and interaction energy between the solvent and the solute, as well as on the bulk density and temperature. In the particle formation experiments, we use supercritical fluids either as solvents, in which case particles are formed by rapid expansion, or as anti-solvents, in which case particles are formed by rapid evaporation of an organic solvent into a supercritical fluid. The goal of the solid formation studies is to understand the relationship between particle size and morphology, and experimental conditions.

TECHNICAL DISCUSSION

There is considerable interest in understanding the local environment (microstructure) surrounding solute molecules in a supercritical solvent [e.g., 1,2]. This interest is driven by the intriguing possibility of exploiting differences between local and bulk conditions for reaction and separation purposes [3]. In our work, we use computer simulations to gain fundamental, microscopically-based understanding of solvation mechanisms in supercritical solvents. In an ongoing study, we use molecular dynamics to investigate the system benzene (solute) - carbon dioxide (supercritical solvent). We model benzene as a rigid six-site molecule [4], and carbon dioxide as a rigid, linear, three-site molecule with a point quadrupole [5].

The simulations employ one solute and 255 solvent molecules. Periodic boundary conditions are used to eliminate finite-size and surface effects. Since there are no solute-solute interactions, the system is effectively at infinite dilution with respect to the solute. We are investigating the microstructure around benzene, and the way in which it affects benzene's rotational and translational diffusion. Simulations are run at supercritical temperatures and over a range of densities spanning the dilute gas and liquid-like regimes. The quantities under investigation are orientation-dependent molecular distribution functions, the dynamics of density fluctuations within the solvation shell, solute rotational and translational diffusivity, and the distribution of solvent orientations around benzene. Figure 1, for example, shows the autocorrelation function for carbon dioxide density fluctuations within the first solvation shell (7.7 Å, distance to the first "valley" of the solute-solvent radial distribution function) around the benzene molecule. From it we obtain a relaxation time for the decay of density fluctuations of roughly 15 psec.

We have also studied solute-solute aggregation in dilute supercritical mixtures [6]. This problem is computationally demanding, because one is interested in dilute mixtures (mole fraction $< 10^{-3}$), which require large sample sizes and long simulations in order for solute-solute statistics to converge. Because of this we have studied simple, spherically symmetric model systems, with potential parameters chosen to simulate so-called attractive behavior [7], which is characteristic of most supercritical systems of practical interest. In this kind of mixture, the solute's partial molar volume and enthalpy are large and negative, and the short- and long-range environment around the solute is solvent-rich with respect to the bulk. In attractive mixtures, the solute is larger than the solvent, and the characteristic energy for solute-solute interactions is larger than for solvent-solvent interactions. We have derived exact equations that allow the classification of a mixture into attractive or repulsive (solvent-lean microstructure) from knowledge of the differences in size and energy between solute and the solvent [7].

Figure 2 shows the lifetimes of dimers over the density range $0.5 < \rho/\rho_C < 2$. It can be seen that nothing remarkable happens to dimer lifetimes in the near-critical region. Dimers stay together for roughly 0.8 psec., the only noticeable effect being a broadening of the distribution at high densities. We see no evidence of extensive solute-solute aggregation at near-critical conditions.
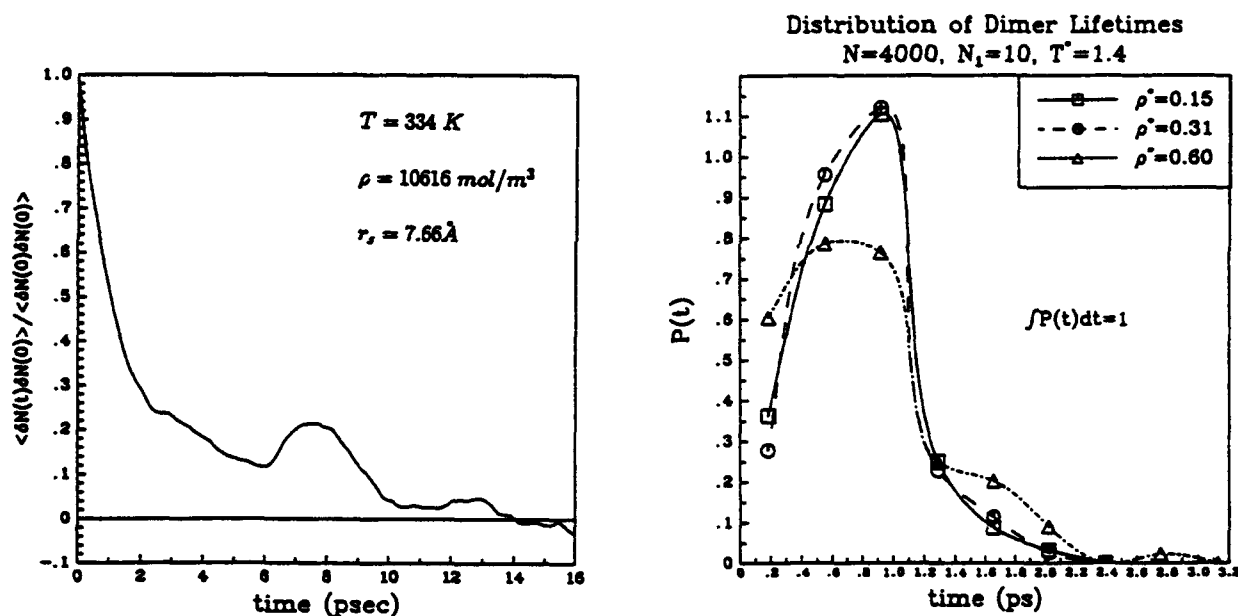
Figure 1: Autocorrelation of carbondioxide density fluctuations in the vicinity of a benzene molecule, calculated by molecular dynamics.

Figure 2: Density dependence of the distribution of pyrene dimer lifetimes in supercritical carbon dioxide, calculated by molecular dynamics. Pyrene mole fraction is 0.0025. The solvent's critical density and temperature are $T^* = kT/\varepsilon = 1.31$, $\rho^* = \rho\sigma^3 = 0.31$, where ε and σ are Lennard-Jones parameters.

An important result from simulations and integral equation calculations is the fact that differences between local and bulk conditions are always more pronounced at substantially subcritical densities. For example, in integral equation calculations of the system naphthalene-carbon dioxide, we found that the first peak of the solute-solute correlation function attained its maximum value at 60% of the solvent's critical density. Analogous results were obtained for the solute-solvent local density augmentation by molecular dynamics. This confirms that short-ranged interactions, and in particular solvation, are unaffected by the proximity to critical points. Although this point seems obvious, there has been considerable confusion in the literature about the separation of long- and short-ranged effects in dilute supercritical mixtures [8].

Supercritical fluids are an extremely interesting medium for particle formation. There exist two routes to supercritical particle formation: rapid expansion (RESS) and the anti-solvent process (SAS).

In RESS, nucleation and growth are triggered by the partial decompression of a supercritical solvent, which causes a pronounced loss of solvent power and the precipitation of solutes. Fast expansions (e.g., $< 10^{-5}$ sec., which can be easily attained in nozzle flows) lead to appreciable supersaturations. In the case of supercritical solutions, the range of attainable supersaturations is especially high because of the enormous enhancement in the solubility of a given solute with respect to ideal gas conditions at the same temperature and pressure, a quantity that can be as high as 10^6. Furthermore, precipitation is triggered mechanically rather than thermally. Mechanical perturbations travel at the speed of sound, which favors the attainment of uniform conditions within the expanding fluid. The combination of large supersaturations and small gradients is a distinguishing feature of fast supercritical expansions, and favors the formation of small and uniform particles. RESS is relevant whenever a supercritical solvent is depressurized. For example, if a supercritical fuel containing dissolved autooxidation or pyrolysis products loses ca. 200 psi. in a nozzle, solids will be formed due to the drop in the carrier fluid's solvent power. In our laboratory, we have used RESS to produce polymer particles for use in controlled release applications [9]. Other groups have investigated the formation of ceramic precursor particles by rapid expansion of supercritical water [10]. Figure 3 shows bioerodible polymer microspheres formed by RESS of supercritical carbon dioxide.
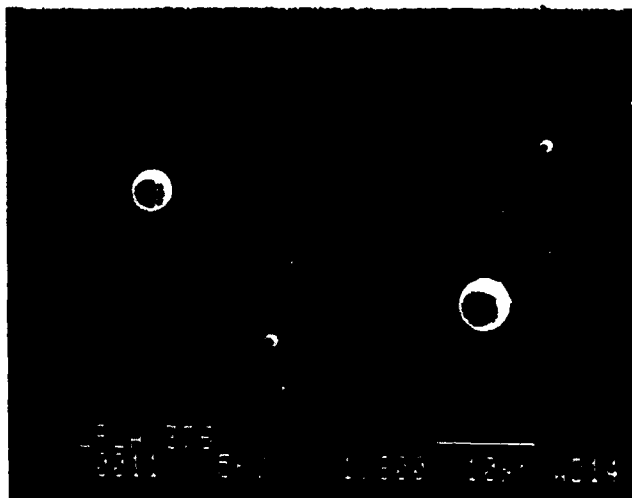
Figure 3: Poly (L-lactic acid) microspheres obtained by rapid expansion of a supercritical solution (RESS) of the polymer in 70 wt% CO_2 - 30 wt% $CHClF_2$.

In SAS, the solid of interest is dissolved in a liquid, and a supercritical fluid having low solvent power with respect to the solute, but miscible with the liquid, is added to precipitate the solid. When this process is run in continuous mode, the liquid and supercritical phases are fed

continuously into a precipitator. Small droplets are sprayed into a co-currently flowing continuum supercritical phase. The liquid solvent is rapidly flashed into the supercritical phase, and dry powders result. In our laboratory we have used the SAS concept to produce biologically active powders of insulin (controlled release applications) [11], and aromatic polyamide (aramid) microfibers (heat resistance, high-modulus, high tensile strength applications) [12]. Figure 4 shows a bundle of aramid fibers obtained by SAS-processing with supercritical carbon dioxide.
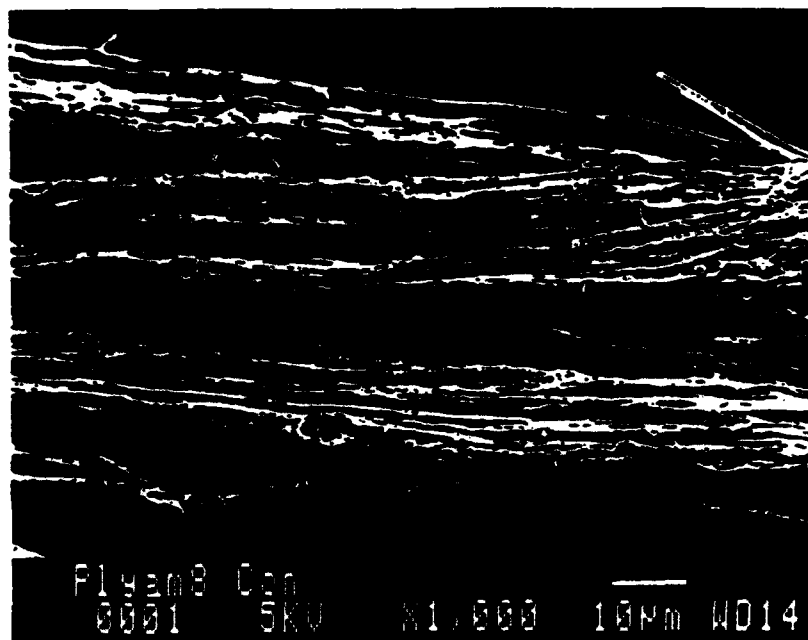
Figure 4: Aramid fiber bundle obtained by supercritical anti-solvent (SAS) contacting of a solution of the polymer in dimethylsulfoxide with supercritical carbon dioxide.

RESS can be used to form fine particles of substances that are soluble in a supercritical solvent. SAS is used for sparingly soluble materials. Together, these techniques allow the processing of a wide range of materials into solid phases with extremely useful properties and morphologies. Possible applications include ceramics, improved controlled drug release devices, and high-performance polymeric fibers.

[1] Brennecke, J.F., Tomasko, D.L., and Eckert, C.A. *J.Phys.Chem.*, *94*, 7692, 1990.
[2] Tom, J.W., and Debenedetti, P.G. *Ind. Eng. Chem. Res.*, *32*, 2118, 1993.
[3] Brennecke, J.F., and Eckert, C.A. *AIChEJ.*, *35*, 1409, 1989.
[4] Luo, H., and Hoheisel, C. *J.Chem.Phys.*, *96*, 3173, 1992.
[5] Murthy, C.S., and Singer, K. *Mol.Phys.*, *44*, 135, 1981.
[6] Chialvo, A.A., and Debenedetti, P.G. *Ind. Eng. Chem. Res.*, *31*, 1391, 1992.
[7] Petsche, I.B., and Debenedetti, P.G. *J. Phys. Chem.*, *95*, 386, 1991.
[8] Debenedetti, P.G. *Chem. Eng. Sci.*, *42*, 2203, 1987.
[9] Tom, J.W., and Debenedetti, P.G. *Biotech. Prog.*, *7*, 403, 1991.
[10] Matson, D.W., Petersen, R.C. and Smith, R.D. *Adv. Ceram. Mater. 1*, 242, 1986.
[11] Yeo, S.-D., Lim, G.-B., Debenedetti, P.G., and Bernstein, H.B. *Biotech. and Bioeng.*, *41*, 341, 1993.
[12] Yeo, S.-D., Debenedetti, P.G., Radosz, M., and Schmidt, H.-W. *Macromolecules*, *26*, 6207, 1993.

PLASMA
PROPULSION

(Not Presented)

FUNDAMENTAL STUDIES OF THE ELECTRODE REGIONS IN ARCJET THRUSTERS

Principal Investigator: M.A. Cappelli

High Temperature Gasdynamics Laboratory
Stanford University
Stanford, CA 94305-3032

SUMMARY/OVERVIEW

The purpose of this research program is to develop a fundamental understanding of the physical processes that occur in the vicinity of hydrogen arcjet thruster electrodes. Our present research program is an extension of past efforts that employ optical-based arcjet thruster diagnostics. Previously, we have used laser-induced fluorescence, optical emission spectroscopy, and absorption spectroscopy, to measure flowfield properties such as temperature and velocity, and to characterize nonequilibrium behavior in arcjet plume flows. In the AFOSR funded program, these diagnostic strategies are being extended to interrogate the internal arcjet flow. Together with physical models of arc attachment, these measurements help us to understand the fundamental behavior of the near-electrode regions in these devices, and assist in identifying the necessary physics to be included in more elaborate models of overall arcjet thruster performance.

TECHNICAL DISCUSSION

During the past several years, there has been an evolution of arcjet technology from laboratory devices to flight-qualified hardware, and finally, to deployment. As demands are made for higher arcjet operating power and higher performance (efficiencies), so increases the need to better understand the performance and life-limiting processes such as cathode erosion and anode heat transfer resulting in both anode erosion and the flow of tungsten at the throat in response to thermal stresses. In principle, reliable arcjet models, if they existed, could be used determine appropriate arcjet designs for extended life and performance. At present, only a few models exist[1,2], and the physics that enters into these models are often highly simplified in order to render the numerical problem tractable. As such, many of the features responsible for heat transfer are neglected, in particular, the near-electrode physics which above all, determines cathode and anode arc attachment. A better understanding of the physical processes in the interior of arcjet thrusters will come from a combination of measurements of internal flow properties and modeling. It is our aim in this program to advance the state of the art in arcjet diagnostics, and to acquire information of the near-electrode regions of arcjets that may be used in the development of arcjet performance models.

Many studies have been conducted to investigate arcjet performance under different operating conditions, electrical configurations and geometries[3]. However, understanding the physical processes governing the arcjet operation requires a detailed knowledge of the plasma properties everywhere in the flow field. A great deal of research has been conducted to measure the flow properties in the plume of the arcjet thruster using several optical techniques including emission, absorption, LIF, and Raman spectroscopy[4-6]. Much less is known about the plasma properties within the core and nozzle of the arcjet, yet it is here where the plasma behavior controls the arcjet performance.

We summarize here our ongoing research into the determination of plasma properties in the near-cathode region of the hydrogen arcjet, and in the expansion nozzle where the arc attaches in the so-called "high mode" at the anode. During the past year, we have studied the properties of the near-

cathode region by investigating the axially radiated emission of atomic hydrogen from this region. The research consists of both a numerical prediction and the experimental measurement of atomic hydrogen axial emission line and continuum spectra. The numerical modeling has demonstrated the promise of obtaining plasma properties (electron number densities, cathode temperature, and possibly velocities) within the throat of the arcjet by optical emission measurements. Experiments have been performed on both 1 kW class and nominally 5 kW class hydrogen arcjets. The experimental results have been compared to single-fluid model predictions.[7] Ongoing activities also include an extension of our LIF measurements into the expansion nozzle, to measure electron number densities, temperatures, and velocities in the vicinity of the anode.

The numerical calculations to simulate the axial hydrogen plasma emission consisted of an integration of the radiative transfer equation along the centerline of the arcjet from the cathode tip to the exit plane and beyond into the plume of the plasma. The spectral emission and absorption coefficients were expressed in terms of the excited state number densities and a lineshape function for each transition. The lineshape function included both Stark and Doppler broadening and Doppler shift. The number densities were calculated from a ten-level collisional-radiative model including the ion, the ground state atom and eight excited states. Semi-empirical rate coefficients were used for the greatest calculation speed. The plasma was assumed optically thin for all transitions other than Lyman radiation, which was assumed fully trapped. The electrons were assumed to have a Maxwellian velocity distribution. A stationary-state approximation was used which permitted neglecting the convective and diffusive flux of excited states on the assumption that such processes are slower than the collisional and radiative transitions between the states. This was shown to be the case under the conditions of the plasma within the arcjet. Hence, the distribution of excited state populations could be determined by the local plasma properties. These properties, namely pressure, electron and atom kinetic temperatures, dissociation fraction, and axial velocity, were entered into the calculations from MHD model predictions[7].

A sample of the results of these calculations is shown in Figure 1. Here the spectral intensity of the H_α transition has been integrated from the cathode (z=-0.4 mm) to the arcjet exit plane, z = 12.1 mm, and to three intermediate positions for comparison. The plot shows that the largest contribution to the emission comes from the inner ten percent of the arcjet, that is, from within the arc root (immediately adjacent the cathode). The extent of reabsorption by the cooler expansion flow is seen to be about 20 percent at line center. However, away from line center, the plasma is still emitting. Consequently the emission linewidth is broadened and flattened as the radiation passes through the expansion flow. The effect of the Doppler shift is seen as an asymmetry that is most pronounced at z = 5 mm. We assume that the Stark shift of the H_α is negligible and so the absorption dip is calculated to be to towards longer wavelengths as the colder gas in the plume is decelerated on centerline. It has been shown that there is little change in the spectrum as the radiation passes through the arcjet plume. Thus, axial line-of-sight emission measurements are expected to yield lineshapes similar to those at the arcjet exit plane. An important feature of our modeling studies is that it is also evident that the continuum emission between electronic transition lines is dominated by gray-body emission from the cathode. As a result, a complete scan of the continuum region between the H_α and H_β transistions afford a measurement of the cathode temperature.

Axial emission measurements of atomic hydrogen have been completed on both a 1 kW class and 5 kW class radiatively-cooled laboratory-type arcjet thruster. During optical alignment, the throat of the arcjet is magnified and imaged onto the entrance slit of a 0.5 m Jarrell-Ash monochromator by the optical train. The intensity is measured with a photomultiplier tube and recorded on a personal computer. Spatial resolution of approximately 0.1 mm is achieved by field stopping the magnified image. The arcjets are either mounted on a translation stage which allows measurements at different radial positions, or, in the case of the 5 kW arcjet, spatial discrimination is obtained by translating the collection optics. A representative set of data for the 5 kW arcjet is illustrated in Figure 2. Here we plot the H_α lineshapes for a range of arcjet specific power. In this figure, we draw your attention to the notable increase in the width of the spectral line. This reflects an

152

increase in the electron density. Also, we note that the absorption feature near line center is on the opposite side of the peak, in contrast to the simulations shown in Figure 1. This discrepancy is attributed to an anomalous stark shift associated with the Balmer series transitions not accounted for in the simulation.

Figure 3 summarizes our most recent results for the arc root electron density variation with specific power. Also shown in this figure are single-fluid model calculations from Olin Aerospace Co. Reasonable agreement between model predictions and experimental measurements are apparent. Figure 4 is a representative set of data depicting the directional spectral intensity as measured over the entire visible wavelength region, for three arcjet powers (mass flow rates of 18.5 mg/s). Also drawn in this figure is the predicted cathode gray body spectra for two cathode temperatures. At low specific powers (and hence lower electron number densities, cathode temperatures close to the melting point of tungsten accurately reproduce the continuum spectrum in the 500 - 650 nm range. It is clear however, that at higher specific powers, the continuum may have a strong contribution from free-free and free-bound electron transitions.

Future work will continue to focus on emission based measurements for internal arcjet diagnostics. In addition, we are in the process of extending our laser-induced fluorescence and spontaneous Raman measurements to measure flow properties in the expansion nozzle.

REFERENCES

1. G.W. Butler, B.A. Kashiwa, and D.Q. King, "Numerical Modeling of Arcjet Performance," AIAA 90-1474, 21st Fluid Dynamics, Plasmadynamics, and LasersConference, Seattle, WA, June 1990.

2. G.W. Butler, and D.Q. King, "Single and Two-fluid Simulations of Arcjet Performance", AIAA 92-3104, 28th Joint propulsion Conference, Nashville, TN, July 1992.

3. D.H. Manzella, F.M. Curran, R.M. Myers, and D.M. Zube; "Preliminary Plume Characteristics of an Arcjet Thruster"; AIAA-90-2645; 21st AIAA/DGLR/JSASS International Electric Propulsion Conference, July 1990.

4. J.G. Liebeskind, R.K. Hanson, and M.A. Cappelli; "Flow Diagnostics of an Arcjet Using Laser-Induced Fluorescence"; AIAA-92-3243; 28th AIAA/SAE/ASME/ASEE Joint Propulsion Conference, July 1992.

5. M.A. Cappelli, R.K. Hanson, J.G. Liebeskind, and D.H. Manzella; "Optical Diagnostics of a Low Power Hydrogen Arcjet"; IEPC-91-091; 22nd AIDAA/AIAA/DGLR/JSASS International Electric Propulsion Conference, October 1991.

6. D.R. Beattie and M.A. Cappelli, "Molecular Hydrogen Raman Scattering in a Low Power Arcjet Thruster", AIAA 92-3566; 28th AIAA/SAE/ASME/ASEE Joint Propulsion Conference, July 1992.

7. M.A. Cappelli, J.G. Liebeskind, R.K. Hanson, G.W. Butler, and D.Q. King; "A Comparison of Arcjet Plume Properties to Model Predictions"; AIAA-93-0820; 31st Aerospace Sciences Meeting and Exhibit, January 1993.
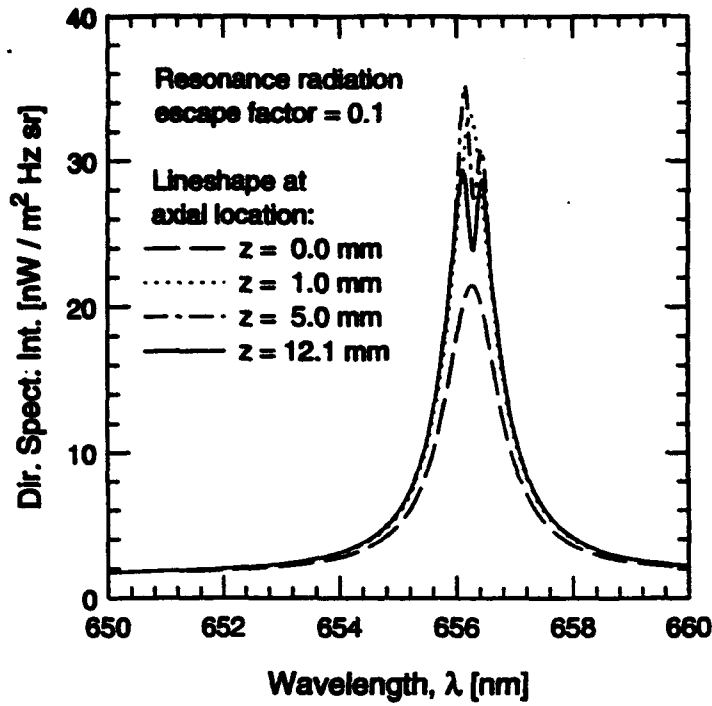
Fig. 1. Simulated Axial Emission Evolution Along Arcjet Centerline
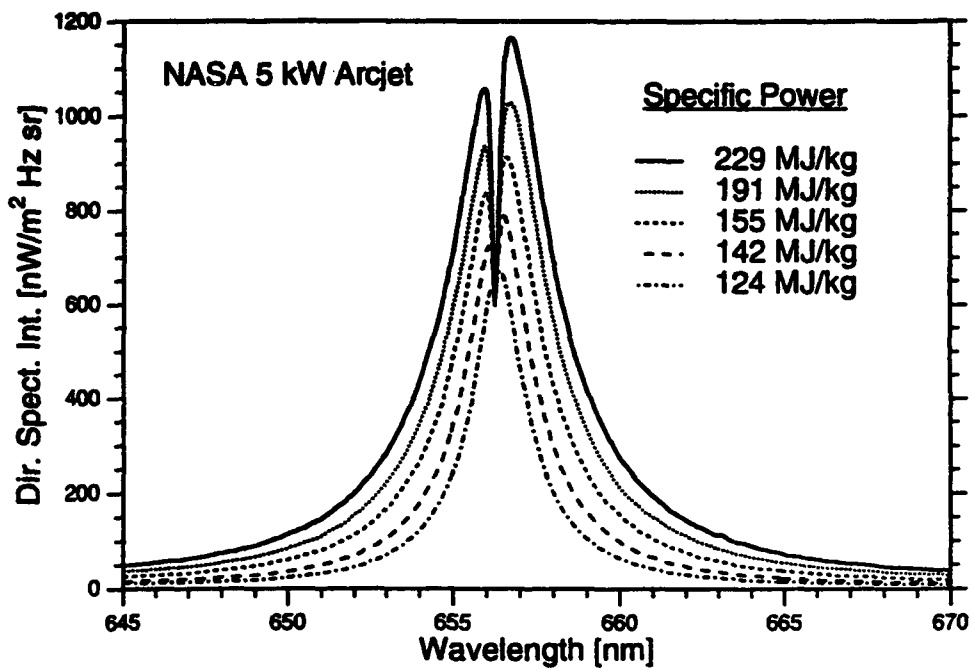
Fig. 2. H_α Axial Emission Line Spectra from a 5 kW Hydrogen Arcjet Thruster

154
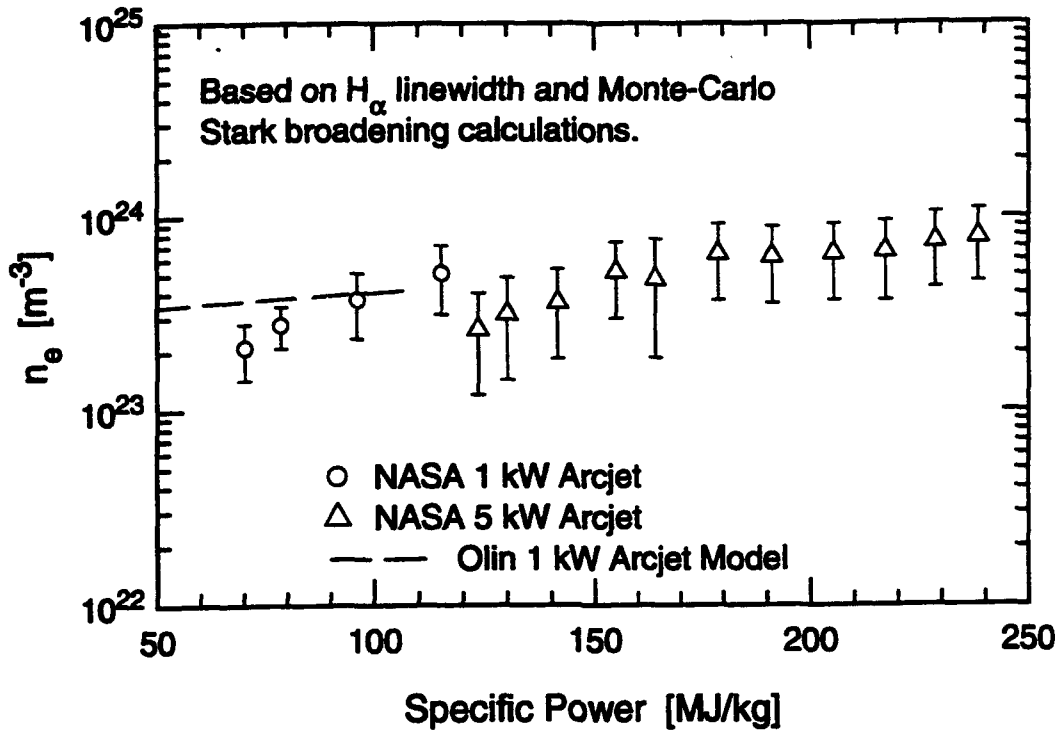
Fig. 3. Centerline Arc Root Electron Number Density
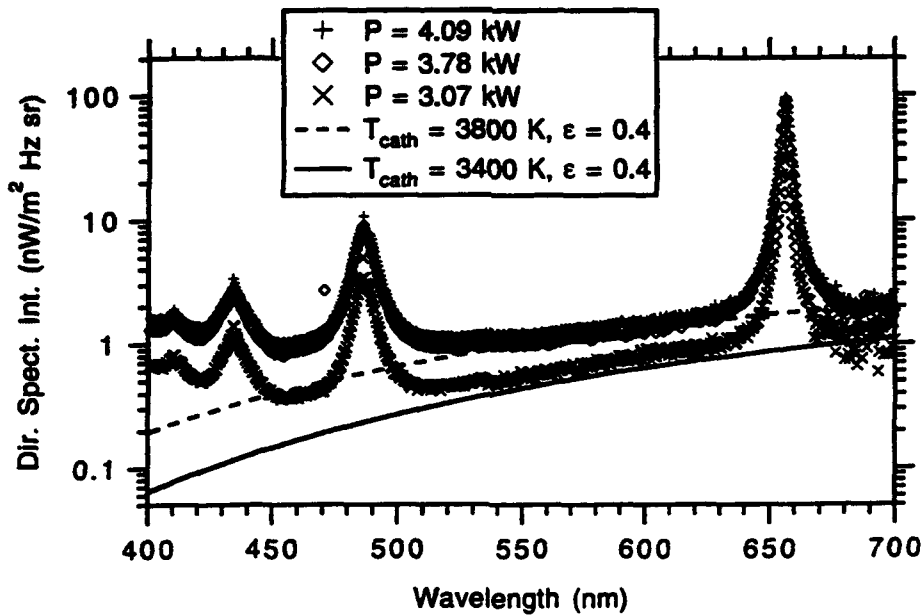
Fig. 4. Axial Visible Emission from a 5 kW Hydrogen Arcjet Thruster

ANOMALOUS IONIZATION AND THE MPD THRUSTER:
Investigations of the Critical Ionization Velocity (CIV) Phenomenon in Space*

PI's: Edgar Y. Choueiri, Robert G. Jahn and Arnold J. Kelly
Electric Propulsion and Plasma Dynamics Lab. (EEPDyL)
Princeton University
Princeton, NJ. 08544

1 Summary/Overview

We have been using analytical tools, computer particle in cell (PIC) simulations, observations made during active experiments in space and available experimental data to characterize the ionization mechanism in the MPD thruster. An understanding of the physics of ionization in plasma thrusters is of utmost importance since ionization losses are highly irrecoverable and are a major cause of inefficiency in many plasma thrusters. Using analytical tools we show that the experimentally measured ionization length in a typical MPD thruster is at least 10 times smaller than that calculated assuming Maxwellian statistics and is more consistent with distributions having suprathermal tail fractions and energies that could be produced by plasma microturbulence (i.e. anomalous ionization). In order to study this complex ionization mechanism we combine advanced PIC simulations and active space experiments. Active space experiments are ideal to stage plasma interactions involving turbulence-driven ionization, such as the critical ionization velocity (CIV) interaction, which can be monitored and studied using onboard plasma diagnostics. We have staged such interactions by performing neutral gas releases onboard the Russian APEX satellite. We analyze recent data from APEX and similar releases from another experiment called ATLAS-1. We use specialized PIC simulations to interpret these releases in order to gain the understanding required to develop experimentally verified ionization models. These models are intended to be included in state of the art MPD thruster fluid codes to improve their realism and accuracy.

2 Technical Discussion

The work described in this abstract is discussed in more detail in the following references: [1, 2, 3, 4, 5]

2.1 Background

Ionization represents a largely irrecoverable energy sink in magnetoplasmady-namic (MPD) thrusters. This is mostly due to the fact that, for typical temperatures and pressures of most plasma thrusters, the plasma flow through the chamber is essentially "frozen" with respect to recombination. Most recently, (1992) Randolph et. al. reported the results of a detailed spectroscopic study of ionization[6]. In that study, the ionization front was observed and its thickness measured at a few millimeters which was shown to be 1 to 3 orders of magnitude smaller than what would be consistent with a Maxwellian electron distribution.

The goals of our study are to investigate the fundamentals of anomalous ionization using analytical tools, active space experiments and PIC codes to develop experimentally verified models and to include the resulting models in state of the art MPD thruster fluid codes much like we did for anomalous resistivity and heating in our previous AFOSR-sponsored work.

2.2 Analytical Work

We derived a prescription for the electron energy distribution function that allows the representation of suprathermal electron tails such as those produced by the nonlinear effects of plasma microturbulence. The details of our derivation can be found in ref. [7]. The model is specified by a bulk temperature T_B, a tail fraction μ, a tail energy scaling parameter and a tail spread parameter. Some sample distribution functions with tails are shown in Fig. (1) The parametric distribution function was combined with a multi-level atomic model of argon and used to calculate the reaction rates for 23 collisional excitation transitions from ground state by electron impact by applying a high-accuracy quadrature on the convolution integrands containing the appropriate cross-sections. The prime goal was the study of the parametric dependencies of the minimum ionization characteristic length on the tail parameters. Calculations are compared with the recent measurements of the dimensions of an ionization "front" observed in a low-power MPD thruster by Randolph et. al.[6]. Figure (2) shows results from these calculations along with the experimental bounds. It is thus clear that even under the most favorable conditions, Maxwellian electrons cannot account for the smallness of λ_i. It is also clear that at these conditions, tail fractions of the order of a few percent can bring down λ_i in the millimeter range that contains the experimentally measured values.

2.3 Insight from Active Space Experiments

The use of active space experiments to gain insight into anomalous ionization has been described in the abstract of last year's contractors meeting. We have finished the development of specialized software to decode and analyze teleme-try data. We have been analyzing particle, field and wave data rec   uring
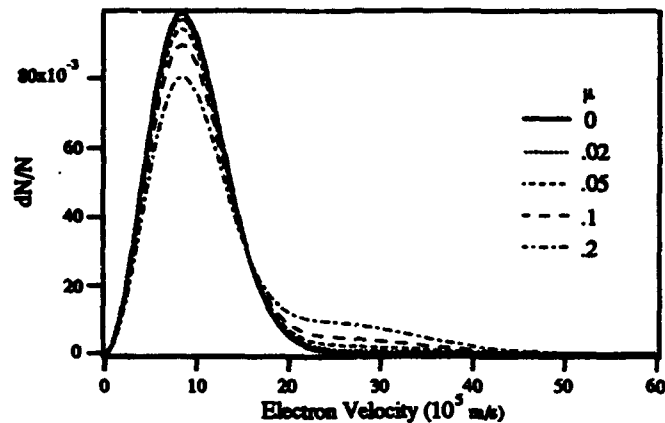
Figure 1: Adopted distribution model for a range of tail fractions, μ. Other conditions are specified in ref. [7].

active neutral gas injections from two space experiments. The first is called ATLAS-1 (conducted from the space shuttle in April 1992) and the second is APEX-CIV conducted from the Russian satellite APEX (the instrumentation we used is described in last year's abstract). While results from APEX are currently being reduced, we have reported our results on ATLAS-1 to-date in detail in refs [1, 3, 4, 5]. Results from both experiments will be presented at the contractors meeting. In brief, ATLAS-1 yielded wave, optical, and particle evidence of strong ionization with factor of 60 enhancement of plasma density over that of the ionospheric background. Whether this ionization can be attributed to plasma turbulence is a question being explored with PIC simulations.

2.4   Results from PIC simulations

We have developed a two-and-one-half-dimensional (two positions and three velocities) particle simulation model in order to study the neutral gas releases[2]. The electrons are assumed guiding center particles while the full dynamics of the ions (with real masses) are followed in time and space. Various ionization processes of the neutral gas including charge exchange and electron impact are included by means of the Monte Carlo technique. We showed that the model can be used to simulate the neutral gas interaction with the ionosphere up to a few millisecond using realistic experimental parameters within a reasonable computing time. The model was applied to study the critical ionization velocity (CIV) tests recently conducted as part of the Atlas-1 xenon gas releases from the the space shuttle. The simulation results show how suprathermal electrons produced by a beam instability of the lower hybrid mode, create, through electron impact, an ion population that exceeds that produced by classical (thermal) means, indicating the prevalence of a turbulence-driven (CIV-type) ionization mechanism.
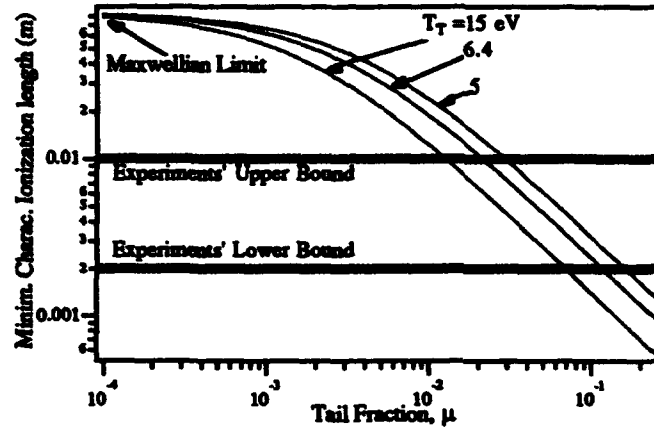
Figure 2: Calculated minimum values of λ_i as a function of the tail fraction. Experimental values from ref. [6]. Other conditions are specified in ref. [7].

References

[1] J.A. Marshall, J.L. Burch, E.Y. Choueiri, and N. Kawashima. CIV experiments on ATLAS-1. *Geophysical Research Letters*, 20(6):499–502, 1993.

[2] H. Okuda and E.Y. Choueiri. Numerical Simulation of Neutral Gas Release Experiments in the Ionosphere, 1994. Accepted for publication in *Physics of Plasmas*, to appear in July.

[3] E.Y. Choueiri and J.A. Marshall. CIV experiments on ATLAS-1 In the May/June Bimonthly Progress Report of the Electric Propulsion and Plasma Dynamics Laboratory. Technical Report MAE 1776.37, EPPDyL, Princeton University, 1992.

[4] E.Y. Choueiri and J. Marshall. Processing of wave data recorded during the CIV tests on ATLAS-1 In the November/December Bimonthly Progress Report of the Electric Propulsion and Plasma Dynamics Laboratory. Technical Report MAE 1776.40, EPPDyL, Princeton University, 1992.

[5] J.A. Marshall, J.L. Burch, E.Y. Choueiri, and N. Kawashima. CIV results from ATLAS-1: Comparison with models. In *1992 Fall Meeting of the American Geophysical Union*, page 411, San Francisco, CA, 1992. SA12A-3.

[6] T.M. Randolph, W.F. Von Jaskowsky, A. J. Kelly, and R. G. Jahn. Measurement of ionization levels in the interelectrode region of an MPD thruster. In 28th *Joint Propulsion Conference*, Nashville, TN, 1992. AIAA-92-3460.

[7] E.Y. Choueiri and H. Okuda. Anomalous ionization in the MPD thruster. In 23rd *International Electric Propulsion Conference*, Seattle, WA, 1993. IEPC-93-067.

A Comprehensive Investigation of Arcjet Operation

Principal Investigator: D. A. Erwin

Aerospace Engineering Department
University of Southern California
Los Angeles, CA 90089-1191

Summary

The primary objective of this research program is to provide measurements of key physical parameters in arcjet plumes. While a great deal of theoretical and numerical work has been done in the area of arcjet operation, there is a shortage of experimental data to validate such work. Furthermore, there are aspects of arcjet operation, such as frozen-flow losses, which are not convincingly explained by current theories. Experimental data may provide the necessary insight to understand such processes. Therefore, we have embarked on an effort to produce comprehensive measurements of flow density and velocity and electron temperature and density throughout the arcjet plume. Measurements of flow velocity and of electron properties have been made, and ongoing work is dedicated towards measuring heavy-particle density.

Technical Discussion

In order to properly understand the physics of arcjet operation, and to construct and verify numerical models, it is necessary to measure experimentally certain physical parameters of the arcjet flow. The current effort at USC is aimed at measuring four important parameters in the arcjet plume: heavy particle number density and velocity and electron number density and temperature. The ultimate goal is to produce a complete and accurate map of the values of these parameters throughout the plume.

Our original plan was to use pulsed electron-beam fluorescence to measure neutral-particle density, Thomson scattering for electron density and temperature, and emission-ripple velocimetry for flow velocity. The pulsed electron-beam fluorescence (PEBF) work is currently underway, and initial results are expected shortly. In the interest of determining time-resolved electron densities and temperature, a triple Langmuir probe technique was employed rather than Thomson scattering. Finally, the emission-ripple velocimetry technique was expanded to a more general form, called current modulation velocimetry (CMV). The initial results of the Langmuir probe and CMV studies were presented last year at IEPC-93, and more comprehensive results are now available.

1. Pulsed Electron-Beam Fluorescence

One of the most difficult problems in understanding the physics of arcjet operation is determining the density of various atomic, molecular, and ionic species in the plume. Conventional diagnostic techniques, such as laser-induced fluorescence and emission spectroscopy, cannot easily provide such measurements, and without species-specific density measurements it is difficult to determine the magnitude and nature of frozen-flow losses in the arcjet nozzle flow. Thus, a new diagnostic method is required.

Electron-beam fluorescence using continuous, low-current beams has been a common technique for several decades, and is capable of measuring species-specific density.[1] Electron impact with particles in the flow field creates excited states which radiate at various wavelengths. This fluorescence is collected and analyzed. The wavelength of the fluorescence signal is a function of the electronic configuration of the radiating particle,

160

and is therefore different for each species. The intensity of the fluorescence at a particular wavelength is proportional to the density of particles of the appropriate species in the flow field. However, it is limited to extremely rarefied flows due to problems with beam divergence and collisional quenching.

We have recently explored the use of pulsed, high-current electron beams as a rarefied flow diagnostic technique.[2] This overcomes both objections to the use of electron-beam fluorescence at higher densities. The high current density causes a self-focusing effect, due to the creation of a narrow channel of positive ions surrounded by a sheath of scattered electrons, and the short pulse length allows measurement of peak emission before collisional effects can affect the results. We believe that the use of pulsed electron-beam fluorescence (PEBF) can provide the species-specific density measurements needed for a more complete understanding of arcjet flow physics.

In order to verify the effectiveness of PEBF in this application, a series of measurements will be taken in the plume of a 1-kW helium arcjet provided by Aerospace corporation, similar to the standard NASA-Lewis design. The electron beam is generated by a pseudospark discharge, producing a beam with peak currents of hundreds of amps and a pulse length of tens of nanoseconds. Beam diameter at the test area, and thus the spatial resolution of the technique, is approximately one millimeter. The beam will be generated downstream of the arcjet and introduced to the arcjet along the centerline, and the collection optics mounted perpendicular to the arcjet to minimize any Doppler shift of the fluorescence signal. For the initial tests, the fluorescence signal will be detected by a photomultiplier tube, with narrow-band filters excluding all but the 501.7nm Helium line.

The fluorescence signals measured during the experiment will be normalized by electron-beam current and compared to calibration benchmarks obtained by passing the electron beam through a chamber containing a static gas of known density and composition, using the same collection optics and experimental geometry. Preliminary calculations suggest that the total fluorescence signal in the probe volume in the 10ns period following excitation will be approximately 6.0×10^8 photons for a local number density of 10^{16} cm^{-3}. This signal is well above the expected background, and occurs at a timescale small compared with the quenching timescale of 300ns. Theoretical calculations also confirm that the beam will self-focus in the density regime under consideration, and beam divergence or attenuation will not be a problem[3].

Currently, the pulsed electron gun is being tested in a dedicated test and calibration facility. This allows us to determine the proper operating parameters (discharge chamber pressure and voltage) of the electron gun, and conduct a preliminary calibration, without requiring the use of the main arcjet chamber. This chamber, consisting of a 1.5m diameter vacuum tank with a 6,000cfm roots-stokes pump combination, is being overhauled to allow unrestricted arcjet operation and diagnostics, including both PEBF and thrust stand measurements.

It is expected that both the chamber overhaul and the initial electron gun tests will be completed shortly. At this point, we will be able to attach the electron gun to the main test chamber. A vacuum isolation system will allow the gun to be operated under optimum conditions regardless of the conditions in the test area, and we will then proceed to conduct a final calibration. At this point, it will be possible to measure the density at points in the plume, with the ultimate goal of making a complete density map. Initial measurements will be made only for atomic helium, due to the ease of calibration.

Once the technique is verified, more comprehensive measurements will be taken. This will include observations of other species in the plume, as well as observation of 1-kW and possibly 30-kW hydrogen and ammonia arcjets. The technique will be used in conjunction with species-specific velocimetry (laser-induced fluorescence or current modulation velocimetry) to obtain the species-specific momentum flux.

2. Triple Langmuir Probe Measurements

At the Phillips Laboratory site, a triple Langmuir probe[4,5] was used to measure the electron temperature and electron density during the PPU switching cycle. The technique used to interpret the triple probe results and the

161

explanation of triple probe theory is principally taken from Tilley et al.[4] The triple probe technique was chosen due to its simplicity of data reduction and its ability to instantaneously follow fluctuations of the plasma properties in the arcjet plume. A triple probe consists of three Langmuir probes that are electrically set up so that no voltage potential sweeps of the probes are required. Since curve fitting is not needed, data analysis is also much easier than for single or double probe techniques. This is believed to be the first use of a triple probe on an arcjet; in reference 4, MPD thruster plumes were investigated.

Shown in Figure 1 is a comparison of how four arcjet operating parameters behave as a function of time: electron temperature, electron density, arcjet current modulation and the observed plume emission ripple of the Hα line. The modulation in the current delivered to the arcjet causes time-dependent variations in other operating parameters. The PPU current amplitude varies about 20% (p-p) around the mean value of 8.2 amps and modulates with the PPU switching frequency of 16.6 kHz. The electron temperature is observed to vary over a 20% range about the mean while electron densities fluctuate about 7% throughout the typical modulation cycle. Note that the current modulation, electron temperature and plume optical signals are all at the same frequency and almost in phase. A time delay between current ripple and both the observed electron temperature and plume emission fluctuations, which were observed at an axial location 2.5 cm downstream of the nozzle exit, is to be expected. There is approximately a 5.2 μsec delay as the gas is convected downstream from the principal arcjet heating zone just in front of the cathode tip. The electron number density, although also strongly correlated with current, is 180° out of phase with the electron temperature. However, the observed plume emission is in phase with the electron temperature fluctuations. These observations imply that the electron temperature drives the excited state populations.

3. Chamber and PPU Effects / Current Modulation Velocimetry

In our previous work[6] a velocity diagnostic called emission ripple velocimetry (ERV) was presented. In ERV, local optical emission oscillations are observed in the plume which are a result of current modulations from a high frequency switching power supply. Measurement of the delay of the emission signal with respect to the current waveform, as a function of axial position, allowed the axial flow velocity (averaged over the distance between two successive observation stations) to be calculated.

ERV, as implemented in reference 6, had two disadvantages which limited its usefulness:
   1. An ERV measurement can only be obtained in the presence of significant high-frequency current ripple. It is thus inappropriate for use with, e.g., traditional ballasted welding power supplies.
   2. The emission signals at different axial stations were obtained at different times (only one detector was used). Velocities so obtained must be time-averaged in order to be meaningful.

We developed a modification to the ERV technique, which we call current modulation velocimetry or CMV, which avoids these difficulties. In CMV, ambient current ripple is not used. Instead, a current spike is superimposed on the arcjet current. The consequent spike in emission is observed simultaneously at two axial locations (using two detectors) separated by several millimeters. The current spike and the emission spikes are all of duration a few microseconds. The time delay between the emission spikes at the two locations can be resolved to about one nanosecond, leading to a velocity measurement whose accuracy is in the range 30–60 m/s for plume velocities of order 5–10 km/s; this accuracy is comparable to those of recent CW-LIF results.[7,8]

Note that the velocity measurements obtained with CMV, while still position-averaged over the detector separation (here, 3.29±0.05 mm), are instantaneous. We know of no other plume velocimetry technique which has this property. LIF measurements, for example, determine the absorption lineshape by scanning in laser wavelength, which takes a minimum of several seconds to determine a velocity. In principle, a Doppler-shifted emission lineshape could be recorded instantaneously by a spectrograph and a gated imaging detector, but we know of no plume measurements in which Doppler shifts have been so measured.

Using the current modulation velocimetry technique, arcjet plume velocity measurements were taken along the centerline as a function of background pressure. Velocity measurements for the lowest three pressure levels are

very similar between the nozzle exit and two cm downstream. At this location, velocities for the 40 mTorr level remain constant or even are observed to rise slightly while velocities for 150 and 300 mTorr can be seen to decrease out to 3.5 cm downstream. Velocity measurements for 1.5 Torr chamber pressure are substantially lower than for the other background pressures tested. As expected, the 800 mTorr velocity curve falls between the high pressure level and the three lower pressure levels.

The trend for all the curves in Figure 2, for axial velocity to decrease with distance from the nozzle, is consistent with the measurements of Liebeskind et al.[7]

Figure 3 presents the same data as Figure 2, for the lowest and highest pressure. Error bars are shown which represent one standard deviation of ten velocity measurements taken at separate times. We see that the plume velocity is not constant, but fluctuates by several percent or more.

References

1) E.P. Muntz, AGARDograph 132, December 1968
2) R.M. Wojcik, J.H. Schilling, and D.A. Erwin, AIAA-90-1515 June 1990.
3) J.H. Schilling. J.A. Pobst, and D.A. Erwin, IEPC-93-130 September 1993
4) D.L. Tilley, A.J.Kelly, and R.G. Jahn, AIAA-90-2667 July 1990
5) S.L. Chen and T. Sekiguchi, "Instantaneous Direct-Display System of Probe Parameters by Means of Triple Probe," J. Appl. Phys, Vol.36, No. 8, 1965 pp.2363-2375
6) R.A. Spores, J.A. Pobst, J.H. Schilling, and D.A. Erwin, AIAA-92-3238 July 1992
7) J.G. Liebeskind, R.K. Hanson, and M.A. Cappell,i AIAA-93-2530 June 1993
8) W.M. Ruyten and D. Keefer, IEPC-91-093 October 1991
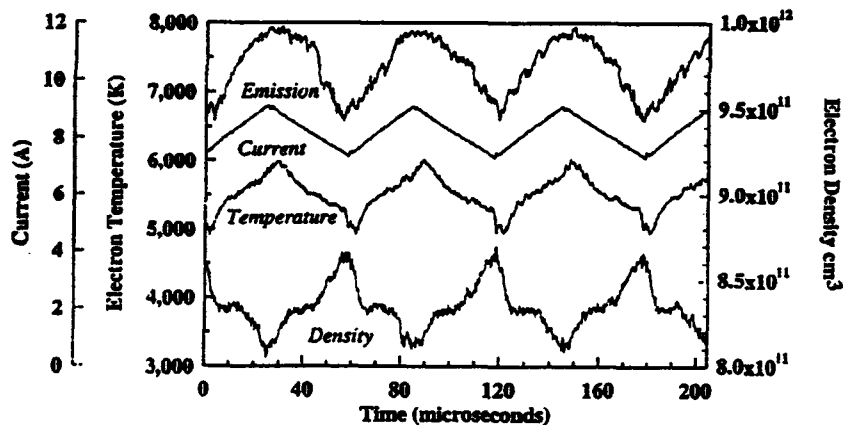
Figure 1
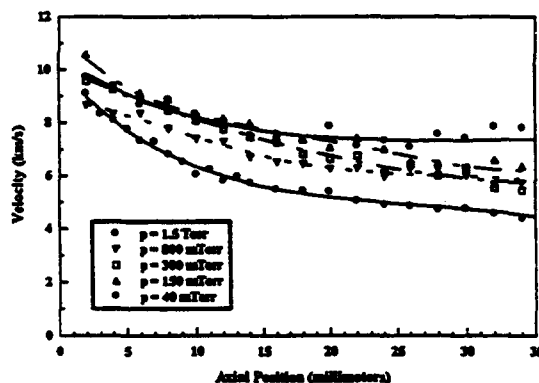
Figure 2
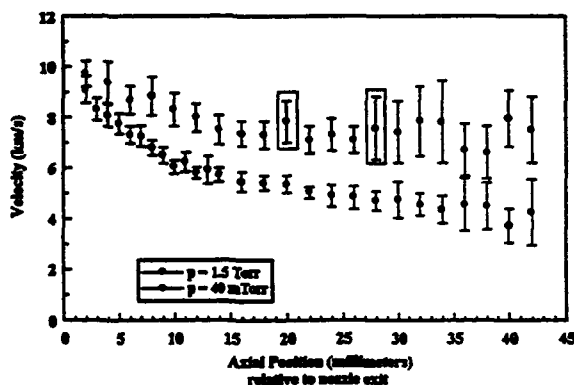
Figure 3

Electrostatic Ion Propulsion Using C60 Molecules
1993-1994 Research Program Overview

S.D. Leifer, D.G. Goodwin, J. Anderson, M. Anderson,
S. Srivastava, S. Trajmar, F.E.C. Culick
California Institute of Technology
Pasadena, California

Introduction

In the past year, the number of technical papers reporting research on the all-carbon molecules known as the fullerenes has continued to increase drastically. Knowledge of the chemical and physical properties of fullerenes, especially C_{60}, is growing. In this time, our research on the use of C_{60} molecules as a propellant for ion propulsion has progressed. While we have continued our investigations of electron impact induced behavior of fullerenes such as ionization, excitation and emission, our studies of C_{60} plasma discharge phenomena have received more attention.

Program Objectives and Accomplishments

Discharge Chamber Experiments

We have successfully sustained a C_{60}/C_{70} plasma in a filament cathode graphite wall discharge chamber for 45 minutes with a discharge voltage as low as 22 V. The ion beam extracted from this discharge was characterized with a crossed electric and magnetic field (EXB) probe. The resolution of this probe at high mass-to-charge ratios was not high enough to discern fullerene fragments, though C_2 and C_4 fragments were not observed. However, significant ion peaks corresponding to either CO, a known oxidation product of C_{60}, or N_2 are present, as well as a peak corresponding to CO_2. The background gas peak intensities decrease over the course of the experiments.

Filament erosion continued to be a severe problem. Hence, we have constructed a quartz walled RF discharge chamber for further experiments. The RF discharge chamber has been operated with Argon gas in initial experiments. The discharge chamber is not cooled, and will attain a wall temperature of approximately 400 °C without additional heating elements. Because of the lack of carbide-forming electrodes and quartz walls, we anticipate greater ease in sustaining a C_{60} plasma with this apparatus. Takegahara and Nakayama (1993) have prepared a C_{60} plasma by this technique.

An automated data acquisition system has been installed for long duration experiments. It simultaneously monitors beam current and voltage, discharge chamber and effusive cell temperatures, flow rate, and diagnostic probes. A residual gas analyzer has also been added to the system to monitor background gas levels. The RGA resolves ion mass up to 100 amu.

Mass flow rate measurements of fullerene into the discharge chamber were attempted unsuccessfully by measuring capacitance changes of the effusive cell as the fullerenes effused. The capacitance change due to thermal effects were of the same order of magnitude as the change due to loss of the C_{60} dielectric. We have since obtained a quartz crystal microbalance to perform calibrated mass flow measurements.

We have obtained an infrared spectrophotometer which we intend to use for ion beam analysis. The instrument is sensitive in the 4000 to 600 cm^{-1} range. Modifications to the EXB probe are also being made to improve resolution in the high mass range.

In addition to erosion of the cathode filament, a large quantity of toluene-insoluble material was found to remain in the effusive cell after long duration, high temperature runs. It was found that this material was amorphous carbon thought to be formed as a result of reactions with entrapped water and solvents. However, annealing of samples prior to sublimation did not inhibit the fullerene breakdown. Annealing was performed at 200 °C for 12 hours prior to operation of the discharge. However, some reports (Milliken et al., 1991) state that toluene contamination of fullerene samples was present up to temperatures of 600 °C.

High Temperature Stability and Material Compatibility Tests

Between 600 and 700 °C, little disintegration of the fullerene material is observed. However, above 800 °C, the fragmentation becomes quite pronounced (Sundar et al., 1992). Such temperatures are necessary for high propellant flow rates. Other reports indicate that C_{60} should remain stable at much higher temperatures than those used in our experiments (Zhang et al., 1993 and Baum et al., 1992). We have started conducting experiments of thermal disintegration of fullerenes. Measured quantities of fullerene powder are placed in quartz tubes, and heated under Helium flow to 250 °C for 24 hours. The tubes are then vacuum sealed and placed in a tube furnace for various durations. After removal from the furnace, solvent is added to each tube and concentration of soluble material measured with FTIR spectroscopy. Because fullerene crystals may trap impurities via "clathrate type" intercalation (Kamaras et al., 1993), the tests are also being conducted by vacuum deposition of fullerene film into the quartz tubes. Furthermore, the effect of various materials on fullerene decomposition is being investigated by the addition of samples to the tubes.

IR Spectroscopy of Fullerenes

The first publications showing IR absorption spectra of C_{60} (Kratschmer et al., 1990 and Kamaras et al., 1993) showed, in addition to the four main dipole peaks theoretically predicted, a moderate intensity peak in the region where CO_2 twin features are typically observed. Indeed, these features which appear at 2349 cm^{-1} and 2328 cm^{-1} were attributed

to CO_2 adsorbed by the fullerene. However, the peaks are shifted and their relative intensities switched from commonly observed CO_2 contamination features.

To investigate this discrepancy, we performed diffuse reflectance fourier transform infrared spectroscopy on fullerene samples prepared by three separate techniques: films formed on KBr by vacuum evaporation, freshly formed fullerene containing soot transported with ascerite (a CO_2 absorber), and purified C_{60} obtained from MER corporation dissolved in CS_2. Though each of the samples should have been free of CO_2 contamination, the twin peaks were present in all three spectra with the same relative intensity. Therefore, we believed that the features were due to either combination modes or vibrational modes allowed by the presence of ^{13}C isotope.

Several papers have since been published (Chase, et al., 1992, Wang et al., 1993) which show C_{60}'s very rich vibrational spectrum. Theoretically predicted modes are assigned to each observed peak, including those originally attributed to CO_2. However, these peak assignments have not yet been confirmed by analysis of isotopically enriched or isotopically pure fullerenes. We have attempted formation of pure ^{13}C fullerenes by laser vaporization techniques, but found no toluene extractable material in the soot. Subsequently, we attempted to form isotopically enriched fullerenes by the arc method. Hollow graphite rods were packed with amorphous ^{13}C powder mixed with a carbon binder. Though fullerenes were produced from these rods, no peak shifting or growth was observed in the spectrum. We believe that only the graphite portions of the rod actually vaporized and contributed to fullerene formation. We are continuing our attempts at producing isotopically pure fullerenes by compressing amorphous carbon powder at high temperatures to form rods for arc method fullerene production. This technique has been successfully employed (Kratschmer, Fostiropoulos, and Huffman, 1990) to demonstrate peak shift of the four main dipole peaks of C_{60}.

We also obtained 99.97% pure C_{70} from Term Ltd. to examine its vibrational structure and to have a standard for comparison with the C_{60} samples. In this way, C_{70} impurities contributing to the IR spectra of the C_{60} samples could be detected.

Luminescence of Gas Phase C_{60}

Experiments performed to determine UV and visible luminescence from gas phase fullerenes subjected to electron impact were performed. It has ince been determined that the emission features observed in these experiments resulted from water and its associated fragments, again indicating the tendency of C_{60} to trap water upon crystallization. In fact, no emission features in the UV or visible spectrum can be attributed to C_{60} from these investigations.

References

T. Baum, S. Loffler, P. Loffler, "Fullerene Ions and Their Relation to PAH and Soot in Low-Pressure Hydrocarbon Flames," Int. J. of Phys. Chem., Vol 96 (7), pp. 841-857, 1992.

B. Chase, N. Herron, E. Holler, "Vibrational Spectroscopy of C_{60} and C_{70} Temperature dependent Studies," J. Phys. Chem., Vol. 96 (11), pp. 4262-4266, 1992.

K. Kamaras, L. Akselrod, S. Roth, Mittelbach, W. Honle, H.G. von Schnering, "The Orientational Phase Transition in C_{60} Films Followed by Infrared Spectroscopy," Accepted, Chemical Physics Letters, 1993.

W. Kratschmer, K. Fostiropoulos, D.R. Huffman, "The Infrared and Ultraviolet Absorption Specta of Laboratory-Produced Carbon Dust: Evidence for the Presence of the C_{60} Molecule," Chem. Phys. Lett., Vol. 170 (2,3), pp 167-169, 1990.

W. Kratschmer, L.D. Lamb, K. Fostiropoulos, D.R. Huffman, "Solid C_{60}: a New Form of Carbon," Nature, Vol. 347, 1990.

J. Milliken, T.M. Keller, A.P. Baronavski, S.W. McElvany, J.H. Callahan, H.H. Nelson, "Thermal and Oxidative Analyses of Buckminsterfullerene," Chem. Mater., Vol 3, pp. 386-387, 1991.

C.S. Sundar, A. Bharathi, Y. Hariharan, J. Janaki, V. Sankara Sastry, T.S. Radhakrishnan, "Thermal Decomposition of C_{60}," Sol. State Comm. Vol. 84 (8), pp 823-826, 1992.

H. Takegahara, Y. Nakayama, "C_{60} Molecule as a Propellant for Electric Propulsion," 23rd International ELectric Propulsion Conference, IEPC-93-032, Seattle, WA September 1993.

K.A. Wang, A.M. Rao, P.C. Eklund, M.S. Dresselhaus, G. Dresselhaus, "Observation of Higher Order Infrared Modes in Solid C_{60} films," Phys Rev. B, Vol. 48 (15), pp 11375-11380, 1993.

B.L. Zhang, C.Z. Wang, C.T. Chan, K.M. Ho, "Thermal Disintegration of Carbon Fullerenes," Phys. Rev. B, Vol. 48 (15), pp11381-11384, 1993.

PARTICLE-IN-CELL AND MONTE CARLO MODELING OF ADVANCED PLASMA THRUSTERS

AFOSR Grant Contract No. F49620-93-1-0317

Principal Investigator:
Daniel Hastings

Massachusetts Institute of Technology
Department of Aeronautics & Astronautics
77 Massachusetts Avenue, Room 33-207
Cambridge, MA 02139

SUMMARY/OVERVIEW:

In order to confidently integrate advanced plasma thrusters on future spacecraft, it is vitally important to assess their backflow contamination potential. Currently, there is no accurate predictive capability to determine the impact of plasma thruster-spacecraft interactions. We employ the hybrid electrostatic plasma particle-in-cell (PIC) method to simulate the transport of low energy ions that are transported from the plume into the backflow region around a spacecraft. Due to the large-scale nature of the problem, we are harnessing state-of-the-art parallel computers, and are able to make backflow predictions over 3-dimensional realistic spacecraft.

AUTHORS:

Daniel Hastings and Robie SamantaRoy,
MIT Department of Aeronautics and Astronautics

Steven Taylor
CalTech
Department of Computer Science

TECHNICAL DISCUSSION:

With renewed interest in electric propulsion for a number of planned missions, as well as station keeping applications for geostationary communication satellites, the important issues of spacecraft contamination are receiving increased attention. For example, in ion thruster plumes, a low-energy plasma is created by charge-exchange processes, and can expand around a spacecraft leading to a current drain on high voltage surfaces. The enhanced plasma density can also lead to attenuation and refraction of electromagnetic wave transmission and reception. In addition, many thrusters emit heavy metal species, both charged and uncharged, due to erosion which can easily adhere to spacecraft surfaces. It is vitally important to understand and predict the backflow transport of these species from the plume onto a spacecraft. Thus, a clear understanding of the plumes of electric propulsion thrusters and the transport of contaminating effluents in them is necessary. Backflow contamination can lead to sputtering and effluent deposition that can affect such aspects of the spacecraft as solar arrays, thermal control surfaces, optical sensors, communications, science instrumentation, general structural properties of materials, and spacecraft charging. This is illustrated in Fig. 1

We are currently developing a numerical model of an ion thruster plume. We have chosen ion thrusters due to their maturity and the relatively large data base with which to

compare our results with. One issue associated with ion thrusters is that complete ionization can not be achieved with reasonable levels of power, and hence, neutral gas is emitted at thermal speeds. We are interested in these slow neutrals because they charge-exchange with the fast beam ions producing fast neutrals and slow ions which can be influenced by local electric fields in the plume. The electric field structure in the plume, as seen in experiments[1] and in computational models[2], is radial, and hence the slow ions are pushed out of the beam and move back towards the spacecraft. The plasma particle-in-cell (PIC) technique is applied to the slow charge-exchange (CEX) ions produced in the beam and their transport in the region exterior to the beam. These CEX ions are transported into the backflow region and can present a contamination hazard for the spacecraft. The self-consistent electrostatic potential is determined by solving Poisson's equation over the entire computational domain.

Historically, PIC techniques have been applied to small-scale problems. However, we are harnessing the power of massively parallel computers, like the Intel Touchstone Delta, and have developed a fully three-dimensional PIC code that can simulate the backflow over an entire realistic spacecraft - a feat never before attempted. Our goal is to gain insight into the contamination process, and to accurately provide estimates of contaminating fluxes so that spacecraft designers can integrate electric propulsion thrusters unto spacecraft with a much higher level of confidence. As an example, in Fig 2 we show the nondimensional backflow current for an ion engine as a function of the ion beam current. This figure shows that the backflow is typically a few percent of the beam current. Note however that for 6 Amperes of ion beam current, this is a backflow of 10^{18} particles/sec. For a molecular diameter of a few Angstroms, then this backflow flux can cover areas of fractions of a square meter with monolayers of propellant and contaminants. We also see that the scaling of the nondimensional backflow current is not linear as might be expected based on the scaling of the charge exchange source term. This is because of the focusing effect of the potential as the current increases.

1) Carruth, M.R., A Review of Studies on Ion Thruster Beam and Charge-Exchange Plasmas, AIAA 82-1944, 16th International Electric Propulsion Conference, New Orleans, LA, Nov. 1982.
2) Samanta Roy, R.I. et al, Modelling of Ion Thruster Plume Contamination, IEPC 93-142, 23rd International Electric Propulsion Conference, Seattle, WA Sept. 1993.
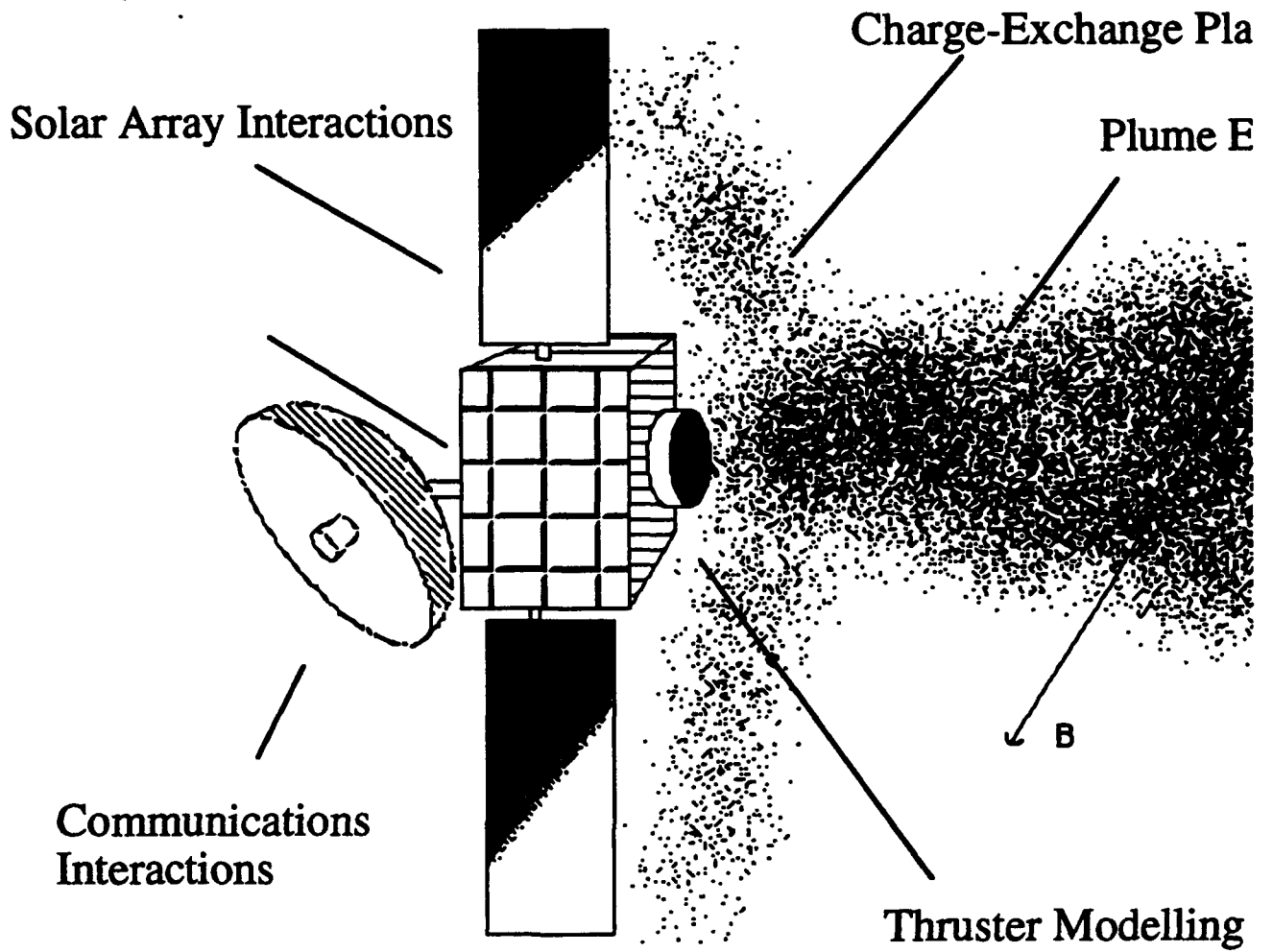
Fig. 1 Schematic of ion thruster spacecraft interactions

The labels in the figure read:

- Solar Array Interactions
- Communications Interactions
- Charge-Exchange Pla
- Plume E
- Thruster Modelling
- B
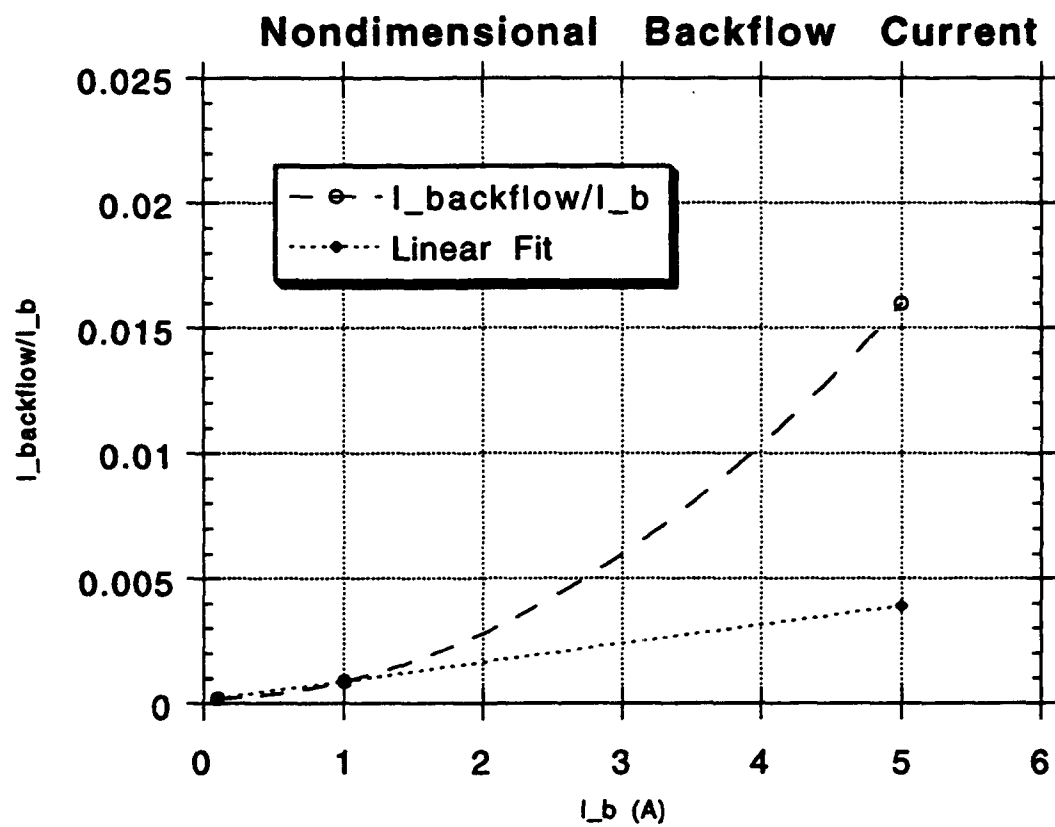
Fig. 2 Backflow Scaling with current

A HIGH THRUST DENSITY, C_{60} CLUSTER, ION THRUSTER[*]

V. Hruby[**]

BUSEK CO. INC.

19 Kearney Road

Needham, MA   02194

INTRODUCTION

Electrostatic thrusters require propellants with high atomic or molecular mass and low ionization potential.   A fullerene (C_{60}) has these and other important attributes which make it ideally suited to replace xenon (Xe) as the preferred ion thruster propellant.   Fullerenes are recently discovered carbon   molecules that in their atomic arrangement resemble the geodesic dome designed by Buckminster Fuller.   A C_{60} fullerene ion thruster has the potential to achieve unprecedented performance.   It could deliver up to 30 times larger thrust density than Xe fueled thruster while simultaneously reducing the relative losses by a factor up to 5.5.   This makes it suitable for current ion thruster missions as well as future multimegawatt interplanetary missions where it would function as the main thruster.

During the initial stage of the program (Phase I SBIR), the basic feasibility issues were addressed.   This included experiments in vapor generation and control, electrode poisoning, fragmentation of C_{60} upon ionization and acceleration.   A schematic of the apparatus is shown in Fig. 1.   It was shown that fullerene vapor mass flow can be controlled, discharged in pure fullerene vapor was demonstrated and that C_{60} fragmentation occurred only in overheated locations that experienced temperatures exceeding 800°C.[1]   This proved the basic feasibility of the fullerene ion thruster.

---

[1] V. Hruby, et al., "A High Thrust Density, C_{60} Cluster, Ion Thruster," 25th AIAA Plasmadynamics and Lasers Conference, Paper No. 94-2466, June 1994.

BUSEK

The greatest difficulty was encountered with the cathodes which were made of spiraled 2% thoriated tungsten wire. The cathodes were bombarded and coated by fullerene ions which degenerated into graphite cutting down on emission while shortening the cathode life. Similar problems are anticipated with hollow cathodes operating on C_{60}. Thus, cathode investigation and alternative methods of fullerene ionization (e.g., electron cyclotron resonance) are the initial subjects of investigation in the current Phase II SBIR effort that was recently started.

PROGRAM OBJECTIVES

The overall Phase II program objective is to develop and construct a laboratory fullerene fueled ion thruster and perform experiments to explore its performance. The work is focused on cathodes and fullerene discharge phenomena and identification of preferred fullerene ionization methods.

CURRENT STATUS

The following work was accomplished since the initiation of Phase II work four months ago.

1) Hollow cathode to operate on fullerenes, xenon and argon with replaceable orifice has been designed and is being procured. Assuming that fullerene fed hollow cathode is not feasible, several alternatives are being investigated.

   a) Operating the hollow cathode on Xe (or Ar) at minimal mass flow.

   b) Assessing the effect of mixed Xe/C_{60} flow on the discharge and on the grid erosion which must necessarily be designed for C_{60} mass over charge ratio.

   c) Investigation of alternative electron sources for electron bombardment ionization of fullerenes.

   d) Investigation of electron cyclotron resonance (ECR) fullerene ionization as an alternative to electron bombardment.

BUSEK

2) Fullerene discharge chamber to be made of explosion bonded Cu/SST laminate was designed and is being procured.

3) Discharge chamber with electromagnets providing the cusp magnetic field distribution for better primary electron utilization is being designed.

4) Facility upgrade was designed and is being implemented. The experiment will be controlled by PC based control and data acquisition system. LabView generic software is being adapted for this purpose. Safe electrical floating of all power supplies and data acquisition equipment was the major challenge in this task.

5) Experiments to expand the fullerene vapor pressure database are being carried out using equipment designed and constructed during Phase I of the program. The objective is to obtain mass flow/vapor pressure data at 600, 650, 680, and 700°C for a given orifice size.

6) Subcontracts to McDonnell Douglas and SRI International to provide system analysis and fullerene analysis respectively were negotiated and put in place.
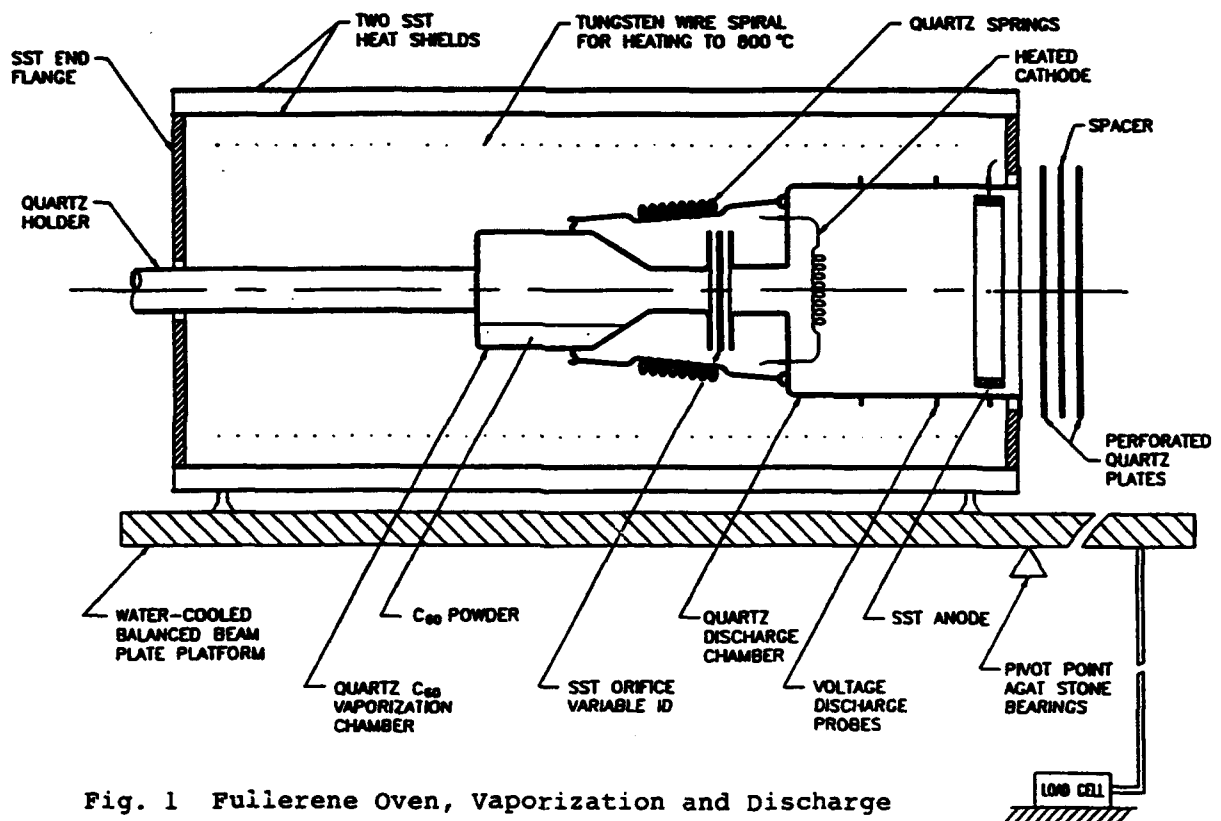

Fig. 1   Fullerene Oven, Vaporization and Discharge Chamber Schematic

174

BUSEK

LASER FLUORESCENCE DIAGNOSTICS FOR ARCJET THRUSTERS

Principal Investigator: Dennis Keefer

The University of Tennessee Space Institute
B. H. Goethert Parkway
Tullahoma, Tennessee 37388-8897

SUMMARY/OVERVIEW:

A multiplexed laser induced fluorescence (LIF) method is being used to provide accurate measurements of velocity and temperature in the exhaust flow of small arcjets. The narrow linewidth of a single frequency stabilized ring dye laser is used to measure the velocity distribution function of an excited state in the flow, which then determines the velocity and temperature. The laser beam is divided, then each beam is modulated at a different chopper frequency and recombined at an angle to provide a point measurement of two vector components of the flow velocity. Neutral excited state species of argon, hydrogen and nitrogen have been used to provide measurements near the exit plane of an argon arcjet and an arcjet operated with simulated ammonia and hydrazine propellants. These flowfield measurements have been compared with predictions from the UTSI numerical arcjet code. The measured velocity was larger than predicted for the hydrogen-nitrogen propellants and showed a velocity separation between the hydrogen and nitrogen constituents. A new, nonequilibrium, two-temperature plasma model has been incorporated into the UTSI code. Detailed comparisons with the LIF measurements will also require a computation of the plume expansion region downstream of the nozzle exit.

TECHNICAL DISCUSSION

A multiplexed LIF diagnostic method was developed to provide accurate measurements of the velocity distribution function of an excited atomic state in an arcjet exhaust plume. Point measurements of two velocity components are obtained simultaneously using a multiplex method. The beam from a frequency stabilized (Coherent 699-21) dye laser is split into two parallel beams, each of which is modulated at a different chopper frequency. The modulated beams are crossed at an angle to provide a measurement volume which samples two vector components of the velocity distribution function simultaneously. An absolute frequency reference is determined at the same time using the optogalvanic effect from the same atomic transition in a hollow cathode lamp. The narrow linewidth of the laser (approx. 500 kHz) provides an ultimate precision of approximately 1 m/s.

Extensive flowfield measurements were made in the exhaust flow of a small water-cooled arcjet operated with argon propellant to demonstrate the measurement technique [1]. We have now extended this method to excited states of hydrogen and nitrogen species, and made measurements on a NASA 1 kW arcjet using simulated ammonia and hydrazine propellants.

Experimental tests on our arcjet were conducted at NASA Lewis Research Center to establish to determine thrust and efficiency for comparison with the code predictions. High resolution emission spectra were recorded for the hydrogen-nitrogen arcjet to determine the chemical species present in the exhaust flow and provide an independent estimate of the temperature. These spectra were used to identify candidate excited nitrogen species to use in the LIF measurements. The Balmer alpha line of hydrogen is the only practical choice in hydrogen.

Large LIF signals could be obtained in the original experiments with argon, but the signals available from hydrogen and nitrogen were much weaker. To improve the signal-to-noise ratio, we moved the detector outside the chamber where a photomultiplier tube could easily be used. The signal was collected with a cassegrain telescope and passed through a 1.25 m monochrometer to provide wavelength filtering. Using this detection system it was possible to use different excitation and detection wavelengths with nitrogen to eliminate the problem of laser radiation scattered from optical elements and the arcjet nozzle.

The tunable dye laser used for these experiments has a maximum scan width of 30 GHz. This is comparable to the doppler width of the H-alpha line in arcjet flows and makes it difficult to accurately measure the shift and broadening of the several fine structure components of this line. The line width of nitrogen is smaller because of its larger mass and, therefore, it provides a better diagnostic. The $3s^4P - 3p^4S^\circ$ transition of nitrogen at a wavelength of 746.83 nm was excited by the laser, and the fluorescence emission at a wavelength of 744.23 nm was used for detection to eliminate problems associated with laser scattering. A typical measured doppler profile for both the perpendicular and angled beam is shown in Figure 1, together with the optogalvanic reference signal from a specially constructed hollow cathode lamp.

Axial and radial velocity profiles obtained using both hydrogen and nitrogen atoms are shown in Figure 2, together with the predictions from the UTSI equilibrium code. The axial velocity of the nitrogen is larger than the hydrogen, and both are larger than the code predictions. The radial velocity of hydrogen is larger than nitrogen, which agrees reasonably well with the code predictions. These data were taken approximately 1 mm downstream of the nozzle exit, and demonstrate the effects of the free-jet expansion past the nozzle, which is not modeled by the code.

Since the chamber pressure in these experiments was approximately 1 Torr, these data suggest that it may be necessary in a comprehensive arcjet code to model velocity separation of hydrogen and nitrogen species during nozzle expansion.

The UTSI code [2], developed under the sponsorship of NASA/LeRC, has now been modified to include finite rate chemistry, species diffusion and separate energy

equations for the electrons and heavy particles. Currently, the code uses only hydrogen for the propellant and has four species: molecular hydrogen, atomic hydrogen, positive hydrogen ions and electrons. There are several possible choices for the two energy equations used to determine the electron and heavy particle temperatures. We chose to use the electron energy equation and a separate equation for the static energy of the mixture of electrons and heavy species.

Chemical rate coefficients, with one exception, were taken from the work of McCay [3]. This exception is the rate of ionization of H atom by electrons which was calculated from ionization cross-section data. Ionization may occur by a two-step process where an electron first excites an H atom and this excited atom is then ionized by a collision with a second electron. This second process will be fast compared to the first because of the relatively small energy required to ionize an excited atom. To implement this effect without introducing a new species (excited H), the threshold energy for the ionization cross section was taken to be the excitation potential (10.2 ev) rather than the ionization potential (13.5 ev).

The nonequilibrium code has experienced some problems with convergence. We have relaxed some of the constraints used in the equilibrium version of the code, and have now obtained satisfactory convergence. Specifically, we have removed the fixed power constraint and the linear anode current assumption. The computation of the electromagnetic field in plasma codes are often plagued with consistency problems.

Typically, only two of the four Maxwell's equations are needed to calculate the electric and magnetic field. The curl of the electric field must vanish for a steady state problem, and tests of vanishing curl of the electric field revealed some numerical problems with our code which have now been corrected. Arcjet codes are under development in several other laboratories, but these codes are time dependent and require considerable computer resources. The UTSI code is a steady-state code and requires less computer time. Therefore, we are continuing to develop and refine this code.

REFERENCES

1. D. Keefer and W. Ruyten, "Laser Fluorescence Velocimetry of an Arcjet Exhaust Plume," AIDAA/AIAA/DGLR/JSASS 22nd International Electric Propulsion Conference, Viareggio, Italy, October 14-17, 1991, IEPC-91-093.

2. R. P. Rhodes and D. Keefer, "Comparison of Model Calculations with Experimental Data from Hydrogen Arcjets," AIDAA/AIAA/DGLR/JSASS 22nd International Electric Propulsion Conference, Viareggio, Italy, October 14-17, 1991, IEPC-91-111.

3. T. D. McCay and C. E. Dexter, "Chemical Kinetic Performance Loss for a Hydrogen Laser Thermal Thruster," J. Spacecraft, Vol 24, No. 4, 1987, pp. 372-376.
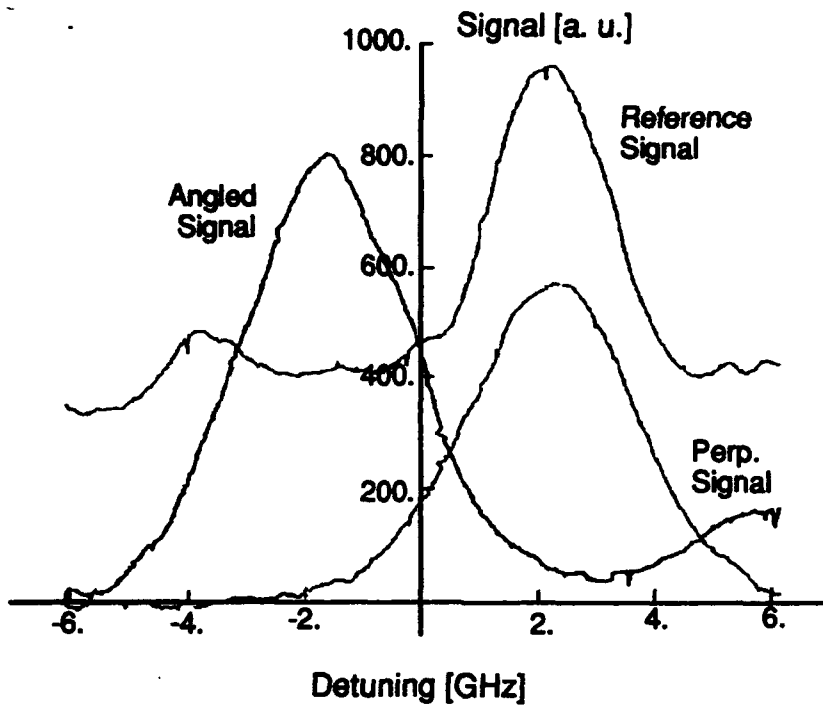
Fig. 1 Experimental LIF Signals from the Perpendicular and Angled Beams and the Optogalvanic Reference Signal.
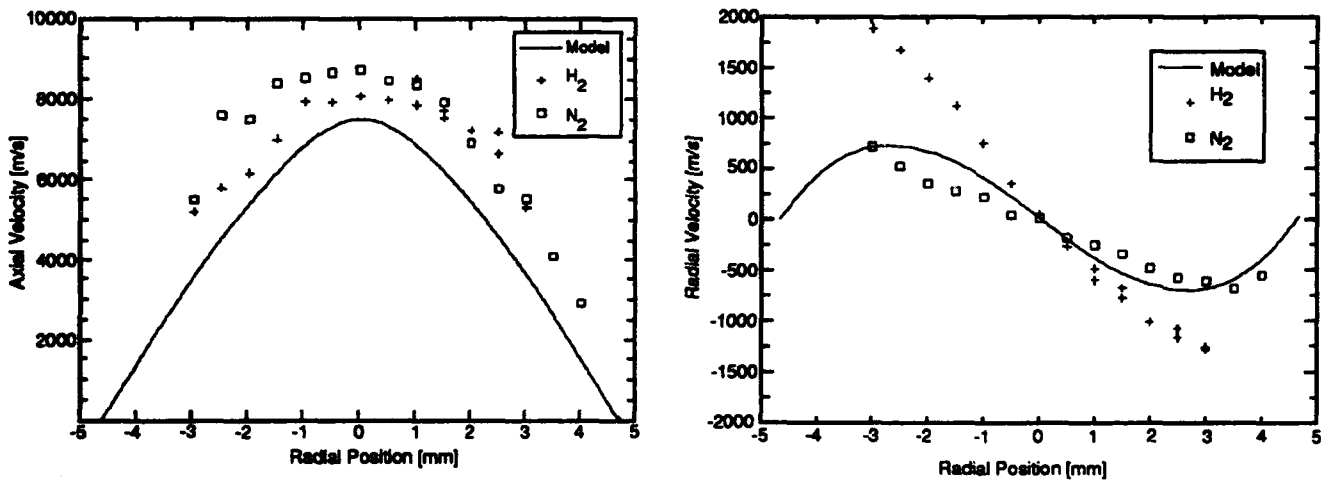
Fig. 2 Comparison of Computed and Measured Axial and Radial Velocities at the Nozzle Exit.

178

TWO TEMPERATURE MODELING
OF MULTICOMPONENT ARCJETS
WITH EXPERIMENTAL VALIDATION

Principal Investigators: Herman Krier and Rodney L. Burton

Department of Mechanical & Industrial Engineering
Department of Aeronautical & Astronautical Engineering
University of Illinois at Urbana-Champaign

Overview

The primary interest of the Air Force for electric propulsion is with storable propellants. Our research emphasizes a gaseous mixture of N_2 and H_2 for the simulation of hydrazine arcjets. Because the arcjet is a low Reynolds number (<1000) device, viscous behavior dominates energy transfer processes in the thermal and viscous boundary layers, which couple with multi-dimensional heat conduction in and from the massive conducting anode wall. Therefore, energy transfer must be described by coupled Navier-Stokes conservation relations and an electromagnetic heating equation, which depend on a complex way on the fluid properties.

Energy transport from plasma in the equilibrium constrictor region of the arcjet is a strong function of the number density distribution of electrons from ionized species. The diffusion of species, particularly electrons, is likewise important. The electric current distribution, not known, is strongly coupled to the n_e and T_e distribution in the vicinity of the relatively cold constrictor and anode walls. Here, non-equilibrium plays a dominant role in determining the spatial variation in the current attachment and anode heating. The proper description of this aspect of arcjet nozzle flow is the primary goal of the research.

All of the above factors vary significantly with power input (the scaling problem). Note that a given arcjet operates over a relatively narrow power range, and arcjets as a class begin to be unstable below ~0.5 kW. We feel that is important to perform experiments away from this stability limit; e. g. at 0.5 kW; e. g. at 1-3 kW. We also feel that a model, to be valid, must be successfully exercised over this power range.

The degree to which an imposed (applied) magnetic B field alters electron drift and hence current distribution and arcjet performance is not well understood, but can be used in conjunction with a numerical model to describe the complex physics of flow and energy transfer in this region of intense plasma heating. The applied field may be used to modify the current distribution in a predictable way, and can therefore be used as another independent variable to validate a numerical model.

We are concerned that the widespread use of the NASA 1 kW thruster may generate non-repeatable results, because of the poorly-defined heat transfer interface between

the nozzle and the body. We also note that the NASA thruster is not well adapted to interior diagnostics or anode heat transfer studies, and are implementing a new anode design.

The emphasis of the AFOSR program at UIUC is experimental, with our code validation as the primary goal. We are in the process of implementing a quadruple Langmuir probe, capable of n_e, T_e, and u measurements in the plume. We are also designing and implementing a fast response total enthalpy probe for measurements of heavy particle temperature in the plume. With a new anode we will measure T_e inside the nozzle and constrictor, using a novel Langmuir pin configuration (Fig. 1). Spectroscopic methods include line-to-line and/or line-to-continuum of seeded gases (e.g. xenon) by an optical multichannel analyzer (OMA).

Experimental Approach

Several diagnostic techniques are employed to validate the predictions of the computational model. Using a NASA 1 kW hydrazine arcjet, Langmuir probe techniques are employed in the plume at the exit plane. Multiple and single probe techniques are used to determine the electron temperature T_e, electron density n_e and the plasma streaming velocity (speed and direction). The flow divergence angle is measured with rotating single probes and fixed-angle probe techniques. Triple Langmuir probes (Chen and Sekiguchi, JAP, 1965), which can be rapidly swept through the plume, are used to determine T_e and n_e simultaneously (Fig. 2). The magnitude of the plume velocity is determined for certain flow conditions using the crossed double probe (Kanal, JPP, 1964) technique. Quadruple probes (Burton, DelMedico and Andrews, JPP, 1993), which combine the triple probe and crossed probe techniques for simultaneous determination of T_e, n_e and plasma velocity are ultimately used to characterize the plume region. Of paramount importance to these probe techniques is understanding the effect of two ionized species (nitrogen and hydrogen) on the ion probe current, and hence on the measured T_e, n_e and plasma velocity. Calculations show that measurements of T_e are unaffected by the presence of multiple ions, while the error in the measured values of n_e is expected to be ±5% due to the presence of the two ionized species. Effects due to the velocity slip due to diffusion are also being considered. The details of these analyses and experimental data will be presented at the 30th Joint Propulsion Conference (1994) as paper AIAA 94-3299, "Application of Multiple Electrostatic Probes in the Plume of a Low Power Arcjet."

Modeling/Interpretation of Experiments

With our present understanding of arcjet modeling, the thrust can be predicted fairly well; i. e., the models can predict the static pressure distribution in the nozzle. Voltage, electric field, and current distribution, however, are poorly understood. The UIUC model includes a self-consistent solution for the voltage; i. e., the anode potential is assumed, the voltage is determined from Poisson's equation, and the current is calculated from Ohm's Law. The volumetric ohmic heating, j^2/σ, determines where the energy is deposited, which in turn determines the electrical conductivity σ, which in turn determines and voltage and current distributions. With this scheme the arc attachment is coupled to the flow field.

180
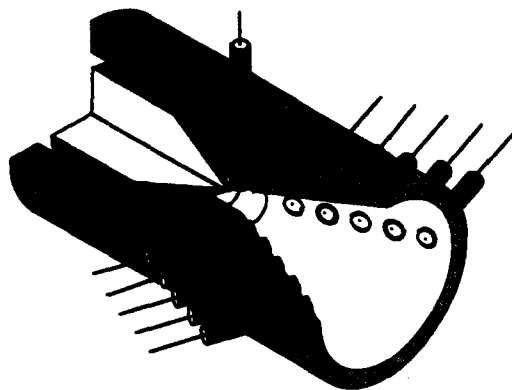
Fig. 1. New anode design with planar Langmuir pins for internal T_e measurements.
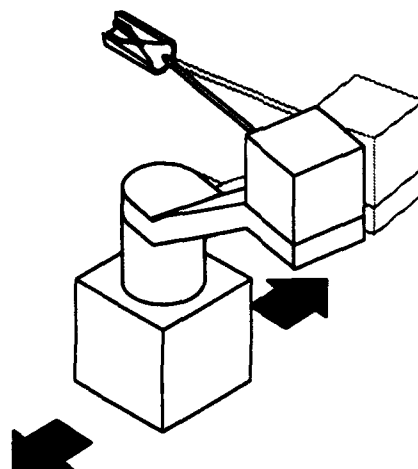

Fig. 2. Carriage for multiple probe diagnostics at the exit plane.

An improved 2 kW arcjet nozzle has been designed for internal probing of the nozzle. Flush-mounted single and double Langmuir pins (Fig. 1) are being employed to obtain n_e, T_e and j in the plasma viscous layer, to better understand the ohmic heating distribution and current symmetry inside the constrictor and nozzle regions, and permit model validation. Other diagnostics considered for model verification include static pressure measurements and emission spectroscopy probing of the constrictor.

The UIUC arcjet model is a steady-state, two-temperature, single-fluid model which includes flow swirl and anode heat transfer in a converging-diverging nozzle geometry. The model assumes plasma radiation to be optically thin. The gas is a combination of nitrogen and hydrogen written generically as $xN_2 + H_2$. Input parameters are x, the thruster geometry, mass flow rate, total applied current, and the inlet swirl angle.

The solution algorithm for the arcjet model is based upon the two temperature plasma model of Mertogul and Krier (AIAA 93-3224). Distinct energy equations for electrons and the gas yield separate electron T_e and gas T_g temperatures. Three scalar momentum equations yield the axial, radial, and azimuthal velocity fields. Species densities are computed assuming quasi-neutrality and two-temperature chemical equilibrium; the appropriate laws of mass action are solved along with a two-temperature equation of state. This allows a computationally efficient parametric investigation of various propellant mixtures.

We note that the electrical conductivity σ is strongly coupled to the electron temperature and number density fields. Ohm's law is combined with $\nabla \cdot j = 0$ to solve for the voltage and current distributions. An example of this is illustrated in Fig 3, where enclosed current contours are shown for an assumed analytical form for the conductivity of $\sigma = \sigma_{max}(x)\exp(-(r/r_{anode})^2)$. As we incorporate ohmic heating, radiation loss, and elastic energy transfer source terms into the electron and heavy particle energy equations, the electrical conductivity is calculated as $\sigma = \sigma(T_e, n_e)$ so that a fully coupled, self-consistent solution for the current distribution is obtained.

181

The j^2/σ term for this σ distribution is non-monotonic and suggests electron heating at the wall of the same order as that at the centerline of the constrictor.

The equations are solved iteratively using a finite volume method. The mass continuity and momentum equations are solved using the PISO algorithm. (Issa, JCP, 1985). These have been successfully solved for adiabatic flow. The results are shown in Fig. 4, where Mach contours are illustrated for a low Reynolds number (Re=117) nozzle flow. The results agree qualitatively with published results (Chung, et al., AIAA 93-0727) as the centerline Mach number increases to a peak value of M=2.4 at a downstream distance of x/R_{throat}=8; M then begins to decrease as the flow thermalizes due to viscous losses. Results will be presented at the 25th AIAA Plasmadynamics and Lasers Conference in June, 1994.
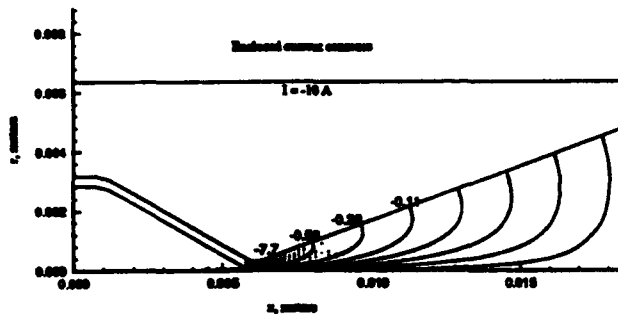
Fig. 3. Enclosed current contours for analytic form of electric conductivity σ.
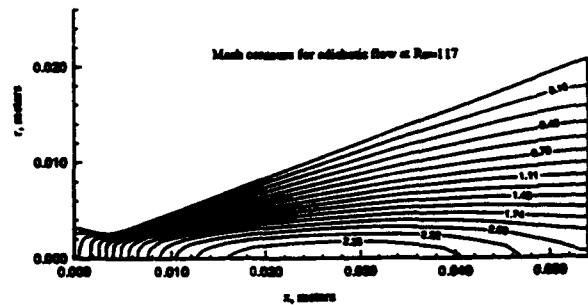
Fig. 4. Mach contours showing maximum in M at x/R_{throat}=8.

Research Applications

The proposed research will lead to improved efficiency and operation with storable arcjet propellants based on nitrogen and hydrogen. Scaling studies over a 1-3 kW range will validate numerical models over a power range, and permit extrapolation to 10 kW. Development of two new probe diagnostic techniques, both inexpensive, will benefit in-flight diagnostics of arcjet missions. Development of a new and inexpensive spectroscopic technique, coupled with an applied magnetic field, may lead to performance improvements for the constricted arcjet. In all of these efforts, modeling will be used to understand the results and lead the way to more efficient arcjets.

Reporting

Bufton, S. A., Burton, R. L. and Krier, H., "Application of Multiple Electrostatic Probes in the Plume of a Low Power Arcjert," to be presented at the 30th JPC, Indianapolis, 1994.

Megli T. W., Mertogul A., Krier H., and Burton R. L. "Two-Temperature Modeling of N_2/H_2 Arcjets," AIAA Paper 94-2413, to be presented at the 25th AIAA Plasmadynamics and Lasers Conference, June 20-23, 1994.

Investigation of Energy Distribution in the Interior of a 30kW class Arcjet

Principal Investigator: Ronald Spores

Air Force Phillips Laboratory
Rocket Propulsion Directorate
Edwards AFB, CA 93524

SUMMARY/OVERVIEW

The internal energy distribution of a 30kW class arcjet operating on ammonia is being investigated using emission spectroscopy. Analysis of the information determined from the hydrogen, NH, and nitrogen spectra will provide a clearer picture of the chemistry within the arcjet nozzle and lead to methods for improving overall efficiency. Optical access holes .020" in diameter were made at three axial locations in the nozzle region between the constrictor and nozzle exit plane. Spectroscopic measurements of excited state atomic hydrogen temperatures, electron density via stark broadening, nitrogen vibrational and rotational temperatures inside the arcjet nozzle are being conducted. As anticipated, results show that the expansion flow is in nonequilibrium.

TECHNICAL DISCUSSION

Over the past 10 years the Air Force has taken the lead in the development of a high power, 30 kW class arcjet for orbital transfer applications. In December 1995, the Air Force will be launching a space experiment, ESEX, to demonstrate a high power arcjet. As part of this effort, the Phillips Laboratory has been investigating various operational issues of concern, i.e. electromagnetic interference, arcjet ignition, spacecraft thermal loading and plume contamination due to high power arcjets. One of the more critical issues that needs to be addressed for the long term development of this technology is overall efficiency which directly correlates to the needed solar array size. A better understanding of the fundamental energy loss mechanisms in the arcjet is needed in order to increase efficiency and reduce trip times from LEO to GEO.

This research utilizes emission spectroscopy to obtain information about the internal energy distributions and temperatures along the length of the arcjet nozzle. This work will lend insight into: recombination rates, propellant enthalpy mixing between the central hot gas from the arc and cooler boundary layer flow, and heat transfer to the anode walls. Much of this work compliments that of Zube and Myers [1] who looked into the nozzle of a 1 kW arcjet through optical access holes. Our technique is similar with the exception that it employs a high power arcjet operating on ammonia propellant. Through comparisons of our work and reference 1 new insight into the differences in internal energy depositions of a 1 and 30 kW class arcjet hope to be obtained. The results of this effort will also be used to enhance the predictive capability of arcjet computational codes currently being developed by AFOSR.

The arrangement of spectrometer and collection optics for the emission spectroscopy system is shown in figure 1. The system consists of an Acton Research SP-500 0.5 m spectrometer with a 2400 holographic grating and a 384x576 CCD detector; approximately

20nm of the spectra could be viewed at once. Optical access holes have been placed at locations along the arcjet nozzle corresponding to expansion ratios of 6.6, 78 and 229, refer to figure 2. The farthest upstream hole is just 0.1" downstream of the constrictor with the other two holes equally spaced to the nozzle exit. In order to eliminate internal wall reflections into the optical access ports, holes were drilled straight through both nozzle walls.

Although the arcjet is capable of being run at power levels as high as 30 kW, tests are currently being carried out at levels closer to 15 kW due to the projected maximum power available onboard spacecraft over the next 10 years. Measurements are first being conducted in the nozzle exit plane with experiments through the optical access holes and into the arcjet interior to be starting shorlty.

Measurements already taken in the plume of the first 8 hydrogen Balmer lines reveal the typical arcjet nonequilibrium of the lower lines in the Boltzmann plot of figure 3. It is believed that this upper excited state temperature is in good agreement with the electron temperature. The underpopulation which is observed in the lower electronic levels is consistent with PLTE and it is anticipated that this will also be seen during a similar examination of nitrogen vibrational spectra. NH rotational temperatures will be determined by comparing experimental and analytical spectra of the P(0,0) band which is found to be sufficiently free of spectra overlap, refer to figure 4. The model of NH emission spectra which was used for these calculations was developed by R Welle[2]. Initial measurements have shown that two of the vibrational-rotational bands of the second positive series of nitrogen are sufficiently distinct to also measure the nitrogen vibrational temperature. Vibrational measurements taken to date at the exit plane, part of the spectra measured is shown in figure 5, indicate a temperature of 3700K.

Specific power (Power / mass flow rate) operating conditions of the ref. 1 arcjet was between 21- 25 MJ/kg while the thruster investigated here is operating at 63 MJ/kg. Due to this much higher specific power level, it is anticipated that there will be a number of differences in results as compared to Zube and Myers.[1] The higher specific impulse should lead to higher centerline temperatures for the high power arcjet. This result is partially bore out by comparing the farthest downstream temperature measurements of ref. 1, which was 3100K, to the exit plane results obtained here of 3800K. Just downstream of the constrictor, the measured temperature for ref. 1 was ~19000K, we anticipate measuring an even higher temperature at this location. An interesting observation in ref. 1 is that electron density increased with mass flow rate (a decrease in specific power); the higher mass flow is thought to cool and constrict the arc, thus driving both the centerline temperature and ionization up. Another observation is that higher recombination rates occur with increased mass flow, as expected. The extent to which changes in the mass flow, or specific power, affect the energy distribution in the 30kW class arcjet is likewise being investigating here. We are also interested in how the longer nozzle length of this study enhances the recombination process.

1.   Dieter Zube, Roger Myers, "Nonequilibrium in a Low Power Arcjet Nozzle", AIAA 91-2113, 27th Joint Propulsion Conference, June, 1991, Sacramento, CA.
2.   M. Crofton, R. Welle, S. Janson, R Cohen, "Rotational and Vibrational Temperatures in the Plume of a 1-kW Ammonia Arcjet", AIAA 91-1491, 22nd Fluid Dynamics, Plasma Dynamics and Lasers Conference, June 1991, Honolulu, Hawaii.
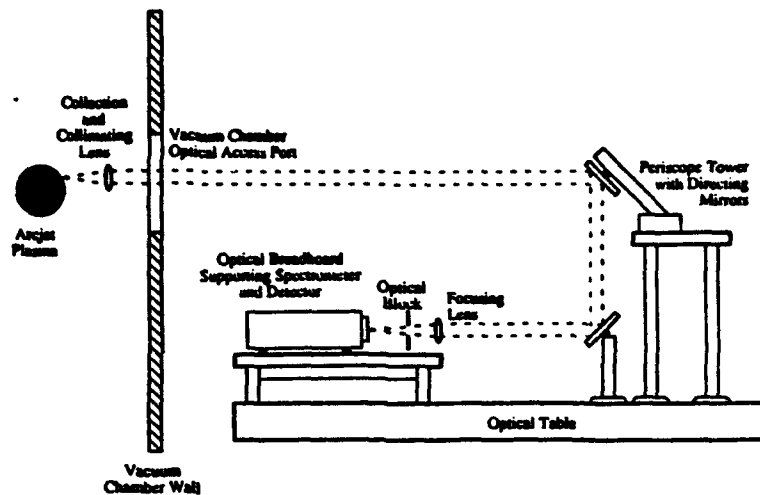
Fig. 1. Emission Spectroscopy Experimental Setup
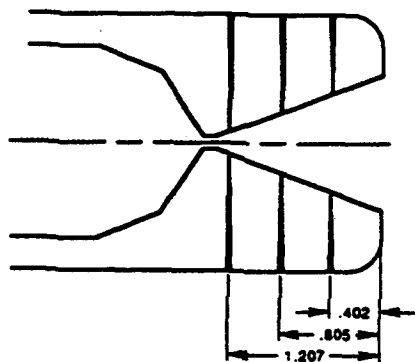
Fig. 2. Arcjet Nozzle with Optical Access
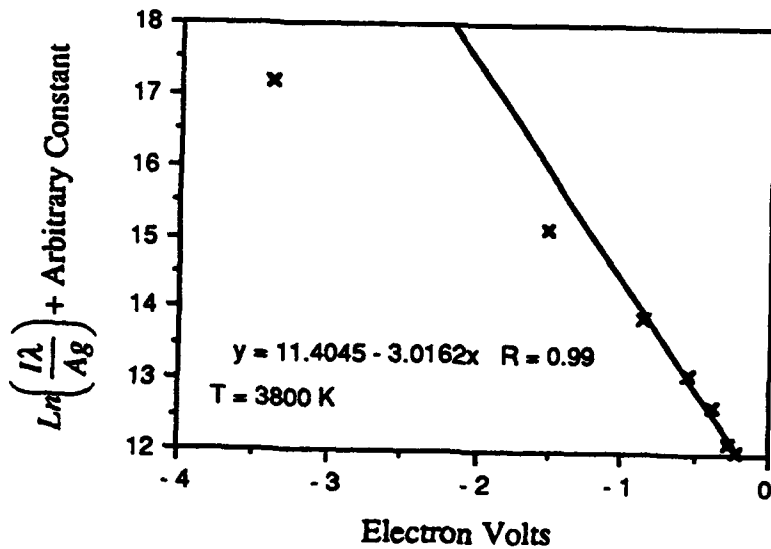
Fig. 3. Boltzmann Plot of Hydrogen Balmer Series
5 mm Downstream of Exit Plane

185
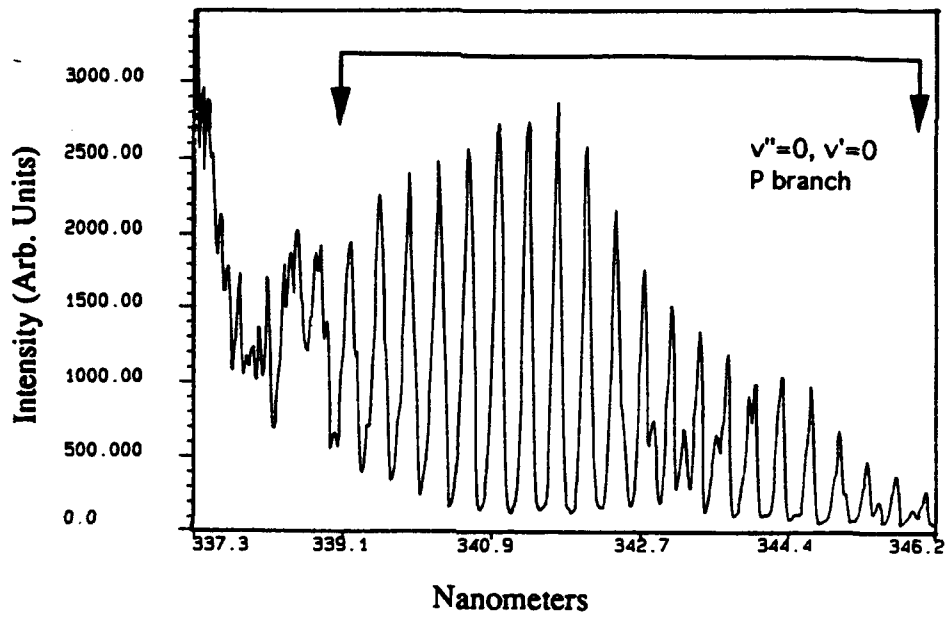
Fig. 4. $A^3\Pi - X^3\Sigma^-$ P_{oo} Rotational Transition of NH
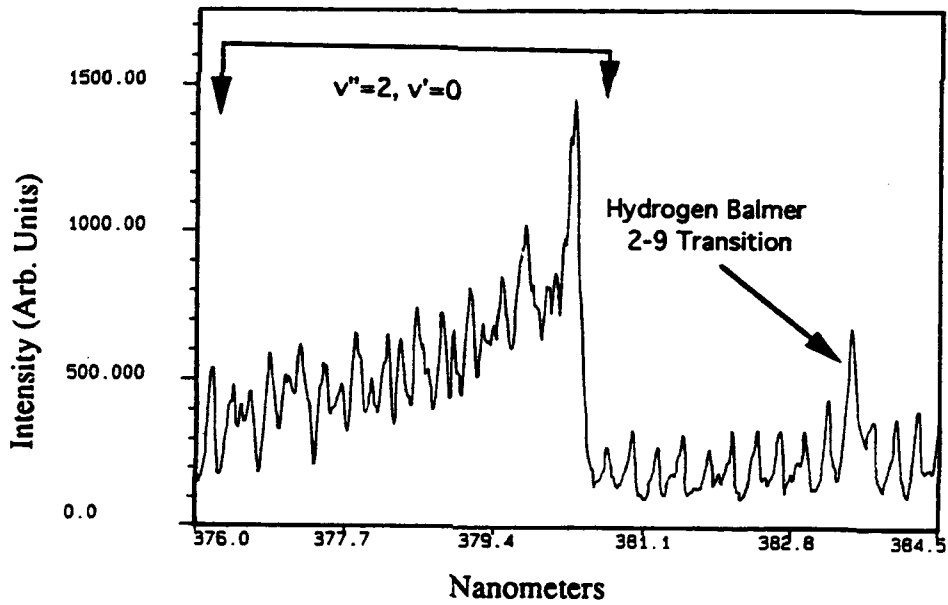
Fig. 5. $C^3\Pi_u - B^3\Pi_g$ Vibrational Transition of Nitrogen

186

THERMAL-ELECTRIC PROPULSION WITH MAGNETOPLASMADYNAMIC ACCELERATION

Principal Investigator: Bagher M. Tabibi

Department of Physics
Hampton University
Hampton, VA. 23668

SUMMARY

The thermal-electric propulsion (TEP) system is an advanced propulsion concept that integrates thermal and electric propulsion systems in a tandem arrangement to take advantages of both systems. In the TEP system, a working medium is preheated to its maximum achievable temperature (~3000 K) by solar thermal flux for generation of an ionized propellant. The heated propellant then expands through a hallow cathode for the MPD that serves an expansion nozzle where the medium is additionally heated by Ohmic heating and accelerated further by $\mathbf{J} \times \mathbf{B}$ forces. These additional gains in the MPD enhance the specific impulse and thrust of the propulsion system. Also the initial plasma from the thermal chamber may assist overcoming the so-called onset current limit.

Thermal-Electric propulsion System

Introduction

The thermal-electric propulsion (TEP) is an advanced concept which provides a high specific impulse ($I_{sp} \geq 1200$ s) and medium thrust level to fill the gap between the very high thrust ($\geq 10^5$ lbf) chemical or nuclear thermal which have very low I_{sp} (≤ 1000 s) and very low thrust (≤ 1 lbf) ion or arcjet which have very high I_{sp} ($\geq 10^4$ s). The concept of the TEP, as shown in Fig. 1, utilizes the principles of a conventional thermal propulsion and magnetoplasmadynamic (MPD) accelerator in tandem arrangement to enhance the I_{sp} as well as its thrust level. For the TEP, input power could be drawn from concentrated solar (STEP) flux or nuclear thermal (NTEP) energy. In other words, the principle of the TEP could be applied either to the solar thermal or to the nuclear thermal propulsion systems to improve their thrust and I_{sp}.

The experimental setup for the test of STEP concept is being constructed at Hampton University under an Air Force Office of Scientific Research (AFOSR) grant.

Solar Thermal propulsion (STP)

The basic mechanism involved in the STP is illustrated in the left portion of TEP diagram in Fig. 1, where it shows energy sources injected into the thermal chamber. Solar radiation is focused within an absorption chamber. Inside the thermal chamber the propellant is heated to a high temperature (~3000 K). The heated propellant than expands through a nozzle to generate thrust. The STP provides the I_{sp} and thrust levels between those of a chemical and an ion propulsion system (see Fig. 2).

A few research activities on the STP has been vigorously pursued until now. A noticeable research activity is carried out for the proof-of-principle of the STP by Rocketdyne Division of Rockwell International Corp., under the contract sponsored by U.S. Air Force Rocket Propulsion Laboratory[1-3]. Recent experimental test of the STP system with the heat exchanger cavity absorber results in I_{sp} ~ 872 lbf.sec/lbm. The projected I_{sp} is 1200 lbf.sec/lbm once the propellant temperature of 4,500 °F is achieved using windowed porous material absorber.
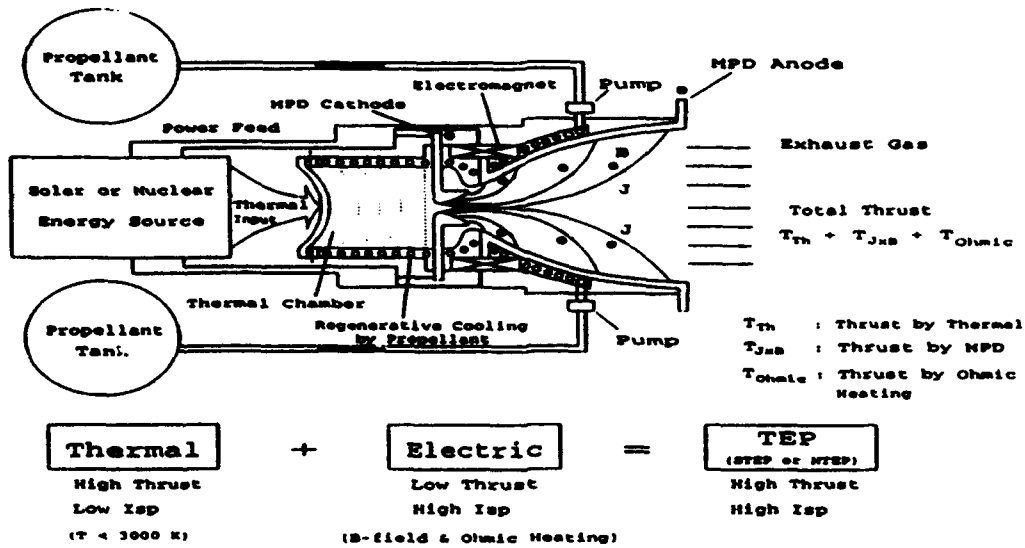
Fig. 1 Concept of Thermal/Electric Propulsion (TEP) System
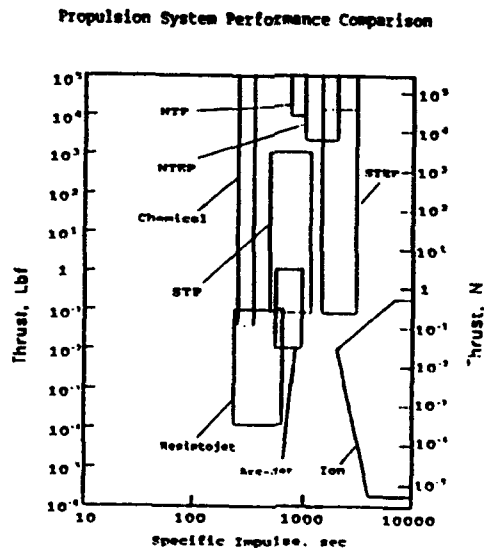
Fig. 2 Performance of Various Thruster Concepts

189

Electrical Propulsion

The electric propulsion in the TEP system uses the high temperature gas exhausted from a thermal propulsion system and partially ionized by thermionic emission of electrons from the nozzle material and /or possibly by seeded plasma. The use of partially ionized plasma in the MPD channel is a strong contrast to the conventional arc-jet and MPD thruster which must be initiated with a cold-gas propellant. The three key concerns in electric propulsion are the electrical conductivity for a low breakdown voltage, the limit of onset current which limits the flow rate of propellant, and the initial ionization for voluminous production of a plasma. The use of high temperature gas that enables thermionic emission of electrons and seeding for the initial ionization processes provide a voluminous plasma that will relax these three key concerns.

Thrust and Specific impulse

The thrust of the STEP system depends on the flow rate of propellant. The capability of the STEP to produce a large volume plasma at the pre-MPD channel enables the discharge currents of the MPD to be stable. Thus, further increment of propellant flow rate and subsequently thrust are possible. Figure 2 shows the estimations of thrust and I_{sp} for various propulsion systems. As shown in Fig. 2, the STEP and NTEP are positioned in the medium ranges of both thrust and I_{sp} as compared to the chemical, NTP, and other high I_{sp} systems.

References

[1] Shoji, J.M.:"performance Potential of Advanced Solar Thermal Propulsion," AIAA Paper 83-1307, AIAA/SAE/ASME 19th joint Propulsion Conference, June 27-29, 1983.

[2] Rault, D. F. G. and A. Hertzberg: "Radiation Energy Receiver for Laser and Solar Propulsion Systems," AIAA Paper 83-1207, AIAA/SAE/ASME 19th Joint Propulsion Conference, Seattle, WA, June 27-29, 1983.

[3] Shoji, J. M., Perry, F. J., Lim, D. P., and Pard, A. G.: "Windowed Porus Material Absorption Concept-A New Solar Thermal Propulsion Concept," The Proceedings of 1986 JANNAF Propulsion Meeting, New Orleans, Louisiana, August 1986.

AIRBREATHING COMBUSTION

AND

PROPULSION DIAGNOSTICS

(Not Presented)

RESEARCH ON SUPERSONIC REACTING FLOWS

AFOSR Grant No. F49620-94-1-0152

Principal Investigators: C. T. Bowman, R. K. Hanson, M. G. Mungal and W. C. Reynolds

Department of Mechanical Engineering
Stanford University
Stanford, CA 94305-3032

SUMMARY/OVERVIEW:

A combined experimental and computational investigation of supersonic reacting flows is being conducted to gain a more fundamental understanding of flow physics and chemistry interactions in compressible reacting flows. The research effort involves two interrelated efforts: (1) an experimental study of mixing and combustion in supersonic flow that utilizes recent advances in laser-based diagnostics, and (2) simulation and modeling of compressible reacting flows using advanced analytical and numerical techniques.

TECHNICAL DISCUSSION:

Experiments in Supersonic Flows

This element of our research comprises three elements: (1) a study of the structure of compressible reacting mixing layers; (2) an investigation of strategies for enhancing mixing in compressible mixing layers; and, (3) application of promising mixing enhancement techniques to reacting compressible mixing layers.

Compressible Combustion Studies

A major focus of our research is on the further examination of the structure of compressible reacting mixing layers as a function of three parameters that simulations and initial experiments indicate will have the largest influence on structure - convective Mach number, heat release and the mean vorticity-density profile. Structural features of the layer will be visualized using simultaneous planar laser-induced fluorescence (PLIF) images of OH (a marker of chemical reaction) and acetone (a marker of fuel). In addition, quantitative images of static temperature will be obtained using PLIF NO and OH thermometry. The time evolution of the large-scale structures will be obtained using a recently-developed double-pulse PLIF imaging technique, described below. All of these flow visualization techniques were developed in our laboratory.

The approach in these experiments is to fix convective Mach number and to vary heat release by varying the hydrogen and oxygen concentration in the feedstreams from low values, where simulations suggest that the flow structure resembles its nonreacting counterpart, to high values where simulations suggest the existence of colayers at convective Mach numbers greater than about 0.5. Experiments have been completed at low heat release for high and low convective Mach numbers, and the observed flow structure resembles that of nonreacting flows (Miller et al., 1994).

Double-Pulse PLIF Imaging

A new method for recording the evolution of large-scale structures in high-speed reacting mixing layers has been recently developed and demonstrated (Seitzman et al., 1994) The technique

192

utilizes a single frequency-doubled dye laser which produces two pulses of laser light separated by an adjustable interval. The laser wavelength is selected to simultaneously excite fluorescence from acetone, seeded into the fuel stream, and from OH, which marks the hot combustion products. The fluorescent signals can be spectrally separated, allowing recording of four independent images (i.e., an OH/acetone image pair for each of the two pulses) using four intensified CCD cameras.

A schematic diagram of the experimental arrangement is shown in Fig. 1 and typical results, combined into two overlaid OH/acetone images, are shown in Fig. 2.
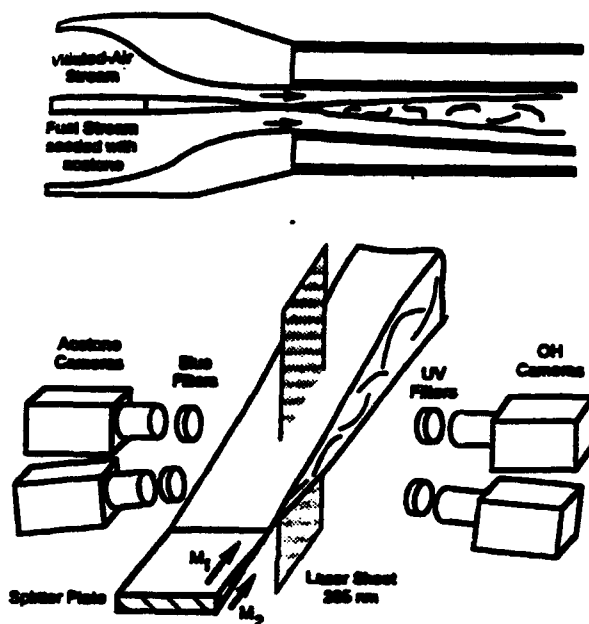
Figure 1. Schematic of mixing layer facility, and optical arrangement of laser sheet and cameras.
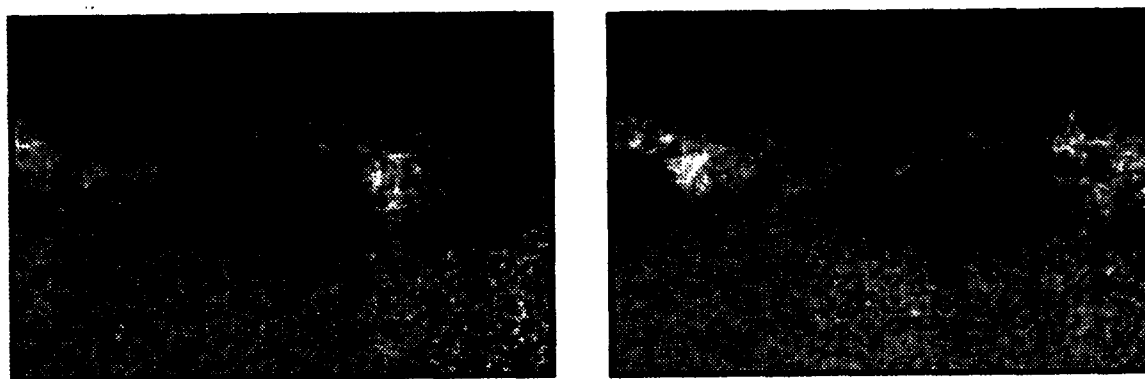
Figure 2. Overlaid double-pulse sideview images (77×50 mm) of acetone and OH in the mixing layer with Mc=0.32: (upper) first pulse image and (lower) second pulse image with a 50 μs delay.

For the low-compressibility conditions of Fig. 2, it is easy to identify and follow the movement of distinct structural features. The OH containing structures convect at a velocity that is similar to (but slightly higher than) the calculated mean convective speed of the layer, while the edge of the acetone-containing structure moves at nearly the speed of the slow stream.

Mixing Enhancement Studies

In addition to the reacting flow experiments described above, we have performed experiments in non-reacting flows aimed at understanding the instantaneous three-dimensional structure of the mixing layer. The approach is as follows: The low-speed side of the supersonic mixing layer is seeded with small amounts of alcohol vapor which condenses in the layer upon mixing with the cold high-speed stream. A laser pulse from a Candela laser is rapidly swept through the mixing region and the light scattered from the fine alcohol droplets is recorded as 16 planar images using an Imacon image converter camera. The images are then re-assembled to produce an instantaneous representation of the mixed fluid region in the layer using volume rendering. An example is shown in Fig. 3.
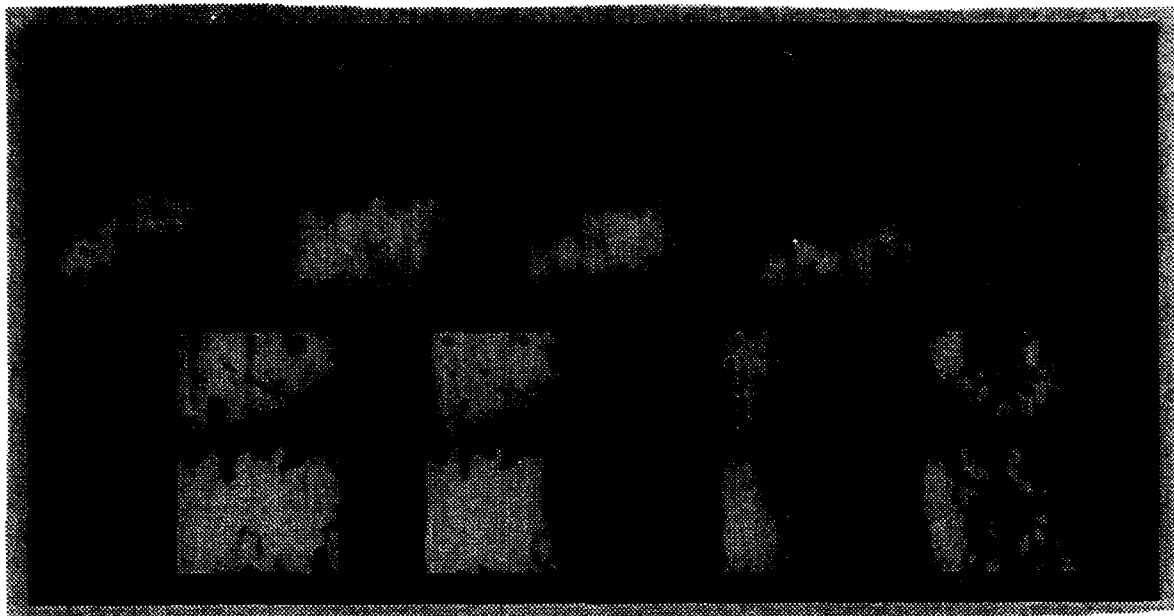
Figure 3.   Instantaneous structure of supersonic mixing layers. Upper images are planar cuts. Lower is volume rendering rotated to various viewing angles.

The upper image set shows 5 of the recorded slices as the sheet sweeps through a low-compressibility mixing layer. The bottom image set shows the volume rendering resulting from the full image set. The volume rendering clearly reveals the quasi two-dimensional structure of the layer, expected at low compressibility. Similar renderings at higher compressibilities show a considerably less organized structure, but with several prominent diagonal bands. This new technique will find further use, as needed, as our studies on mixing enhancements continue.

Stability Analyses and Numerical Simulations

The objectives of this element of our research are to conduct analytical and computational studies of reacting supersonic mixing layers that not only provide insight into the behavior of the layer that guides the experiments and aids in their interpretation, but also provides detailed information on flow physics not directly available from the experiments.

A focus of the computational effort will be on effects of chemistry models on results. Initial efforts will consider differences between single-step and multi-step chemistry models.

Publications:

1. B. K. McMillin, J. L. Palmer and R. K. Hanson (1993), Instantaneous Temperature Imaging of a H_2/NO Jet in Supersonic Crossflow using Two-Line PLIF, Applied Optics **32**, 7532.

2. M. F. Miller, T. C. Island, J. M. Seitzman, C. T. Bowman, M. G. Mungal and R. K. Hanson (1993), "Compressibility Effects in a Reacting Mixing Layer," AIAA-93-1771, AIAA/SAE/ASME/ASEE 29th Joint Propulsion Conference, Monterey, CA.

3. M. F. Miller, T. C. Island, J. M. Seitzman, C. T. Bowman, M. G. Mungal and R. K. Hanson (1994), "An Experimental Investigation of Supersonic Reacting Mixing Layers," AIAA-94-0823, 32nd AIAA Aerospace Sciences meeting, Reno, NV.

4. B. Yip, M. F. Miller, A. Lozano, and R. K. Hanson (1994), "A Combined OH/Acetone Planar Laser-Induced Fluorescence Imaging Technique for Visualizing Combusting Flows," Experiments in Fluids (in press).

5. J. Seitzman, M. F. Miller, T. C. Island and R. K. Hanson (1994), "Double-Pulse Imaging using Simultaneous OH/Acetone for Studying the Evolution of High-Speed Reacting Mixing Layers, 25th Symposium (International) on Combustion, accepted.

MECHANISTIC MODELS FOR SOOT FORMATION

Principal Investigators: M.B. Colket, III and R.J. Hall

United Technologies Research Center
East Hartford, CT 06108

SUMMARY/OVERVIEW

The overall objectives of this work are to (1) refine and update an existing soot formation model and (2) with the assistance of M. Smooke of Yale University, incorporate this soot model into a code describing a laminar, opposed jet diffusion flame. Pyrolysis data obtained in previous years from a single-pulse shock tube have been interpreted to develop a detailed pyrolytic model of toluene decay and polyaromatic hydrocarbon formation. The soot model has been refined and incorporated into the diffusion flame model. The resultant code describes a strongly coupled gas-particulate system which includes effects of (gas and particulate) radiation, species scavenging by the particles, thermophoresis and oxidation.

TECHNICAL DISCUSSION

A. Toluene Pyrolysis and Formation of Polyaromatic Hydrocarbons

As part of the effort to develop a model for soot production in an opposed jet diffusion flame, the reaction kinetics and mechanisms associated with ring and polyaromatic hydrocarbon formation during the oxidative pyrolysis of alkane fuels need to be established. In the previous years, the mechanism for benzene formation during the decomposition of methane was investigated[1] and toluene, phenylacetylene, norbonadiene and cyclopentadiene were pyrolyzed. Along with the hydrocarbon decomposition, information was collected on the formation of polyaromatic hydrocarbons (PAH). Detailed chemical kinetic modeling[2] has offered some answers to some key issues related to benzyl radical decay. The existence of a low temperature decomposition pathway has been confirmed and the likely products have been identified. Furthermore, the rate of PAH production exceeded that predicted using the standard mechanism involving sequential acetylene addition. This result is not unexpected since, in the case of toluene pyrolysis, bimolecular reactions involving aromatics should lead to a substantial increase in growth rates. Rapid formation of anthracene was found during toluene pyrolysis at low temperatures but phenanthrene (a more stable isomer of anthracene) was produced much more readily during phenylacetylene pyrolysis. These results provide a basis for suggesting specific mechanisms for formation of these $C_{14}H_{10}$ species. Since equilibrium levels of anthracene and phenanthrene were approached above 1600K for these experiments, a rate constant of $8 \times 10^{12} \exp(-65 \text{kcal/mole/RT}) \text{ sec}^{-1}$ for the isomerization, anthracene $\leftrightarrow$ phenanthrene, was estimated. Finally, four-centered, concerted reactions involving direct H_2 elimination and ring closure were suggested to explain the rapid production of selected PAH species. Rate constants of $10^8 \exp(-E/RT) \text{ sec}^{-1}$, where $30 < E < 40$ kcal/mole, were used to describe this overall process.

B. Soot Formation in an Opposed Jet, Laminar Diffusion Flame

B.1. Description

A new tool for studying soot formation in opposed jet diffusion flames has been developed[3] by integrating the dynamical equations for spheroid growth with the conservation equations and complex chemistry of counterflow diffusion flames. The approach is an extension of recently reported work on soot formation in premixed flames[4], although a revised inception mechanism based on

quasi steady-state expressions for intermediates formed during the production of naphthalene and phenanthrene has been utilized. The growth of spheroids has been treated as a classical aerosol dynamics problem; the size range of interest is divided into discrete intervals or classes with a logarithmic transformation and the size class mass densities are derived using terms representing inception, surface growth (and oxidation), and coalescence. It is assumed that surface growth and coalescence have the free molecule form, and that the spheroids consist of carbon. Particle inception, surface growth, and oxidation are calculated from local concentrations of gaseous species determined from a complex chemical kinetic mechanism. Scrubbing of species due to inception, growth and oxidation of the particles is included in the species and conservation equations. Particle transport by thermophoresis and diffusion with an effective sectional diffusion coefficient have been included. Non-adiabatic radiative loss by both gas and particle emission is also included in the energy equation. The resultant algorithm accurately predicts soot volume fraction with as few as two or three size classes. Reliable predictions of average particle size or number density require fifteen or more sections.

B.2. Evolution of soot volume fraction

A methane/air opposed jet, laminar flame was modeled over a range of strain rates. For the base case discussed here, T_{inlet}=298K, P=1atm, maximum strain rate is 17.2 sec^{-1}, and the number of particle sections was 15. The kinetic mechanism contained 33 gaseous species and 102 elementary reactions. Calculated evolution of the total volume fraction and the profiles of the sections are shown in Fig. 1. The volume fractions are plotted as a function of a normalized coordinate, y', which is zero at the stagnation plane of the opposed jet flame and is one at the location of the peak flame temperature. The average size (optical diameter, D_{63}) for some of the sections (denoted by numbers in Fig. 1) are: (1)0.762, (5)5.996, (7)16.82, (9)47.2, (11)132.4, and (15)1042.0 nanometers. This range of diameters represents a mass range more than 9 orders of magnitude.

Evolution toward larger mass particles occurs due to surface growth and coalescence. The smaller sizes appear in the vicinity of the acetylene peak, but never acquire an appreciable fraction of the total soot mass. Most of the soot growth occurs in a narrow range between about 0.5 to 0.8 in the normalized coordinate. Falling temperature, acetylene, and benzene concentrations give rise to rapid reductions in surface growth rates as the stagnation plane is approached. As the particles grow, convection and thermophoresis push them in the direction of the stagnation plane. At the stagnation plane, thermophoresis causes some spilling of large particles to the fuel side of the plane, but convection pushes them back. A balance between convection and thermophoresis leads to a peak on the fuel side of the stagnation plane. The population in bins above class 11 is negligible. Qualitative comparisons with the data of Zhang, Atreya, and Lee[5] are quite satisfactory, most notably in the way the model reproduces the profile of the total soot volume fraction and the accumulation of soot at the stagnation plane.

The Harris-Weiner[6] (HW), Frenklach-Wang[7] (FW), and modified Frenklach-Wang[4] (MODFW) surface growth rates are compared with oxidation in Fig. 2. It is apparent that only the Harris-Weiner expression results in significant net surface growth and the HW expression was used in the base case calculations. The MODFW expression for growth never exceeds the oxidation rate, and the FW expression ($\alpha = 1$) is only marginally so in a restricted region. Near the flame front (peak temperature regime), the FW mechanism predicts significant growth rates because of increased temperature and the high concentrations of H-atoms. However, oxidation rates (by OH and O_2) by far dominate this growth expression. Inclusion of Soret diffusion did not alter the H-atom profile enough to change this conclusion.

B.3. Effects of radiation, oxidation and thermophoresis

Radiation from gas bands and soot depresses peak temperature by about 70 K for the base strain rate. This cooling represents about 7% conversion of flame enthalpy to radiation and is large enough to perturb significantly the soot growth species benzene and acetylene. The consequence is a marked sensitivity of volume fraction to radiation, as seen in Fig. 3. Without radiation, the predicted volume fraction is nearly a factor of three higher. This increase arises not just from the larger levels of acetylene and benzene, but also from the Arrhenius terms in the inception and surface growth expressions. Radiation effects decrease monotonically with increasing strain rate, as the flames become thinner and there is less residence time for radiation. This very strong sensitivity of radiation on soot predictions is consistent with results of Sivathanu and Gore[8]. Thus, accurate, coupled calculations of radiation phenomena is a key ingredient in the prediction of soot profiles in flames. For the methane flames studied, most of the radiative gas cooling is actually due to gas bands, because the soot radiation temperature and volume fractions are relatively low.

Figure 3 also shows the importance of oxidation. Suppressing it entirely results in the increase in volume fraction shown. Oxidation in the soot growth region is mainly due to molecular oxygen. Suppressing thermophoresis also results in increased soot. Thermophoresis lowers the residence time in the growth region, and thus reduces soot yield. Without thermophoresis, there is no spilling of particles to the fuel side of the stagnation plane.

Because the rate of inception is strongly affected by temperature, removing radiative loss results in much higher levels of particles, at least towards the inception region. Near the stagnation plane, the model predicts less difference in number density, presumably due to a loss of sensitivity to initial conditions in a coalescence-dominated regime. Number density decreases toward the stagnation plane, of course, because of coalescence. Figure 4 shows interesting effects on the average particle size, or optical diameter D_{63}. More rapid surface growth resulting from removal of radiation, and faster coalescence from higher number densities results in much larger particles. The particles that do penetrate to the fuel side of the stagnation plane evidently do not further coalesce; the number densities and collision frequencies are too low for this to proceed on a reasonable time scale. Without thermophoresis, the particles have more time to grow to a larger size at the stagnation plane.

REFERENCES

1. Colket, M. B., and Smooke, M. D. (1993). *The Formation of Benzene from Methane*, presentation at joint Central/Eastern States Section of the Combustion Institute, New Orleans, LA.
2. Colket, M. B. and Seery, D. J. (1994), "Reaction Mechanisms for Toluene Pyrolysis", accepted for presentation to Twenty-Fifth International Symposium on Combustion, Irvine CA.
3. Hall, R. J., Smooke, M. D., and Colket, M. B. (1994), "Predictions of Soot Dynamics in Opposed Jet Diffusion Flames", Submitted for publication in special Combustion and Science Technology book in honor of I. Glassman.
4. Colket, M. B. and Hall, R. J. (1994), "Successes and Uncertainties in Modeling Soot Formation in Laminar, Premixed Flames," *Proceedings of the International Workshop on Mechanisms and Models of Soot Formation* (H. Bockhorn, Ed.), Springer-Verlag, Heidelberg.
5. Zhang, C., Atreya, A., and Lee, K. (1992). *Twenty-First Symposium (International) on Combustion*, The Combustion Institute, pp. 1049-1057.
6. Harris, S. J. and Weiner, A. M. (1983). Comb. Sci. Tech. 31, 155.
7. Frenklach, M. and Wang, H. (1990). *Twenty-third Symposium (International) on Combustion*, The Combustion Institute, p. 1559.
8. Sivathanu, Y. R. and Gore, J. P. (1994), Combustion and Flame, 97, 161.

Fig. 1 Spatial Evolution of Size Classes (q_{max} = 17.2 sec^{-1})
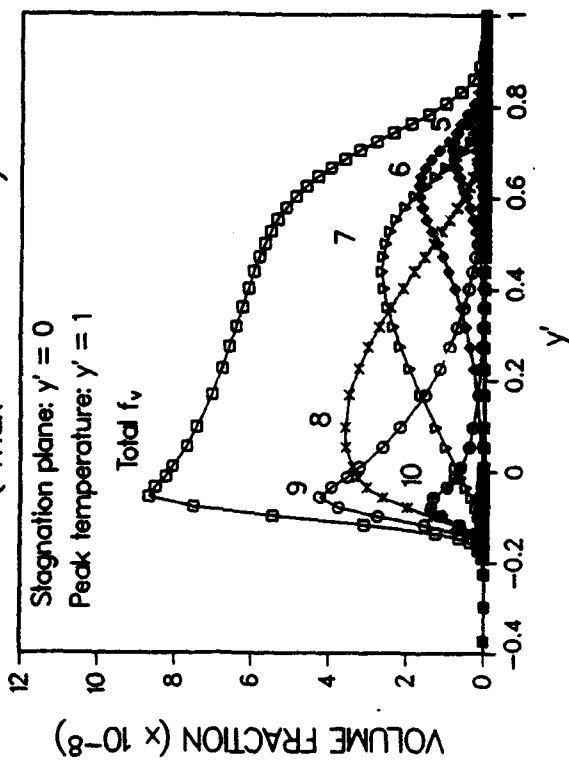
Fig. 2 Comparison of Surface Growth Models with Rate of Oxidation
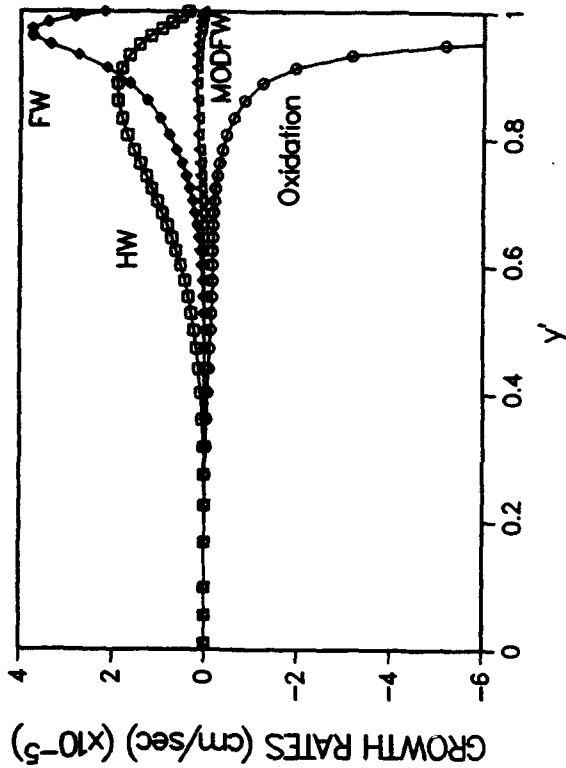
Fig. 3 Effect of Radiation, Oxidation and Thermophoresis on Soot Volume Fraction
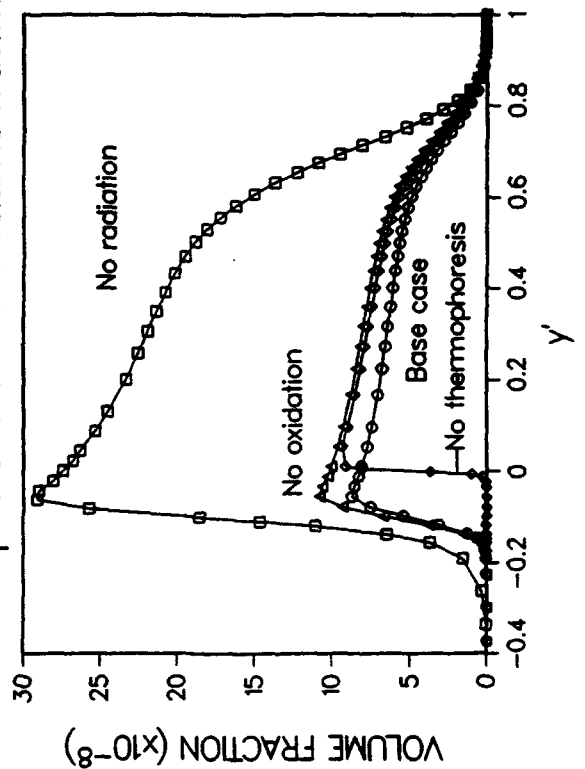
Fig. 4 Effect of Radiation, Oxidation and Thermophoresis on Average Particle Size
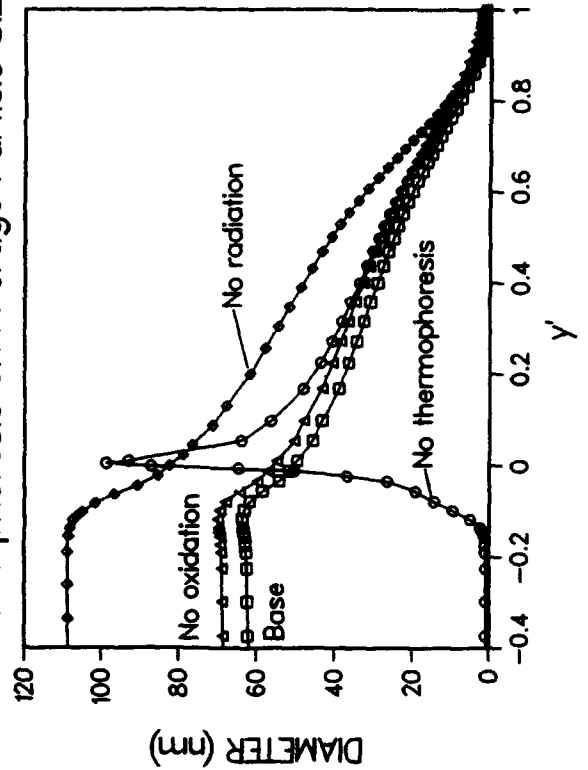
TURBULENCE-CHEMISTRY MODELS IN HIGHLY STRAINED NON-PREMIXED FLAMES

Sanjay M. Correa
General Electric Research Center
Schenectady, New York, 12301

SUMMARY: OBJECTIVES AND PRIOR RESULTS

The objective of this research program is to develop and assess models for turbulence-chemistry interactions in highly strained flames. The framework provided by particle-tracking pdf models is emphasized. The data are typically obtained by laser Raman spectroscopy. The flame is stabilized by recirculation, and so is more complex and realistic than simpler "parabolic" jet flames. The models can then be combined with CFD codes to predict flame stability, flow/temperature fields and trace emissions from air-breathing combustors. Previously, a conventional pressure-corrected "elliptic" CFD code was combined with the joint velocity-composition pdf model. A two-variable partial equilibrium scheme was used for the CO/H_2 oxidation chemistry. The calculations compared favorably with Raman data (mixture fraction, major species, and temperature) in a 27.5% CO/ 32.3% H_2/ 40.2% N_2 – air flame stabilized in the recirculation zone behind a bluff body [1]. Also, the Partially Stirred Reactor (PaSR) model was developed to study the interactions between turbulence and full chemistry schemes for (i) CO/H_2 [2] and (ii) CH_4 [3]. Detailed analyses of the chemical pathways in various stages of the mixing process for oxidation and emissions chemistry are provided in Ref. 4. Progress made over the past year follows.

PROGRESS IN THE PAST YEAR

I. The CFD/joint pdf model has been used to calculate the non-premixed bluff-body methane-air flame, according to a four-step steady state chemistry scheme, and compared with the Raman data [5]. Figure 1 shows the experimental set-up. More details are given in Refs. 1 and 5.
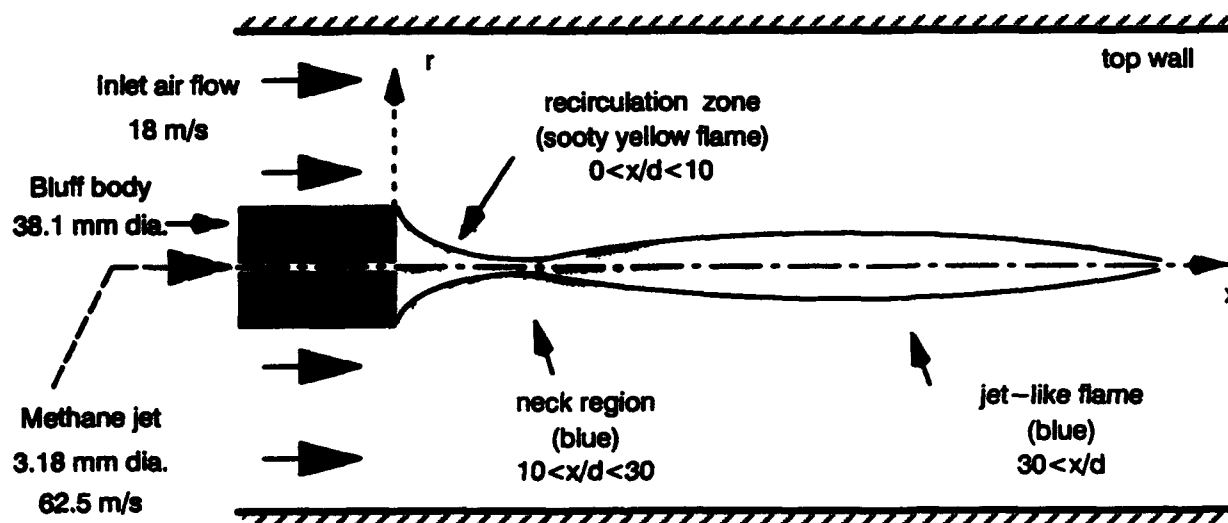
Figure 1. Bluff-body stabilized methane "diffusion" flame in 15 cm x 15 cm tunnel.

The Raman system was modified to account for the significant levels of laser–induced fluorescence and incandescence encountered in the rich sooty zone of the flame. The joint pdf contains three velocity components which are modeled by Langevin equations, and five thermochemical scalar variables with mixing given by linear deterministic relaxation to the mean and chemistry by a 4–step steady–state reduced scheme. The flame is characterized by significant finite–rate chemistry including, unlike the $CO/H_2/N_2$ fuel in the same apparatus, strong bimodality in the temperature–mixture fraction scatterplots. Calculations are compared with the Raman data on temperature and major species. Computed radial profiles of the mean and r.m.s. mixture fraction at $x/d=20$ compare well with the Raman data (Fig. 2a). The measured radial profiles are shown in full, revealing the degree of symmetry, while the computed profiles are by assumption axisymmetric. Major species profiles also agree quite well (Fig. 2b). The mean O_2 is depleted in the wake of the bluff–body but coexists with mean CH_4, a consequence of finite–rate chemistry. The largest discrepancies are caused by the breakdown of the assumption of a chemical steady state for the cool fuel–rich gas at the core of the flame. Additional results are discussed in Ref. 5.
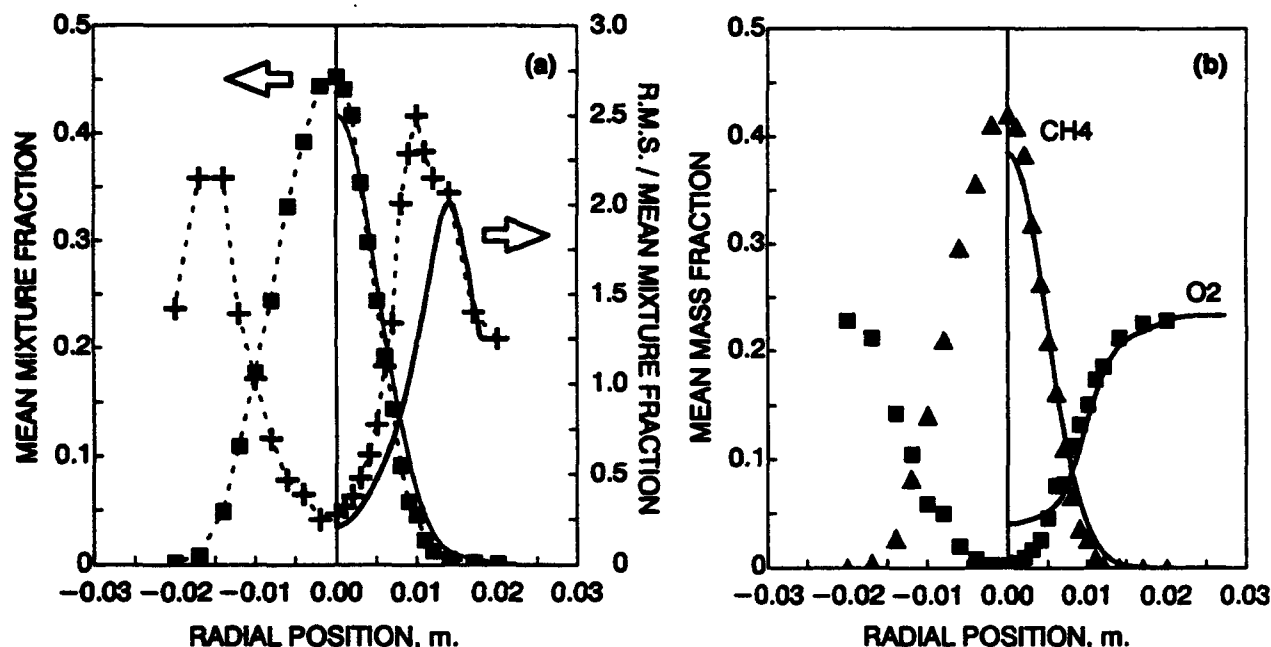
Figure 2. Radial profiles at $x/d=20$. (a) Mean and r.m.s. of mixture fraction. (b) Selected major species.

The calculated CO scatterplots have maxima of 3% (inset: Figure 3) whereas the data peak at about 10%. Similar 10% levels were measured in other bluff body flames and in pilot–stabilized flames, and 2–3% peaks were predicted in the latter using the 4–step scheme within a (scalar) pdf/Reynolds stress model. Hence this discrepancy on CO maxima has appeared in diverse circumstances (but always in combustion gases that are near local extinction). There are many potential contributors, including: (i) the assumption of a steady state for the radicals in the 4–step mechanism; (ii) the errors in Raman–based CO and CO_2 data; and (iii) neglection of phenomena such as unsteady flamelets or micromixed gases (perfectly stirred reactors) which have been shown to lead to high CO. In intense turbulence, however, the microscale may be better simulated by the PaSR since it is the degenerate form of the pdf equation for spatially homogeneous systems. For example, at 30 atm the PaSR indicates that approximately 2% peak CO levels are encountered until the fuel is pyrolyzed and CO oxidation can commence [4]. CO is an important clue to the microstructure of highly turbulent combusting gases, and accurate measurements will be critical.
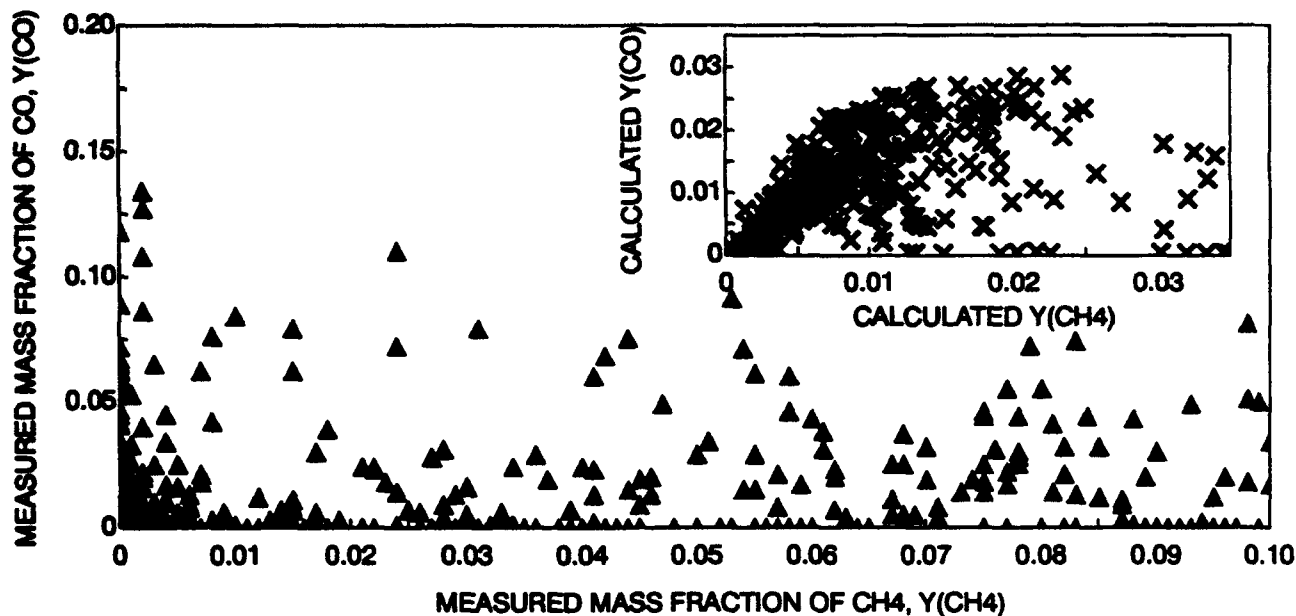
Figure 3. Scatterplot of measured CH₄ and CO. Inset: calculated scatterplot.

II. The PaSR model has been described previously [2−4]. Prior work concentrated on the IEM mixing model and different (full and reduced) chemistry schemes, none of which will be discussed here. The IEM model is attractive because it permits highly "parallelizable" computation, but the consequences of certain peculiarities − such as determinism and the shape−preserving relaxation of the initial pdf of a conserved scalar − need to be examined in the context of combustion. In the present reporting period, two pair−exchange mixing models, viz., the original Curl model and a modification thereof, were compared with the "Interaction−by−Exchange−with−the−Mean" (IEM) model, in the context of homogeneous combustion. The details are available in Ref. 6.

(i) The Curl model randomly chooses N_{mix} pairs of particles, mixes them by averaging their scalar values, and finally returns them to the ensemble. The mean is unchanged whereas the variance decreases, in the inert case.

(ii) The Modified Curl model also randomly chooses pairs of particles, but mixes them by averaging their scalar values in a weighted manner. The weight is α varied randomly between zero and one according to the flat pdf $P(\alpha)=1$.

Under the Curl and the modified Curl models, the post−mixing mass fractions and temperature of each particle in the ensemble are advanced in time by integration of the chemical kinetics equations.

(iii) The so−called "Interaction−by−Exchange−with−the−Mean" or "IEM" model relates each particle to the ensemble, rather than to a partner [2, 3]. It accounts simultaneously for chemistry and mixing.

All three mixing models fail to yield the Gaussian expected of a conserved scalar pdf in the limit of large time; however, the significance of this failure is not obvious in the reacting case and motivates the present work.

The fuel is 50%CO/50%H₂ (by vol.). The kinetic scheme consists of 11 species and 23 reactions. The inlet conditions are 1 atm and 900K. The stoichiometry of the premixed inflow leads to a PSR temperature of 1740K at a residence time of 5 ms (1800K in equilibrium), but to blowout in a PFR. The PaSR mixing fre-

quency was varied in the range 10 – 10^4 Hz, by factors of $\sqrt{10}$; it has been shown that this range more than covers the mixing frequencies encountered in a practical combustor [3].

The stochastically steady mean temperature and mass fraction of CO are shown in Fig. 4. At frequencies >1000 Hz all three models approach the PSR, which was computed by an independent code. At lower frequencies, however, the pair–exchange models tend to blow out while the IEM model sustains combustion. Despite these differences, the pdf's and scatterplots of temperature, CO, OH, and O – selected because of their intrinsic importance as well as their influence on NO_x emissions – are very similar between the three models. The similarity increases with the mixing frequency, which is significant given that practical (e.g., gas–turbine) combustors operate at high mass–loadings and therefore necessarily at high mixing rates. Hence the IEM model appears to be reasonable for highly turbulent premixed combustion.
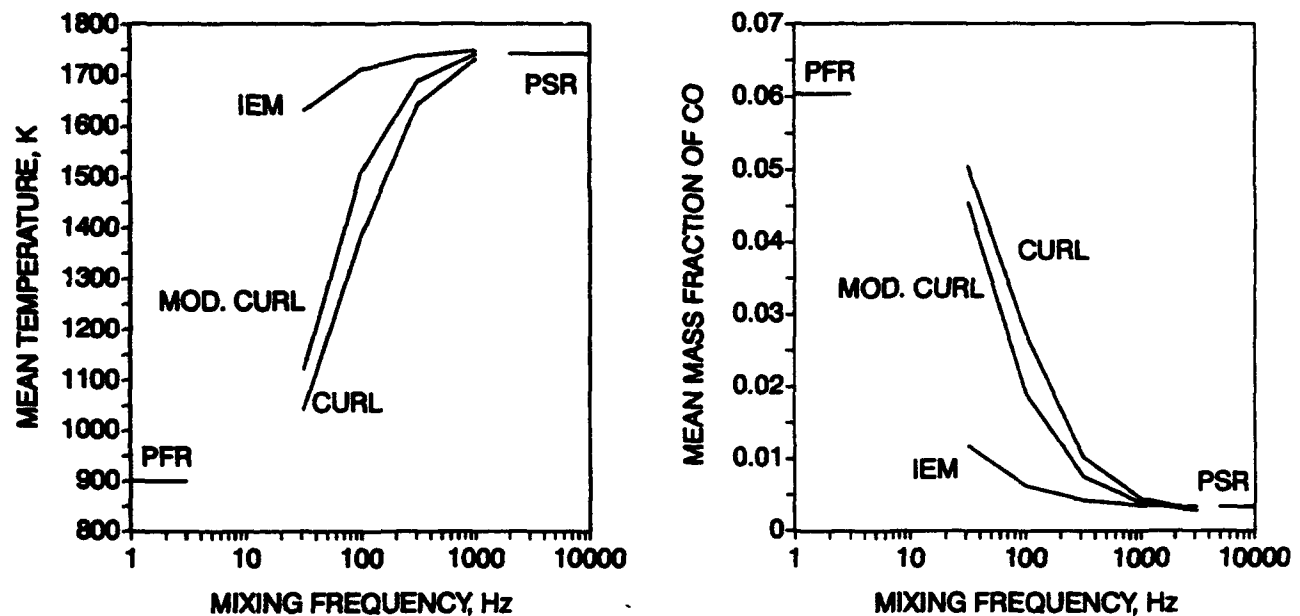
Figure 4. Variation of PaSR under different mixing models.

REFERENCES

1. Correa, S.M. and Pope, S.B.,"Comparison of a Hybrid Monte–Carlo PDF/Finite–Volume Mean Flow Model with Bluff–Body Raman Data," Twenty–Fourth (International) Symposium on Combustion, The Combustion Institute, Pittsburgh, PA, pp. 279–285, 1992.

2. Correa, S.M.,"Turbulence–Chemistry Interactions in the Intermediate Regime of Premixed Combustion," *Comb. and Flame*, 93, pp. 41–60, 1993.

3. Correa, S.M. and Braaten, M.E.,"Parallel Simulations of Partially–Stirred Methane Combustion," *Comb. and Flame*, 94, pp. 469–486, 1993.

4. Correa, S.M.,"Models for High–Intensity Turbulent Combustion," in press, *J. Computing Systems in Engineering*, 1994.

5. Correa, S.M., Gulati, A. and Pope, S.B.,"Raman Measurements and Joint PDF Modeling of a Non–Premixed Bluff Body–Stabilized Methane Flame," accepted for Twenty–Fifth (International) Symposium on Combustion, Irvine, CA, July 31 – August 5, 1994.

6. Correa, S.M.,"A Direct Comparison of Pair–Exchange and IEM Models for Scalar Mixing in Premixed Combustion," submitted to *Comb. and Flame*, April 1994.

HIGH RESOLUTION MEASUREMENTS OF
MIXING AND REACTION PROCESSES IN TURBULENT FLOWS

AFOSR Grant No. 89-0541

Werner J.A. Dahm

Gas Dynamics Laboratories
Department of Aerospace Engineering
The University of Michigan
Ann Arbor, MI 48109-2140

Summary/Overview

This research program is an experimental and theoretical investigation into the fine scale structure of mixing and combustion processes in turbulent flows. It has the following three specific objectives: *(i)* to develop and implement new, high-resolution, four-dimensional, quantitative imaging methods for direct experimental measurements of the small scale structure of mixing and chemical reaction processes in turbulent flows, *(ii)* to use these new imaging methods to investigate the detailed physical structure and dynamics of molecular mixing and chemical reactions in turbulent flows, and *(iii)* to incorporate results from these experimental studies into improved models of reacting turbulent flows. Results are providing remarkable new insights into the nature of the small scales of mixing and combustion processes in turbulent flows. These are contributing to predictive submodels allowing computations of the fine structure of reacting flows for improved high-speed air-breathing propulsion systems.

Technical Discussion

The molecular mixing of one or more dynamically passive conserved scalar quantities in turbulent flows is the rate limiting step in combustion processes involving non-premixed reactant systems. Applications range from combustor design for reacting flows in high speed airbreathing propulsion systems, to the reduction of environmental pollutants in industrial combustion systems. The arbitrary scalar quantity in that case is an elemental mixture fraction evolving in a chemically reacting turbulent flow. The first phase of our work involves results from experiments on the structure and dynamics of conserved scalar mixing at the small scales of turbulent shear flows. Our measurements are conducted in the self-similar far field of an axisymmetric turbulent jet. We use a unique laser induced fluorescence imaging system (see our previous reports) developed specifically for these highly resolved, three- and four-dimensional, spatio-temporal measurements of the full space- and time-varying conserved scalar field. Each measurement produces the fully-resolved scalar field at over 3 billion individual points in a small four-dimensional space-time volume in the flow. The spatial separation between adjacent points within each three-dimensional spatial data volume is smaller than the local strain-limited molecular diffusion lengthscale λ_D of the scalar field, and the temporal separation between the same data point in successive data volumes is shorter than the local molecular diffusion scale advection time λ_D/u. Examples of these data volumes are shown in Figure 1. Work during the past year has concentrated on analyses of data obtained from measurements in both three-dimensional (spatial) and four-dimensional (spatio-temporal) form. Examples of these data volumes are shown in Figures 2-3.

The first experimental measurements are presented for the full three-dimensional spatial scalar energy spectrum $E_\zeta(k)$ resulting from the molecular mixing of a $Sc \gg 1$ conserved scalar quantity in a turbulent flow at local outer-scale Reynolds numbers Re_δ between 3,000 and 6,000. The

three-dimensional character of these measurements allows direct evaluation of the three-dimensional spatial scalar spectrum $E_\zeta(\mathbf{k})$ associated with turbulent mixing. The resulting isotropic spectrum function $E_\zeta(k)$, integrated from this full spectrum, is compared with its individual one-dimensional counterparts $E_\zeta(k_x)$, $E_\zeta(k_y)$ and $E_\zeta(k_z)$ as a test of the small-scale isotropy hypothesis. These one-dimensional spatial spectra are compared with previous temporal spectrum measurements, and with Batchelor's classical theory of the high wavenumber spectrum for $Sc \gg 1$ scalar mixing in turbulent flows.

In the second phase of our work, a physically-based formulation is being developed to relate the chemical state of nonequilibrium combustion in turbulent nonpremixed flows to the mixing state of one or more conserved scalars by the underlying turbulent flow. The approach is motivated by results from our detailed imaging studies of scalar mixing in turbulent flows, which show that essentially all the instantaneous scalar energy dissipation rate field is confined to locally one-dimensional dissipation layers. The ubiquity of these dissipation layers is independent of the extent of chemical nonequilibrium in the flow, and instead is a direct consequence of the dynamics of scalar mixing. The presence of these layer-like dissipation structures in turn indicates a locally one-dimensional structure in the underlying chemical species fields. The resulting strained dissipation and reaction layer model has certain similarities with the classical "flamelet" model, however it is based on entirely different physical observations, is derived from entirely different arguments, and is limited by an entirely different and more widely applicable set of conditions. Moreover, the boundary conditions for solution of the local chemical state differ fundamentally from those used in flamelet models. Results obtained when this formulation is applied to imaging measurements of conserved scalar fields in turbulent flows, for conditions ranging from near equilibrium to deep nonequilibrium, demonstrate remarkable resemblances to direct imaging measurements of chemical species under similar combustion conditions (see Fig. 4). Notably, the present strained dissipation and reaction layer formulation inherently produces results showing the predominance of thin (flamelet) reaction zones under conditions of relatively weak chemical nonequilibrium, and the natural emergence and dominance of broad (distributed) reaction zones with increasing equilibrium departures. It thus provides a physical and theoretical framework that unifies these two widely disparate views of the coupling of the underlying mixing dynamics to the reaction chemistry in turbulent combustion.

References

1. Southerland, K.B. & Dahm, W.J.A. (1993) Four-dimensional laser induced fluorescence study of the structure of molecular mixing in turbulent flows; AIAA Paper No. 94-0820, 32nd AIAA Aerospace Sciences Mtg.

2. Bish, E.S. & Dahm, W.J.A. (1993) Non-equilibrium structure of H_2-Air combustion in turbulent jets; AIAA Paper No. 94-0100, 32nd AIAA Aerospace Sciences Mtg.

3. Bish, E.S. & Dahm, W.J.A. (1993) Strained dissipation and reaction layer analyses of turbulent reacting flows; AIAA Paper No. 94-2310, 25th AIAA Fluid Dynamics Conference.

4. Southerland, K.B. & Dahm, W.J.A. (1993) A structural and spectral study of fine-scale mixing in turbulent flows; AIAA Paper No. 94-2392, 25th AIAA Fluid Dynamics Conference.

5. Bish, E.S. & Dahm, W.J.A. (1993) Strained dissipation and reaction layer analyses of nonequilibrium chemistry in turbulent reacting flows; 25th International Symposium on Combustion; to appear in Combustion & Flame.

6. Dahm, W.J.A. and Bish (1993) High resolution measurements of molecular transport and reaction processes in turbulent combustion; in Turbulence and Molecular Processes in Combustion, pp. 287–302, (T. Takeno, Ed.) Elsevier Science Publishers B.V.
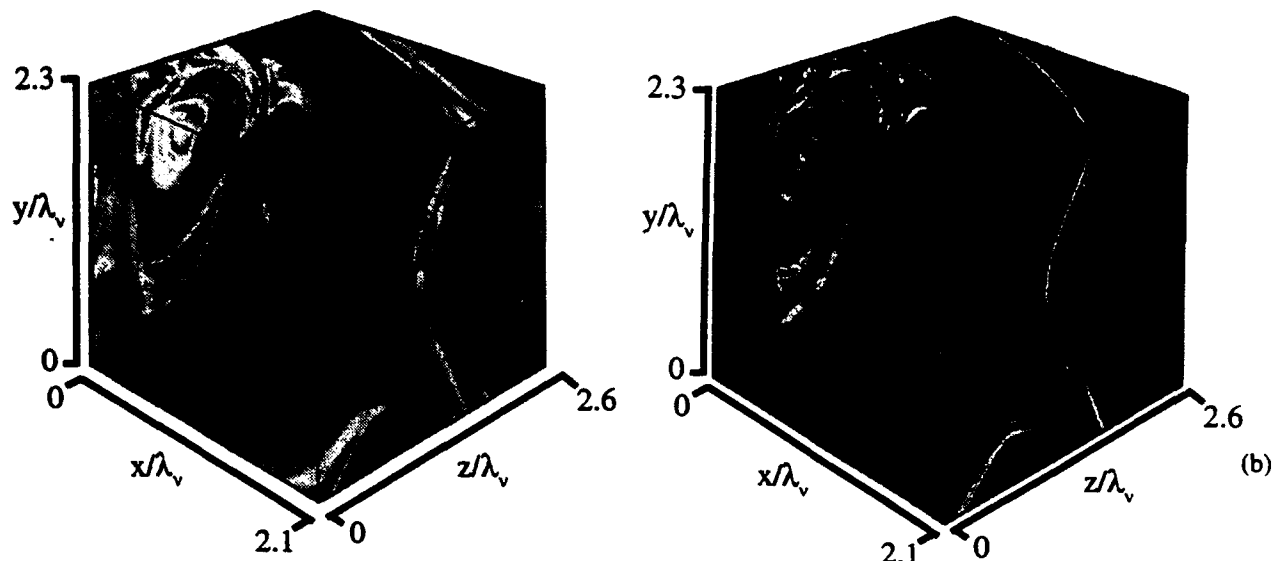
Fig. 1. Example of a 256^3 spatial data volume from the four-dimensional, fully-resolved, conserved scalar measurements. Shown are the scalar field (left) and the dissipation field (right).
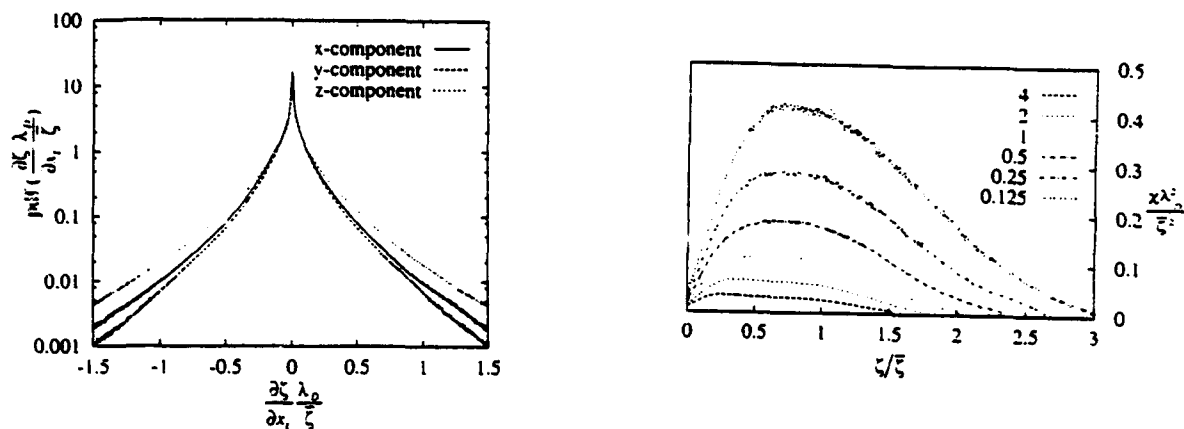
Fig. 2. Probability densities of the individual scalar gradient vector components fields $\partial\zeta/\partial x_i$ (right) and the joint probability density of conserved scalar and scalar dissipation (left).
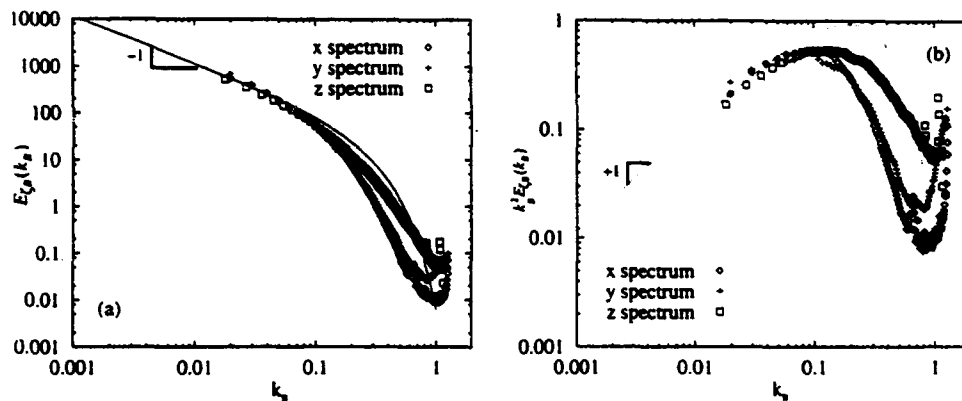
Fig. 3. One-dimensional fine-scale spectra obtained from the three-dimensional spatial scalar field data, showing the scalar spectra (left) and the dissipation spectra (right). Overlayed is Batchelor's theory for the high wavenumber scalar mixing for $q = 5$.
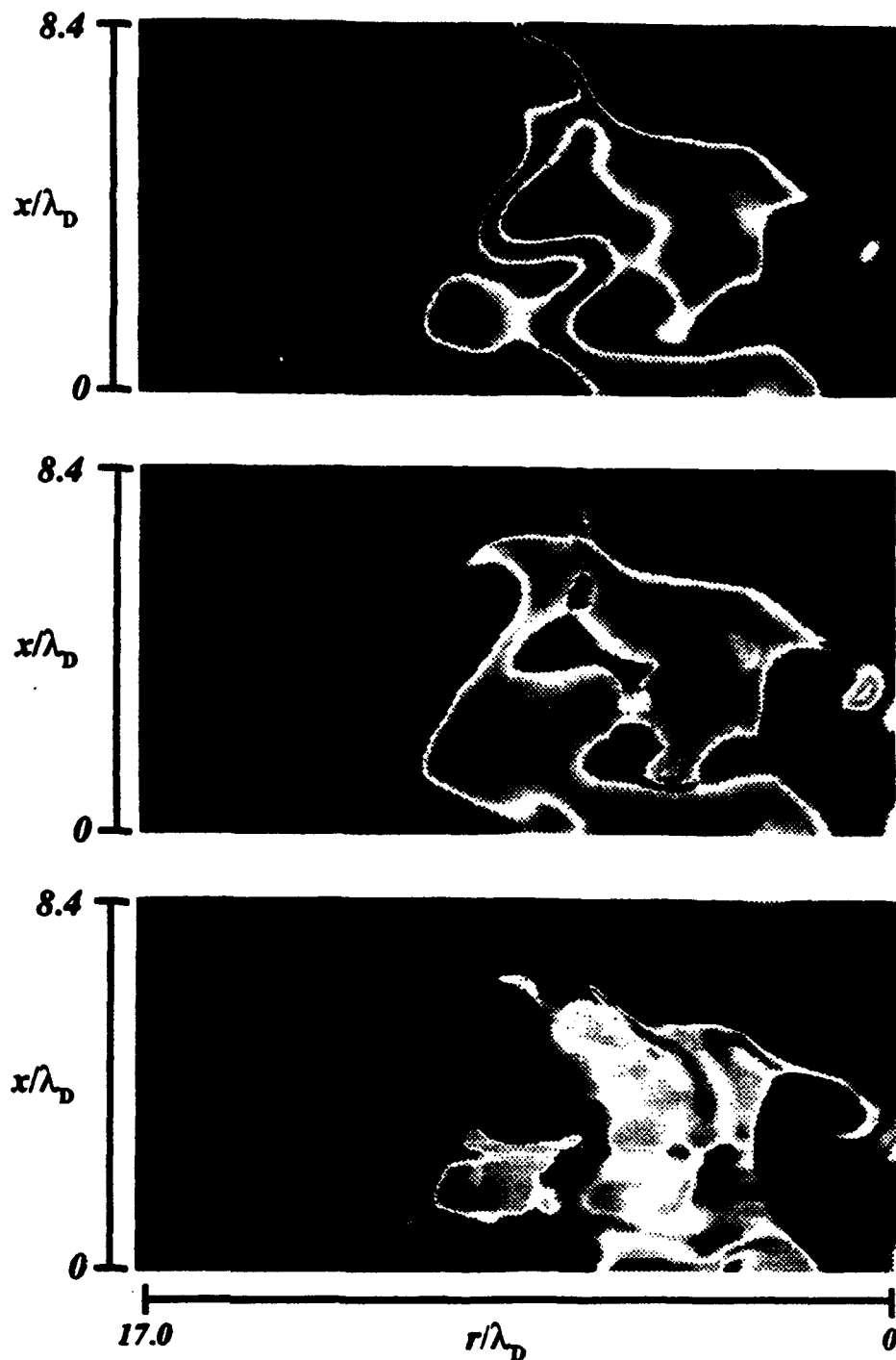
Fig. 4. Results for OH mass fraction field in a hydrogen-air turbulent jet diffusion flame, obtained from conserved scalar mixing measurements and the strained dissipation and reaction layer (SDRL) model for equilibrium (top), moderate non-equilibrium (middle), and deep nonequilibrium (bottom). Note the progression from thin "flamelet-like" OH zones near equilibrium to broad "distributed" OH structures with increasing chemical non-equilibrium.

207

CHEMICAL REACTIONS in TURBULENT MIXING FLOWS

P. E. Dimotakis and A. Leonard

Graduate Aeronautical Laboratories
California Institute of Technology, Pasadena, CA 91125

Summary/Overview

The purpose of this research is fundamental investigations of mixing, chemical reaction, and combustion processes; in turbulent, subsonic, and supersonic free-shear flows. The program is comprised of an experimental effort; an analytical, modeling, and computational effort; and a diagnostics and data-acquisition development effort, as directed by the specific needs of our experiments. The computational studies are focused on fundamental issues pertaining to the numerical simulation of compressible flows with strong fronts, in both chemically-reacting and nonreacting flows. Parts of this effort are cosponsored by AFOSR URI Grant No. F49620–93–1–0338.

Technical discussion

New experiments have been performed in the Supersonic Shear Layer (S^3L) facility in an attempt to separate Reynolds number and compressibility effects on molecular mixing in turbulent shear layers. The velocities and pressures required to produce compressible, kinetically fast, chemically-reacting experiments are such that existing data have Reynolds numbers an order of magnitude higher than previous experiments. Previous measurements in the compressible shear layer indicated a (weak) reduction in the mixed-fluid fraction.[1,2] Because increases in Mach number were also accompanied with increases in Reynolds number, this reduction could be due to either Mach- or Reynolds-number effects. In an attempt to decouple these effects, two sets of experiments have been performed. In each set, the Reynolds number is varied by a factor of two, with other relevant parameters held constant. The results of these experiments are plotted, along with previous data, in Fig. 1. As noted in previous discussions,[3] the data can be seen to be consistent with an extrapolation of the decrease observed in the mixed fluid fraction in incompressible flow data, *i.e.*, a reduction attributable to Reynolds number effects alone.

The S^3L facility has been upgraded to support bi-supersonic flow ($M_1 > 1$, $M_2 > 1$) and we have begun an experimental investigation of the interaction between two compressible gas streams, in the transonic Mach number regime. An example of this initial study is the schlieren image in Fig. 2. The inlet conditions for this shear layer were: $M_1 = 0.65$ [N_2], $M_2 = 1.13$ [N_2]. The image captures the interaction of an initial expansion fan, produced by a 5° turn at the test section inlet (lower left). This wave structure curves the shear layer
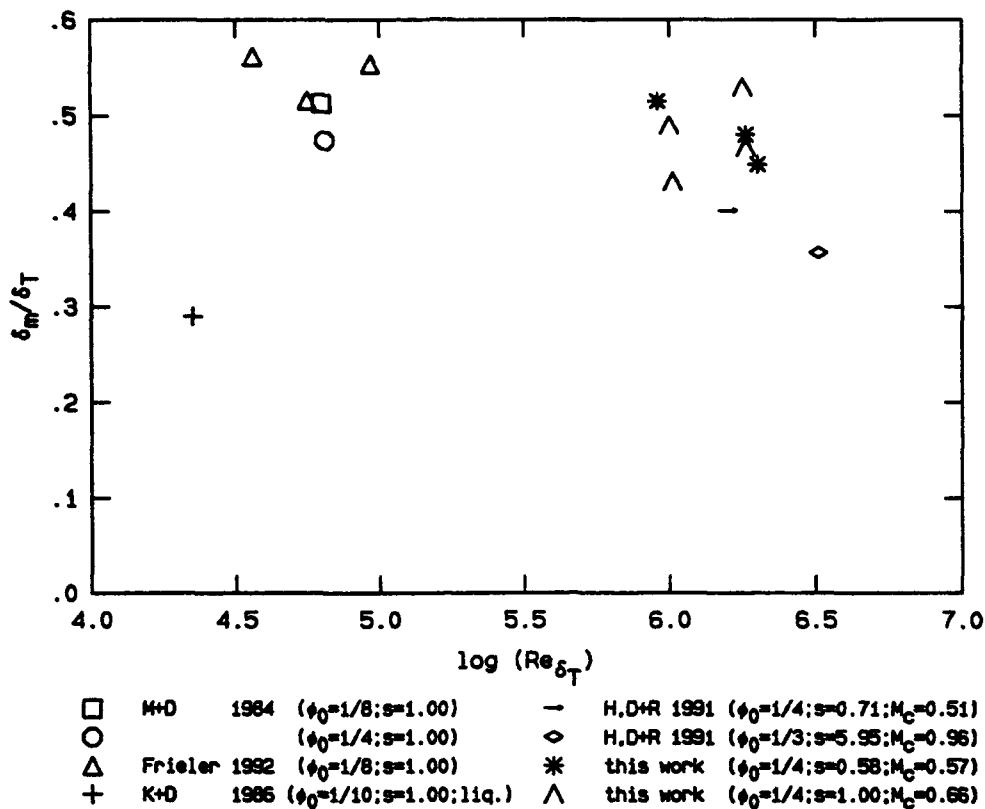
FIG. 1 Normalized mixed-fluid thickness vs. Re.

towards the bottom guidewall, producing an effective converging-diverging nozzle in the upper, initially subsonic freestream, and a divergence in the lower, supersonic freestream. This produces a flow in which both streams are accelerated.

We have continued the development of planar, laser-imaging techniques. In recent experiments, previous measurements[4] were extended with improvements in image signal-to-noise ratio. New time-resolved, planar, laser-Rayleigh scattering images have been recorded, in non-reacting shear layers, for convective Mach numbers with respect to the low-speed stream in the range of $0.5 \leq M_{c2} \equiv (U_c - U_2)/a_2 \leq 1.5$. These results were presented at the 1993 Annual Meeting of the American Physical Society, Division of Fluid Dynamics.[5] The experiments were conducted in the S^3L facility, in previously documented flow conditions. The beam of a frequency-doubled Nd:YAG laser (250 mJ in a 9 ns pulse) was steered through an optical window into the experimental test-section and shaped into a sheet of light. The sheet was passed through slits in the guide walls that acted as "aerodynamic" optical windows and aligned with the flow direction. The Rayleigh-scattered light was collected at right angles to the planar probe region and imaged onto a cryogenically-cooled, 1024^2 pixel, CCD array.

Figures 3 and 4 depict examples of such planar-image data. The high-speed stream occupies
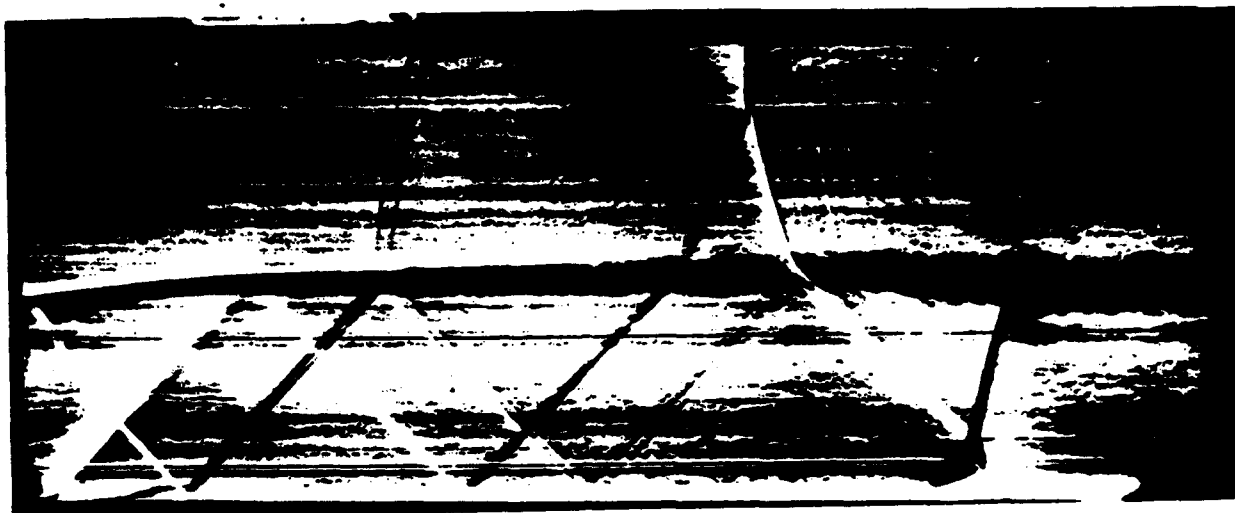
FIG. 2 Shear layer inlet conditions: $M_1 = 0.65$ [N_2], $M_2 = 1.13$ [N_2].
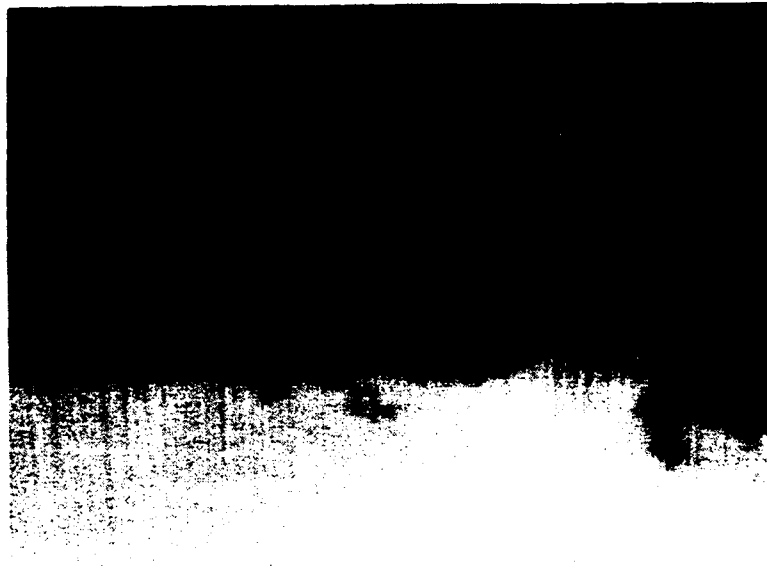
FIG. 3 Supersonic-subsonic flow. $M_c = 0.54$.

the upper part of the image and the low-speed stream the lower part of the image. The imaged region extends 3.2 cm in the streamwise direction, *i.e.*, roughly twice the width of the shear layer at that location (17 cm downstream from the tip of the splitter plate).

In Fig. 3, the high-speed stream fluid is N_2. In Fig. 4. the high-speed side stream fluid is He. In both cases. the low-speed stream fluid is C_2H_4 (ethylene). Even at relatively low compressibility, *i.e.*, $M_c = 0.54$ (Fig. 3), the mixing layer exhibits a different structure than the large-scale roller-like structures observed in incompressible shear layers. The low-speed fluid is seen to be peeled off by the high-speed stream. The transport of fluid across the layer appears to occur more through relatively well-defined intrusions of fluid into the opposite

210

FIG. 4 Supersonic-subsonic flow. $M_c = 0.94$.

stream, rather than through an entrainment process through the rotational motion of organized, large-scale vortical structures. In the higher compressibility flow image data (Fig. 4), the structure of the shear layer is different yet from the previous, lower-compressibility case. In addition, a wave system can be observed in the low-speed stream. These waves were observed in the same facility using Schlieren imaging[1,6] and can be seen to be generated by large-scale structures in the shear layer, convecting with a velocity higher that the speed of sound in the low-speed stream, i.e., $M_{c2} > 1$. A directly-estimated convective Mach number with respect to the low-speed stream, of $M_{c2} \simeq 2.5$ for this wave system can be inferred from the wave angles. This estimate compares well with previous findings, which were based on schlieren data as well as cross-correlation data derived from wall-mounted, high-speed, pressure transducers.[6]

In our investigation of turbulent mixing in liquid-phase jets, we have obtained high-resolution ($1,024^2$, high signal-to-noise ratio ($> 300 : 1$) images of the scalar field using planar laser-induced-fluorescence (LIF) techniques. The images were recorded in the far-field of a turbulent jet, perpendicular to the axis of symmetry, in the Reynolds number range of $4.5 \times 10^3 \leq Re \leq 18 \times 10^3$, and span the full transverse extent of the turbulent jet. Each image was calibrated and normalized using several background and uniform-illumination images. An example of an image at $Re = 18 \times 10^3$ is shown in Fig. 5a. From such images, contours of constant jet-fluid concentration have been produced, as shown in Fig. 5b. We have found that qualitative differences between low and high Reynolds number images are reflected on the individual probability density functions of the scalar field, as well as on other statistics. We are studying iso-scalar contours, over a range of scalar values, to uncover their statistical geometrical properties.

The new multidimensional Godunov scheme[7] is used to compute a two-dimensional invis-
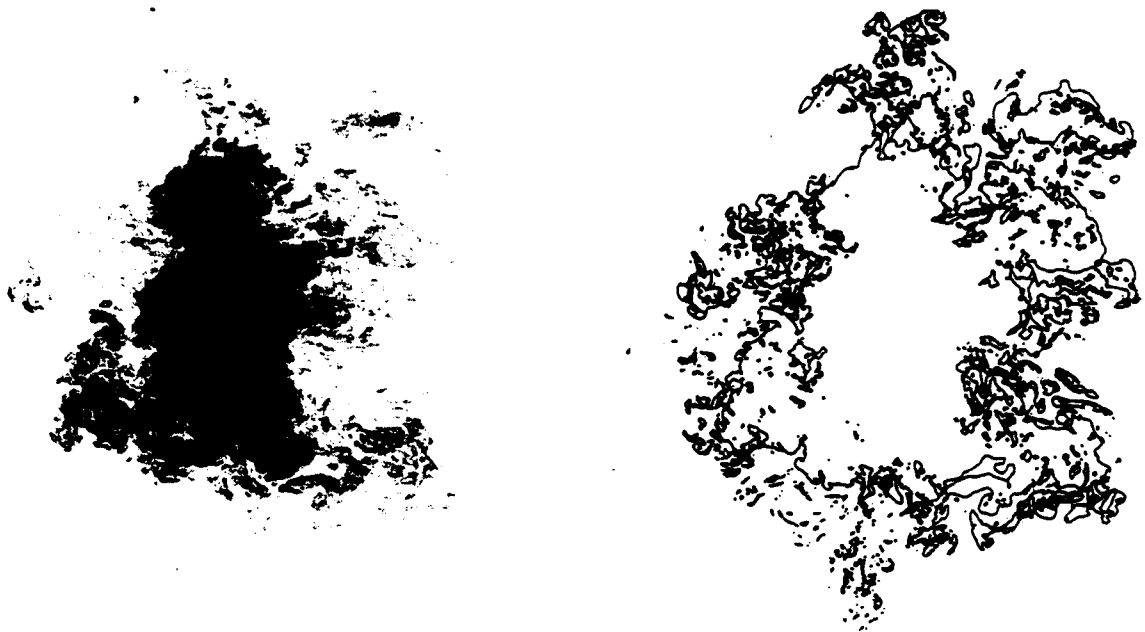
FIG. 5 (a) Planar LIF image in the far-field of a liquid-phase turbulent jet ($Re = 18 \times 10^3$).
(b) Iso-scalar contour.

cid shear layer. This employs the method of Riemann Invariant Manifolds, which can be viewed as the extension of the method of characteristics to the general case of unsteady multidimensional flow. These computations are performed in order to compare with the experimental results obtained from the GALCIT supersonic shear layer facility (cf. Fig. 2). The parameters are chosen to permit a direct comparison with experimental results. A perfect gas is assumed, with constant, specific-heat ratio of $\gamma = 1.4$. The computational domain is the rectangle $0 \le x \le 2$ and $0 \le y \le 1$. The lower boundary, $y = 0$, and upper boundary, $y = 1$, are reflecting walls, and at the right boundary, $x = 2$, outflow boundary conditions are imposed based on the local Riemann Invariants. Inflow boundary conditions are specified at the left boundary ($x = 0$). One such run is presented in Fig. 6. Mach number contours are given for the case with the low speed side corresponding to Mach number $M_1 = 0.65$ and the high speed side to Mach number $M_2 = 1.13$. The high speed stream enters the test section at a 5 degree angle. The inlet pressure ratio is $p_1/p_2 = 1.5$. As noted in the discussion of Fig. 2, the main feature of the computed flow is that the subsonic low speed stream is accelerated and becomes supersonic. The shear layer curves and acts as the lower boundary of gas-dynamic convergent-divergent nozzle for the low-speed stream.

212
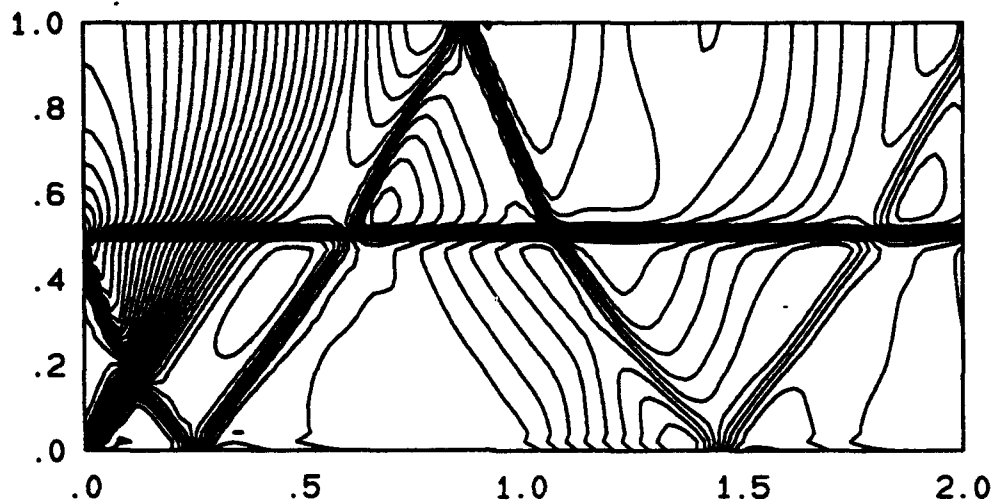
FIG. 6 Mach number contour levels for pressure ratio $p_1/p_2 = 1.5$. 60 contour levels in the range $0.6 < M < 1.4$. The resolution is 100×50 cells.

References

[1] Hall, J. L., *An Experimental Investigation of Structure, Mixing and Combustion in Compressible Turbulent Shear Layers*, Ph.D. thesis, California Institute of Technology (1991).

[2] Hall, J. L., Dimotakis, P. E., and Rosemann, H., "Some measurements of molecular mixing in compressible turbulent mixing layers," *AIAA 22nd Fluid Dynamics, Plasma Dynamics and Lasers Conference*, Paper 91-1719 (1991).

[3] Dimotakis, P. E., "Some issues on turbulent mixing and turbulence," GALCIT Report FM93-1a (1993).

[4] Rosemann, H., Dimotakis, P. E., and Hall, J., "Flow Visualization in Compressible Turbulent Shear Layers," IUTAM Symposium, *Eddy Structure Identification in Free Turbulent Shear Flows*, 12-14 October 1992 (Poitiers, France) (1992).

[5] Fourguette, D. C., Bond, C. L., and Dimotakis, P. E., "Scalar field measurements in supersonic shear layers," *Bull. Am. Phys. Soc.* 38(12), 2202 (1993).

[6] Hall, J. L., Dimotakis, P. E., and Rosemann, H., "Experiments in non-reacting compressible shear layers," *AIAA J.* 31(12), 2247-2254 (1993).

[7] Lappas, T., *An Adaptive Lagrangian Method for Computing 1-D Reacting Flows and the Theory of Riemann Invariant manifolds for the Compressible Euler Equations*, Ph.D. thesis, California Institute of Technology (1993).

213

REACTION ZONE MODELS
FOR VORTEX SIMULATION OF TURBULENT COMBUSTION

(AFOSR Grant No. 92-J-0445)

Principal Investigator: Ahmed F. Ghoniem

Department of Mechanical Engineering
Massachusetts Institute of Technology
Cambridge, MA 02139

SUMMARY/OVERVIEW

The objectives of this work are to (1) construct reaction zone models, incorporate these models in turbulent flow simulations, and exploit massive parallel processing in the computations; (2) develop approaches to incorporate flow-combustion interaction mechanisms which are compatible with Lagrangian simulation algorithms; and (3) use simulation results to reveal turbulent combustion physics with emphasis on approaches to enhance burning rates and reduce emissions. The approach used to simulate the turbulent flow is vortex methods in two and three dimensions, and that for modeling the reaction zone is based on unsteady strained thin flames. During the 93-94 year, we focused our efforts on three connected projects (1) massively parallel implementation of three dimensional vortex simulations, (2) development of unsteady thin flame models with detailed chemistry and transport, and (3) analysis of the reacting shear layer simulation results to shed more light on flow-combustion interaction mechanisms. The following discussion describes in some detail the motivations behind, accomplishments and current status of each project. Except for the third project, most of the work during this year has gone into methodology development, i.e. model formulation, computer codes construction, and validation of results.

TECHNICAL DISCUSSION

Progress in the application of advanced simulation methods in turbulent combustion relies on developing algorithm which take full advantage of the most powerful computer architecture available. Developing a massively parallel version of the vortex simulation codes has been motivated by several factors. (1) The computational needs of these codes scale as $O(N^2)$, where N in the total number of vortex elements used to discretize the vorticity field. Moreover, the ratio between the integral and the smallest (Kolmogorov) flow length scales which must be captured in a simulation is $O(R^{3/4})$ where R is the Reynolds number. Since vortex elements must be distributed in the cross section of the vorticity structures to properly capture their dynamics, the number of elements increase as $R^{3/2}$, making the computational effort increase almost cubically with the flow Reynolds number. (2) Recent trends in hardware and system software emphasize the parallel operation of several to several hundred processors connected to a common memory (shared memory) or possessing their individual memory (message passing). Load balancing and synchronizing among the processor determines the parallel efficiency. (3) The apparent compatibility of the computational algorithms of the vortex method with the computing environment of a massively parallel architecture. This is because the basic ingredients of the method consist of computing the velocity field as a sum over the elliptic contributions of all the vortex elements in the field, amounting to the N^2 operations, and updating the location and strength of the vortex elements, leading to an extra N operations. This strategy, which maintains the grid-free, adaptive nature of the algorithm, sets a limit on the number of elements according to the available computer resources. On the other hand, it is this very property which makes these methods ideal for parallel operation. In a parallel environment, especially with a shared memory architecture, the actual clock time, equivalent to almost a single processor time, required to compute the vortex interactions on an M-processor machine is $O(N^2/M^2)$, and hence the total time is $O(N^2/M)$, i.e. one can, given efficient communication links, achieve linear improvement of the computational speed with the number of processors.

Empowered by these observations, we proceeded towards developing a fully three dimensional internal flow vortex simulation code and testing this code on a number of massively parallel machines. As a first accomplishment, we were able to demonstrate the validity of the prediction described above, i.e. the linear parallel efficiency of vortex codes, by running a three dimensional vortex interactions code on a Connection Machine CM-5, and comparing the time required to compute a field using up to 35,000 elements on the fastest vector machine available, the CRAY C-90, and a CM-5 using up to 128 processors. The quadratic increase in time required by the C-90 is clearly shown in figure 1, as well as the better than order of magnitude improvement when the same code is adopted to the CM-5. The nearly linear improvement exhibited by the time required on the CM-5 as more processors are used is another indication of the enormous potential and impact of this technology. We expect to get even better performance by incorporating machine dependent directives which perform functions at the machine language level.

The effort to develop a computationally efficient and accurate unsteady thin flame models in which some detailed chemical kinetics and transport models within the flame structure can be incorporated, while, outside the flame, the flow is treated as essentially non reacting, has proceeded according to the plan described in last year's report. The efficiency of our unsteady strained flame models is achieved by adopting a number of coordinate maps and imposing some weak restrictions on the variation of the transport coefficients inside the flame zone, to transform the original unsteady reaction-convection-diffusion equations into a set of unsteady reaction-diffusion equations which are much easier to integrate. The problem is actually reduced to a two-point boundary value problem solved using adaptive girding to optimize the placement of the computational points between the two streams; unburnt and burnt mixtures in a premixed combustion simulation and fuel and oxidizer in a diffusion combustion simulation. We proceeded to test our modeling assumptions with regard to the variation of the transport properties against the actual variation within typical flame structures and found them to be consistent with the expected behavior. Our effort this year amounted to testing our models against results of a strained premixed flame computations of methane flames.

A sample result of the unsteady flame model, pertaining to the response of a premixed flame to a stepwise change in the applied strain rate, is shown in figure 2. In this calculations, a one-step reaction model is used and the effect of the Lewis number on the time required by the flame to reach steady state, the settling time, is shown. At non unity Lewis number, the settling time can be significant, $O(10^{-3}$ s$)$ and the response of the flame to changes in the flow field may not be instantaneous as often assumed in turbulent combustion simulations. We find that, at non unity Lewis number conditions, the response time of the flame is that associated with the convection-diffusion zone and not the reaction-diffusion zone. The implications here are that some basic assumptions in conventional thin flame and flamelet models should be revised. The study was also extended to the case of a periodic strain where it was found that the most important impact of the frequency of fluctuation, as long as the amplitude of fluctuation keeps the maximum strain below the extinction value, is to create a phase lag between the applied strain, and hence the velocity field, and the change in the burning velocity. This lag may not be of much significance to, e.g., the overall heat release, but it is certainly of concern to problems associated with combustion instability. W are pursuing the effort to incorporate reduced chemical mechanisms in our simulations.

The third project is concerned with analyzing simulations of spatially developing reacting shear layers to reveal the vorticity dynamics of exothermic flows. Simulation with finite, Arrhenius-rate chemistry and infinitely fast chemistry were compared and both agreed well as far as the effect of energy release on the vorticity dynamics is concerned, showing that implementing flame sheet models will not compromise the flow physics in a significant way . Results indicate that exothermic reactions modify the shape, size, speed and orientation of the large eddies and alters there interaction mechanisms from the conventional pairing mode into a tearing mode, leading to an overall reduction of the overall cross stream growth of the layer. We show that all the observed effects can be traced back to the primary mechanisms by which heat

release can modify the vorticity dynamics, volumetric expansion and baroclinic vorticity generation. The local reduction in the magnitude of the vorticity due to the expansion of the material elements transporting the vorticity diminishes the mixing zone by aligning the eddies major axis with the flow direction. On the other hand, baroclinic vorticity generation is manifested in the formation of a band of positive vorticity around the eddies whose sign is predominantly negative, thus inhibiting entrainment and affecting the eddy interaction mode as described above.

REFERENCES

1.   Soteriou, M.C. and Ghoniem, A.F., "Numerical Study of Exothermic Combustion on Mixing Layer using Finite and Infinite Reacting Rate Models," presented at ICDERS, August 3, 1993, Portugal, to appear in *Combust. Sci. Tech.*
2.   Soteriou, M.C. and Ghoniem, A.F., "Simulation of Flow Combustion Interactions on a Spatially Developing Layer," presented at the Second U.S. National Congress on Computational Mechanics, Aug. 16, 1993, Washington, D.C., to appear in a special volume.
3.   Soteriou, M.C. and Ghoniem, A.F., "Dynamics of Reacting Shear Flows, Effects of Exothermicity and Forcing," presented at the 32nd Aerospace Sciences Meeting, Reno, NV, January 1994, submitted to the *AIAA Journal*.
4.   Soteriou, M.C. and Ghoniem, A.F., "Vorticity Dynamics of an Exothermic Spatially Developing, Forced, Reacting Shear Layer," accepted for presentation at the *25th Symposium (International) on Combustion*, UC Irvine, August 1994, to appear in Proceedings.
5.   Petrov, C.A. and Ghoniem, A.F., "An Unsteady Strained Flame Model for Turbulent Combustion Simulation," presented at the 32nd Aerospace Sciences Meeting, January 1994, Reno, NV.
6.   Petrov, C.A. and Ghoniem, A.F., "The Transient Response of Strained Laminar Premixed Flames," submitted for publication in *Combust. Flame*.
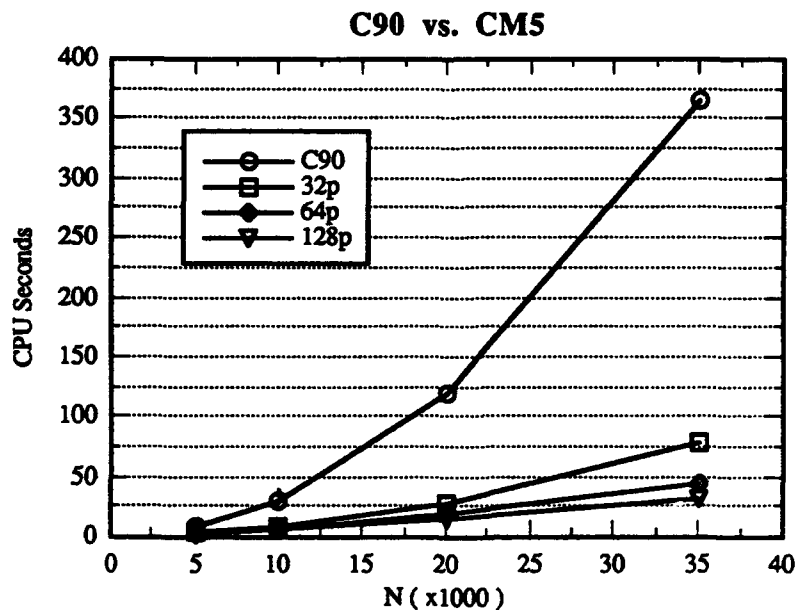
Figure 1.   Comparison between the CPU time required to compute the vortex interactions a single processor C90 and a CM-5 with different numbers of processors.

Figure 2.   The steady state burning velocity and flame location, left, and the settling time, right, plotted against the Karlovitz number for different L_e for $T_b = 1950\ K$.

Figure 3.   The vorticity field in a uniform density, top, and variable density, bottom, reacting shear layer. The gray scale corresponds to the magnitude and sign of vorticity. The density ratio of the unburnt to the burnt mixture is five while the stream velocity ratio is two.

217

Figure 2. The steady state burning velocity and flame location, left, and the settling time, right, plotted against the Karlovitz number for different L_e for $T_b = 1950\ K$.

Figure 3. The vorticity field in a uniform density, top, and variable density, bottom, reacting shear layer. The gray scale corresponds to the magnitude and sign of vorticity. The density ratio of the unburnt to the burnt mixture is five while the stream velocity ratio is two.

NUMERICAL STUDIES FOR THE RAM ACCELERATOR

(AFOSR-MIPR-94-0004)

Chiping Li, K. Kailasanath, Elaine S. Oran, and Jay P. Boris

Laboratory for Computational Physics, Code 6400
Naval Research Laboratory, Washington, DC 20375

SUMMARY/OVERVIEW

Time-accurate, multidimensional Euler and Navier-Stokes simulations have been performed to study reactive flows in the ram accelerator. In the past year, we have studied the structure and dynamics of shocks and detonations on accelerating projectiles. Our studies show that: (1) behind the reflected shocks on the projectile, the detonation structure interacts with more than one shock and is significantly more complex than that of an oblique detonation generated by a single, wedge-induced shock; (2) during acceleration, the detonation structure remains stable and consistently generates the high pressure which produces strong thrust on the projectile; (3) the detonation structure moves upstream as the reflected shocks on the projectile are strengthened by the projectile acceleration. Furthermore, the pressure distribution on the projectile from these simulations provides useful information on the projectile stability. In the last year, we have also studied the boundary layer behind moving shocks on the wall of the launch tube. The results show that the boundary layer weakens the shock and the overall effect of the boundary layer on the combustion process is rather small.

TECHNICAL DISCUSSION

In the ram accelerator, a projectile is accelerated by the high pressure generated in the shock-induced combustion in premixed fuel-oxidizer mixtures. In order to achieve strong, sustainable projectile acceleration, many basic issues, such as the dynamics of shocks and detonations, the mechanism of different forms of shock-induced combustion and the effect of different types of boundary layers, need to be understood. Our approach is to use the time-accurate, multidimensional numerical simulation as a tool to study these issues.

Detonation Structures on Accelerating Projectiles

In the past, we have studied the structure and stability of detonations generated by a single, wedge-induced shock. Those studies show that in a wide range of flow and mixture conditions, the detonation structure is stable and very resilient to disturbances in the flow and very suitable for ram-accelerator applications. This structure is multidimensional and consists of a nonreactive shock, an induction region, a set of deflagration waves, and a detonation wave in which the pressure rise generated by the energy release is coupled with the shock front. The detonation structure on the ram-accelerator projectile is likely to have many similarities to the oblique detonation structure generated by a single, wedge-induced shock. However, the complexity of the multiple shock reflections and the expansion waves on the projectile as well as the projectile acceleration may significantly affect the structure and stability of the detonation in the ram accelerator.

In order to study the structure and dynamics of the detonation during the acceleration process, we conducted highly resolved simulations for the reactive flow in a small region (Fig. 1) where multiple shock reflections are formed between the projectile and the wall of the launch tube. We have simulated the detonation structure on the ram-accelerator projectile in the stoichiometric hydrogen-air mixture (H_2:O_2:N_2/2:1:3.76) at Mach numbers ranging from 7.0 to 10.0. These simulations show that the detonation structure in the ram accelerator has the same basic elements as those in the oblique detonation structure generated by a single, wedge-induced shock. However, in the ram accelerator, the induction region typically interacts with more than one shock and also with expansion waves. These expansion waves weaken the induction process and further complicate the detonation structure. The configuration of the detonation structure in the ram accelerator can be quite different from and significantly more complex than that generated by a single shock.

For example, in the case of $M = 7.6$, the detonation only exists in a very small region close to the projectile surface and the energy release becomes decoupled from the shock not far from the projectile because of the expansion waves generated at the projectile shoulder. At $M = 8.0$, the second reflected shock becomes an oblique detonation near the projectile and, away from the projectile, the second

reflected shock follows the water, formation and energy release. However, at M = 8.4, the structure of the detonation is rather similar to that of a detonation generated by a single shock. Figures 2-4 show contours of the induction parameter, water concentration and pressure from the simulations for M = 7.6, 8.0 and 8.4. These figures also show pressure profiles on the projectile surface and tube wall.

As the projectile Mach number increases, the detonation moves upstream from one reflected shock to another. The multiple shock reflections provide many possible configurations for a stable detonation structure in a wide range of Mach numbers. This explains why the detonation structure can be maintained on the projectile for a significant amount of time to generate continuously strong projectile acceleration, as observed in our earlier studies.

Projectile Stability

In the past year, we began to use the pressure information obtained from our simulations to analyze the stability of the ram-accelerator projectile. The projectile stability is an important issue in ram-accelerator development. An unstable projectile design can lead to canting and premature destruction of the projectile. Our simulations show that the peak pressure occurs on the rear part of the ram-accelerator projectile during acceleration, unlike projectiles in open air. Therefore, the conclusion from the standard projectile analysis may not be valid for the projectile during acceleration. Our analysis indicates that, to maintain projectile stability, the location of the center of mass has to be significantly behind those of conventional projectiles in open air. Information from such analyses is very useful to the experimental efforts conducted at the Eglin AFB and other sites. However, our finding is still preliminary and this issue will be further investigated.

Shock-Boundary-Layer Structure

Previously, we have studied the effect of the boundary layer behind the shock generated at the leading tip of the projectile. The results show that the expansion waves behind the shock decrease the temperature and pressure in the main flow and significantly limit the overall effect of the boundary layer on the combustion process. In the past year, we have numerically simulated the boundary layer behind the moving shock on the launch tube. In the simulations, a coordinate transformation is performed so that the top boundary is moving at the original shock speed and the shock is nearly stationary. The simulations show the detailed structure of the shock and the boundary layer. Near the wall, the shock curves downstream due to the velocity difference between the shock and the wall. Behind the shock, the pressure and temperature increase in a small region near the wall. However, these increases are much smaller than those in the boundary layer on the projectile under similar flow conditions. Unlike the temperature and pressure increases in boundary layers on the projectile, the temperature and pressure increases here are likely to be due to direct viscous effects such as viscous heating rather than indirect viscous effects such as compression generated by the boundary-layer-induced shock. In the cases studied , the the effect of the boundary layer behind a moving shock on the combustion process is much less than that of the boundary layer behind a stationary shock generated at the projectile tip.

PUBLICATIONS AND PRESENTATIONS

Structure of Reaction Waves behind Oblique Shocks, C. Li, K. Kailasanath, and E.S. Oran, *Progress in Aeronautics and Astronautics*, 153:231, 1993.

Numerical Simulations of Reactive Flows in Ram Accelerators, Li C., Kailasanath K., and Oran E.S., the 1st Int. Meeting on Ram-Accelerators, Saint-Louis, France, 1993.

Analysis of Transient Flows in Thermally Choked Ram Accelerators, C. Li, K. Kailasanath, E.S. Oran, A.M. Landsberg, and J.P. Boris, AIAA-93-1916, 1993.

Structure of Different Types of Supersonic Boundary Layers, C. Li and K. Kailasanath, *the 46th APS Meeting of Fluid Dynamics*, Albuquerque, NM, 1993.

Numerical Simulations of Transient Reactive Flows in Ram Accelerators, C. Li, K. Kailasanath, E.S. Oran, A.M. Landsberg, and J.P. Boris, Submitted to *Shock Waves*, 1993.

Detonation structure on Ram-Accelerator Projectiles , C. Li, K. Kailasanath, and E.S. Oran, AIAA-94-0551, 1994.

Detonation Structures behind Oblique Shocks, C. Li, K. Kailasanath, and E.S. Oran, *Physics of Fluids*, 6:1600, 1994.
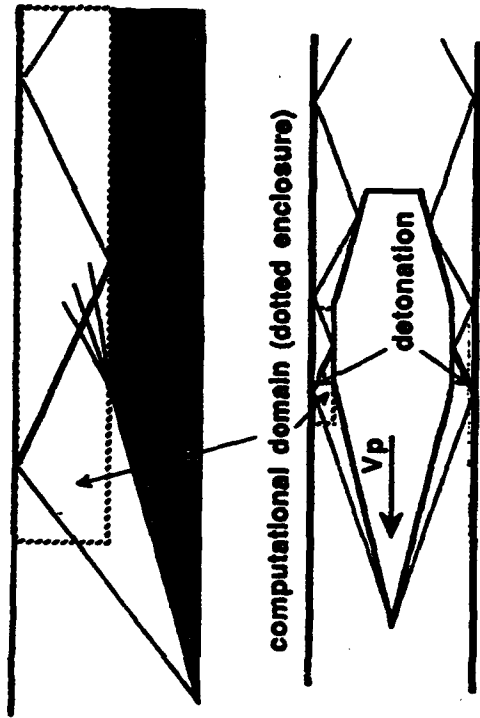
Figure 1 Schematic of the computational domain used to study the detailed detonation structure on the ram-accelerator projectile.
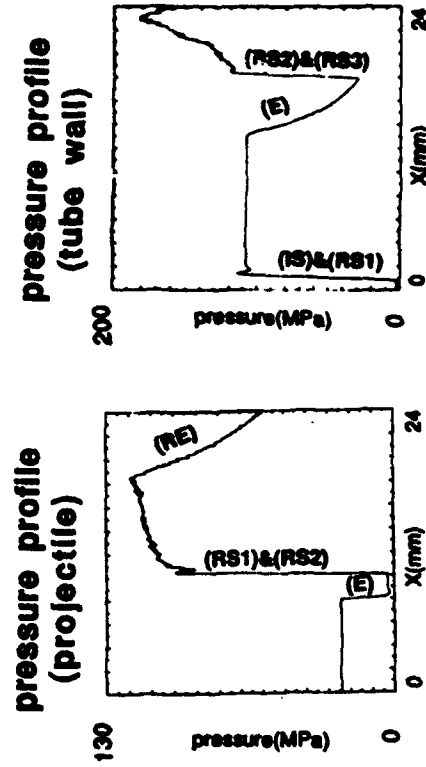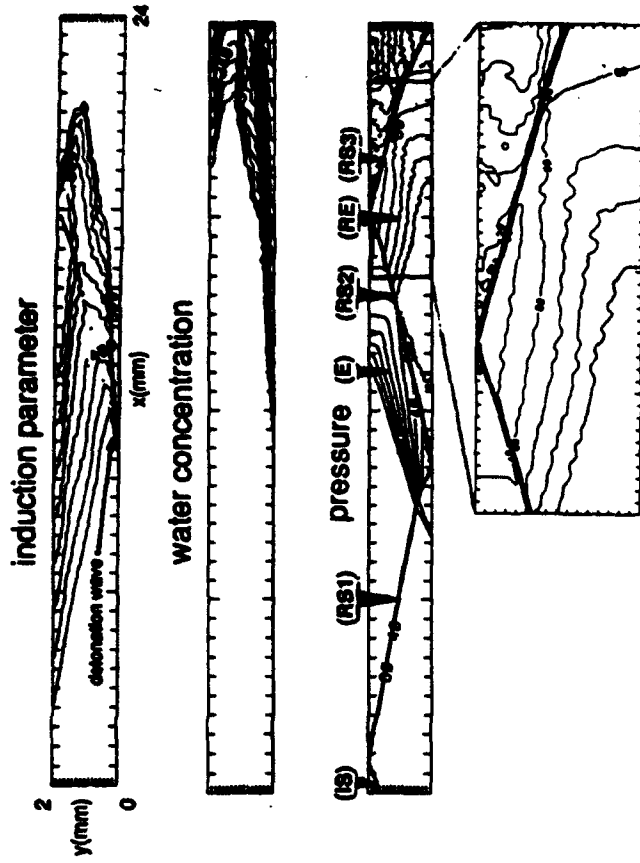
Figure 2 Flow properties from the simulation for the detailed detonation structure generated by a series of reflected shocks on the ram-accelerator projectile. The inflow Mach number is 7.6 and the mixture ratio is $H_2:O_2:N_2/2:1:3.76$. The leading angle of the projectile is $16°$. The size of the computational domain is 2.4×0.2 cm². In the flow field, the incident shock (IS) impinges on the tube wall and is reflected (RS1). RS1 is weakened by the expansion waves (E) generated at the corner of the projectile shoulder and, then, collides with the projectile generating RS2. E is further reflected back from the tube wall (RE). RS2 is also reflected back from the tube wall creating RS3. The detonation exists in a very small region near the projectile.

221

Figure 4 Flow properties from the simulation for the detailed detonation structure generated by a series of reflected shocks on the ram-accelerator projectile. The inflow Mach number is 8.4 and the mixture ratio is $H_2:O_2:N_2/2:1:3.76$. The leading angle of the projectile is 16°. The size of the computational domain is 2.4×0.2 cm^2. The detonation structure here is rather similar to that of a detonation generate by a single shock.

Figure 3 Flow properties from the simulation for the detailed detonation structure generated by a series of reflected shocks on the ram-accelerator projectile. The inflow Mach number is 8.0 and the mixture ratio is $H_2:O_2:N_2/2:1:3.76$. The leading angle of the projectile is 16°. The size of the computational domain is 2.4×0.2 cm^2. Near the projectile, a significant part of the second reflected shock becomes an detonation.

222

STUDIES ON HIGH PRESSURE AND UNSTEADY FLAME PHENOMENA

Principal Investigator: Chung K. Law

Princeton University
Princeton, NJ 08544

SUMMARY/OVERVIEW

The objective of the present program is to study the structure and response of steady and unsteady laminar premixed and nonpremixed flames in reduced and elevated pressure environments through (a) non-intrusive experimentation, (b) computational simulation using detailed flame and kinetic codes, and (c) asymptotic analysis with reduced kinetic mechanisms. During the reporting period progress has been made in the following projects: (1) a theoretical and experimental study of unsteady diffusion flames; (2) a computational and experimental study of hydrogen/air diffusion flames at sub- and super-atmospheric pressures; (3) an asymptotic analysis of the structure of premixed flames with volumetric heat loss; and (4) asymptotic analyses of ignition in the supersonic hydrogen/air mixing layer with reduced mechanisms.

TECHNICAL DISCUSSIONS

1. Studies on Unsteady Diffusion Flames

A crucial influence on the flame behavior which so far has not been adequately addressed is the effect of unsteadiness of the environment on the flame behavior. This issue is of particular relevance to the modeling of turbulent flames through the concept of laminar flamelets. These flamelets are subjected to fluctuating flows with various intensities of straining, and it is reasonable to expect that the flame would respond differently in an oscillating strained flow field than in a steady strained flow field.

During the reporting period we have analyzed the response of a counterflow diffusion flame subjected to an oscillating strain rate, using large activation energy asymptotics. The characteristic oscillation time of practical interest is found to be of the same order as the characteristic diffusion time of the flame, so that the flame structure consists of a quasi-steady reactive-diffusive layer embedded in the outer unsteady-convective-diffusive zones. A linear analysis is conducted by assuming that the amplitude of the strain rate oscillation is small relative to the mean strain rate.

Figure 1 shows the real parts of the fluctuations in heat release as a function of the frequency of oscillation, when the mean flame is either near equilibrium or near extinction. It has been found that the flame response is controlled mainly by two effects: (a) the response of the convective mass flux into the reaction sheet, which is directly related to the flow-field variation applied at the boundary, and (b) the response of the reaction sheet to adjust the reduced residence time due to finite-rate chemistry. For flames near equilibrium, the former effect tends to be dominant, so that the response of the net heat release is in phase (i.e. positive real) with the strain rate oscillation. For flames near extinction, however, the finite-rate chemistry effect overtakes the fluid-dynamic effect such that increasing strain rate leads to a reduction of the reactivity of the flame during the oscillatory cycle. As such, the net heat release response of the near-extinction flame becomes out of phase with the strain rate oscillation in the sense of the Rayleigh's criterion. Results of the present study suggest the possibility that the unsteady characteristics of the near-extinction diffusion flame can be significantly different from those in the Burke-Schumann limit.

A parallel experimental study is also in progress. Figure 2 shows the schematic of the experimental setup. To achieve the instantaneous measurement of the unsteady counterflow flame, the laser beam is modulated by an optical chopper at the applied perturbation frequency. Then the signal is delayed and sent to the loudspeakers, which generate the acoustic perturbation of the flow in the nozzle. By comparing the signal sent to the loudspeakers with the chopped laser signal detected by the photodiode, the entire applied sine wave can be mapped out. We shall measure the instantaneous snapshots of the strain rate field and flame responses in order to provide more deterministic information of the unsteady flame phenomena.

The theoretical part of this work is reported in Publication No. 1.

2. Pressure Effects on Extinction of Hydrogen-Air Diffusion Flames

Recent interests in high-speed aero-propulsion have led to considerable research on hydrogen/oxygen chemistry, as well as its coupling to fluid flows. Because of the high-speed nature of the flow, the available residence time for mixing and chemical reaction is significantly reduced. Furthermore, the combustion chamber within aero-engines not only operates at higher pressures, but the chamber pressure can also undergo strong fluctuations, such that chemical kinetics and the flame behavior can be significantly modified from those at the atmospheric condition. Consequently, it is of importance to understand the ignition and extinction phenomena involving hydrogen/oxygen mixtures under variable pressures.

We have conducted LDV measurements of local extinction strain rates of nonpremixed counterflow flames of diluted hydrogen against air, at pressures of 0.5 to 1.0 atmosphere. The measured data compare well with results obtained from computational simulation with detailed chemistry and transport. We have subsequently performed additional computational studies of the pressure effect on flame extinction. Figure 3 shows extinction flame temperatures calculated for a 13% hydrogen mixture as a function of the system pressure. The relationship of extinction temperatures with pressure for this system exhibits the familiar non-monotonic "Z" shaped dependency as observed for the homogeneous hydrogen/oxygen explosion limits. This implies that an increase in pressure could render a mixture to change from an extinguished state, to a burning state, and back to an extinguished state. This behavior is explained on the basis of the intrinsic chain branching-termination kinetics of hydrogen oxidation.

This work is reported in Publication No. 2.

3. Asymptotic Analysis of Premixed Flames with Volumetric Heat Loss

A classical model problem for the study of premixed flame extinction is that of Spalding, who analyzed a one-dimensional freely-propagating flame with a temperature-sensitive one-step overall reaction and radiative heat loss. More sophisticated analyses have since been performed using one-step chemistry and activation energy asymptotics. These studies predict that extinction occurs when the ratio of the burning rate to its adiabatic value is reduced to $e^{-1/2} \approx 0.61$, a result that is insensitive to the nature of the heat loss. Subsequent numerical computations that consider detailed transport and chemistry also predict extinction when the burning rate is reduced to roughly 60% of its adiabatic value, suggesting that this value may represent a universal constant, independent of reaction and loss mechanisms.

In order to gain a better understanding of the role of dominant kinetic parameters, we have revisited this classical problem and have performed asymptotic analyses with multi-step reaction mechanisms. We first employed the two-step Zel'dovich-Liñán mechanism which consists of a branching reaction and a competing recombination reaction, thus capturing the chain nature of real flames. The analysis again predicts the normalized burning rate at extinction to be $e^{-1/2}$.

We have also made considerable progress in understanding the extinction characteristics of nonadiabatic methane/air flames by considering a reduced reaction mechanism that has been systematically derived from larger detailed mechanisms. Thus the reduced mechanism contains many important chemical parameters that are dominant in the chemistry of "real" flames. Extinction conditions were found explicitly in terms of these parameters. Results show that the critical value of the burning rate at extinction, though not a universal constant, varies only slightly, in the range between 0.61 and 0.64. In figure 4 we have plotted the nondimensional burning rate as a function of the loss parameter. At the (extinction) turning point, the burning rate is nearly the

same for all curves, but the critical value of the heat loss parameter is seen to be less than that for one-step models. The corresponding reduction in flame temperature needed for extinction is therefore substantially less than that predicted by one-step models.

These works for the two-step model and the methane/air flames are respectively reported in Publication Nos. 3 and 4.

4. Ignition in the Supersonic Hydrogen/Air Mixing Layer

The development of the scramjet engine for supersonic propulsion and the scramaccelerator for hypervelocity projectile launching has renewed interest in supersonic combustion. Fundamental studies such as ignition within chemically-reactive supersonic boundary layer flows can provide better understanding of the key factors in developing supersonic combustors. In our previous studies of one-step chemistry model, several distinct ignition situations are identified, and it was shown that ignition can be greatly facilitated by use of the kinetic energy of the high-speed flow through viscous heating. In the present study we take one step further and consider more realistic hydrogen/air mixing layer using reduced mechanisms. In particular, two distinct reduced mechanisms are identified depending on the maximum characteristic ignition temperature (T^*) relative to the crossover temperature (T_c), at which the rates of the chain branching and termination reactions are equal. Each regime is further subdivided into two distinct cases, namely the hot stream ($\beta > \mu$) and the viscous heating ($\beta < \mu$) case, depending on the relative dominance of the external and internal ignition sources. These four cases are analyzed separately using asymptotic technique, and the analysis properly captures the ignition process in a well-defined manner.

Figure 5 shows the minimum ignition distance as a function of the flow Mach number. Although the gross trend is similar to that of the one-step analysis, it is clearly shown that the system response is significantly enriched when realistic chemistry is properly taken into account. For example, ignition in the low temperature regime (region I, II) is controlled by a large activation energy process, so that the ignition distance is more sensitive to its characteristic temperature than that in the high temperature regime (region III, IV). In figure 6, it is also shown that the ignition distance varies non-monotonically with the system pressure in the manner of the well-known hydrogen/oxygen explosion limits, thereby further substantiating the importance of chemical chain mechanisms in this class of chemically-reacting boundary layer flows.

This work is reported in Publication No. 6.

MAJOR PUBLICATIONS (April, 1993 – March, 1994)

1. "Response of counterflow diffusion flames to oscillating strain rates," by H. G. Im, C. K. Law, J. S. Kim and F. A. Williams, to appear in *Combustion and Flame* as part of the *Twenty-Fifth Symposium (International) on Combustion* (1994).

2. "Effects of pressure and dilution on the extinction of counterflow nonpremixed hydrogen-air flames," by P. Papas, I. Glassman and C. K. Law, to appear in the *Proceedings of the Twenty-Fifth Symposium (International) on Combustion*, the Combustion Institute, Pittsburgh, PA (1994).

3. "Laminar flame propagation with volumetric heat loss and chain branching-termination reactions," by B. H. Chao and C. K. Law, *International Journal of Heat and Mass Transfer*, Vol. 37, pp. 673-680 (1994).

4. "Extinction of premixed methane-air flames with volumetric heat loss," by J. K. Bechtold and C. K. Law, submitted.

5. "Analysis of thermal ignition in the supersonic mixing layer," by H. G. Im, B. H. Chao, J. K. Bechtold and C. K. Law, *AIAA Journal*, Vol. 32, No. 2, pp. 341-349 (1994).

6. "Ignition in the supersonic hydrogen/air mixing layer with reduced reaction mechanisms," by H. G. Im, S. R. Lee and C. K. Law, submitted.

Figure 1

EXPERIMENTAL SET-UP
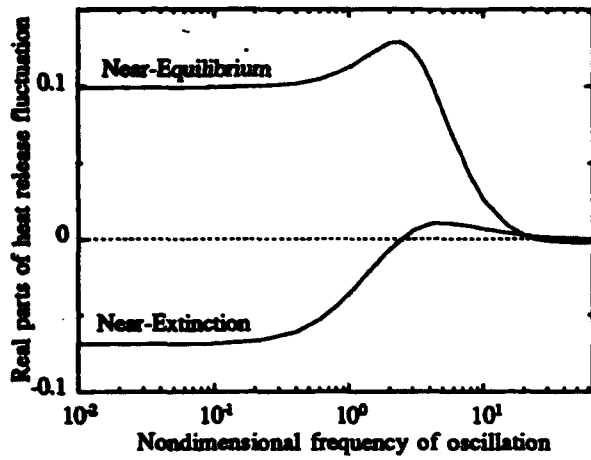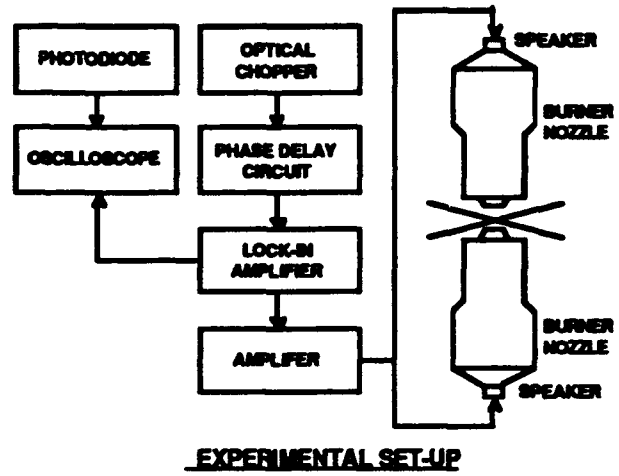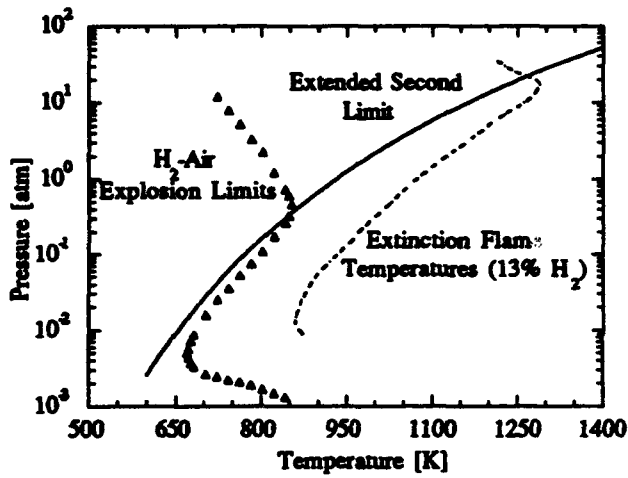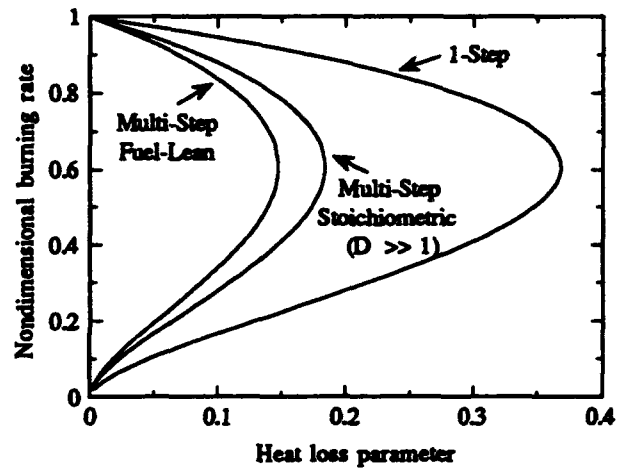
Figure 2

Figure 3

Figure 4
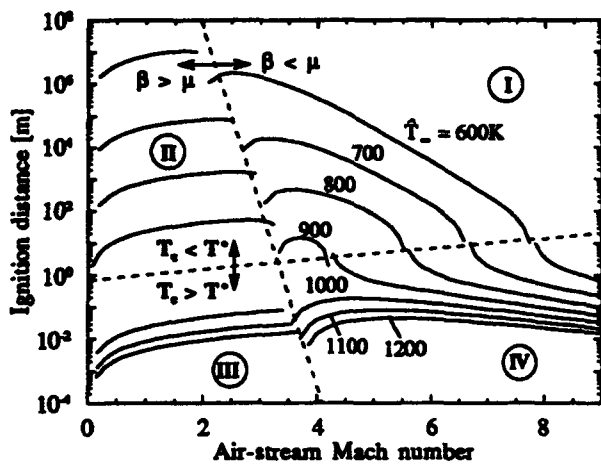
Figure 5
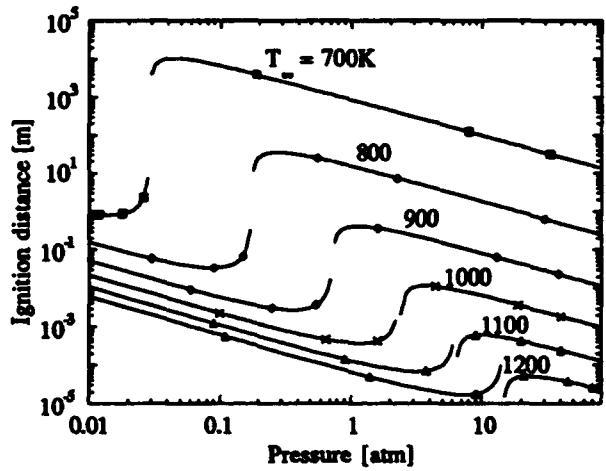
Figure 6

226

FUNDAMENTAL RESEARCH TO ADVANCE RAM ACCELERATOR TECHNOLOGY

Donald M. Littrell and Capt. Keith Clutter
WL/MNAA, Eglin AFB, Florida 32542-6810

Raj Sinha
SAIC, Ft. Washington, Pennsylvania 19034-3211

Glenn E. Rolader
SAIC, Shalimar, Florida 32579

Eugene Clothiaux
Department of Physics, Auburn University, Alabama 36849

SUMMARY/OVERVIEW:

right Laboratory's Armament Directorate (WL/MN), in conjunction with the Air Force Office of Scientific Research (AFOSR), has a multi-year program to advance the understanding of the fundamental processes (e.g., shock-boundary layer interaction, boundary layer combustion, transient compressible turbulence, high pressure kinetics, the transition from deflagration to detonation) that occur in a high pressure combustible environment such as the ram accelerator. The research objectives are: (1) to develop computational fluid dynamic (CFD) techniques to simulate fundamental fluid dynamic, kinetic, and combustion/detonation processes, and (2) to validate these CFD codes through the development of optical diagnostic techniques for characterizing flow fields in high pressure combustion environments. During the reporting period, progress has been made in determining: the effect of the subgrid on the large scale vortices in a large eddy simulation of a high pressure reacting gas; and the detonation characteristics of a sub-atmospheric methane/oxygen mixture.

TECHNICAL DISCUSSION:

1. Computational Fluid Dynamic Research:

Direct Numerical Simulation (DNS) of turbulence is desirable, but for the high Reynolds number and geometry of interest in the ram accelerator, it is not currently practical. It can, however, be utilized to simulate specific geometric regions of the flow field, such as the projectile nose tip region. Recognizing this role, researchers at the Naval Research Laboratory are performing DNS simulations of high-pressure wedge-induced oblique detonation [1]. Conventional time-averaged Reynolds-stress (RS) models can be used to approximate the effect of turbulence from a "system point-of-view," and researchers at the Army Research Laboratory have utilized the Baldwin-Lomax model to aid in the development of their 120mm ram accelerator.

While RS models are valuable for system design and operation, they do not directly calculate any of the turbulence, and for unsteady flows, they require that the turbulent time-scales are small in comparison to convection time scales. Such averaging may be adequate for slowly accelerating flows or flows with low frequency periodic behavior, but it is not appropriate for short duration transient flows and flows with higher frequency periodic behavior, where the time-scales of the large scale turbulent structure and the convective processes are comparable. For such flows, the optimum approach is Large Eddy Simulation (LES), where the large scale turbulent structure is directly simulated by the flow solver, but the finer dissipate structure is modeled with a sub-grid. Consequently, this research takes an LES approach to simulate the high-pressure ram accelerator environment. The goal is to start with fundamental unit

problems and ascertain the utility and necessity of various subgrid models in the complex ram accelerator flowfield. The first unit problem considered is a backward facing step similar to the ram accelerator wake region. In the remainder of this section, the effect of the subgrid on the simulation of vortex shedding in the wake region is discussed.

The unsteady flow in an axisymmetric ducted flow with a backward-facing step has been simulated with and without a subgrid model. The geometry is similar to that used by Menon [2]. The backward-facing in this geometry leads to periodic vortex shedding from the edge of the step. The Reynolds number based on the step height and the inlet velocity is approximately 5,000. The boundary conditions used are as follows: no-slip conditions at the solid walls and symmetry conditions at the centerline. At the inflow boundary, the flow is assumed to be in the axial direction with uniform a stagnation pressure of 0.23 atmospheres, a stagnation temperature of 300 ^{O}K, and a Mach number of 0.23. Since the inflow is subsonic, only three of the four conditions can be specified and the fourth one is obtained by extrapolating the characteristic variable corresponding to the left-going characteristic from inside the domain. The flow at the nozzle exit is supersonic, and non reflective conditions are therefore used at the outflow boundary.

First, a simulation without a subgrid model was performed for approximately 25,000 time steps with a time increment of approximately 6 microseconds. The "average" Courant number utilized was about 3.5. The reported data were obtained over the last 6,000 time steps after periodic vortex shedding had been established. The pressure fluctuations normalized with time mean pressure at the base of the step over 8 shedding cycles are shown in Figure 1. The peak-to-peak amplitude of the fluctuations is approximately five percent of the mean pressure level. The corresponding frequency spectra of the pressure fluctuations is shown in Figure 2 and the dominant modes are found to be 243Hz, 486Hz, and 729Hz. The principle mode agrees exactly with the duct longitudinal acoustic mode.

The temporal evolution of the shedding cycle is best illustrated by the contours of the fluctuating component of the spanwise vorticity. A set of instantaneous plots of fluctuating spanwise vorticity at several time intervals is shown in Figure 3. A time interval of 4.1ms represents one characteristic shedding cycle, i.e., a vortex passage frequency of 243Hz. As the separated shear layer generated at the corner of the step becomes unstable, a vortex grows at the edge of the shear layer. A complex sequence of vortex merging occurs before the vortex detaches from the shear layer and rolls into an independent structure which is then convected by the local flow.

Next, calculations are performed with a compressible extension of the Smagorinsky subgrid model [3]. The solution was integrated in time for 16,000 steps, and the results from the last 5,000 steps are presented. The pressure fluctuations at the base of the step are shown in Figure 4, and the frequency spectra of the pressure fluctuations is shown in Figure 5. The dominant frequency of fluctuations is 243Hz and the peak-to-peak amplitude of the fluctuations is approximately five percent of the mean pressure. With the subgrid model included, the pressure fluctuations are more periodic. A comparison of the spectra further reveals that subgrid stresses attenuate the high frequency randomness evident in the simulations without subgrid stresses.

2. Diagnostics Research:

The experimental research is focused on the development and utilization of optical diagnostic techniques for a high-pressure combustion environment typical of the ram accelerator. The goal is to obtain flow visualization data in the high pressure regime for validation of the CFD models. Four optical techniques have been selected for investigation: Schlieren photography, x-ray shadowgraphy, emission spectroscopy, and single-pulse planar imaging using Rayleigh scattering. These techniques have been utilized by other researchers at sub-atmospheric pressures, and in this research the feasibility of applying each of these techniques at higher pressures will be investigated. Initial work has been with Schlieren shadowgraphy and emission spectroscopy.

Since the ram accelerator is not conducive for optical diagnostic development, an independent shock-induced combustion device was designed, built and tested last year. The device consists of a light gas gun that injects 10mm diameter spherically blunted cylinders, "models," into a test chamber filled with

a selected flammable gas mixture. Models have been injected into methane/oxygen mixtures at velocities ranging from 900 m/s to 1100 m/s . At sub-atmospheric pressures with a stoichiometric mixture, combustion is not repeatably achieved, a finding consistent with the observations by Lehr [4]. When combustion does occur, a detonation front traveling at approximately 2100 m/s is observed. This velocity is in agreement with theoretical calculations of the mixture's Chapman-Jouguet detonation velocity. Shock-induced combustion is not observed on either the nose or behind the projectile. The device is being upgraded to include a two-stage light gas gun injector to allow for injection velocities above the mixture detonation velocity.

To further investigate the detonation characteristics of methane, an experiment was performed with an oxygen-rich mixture. As shown in Figure 6, these conditions did not lead to combustion. Consequently, at sub-atmospheric pressures, shock-induced combustion and detonation with a methane based mixture were not consistently achieved. Future experiments will focus on documenting the detonation characteristics of methane/oxygen mixtures and on determining the utility of the optical diagnostic techniques at higher pressures.

REFERENCES:

[1] C. Li, K. Kailasanath, and E.S. Oran, "Detonation Structures Behind Oblique Shocks," Phys. Fluids 6 (4) , 1600-1611 (April 1994).
[2] J. Menon and W.H. Jou, "Numerical Simulations of Oscillatory Cold Flows in an Axisymmetric Ramjet Combustor," J. Propulsion and Power, 525-534 (Sept.-Oct. 1990).
[3] N. Sinha, B. York, R.K. Madabhushi, and S.M. Dash, "Sensitivity Studies to Establish Modeling Requirements for Ram Accelerator Flowfield Simulation," 30th JANNAF Combustion Meeting, Monterey California (November 15-18, 1993).
[4] Personal communication, H. Lehr, Institut Saint Louis (Oct. 1993).
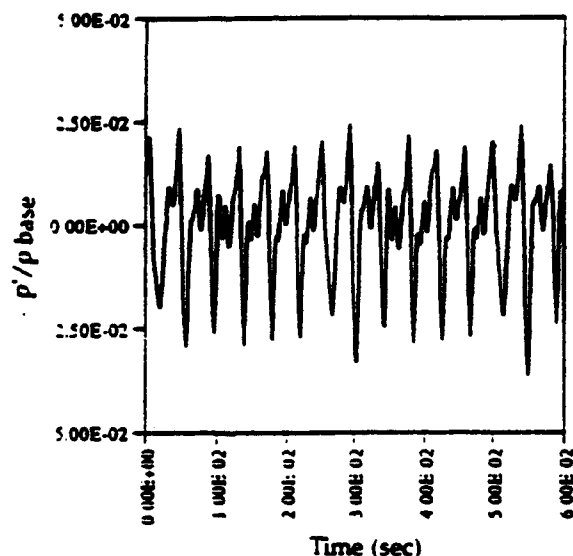
Figure 1. Pressure fluctuations (normalized with time-mean pressure) at the base of the step with no subgrid model.
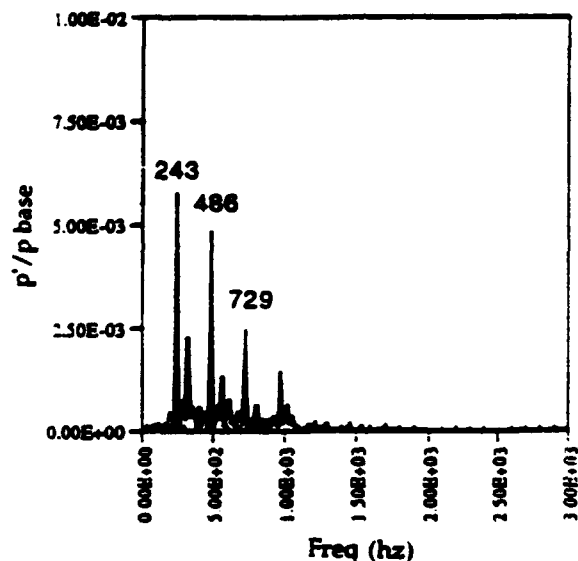
Figure 2. Frequency spectra of pressure fluctuations at the base of the step with no subgrid model.
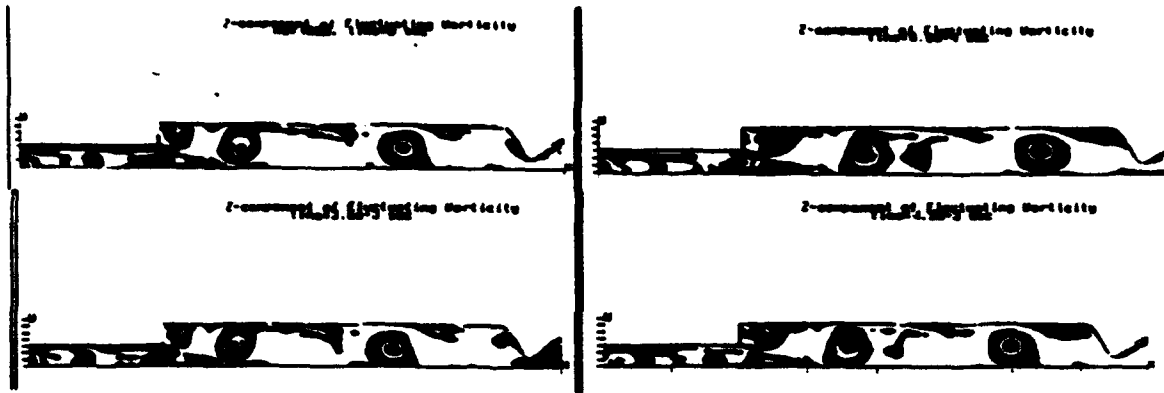
Figure 3. Fluctuating component of spanwise (z) vorticity at 4 instances illustrating the temporal evolution of a typical vortex shedding cycle.
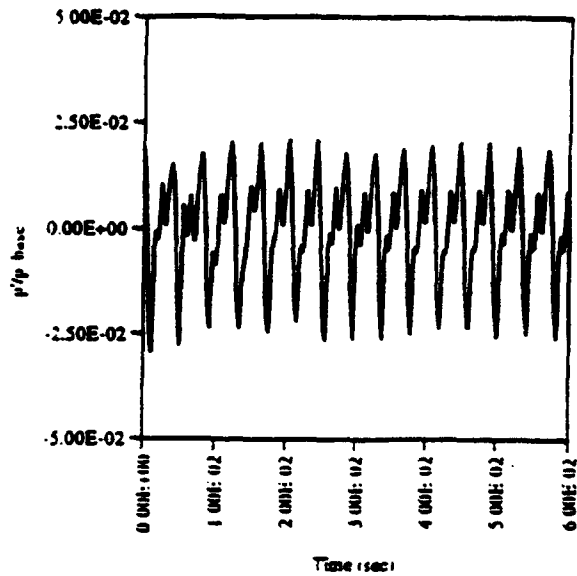
Figure 4. Pressure fluctuations at the base of the step when the subgrid model is included.
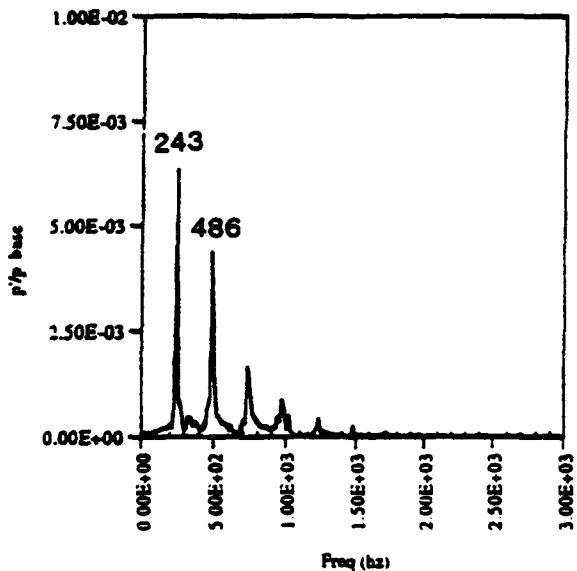
Figure 5. Frequency spectra of pressure fluctuations at the base of the step when the subgrid model is included.

Figure 6. Schlieren shadowgraph of a hemispherically blunted cylinder in a 3:1 O_2:CH_4 mixture (pressure = 0.5 atm, velocity = 1 km/s). Direction of travel is from the bottom of the page to the top.

230

TWO- AND THREE-DIMENSIONAL MEASUREMENTS IN FLAMES

Yale University
Department of Mechanical Engineering and Center for Laser Diagnostics
New Haven, Connecticut 06520-8284

SUMMARY/OVERVIEW

Laser-based imaging techniques are being developed and applied to the study of turbulent reacting flows. These techniques incorporate a variety of light scattering mechanisms to allow the measurement of the spatial distributions of temperature, species concentrations, velocity, and most recently, the mixture fraction. The data provided by these measurements can afford a better understanding of the interaction of turbulence and chemistry in turbulent flames. During the past year, we have concentrated on exploring the capabilities and limitations of a new technique for imaging the mixture fraction in turbulent nonpremixed flames.

TECHNICAL DISCUSSION

In modeling of turbulent nonpremixed flames, the quantity most often used to describe the flow is the mixture fraction. The mixture fraction is defined as the mass fraction of all atoms originating from the fuel stream and is one of many possible conserved scalars that can be defined in the flame. Each of these conserved scalar quantities is independent of the chemical reaction. Under idealized conditions, knowledge of a single conserved scalar can be used to derive essentially all of the scalar quantities of interest in the flow.

Experimentally, the determination of the mixture fraction in nonpremixed flames is quite difficult. The mixture fraction has been determined at a single point from measurements of all major species using spontaneous Raman scattering. The data from single-point measurements are incomplete, however, because of the lack of multi-dimensional information required to obtain gradients. The scalar dissipation, (calculated from the square of the mixture fraction gradient), determines the rate of molecular mixing and is widely used in modeling turbulent reacting flows. Therefore, techniques capable of two-dimensional or preferably three-dimensional measurements of the mixture fraction are needed.

A means of determining the mixture fraction without measuring all of the major species has been proposed by Sten Stårner and Robert Bilger of the University of Sydney. They have shown that the mixture fraction can be determined from simultaneous measurement of only two quantities (with the assumption of unity Lewis number and a one-step reaction between fuel and oxidizer). We have investigated three different experimental approaches to determining the mixture fraction in turbulent nonpremixed hydrocarbon flames. Each of these techniques is based on simultaneous monitoring of the fuel concentration and Rayleigh scattering. The main difference in the approaches is the means for determining the fuel concentration.[1] These experiments were conducted in our laboratory with the collaboration of researchers from the University of Sydney.

The flame selected for our initial study was a turbulent nonpremixed acetaldehyde flame.[2] Acetaldehyde (CH_3CHO) was chosen for its relatively high fluorescence yield and small variation of fluorescence intensity with temperature, which allows the fuel concentration to be found directly from the acetaldehyde fluorescence. In these experiments, the flow was illuminated by two

overlapping laser sheets. The first, formed from the second harmonic of a Nd:YAG pumped dye laser, excited fluorescence from the acetaldehyde fuel. The second illumination sheet, from a flashlamp-pumped dye laser, excited Rayleigh scattering. The fuel fluorescence was imaged onto a gated-image intensifier that was optically coupled to a cooled CCD detector. The Rayleigh scattering was imaged onto a separately gated intensifier optically coupled to the second CCD detector.

The raw images were corrected for background and nonuniform detector response. In addition, since the magnification of the two images and the illumination sheet size were different, the necessary rotation, translation, scaling, and cropping were applied to the images to allow them to be compared on a pixel-by-pixel basis. The fuel was a mixture of acetaldehyde diluted 1/1 by air (on a mass basis) to eliminate soot. It emanated from a piloted burner (d = 3.9 mm) with a velocity corresponding to Re = 18,000. The flame was enshrouded in a low velocity filtered air coflow in order to keep the measurement area clear of particles, which would interfere with the Rayleigh images.

Preliminary data on the calculated temperature and mixture fraction obtained from the instantaneous Rayleigh/fluorescence images show several interesting features. (Fig. 1) Evident in the temperature mappings are the high temperature zones on the outer edge of the flame. As expected, the mixture fraction peaks in the unburned regions near the center of the jet. A closer inspection of the mixture fraction images obtained from the acetaldehyde flame shows a slight decrease in the mixture fraction on the rich side of the stoichiometric value, where the temperature has not yet peaked. A similar dip in the mixture fraction on the rich side of the flame front was noted in measurements performed in a laminar flame. One explanation of this behavior is pyrolysis of the acetaldehyde fuel. To investigate this, experiments were done in which the acetaldehyde fluorescence and fuel Raman scattering were measured simultaneously. The C-H Raman scattering should be relatively insensitive to the breakup of the acetaldehyde into other hydrocarbon fragments. The fluorescence, on the other hand, is expected only from the acetaldehyde molecule itself, so differences in the Raman and fluorescence traces may be indicative of pyrolysis. A comparison was made of acetaldehyde fluorescence and C-H Raman intensity along lines intersecting laminar and turbulent flames. (Fig. 2) In both cases, the agreement was quite good despite the relatively noisy Raman signal. These results support the assertion that acetaldehyde fluorescence is a good alternative to Raman scattering as a means of marking the fuel, but do not explain the anomalous dip in the mixture fraction on the fuel rich side of the stoichiometric value.

In a recent collaboration, Peter Lindstedt of Imperial College performed a detailed calculation of acetaldehyde chemistry in an opposed jet configuration.[3] The results shed considerable light on the mixture fraction obtained in our experiments. Calculation of the mixture fraction from the computed temperature and fuel mass fraction using the two scalar scheme outlined above results in a dip in mixture fraction on the rich side of the flame similar to those obtained in the experiments. One of the most striking features of the calculation is the high concentration of CO (a maximum mole fraction of nearly 20%) present in the flame. The combustion characteristics of acetaldehyde appear to differ significantly from that of methane, so that the two scalar approach that worked well for methane and propane may not work as well for acetaldehyde.

Another technique that has been proposed as a way of marking the fuel in hydrocarbon flames is to introduce acetone as a tracer and detect acetone fluorescence. Acetone is easily seeded into flows and has only mild toxicity. However, an unresolved issue related to the use of acetone as a fuel tracer in flames relates to the behavior of the fluorescence as a function of temperature. To test the use of acetone as a fuel tracer for determination of mixture fraction, the fluorescence/Raman setup described above was used to investigate laminar and turbulent acetone-seeded methane flames. The acetone was seeded into the methane fuel by bubbling methane through liquid acetone to give a final mixture of 70% air, 25% methane, and 5% acetone by volume. A laminar flame was stabilized on a 16 mm diameter nozzle, and the gas mixture had a Reynolds number of 700 at the nozzle exit. Results of the fluorescence/Raman comparison in the laminar flame show a clear departure between the normalized fluorescence and Raman signals, with the fluorescence signal exceeding the Raman signal in the fuel-rich region of the flame. (Fig. 3) This behavior is

232

consistent with the fluorescence increasing as a function of temperature as reported by other researchers. A comparison of the normalized Raman and fluorescence signals in a turbulent flame showed similar results, with the fluorescence signal greater than the Raman signal in some locations.

To avoid the problems related to the use of acetaldehyde or acetone as the fuel, a set of experiments were done in which the concentration of fuel was inferred from the Raman scattering of the vibrational C-H stretch of methane. The main drawback to Raman scattering is the extremely small Raman scattering cross section and, consequently, the difficulty in getting sufficient signals. As early as 1985, we demonstrated simultaneous Raman and Rayleigh imaging, although the data were not used to determine mixture fraction. Previous Raman imaging experiments made use of a multipass optical cell to form the illumination sheet. In this work, a multipass cell was not used, but a two-pass arrangement allowed two components of the scalar gradient to be determined along a line.

In the Raman and Rayleigh line imaging measurements, a flashlamp-pumped dye laser provided up to 1 J of energy at 532 nm. The beam was focused into the flame initially by a spherical lens. After passing through the flame, the beam was re-collimated by a second lens, reflected from a planar mirror, and refocused into the flame. The two beams were aligned so that the reflected beam passed just over the top of the incoming beam. This two-beam approach allowed gradients to be obtained in both the radial and axial directions. The beam waist was measured to be 0.6 mm.

The scattered Raman and Rayleigh light was detected by two intensified CCD detectors oriented perpendicular to the laser beam. The raw Raman and Rayleigh line images were corrected for background and nonuniform detector response. In addition, the necessary rotation, translation, scaling, and cropping were applied to the images to allow them to be compared on a pixel-by-pixel basis. The resulting images consist of two lines radially across the flow corresponding to the main and reflected beams with a pixel resolution of $0.27 \times 0.45 \times 0.6$ mm^3. (Fig. 4)

The flame investigated was an axisymmetric, piloted methane-air flame. The main fuel nozzle had a diameter of 3.8 mm. The main jet was surrounded by an annular premixed pilot flame (pilot diameter 15 mm). A low speed annular coflow of filtered air surrounded the burner to eliminate particles from the flow, which would interfere with the Rayleigh scattering. The methane was diluted 3/1 on a volume basis to eliminate soot. The Reynolds number was 20,600 and the beams intersected the flow 25 nozzle diameters downstream. The signal/noise for the ambient air in the Rayleigh images is $\approx$ 200. Because of the weakness of the Raman signal, the signal/noise for those images is roughly 15. Sets of 500 instantaneous shots were taken at a number of different locations within the flame to allow statistical characterization of the mixture fraction and the scalar dissipation. A complete description of the results obtained from this measurement approach has been accepted for presentation at the Twenty Fifth International Symposium on Combustion.[4]

REFERENCES

1. J.H. Frank, K.M. Lyons, D.F. Marran, M.B. Long, S.H. Stårner, and R.W. Bilger, "Mixture Fraction Imaging in Turbulent Nonpremixed Hydrocarbon Flames," accepted for publication Twenty-*Fifth Symposium (International) on Combustion*, Irvine CA, July 1994.
2. M.B. Long, J.H. Frank, K.M. Lyons D.F. Marran, and S.H. Stårner, "A Technique for Mixture Fraction Imaging in Turbulent Nonpremixed Flames," *Ber. Bunsenges. Phys. Chem.*, 97, 1555-1559 (1993).
3. P. Lindstedt and M.B. Long, "Comments on the Pyrolysis Properties of Acetaldehyde," to be submitted (1994).
4. S.H. Stårner, R.W. Bilger, K.M. Lyons, J.H. Frank, and M.B. Long, "Conserved Scalar Measurements in Turbulent Diffusion Flames by a Raman and Rayleigh Ribbon Imaging Method," accepted for publication *Twenty-Fifth Symposium (International) on Combustion*, Irvine CA, July 1994.

Mixture Fraction (0 - .8)

Temperature (300 - 1900)

Min   Max
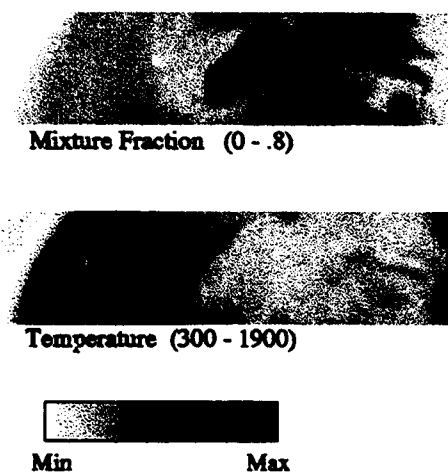
Figure 1.

The conserved scalar and temperature fields calculated from the acetaldehyde fluorescence/Rayleigh scattering experiment. In each image, the scalar value is represented by a linear gray scale with darker shades corresponding to larger values.

Radial Position

Figure 2.

Comparison of Raman and acetaldehyde fluorescence intensity at various downstream locations in a laminar acetaldehyde-air flame. Shots (a) - (d) correspond to different downstream locations from a 16 mm diameter nozzle. Downstream locations were (a) 43.5 mm, (b) 33.5 mm, (c) 23.5 mm, and (d) 13.5 mm. The fluorescence was excited at 320 nm.

Radial Position

Figure 3.

Comparison of Raman and acetone fluorescence intensity at various downstream locations in a laminar methane-air flame seeded with acetone vapor. Downstream locations were (a) 88.5 mm, (b) 63.5 mm, (c) 38.5 mm and (d) 13.5 mm. The fluorescence was excited at 320 nm.

Rayleigh

Raman

Temperature

Mixture Fraction
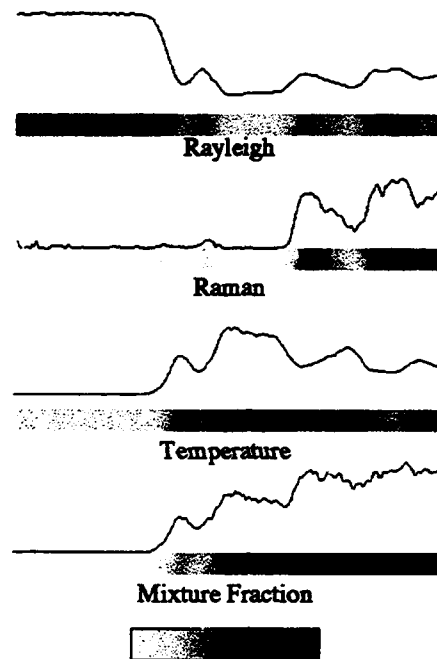
Figure 4.

At top, the Rayleigh and Raman images from a turbulent methane-air flame are shown. Scattered intensity along each of the lines is represented as a gray scale image and directly above it, the intensity along one of the lines is plotted. For the data shown, the Reynolds number was 20,600 and the beams intersected the flow 25 nozzle diameters downstream. The mixture fraction and temperature calculated from the raw data are shown at the bottom. The right side of the image corresponds to the jet centerline.

234

MODELLING MIXING AND REACTION
IN TURBULENT COMBUSTION

Principal Investigator: S.B. Pope

Mechanical & Aerospace Engineering
Cornell University
Ithaca, NY 14853

SUMMARY

The overall objective of the research project is to develop, test and demonstrate a combined methodology for modelling turbulent combustion. The three principal ingredients in the method are: manifold methods for simplifying the chemical kinetics; the EMST mixing model; and, the PDF method for treating the inhomogeneous turbulent reactive flows. When developed, the method will be applied to piloted jet diffusion flames, and comparison will be made with the available experimental data.

INTRODUCTION

In the following three sections. recent progress is described on manifold methods, the EMST mixing model, and application of PDF methods to piloted jet diffusion flames.

MANIFOLD METHODS

Our quantitative knowledge of combustion chemistry is embodied in detailed reaction mechanisms, which continue to advance in their scope and accuracy. In computations of combustion in complex flows (e.g. multidimensional laminar flows, turbulence simulations or turbulent combustion modelling) the computational cost of using a detailed reaction mechanism is excessive, and usually prohibitive. Consequently, there is motivation to develop computationally-simpler approximate methods based on detailed reaction mechanisms.

A fundamental assumption in all simplification strategies—made explicit in manifold methods—is that the thermochemical compositions everywhere in a reactive flow lie close to a low-dimensional manifold in the high-dimensional composition space. We previously developed the Intrinsic Low-Dimensional Manifold method (ILDM) (Maas & Pope 1992a, b), and have recently shown that it is accurate in application to premixed laminar flames (Maas & Pope, 1994).

We recently developed an alternative Trajectory-Generated Low-Dimensional Manifold method (TGLDM) (Pope & Maas 1993), which has some advantages. Figures 1 and 2 show the application of the 1D and 2D TGLDM method to a transient perfectly-stirred reactor operating on a $CO/H_2/N_2$-air mixture. It may be seen that the 2D method is accurate both for major and minor species.

EMST MIXING MODEL

The term "mixing model" refers to a turbulence sub-model that describes the evolution of the pdf of composition. In the Lagrangian-pdf framework, the mixing model specifies how the composition $\phi(t)$ evolves following a fluid particle. In one popular model (IEM) $\phi(t)$ relaxes to the local mean value $\langle\phi\rangle$ at a specified rate. In another class of models (particle-interaction models), the composition of the n-th particle in an ensemble $\phi^{(n)}(t)$ changes by an exchange with another randomly selected particle (m, say, with composition $\phi^{(m)}(t)$).

Such mixing models have been extensively examined for inert flows (e.g. Pope 1982) and several shortcomings have been identified and are now well-appreciated. More recently a different shortcoming—peculiar to reacting flows—has been identified. Specifically, the physics of the problem shows that mixing is *local in composition space* whereas the models cited above are non-local.

We have developed a model which is asymptotically local, and which reduces to the mapping closure in the one-composition case. It is based on Euclidean minimum spanning trees (EMST). An example of an

EMST (for 4D, $N = 400$) is shown in Fig. 3. By definition, the EMST is the set of edges joining the points, such that all points are connected, with the $N - 1$ edges chosen (out of the N^{-2} possibilities) so that their total length is minimal. By this construction, one or more neighbors are identified for each particle.

This model has been implemented and tested in up to 10 dimensions. Figure 4 shows results from a revealing test case in which there is a mean scalar gradient. In this instance, the variance (and indeed all other statistics) attains a stationary value. The results agree well with experiments and DNS, and the skewness and kurtosis are close to Gaussian values.

PILOTED JET DIFFUSION FLAMES

The objective of the project is to combine manifold methods, the EMST mixing model and PDF methods to make calculations of piloted jet diffusion flames. We have performed some preliminary studies using the simpler and more conventional IEM model (Norris 1993, Norris & Pope 1994).

Figures 5 and 6 compare experimental and calculated scatter plots in a piloted jet diffusion flame at two different jet velocities. The fuel is a $CO/H_2/N_2$ mixture, and the measurement location is at $x/D = 10$, $r/D = 0.9$. At the lower jet velocity (Fig. 5) it may be seen that the calculations accurately reproduce the measured conditional means. Evidently the experimental data show more scatter about this conditional mean than do the calculations. The extent to which this difference can be attributed to experimental error is an open question.

At the higher jet velocity (Fig. 6) the flame is close to being extinguished. The calculations are in accord with the data showing almost complete extinction except close to stoichiometric.

REFERENCES

Maas, U. and Pope, S.B. (1992a) Combust. Flame **88**, 239.

Maas, U. and Pope, S.B. (1992b) Twenty-fourth Symp. (Int'l.) on Combust., p. 103.

Maas, U. and Pope, S.B., (1994) Twenty-fifth Symp. (Int'l.) on Combust., to be published.

Norris, A.T. (1993) Ph.D. Thesis, Cornell University.

Norris, A.T. & Pope, S.B. (1994) Twenty-fifth Symp. (Int'l.) on Combust., to be published.

Pope, S.B. (1982) Combust. Sci. Technol. **28**, 131.

Pope, S.B. and Maas, U. (1993) Cornell University Report FDA-93-11.
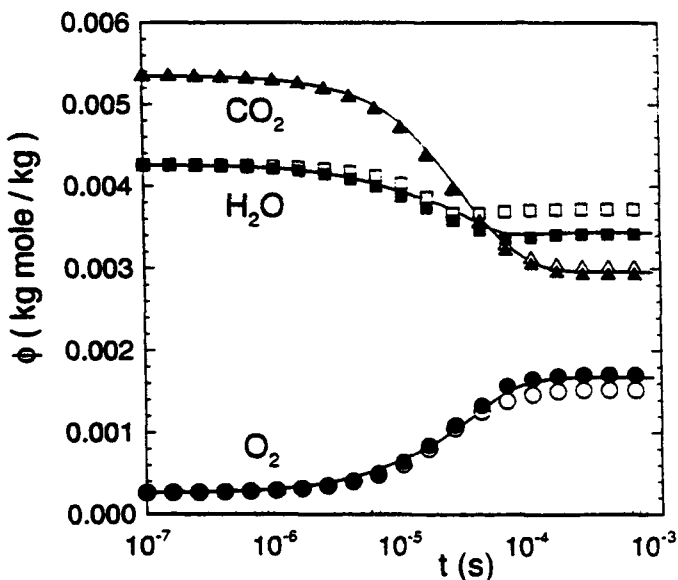
Fig. 1: Specific mole numbers of major species against time for the transient PSR test case. with $\omega = 10^4 s^{-1}$. Solid line. full kinetics: solid symbols. 2D TGLDM: open symbols. 1D TGLDM.
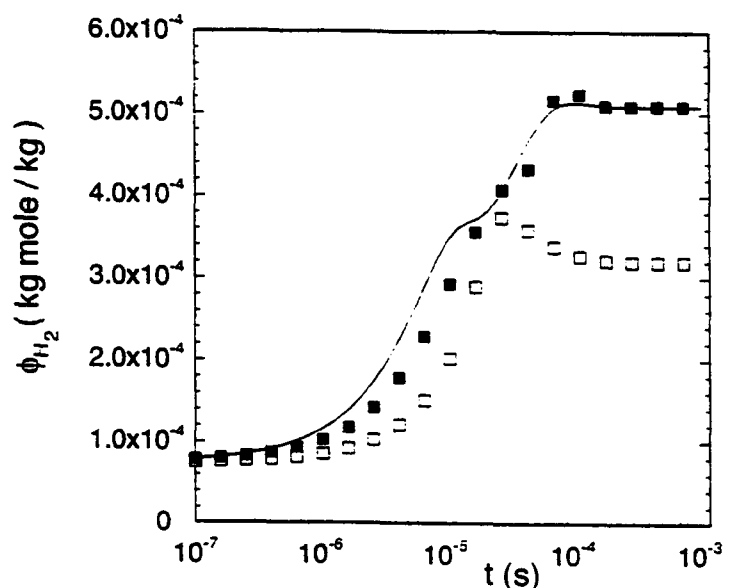
Fig. 2: Specific mole number of H_2 against time for the transient PSR test case. with $\omega = 10^4 s^{-1}$. Solid line. full kinetics: solid symbols. 2D TGLDM: open symbols. 1D TGLDM.

236
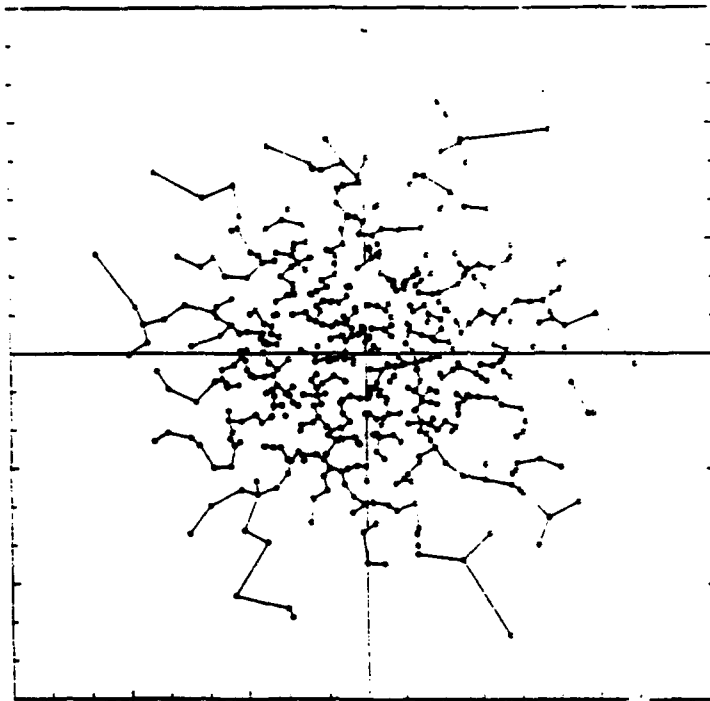
Fig. 3: Example of a 2D Euclidean Minimum Spanning Tree (EMST)
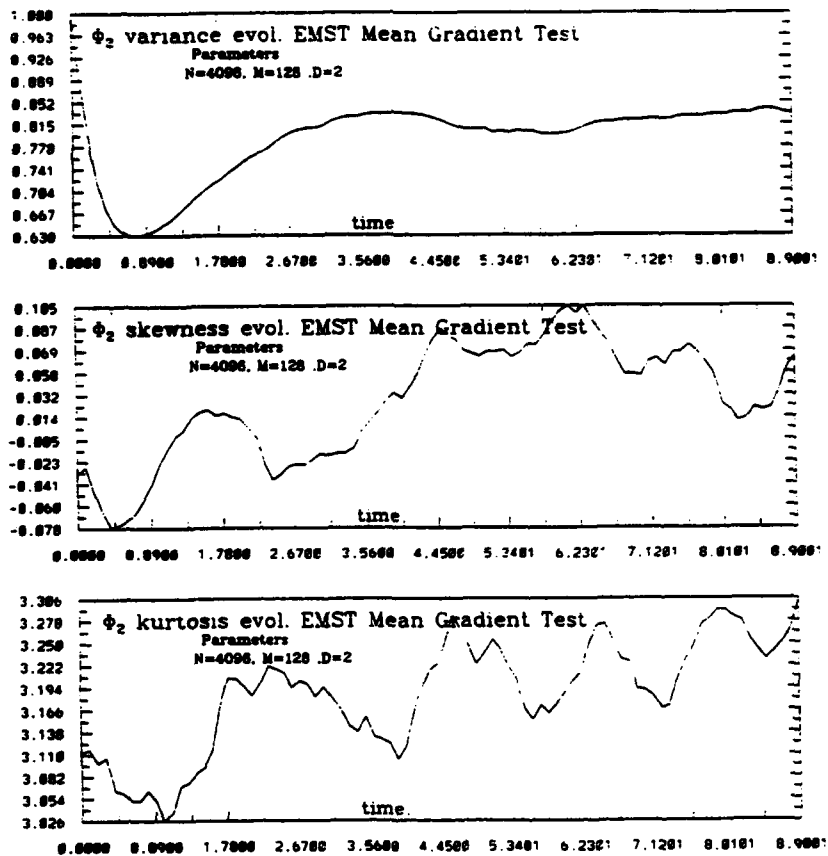
Fig. 4: EMST mixing model applied to two scalars with mean gradients
in isotropic turbulence. Temporal evolution of a) the variance b) the
skewness and c) the kurtosis of one scalar.

237
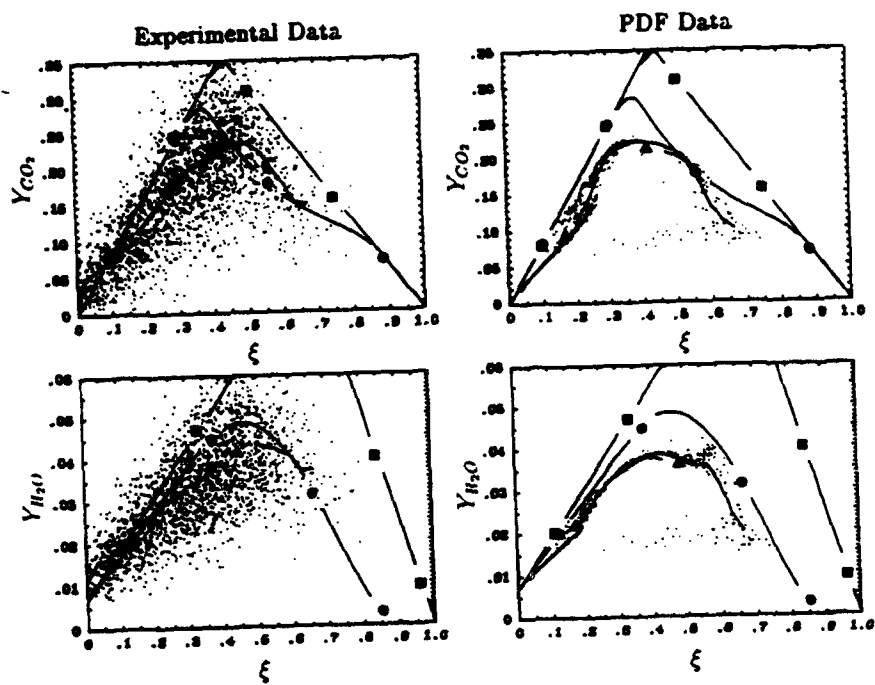
Fig. 5: Scatter plots of species mass fractions against mixture fraction in a piloted $CO/H_2/N_2$-air turbulent jet diffusion flame. with jet velocity 98 m/s.
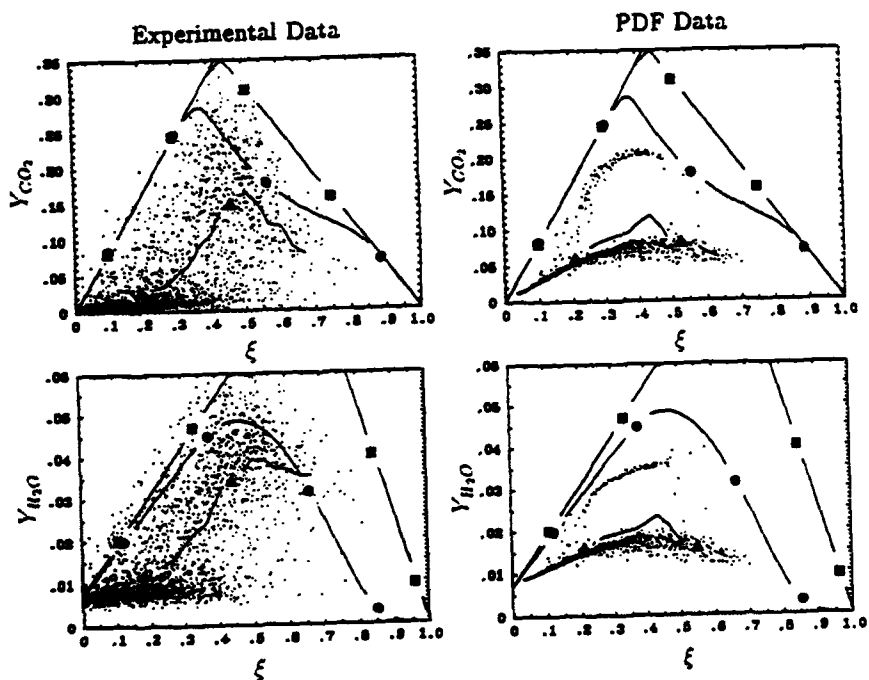
Fig. 6: Scatter plots of species mass fractions against mixture fraction in a piloted $CO/H_2/N_2$-air turbulent jet diffusion flame. with jet velocity 164 m/s.

238

AFOSR SPONSORED RESEARCH IN PROPULSION DIAGNOSTICS

PROGRAM MANAGER: JULIAN M. TISHKOFF

AFOSR/NA
110 Duncan Avenue, Suite B115
BOLLING AFB DC 20332-0001

SUMMARY/OVERVIEW: The Air Force Office of Scientific Research (AFOSR) program in propulsion diagnostics currently is focused on three areas of study: gas-phase measurements, plasmas, and particle/droplet measurements. An assessment of major research needs in each of these areas is presented.

TECHNICAL DISCUSSION

AFOSR is the single manager for Air Force basic research, including efforts based on external proposals and in-house work at Air Force laboratories. The propulsion diagnostics subarea is assigned to the AFOSR Directorate of Aerospace and Engineering Sciences along with programs in rocket propulsion, airbreathing combustion, and fluid and solid mechanics.

Interests of the AFOSR propulsion diagnostics subarea are given in the SUMMARY section above. This program, now in its eleventh year, has produced many "first-ever" laser-based measurements. The instrumentation with which these measurements were made is becoming commonly available for laboratory and bench test utilization. Measurements range from microscopic to macroscopic scales with relevance to: plasma acceleration; combustion aerothermochemistry; the behavior and synthesis of advanced energetic materials; characterization of exhaust plume formation and radiation; and dynamic control of propulsion, weapon and power generation systems.

Decisions on support for research proposals are based on scientific opportunities and technology needs. Research areas with the greatest growth potential are plasmas and measurements in supercritical fluids.

In the rapidly changing international environment we also are examining how we conduct our research activities in relation to both Air Force and civilian needs. We now recognize a new set of research objectives, including achieving rapid technology transitioning and dual military and civilian technological use for Air Force basic research. A new concept under consideration by AFOSR is the establishment of multi-investigator university research centers with links to industry and the Air Force laboratories to enhance the university-industry-Government research infrastructure.

We welcome your ideas on fostering better working relationships among universities, industry, and Government scientists and technologists.

The purpose of this abstract has been to communicate AFOSR perceptions of research trends to the university and industrial research communities. However, communication from those communities back to AFOSR also is desirable and essential for creating new research opportunities. Therefore, all proposals and inquiries for fundamental research are encouraged even if the content does not fall within the areas of emphasis described herein. Comments and criticisms of current AFOSR programs also are welcome.

AFOSR SPONSORED RESEARCH IN AIRBREATHING COMBUSTION

PROGRAM MANAGER: JULIAN M. TISHKOFF

AFOSR/NA
110 Duncan Avenue, Suite B115
BOLLING AFB DC 20332-0001

SUMMARY/OVERVIEW: The Air Force Office of Scientific Research (AFOSR) program in airbreathing combustion currently is focused on seven areas of study: supersonic combustion, reacting flow, soot, sprays, kinetics, ram accelerators, and supercritical fuel behavior. An assessment of major research needs in each of these areas is presented.

TECHNICAL DISCUSSION

AFOSR is the single manager for Air Force basic research, including efforts based on external proposals and in-house work at Air Force laboratories. Airbreathing combustion is assigned to the AFOSR Directorate of Aerospace and Engineering Sciences along with programs in rocket propulsion, propulsion diagnostics, and fluid and solid mechanics.

Interests of the AFOSR airbreathing combustion subarea are given in the SUMMARY section above. Many achievements can be cited for these interests, yet imposing fundamental research challenges remain. The objective of the program is publications in the refereed scientific literature describing significant new understanding of multiphase turbulent reacting flow. Incremental improvements to existing scientific approaches, hardware development, and computer codes fall outside the scope of this objective.

Decisions on support for research proposals are based on scientific opportunities and technology needs. In recent years two major emphases have defined the main thrusts of this research activity: supersonic combustion to support hypersonic airbreathing propulsion technology and issues affecting the future utilization of hydrocarbon fuels. Starting in 1987 new research efforts were directed at novel means for achieving ignition, combustion enhancement, low-loss flameholding, and complete chemical energy release in supersonic combustion. The year 1989 saw new research in interactive control of fluid transport processes. These opportunities reflect a generic interest in interdisciplinary efforts between researchers in control theory and fluid transport behavior. For hypersonic propulsion a particular focus of interactive flow control is the investigation of means to overcome the suppression of mixing that high Mach number flows experience in relation to subsonic flows.

Future systems will require fuels to absorb substantial thermal energy, raising fuel temperatures to supercritical thermodynamic conditions. Understanding and controlling fuel properties at these conditions will be crucial for avoiding thermal degradation and for subsequent processes within the combustor. Environmental concerns and the availability of petroleum supplies also will contribute to future propulsion system design and operational needs.

Designing propulsion systems that will offer reliability, maintainability and long service life represents a new motivation for propulsion research. Future budgets likely will dictate the acquisition of reduced quantities of new operational aerospace vehicles, with a corresponding increase in requirements for durability. Research topics such as soot and supercritical fuel behavior will be relevant to these new service constraints.

With funding provided by the Department of Defense, AFOSR will sponsor a Focused Research Initiative topic on high performance, low emissions gas turbine combustors. Information for submitting proposals to this initiative is given in a recently issued Broad Agency Announcement. In the rapidly changing international environment we also are examining how we conduct our research activities in relation to both Air Force and civilian needs. We now recognize a new set of research objectives, including achieving rapid technology transitioning and dual military and civilian technological use for Air Force basic research. Through this initiative we hope to foster better working relationships among universities, industry, and Government scientists and technologists.

A new concept under consideration by AFOSR is the establishment of multi-investigator university research centers with links to industry and the Air Force laboratories. These centers also are intended to enhance the university-industry-Government research infrastructure.

The purpose of this abstract has been to communicate AFOSR perceptions of research trends to the university and industrial research communities. However, communication from those communities back to AFOSR also is desirable and essential for creating new research opportunities. Therefore, all proposals and inquiries for fundamental research are encouraged even if the content does not fall within the areas of emphasis described herein. Comments and criticisms of current AFOSR programs also are welcome.

THEORIES OF TURBULENT COMBUSTION IN HIGH SPEED FLOWS
(AFOSR Grant No. F49620-92-J0184)

Principal Investigators: F. A. Williams and P. A. Libby

Department of Applied Mechanics and Engineering Sciences
University of California San Diego, La Jolla, CA 92093-0310

SUMMARY/OVERVIEW

The objective of this research is to improve our understanding of the chemical kinetics and fluid dynamics of turbulent combustion in high speed flows. At present emphasis is being placed on understanding the ignition processes in nonpremixed counterflow systems of hydrogen and air. In addition, to understand the effects of heat release on the high-speed compressible turbulence a direct numerical simulation study is also being initiated. The results may help to improve abilities to design propulsion systems that employ high-speed turbulent combustion.

TECHNICAL DISCUSSION

The previous summary described research on ignition in hydrogen-air mixtures, on nonpremixed flames in stagnating turbulence and on structures of counterflow diffusion flames with small stoichiometric mixture fractions. The complete reference citation for publication of the work on the last of these topics was not available last year and therefore is included here as the first reference [1]. The present summary focuses on the new research performed during the past year. This research emphasizes ignition phenomena as well as extinction, introduces methods of bifurcation theory and offers some experimental measurements to test theoretical predictions.

This research emphasizes the flamelet regime of turbulent diffusion flames. It is important to use the most up-to-date information to assess whether applications are most likely to fall in flamelet (flame-sheet) or distributed-reaction regimes. Such assessments have recently been completed for hypersonic propulsion employing hydrogen-air diffusion flames [2], and the results support continued emphasis on the flamelet regime. Attention was thus focused on flamelets in the hydrogen-air system, and four separate studies presently underway are reported here, all of them involving counterflowing configurations in one way or another.

Numerical Investigation of Ignition in Hydrogen-Air Mixtures

The critical parameters and the structure of the ignition kernel in hydrogen-air nonpremixed counterflowing configurations were calculated for a range of pressures from 0.5 to 40 atmospheres, for a range of initial temperatures and for a range of equivalence ratio. The conservation equations for the counterflow system with an updated chemical mechanism [2] were numerically integrated using the arc-tracing continuation technique [3]. The results of such complete calculations are not only useful for assessing the adequateness of various approximate models required in theoretical modeling and in large-scale simulation of these flames, but also provide guidance for combustor designers concerning the ranges of operations in which the ignition is controlling.

Representative results for the peak temperature as a function of the strain rate are shown in Figs. 1 and 2. The extinction strain rate for hydrogen flames, unlike that for methane flames, is seen to increase rapidly with increasing pressure. These results are consistent with the dependences of the crossover temperatures on the pressures for the two fuels. The crossover temperature for hydrogen flames is the temperature at which the rate of the chain branching reaction $H + O_2 \rightarrow OH + O$ becomes equal to that of the chain termination step $H + O_2 + M \rightarrow HO_2 + M$, while for methane flame the rate of the branching step is to be compared with the rate of the radical-removing step $CH_4 + H \rightarrow CH_3 + H_2$, which is bimolecular rather than three-body.

The critical strain rate for ignition is seen to be very sensitive to the oxidizer temperature. Above a transition value of the oxidizer temperature, no abrupt ignition or extinction phenomena are observed. This transition temperature, which is slightly larger than the crossover temperature for reasons discussed below, is shown along with the corresponding transition strain rate as a function of pressure in the inset of Fig. 2. As the oxidizer temperature is reduced the critical ignition strain rate decreases rapidly and soon reaches values where the convective effects of the flowfield have a minimal influence on the ignition processes. In addition, the middle branch of the S-curve is seen to approach the frozen branch increasingly tangentially with decreasing oxidizer temperature. It is extremely difficult to determine the ignition strain rate accurately by the continuation method for these cases; the solutions are extremely sensitive to the initial conditions and may converge to the middle branch. It is uncertain whether any currently available computational approach can circumvent this difficulty and attention is being given to this question.

Another application of the results from full integrations relates to the assessment of reduced mechanisms for the treatment of hydrogen oxidation in practical devices. In the calculation of multidimensional problems, it is computationally desirable to reduce the number of species that must be taken into account. A four-step mechanism was obtained by imposing steady-state approximations for HO_2 and H_2O_2. Three different three-step mechanism results from the four-step scheme by introducing a steady-state approximation for O or OH, or by employing steady states for both O and OH simultaneously and relaxing the HO_2 steady-state assumption. Finally a two-step mechanism is obtained by putting all species except H in steady state. Figure 3 shows the peak temperature as a function of the strain rate, according to the prediction of the full and these reduced chemical schemes for a diluted hydrogen-air diffusion flame at atmospheric pressure; results are similar without dilution. It is found that the two-step chemistry gives higher maximum temperature consistent with the higher H concentration predicted by the two-step chemistry in the reaction zone, yet the extinction and ignition strain rates differ only by approximately 10% and 15%, respectively for the undiluted flames and up to 25% and 40%, respectively for extreme dilutions (15% molar concentration of H_2 in the fuel stream.) It is interesting to observe from the intermediate curves in Fig. 3 that the discrepancy between the predictions of the two-step and full-mechanisms arises largely from the O steady-state assumption. On the other hand, calculations imposing H steady-state with the O steady-state relaxed gave results too poor to plot on the figure, thus suggesting that though the ignition may occur far on the air side of the mixing layer, the attack of H-atoms on O_2 (the chain-branching step) still plays a dominant role in initiating and propagating the ignition process. These results are being published [3].

Asymptotic Analysis of the Ignition Processes in Hydrogen-Air Systems

In a theoretical study, the slope of the ignition branch for steady, counterflow, hydrogen-oxygen diffusion flames, with dilution permitted in both streams, was investigated for two-step reduced chemistry by methods of bifurcation theory. Attention was restricted to fuel-stream temperatures less than or equal to the oxidizer-stream temperature T_∞ and to T_∞ larger than or of the order of the crossover temperature at which the rates of the H + O_2 chain-branching and chain-terminating steps are equal. Two types of solutions were identified, a frozen solution that always exists in this kinetic approximation because all rates are proportional to the concentration of the intermediate H atom, and an ignited solution that bifurcates from the frozen solution if a Damköhler number constructed from the strain rate and the rate of the branching step H + $O_2 \rightarrow$ OH + O is increased to a critical value at which the strain rate becomes small enough for autoignition to occur in this flow field. Along the ignited branch, the original two-step chemistry soon fails near the hot oxidizer stream, necessitating consideration of O + $H_2 \rightarrow$ OH + O as the dominant chain-branching step, the effect of which was included in the analysis by introducing a finite position of H_2 depletion, with frozen flow beyond, to the oxidizer boundary. The critical Damköhler number for ignition, and the slope of the curve of the maximum radical concentration as a function of Damköhler at the ignition point, were calculated parametrically as functions of the hydrogen Lewis number, and different limiting behaviors were clarified for Lewis numbers of zero and unity. It was shown that

when effects of chemical heat release are neglected, so that the ignition involves only a branched-chain explosion, a good approximation at sufficiently high T_∞, the ignition is always gradual in the sense that the limiting ignited-branch slope is positive (supercritical bifurcation) and there is no S curve. At high T_∞ the radical-production step alone affords a good one-step approximation for ignition, but its heat release is too small 11 to remove the gradual-ignition behavior, even as T_∞ drops below crossover. Near crossover it becomes necessary to include the radical-consumption step as well, while which is much more exothermic, and even before crossover the augmentation of the branched-chain explosion by its associated heat release readily produces abrupt ignition, a negative limiting ignition-branch slope (subcritical bifurcation) which leads to an S curve. For T_∞ somewhat below crossover, the branched-chain contribution to ignition ceases entirely, and a thermal-explosion character must develop. The results are a first step towards analytical description of nonpremixed H_2-O_2 autoignition. This work is being published [4].

Experimental Investigation of Hydrogen-Air Diffusion Flames

Most of the research on hydrogen-air diffusion flames has been of a theoretical or numerical nature. Very few experiments have been performed to test the detailed numerical diffusion-flame models. To remedy this deficiency, an experimental investigation was initiated to ascertain how well the chemical-kinetic mechanism which has been used in the present work for the hydrogen-oxygen-nitrogen systems can predict measured diffusion-flame extinction conditions. The results from this study are shown in Fig. 4. It can be seen that the measurements and computations of extinction strain rates for an axisymmetric counterflow configuration agree very well for diluted flames. Experimental data begin to depart from theory at the highest hydrogen mole fractions shown because of the onset of experimental difficulties that prevent good tests from being made at higher hydrogen concentrations. The results of these studies have been accepted for publication [5].

Nonpremixed Flames in Stagnating Turbulence

Our analysis of nonpremixed flames in stagnating turbulence is continuing. The principal focus of this study is the comparison of theory with the experimental results or methane-air flames reported by the Whitelaw Group at Imperial College. Since these flames occupy approximately 40% of the gap between the two jets carrying the turbulent fuel and oxidizer streams, the thin flame analysis used in all previous treatments of flames in stagnating turbulence is inapplicable and a new approach based on solving the conservation equations from one exit plane to the other has been developed. Our present fluid mechanical treatment is based on the $k - \epsilon$ theory while a presumed pdf-flame sheet description is used to deal with the chemistry. The numerical analysis of the resulting system of ordinary differential equations is extremely difficult but solutions have now been obtained and compared with experimental data. In making the comparison with the available data, we confront the problem of dealing with predictions based on Favre-averaging and experimental data presumably involving conventional averaging. Thus in the present case only fluid mechanical quantities in the two constant density regions outside of the flame and the state variables within the flame are subject to comparison. Somewhat surprising is the finding of qualitative agreement with the former data but excellent agreement with the latter. We intend to conclude this study and then apply the theory to hydrogen-air flames perhaps with a Reynolds stress theory for the description of the fluid mechanical behavior.

References

[1] J. S. Kim and F. A. Williams. Structures of flow and mixture fraction fields for counterflow diffusion flames with small stoichiometric mixture fractions. *SIAM Journal on Applied Mathematics*, 53(6):1551–1566, December 1993.

[2] G. Balakrishnan and F. A. Williams. Turbulent combustion regimes for hypersonic propulsion employing hydrogen-air diffusion flames. *Journal of Propulsion and Power*, to appear, 1994.

[3] G. Balakrishnan, M. D. Smooke, and F. A. Williams. A numerical investigation of the ignition and extinction limits in laminar nonpremixed counterflowing hydrogen-air streams. *Combustion and Flame*, submitted, 1994.

[4] A. Sánchez, A. Liñán, and F. A. Williams. A bifurcation analysis of high-temperature ignition of H_2 - O_2 diffusion flames. *Twenty-Fifth Symposium (International) on Combustion*, to appear, 1994.

[5] G. Balakrishnan, D. Trees, and F. A. Williams. An experimental investigation of strain-induced extinction of diluted hydrogen-air counterflow diffusion flames. *Combustion and Flame*, to appear, 1994.
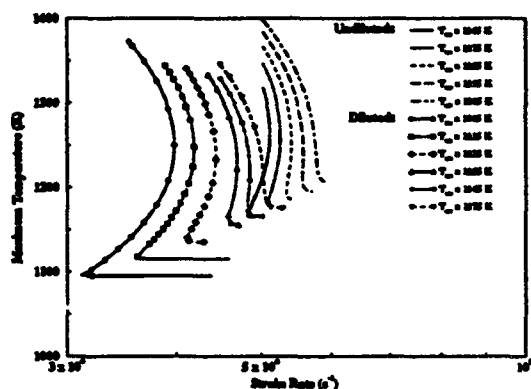
Figure 1: The variation of maximum temperature with the strain rate for an undiluted hydrogen-air flame at atmospheric pressure and for the corresponding flame in which the hydrogen is diluted with nitrogen to 60 mole percent nitrogen.
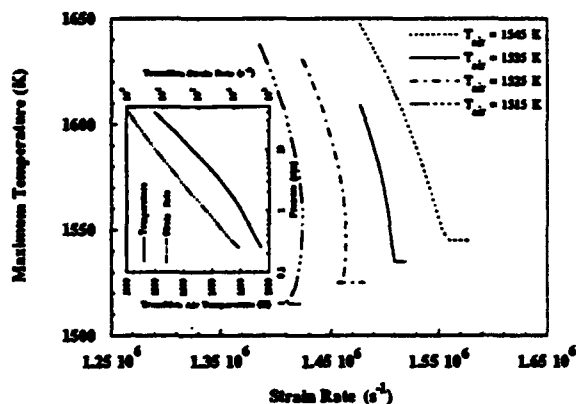
Figure 2: The variation of maximum temperature with the strain rate for an undiluted hydrogen-air flame at 10 atmospheres pressure and in the inset the variation with pressure of the strain rate and air temperature at the transition between monotonic and nonmonotonic behavior.
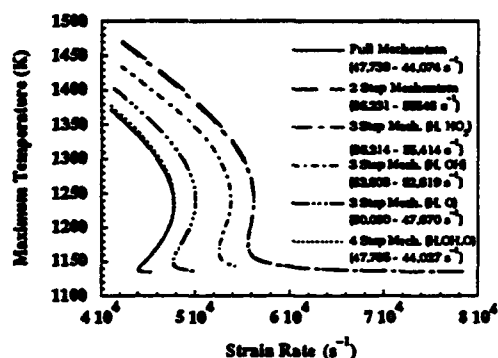
Figure 3: The dependence of the maximum flame temperature on the strain rate for a diluted hydrogen-air flame with T_{air} = 1135 K, T_{fuel} = 300 K and p = 1 atm, as obtained with full chemistry and with two-, three- and four-step mechanisms, the fuel being a mixture of hydrogen with nitrogen having 60 mole percent nitrogen.
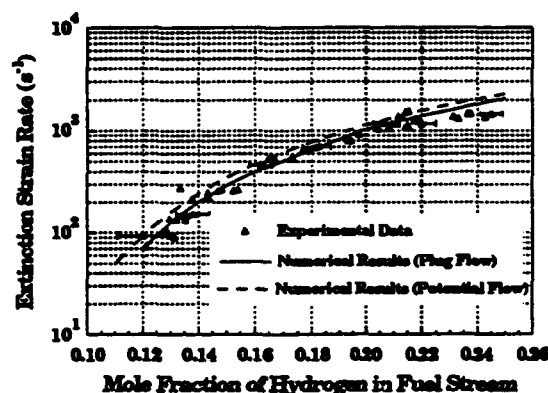
Figure 4: Comparison between theory employing full chemistry and experiment for the dependence of the air-side extinction strain rate on the hydrogen mole fraction in the fuel stream for axisymmetric counterflow flames of hydrogen-nitrogen mixtures with air.

SPACE POWER and PROPULSION
Invitees

Dr William E Anderson
Department of Mechanical
  Engineering
Pennsylvania State University
University Park PA 16802
(814)863-6289

Mr Chris Andrews
OLAC PL/LSVE
Edwards AFB CA 93523-5000
(805)275-5766
AV 525-5766

Dr William Bailey
AFIT/ENP
Wright-Patterson AFB OH 45433-6583
(513)255-4498
AV785-4498

Dr Joseph Baum
SAIC
1710 Goodridge Drive
P.O. Box 1303,
McLean VA 22102
(703)827-4952

Dr Merrill Beckstead
Dept of Chemical Engineering
Brigham Young University
Provo UT 84602
(801)378-6239

Dr Robert Beddini
Univ of Illinois
AAE Department
104 South Mathews Avenue
Urbana IL 61801-2997
(217)333-4239

Dr Oscar Biblarz
Department of Aeronautics
Naval Post Graduate School
Monterey CA 93943-5100
(408)646-2972
AV878-2972

Dr Mitat Birkan
AFOSR/NA
110 Duncan Ave, Suite B115
Bolling AFB DC 20332-0001
birkan@afosr.af.mil
(202)767-4938
fax:(202)767-4938

Dr Fred Blomshield
Code 3892,Propulsion
Research Branch
Naval Weapons Center
China Lake CA 93555
(619)939-3650
AV437-3650

Dr Iain Boyd
Cornell University
Sibley School of Mechanical &
Aerospace Engg,216 Upson H
Ithaca NY 14853-7501
boyd@scotch.mae.cornell.edu
(607)255-4563
FAX: 255-1222

247

Dr Mel Branch
Mechanical Engineering Dept
University of Colorado
Boulder CO 80309-0427
(303)492-6318
(303)492-7151

Dr Thomas Brill
University of Delaware
Department of Chemistry
Newark DE 19716
(302)831-6079

Dr Robert Brown
486 Birch Way
Santa Clara CA 95051
(408)248-8522

Dr Rodney Burton
Dept. of Aero. And Astro. Engg
University Of Illinois-UC
101 Transportation Building
Urbana IL 61801-2997
(217)333-2651

Dr G.W.(Bill) Butler
Rocket Research Company
11441 Willows Rd
P.O. Box 97009
Redmond WA 98073-9709
(206)885-5000
FAX: (206)882-5804

Mr David Byers
NASA Lewis Research Center
MS 500-219
21000 Brookpark Road
Cleveland OH 44135-3127
(216)977-7540

Dr George Caledonia
Physical Sciences Inc.
20 New England Business Center
Andover MA 01810-1077
psiand@pinet.aip.org
(508)-689-0003
FAX: (508)689-3232

Dr David Campbell
OLAC PL/RKFA
10 E. Saturn Blvd
Edwards AFB CA 93524-7660
CAMPBELL@SCIHP1.PLE.AF.MIL
(805)275 6177
fax:(805)275-5471

Dr Mark Cappelli
Stanford University
Mechanical Engineering Dept.
Stanford CA 94305-3032
(415)723-1745
Fax 723-1748

Dr Leonard Caveny
OSD/SDIO/IST
Pentagon
Washington DC 20301-7100
(703)693-1687

Dr Yunus Ali Cengel
University of Nevada-Reno
Dept of Mechanical Engg
Reno NV 89557-0030

Dr Baki M. Cetegen
Mechanical Engineering Dept
U-139 ME
University of Connecticut
Storrs CT 06268
(203)486-2966

Dr C I Chang
AFOSR/NA
110 Duncan Ave, Suite B115
Bolling AFB DC 20332-6448
(202)767-4987
FAX:767-4988

Dr Franklin Chang-Diaz
Lyndon B Johnson Space Center
Code CB
Houston TX 77058
(713)483-2714

Dr Malcolm Chase
Center for Chemical Physics
National Inst of Stds & Tech
Building 222, Room A158
Gaithersburg MD 20899
(301)975-2526

Dr Fan-Bill Cheung
Penn State University
208 Mechanical Engineering
University Park PA 16802
(814)863-4281
FAX 865-3389

Dr Peck Cho
Dept. of Mechanical Engg.
College of Engineering
Michigan Technological Univ.
Houghton MI 49931

Dr Won-Ho Choe
214 Nuclear Engineering Lab
University of Illinois
103 South Goodwin Avenue
Urbana IL 61801
(217)333-2821

Dr Chan K Choi
Purdue University
School of Nuclear Engrg
West Lafayette IN 47907
(317)494-6789

Dr Edgar Choueiri
Department of Mechanical And
Aerospace Engineering
Princeton University
Princeton NJ 08544-5263
choueiri
(609)258-5221
FAX:(609) 258-6875

Dr T J Chung
University of Alabama
Huntsville AL 35801
(205)895-6394

Dr George Clark
Aerojet Tactical Systems
PO Box 13400
Building 0525
Sacramento CA 95813
(916)988-6919

Dr William Clark
Naval Weapons Center
Code 3895
China Lake CA 93555-6001

Dr Ronald Cohen
The Aerospace Corporation
PO Box 92957
Mail Stop M5-754
Los Angeles CA 90009
cohen@qmail2.aero.org
(310)336-5946
FAX: (310)336-7680

Dr Norman Cohen
Aerospace Corporation
PO Box 92957
M/S 747
Los Angeles CA 90045
(213)648-7427

Dr Norman Cohen
Professional Services
141 Channing St
Redlands CA 92373
(714)792-8807

Dr Robert Corley
OLAC PL/DYC
Stop 24
Edwards AFB CA 93523-5000
(805)275-5620
AV525-5353

Dr John Cox
Grummen Corp.
2411 Dulles Corner Park
South Bldg,Suite 500
Herndon VA 22071
cox@gidstech.grumman.com
(703) 713-4298
FAX: 713-4067

Dr George Cox
United Technologies
Pratt-Whitney
P.O. Box 109600
West Palm Beach FL 33410-9600
(407)796-2887
FAX 796-5825

Dr F E C Culick
Engrg and Appl Sci Dept
California Institute of
    Technology
Pasadena CA 91125
(818)356-4470

250

Dr John Daily
University of Colorado
Engineering Center ME 1-13
Campus Box 427
Boulder CO 80309-0427
(303)492-7110

Dr B R Daniel
School of Aerospace Rngrg
Georgia Institute of
    Technology
Atlanta GA 30332

Lt Col Larry Davis
HQ AFSC/XTR
Andrews AFB DC 20334
(301)981-7882

Dr Gregory Dobbs
United Technologies Res. Ctr.
MS 129-90 Silver Lane
East Hartford CT 06108
(203)727-7145
FAX 727-7669

Dr Jim Drakes
Sverdrup Technology/AEDC
1099 Avenue C
Arnold AFB
 TN 37389-9013
drakes@hap.arnold.af.mil
(615)454-7420
FAX: 454-6317

Dr Joel Dubow
Materials Science
Univ of Utah
2008B Mechanical Engrg Bldg
Salt Lake City UT 84112
(801)581-8388

Dr J T Edwards
WL/POSF
Wright Patterson AFB OH 45433-6563
(513)476-7393
FAX:255-1125

Dr Daniel A Erwin
Dept of Aerospace Engg
University of Southern
California
Los Angeles CA 90089-1191
(213)740-5358

Dr William Escher
NASA Headquarters
Code RP
Washington DC 20546
(202)453-9111

Dr James Fang
Rockwell/Rocketdyne Division
6633 Canoga Park
Canoga Park CA 91303
(818)718-3728
FAX 718-3600

251

Dr John Fischer
Code 3853
Naval Weapons Center
China Lake CA 93555-6001
(619)939-1641
AV437-1641

Dr J E Flanagan
Rocketdyne
6633 Canoga
Canoga Park CA 91304
(818)710-2466

Dr Gary Flandro
Univ. of Tennessee
Space Institute
Tullahoma TN 37388
(615)455-0631
(615)393 7217

Dr Arthur Fontijn
Chemical & Environmental
    Engineering Department
Rensselaer Polytechnic Inst.
Troy NY 12180-3590
fontijn@rpitsmts
(518)276-6508
FAX: 276-4030

Dr R A Frederick
Sverdrup Technology, Inc
Mail Stop 900
Arnold AFB TN 37389-9998
(615)454-3130

Dr Bish Ganguly
WL/POOC-3
Wright-Patterson AFB OH 45433-6563
(513)255-2923
AV785-2923

Dr Robert Ghirardelli
U.S. Army Research Office
P.O. Box 12211
Research Triangle Pk NC 27709-2211
(919)549-0641
AV935-3331

Dr David Golden
SRI International
333 Ravenswood Avenue
Menlo Park CA 94025-3696
(415)859-0811

Dr David Gonzales
MIT
Dept. of Aero&Astro
Room 37-441
Canbridge MA 02139
gonzales@mit.edu
(617)253-7773
FAX: 258-5143

Dr D Goodwin
Mech. Engg&Applied Science
California inst. of Tech.
Mail Stop 213-6
Pasadena CA 91125
dgoodwin@caltech.edu
(818)356-4249
FAX: (818)568-2719

252

Dr B B Goshgarian
OLAC PL/MKPB
Stop 24
Edwards AFB CA 93523-5000
(805)275-5183
AV525-5183

Prof. Robert Goulard
CME Dept.
George Washington Univ.
802 22nd Str, NW
Washington DC 20052
(202)994-7510
FAX 994-0238

Dr William Graham
Morton Thiokol, Inc
Huntsville Division
Huntsville AL 35807-7501
(205)882-8397

Dr Alten Grandt
Department of Aeronautics
   and Astronautics
Purdue University
West Lafayette IN 47907

Dr Ashwani K Gupta
Director, Combustion Lab.
The University of Maryland
Dept. of Mechanical Engrg.
College Park MD 20742
(301)454-8865

Mr Eugene Haberman
OLAC PL/MK
Stop 24
Edwards AFB CA 93523-5000
(805)275-5420
AV525-5420

Dr Kirk E. Hackett
EOARD
PSC 802 BOX 14
FPO, AE 09499-0200
071-409-4354
F071-402-9618

Dr Marc Hallada
PSC 802 BOX 14
FPO AE 09499-0200
71 409-4437
fx71402-9618

Dr V E Haloulakos
Advanced Propulsion
McDonnell Douglas
5301 Bolsa Avenue
Huntington Beach CA 92647
(714)896-3456

Dr Elmer Hansen
Department of Mechanical
   Engineering
University of Florida
Gainesville FL 3261'
(904)392)802

253

Dr Ron Hanson
Mechanical Engineering Dept
Stanford Univ -
Stanford CA 94305-3032
(415)723-1745

Dr Kenneth Harstad
Jet Propulsion Laboratory
4800 Oak Grove Drive
Pasadena CA 91109

Dr David Hastings
Department of Aeronautics
   and Astronautics
Massachusetts Inst of Tech
Cambridge MA 02139
hastings@werner.mit.edu
(617)253-0906
FAX: (617)258-7566

Ms Sharon Hasty
John Hopkins Univ/APL
CPIA
John Hopkins Road
Laurel MD 20707
(301)992-7306

Dr Donald Hautman
United Technologies Res. Ctr.
Silver Lane
East Hartford CT 06108
(203)727-7424

Dr Clark W. Hawk
Mechanical Engineering Dept
College of Engineering
Propulsion Research Center
Huntsville AL 35899
(205)895-6474
Fax 895-6758

Dr Thomas Hawkins
OLAC/PL/LKLR
Stop 24
Edwards AFB
 CA 93523-5000
(805)275-5749
AV 525-5749

Dr Stephen D Heister
School of Aeronautics
and Astronautics
323 Grissom Hall
West Lafayette IN 47907
(317)494-0307
F 494-0307

Dr Helmut Hellwig
AFOSR/CC
110 Duncan Ave,Suite B115
Bolling AFB DC 20332-0001
(202)767-5017
AV297-5017

Dr Alan Hersh
Hersh Acoustical Engineering
9545 Cozycroft Avenue
Chatsworth CA 91311
(818)998-8311
FAX 341-0978

Dr Marc Holiday
PSC 802 BOX 14
FPO AE 09499-0200
44-71-514-4437

Dr Vlad Hruby
Busek Co. Inc.
19 Kearney Road
Needham MA 02194
(617) 449-3929
FAX: (617) 449-9263

Dr Robert Huffman
Phillips Lab,Geophysics Dir.
PL/GPIM
29 Randolph Rd
Hanscom AFB MA 01731-3010
(617) 377-3311
FAX: 377-9950

Dr H R Jacobs
Mechanical Engg Bldg, 208
Penn State University
University Park PA 16802
(814)863-2519
FAX 865-3389

Dr J I Jagoda
Aerospace Engineering Dept
Georgia Institute of
    Technology
Atlanta GA 30329
(404)894-3060

Dr Donald Jassowski
Aerojet Technical Systems Co
PO Box 13222
Sacramento CA 95813
(916)355-2849

Dr Jay Jeffries
Molecular Physics Lab
SRI International
333 Ravenswood Avenue
Menlo Park CA 94025-3696
(415)859-6341

Dr S M Jeng
Dept. of Aero&Engineering
University of Cincinnati
797 Rhodes Hall#70
Cincinnati OH 45221-0070

Dr Robert Jensen
Rockwell/Rocketdyne Division
6633 Canoga Ave
Canoga Park CA 91303
(818)718-3730
FAX 718-3600

Dr Abraham Kadish
Earth and Space Sciences Div.
Atmospheric Sciences Group
Mail Stop D466, LANL
Los Alamos NM 87545

255

Dr Jordin Kare
Building 197, Room 1020
Lawrence Livermore Nat'l Lab
P O Box 808
Livermore CA 94550
(415)423-8300

Dr David Kassoy
Dept of Mechanical Engineering
University of Colorado at
Boulder, Campus Box 427
Boulder CO 80309
(303)492-2991
(303)492-7694

Dr Dan Katayama
Phillips Laboratory(GPID)
PL/GPID
29 Randolph RD
Hanscom AFB MA 01731-3010
dhkata@al.phl.af.mil
(617)377-5088
FAX: 377-7091

Dr Myron Kaufman
Department of Chemistry
Emory University
Atlanta GA 30322
(404)727-6619

Dr Dennis Keefer
University of Tennessee
Space Institute
Tullahoma TN 37388
(615)455-0631
FAX: (615)454-2271

Dr Arnold A Kelly
Department of Mechanical and
    Aerospace Engineering
Princeton University
Princeton NJ 08544-5263
(206)452-5221

Dr Philip Kessel
OLAC PL/LSCF
Edwards AFB CA 93523-5000

Dr Sue Kim
California State University
6000 J Street
Sacramento CA 95819
(916)454-6712

Mr Mark Kleim
NASA Lewis Research Center
21000 Brookpark Rd
MS 510-219
Cleveland OH 44135

Dr Herman Krier
Dept of Mechanical and
    Industrial Engineering
University of Illinois
Urbana IL 61801
(217)333-0529
FAX:(217)244-6907

Prof M Kristiansen
P.W. Horn Professor
Dept of Electrical Engg,MS3102
Texas Tech University
Lubbock TX 79409-4439
(806)792-3007

Dr Warren Krueger
167 Alvana Street, NW16-160
Massachusetts Institute of
   Technology
Cambridge MA 02139
(617)253-0236

Dr Paul Kuentzmann
Office National D'Etudes et de
rechersches Aerospatiales
29,Ave. de la Division Leclerc
Chatillon-sous-Bagneux France

Dr Kenneth Kuo
Penn State University
208 Mechanical Engineering
University Park PA 16802
(814)863-6741
FAX 863-3203

Prof. Peter W Langhoff
Department of Chemistry
INDIANA UNIVERSITY
Bloomington IN 47405
(812)855-8621

Dr William Larson
OLAC PL/LSVF
Edwards AFB CA 93523-5000
(805)275-5657
AV525-5657

Dr C K Law
Department of Mechanical and
   Aerospace Engineering
Princeton University
Princeton NJ 08544-5263
(609)258-5271

Dr Joel Lebowitz
Rutgers-The State University
Department of Mathematics
Hill Center-Busch Campus
New Brunswick NJ 08903
(201)932-3117

Dr G Lengelle'
Office National D'Etudes et de
Recherches Aerospatiales
29,Ave de la Division Lecherc
   France

Dr Debbie Levin
Institute for Defense Analysis
1801 North Beaugard Street
Alexandria VA 22311
(703)578-2868
FAX: 578-2877

Mr Jay Levine
OLAC PL/LSCF
Edwards AFB CA 93523-5000
(805)275-5366
AV 525-5366

Dr P Y Liang
Advanced Combustion Devices
Rocketdyne Div, Rockwell Int.
6633 Canoga Avenue
Canoga Park CA 91303

Dr Thomas A Litzinger
Dept. of Mechanical Engg.
The Pennsylvania University
University Park PA 16802
(814)865-3743
FAX: (814)863-4848

Dr Shankar Mahalingam
Dept of Mechanical Engineering
The University of Colorado
Boulder CO 80309-0019
(303)492-7236

Dr David Mann
Army Research Office
P.O. Box 12211
Research Triangle Pk NC 27709-2211
david@aro-emh1.army.mil
(919)549-4249
FAX: 549-4310

Prof Alan Marchand
Dept of Chemistry
North Texas State Univ
NTSU Station, Box 13767
Denton TX 76203-5068
(817)565-3823

Dr Stephen Margolis
Combustion Research Facility
Sandia National Laboratories
Livermore CA 94551-0969

Dr Manuel Martinez-Sanchez
Aeronautics and Astronautics
Massachusetts Inst of Tech
Building 37-401
Cambridge MA 02139
(617)253-5613
FAX: (617)258-5143

Dr Jyotirmoy Mazumder
Department of Mechanical and
    Industrial Engineering
University of Illinois
Urbana IL 61801
(217)333-1964

Dr Wheeler McGregor
Sverdrup Technology/AEDC
1099 Avenue C
Arnold AFB
 TN 37389-9013
(615)454-7420
FAX 454-4611

Prof. Vincent McKoy
California Inst.of Tech.
Division of Chemistry
Mail Code 127-72
Pasadena CA 91125
bvm@starbase1.caltech.edu
(818)395-6545
FAX:568-8824

Dr Franklin Mead
OLAC PL/LKVE
Edwards AFB CA 93523-5000
(805)275-5540
AV525-5540

Dr Carl Melius
Sandia National Laboratories
Livermore CA 94551-0969
(415)294-2650

Dr Charles Merkle
205 ME
Pennsylvania State University
University Park PA 16802
(814)863-1501
FAX 865-3389

Dr Claude Merrill
OLAC PL/MKPL
Stop 24
Edwards AFB CA 93523-5000
(805)275-5169
AV525-5169

Prof Dr Ernst Messerschmid
University of Stuttgart
Pfaffenwaldring 31
D-7000, Stuttgart 80
Germany
0711-685-2375
fax 685-2010

Dr Michael Micci
233 Hammond Building
Pennsylvania State University
University Park Pa 16802
(814)863-0043
FAX: 865-3389

Dr George Miley
University of Illinois
103 South Goodwin Avenue
214 Nuclear Engineering Lab
Urbana IL 61801
(217)333-3772

Dr Richard Miller
Office of Naval Research
Mechanics Division, Code 432
800 North Quincy Street
Arlington VA 22217-5000
(202)696-4403

Dr Charles Mitchell
Dept. of Mechanical Engineerin
Colorado State University
Fort Collins CO 80523
(303)491-6654

259

Dr Andrzej Miziolek
Ballistic Research Laboratory
SLCBR-IB-1
Aberdeen Proving Gnd MD 21005-5066
(410)278-6157
FAX:278-6094

Mr T S Mogstad
McDonnell Douglas Astr.Co-West
Design And Tech. Center
Huntington Beach CA 92647
(714)896-3437

Dr Robert Moriarty
University of Illinois
    (Chicago Circle)
Department of Chemistry
Chicago IL 60680
(312)996-2364

Dr Kenneth Moses
Fusion Physics and Technology
3547 Voyager Street, Suite 104
Torrance CA 90503-1667
(213)542-3800

Dr Philip Muntz
Dept. of Aerospace Engineering
University of Southern
    California
Los Angeles CA 90089

Dr S N B Murthy
Dept of Mechanical Engineering
Purdue University
West Lafayette IN 47907
(317)494-1509
(317)494-5639

Dr Vittorio Nardi
Stevens Institute of
    Technology
Castile Point Station
Hoboken NJ 07030
(201)420-5938

Dr Thong Nguyen
Aerojet Techsystems
P.O. Box 13222
Sacramento CA 95813
(916)355-3664

Dr Jim Nichols
OLAC PL/RKLB
Edwards AFB CA 93523-5000
(805)275-5249
AV 525-5249

Dr Gary Nickerson
Software&Engineering Assoc.
1000 E. William St., Suite 200
Carson City NV 89701
(702)882-1966

260

Dr Arnold Nielsen
Naval Weapons Center
China Lake CA 93555-6001
(619)939-1614
AV437-1614

Mr Randy Nishiyama
R/E/WPS
US Dept of Commerce
NOAA, 325 Broadway
Boulder CO 80303-3328

Dr Douglas Olson
AeroChem Research Laboratories
    Inc.
P. O. Box 12
Princeton NJ 08542
(609)921-7070

Dr John Paulson
Phillips Lab,Geophysics Dir.
PL/GPID
29 Randolph RD
Hanscom AFB MA 01731-3010
(617)377-2109
FAX: 377-7091

Col Arthur Pavel
RL/XP
26 Electronic Parkway
Griffiss AFB NY 13441-4514
(202)767-5018
AV587-4058

Dr Blaine E. Pearce
Calspan Corporation,Adv. Tech.
Ctr, P.O. Box 400
4455 Genesee Street
Buffalo NY 14225
pearce@calspan,COM
(716) 631-6789
FAX: 631-6815

Ms Dorothy Pecker
The John Hopkins Univ/APL
John Hopkins Rd
Laurel MD 20707

Dr Don Penn
OLAC PL/RKLB
Edwards AFB CA 93523-5000
(805)275-5316
AV525-5316

Dr Jerry Pieper
Aerojet Techsystems
P.O. Box 13222
Sacramento CA 95813
(916)355-3087

Dr Robert Poeschel
Plasma Physics Department
Hughes Research Laboratories
3011 Malibu Canyon Road
Malibu CA 90265
(213)317-5443

Dr Dimos Poulikakos
University of Illinois
(Chicago Circle)
Dept. of Mechanical Engg.
Chicago IL 60680
(312)996-5239
FAX: 413-0447

Dr Edward Price
School of Aerospace Engrg
Georgia Institute of
   Technology
Atlanta GA 30332-0420
(404)894-3063

Dr Richard Priem
Priem Consultants
13533 Mohawk Trail
Cleveland OH 44130
(216)845-1083

Dr Lawrence Quinn
OLAC PL/DYC
Edwards AFB CA 93523-5000
(805)275-5353
AV 525-5353

Dr Frederick Reardon
Cal State U.-Sacramento
Dept of Mechanical Engineering
6000 J Street
Sacramento CA 95616
(916)278-6727

Dr Mike Redmond
Hughes STX
OLAC PL/RKFE
10 E. Saturn Blvd
Edwards AFB CA 93524-7660
(805) 275-5762
FAX: 275-5471

Dr Bob Reed
Sverdrup Technology/AEDC
1099 Avenue C
Arnold AFB
 TN 37389-9013
(615)454-7420
FAX:454-4611

Dr Russell Reed
Naval Weapons Center
China Lake CA 93555-6001
(619)939-7296
AV437-7296

Dr Robert Rhein
Research Chemist
Code 3244
Naval Weapons Center
China Lake CA 93555-6001
(619)939-7392
AV 437-7310

Dr J W Rich
Department of Mechanical Engg
206 West 18th Ave
The Ohio State University
Columbus OH 43210
(614)292-6309
Fax: 292-3163

262

Dr Stephen Rodgers
OLAC PL/LKL ⁿ
Stop 24
Edwards AFB CA 93523-5000
(805)275-5416
AV525-5416

Mr Wayne Roe
OLAC PL/XRX
Stop 24
Edwards AFB CA 93523-5000
(805)275-5206
AV525-5206

Dr David Ross
Director,Physical Organic Chem
SRI International
333 Ravenswood Avenue
Menlo Park CA 94025-3696
(415)859-2430

Dr J Reece Roth
Dept of Elec and Comp Engrg
316 Ferris Hall
The University of Tennessee
Knoxville TN 37996-2100
(615)974-4446

Dr Gabriel Roy
ONR Code 1132P
800 North Quincy Street
Arlington VA 22217
(202)696-4405

Dr Len Sakell
AFOSR/NA
110 Duncan Ave, Suite B115
Bolling AFB DC 20332-0001
(202)767-4935
AV297-4935

Dr Mark Salita
Morton Thiokol/Wasatch Div
MS 280B
PO Box 524
Brigham City UT 84302
(801)863-2163

Dr Michael Salkind
President
Ohio Aerospace Institute
2001 Aerospace Parkway
Brookpark OH 44142
(216)891-2100

Dr Robert Santoro
Penn State University
Mechanical Engineering Dept
208 Mechanical Engineering
University Park PA 16801
(814)863-1285
FAX 865-3389

Dr Robert Schmitt
Chemistry Lab
SRI International
333 Ravenswood Avenue
Menlo Park CA 94025-3696
(415)859-5579

Dr Keith Schofield
Quantum Institute
University of California,
    Santa Barbara
Santa Barbara CA 93106

Dr Herbert Schrade
Institut Fur Raumfahrtantriabe
Universitat Stuttgart
Pfaffenwaldring 31
D-7000 Stuttgart GE
7116-852-383
or 375

Dr Michael Schuller
Phillips Lab/VTPN
Kirtland AFB
Albuquerque NM 87117
(505)846-2878

Dr Ilter Serbetci
Cleveland State University
Mechanical Engineering Dept.
MC-219
Cleveland OH 44115
(216)687-2576

Maj Scott Shackelford
F J Seiler Research Laboratory
United States Air Force Acad
Colorado Springs CO 80840
(719)472-2655

Dr R Shoureshi
School of Mechanical
    Engineering
Purdue University
West Lafayette IN 47907
(317)494-5639

Dr Isaac F Silvera
Harvard University
Department of Physics
Cambridge MA 02138
(617)495-9075

Dr William Sirignano
College of Engineering
University of California
Irvine CA 92717
(714)856-6002

Dr Tom Smith
Phillips Laboratory
OLAC PL/RKFT
8 Draco Dr
Edwards AFB CA 93524-7230
(805) 275-5432
FAX: 275-5034

Dr Mitchell Smooke
Mechanical Engineering Dept.
Yale University
New Haven CT 06520
(203)432-4344

Dr Ronald Spores
OLAC PL/LSVE
Edwards AFB CA 93523-5000
(805)275-5766
FAX: (805)275-5203

Dr William C Stwalley
The University of Iowa
Iowa Laser Facility
Chemistry and Physics
Iowa City IA 52242-1294
(319)335-1299

Dr V V Subramaniam
Department of Mechanical Engg
206 West 18th Avenue
The Ohio State University
Columbus OH 43210
vsubrama@magnus.acs.ohio-state.edu
(614)292-6096
FAX: (614)292-3163

Dr Bagher M Tabibi
Department of Physics
Hampton University
Hampton VA 23668
(804)727-5277
FAX: (804)727-5955

Dr Douglas Talley
OLAC PL/RKFT
Edwards AFB CA 93523-5000
(805)275-6174
AV525-6174

Mr Robert L Talley
Viritay Technologoies, Inc
4845 Millersport Highway
East Amherst NY 14051
(716)689-0177

Dr Steve Taylor
California Inst. of Tech.
Computer Science
Mail Code 256-80
Pasadena CA 91125
steve@scp.caltech.edu
(818)395-6844
FAX: 792-4257

Dr James Tien
Case Western Reserve
   University
Glennan Building, Room 415
Cleveland OH 44106
(216)368-4581

Dr Julian Tishkoff
AFOSR/NA
110 Duncan Ave,Suite B115
Bolling AFB DC 20332-0001
(202)767-0465
AV297-0465

Prof William Trogler
Department of Chemistry
University of California, San
   Diego
La Jolla CA 92093-0310
(619)452-6175

Dr Wing Tsang
National Institute of Standard
and Technology
Chemical Kinetics Division
Gaithersburg MD 20899
(301)975-3507

Dr Peter Turchi
Aero/Astro Engineering
328 CAE Building
Ohio State University
Columbus OH 43210
(614)292-2691

Dr Gammy Vajianni
OLAC PL/RKFA
Hughes STX
10 E. Saturn Blvd
Edwards AFB CA 93524-7660
(805)275-5657
Fax:(805)275-6233

Dr Phillip L. Varghese
ASE-EM DEPT.
University of Texas, Austin
Austin TX 78712
varghese@cfdlab.ae.utexas.edu
(512) 471-3110
Fax: 471-3788

Dr Robert Vondra
PO Box 596
Wrightwood CA 92397
(619)249-3451

Dr Francois Vuillot
Office National D'Etudes et de
resherches Aerospatiales
29,Ave de la Division Lecherc
Chatillon-sous-Bagneux France

Dr Paul Waltrup
Johns Hopkins University
Applied Physics Laboratory
Johns Hopkins Road
Laurel MD 20707
(301)953-5000
ext 4186

Dr David Weaver
OLAC PL/DYCR
Edwards AFB CA 93523-5000
(805)275-6177
fax 275-5886

Dr Richard Weiss
OLAC PL/CA
Edwards AFB CA 93523-5000
(805)275-5622
AV525-5622

Dr Forman A Williams
Center for Energy and
    Combustion Research, 0411
University of California
La Jolla CA 92093-0411
(619)534-5492

Dr W S Williamson
Plasma Physics Department
Hughes Research Laboratories
3011 Malibu Canyon Road
Malibu CA 90265
(213)317-5443

Dr Curt Wittig
Department of Chemistry
University of Southern CA
Los Angeles CA 90089-0482
wittig@pern.usc.edu
(213)740-7368
FAX: 746-4945

Dr Hans Wolfhart
Institute for Defense Analysis
1801 North Beauregard Street
Alexandria VA 22311
(703)578-2969
FAX: 578-2877

Dr D O Woolery
Rocketdyne
6633 Canoga Avenue
Canoga Park CA 91304

Dr Ted Yang
Massachusetts Institute of
    Technology
167 Albany Street
Cambridge MA 02139
(617)253-8453

Dr Vigor Yang
Department of Mechanical
    Engineering
Pennsylvania State University
University Park PA 16802
(814)863-1502
FAX 865-3389

Dr Thomas York
AERO/ASTRO Engineering
328 CAE Building
Ohio State University
Columbus OH 43210
(614)292-2691

Dr Ben Zinn
School of Aerospace Engrg
Georgia Institute of
    Technology
Atlanta GA 30332
(404)894-3033

Dr Paul Zittel
(310)336-6642
FAX: 336-1636

Mr Robert Zurawski
Program Manager
Propulsion Technology Programs
NASA HQA, OAST-MAIL CODE RP
Washington DC 20546
(202)453-2261

PROPULSION DIAGNOSTICS

Invitees

Dr William Bachalo
Aerometrics, Inc.
550 Del Rey Avenue
Unit A
Sunnyvale CA 94086
(408)738-6688

Dr Edward Beiting
Aerophysics Lab, Prop & Env Sc
The Aerospace Corporation
P O Box 92957, M5/754
Los Angeles CA 90009-2957
(310)336-7035

Dr Richard Chang
Applied Physics Department
P. O. Box 208284
Yale University
New Haven CT 06520-8284
(203)432-4272
FAX: 432-4274
RK_CHANG@RAMAN.ENG.YALE.EDU

Dr Wai K Cheng
Department of Mechanical
   Engineering
MIT
Cambridge MA 02139
(617)253-4531

Dr David Crosley
Molecular Physics Department
SRI International
333 Ravenswood Avenue
Menlo Park CA 94025-3696
(415)326-6200

Dr Gregory Dobbs
United Technologies Research
   Center - Mail Stop 90
Silver Lane
East Hartford CT 06108
(203)727-7145

Dr A C Eckbreth
United Technologies Research
   Center
Silver Lane
East Hartford CT 06108
(203)727-7269

Dr Thomas Ehlert
Department of Chemistry
Marquette University
Milwaukee WI 53233
(414)288-7066

Dr Gregory Faris
SRI International
333 Ravenswood Avenue
Menlo Park CA 94025-3493
(415)859-4131

Dr Richard Field
U. S. Army Armament R&D Center
DRSMC-LCA-G(D)
Building 382-S
Dover NJ 07801
(201)724-5844
(201)724-5682

Dr Bish Ganguly
WL/POOC-3
Wright-Patterson AFB OH 45433-6563
(513)255-2923
DSN 785-2923
FAX:476-4095

Dr Alan Garscadden
WL/CA-P
Building 18
1921 Sixth Street, Suite 5
Wright-Patterson AFB OH 45433-7650
(513)255-2246
DSN 785-2246
FAX:476-4657

Dr Larry Goss
Research Applications Division
Systems Research Labs, Inc.
2800 Indian Ripple Road
Dayton OH 45440-3696
(513)252-2706

Dr Ronald Hanson
Department of Mechanical
    Engineering
Stanford University
Stanford CA 94305-3032
(415)723-1745
FAX:723-1748
hanson@navier.stanford.edu

Dr D L Hartley
Combustion Sciences
Sandia National Laboratories
Livermore CA 94551-0969

Dr Cecil F. Hess
MetroLaser
18006 Skypark Circle
Suite 108
Irvine CA 92714-6428
(714)553-0688
FAX:553-0495

Dr L Hesselink
Department of Aeronautics and
    Astronautics
Stanford University
Stanford CA 94305-3032
(415)723-3466

Dr E D Hirleman
Department of Mechanical and
    Aerospace Engineering
Arizona State University
Tempe AZ 85287
(602)965-3895
FAX:965-1384

Dr Donald Holve
Insitec
28 Bobbie Court
Danville CA 94526
(415)837-1330

Dr David Huestis
SRI International
333 Ravenswood Avenue
Menlo Park CA 94025-3493
(415)859-3464

Dr Thomas Ishii
Department of Electrical
    Engineering
Marquette University
Milwaukee WI 53233
(414)288-6998
FAX:288-7082

Dr Roman Kuc
Department of Electrical
    Engineering
Yale University
New Haven CT 06520
(203)432-4891

Dr Bruce MacDonald
Research Applications Division
Systems Research Labs, Inc.
2800 Indian Ripple Road
Dayton OH 45440-3696
(513)252-2706

Dr Timothy Parr
Naval Weapons Center
Code 3893
China Lake CA 93555
(619)939-2521

Dr Emil Pfender
Department of Mechanical Engrg
125 Mechanical Engineering
The University of Minnesota
Minneapolis MN 55455

Dr Jay Jeffries
SRI International
333 Ravenswood Avenue
Menlo Park CA 94025-3493
(415)859-6341

Dr Marshall Long
Department of Mechanical
    Engineering
Yale University
New Haven CT 06520
(203)432-4229

Dr T E Parker
Physical Sciences
20 New England Business Center
Andover MA 01810
(508)689-3232

Dr S S Penner
Center for Energy and
    Combustion Research, 0411
University of California
La Jolla CA 92093-0411
(619)534-4284

Dr Won B Roh
Department of Engrg Physics
Air Force Institute of
    Teechnology
Wright-Patterson AFB OH 45433-6583

270

Dr Gregory Smith
Department of Chem Kinetics
SRI International
333 Ravenswood Avenue
Menlo Park CA 94025-3493
(415)859-3496

Dr Alan Stanton
Southwest Sciences, Inc.
1570 Pacheco Street
Suite E-11
Santa Fe NM 87501
(505)984-1322

Dr James Trolinger
MetroLaser
18006 Skypark Circle
Suite 108
Irvine CA 92714-6428
(714)553-0688
FAX:553-0495

Dr John Vanderhoff
Ballistic Research Laboratory
DRSMC-BLI(A)
Aberdeen Proving Ground MD 21005
(410)278-6642

Dr James Verdieck
Rockwell International
Rocketdyne Div, M/S FA26
6633 Canoga Avenue
Canoga Park CA 91303
(818)700-4709

Dr Joda Wormhoudt
Aerodyne Research, Inc.
45 Manning Road
Manning Park Research Center
Billerica MA 01821-3976
(508)663-9500
FAX:663-4918

AIRBREATHING COMBUSTION

Invitees

Dr Suresh P Aggarwal
Mechanical Engineering Dept
University of Illinois
  at Chicago
Chicago IL 60680
(312)996-2235

Dr Griffin Anderson
NASA Langley Research Center
M/S 168
Hampton VA 23665
(804)864-3772

Dr Scott Anderson
Department of Chemistry
State University of New York
Stony Brook NY 11794-3400
(516)632-7915

Dr K Annamalai
Mechanical Engineering Dept
Texas A&M University
College Station TX 77843-3123

Dr Kurt Annen
Aerodyne Research, Inc.
45 Manning Road
Manning Park Research Center
Billerica MA 01821-3976
(508)663-9500
FAX:663-4918

Dr Jad Batteh
Science Applications
International Corporation
1519 Johnson Ferry Rd #300
Marietta GA 30062
(404)973-8935
FAX:973-6971

Dr Simon Bauer
Department of Chemistry
Cornell University
Ithaca NY 14853-1301

Dr S L Baughcum
Boeing Company
P O Box 3999, MS 87-08
Seattle WA 98124
(206)965-0426
FAX:234-4543

Dr Howard Baum
National Institute of
Standards and Technology
Center for Fire Research
Gaithersburg MD 20899
(301)975-6668

Dr John Bdzil
Los Alamos National Laboratory
Los Alamos NM 87545

Dr H L Beach
NASA Langley Research Center
MS 168
Hampton VA 23665-5225
(804)864-3772
(804)864-2658

Dr Josette Bellan
Applied Technologies Section
Jet Propulsion Laboratory
4800 Oak Grove Drive
Pasadena CA 91109
(818)354-6959

Dr Michael Berman
AFOSR/NC
110 Duncan Avenue, Suite B115
Bolling AFB DC 20332-0001
(202)767-4963
DSN 297-4963

Dr Paul Bonczyk
United Technologies Research
    Center
Silver Lane
East Hartford CT 06108
(203)727-7162

Dr Gary Borman
University of Wisconsin
Engine Research Lab, ME Dept
1500 Johnson Drive, Rm 119 ERB
Madison WI 53706
(608)263-1616
FAX:262-6707

Dr Kevin Bowcutt
Rockwell International
Mail Code NA40
12214 Lakewood Boulevard
Downey CA 90241
(213)420-0317

Dr C T Bowman
Department of Mechanical
Engineering
Stanford University
Stanford CA 94305-3032
(415)723-1745
FAX:723-1748
bowman@navier.stanford.edu

Dr K N C Bray
University of Cambridge
Department of Engineering
Trumpington Street
Cambridge CB2 1PZ, England UK
0223 332744
0223 337733
FAX0223 332662

Dr Robert Breidenthal
Department of Aeronautics and
    Astronautics
University of Washington, FS10
Seattle WA 98195
(206)685-1098

Dr Kenneth Brezinsky
Department of Mechanical and
    Aerospace Engineering
Princeton University
Princeton NJ 08544-5263
(609)258-5225

Dr J E Broadwell
Graduate Aeronautical Labs
California Institute of
Technology
Pasadena CA 91125

Dr Garry Brown
Department of Mechanical and
Aerospace Engineering
Princeton University
Princeton NJ 08544-5263
(609)258-6083

Dr R C Brown
Aerodyne Research, Inc.
45 Manning Road
Manning Park Research Center
Billerica MA 01821-3976
(508)663-9500
FAX:663-4918

Dr John D Buckmaster
Department of Aerospace
Engineering
University of Illinois
Urbana IL 61801

Dr Dennis Bushnell
NASA Langley Research Center
Mail Stop 168
Hampton VA 23665
(804)864-4546

Dr Ron Butler
WL/POSF
Building 490
1790 Loop Road, N
Wright-Patterson AFB OH 45433-7103

Dr T D Butler
Group T-?
Los Alamos National Laboratory
Los Alamos NM 87545
(505)667-4156

Dr H F Calcote
AeroChem Research Laboratories
Inc.
P. O. Box 12
Princeton NJ 08542
(609)921-7070

Mr. Donald Campbell
NASA Lewis Research Center
21000 Brookpark Road
Mail Stop 3-2
Cleveland OH 44135
(216)433-2929
(216)433-5266

Dr Graham V Candler
Department of Aerospace
Engineering & Mechanics
University of Minnesota
Minneapolis MN 55455

274

Dr Brian Cantwell
Department of
    Mechanical Engineering
Stanford University
Stanford CA 94305-3032
(415)723-4825

Dr Tryfon Charalampopoulos
Mechanical Engineering Dept.
Louisiana State University
Baton Rouge LA 70803
(504)388-5792
(504)388-5799

Dr Lea D Chen
Mechanical Engineering Dept
University of Iowa
Iowa City IA 52242
(319)335-5674
FAX:335-5669
ldchen@icaen.uiowa.edu

Dr Norman Chigier
Department of Mechnanical
    Engineering
Carnegie-Mellon University
Pittsburgh PA 15213-3890
(412)578-2498

Dr Robert Childs
Nielsen Engineering and
    Research, Inc.
510 Clyde Avenue
Mountain View CA 94043-2287
(415)968-9457

Dr S Y Cho
Department of Mechanical and
    Aerospace Engineering
Princeton University
Princeton NJ 08544-5263

Dr M-S Chou
Building R1, Room 1044
TRW Space and Technology Group
One Space Park
Redondo Beach CA 90278
(213)535-4321

Mr R.W. Claus
NASA Lewis Research Center
21000 Brookpark Road
Cleveland OH 44135-3127
(216)433-5869

Mr Steven Clouser
Research and Technology Group
Naval Air Propulsion Center
Trenton NJ 08628
(609)896-5752
DSN 442-7752

Capt Keith Clutter
WL/MNAA
Eglin AFB FL 32542-6810
(904)882-0207
DSN 872-0207
FAX: 872-0341

275

Dr M B Colket
United Technologies Research
   Center
Silver Lane
East Hartford CT 06108
(203)727-7481

Mr Stephen Corda
Applied Physics Laboratory
Johns Hopkins University
Johns Hopkins Road
Laurel MD 20707-6099
(301)953-5000
Ext 4654

Dr S M Correa
General Electric - Corporate
Research and Development
P. O. Box 8
Schenectady NY 12301
(518)387-5853

Dr C Criner
Mach I, Inc
346 East Church Road
King of Prussia PA 19406
(803)292-3345

Dr Clayton Crowe
Department of Mechanical
   Engineering
Washington State University
Pullman WA 99164-2920
(509)335-3214

Dr E T Curran
WL/PO
Building 18
1921 Sixth Street, Suite 5
Wright-Patterson AFB OH 45433-7650
(513)255-2520
DSN 785-2520
FAX:476-4657

Dr Eli Dabora
Mechanical Engineering Dept
University of Connecticut
Box U-139 ME
Storrs CT 06268
(203)486-2415
(203)486-2189

Dr Werner Dahm
Department of Aerospace
   Engineering
The University of Michigan
Ann Arbor MI 48109-2140
(313)764-4318
FAX:763-0578
wdahm@engin.umich.edu

Dr Sanford M Dash
Science Applications
International Corporation
501 Office Ctr Dr, Suite 420
Fort Washington PA 19034-3211
(215)542-1200
FAX:542-8567

Dr Ron Davis
Chemical Science and Techn Lab
Building 221, Room B312
National Inst of Stds & Tech
Gaithersburg MD 20899

Lt Col Larry Davis
AFOSR/ST
110 Duncan Avenue, Suite B115
Bolling AFB DC 20332-0001
(202)767-4937
DSN 297-4938
(202)767-4973

Dr George Deiwert
NASA Ames Research Center
MS 230-2
Moffett Field CA 94035
(415)604-6198

Dr Paul Dimotakis
Graduate Aeronautical Labs
California Institute of
    Technology
Pasadena CA 91125
(818)395-4456
(818)395-4447
pavlos@caltech.edu

Dr David Dolling
Department of Aerospace Engrg
    and Engineering Mechanics
University of Texas at Austin
Austin TX 78712
(512)471-4470
(512)471-7593

Dr Michael Drake
Physical Chemistry Department
General Motors Research Labs
Twelve Mile and Mound Roads
Warren MI 48090-9055

Dr Pablo G Debenedetti
Department of Chemical
    Engineering
Princeton University
Princeton NJ 08544-5263
(609)258-5480
PDEBENE@pucc.princeton.edu

Dr R W Dibble
Department of Mechanical Eng
6159 Etcheverry Hall
University of California
Berkeley CA 94720
(415)642-4901
FAX:642-6163

Mr Lee Dodge
Southwest Research Institute
P O Drawer 28510
San Antonio TX 78284
(512)684-5111
Ext 3251

Capt Randy Drabczuk
WL/MNAA
Eglin AFB FL 32542-6810
DSN 872-0207
(904)882-0207
FAX: 872-0341

Dr Frederick Dryer
Department of Mechanical and
    Aerospace Engineering
Princeton University
Princeton NJ 08544-5263
(609)258-5206

Dr C Dutton
Department of Mechanical and
  Industrial Engineering
University of Illinois
Urbana IL 61801

Dr Harry Dwyer
Department of Mechanical
  Engineering
University of California
Davis CA 95616

Dr Raymond Edelman
WC 70
Rocketdyne
6633 Canoga Avenue
Canoga Park CA 91304
(805)371-7196

Dr J T Edwards
WL/POSF
Building 490
1790 Loop Road, N
Wright-Patterson AFB OH 45433-7103
(513)255-1945
DSN 785-1945
FAX:255-1125

Ms Charlotte Eigel
WL/POSF
Building 490
1790 Loop Road, N
Wright-Patterson AFB OH 45433-7103
(513)255-5106
DSN 785-5106

Dr Said Elghobashi
Department of Mechanical
  Engineering
University of California
Irvine CA 92717
(714)856-6002

Dr Phillip Emmerman
Harry Diamond Laboratories
Attn. SLCHD-ST-RD
2800 Powder Mill Road
Adelphi MD 20783-1197
(301)394-3000

Mr Peter Erbland
National Aero-Space Plane JPO
ASC/NAF, Building 52
2475 K Street, Suite 3
Wright-Patterson AFB OH 45433-7644
(513)255-9757
DSN 785-9757

Dr K C Ernst
Pratt and Whitney Aircraft
  Group
Government Products Division
West Palm Beach FL 33402

Mr John Facey
Code RP
NASA
400 Maryland Avenue, SW
Washington DC 20546
(202)453-2854

Dr G M Faeth
Department of Aerospace
    Engineering
University of Michigan
Ann Arbor MI 48109-2140
(313)764-7202
FAX:764-0578

Dr Francis Fendell
TRW Space and Technology Group
Building R1, Room 1022
One Space Park
Redondo Beach CA 90278
(213)812-0327

Dr Michael Frenklach
202 Academic Projects Building
The Pennsylvania State
    University
University Park PA 16802
(814)865-4392

Mr Jack Fultz
WL/POPR
Wright-Patterson AFB OH 45433-6563
(513)255-2175
DSN 785-2175

Dr David Fyfe
Laboratory for Computational
    Physics & Fluid Dynamics
Naval Research Laboratory
Washington DC 20375-5344
(202)767-6583
DSN 297-6583

Dr Alon Gany
Department of Mechanical and
    Aerospace Engineering
Princeton University
Princeton NJ 08544-5263
(609)258-5041

Dr Alon Gany
Department of Aeronautical Eng
Technion-Israel Institute of
    Technology
32000 Haifa, ISRAEL
04-292308

Dr Ahmed Ghoniem
Department of Mechanical
    Engineering
MIT
Cambridge MA 02139
(617)253-2295
FAX:253-5981

Mr R Giffen
General Electric Company
Aircraft Engine Group
Neumann Way
Cincinnati OH 45215

Dr P Givi
Department of Mechanical and
    Aerospace Engineering
State University of New York
Buffalo NY 14260

Dr Irvin Glassman
Department of Mechanical and
   Aerospace Engineering
Princeton University
Princeton NJ 08544-5263
(609)258-5199
(813)442-1118

Dr A D Gosman
Department of Mechanical Engrg
Imperial College of Science
   and Technology
London WS7 2BX UK

Dr Frederick Gouldin
Department of Mechanical and
   Aerospace Engineering
Cornell University
Ithaca NY 14853-1301
(607)255-5280

Dr F Grinstein
Laboratory for Computational
   Physics & Fluid Dynamics
Naval Research Laboratory
Washington DC 20375-5344

Dr Ephraim Gutmark
Research Department
Code 3892
Naval Air Warfare Center
China Lake CA 93555-6001
(619)939-3745
DSN 437-3745

Dr. Robert B. Hall
SAF/AQT
1500 Air Force Pentagon
Washington DC 20330-1500
(703)695-7866
DSN 225-7866
(703)695-4580
campbell@aqpo.hq.af.mil

Dr Howard Hanley
Chem & Sci Tech Lab
National Inst of Stds & Tech
325 Broadway
Boulder CO 80303-3328
(303)497-3320

Dr Robert Hansen
Office of Naval Research
Code 1215
800 North Quincy Street
Arlington VA 22217-5000
(202)696-4715

Dr Stephen Harris
Physical Chemistry Department
General Motors Research Labs
30500 Mound Road
Warren MI 48090-9055
(313)986-1305

Dr S Henbest
Aeronautical Research Labs
506 Lorimer St, Fishermen's Bn
Box 4331, P O
Melbourne, Victoria AUSTRALIA 3207
(03)647 7585
FAX:646 6771
henbests@aedmel.arl.dsto.gov.au

Dr James Hermanson
Propulsion Technology
United Technologies Research
    Center
East Hartford CT 06108

Mr Norman Hirsch
WL/POPR
Wright-Patterson AFB OH 45433-6563
(513)255-2175
DSN 785-2175

Dr David Hofeldt
125 Mechanical Engineering
111 Church Street, S E
University of Minnesota
Minneapolis MN 55455
(612)625-2045

Mr Robert Holland
United Technologies Chemical
    Systems Division
P O Box 49028
San Jose CA 95161-9028
(408)224-7656

Dr Hans G Hornung
Graduate Aeronautical Labs
California Institute of
    Technology
Pasadena CA 91125
(818)395-4551

Dr Lawrence Hunter
Applied Physics Laboratory
Johns Hopkins University
Johns Hopkins Road
Laurel MD 20707-6099
(301)953-5000
Ext. 7406

Dr M Y Hussain
ICASE, Mail Stop 132C
NASA Langley Research Center
Hampton VA 23665
(804)864-2175

Dr A K M F Hussain
Department of Mechanical
    Engineering
University of Houston
Houston TX 77004
(713)749-4444

Dr Essam A Ibrahim
Department of Mechanical
    Engineering
Tuskegee University
Tuskegee AL 36088
(205)727-8974

Dr T A Jackson
WL/POSF
Building 490
1790 Loop Road, N
Wright-Patterson AFB OH 45433-7103
(513)255-6462
DSN 785-6462
FAX:255-1125

Mr Gordon Jensen
United Technologies Chemical
    Systems Division
P O Box 49028
San Jose CA 95161-9028
(408)365-5552

Dr Sheridan Johnston
Combustion Sciences
Sandia National Laboratories
Livermore CA 94551-0969
(510)294-2138

Dr K Kailasanath
Code 6410, LCP&FD
US Naval Research Laboratory
4555 Overlook Avenue, SW
Washington DC 20375-5344
(202)767-2402
FAX:767-4798
KAILASANATH@lcp.nrl.navy.mil

Dr Ann Karagozian
Mechanical, Aerospace and
Nuclear Engineering Department
University of California, LA
Los Angeles CA 90024
(213)825-5653

Dr Laurence R Keefe
Nielsen Engineering and
    Research, Inc.
510 Clyde Avenue
Mountain View CA 94043-2287
(415)968-9457
FAX:968-1410

Dr Arnold Kelly
Department of Mechanical and
    Aerospace Engineering
Princeton University
Princeton NJ 08544-5263
(609)258-5221

Dr John Kelly
Altex Technologies Corporation
650 Nuttman Road
Suite 114
Santa Clara CA 95054
(408)980-8610

Dr Lawrence A Kennedy
Department of Mechanical
    Engineering
The Ohio State University
Columbus OH 43210-1107
(614)292-5782

Dr Ian Kennedy
Mechanical Engineering Dept
University of California,
    Davis
Davis CA 95616
(916)752-2796
IMKENNEDY@poppy.engr.ucdavis.edu

Dr James Kezerle
Gas Research Institute
8600 West Bryn Mawr Avenue
Chicago IL 60631
(312)399-8331

Dr Merrill K King
NASA Headquarters
Code SNB
300 E Street, SW
Washington DC 20546
(202)358-0818

Dr Galen King
Department of Mechanical
  Engineering
Purdue University
West Lafayette IN 47907
(317)494-2713

Dr William H Kirchhoff
Division of Chemical Sciences
Office of Basic Energy Science
Department of Energy
Washington DC 20585
(301)903-5820
william.kirchhoff%er@mailgw.er.doe.

Dr Charles Kolb
Aerodyne Research, Inc.
45 Manning Road
Manning Park Research Center
Billerica MA 01821-3976
(508)663-9500
FAX:663-4918

Dr Wolfgang Kollmann
Mechanical Engineering Dept
University of California,
  Davis
Davis CA 95616
(916)752-1452

Mr William E Koop
HQ AFMC/STTA
4375 Chidlaw Road, Suite 6
Wright-Patterson AFB OH 45433-5006

Dr George Kosaly
Department of Mechanical
  Engineering
University of Washington
Seattle WA 98195
(206)543-6933
FAX:685-8047

Dr C R Krishna
Department of Nuclear Energy
Brookhaven National Laboratory
Upton NY 11973

Mr David Kruczynski
Attn SLCBR-IBA
Interior Ballistics Division
Army Research Laboratory
Aberdeen Proving Gnd MD 21005-5066
(410)278-6202
DSN 298-6202

Dr Kenneth Kuo
Department of Mechanical
  Engineering
Pennsylvania State University
University Park PA 16802
(814)865-6741
FAX:863-3203

Dr Samuel C Lambert
WL/CA-M
101 West Eglin Boulevard
Suite 101
Eglin AFB FL 32542-6810
(904)882-3002
DSN 872-3002
FAX:882-8689

Dr Marshall Lapp
High Temperature Interfaces
  Division
Sandia National Laboratories
Livermore CA 94551-0969
(510)294-2435

Dr John Larue
Department of Mechanical
  Engineering
University of California
Irvine CA 92717

Dr A Laufer
Office of Energy Research
U. S. Department of Energy
1000 Independence Avenue, N.W.
Washington DC 20585
(202)903-5820
allan.laufer%er@mailgw.er.doe.gov

Dr N M Laurendeau
Department of Mechanical
  Engineering
Purdue University
West Lafayette IN 47907
(317)494-2713

Dr Moshe Lavid
ML Energia, Inc.
P. O. Box 1468
Princeton NJ 08540
(609)799-7970

Dr C K Law
Department of Mechanical and
  Aerospace Engineering
Princeton University
Princeton NJ 08544-5263
(609)258-5271
FAX:258-6109

Dr Stan Lawton
McDonnell Douglas Research Lab
McDonnell Douglas Corporation
PO Box 516
St Louis MO 63166-0516
(314)233-2547

Dr J Carl Leader
McDonnell Douglas Research Lab
McDonnell Douglas Corporation
PO Box 516
St Louis MO 63166-0516
(314)232-4687

Dr C C Lee
Environmental Protection
  Agency
Cincinnati OH 45268
(513)569-7520

Dr Spiro Lekoudis
Office of Naval Research
Mechanics Division, Code 432
800 North Quincy Street
Arlington VA 22217-5000
(703)696-4406

Dr Anthony Leonard
Graduate Aeronautical Labs
California Institute of
    Technology
Pasadena CA 91125
(818)395-4465

Dr R S Levine
National Institute of
Standards and Technology
Center for Fire Research
Gaithersburg MD 20899
(301)921-3845

Dr Erwin Lezberg
NASA Lewis Research Center
21000 Brookpark Road
Cleveland OH 44135-3127
(216)433-5884

Dr Chiping Li
Laboratory for Computational
    Physics & Fluid Dynamics
Naval Research Laboratory
Washington DC 20375-5344
(202)767-3254
FAX:767-4798
LI@lcp.nrl.navy.mil

Dr Paul Libby
Center for Energy and
    Combustion Research, 0411
University of California
La Jolla CA 92093-0411
(619)534-3168

Dr Wilbert Lick
Department of Mechanical and
    Environmental Engineering
University of California
Santa Barbara CA 93106

Dr Hans Liepmann
Graduate Aeronautical Labs
California Institute of
    Technology
Pasadena CA 91125
(818)395-4535

Dr. Don Littrell
WL/MNAA
Eglin AFB FL 32542-6810
DSN 872-0395
(904)882-0395
FAX: 872-0341

Dr Lyle N Long
Department of Aerospace Engrg
233 Hammond Building
Pennsylvania State University
University Park PA 16802
(814)865-1172

Dr Marshall Long
Department of Mechanical
  Engineering
Yale University
New Haven CT 06520
(203)432-4229

Dr F E Lytle
Department of Chemistry
Purdue University
West Lafayette IN 47907
(317)494-5261

Dr Andrej Macek
National Institute of
Standards and Technology
Physics Building, B-312
Gaithersburg MD 20899
(301)975-2610

Dr James Madson
McDonnell Douglas Research Lab
McDonnell Douglas Corporation
PO Box 516
St Louis MO 63166-0516

Dr Edward Mahefkey
WL/POOC-5
Wright-Patterson AFB OH 45433-6563
(513)255-6241
DSN 785-6241

Mr Nick Makris
SA-ALC/SFT
Kelly AFB TX 78241-5000
AV945-8212
FAX:945-9964

Dr Oscar Manley
US Department of Energy
Office of Energy Research
1000 Independence Avenue, SW
Washington DC 20585
(202)353-5822

Dr David Mann
U. S. Army Research Office
Engineering Sciences Division
P. O. Box 12211
Research Triangle Pk NC 27709-2211
(919)549-4249
DSN 832-4249
FAX:549-4310
david@aro-emh1.army.mil

Dr Nagi Mansour
Computational Fluid Mechanics
  Branch, RFT 202A-1
NASA Ames Research Center
Moffett Field CA 94035
(415)604-6420

Dr Frank Marble
Engrg. and Appl. Sci. Dept.
California Institute of
  Technology
Pasadena CA 91125
(818)395-4784

Dr John Marek
NASA Lewis Research Center
21000 Brookpark Road
Cleveland OH 44135-3127

Dr Bruce Masson
PL/ARDF
Kirtland AFB NM 87117-6008
(505)844-0208
DSN 244-0208

Dr James McDonald
Code 6110
Naval Research Laboratory
Chemistry Division
Washington DC 20375-5342
(202)767-3340
DSN 297-3340

Dr D K McLaughlin
233 Hammond Building
Pennsylvania State University
University Park PA 16802
(814)865-2569

Dr James McMichael
AFOSR/NA
110 Duncan Avenue, Suite B115
Bolling AFB DC 20332-0001
(202)767-4936
DSN 297-4936
FAX:767-4988
mcmichael@afosr.af.mil

Dr Constantine M Megaridis
University of Illinois-Chicago
Mechanical Engineering Dept
842 West Taylor St, Box 4348
Chicago IL 60680
(312)996-3436
cmm@dino.me.uic.edu

Dr A M Mellor
Mech & Matls Eng Department
Station B, Box 6019
Vanderbilt University
Nashville TN 37235
(615)343-6214

Dr Lynn Melton
Programs in Chemistry
University of Texas, Dallas
P. O. Box 830688
Richardson TX 75083-0688
(214)690-2913
FAX:690-2925

Dr R Metcalfe
Department of Mechanical
    Engineering
University of Houston
Houston TX 77004
(713)749-2439

Maj Howard Meyer
AL/EQC
139 Barnes Drive
Suite 2
Tyndall AFB FL 32403-5319
(904)283-6038
DSN 523-6038
FAX:283-6090
MeyerH@AFCESA1.AF.MIL

Dr Michael M Micci
Department of Aerospace Engrg
233 Hammond Building
Pennsylvania State University
University Park PA 16802
(814)863-0043

Dr D L Mingori
Mechanical, Aerospace and
    Nuclear Engineering Dept
University of California
Los Angeles CA 90024
(213)825-1265

Dr Andrzej Miziolek
Ignition and Combustion Branch
Interior Ballistics Division
Army Research Laboratory
Aberdeen Proving Gnd MD 21005-5066
(410)278-6157
FAX:278-6094

Dr Parviz Moin
Center for Turbulence Research
Stanford University
Stanford CA 94305-3032
(415)725-2081

Dr H Mongia
General Motors Corporation
Allison Gas Turbine Operations
P. O. Box 420
Indianapolis IN 46206-0420
(317)230-5945

Dr Peter Monkewitz
Mechanical, Aerospace and
    Nuclear Engineering Dept
University of California
Los Angeles CA 90024
(213)825-5217

Dr P J Morris
233-L Hammond Building
Pennsylvania State University
University Park PA 16802
(814)863-0157

Dr Edward Mularz
Aviation Res. and Tech. Activ.
NASA Lewis Res. Ctr., MS 5-11
21000 Brookpark Road
Cleveland OH 44135-3127
(216)433-5850

Dr M G Mungal
Department of Mechanical
    Engineering
Stanford University
Stanford CA 94305-3032
(415)725-2019
FAX:723-1748

Dr Phillip E Muntz
Department of Aerospace Engrg
Univ of Southern California
854 West 36th Place, RRB 101
Los Angeles CA 90089-1191
(213)740-5366

288

Dr Arje Nachman·
AFOSR/NM
110 Duncan Avenue, Suite B115
Bolling AFB DC 20332-0001
(202)767-5028
DSN 297-5028
nachman@afosr.af.mil

Dr. Hassan M Nagib
Department of Mechanical and
    Aerospace Engineering
Illinois Institute of Tech
Chicago IL 60616

Dr Abdollah Nejad
WL/POPT
Building 18
1921 Sixth Street, Suite 10
Wright-Patterson AFB OH 45433-7655
(513)255-9991
DSN 785-9991
FAX:255-1759

Dr Herbert Nelson
Code 6110, Chemistry Division
Naval Research Laboratory
4555 Overlook Avenue, SW
Washington DC 20375-5342
(202)767-3686

Dr David Nixon
Department of Aeronautical Eng
The Queen's Univer of Belfast
Stranmillis Road
Belfast BT9 5AG N Ireland UK
(0232)245133
FAX0232 382701

Dr G B Northam
NASA Langley Research Center
MS 168
Hampton VA 23665-5225
(804)864-6248

Dr R C Oldenborg
Chemistry Division
Los Alamos National Laboratory
Los Alamos NM 87545
(505)667-2096
(505)667-3758

Dr A K Oppenheim
Department of Mechanical
    Engineering
University of California
Berkeley CA 94720
(415)642-0211

Dr Elaine Oran
LCP&FD, Code 6404
US Naval Research Laboratory
4555 Overlook Avenue, SW
Washington DC 20375-5344
(202)767-2960
FAX:767-4798
ORAN@lcp.nrl.navy.mil

Dr Simon Ostrach
Case Western Reserve Univ
Department of Mechanical and
    Aerospace Engineering
Cleveland OH 44106

Dr Richard Peterson
Department of Mechanical
   Engineering
Oregon State University
Corvallis OR 97331-6001
(503)754-2567

Dr W M Pitts
National Institute of
Standards and Technology
Center for Fire Research
Gaithersburg MD 20899
(301)975-6486

Dr Robert Pitz
Department of Mechanical and
   Materials Engineering
Vanderbilt University
Nashville TN 37235
(615)322-0209

Dr S B Pope
Department of Mechanical and
   Aerospace Engineering
Cornell University
Ithaca NY 14853-1301
(607)255-4314
pope@pdf.tn.cornell.edu

Dr C L Proctor II
Department of Mechanical
   Engineering
University of Florida
Gainesville FL 32611
(904)392-7555

Dr Herschel Rabitz
Department of Chemistry
Princeton University
Princeton NJ 08544-1009
(609)258-3917
FAX:258-6746

Dr Saad Ragab
Engrg Sci & Mechanics Dept
Virginia Polytechnic Institute
   and State University
Blacksburg VA 24061
(703)231-5950

Dr S R Ray
National Institute of
Standards and Technology
Center for Chemical Engrg
Gaithersburg MD 20899

Mr. Robert Reed
Sverdrup Technology, Inc.
AEDC
1099 Avenue C
Arnold AFB TN 37389-9013
(615)454-4648
DSN 340-4648
(615)454-6317

Dr R G Rehm
National Institute of
Standards and Technology
Center for Fire Research
Gaithersburg MD 20899
(301)975-2704

Dr Rolf D Reitz
Mechanical Engineering Dept
University of Wisconsin
1500 Johnson Drive
Madison WI 53706
(608)262-0145
FAX:262-6717

Dr M Renksizbulut
Department of Mechanical
    Engineering
University of Waterloo
Waterloo, Ontario CN N2L 3G1
(519)885-1211
Ext 3977

Dr David Reuss
Fluid Mechanics Department
General Motors Research Labs
30500 Mound Road
Warren MI 48090-9055
(313)986-0029

Dr William Reynolds
Department of Mechanical
    Engineering
Stanford University
Stanford CA 94305-3032
(415)723-3840

Dr James Riley
Mechanical Engineering Dept
University of Washington
Seattle WA 98195
(206)543-5347

Dr Michael Roco
National Science Foundation
Chemical and Thermal Syst Div
1800 G Street, N W
Washington DC 20550
(202)357-9606

Dr U S Rohatgi
Department of Nuclear Energy
Brookhaven National Laboratory
Upton NY 11973
(516)282-2475

Dr Glenn Rolader
Science Applications
International Corporation
1247-B N Eglin Parkway
Shalimar FL 32579
DSN 872-0391
(904)882-0391

Dr W M Roquemore
WL/POSF
Building 490
1790 Loop Road, N
Wright-Patterson AFB OH 45433-7103
(513)255-6813
DSN 785-6813
FAX:255-1125
Roquemwm@wl.wpafb.af.mil

Dr Anatol Roshko
Graduate Aeronautical Labs
California Institute of
    Technology
Pasadena CA 91125
(818)395-4484

Dr Daniel Rosner
Department of Chemical
    Engineering
Yale University
New Haven CT 06520
(203)432-4391

Dr John Ross
Department of Chemistry
Stanford University
Stanford CA 94305-3032
(415)723-9203

Dr Gabriel Roy
Office of Naval Research
Mechanics Division, Code 1132
800 North Quincy Street
Arlington VA 22217-5000
(703)696-4405
FAX:696-0934
roy@ocnr-hq.navy.mil

Mr Kurt Sacksteder
NASA Lewis Research Center
MS 500-217
21000 Brookpark Road
Cleveland OH 44135
(216)433-2857

Dr Leonidas Sakell
AFOSR/NA
110 Duncan Avenue, Suite B115
Bolling AFB DC 20332-0001
(202)767-4935
DSN 297-4935
FAX:767-4988
sakell@afosr.af.mil

Dr Mohammad Samimy
Ohio State University
Mechanical Engineering Dept
206 West 18th Street
Columbus OH 43210-1107
(614)422-6988

Dr G S Samuelsen
Department of Mechanical
    Engineering
University of California
Irvine CA 92717
(714)856-5468

Dr Billy Sanders
University of California
Davis CA 95616

Dr Joseph Sangiovanni
United Technologies Research
    Center
Silver Lane
East Hartford CT 06108
(203)727-7328

Dr Lakshmi Sankar
School of Aerospace Engrg
Georgia Institute of
    Technology
Atlanta GA 30332
(404)894-3014

Dr Domenic Santavicca
Department of Mechanical
   Engineering
Pennsylvania State University
University Park PA 16802
(814)863-1863

Dr R J Santoro
Department of Mechanical
   Engineering
Pennsylvania State University
University Park PA 16801
(814)863-1285

Mr William Scallion
NASA Langley Research Center
Mail Stop 408
Hampton VA 23665
(804)864-5235

Dr Klaus Schadow
Naval Air Warfare Center
Code 3892
China Lake CA 93555-6001
(619)939-6532
DSN 437-6532
FAX:939-6569

Dr John Schaefer
Energy and Environmental Div.
Acurex Corporation
555 Clyde Ave., P. O. Box 7555
Mountain View CA 94039

Dr W H Schofield
Aeronautical Research Labs
506 Lorimer St, Fishermen's Bn
Box 4331, P O
Melbourne, Victoria AUSTRALIA 3001

Dr D J Seery
United Technologies Research
   Center
Silver Lane
East Hartford CT 06108

Dr Hratch Semerjian
National Institute of
   Standards and Technology
Chem Sci & Tech Laboratory
Gaithersburg MD 20899
(301)975-3145
FAX:975-3845
HRATCH@micf.nist.gov

Dr K Seshadri
Center for Energy and
   Combustion Research, 0411
University of California
La Jolla CA 92093-0411
(619)534-4876

Dr G S Settles
309 Mechanical Engrg Building
Pennsylvania State University
University Park PA 16802
(814)863-1504

Dr Robert Shaw
Division of Chemical and
   Biological Sciences
U S Army Research Office
Research Triangle Park NC 27709-221
(919)549-0641

Mr Harold Simmons
Parker Hannifin Corporation
Gas Turbine Fuel Systems Div.
17325 Euclid Avenue
Cleveland OH 44143
(216)531-3000
Ext 2309

Dr Neeraj Sinha
Science Applications
International Corporation
501 Office Ctr Dr, Suite 420
Fort Washington PA 19034-3211
(215)542-1200
FAX:542-8567

Dr William Sirignano
School of Engineering
University of California
Irvine CA 92717
(714)856-6002

Dr F Dee Stevenson
Office of Basic Energy Science
U. S. Department of Energy
1000 Independence Avenue, N W
Washington DC 20585

Dr David Stewart
Department of Theoretical and
   Applied Mechanics
University of Illinois
Urbana IL 61801

Dr Anthony Strawa
NASA Ames Research Center
MS 230-2
Moffett Field CA 94035
(415)604-3437

Dr F D Stull
WL/POPS
Wright-Patterson AFB OH 45433-6563
(513)255-5210
DSN 785-5210

Dr Geoffrey J Sturgess
Pratt & Whtiney Aircraft Group
United Technologies Corp
400 Main Street M/S 163-16
East Hartford CT 06108
(203)565-5437
(203)557-0687

Dr B Sturtevant
Engrg and Appl Sci Dept
California Institute of
   Technology
Pasadena CA 91125

Dr G Sullins
Applied Physics Laboratory
Johns Hopkins University
Johns Hopkins Road
Laurel MD 20707-6099
(301)953-5000

Dr Dexter Sutterfield
National Institute for
Petroleum and Energy Research
Post Office Box 2128
Bartlesville OK 74005
(918)337-4251

Dr Larry Talbot
Department of Mechanical
    Engineering
University of California
Berkeley CA 94720
(415)642-6780

Dr Richard Tam
Department of Mathematics
Indiana University-Purdue
    University
Indianapolis IN 46205

Dr Christopher Tam
Department of Mathematics
Florida State University
Tallahasee FL 32306-3027
(904)644-2455

Dr. Richard Tankin
Mechanical Engineering Dept
Northwestern University
Evanston IL 60208-3111
(708)491-3532

Dr Julian Tishkoff
AFOSR/NA
110 Duncan Avenue, Suite B115
Bolling AFB DC 20332-0001
(202)767-0465
DSN 297-0465
FAX:767-4988
tishkoff@afosr.af.mil

Dr T Y Toong
Department of Mechanical
    Engineering
MIT
Cambridge MA 02139
(617)253-3358

Dr Michael Trenary
Department of Chemistry
The University of Illinois
Chicago IL 60680

Dr Timothy Troutt
Department of Mechanical
    Engineering
Washington State University
Pullman WA 99164-2920

Dr Allen Twarowski
Rockwell International Sci Ctr
1049 Camino dos Rios
P O Box 1085
Thousand Oaks CA 91360
(805)373-4576
ajtwarow@scimail.remnet.ab.com

Dr A D Vakili
University of Tennessee
Space Institute
Tullahoma TN 37388

Dr Earl VanLandingham
National Aeronautics & Space
    Administration, Code RB
400 Maryland Avenue, SW
Washington DC 20546
(202)453-2847

Dr Joe Wanders
AL/EQS
139 Barnes Drive
Tyndall AFB FL 32403-5319
(904)283-6026
DSN 523-6026

Dr. Phillip R. Westmoreland
Department of Chemical
    Engineering
University of Massachusetts
Amherst MA 01003
(413)545-1750
(413)545-2507
(413)545-1647
westm@ecs.umass.edu

Dr C J Ultee
United Technologies Research
    Center
Silver Lane
East Hartford CT 06108

Dr S P Vanka
Department of Mechanical
    and Industrial Engrg
University of Illinois
Urbana IL 61801

Dr P J Waltrup
Applied Physics Laboratory
Johns Hopkins University
Johns Hopkins Road
Laurel MD 20707-6099
(301)953-5000
Ext. 5626

Dr Charles Westbrook
Lawrence Livermore National
    Laboratories
P. O. Box 808
Livermore CA 94550

Dr James Whitelaw
Department of Mechanical Engrg
Imperial College of Science
    and Technology
London SW7 2BX UK

Dr Forman Williams
Center for Energy and
    Combustion Research, 0411
University of California
La Jolla CA 92093-0411
(619)534-5492

Dr Michael Winter
Propulsion Science
United Technologies Research
    Center
East Hartford CT 06108
(203)727-7805

Mr Steve Wirick
WL/AAWW-3
Wright-Patterson AFB OH 45433-6543
(513)255-4174
DSN 785-4174
FAX:476-4642

Dr Bernard T Wolfson
Wolfson Associates
    International
4797 Lake Valencia Blvd West
Palm Harbor FL 33563
(813)786-3007

Dr J M Wu
University of Tennessee
Space Institute
Tullahoma TN 37388

Dr Richard Yetter
Department of Mechanical and
    Aerospace Engineering
Princeton University
Princeton NJ 08544-5263

Dr Pui-kuen Yeung
School of Aerospace Engrg
Georgia Institute of
    Technology
Atlanta GA 30332-0150
(404)894-9341
FAX:894-2760
yeung@peach.gatech.edu

Dr Shaye Yungster
Institute for Computational
Mechanics in Propulsion
NASA Lewis Research Ctr
Cleveland OH 44135
(216)433-6680

Dr Michael Zachariah
National Institute of
Standards and Technology
Center for Chemical Engrg
Gaithersburg MD 20899
(301)975-2063

Mr Fred Zarlingo
Code 3246
Naval Air Warfare Center
China Lake CA 93555-6001
(619)939-7395
DSN 437-7395

Dr E E Zukoski
Engrg. and Appl. Sci. Dept.
California Institute of
    Technology
Pasadena CA 91125
(818)395-4785